PARTICLE ACCELERATION AND DETECTION

P. Strehl

Beam Instrumentation and Diagnostics

Springer

Beam Instrumentation and Diagnostics

Particle Acceleration and Detection

springer.com

The series *Particle Acceleration and Detection* is devoted to monograph texts dealing with all aspects of particle acceleration and detection research and advanced teaching. The scope also includes topics such as beam physics and instrumentation as well as applications. Presentations should strongly emphasise the underlying physical and engineering sciences. Of particular interest are

- contributions which relate fundamental research to new applications beyond the immediate realm of the original field of research
- contributions which connect fundamental research in the aforementioned fields to fundamental research in related physical or engineering sciences
- concise accounts of newly emerging important topics that are embedded in a broader framework in order to provide quick but readable access of very new material to a larger audience

The books forming this collection will be of importance for graduate students and active researchers alike.

Peter Strehl

Beam Instrumentation and Diagnostics

With 301 Figures

Springer

Peter Strehl
Händelstrasse 32
64291 Darmstadt
Germany
E-mail: hpstrehl@aol.com

Library of Congress Control Number: 2005937154

ISSN 1611-1052

ISBN-10 3-540-26401-9 Springer Berlin Heidelberg New York
ISBN-13 978-3-540-26401-9 Springer Berlin Heidelberg New York

Springer is a part of Springer Science+Business Media
springer.com

Printed in The Netherlands

Typesetting: by the author and TechBooks using a Springer LaTeX macro package
Cover design: *design & production* GmbH, Heidelberg

Printed on acid-free paper SPIN: 10989920 54/TechBooks 5 4 3 2 1 0

To Irene,
showing always sympathy for my professional work

Schreiben ist hart;
man kommt nur schwer dahinter,
wann man aufhören muss.

PETER USTINOV

Preface

This book summarizes the experience of many years of teamwork with my group, the beam diagnostics group of GSI. For a long time the group was also responsible for operating the machines and application programming. In my opinion, this connection was very efficient: first, because a beam diagnostic system has to place powerful tools at the operators' disposal; second, because data evaluation and presentation of results for machine operation demand application programs which can be handled not only by skilled experts.

On the other hand, accelerator developments and improvements as well as commissioning of new machines by specialists require more complex measurements than those for routine machine operation. A modern beam diagnostic system, including the software tools, has to cover these demands, too.

Therefore, this book should motivate physicists, constructors, electronic engineers, and computer experts to work together during the design and daily use of a beam diagnostic system. This book aims to give them ideas and tools for their work.

I would not have been able to write this book without a good education in physics and many discussions with competent leaders, mentors, and colleagues. After working about 40 years in teams on accelerators, there are so many people I have to thank that it is impossible to mention them all by name here.

In recognition, of all, I would like to thank very much my first teachers, Peter Brix and Friedrich Gudden for filling me with enthusiasm for nuclear physics, electron scattering, and accelerator physics at the DALINAC nearly 40 years ago. Starting in 1970 at GSI, it was Christoph Schmelzer, who was always a sympathetic listener, helping me with discussions and many suggestions. Under the leadership of Dieter Böhne, who managed most accelerator projects of GSI, the beam diagnostics group, responsible for all beam diagnostics up to the target, was established. I gratefully acknowledge this in memory of both.

I thank Norbert Angert and Klaus Blasche for helpful discussions and support during their leadership of the accelerator department. Furthermore,

I would especially like to thank Jürgen Klabunde for many years of collaboration. Specification of beam diagnostic elements, elaboration of program algorithms, performing of accelerator experiments, and organization of machine operation was our common job.

This job could not have been done without the members of the beam diagnostics group. Especially, many thanks to Volker Schaa, for implementing many application programs and together with his team always available in case of software problems. Many thanks also to Fritz Bock, keeping the process computer system available day and night. In memory of Helgi Vilhjalmsson, I gratefully acknowledge his professional work and his very much respected engagement in the group.

It would be unforgivable not to acknowledge here Frank Peldzinski, together with Alfons Suderleith who were responsible for service, maintenance, and new installations of beam diagnostic elements. In this connection, the work of Günther Grimm and Horst Graf in the small beam diagnostics workshop contributed a big part to constructing the beam diagnostics system; thanks to both of them. I thank gratefully also Jörg Glatz and Ludwig Dahl for numerous physics discussions, resulting mostly in suggestions and improvements for operating the machines. In this connection, the good collaboration with Dieter Wilms and Uwe Scheeler, now both responsible for the operations group, is gratefully acknowledged.

In recognition of all members of the diagnostic group, I would like to mention Mohamed Fradj, Manfred Hartung, Tobias Hofmann, Wolfgang Kaufmann, Wilhelm Losert, Rolf Mayr, Peter Moritz, Hansjörg Reeg, and Norbert Schneider for professional discussions and their great engagement as operators, shift leaders, and designers. Many thanks to them and all other members of the beam diagnostics group.

Construction design and procuring of nearly all mechanical parts of the GSI beam diagnostic systems were managed by Hubert Kraus with the help of Jochen Störmer. I thank them both very much for their work and many years of close collaboration.

My special thanks go to Andreas Peters and Peter Forck, who now are the leaders of the beam diagnostics group. Designing together the beam diagnostic systems for SIS, ESR (partly), and the high energy beam lines, the collaboration could not have been better. In 2002, Peter Forck took over my courses on "Beam Instrumentation and Diagnostics" at the Joint University Accelerator School (JUAS). He improved and supplemented my lecture notes. Some of the contributions to this book are adapted from our common work.

After retirement, I miss very much the short meetings with Claus Riedel. We met nearly every day for half an hour or even more for discussion. I thank him very much for many suggestions concerning the solution of mathematical-physical problems.

For pictures marked GSI-Foto, I acknowledge the work of Achim Zschau and Gabriele Otto for taking them. The draft version of the book was written

with Scientific Workplace of MacKichan Software Inc. I can recommend it as a powerful tool.

I also thank the editorial board of Springer for helpful suggestions. Finally, I wish to express my special thanks to my editor, Dr. Christian Caron, and his team, especially, Gabriele Hakuba and Birgit Münch.

Darmstadt *Peter Strehl*
December 2005

Commonly Used Abbreviations

AC alternating current
ADC analog-to-digital converter
AlN aluminum nitrite
ATF accelerator test facility (KEK)
BCT beam current transformer
BPM beam position monitor
BNL Brookhaven National Laboratory
BTF beam transfer function
BeO beryllium oxide
CAD computer-aided design
CCC cryogenic current comparator
CCD charge-coupled device
COG center of gravity
CERN European Organisation for Nuclear Research
CT computer tomography
CVD chemical vapor deposition
CW continuous wave
DAC digital-to-analog converter
dc direct current
DESY Deutsches Elektronen Synchrotron
DSP digital signal processing
ECR electron cyclotron resonance
ESR experimental storage ring
FC Faraday cup
FD finite difference
FE finite element
FFT fast Fourier transformation
FWHM full width half-maximum
GSI Gesellschaft für Schwerionenforschung
HILAC heacy ion linear accelerator
IC ionization chamber
IF intermediate frequency

ICT integrating current transformer
ISR intersecting storage ring (CERN)
KEK High Energy Accelerator Research Organisation
LEP large electron-positron storage ring
LHC large hadron collider
LBL Lawrence Berkeley Laboratory
MART multiplicative algebraic reconstruction technique
MCP multichannel plate
MCA multichannel analyzer
MEVVA metal vapor vacuum
MUCIS multicusp ion source
MWPC multiwire proportional chambers
ODR optical diffraction radiation
OTR optical transmission radiation
OTDR optical time domain reflectometer
PC personal computer
PCI industrial personal computer
PIG Penning (ion source)
PLL phase-locked loop
PMT photomultiplier tube
pps particles per second
PS proton synchrotron (CERN)
PSI Paul Scherrer Institut (SIN)
RAM random access memory
RCT resonant current transformer
RHIC Relativistic Heavy Ion Collider
rf radio frequency
RFQ radio-frequency quadrupole
rms root-mean-square
SCM scintillation current monitor
SEM secondary electron emission monitor
SI International Unit System
SIS Schwer Ionen Synchrotron
SLAC Stanford Linear Accelerator Center
SPS super proton synchrotron
SQUID superconducting quantum interference device
TAC time-to-amplitude converter
TDC time to digital converter
TESLA TeV-Energy Superconducting Linear Accelerator
TDR time domain reflectometer
TOF time of flight
UNILAC Universal Linear Accelerator
UV ultraviolet
VCO voltage-controlled oscillator
VSWR voltage standing wave ratio
WEB WorldWide Web

Contents

1

Introduction

Some decades ago, particle accelerators were controlled and optimized mainly by looking at viewing screens – mostly based on ZnS – and simple beam current meters. Developments in the field of beam diagnostics have paralleled the development of computers, sophisticated electronic circuits, and PCI systems. A consequence is the design of more and more complex machines, using powerful simulation programs to describe particle dynamics in modern accelerator structures. Nowadays, computer-aided operation and on-line control of modern accelerators, operated in a great variety of modes, require the availability of many beam parameters. Due to the manifold machines, such as linacs, cyclotrons, synchrotrons, storage rings, and transport lines, the demands on a beam diagnostic system can differ. Taking additionally the broad spectrum of particles, such as electrons, protons, and heavy ions into account, it becomes very clear that the development of versatile measurement techniques became essential in recent years. The main beam parameters and their meaning for characterization of particle beams are

Beam Intensity

In the most general definition, beam intensity I is defined as

$$I = \frac{number\,(N)\;of\;particles}{time\;unit} \tag{1.1}$$

and covers a range from some particles per second (pps) up to 10^x pps with $x > 14$. For charged particles, beam intensity is related to the beam current i

$$Q = i \times t = N\zeta e \;\rightarrow \tag{1.2}$$

$$i = \frac{N\zeta e}{t}\,, \tag{1.3}$$

where $e = 1.602 \times 10^{-19}$ As and ζ is the charge state of the accelerated particle. For dc-machines, the time unit t is 1 s and i corresponds to the dc-current. For rf accelerators working in continuous mode, such as cyclotrons, the time unit is given by the bunch length Δt. Pulsed rf accelerators are characterized by two time units: T_p as the macropulse length and Δt as the bunch length. Defining the duty cycles

$$D_\mathrm{m} = \frac{T_\mathrm{p}}{T_0} \quad T_0, \text{ repetition period} \tag{1.4}$$

$$D_\mathrm{rf} = \frac{\Delta t}{T_\mathrm{rf}} \quad T_\mathrm{rf}, \text{rf period} \tag{1.5}$$

currents in the bunch i_b or macropulse i_p can be related to the average current i_a, measured with a dc-meter

$$i_\mathrm{p} = i_\mathrm{b} D_\mathrm{rf} \tag{1.6}$$

$$i_\mathrm{a} = i_\mathrm{p} D_\mathrm{m} \, . \tag{1.7}$$

The great variety of intensity measuring systems is discussed in Chap. 2.

Beam Profile

In a three-dimensional rectangular coordinate system, "beam profile" means the intensity distribution over one of the coordinates. In accelerator physics, it is usual to distinguish between longitudinal and transverse directions. The longitudinal coordinate runs along the beam axis and determination of the intensity distribution along this axis requires measuring techniques other than those for the two transverse axes. This is explained and discussed in Chaps. 4 and 5.

Beam Position

The beam position is defined only in the two transverse coordinates and can be derived immediately from beam profile measurements. In general, the term "beam position" refers to the center of gravity within the transverse intensity distributions. This holds especially for measuring devices which measure only the beam position. Beam position monitors are of great importance for operation and optimization of circular machines. In these machines, much more information such as tune, chromaticity, and closed orbit is extracted from the beam position monitors (BPM). In most cases, the measuring electrode systems are based on capacitive coupling to the beam. More explicit information is given in Chaps. 5 and 6.

Emittance

The terminus "emittance" was introduced to accelerator physics from the Hamilton formalism. The ease with which a particle beam can be transported, the accuracy of beam energy determination, the bunch shape and microstructure in time, and the precision with which scattering angles and a time focus can be determined in physics experiments, depend on the distributions in the phase spaces. As for the beam profile, it is usual to discriminate between two transverse emittances and a longitudinal one, as derived in Chap. 6.

Beam Energy

Of course, the required beam energy is determined mainly by planned experiments or in industrial use by special applications such as ion implantation, inertial fusion, and sputtering systems. On the other hand, determination of beam energy, energy spread, and the related quantities momentum and momentum spread is of great importance in evaluating beam quality and optimizing machine parameters. We deal with the matter in Chaps. 5 and 7.

Charge States and Mass Numbers

In heavy ion machines, the ratio between the charge number ζ and the mass number A of the ions ζ/A is important, because the rf power needed for acceleration is proportional to $(A/\zeta)^2$. Therefore, the accelerator constructor is faced with the problem of maximizing the ratio ζ/A. Highly ionized ions are preferred in such machines. However, all types of ion sources deliver a spectrum of ions composed of different charge states of different isotopes. Therefore, charge state and mass separation become essential for beam diagnostics. This holds also for the charge state separation behind strippers which are used in most heavy ion machines to reduce the required rf power. This is discussed in Chap. 4.

Q Value

The Q value, respectively, tune, is a quantity defined only in circular machines. It relates the number of betatron oscillations around a circular machine to the settings of the focusing and beam guiding elements. In older machines, the Q value was determined from an appropriate number of position measurements around the machine. As discussed in Chap. 7, measurement of Schottky noise and analysis of the so-called beam transfer function (BTF) in response to beam excitation are now the most applied methods.

Chromaticity

The chromaticity ξ may be considered a proportionality factor in the relation between tune spread and momentum spread. The methods of determination are similar to those used to determine the tune.

Modern beam diagnostic systems should cover mainly the needs of operators and shift leaders during routine machine operation. On the other hand, accelerator developments, improvements, and commissioning of new machines require more complex measurements by skilled experts.

Considering the high demands on beam diagnostic systems, it becomes very clear that many fields of science and technique are involved, mainly

- vacuum and high vacuum technique;
- material research, mainly for the suitability of materials in vacuum systems and their thermal characteristics;
- computer-aided design (CAD) of complex electromechanical devices,
- signal calculations, including
  - electrodynamics, considering also relativistic effects,
  - particle dynamics, including space charge effects;
- analog and digital techniques, applying modern signal analysis; and
- computer techniques, mainly process control and implementation of physical application programs, including tools for operators and accelerator scientists.

A beam diagnostics group has to meet requirements that demand teamwork among technicians, engineers, physicists, and software workers. Experience has shown that members of the diagnostic group should take part in operation and improvements of the machines.

Of course, there is great variety of specialist literature available around the world, covering this matter in scientific journals, numerous articles, and excellent books, e.g., [1–12]. Two well-established international workshops dedicated to beam diagnostics give further detailed information:

- The Beam Instrumentation Workshop (BIW), organized every two (even) years since 1994 by American accelerator centers [13–19]
- The Workshop on Beam Diagnostics and Instrumentation for Particle Accelerators (DIPAC), organized every two (odd) years since 1993 by European accelerator centers [20–25].

It would be an unforgivable omission in the age of the Web not to mention the excellent services in the publication of conference proceedings etc. via the Net, (e.g., [26, 27]).

This book aims to give all experts involved in beam diagnostic system design, routine operation, and improvement of machines application programming and construction design ideas and tools for their work. A recently published book by Minty and Zimmermann [28] is an excellent treatise, showing

very clearly the importance of beam diagnostic data for machine operation and optimization. It deals with linacs and circular machines but is focused mainly on highly relativistic electrons and protons. Besides numerous examples of the use of beam diagnostic data for beam dynamics and optic studies, the book also covers machine theory such as cooling, bunch compression, injection, extraction, synchrotron radiation, and polarized beams.

This new book complements it insofar as the design of beam diagnostics devices and measurement procedures are also described in more detail. Furthermore, instead of considering mainly relativistic light particles, nonrelativistic heavy ions are the subject of this book. As far as beam diagnostics and measurements in synchrotrons are concerned, it aims to complement the book of Minty and Zimmermann by contributions, characteristic of machines accelerating heavy ions from low β values to β near one. Giving examples concerning

- construction design of diagnostic devices,
- signal calculation and signal processing,
- implementation of application programs for operators, shift leaders and skilled experts,

the author would be happy to inspire young engineers and physicists to work in the fascinating field of beam diagnostics.

Most beam diagnostic devices, including signal processing and application software were developed for the accelerator facilities of Gesellschaft für Schwerionenforschung (GSI) and in consequence most of the contents refers to long term work at GSI. The main parameters of the machines under discussion are given in Tables 1.1–1.6, starting with the Universal Linear Accelerator (UNILAC) [29].

Table 1.1. Technical parameters of the UNILAC

Ion source and LEBT	
Ions sources	MEVVA[1], PIG[2], MUCIS[3]
Max A/ζ	65
Injection energy	2.2 keV/u
Relative velocity ($\beta = v/c$)	0.217%
Magnetic rigidity	0.44 Tm
Extraction voltage	10–50 kV
Postacceleration	≤ 135 kV
Transversal emittance (normalized)	$\leq 0.4\,\pi$·mm·mrad
Transversal emittance (not normalized)	≤ 190·mm·mrad
Energy spread $\Delta W/W$	$\leq \pm 1 \times 10^{-4}$
Mass resolution $m/\Delta m$	≤ 210

Table 1.2. Technical parameters of the UNILAC, continued

Prestripper rf accelerator		
Resonator	RFQ	Superlens
Frequency [MHz]	36.136	36.136
Tank length [m]	9.35	0.8
Inner tank diameter [m]	0.762	0.86
Energy range [keV/u]	2.2–120	120
β [%]	0.217–1.605	1.605
100% horiz. rms emittance, norm. [mm·mrad]	0.050	0.069
100% vert. rms emittance, norm. [mm·mrad]	0.050	0.069
100% longitudinal. rms emittance [keV/u·ns]	0.139	0.250
Particle transmission in relation to RFQ input [%]	89	88

Table 1.3. Technical parameters of the UNILAC, continued

Prestripper rf accelerator, cont.		
Resonator	IH1	IH2
Frequency [MHz]	36.136	36.136
Tank length [m]	9.1	10.3
Inner tank diameter [m]	1.829	2.034
Energy range [keV/u]	120–743	743–1395
β [%]	1.605–3.995	3.995–5.473
100% horiz. rms emittance, norm. [mm·mrad]	0.085	0.111
100% vert. rms emittance, norm. [mm·mrad]	0.085	0.111
100% longitudinal. rms emittance [keV/u·ns]	0.390	0.446
Particle transm. in relation to RFQ input [%]	88	88

Table 1.4. Technical parameters of the UNILAC, continued

Stripper section at 1.4 MeV/u			
	IH2 exit	Stripper gas	Alvarez entrance
Bunch frequency [MHz]	36.136	36.136	36.136
β [%]	5.473	5.473	5.473
100% horiz. rms-emitt., norm. [mm·mrad]	0.111	0.122	0.225
100% vert. rms-emitt., norm. [mm·mrad]	0.111	0.123	0.296
95% longitudinal. rms-emitt. [keV/u·ns]	0.264	0.303	1.39
Particle transm. in rel. to RFQ input [%]	88	88	88

Table 1.5. Technical parameters of the UNILAC, continued

Poststripper accelerator		
	Alvarez 1	Alvarez 2
Frequency [MHz]	108.41	108.41
Energy [MeV/u]	3.6	5.9
β [%]	8.761	11.216
100% horiz. rms emitt., norm. [mm·mrad]	0.244	0.269
100% vert. rms emitt., norm. [mm·mrad]	0.306	0.287
95% longitudinal. rms emitt. [keV/u·ns]	1.42	1.52
Particle transm. in rel. to RFQ input [%]	87.7	87.7
Beam intensity [emA]	15	15
Beam power (pulsed) [kW]	459	752
Power (average) [kW] (duty factor 2%)	9	15

Table 1.6. Technical parameters of the UNILAC, continued

Poststripper accelerator, cont.		
	Alvarez 3	Alvarez 4
Frequency [MHz]	108.41	108.41
Energy [MeV/u]	8.6	11.4
β [%]	13.514	15.591
100% horiz. rms emitt., norm. [mm·mrad]	0.320	0.349
100% vert. rms emitt., norm. [mm·mrad]	0.301	0.298
95% longitudinal. rms emitt. [keV/u·ns]	1.47	1.44
Particle transm. in rel. to RFQ input [%]	87.7	87.6
Beam intensity [emA]	15	15
Beam power (pulsed) [kW]	1097	1454
Power (average) [kW] (duty factor 2%)	22	29

Remark. The three types of ion sources are the ones mostly used. Their use may be characterized as follows:

1. MEVVA: Mainly for injection into the Schwer Ionen Synchrotron (SIS), high currents, low repetition rate, short pulses.
2. PIG: Mainly heavy metal ions, long pulses, moderate currents.
3. MUCIS: Gas ions up to Xe, high currents, low repetition rate.

Remark. For further acceleration, deceleration as well as fine-tuning of the output energy, there are 10 single gap resonators installed behind the Alvarez 4. The maximum effective acceleration voltage is 1.2 MV for each of them. Therefore, the maximum beam energy for a $^{238}U^{28+}$ ion is 12.8 MeV/u.

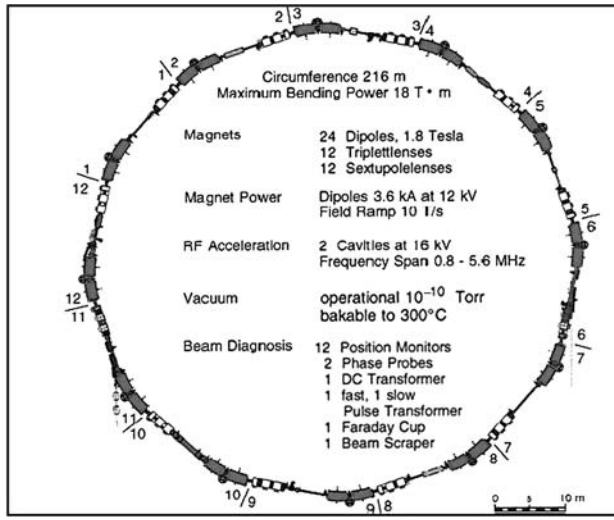

Fig. 1.1. Layout of the SIS

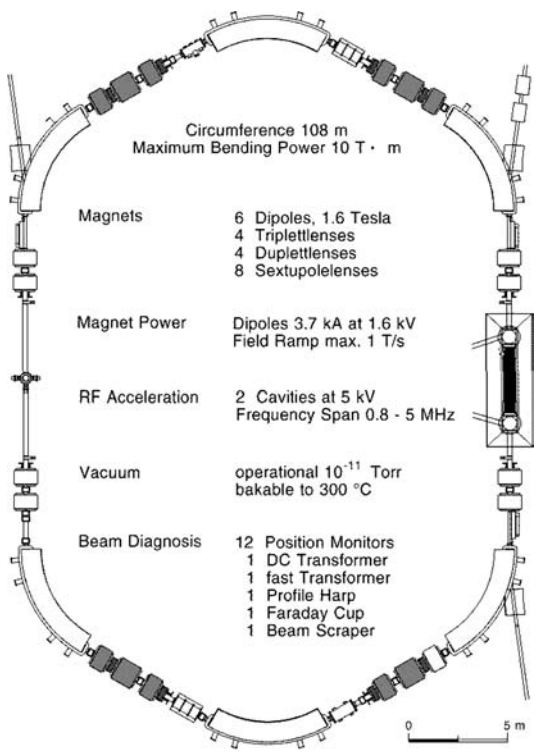

Fig. 1.2. Layout of the ESR

Table 1.7. The most important beam properties of the SIS

SIS Beam properties	
Particle energy	50–1000 MeV/u for U 50–2000 MeV/u for Ne
Energy definition	ca. 10^{-3}
Cycle length	1 to 10 s
Extraction	fast: ca. 1 μs slow: 10–8000 ms
Beam emittance depending on ring filling and extraction time	3–30 π·mm·mrad

Table 1.8. The most important beam properties of the SIS

ESR – main features	
Particle energy	3–560 MeV/u for U 50–830 MeV/u for Ne
Energy definition	ca. 10^{-4} with e-cooling
Cycle length	Field ramp: 1.5 s
Storage time	Minutes to hours
Extraction	Fast: ca. 0.5 µs Slow: to some 10 s
Beam emittance	0.1 π·mm·mrad, with e-cooling
Particle number per cycle	Typically 10^8 with cooling

Figure 1.1 shows a layout of the SIS, including some information about the equipment, and Table 1.7 summarizes the most important beam properties.

The corresponding layout of the experimental storage ring (ESR) is shown in Fig. 1.2, and the main features of the storage ring are given in Table 1.8.

2

Beam Intensity Measurements

Measurement, continuously monitoring and optimizing of beam intensity is one of the most important activities during operation of complex accelerators [30]. In general, a certain intensity measuring system covers only a limited range of intensities, which is caused by

- the great variety of accelerator types,
- the manifold accelerated ion species covering a wide range of energies and charge states, and
- the great variety in the time structure of the particle streams.

As a consequence, detectors and measuring systems show great diversity. The measuring principles applied depend on the expected intensities and cover a wide spectrum ranging from absolute determination by particle counting and simple current measurements to more complicated relative methods, requiring calibration by an absolute measurement. Detector systems may be classified according to properties, such as

(1) on-line measurement
(2) non-destructive
(3) radiation resistant
(4) absolute measurement
(5) vacuum compatible
(6) kind of output signal

Table 2.1 gives a selection of commonly used principles. The classifications 1–6 are marked by + = yes, − = no and o = only under favorable conditions; N = number of particles; ζ = charge state of the particles; ΔW = energy loss; W_{ion} = average energy needed to generate one ion pair, and p = pressure.

From Table 2.1, it becomes evident that absolute determination of beam intensity is possible either at quite low particle streams by counting single particles or at high intensities by using beam transformers. In the range of about $10^7 < N < 10^{12}$ particles, respectively, charges per second (for $\zeta = 1$, it corresponds to $1.6\,\mathrm{pA} < i < 160$ nA), only more or less indirect methods

Table 2.1. Principles of intensity measurements and their classification. TC = track counting, FC = Faraday cup, IC = ionization chamber, SPC = scintillation pulse counter, SCM = scintillation current monitor, SEM = secondary electron monitor, RGM = residual gas ionization monitor, NRM = nuclear reaction monitor, BCT = beam transformer (from P. Heeg, A. Peters, Strehl, P., AIP Conference Proceedings 333, Vancouver, B.C., Canada 1994, pp. 287–293. With permission)

Principle	On-line	Nondes-tructive	Radiation resistant	Absolute calibration	Vacuum compatible	Output signal
TC	−	−	−	+	−	N
FC	+	−	+	+	+	$N\zeta e$
IC	+	−	+	−	−	$Ne \cdot \Delta W / W_{\text{ion}}$
SPC	+	−	−	+	−	N
DD	+	−	+	+	+	N
SCM	+	−	−	−	−	$\sim N \cdot \Delta W$
SEM	+	o	+	−	+	$\sim N \cdot \mathrm{d}W/dx$
RGM	+	+	+	−	+	$\sim N \cdot p \Delta W$
NRM	+	o	+	−		
BCT	+	+	+	+	+	$\sim N\zeta e$

have to be applied. A typical example gives the slow extraction mode of synchrotrons, preferred by nuclear or atomic physicists in their experiments to avoid pile-up in the detectors. Considering a revolution time of the order of 1μs and typical currents of the order of 100 μA, an extraction time of 1s results in a current of 100 pA, which is too high for particle counting and too low for measurement with a beam transformer. Due to effects which are discussed later, even measurements of current with Faraday cups in the pA range can be problematic. Fortunately, there is always an overlap of the ranges of absolute methods with various indirect methods, which allows calibrating them. This is illustrated in Fig. 2.1, which gives an overview of the ranges of different detector systems used in the SIS of GSI.

2.1 Faraday Cups

In principle, a Faraday cup (FC) is a beam stopper, isolated from the beam pipe ground potential and connected to a current meter. The device is the one mostly used to measure beam intensities. Although non-destructive measurements with beam transformers or similar devices are preferred for continuous monitoring of a beam, the Faraday cup, stopping the beam completely and measuring the beam current at the same time, has its advantages, too. For example

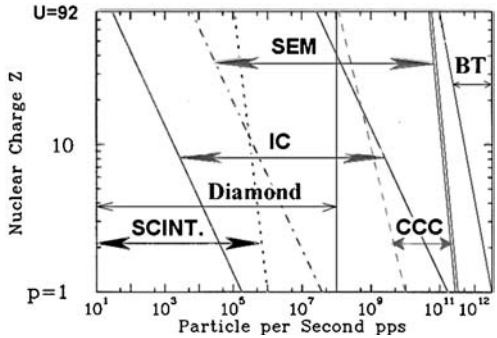

Fig. 2.1. Different detector systems used for slow extraction in the SIS at GSI. The numbers hold for different ions (scale on the left-hand side) with a kinetic energy of 1 GeV/u, an extraction time of 1 s and a beam spot size of 1cm^2. Here CCC stands for "Cryogenic Current Comparator" [31,32], and BT stands for beam current transformer. Due to the destructive character of Faraday cups, they are not used in this case

- if the beam has no time structure (dc-beam), a Faraday cup is the most versatile device for measuring the dc-current of the beam;
- during optimization of machine settings with respect to intensity, components of the following accelerator structures and beam transport system are automatically protected using a Faraday cup for intensity monitoring;
- beam stoppers, respectively, Faraday cups, are often used to stop the beam in case of emergency.

Normally, Faraday cups (FC's) are not provided to measure very fast signals, requiring a large bandwidth of the cup itself and the accompanying signal processing system. With a typical bandwidth up to about 10 MHz, FCs are suitable for measuring the current of dc-beams as well as the average current of pulsed beams having pulse lengths of the order of some microseconds to some milliseconds.

2.1.1 Faraday Cups for Low Power Beams

Due to the electrical insulation of a cup, heat transfer by conduction does not take place and also heat transfer by convection tends to zero in a vacuum system. To avoid heating up, the power loss on a noncooled Faraday cup should not exceed some watts. Cooling by radiation (see Chap. 3, Sect. 3.4) cannot be recommended because thermal emission of electrons arises according to Richardson-Dushmann's law [see (7.33) in Chap. 6, Subsect. 7.1.2].

Designing a non-cooled Faraday cup, the following effects have to be taken into account:

- emission of secondary electrons,

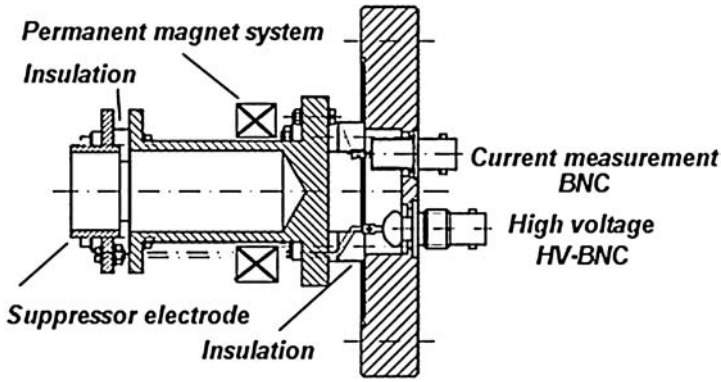

Fig. 2.2. Construction drawing of a simple Farady cup without cooling, mounted on a CF flange [33]

- leak currents arising due to sputtering and deposition of sputtered material onto isolating ceramic parts.

Secondary Electrons

The flux of secondary electrons is $\sim \cos\theta$, where θ is the angle of the electron trajectory against the beam axis. This implies $L_{\mathrm{Fc}} > R$ (L_{Fc} is the length of the open aperture and R is its radius), which is not always possible. Suppression of secondary electrons can be performed by

- an electric field
- a magnetic field
- a combination of both.

Figure 2.2 shows the important parts and typical dimensions of an end Faraday cup, provided for measuring beam currents with low intensity and low beam energy. As a consequence, neither water cooling nor a large thickness of the stopper plate is required. Since most of the emitted secondary electrons are in the energy region below 200 eV, a suppressor voltage of about -500 V is sufficient. Nevertheless, the efficiency of the electrical secondary electron suppression should be checked by measuring the current dependent on the high voltage applied. A permanent magnet system can improve the efficiency of the electric field, especially if the condition $L_{\mathrm{Fc}} > R$ cannot be fulfilled due to spatial limitations. Figure 2.3 is an example of the design of a magnetic suppressor showing also the measured magnetic field strength along the x, y, z-axes. Referring to Eq. (7.74) (Chap. 6, Sect. 7.1.2), the bending radius of a secondary electron with kinetic energy W_{kin} is

$$\rho_{\mathrm{e}} = \frac{\sqrt{2m_{\mathrm{e}}W_{\mathrm{kin}}}}{eB} \approx 3.37\frac{\sqrt{W_{\mathrm{kin}}[\mathrm{ev}]}}{B[\mathrm{mT}]}[\mathrm{mm}]\ . \tag{2.1}$$

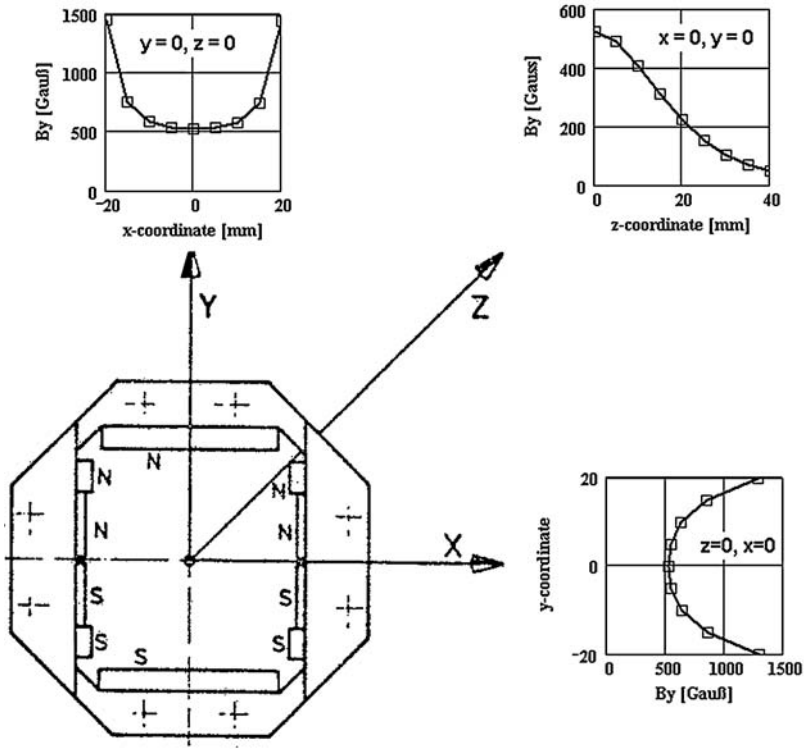

Fig. 2.3. Arrangement of cobalt-samarium permanent magnets in the yoke of a magnetic secondary electron suppressor and the magnetic field strength achieved along the three axes ($1\,\mathrm{Vs/m^2} = 1\mathrm{T} = 10^4\,\mathrm{Gau}\beta$)

For typical field strengths of permanent magnets, bending radii of the order of some millimeters result.

Sputtering

By the sputtering process, atoms of a material hit by energetic particles are removed and deposited elsewhere. Therefore, deposition of sputtered conductive material on electrical insulation can result in leak currents leading to falsification of beam current measurements. The number of sputtered atoms per incident ion depends on many parameters. Measured sputtering rates for a 45-keV Kr beam show relatively high differences between various materials. Table 2.2 gives the sputtering rates [34] for construction materials used mostly in the design of beam intercepting devices such as Faraday cups, and slits.

Table 2.2. Measured sputtering rates for some typical construction materials with a 45 keV Kr beam [34]

Material	C	Al	Ti	Fe	Cu	Mo	Ta	W
Atoms/Ion	2.3	< 1	2	4	12	3	3.1	5

With a sputtering rate of N atoms per incident ion, the amount of material that will be removed can be derived easily from the following relations:

$$\frac{\textit{Number of projectiles}}{\textit{Area}} = \frac{i\,t}{F\zeta e} \tag{2.2}$$

$$\frac{\textit{Number of sputtered atoms}}{\textit{Area}} = N\frac{i\,t}{F\zeta e} \tag{2.3}$$

$$\frac{\textit{Number of Atoms}}{cm^3} = \frac{N_\mathrm{A}\rho}{A}, \tag{2.4}$$

where, A = atomic weight, ρ = density [g/cm^3] of the bombarded material i/F = beam current density [mA/cm^2], ζ = charge state of the incident ion, and $N_\mathrm{A} = 6.022 \times 10^{23}$/mole is Avogadro's number. The thin layer of removed material comes out as

$$R_\mathrm{s}\,[\mu\mathrm{m/h}] = \frac{0.36\,N\,A\,i}{\zeta\rho F}\ . \tag{2.5}$$

To avoid deterioration of the isolating material, the designer should provide appropriate shielding for the isolating parts.

2.1.2 Faraday Cups for High Power Beams

Contact Cooling

If the average power loss in a Faraday cup becomes higher than some watts, contact cooling may be a solution. This can be performed by using an isolating material of relatively high heat conductivity between the cup body and a part, which can take away the heat to the beam pipe by water cooling or via heat conductivity. Experience has shown that beryllium oxide (BeO) and aluminum nitrite (AlN) (especially Shapal M, [35]) are suitable materials with high heat conductivity and low specific electrical resistance. The heat conductivity of BeO and AlN as a function of temperature is shown in Fig. 2.4. Taking the poisoning factor of beryllium into account using AlN is recommended (especially Shapal-M) as isolating material; it can be machined to a certain extent. A practical example is shown in Fig. 2.5. The drawing shows the main parts of a contact cooled Faraday cup provided for the following beam parameters:

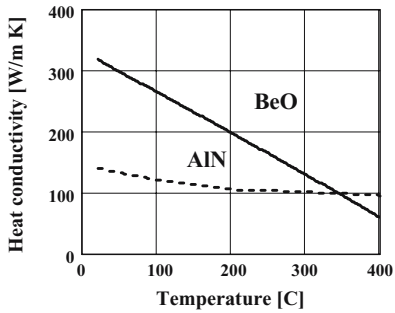

Fig. 2.4. Heat conductivity of beryllium oxide (BeO) and aluminum nitrite (AlN) as function of temperature

Kind of ions: p, α
Beam energy: 400 keV, total
Maximum beam current: 1mA, dc, analyzed
Maximum beam diameter: 25 mm

The maximum dc-beam power is 400 W, which requires cooling. For various reasons, no water cooling could be accepted in this case. As a solution, the total heat of 400 W is conducted to parts of large masses outside the vacuum via AlN insulation and a massive copper rod (see Fig. 2.5). The maximum temperature difference between the end of the massive copper rod and the front face of the cup body can be estimated from the sum of the gradients of temperature over the relevant parts, using the relation:

$$\frac{\dot{Q}}{A_\mathrm{n}} = -\lambda \ \mathrm{grad}\ T \ \rightarrow \frac{\Delta T}{\Delta x} = -\frac{\dot{Q}}{\lambda\, A_\mathrm{n}} \tag{2.6}$$

$$\lambda_\mathrm{Cu} = 0.372\ [\mathrm{W/mm\,K}]\,,\ \lambda_\mathrm{Shapal\ M} = 0.1\ [\mathrm{W/mm\,K}] \tag{2.7}$$

where $\dot{Q}/A_\mathrm{n}$ is the power flow through the cross section A_n.

Contact cooling has the following advantages:

- simpler design,
- no cooling water supply required,
- higher achievable accuracy of current measurement since there are no leak currents via the finite resistance of deionized water,
- safer from the vacuum technical point of view.

Water Cooling

For very intense beams, the following parameters are relevant for the design of a beam intercepting device such as a Faraday cup:

- total beam power,

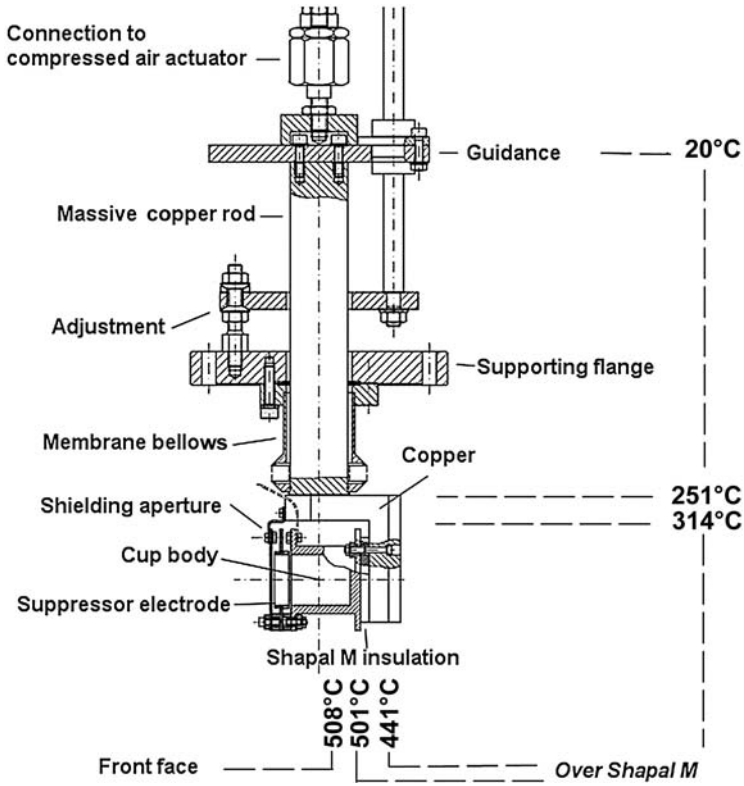

Fig. 2.5. Example of a contact cooled Faraday cup [33] provided for a power loss of 400 W. The temperature gradients over the relevant parts are given below and at the right-hand side of the drawing

- penetration depth of the impinging particles,
- maximum power density,
- time structure of the beam.

Thermal aspects as well as procedures to calculate temperature distributions in beam intercepting devices are detailed in Chap. 3. Beside the thermal aspects, the designer has to consider two additional effects, arising from water cooling:

- Leak currents arising from the conductance of cooling water, even when deionized water with low conductivity is used. The shunt impedance is determined from

$$R_{\mathrm{w}} = \rho_{\mathrm{w}} \frac{l}{A_{\mathrm{n}}} \ , \tag{2.8}$$

where $\kappa = 1/\rho_{\mathrm{w}}$ is the conductance of the cooling water, typically $1\mu\mathrm{S/cm} < \kappa < 10\ \mu\mathrm{S/cm}$. A_{n} and l are the cross section and length of

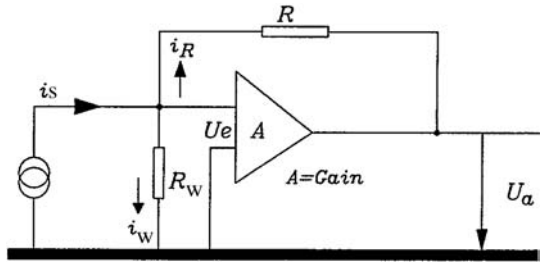

Fig. 2.6. Simplified electrical diagram to calculate the effect of cooling water conductivity

the insulation bridged by the cooling water. Figure 2.6 shows a simplified block diagram to calculate the effect. Taking R_w as calculated from (2.8), the output voltage U_a is given by

$$U_a = \frac{-is\,R}{1 - \frac{1}{A}\left(1 + \frac{R}{R_w}\right)} \,. \tag{2.9}$$

This illustrates the usefulness of modern operational amplifiers, having gains $A \gg 1$, which reduce the error below 1% for a 100-MΩ resistor in the feedback circuit.

- With respect to material selection, the designer has to be careful, especially about those materials that are in touch with the cooling water. Due to the different potentials of materials against each other, the formation of galvanic elements may result in a considerable falsification of current measurement. In practice, there can be currents of the order of some nanoamperes, even if all construction materials have been selected very carefully. Table 2.3 gives the potentials of often used materials measured against an H_2 electrode.

Figure 2.7 is an example of a water-cooled FC, designed as an end cup and provided for some kilowatts of beam power and penetration depths of about 10 mm in copper. The construction design allows the addition of a permanent magnet system to enhance the secondary electron suppression by the electric field. Another example of a water-cooled Faraday cup may be suitable to illustrate the problem between the requirements of an user and the limitations of thermal aspects as well as geometric restrictions. In a first step, the specifications were given as follows:

Table 2.3. Potential of various materials measured against a H_2 electrode.

Material	Al	Ta	Fe	Ni	W	Cu	Ag
Potential [V]	−1.66	−0.75	−0.44	−0.25	−0.1	+0.35	+0.8

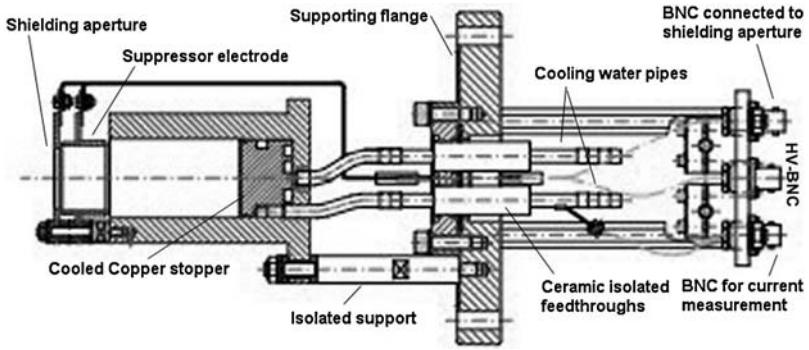

Fig. 2.7. Construction drawing [33] of a water-cooled end Faraday cup. The cup stops high energy particles with a penetration depth up to 10 mm and a beam power up to some kilowatts

Beam energy: 66 MeV $^{+}$, protons
Beam power: 50 kW, dc
Beam spot size (FWHM): horizontal 7 mm, vertical 10 mm
Required aperture *: 150 mm ∅
Maximum allowed insertion length: 1000 mm
Pressure of the cooling water: 5–6 bar
$^{+}$ In addition, a 200-MeV proton beam of low intensity should also be stopped.
* With the relatively large aperture, a controlled offset of the beam should be considered.

The penetration depth of 66-MeV protons in copper is about 6.4 mm, but, to avoid irradiation of the cooling water by the 200-MeV beam (penetration depth $\simeq 45$ mm), at least 50–55 mm of copper have to be in front of the cooling channels. Assuming a Gaussian intensity distribution with $\sigma_x = 7/2.35 \simeq 3$ mm and $\sigma_y = 10/2.35 \simeq 4.3$ mm, one arrives at the enormous power density of about 63 kW/cm^2 at the center of the beam. To avoid melting the material, the stopper plates have to be tilted as discussed in detail in Chap. 3. But, due to the required aperture of 150 mm in diameter and the restricted insertion length, no solution could be found with respect to

- the maximum temperature at the front face which should be well below the melting temperature of the stopping material.
- and the maximum allowed power flow to the cooling water of about 120 W/cm^2 to avoid film boiling. Due to the limitation in cooling water pressure to 6 bar turbulent water flow, allowing higher power flow was not possible.

In consequence, the specifications have been reduced as follows:

- By defocusing the beam, the spot size is enlarged to 14 mm (FWHM) for both directions, which means that nearly 100% of the 50-kW beam is within a diameter of 35 mm.
- Together with the design documents a diagram showing the maximum allowed beam power dependent on the beam diameter should be handed over by the designer.

Figure 2.8 shows the important parts of the FC [33], taking into account the reduced requirements. The small inset at the bottom left shows the reduction in the power density with a maximum of about 22.5 kW/cm^2 at the center of the beam, the inset on the right-hand side has been calculated using programs detailed in Chap. 3. Tilting the two stopping plates, as shown in the figure a reduction in the power density of nearly a factor or $\sqrt{10}$ could be achieved. Note that the thickness of the tilted copper plates is not determined

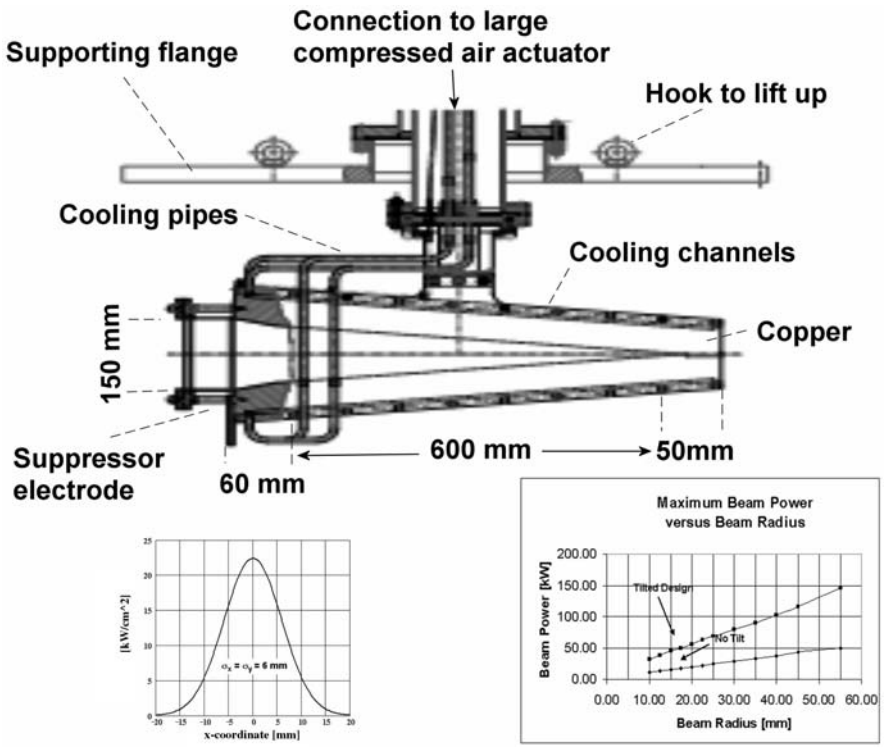

Fig. 2.8. High-power Faraday cup [33] provided to stop 66-MeV protons with a beam power of 50 kW dc. The small inset at bottom left gives the beam power density over the beam cross section. The insert at bottom right gives the allowed beam power dependent on the beam radius for the tilted design and a design without tilting

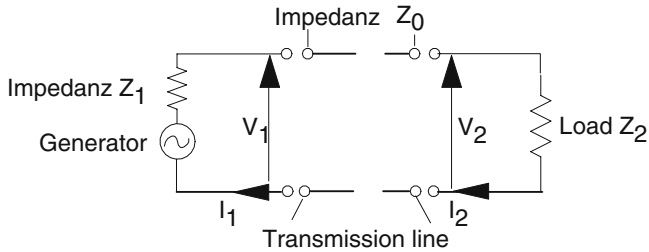

Fig. 2.9. Simplified diagram to clarify the matching conditions for transmission of fast signals measured with a broadband Faraday cup

by the requirement to stop 200-MeV protons also, but by the necessity to distribute the heat flow over the surface, where the cooling channels are located. Of course, the thickness of material at the end of the cup is determined by the requirement to stop 200-MeV protons. The weight of the two stopping plates is of the order of 80 kp and the required cooling water flow is of the order of $2\,\mathrm{m}^3/\mathrm{h}$ assuming a ΔT of 20°C.

2.1.3 Faraday Cups in Broadband Design

Some Definitions and Formulas

To measure fast signals, the bandwidth of a Faraday cup has to be matched to the transmission line and to the load, which is normally a low impedance amplifier. Figure 2.9 shows this schematically. The rise time t_r of a fast signal (normally defined as the time between 10 and 90% of the signal amplitude) is related to the bandwidth (BW) by

$$\mathrm{BW}\ [\mathrm{GHz}] = \frac{0.35}{t_\mathrm{r}\,[\mathrm{ns}]} \tag{2.10}$$

A measure for the quality of matching is the voltage reflection coefficient ρ_V, defined by

$$\rho_\mathrm{V} = \frac{Z - Z_0}{Z + Z_0}\ , \tag{2.11}$$

where Z_0 is the impedance of the transmission line and Z is the impedance of the load. There are three important cases:

- $Z = Z_0$, the matching is perfect, no reflected signal.
- $Z = 0$, $\rho_\mathrm{V} = -1$, short circuit, the reflected signal has the same amplitude but changes the sign. This is often used to generate short pulses (so-called clipping of a signal).
- $Z = \infty$, $\rho_\mathrm{V} = 1$, open circuit, the signal is reflected with the same amplitude and sign.

Another measure for evaluating the quality of a network is the so-called voltage standing wave ratio (VSWR), defined as

$$\mathrm{VSWR} = \frac{Z}{Z_0} = \frac{1+\rho_\mathrm{V}}{1-\rho_\mathrm{V}} \,. \tag{2.12}$$

The impedance of a coaxial transmission line is given by [36]

$$Z_0 = \frac{Z_\mathrm{c}}{2\pi}\ln\frac{b}{a} = \frac{60}{\sqrt{\varepsilon_\mathrm{r}/\mu_\mathrm{r}}}\ln\frac{b}{a}\,[\Omega] \tag{2.13}$$
$$Z_\mathrm{c} = \sqrt{\frac{\mu_0\mu_\mathrm{r}}{\varepsilon_0\varepsilon_\mathrm{r}}}.$$

In (2.13), b is the radius of the outer conductor, a is the radius of the inner conductor, $\mu_0 = 1.257 \times 10^{-6}$ [Vs/Am], and $\varepsilon_0 = 8.854 \times 10^{-12}$ [As/Vm]. Figure 2.10 shows an example of a 50-Ω coaxial Faraday cup with a bandwidth of about 2 GHz. According to (2.13), the ratio b/a has to be 2.3. To design the tapered section, which connects the stopping copper body to the broadband N-connector, a formula given in [36] can be applied:

$$Z_0 = \frac{Z_\mathrm{c}}{2\pi}\ln\frac{\tan\frac{\theta_2}{2}}{\tan\frac{\theta_1}{2}} \,, \tag{2.14}$$

where $\theta_{1,2}$ are the angles between the boundary of the tapered conductor and the horizontal line (θ_2 is the larger one). Because the expected beam power

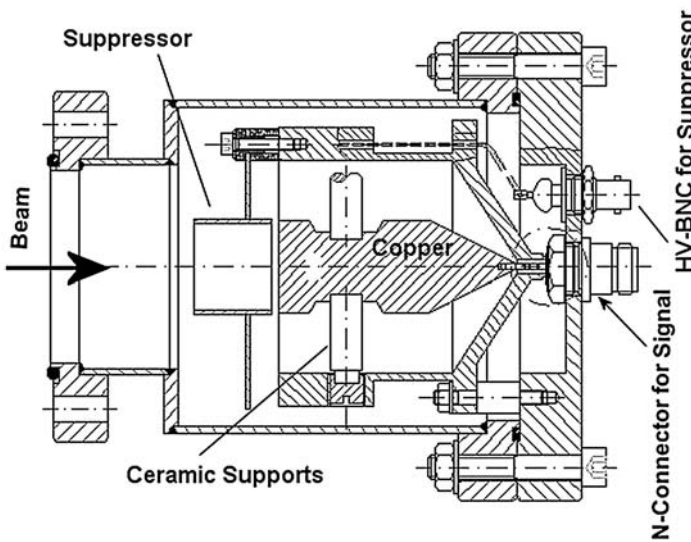

Fig. 2.10. Example of a coaxial Faraday cup [33]

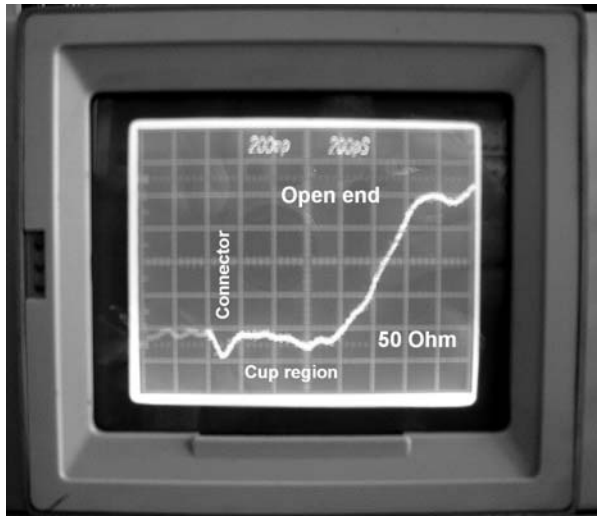

Fig. 2.11. Check of a 50-Ω Faraday cup with a time domain reflectometer (TDR) by measuring the reflection coefficient ρ_{V}

is only of the order of some 100 W, the heat transfer takes place via the three ceramic supports made from Shapal M. The matching to 50 Ω can be tested with a time domain reflectometer (TDR). The device transmits a very fast pulse ($t_{\mathrm{r}} = 25\,\mathrm{ps}$, for example) and measures the reflected signal. Figure 2.11 gives the result of such a measurement. Considering the coaxial cup as a transmission line, $Z \sim \sqrt{L/C}$ where L is the inductance and C is the capacitance per unit length, respectively. Thus, the dip at the position of the commercial connector (see Fig. 2.11) indicates that the capacitance is too high compared to the inductance. The matching of the cup body itself is satisfactory. To compensate for the relatively high ε_{r} of the Shapal M supporting rods, the ratio b/a (see eq. 2.13) has been enlarged by deepening the copper body at this position.

Two important effects have to be considered in evaluating measured signals:

- Broadening of fast signals can occur due to the emission of secondary electrons because the electrons may be emitted with different energies as well as different start times.
- Depending on the charge of the incident ions, the signal amplitude is enhanced ($\zeta_{\mathrm{ion}} > 0$) or attenuated ($\zeta_{\mathrm{ion}} < 0$) by the emission of secondary electrons.

If the particles move with a velocity $v \ll c$ toward the stopper plate, one has to consider the advanced electrical field of bunches, which falsifies the measured signal by an influenced i_{f} (also called displacement current,

see Chap. 5). The influenced current is given by

$$i_{\mathrm{f}} = \frac{d}{dt}\varepsilon_0 \int E_{\mathrm{z}}\, dA = 2\pi\varepsilon_0 \frac{d}{dt} \int_0^R E_{\mathrm{z}}\, r\, dr \tag{2.15}$$

where $A = \pi R^2$ is the area of the cup front face. This means that there is a current flow before the bunch itself hits the stopper plate. The problem can be studied, considering the longitudinal component of the electrical field strength for a moving single particle with unit charge e [39]

$$E_{\mathrm{z}}^{sp}(t) = -\frac{e}{4\pi\varepsilon_0} \frac{\gamma\beta ct}{\left[\sqrt{r^2 + (\gamma\beta ct)^2}\right]^3} \tag{2.16}$$

and composing a bunch by a weighted distribution of this charge e over the selected bunch shape. In a very good approximation, the transverse dimensions of the bunch can be neglected. The composition of a bunch is straightforward (see Chap. 5) and with $P(m)$ as the normalized weights leads to

$$E_{\mathrm{z}}^{b} = -\frac{e}{4\pi\varepsilon_0} \sum_{\mathrm{m}} P(m) \frac{\gamma\beta c(t + m\,\delta t)}{\left[\sqrt{r^2 + [\gamma\beta c(t + m\,\delta t)]^2}\right]^3}\,. \tag{2.17}$$

In (2.17), m is the number of strips and δt is the width of the strips, composing the bunch. Now the integration and derivation according to (2.15) has to be performed. The result is

$$i_{\mathrm{f}}(t) = \frac{e}{2}\gamma\beta c R^2 \sum_{\mathrm{m}} P(m) \frac{1}{\left[\sqrt{R^2 + [\gamma\beta c(t + m\,\delta t)]^2}\right]^3}\,. \tag{2.18}$$

Perhaps the best illustration of the effect is to consider a bunch of square shape. The weights $P(m)$ are constant in this case and defined by $P(m) = \Delta t\,/(N+1)$ with Δt as the bunch length and N $(-N/2 \le m \le N/2)$ as the number of sampling points. It follows immediately that $\delta t = \Delta t/N$. On the left-hand side, Fig. 2.12 shows the calculated signals for a bunch length $\Delta t = 1\,\mathrm{ns}$, corresponding to a bunch current of $e/\Delta t = 160$ pA. A more realistic bunch shape is described by a $\cos^2$ function with (see Chap. 5)

$$P(m) = \frac{P(m) = \cos^2(\pi m\,\delta t/2\Delta t)}{P_0} \tag{2.19}$$

$$P_0 = \sum P(m). \tag{2.20}$$

The results for two different β values are shown in both diagrams on the right-hand side of Fig. 2.12.

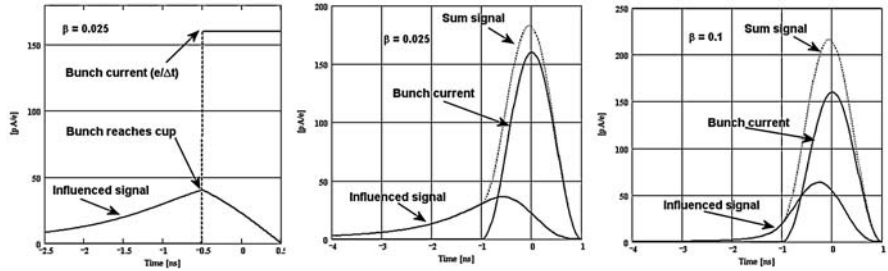

Fig. 2.12. Effect of the advanced longitudinal electrical field on the signals of slowly moving bunches. Left: Signal of a bunch with square shape. Middle and right: Signal of a bunch with $\cos^2$ shape for two different β values. The radius of the stopper plate is $R = 12.5\,\mathrm{mm}$

The effect of the advanced field cannot be shielded by an electric field in front of the cup. However, both effects – the advanced field effect and broadening by secondary electrons – can be suppressed by mounting a shielding grid in front of the stopper plate. If this grid is supplied with a negative voltage, the secondary electrons are repelled to the stopper and the advanced bunch field is shielded by the metallic grid. Figure 2.13 shows the measured bunch signal, using a coaxial cup equipped with a grid, as shown at the right-hand side of the figure. In the example, the bunch with $\Delta t \simeq 1\,\mathrm{ns}$ was moving with a β value of 0.055. Because positive ions have been stopped in the cup, beside a broadening of the signal, a strong enhancement by the escaping secondary electrons is observed, when the suppressor voltage is switched off.

The bunch signal, measured with a coaxial Faraday cup, corresponds directly to the bunch current; bunch shape monitoring with a capacitive pickup

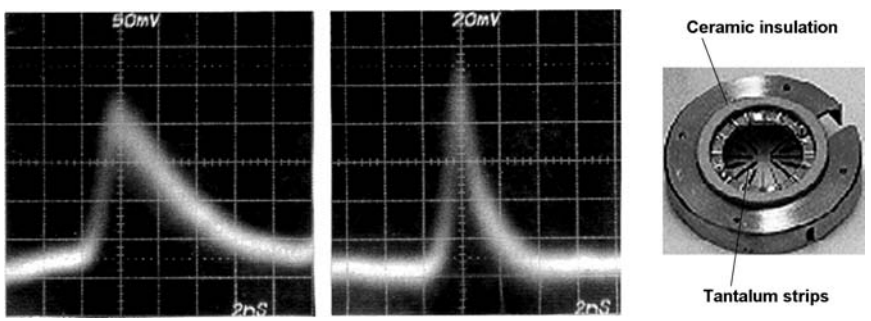

Fig. 2.13. Measured fast bunch signal with a coaxial Faraday cup. Left: No voltage on the suppressor grid. Middle: $-500\,\mathrm{V}$ at the grid; note the different scale of the ordinate. Insert on the right: grid to be mounted in front of the stopper plate. Note that the timescale of the oscilloscope is opposite to the timescale used in the calculated signals of Fig. 2.12

shows the derivation d/dt of the density distribution within the bunch (see Chap. 5). For absolute current measurements, the interception of the beam by the grid structure has to be considered. As becomes clear from Fig. 2.12, the advanced field depends strongly on the β value and may be neglected for higher β's, especially looking only at the bunch shape.

Referring to (2.10), the geometric design of a broadband Faraday cup with a definitive impedance is less critical for signals with rise times of the order of some nanoseconds. Figure 2.14 shows the model of a broadband Faraday cup, provided to measure the shape of bunches with rise times of some nanoseconds. Due to the high requirements concerning the power loss in the cup, the design was determined mainly by thermal considerations. The model was designed, approximating the 50-Ω geometry as well as possible by formulas in the literature [36–38]. Taking advantage of TDR measurements, the matching could be improved afterward by slight changes in the geometry of the model [40]. The beam parameters given to the designer [33] are rather extreme for beam power and beam power density:

beam energy: 2.5 MeV protons,
$\sigma_x = \sigma_y = 1.8$ mm,
Length of the macropulse: 1 ms
length of the bunches: 650 ns (1000 bunches within one macropulse)

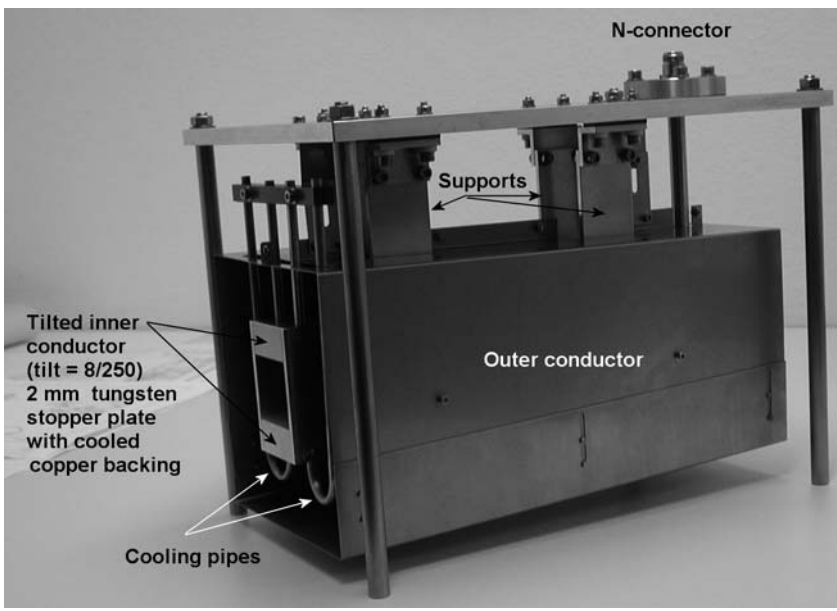

Fig. 2.14. Model of a broadband Faraday cup [33], provided for high beam pulse power with tilted stopper plates. See text for details

repetition frequency: 60/s
average current within one macropulse: 40 mA

Assuming two-dimensional Gaussian intensity distribution results in an extreme power density of 491 kW/cm^2 during the macropulse. The thermal problem was solved by proposing two tilted plates (tilt = 8/250) with a 2 mm sheet of tungsten on a cooled copper backing (in the model, stainless steel was used). Performing the corresponding thermal calculations, as discussed in Chap. 3, results in a maximum temperature of about 250°C on the front face at the center of the beam.

2.1.4 Faraday Cups for Electrons

The designer of Faraday cups for high energy electrons has to take two effects into account, which do not occur for particles with higher mass:

- Generation of "bremsstrahlung", when an electron is accelerated in the Coulomb field of a nucleus. This requires additional measures to protect components of the cup itself as well as to shield the environment against dangerous radiation.
- For bremsstrahlung with an energy higher than two times the rest energy of the electron (2×511 keV), creation of electron–positron pairs begins. To avoid errors in current measurement, one has to prevent the escape of one of them from the cup.

The energy loss by ionization and excitation $(\mathrm{d}W/dx)_{\mathrm{coll}}$ is determined by the well-known Bethe-Bloch formula [41–45, 47], and the mean energy loss by pair production $(\mathrm{d}W/dx)_{\mathrm{rad}}$ is derived in [48]. Comparing both formulas, one finds that the energy loss by ionization and excitation is $\sim Z$ and the energy loss due to bremsstrahlung is $\sim Z^2$. Therefore, the ratio of the two effects depends on the stopping material and on the relativistic region given by [42, 45, 48]

$$\frac{(\mathrm{d}W/dx)_{\mathrm{rad}}}{(\mathrm{d}W/dx)_{\mathrm{coll}}} \approx \frac{(W + mc^2)\, Z}{1600\, mc^2} \,. \tag{2.21}$$

Thus, radiation loss predominates at higher energies. The so-called critical energy W_{c}, where the effects are equal, is given by

$$1 = \frac{(W_{\mathrm{c}} + mc^2)\, Z}{1600\, mc^2} \tag{2.22}$$

$$W_{\mathrm{c}}\,[\mathrm{MeV}] = 0.511 \left(\frac{1600}{Z} - 1 \right) \approx \frac{800}{Z}\,[\mathrm{MeV}] \,. \tag{2.23}$$

Figure 2.15 gives W_{c} dependent on the atomic number. Evidently, this implies using a low Z material to stop high energy electrons with a Faraday cup. Nevertheless, the loss of charges by pair production and Compton scattering from the produced photons has to be prevented. This can be done by placing

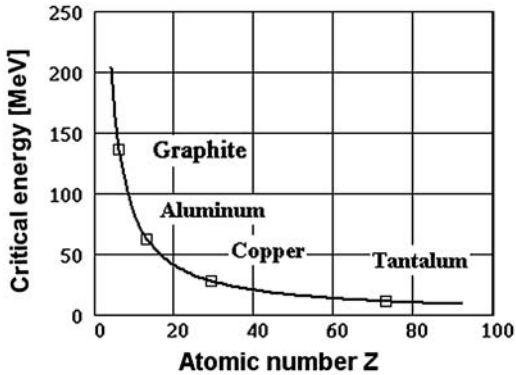

Fig. 2.15. Critcal energy W_c as a function of atomic number Z

an effective absorber behind the low Z material stopper. Combining experimental results [49, 50] with theoretical considerations, a practical formula has been derived [51]. The percentage of charged particle loss from a Faraday cup consisting of t radiation lengths of a low Z material backed by a lead absorber of x radiation lengths is approximately

$$f_p\,[\%] \simeq 2W_0 \left(1 - \frac{D\,t}{W_0}\right) e^{\left[-\sigma\left(x - \ln\frac{W_0}{185}\right)\right]}\,, \tag{2.24}$$

where

- D [MeV/X_0] is the closely approximated average energy loss by collision $\langle(\mathrm{d}W/dx)_{\mathrm{coll}}\rangle$, provided that the primary electron is completely stopped in the initial absorber;
- X_0[g/cm^2] is the radiation length (see Chap. 3, eq. 3.24);
- $\sigma\,[1/X_0]$ is the minimum photon-absorption coefficient of the absorber material. For lead, $\sigma = 1/4.25\,X_0$ [51];
- W_0 is the primary energy of the electrons;
- t $[X_0]$ is the thickness of the stopper plate in units of X_0; and
- $x\,[X_0]$ is the thickness of the absorbing lead cylinder in units of X_0.

Equation 2.24 holds under the condition that the radius of the cup is determined from the expression,

$$r_c\,[X_0] = 0.85x - 2 + r_b \tag{2.25}$$

In Fig. 2.16, the meaning of the parameters in (2.25) is illustrated.

For the designer, it might be helpful to demonstrate the dimensioning by an example. Let us assume $W_0 = 100\,\mathrm{MeV}$ as the primary energy of the electrons, with a beam radius of $r_b = 1\,\mathrm{cm}$, completely stopped in a graphite block, as illustrated in Fig. 2.16.

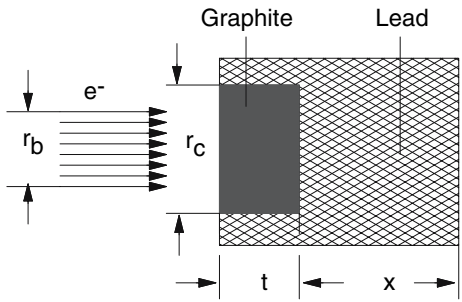

Fig. 2.16. Scheme to explain the parameters of the Faraday cup in (2.25)

The critical energy $W_c = 135.8\,\text{MeV}$. The radiation length of graphite and lead for high energy electrons, including Coulomb correction are $X_0^{\text{carbon}} \simeq 42.7\,\text{g/cm}^2$ and $X_0^{\text{lead}} \simeq 6.37\,\text{g/cm}^2$, taken from a table given in [53]. From (3.24) in Chap. 3, the values are 44.4 and 5.6. Considering the design of a Faraday cup, the differences are not relevant; therefore, we use the values from the table. The value of D for graphite (carbon) is [51] $D = 10 \ln W_0 + 53\,\text{MeV} / X_0$. With W_0=100 MeV and $X_0^{\text{carbon}} = 42.7\,\text{g/cm}^2$, one obtains $D \simeq 2.3$. The penetration depth of energetic electrons can be calculated from the Bethe-Bloch formula and is displayed over the energy range 0–1000 MeV in Fig. 2.17. The penetration depth of 100-MeV electrons is $Pd \simeq 17.4\,\text{cm}$, which corresponds to $t \simeq 0.88\,X_0$. To be on the safe side, we set the thickness of the graphite stopper at $1.3\,X_0$, which corresponds to a thickness of 26 cm. Now all parameters for evaluating (2.24) dependent on x are determined. The result is shown in the diagram of Fig. 2.18. As mentioned above, the diagram

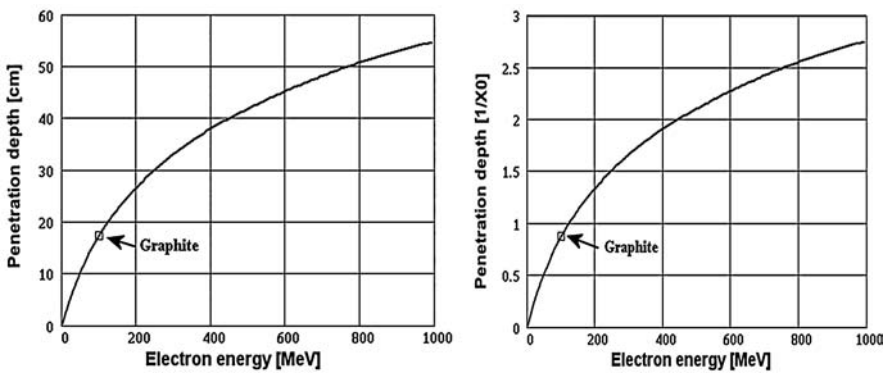

Fig. 2.17. Penetration depth of energetic electrons in graphite [52]. Left: ordinate in cm, with $\rho = 2.15\,\text{g/cm}^2$. Right: ordinate in units of the radiation lengths $X_0 = 42.7\,\text{g/cm}^2$

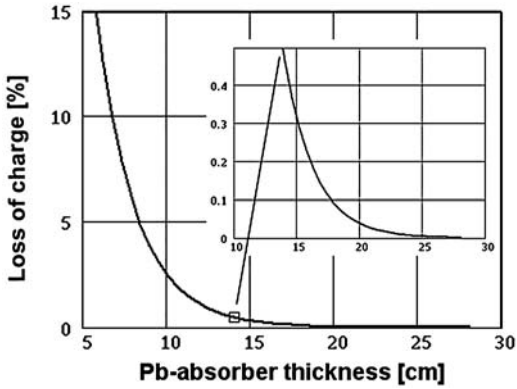

Fig. 2.18. Dimensioning of the Pb-absorber thickness for a given maximum loss of charge due to pair production and escape of electrons or positrons. The insert shows the region around the design values on an enlarged scale

holds, if (2.25), determining the dimensions of the cup according to Fig. 2.16, is fulfilled. Hence, the radius r_c of the Pb absorber has to be determined from the diagram given in Fig. 2.19. Assuming, for example, a maximum allowed loss of charge of 0.1% for the stopped 100-MeV electron beam, the required absorber thickness is $x = 31.53\, X_0^{\text{lead}}$, which with $\rho = 11.35\,\text{g/cm}^3$ leads to a thickness of 17.7 cm and a radius of 13.9 cm.

Of course, to avoid escape of secondary electrons and backscattered electrons, the corresponding measures of suppression have to be provided in the design of a Faraday cup for electrons, too.

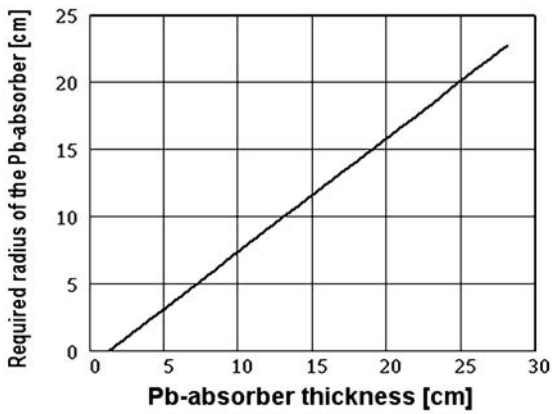

Fig. 2.19. Required radius of the Pb absorber according to (2.25) dependent on the absorber thickness, determined according to (2.24) for a 100-MeV electron beam

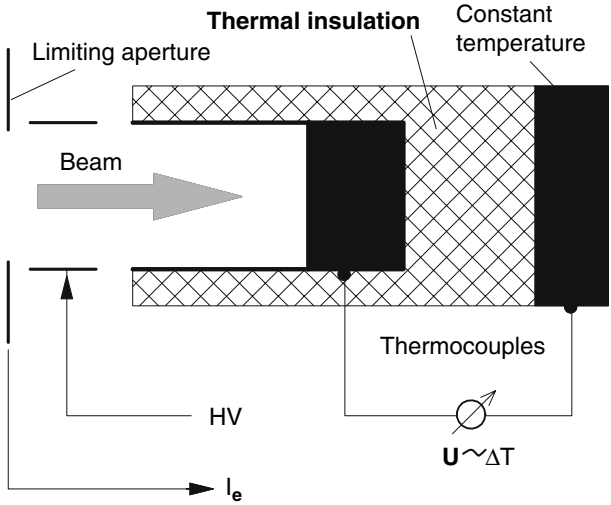

Fig. 2.20. Scheme of a calorimetric beam intensity measurement. The limiting aperture can be used to "focus" the beam into the calorimeter by minimizing the measured current from secondary electron emission

2.2 Calorimetric Intensity Measurements

A very special problem in beam diagnostics is the intensity measurement of neutral beams. Due to the lack of electrical signals, this task requires the application of other methods. One possibility is given by calorimetric measurements. The use of calorimetry has been discussed by a number of authors [54–59]. Assuming that the energy and mass of the energetic neutral particles are known, particle flow can be determined by measuring the change in temperature of a thermally isolated beam stopper, as shown schematically in Fig. 2.20. Measuring the change in temperature in a specific time interval, the beam intensity can be determined from the relations,

$$\frac{dQ}{\Delta t} = \frac{N}{\Delta t}\frac{m}{2}v^2 = m\,c_\mathrm{p}(T)\frac{dT}{\Delta t} = \rho\,V\,c_\mathrm{p}(T)\frac{dT}{\Delta t} \tag{2.26}$$

$$\frac{N}{\Delta t} = \frac{1}{\Delta t}\frac{\rho\,V}{W_\mathrm{sp}}\int_{T_1}^{T2} c_\mathrm{p}(T)\,dT, \quad W_\mathrm{sp} = \frac{m}{2}v^2. \tag{2.27}$$

The slight dependency of c_p on the temperature can be taken into account by a linear approximation of the type of $c_\mathrm{p}(T) = a + bT$. From the values of c_p at 25°C and 2000°C given in Table 3.1 of Chap. 3, one obtains a and b, given in Table 2.4 for some typical materials.

With $c_\mathrm{p}(T) = a + bT$, the number of particles hitting a calorimeter in time Δt can be obtained from

Table 2.4. Coefficients a and b to determine the heat capacity c_p between $T = 25^\circ\mathrm{C}$ and $T = 2000^\circ\mathrm{C}$ from the equation $c_\mathrm{p}(T) = a + bT$

	Graphite	Al	Ti	Fe	Cu	Ta
a [Ws / g K]	0.708	0.901	0.439	0.522	0.385	0.14
$b\,[10^{-4}\mathrm{Ws}\,/\,\mathrm{g\,K^2}]$	1.458	0.947	1.939	1.342	0.557	0.142

$$\frac{N}{\Delta t} = \frac{1}{\Delta t}\frac{\rho V}{W}\left[a\,(T_2 - T_1) + \frac{b}{2}\left(T_2^2 - T_1^2\right)\right] . \tag{2.28}$$

The scheme of Fig. 2.20 and (2.27) may be used slightly modified if water cooling of the stopper block is necessary. In this case, slow changes in the beam energy – caused by changes in the kinetic energy W_sp or the particle flux $N/\Delta t$ – can be monitored by measuring the inlet and outlet temperature of the cooling water. It is evident that the flow rate of the water $\Delta V_\mathrm{w}/\Delta t$ has to be known. With the density of water $\rho_\mathrm{w} = 1\,\mathrm{g/cm^3}$ and the heat capacity $c_\mathrm{w} = 4.18\,\mathrm{Ws\,/g\,K}$, the change in total energy $W = NW_\mathrm{sp}$ is given by

$$\frac{\Delta W}{\Delta t} = \rho_\mathrm{w} c_\mathrm{w} \frac{\Delta V_\mathrm{w}}{\Delta t}\Delta T \tag{2.29}$$

Of course, due to the long time constant of the device, only changes in energy with a rather slow rate of change can be monitored. Furthermore, after moving the device into the beam, one has to wait a suitable time until the cooled block of material achieves a steady state. Since the thermal insulation of the calorimeter, as shown in the scheme of Fig. 2.20, also results in electrical insulation, the calorimetric measurement may be combined with current measurement, if charged particles are stopped.

2.3 Beam Current Transformers

The use of a beam current transformer (BCT) for intensity measurement of charged particle beams has the following advantages:

- Non-destructive signal extraction and, therefore most of the problems discussed for the design of Faraday cups will not arise. Since the ion beam will not be distorted by the measurement, the beam current transformer is well qualified for on-line closed-loop feedbacks to control ion beam intensity.
- Assuming careful design of the transformer system, the measurement will be nearly independent of beam position and beam size.
- Obviously, the most important advantage is the direct proportionality of the output signal to the beam current. Furthermore, precise absolute calibration can be performed by feeding a well-known current pulse from an external current source via a dedicated calibration winding.

One basic shortcoming of beam current transformers is the strong dependence of the sensitivity and time constant on the time structure of the beam. Since there is a great variety in the characteristics of beams, a broad spectrum of solutions is possible in:

- mechanical design,
- type of core material, for example, Vitrovac, Ni–Zn ferrites;
- winding schemes, and for example, bifilar windings to reduce common mode noise signals;
- signal processing electronics connected to the current transformer.

The design and use of beam transformers in accelerator physics and especially for non-destructive intensity measurements are detailed in the literature [30, 60–76, 78]. Nevertheless, it can be helpful to repeat the principles of signal generation as well as some important features, for design and signal processing. Figure 2.21 shows a model of a beam current transformer to explain signal generation. Figure 2.22 shows a simple construction drawing of a beam transformer. In this example, the necessary isolating gap in the beam pipe is achieved using a ceramic insulator, with special metallic sealing rings between the ceramic disk and the supporting metallic parts of the housing. Another cheaper possibility to realize a gap in the beam pipe is shown in Fig. 2.28 where an O-ring is used to avoid a short circuit in the induced signal. This kind of sealing may be used in vacua up to about 10^{-7} mbar and a moderate level of radiation. A newly designed transformer [79], shown in Fig. 2.24, has been inserted completely in a vacuum-sealed housing. As it is clear from the figure, the construction does not require extra insulation around the gap. The stable support, which seems to be slightly oversized, avoids vibrations causing microphonic distortions. The transformer has been designed to measure beam

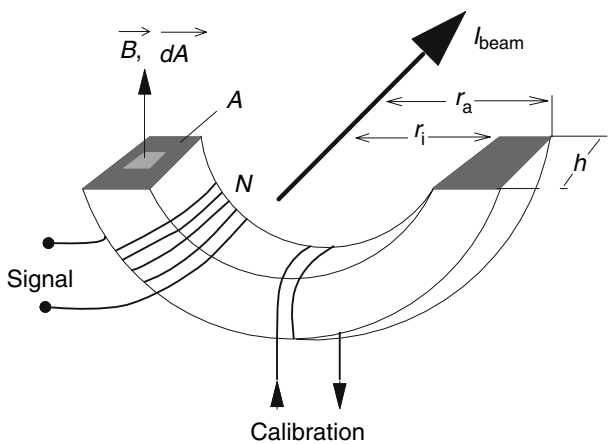

Fig. 2.21. Physical model of a beam transformer showing only one-half of the core

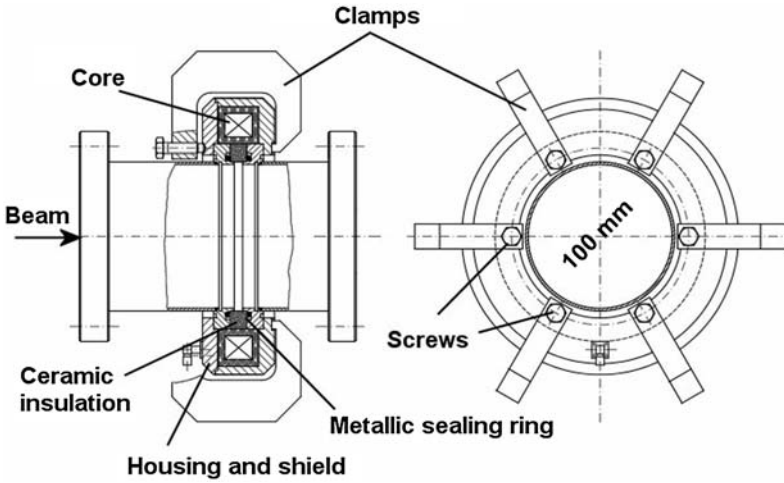

Fig. 2.22. Construction drawing of a beam transformer

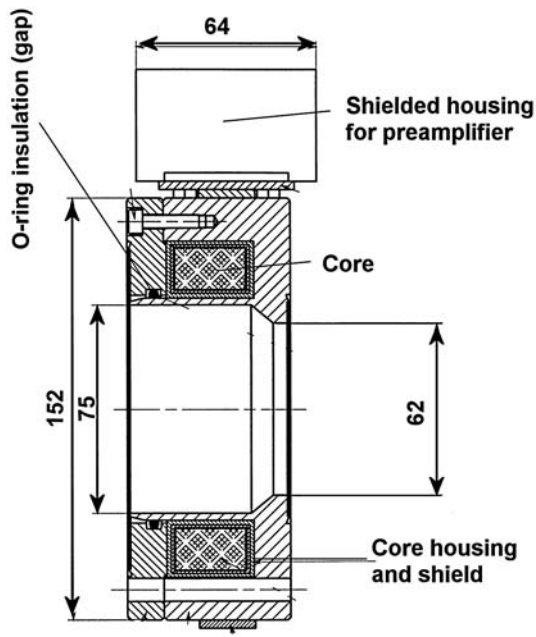

Fig. 2.23. Construction drawing of a beam transformer using an O-ring insulator as the isolating gap. All dimensions in milimeters

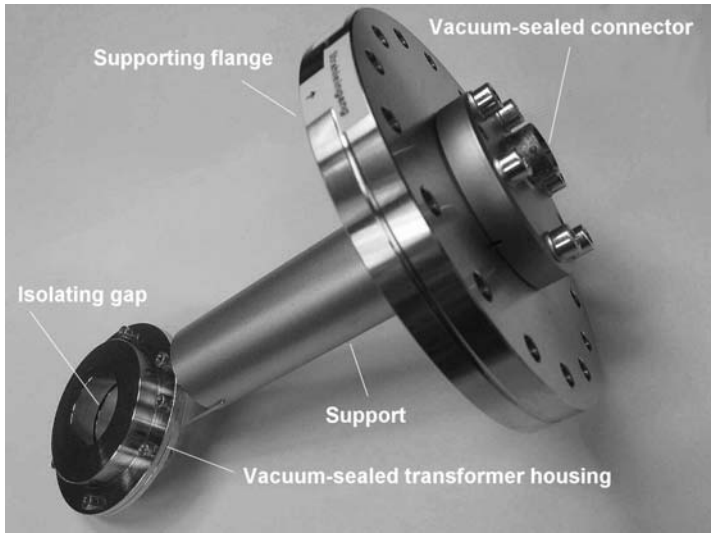

Fig. 2.24. Beam current transformer inside a vacuum-sealed housing [79], GSI Foto

pulses having lengths up to 8 ms with a maximum droop of 3% using a ferrite core shielded by a Mu-metal box inside the vacuum-sealed housing.

Referring also to Chap. 5, the induced voltage in one winding is given by

$$u(t) = -\frac{d}{dt}\int \overrightarrow{B}\,\overrightarrow{dA} = -\frac{d}{dt}\int B_\Phi\, dA = -\frac{d}{dt}\oint \overrightarrow{A_{\mathrm{pot}}}\,\overrightarrow{dl} \tag{2.30}$$

where A_{pot} is the vector potential. Since the signal is nearly independent of the beam position and the transverse dimensions of the beam, only the azimuthal component of the magnetic field B_φ has to be considered. Applying Biot-Savart's law, one obtains

$$\overrightarrow{B_\varphi} = \frac{\mu_0 I_{\mathrm{beam}}}{2\pi r}\overrightarrow{e_\varphi}, \quad \mu_0 = 1.256 \times 10^{-6}\,\mathrm{Vs/Am}\,, \tag{2.31}$$

with $\overrightarrow{e_\varphi}$ as the unit vector in the φ-direction of a cylindrical coordinate system, defined by the two other coordinates z (in the beam direction) and the radial coordinate r. To derive the equivalent electric circuit diagram of a beam transformer and in consequence the transfer function, the most important parts which one has to consider are

- the transformer inductance L,
- the number of secondary windings N,
- the load resistance of the system R,
- the resistance of the cables of the secondary circuit R_{L},
- the stray capacitance between the components (cables, core, windings) C_{L},

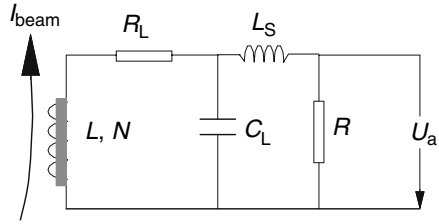

Fig. 2.25. Simplified equivalent electrical circuit diagram of a beam current transformer showing the most important components. The consideration of all stray inductances and capacitances shown in the diagram is only a coarse simplification and may be found in other arrangements in the literature [80, 81]

- the stray inductance between the components L_S, and
- the magnetic losses caused by eddy currents and the magnetization process [80].

The transformer inductance is given by

$$L = \frac{N^2 \mu_0 \mu_r h}{2\pi} \ln \frac{r_a}{r_i} \tag{2.32a}$$

with the dimensions as shown in Fig. 2.21 and μ_r as the relative permeability of the core material.

2.3.1 The Passive Beam Transformer

The equivalent electric circuit diagram of a (passive) beam transformer is shown in Fig. 2.25. The transfer function $f(s)$ with s as the Laplace variable

$$U_a(s) \rightarrow f(s)\, I_{beam}(s) \tag{2.33}$$

and the corresponding solution

$$U_a(t) \rightarrow F(t) I_{beam}(t) \tag{2.34}$$

become rather complex. On the other hand, the most important features of a passive transformer, such as the sensitivity $S = U_a / I_{beam}$ and droop time constant τ can be figured out neglecting the small values of L_s and C_L. Thus, in a first approximation, the transfer function simplifies to

$$U_a(s) = -I_{beam}(s)\, \frac{s\, R\, L}{N} \frac{1}{s\, L + R_L + R}\, . \tag{2.35}$$

Assuming $I_{beam}(s) = i_p / s$, which idealizes the beam current to a step function, the solution of (2.35) is

$$U_{\mathrm{a}}(t) = -i_{\mathrm{p}} \frac{R}{N} \, e^{\left[-\frac{R+R_{\mathrm{L}}}{L} \, t\right]} \; . \tag{2.36}$$

The sensitivity is

$$S = \frac{U_{\mathrm{a}}(0)}{i_{\mathrm{p}}} = \frac{R}{N} \; , \tag{2.37}$$

and the droop time constant τ of the exponential drop is given by

$$\tau = \frac{L}{R + R_{\mathrm{L}}} \approx \frac{L}{R} \; . \tag{2.38a}$$

The effective inductance L according to (2.32a) may be reduced by eddy currents, which results in a reduction of the time constant τ if the relation $\tau_{\mathrm{e}} \ll \tau$ is not fulfilled [69, 82]. The time constant τ_{e}, determined by eddy currents, is given by [82]

$$\tau_{\mathrm{e}} = \frac{\mu_0 \, \mu_{\mathrm{i}} \, d^{\,2}}{\pi^2 \rho_{\mathrm{ec}}} \; , \tag{2.39}$$

where μ_{i} is the relative initial permeability, d is the thickness of the laminate and ρ_{ec} is the specific electric resistance of the core material. Obviously, a small τ_{e} can be achieved by a thin laminate of a core material with high specific electric resistance, whereas the selection of a material with low μ_{i} would contradict (2.32a).

Considering (2.32a), (2.36), (2.37), and (2.38a), a conflict arises with respect to the selection of N since the output voltage is proportional to $1/N$ and therefore requires a low N. On the other hand, the transformer inductance is proportional to N^2 and should be high for good low frequency response, respectively, a large droop time constant τ. To achieve a drop of less than 1% for beam pulse lengths of the order of some microseconds requires a rather high number of windings N and results in low sensitivity.

For illustration, we assume the following parameters:

beam pulse length: $T_{\mathrm{p}} = 5\,\mathrm{ms}$
maximum allowed drop: $D = 3\%$
height of the core: $h = 0.05\,\mathrm{m}$ $(5\,\mathrm{cm})$
inner radius of the core: $r_{\mathrm{i}} = 0.03\,\mathrm{m}$
outer radius of the core: $r_{\mathrm{a}} = 0.06\,\mathrm{m}$
relative permeability of the core $\mu_{\mathrm{r}} = 80.000$ (Ultraperm, $50\,\mu\mathrm{m}$, [83])
load resistance $R = 500\,\Omega$

Neglecting R_{L}, the drop $D = R\,T_{\mathrm{p}}/L$ and the required number of windings N can be determined from the relation $L(N) = RT_{\mathrm{p}}/D$, leading to

$$N(T_{\mathrm{p}}) = \sqrt{\frac{2\pi R T_{\mathrm{p}}}{D \mu_0 \mu_{\mathrm{r}} \, h \ln r_{\mathrm{a}}/r_{\mathrm{i}}}} \tag{2.40}$$

$$N \simeq 388 \quad \rightarrow L = 83.44\,H \tag{2.41}$$

$$S = 1.289\,V/A. \tag{2.42}$$

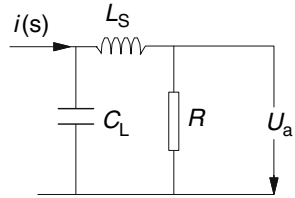

Fig. 2.26. Simplification of the electrical circuit diagram shown in Figure 2.25 to study the effect of stray capacitance and stray inductance

The result is quite a low sensitivity. Furthermore, due to the large number of windings, the beam current transformer acts as a very sensitive microphone, requiring additional measures to avoid vibrations of the core.

The stray C_L and the stray L_s shown in the simplified electrical equivalent circuit of Fig. 2.25 can be taken into account by substituting $R \rightarrow R \parallel C_\mathrm{L}$ and multiplying the result by $R/(L_\mathrm{s} + R)$. This gives

$$U_\mathrm{a}(\mathrm{s}) = -i_\mathrm{beam}(s)\frac{sRL}{N}\frac{1}{R + sL + R_\mathrm{L} + sRC_\mathrm{L}(sL + R_\mathrm{L})}\frac{1}{1 + \frac{L_\mathrm{s}}{R}} \; . \qquad (2.43)$$

A solution can be obtained, using PC programs [84–86]. However, one arrives at a rather complex expression for $U_\mathrm{a}(t)$. On the other hand, to study the effect of L_s and C_L, it will be sufficient to consider only the right-hand part of the electrical circuit diagram shown in Fig. 2.26. It is reasonable to assume $i(\mathrm{s}) = i_0/s$, leading to

$$U_\mathrm{a}(\mathrm{s}) = \frac{i_0}{s}\frac{1}{s^2 L_\mathrm{s} C_\mathrm{L} + sRC_\mathrm{L} + 1} \; . \qquad (2.44)$$

Even for this simplified circuit, the solution for $U_\mathrm{a}(t)$ is quite complex and will not be displayed here. As it becomes clear from Fig. 2.26, the rise time is determined by the elements in this part of the electrical circuit. Furthermore, the combination of L_s and C_L may result in an overshoot and damped oscillation of the signal. This is illustrated in Fig. 2.27 assuming $L_\mathrm{s} = 10\,\mu\mathrm{H}$, $C_\mathrm{L} = 100\,\mathrm{pF}$, and $R = 500\,\Omega$. From this simplified consideration, the influence of L_s and C_L on the rise time, respectively, bandwidth, as well as on the ringing characteristics become clear. For the example, a rise time of about 350 ns can be obtained, corresponding to a bandwidth of 1 MHz. One should also keep in mind that scaling of the rise time is $\sim \sqrt{L_\mathrm{s} C_\mathrm{L}}$. To observe plasma oscillations of ion sources with frequencies of the order of some 100 kHz, the bandwidth of a beam transformer should be about 1 MHz and ringing has to be minimized. Figure 2.28 gives an example of ion source oscillations, observed with a beam transformer having a bandwidth of about 700 kHz. Obviously, the rise time of the signal is determined by the ion source and not by the beam transformer having a rise time of about 0.5 µs. The frequency of the plasma

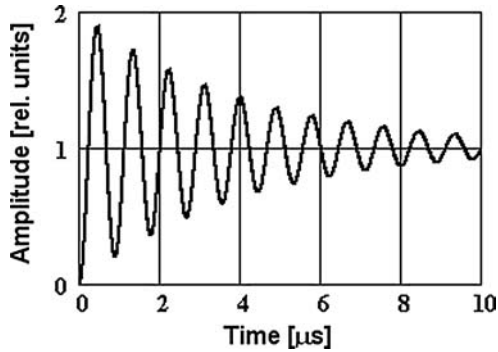

Fig. 2.27. Expected signal $U_a(t)$ according to the simplified electrical cicuit diagram of Figure 2.26. The diagram holds for $R = 500\,\Omega$, $L_s = 100\,\mu H$, and $C_L = 200\,pF$

oscillations of about 100 kHz could be determined with capacitive pickups having a bandwidth of about 2 GHz (see Chap. 5).

Noise and Detection Limit

The signal-to-noise ratio of the passive transformer is determined mainly by the effective thermal noise U_e of the load resistance R, given by

$$U_e = \sqrt{4\,k_b T\,R\,df}, \quad k_b = 1.38 \cdot 10^{-23}\ \text{[Ws/K]}\ . \tag{2.45}$$

Assuming $i_{beam}\,R\,/\,N(T_p) = U_e$, we obtain the required beam current i_{min} for a signal-to-noise ratio of 1. In (2.46), the number of windings for a given R depends on the pulse length T_p and the allowed droop D_r according to (2.40):

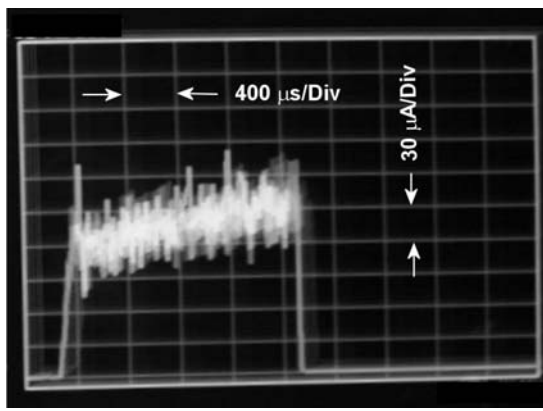

Fig. 2.28. Plasma oscillations of a Penning Ion Source (PIG) observed at GSI with a beam current transformer

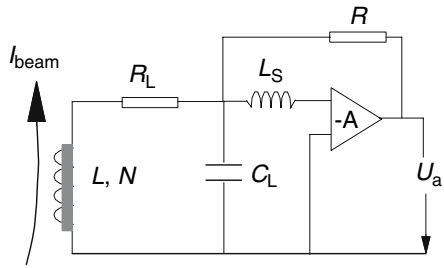

Fig. 2.29. Electrical equivalent circuit of an active beam transformer. A is the complex gain of the operational amplifier

$$i_{\min} = 10^6 \frac{N(T_p)}{R} \sqrt{4\, k_b T\, R\, df} \quad [\mu A] \,. \tag{2.46}$$

For the example discussed ($N = 387$, $R = 500\,\Omega$, $df = 4.4\,\mathrm{MHz}$), this yields $4.6\,\mu\mathrm{A}$.

Remark. Due to the disadvantageous relation between the sensitivity $\sim 1/N$ and the droop time constant $\sim N^2$, pure passive transformers are scarcely used any longer in beam diagnostics. Nevertheless, it is an excellent example for studying the characteristics of this type of a non-destructive beam current monitor.

2.3.2 The Active Beam Transformer

In the last 20 years, the development of beam current transformers has followed the development of modern electronic circuits. One important step was the extension of the low frequency range by placing the current transformer in the feedback loop of an operational amplifier (see e.g., [30, 61, 62]), as shown in the modified electrical equivalent circuit of Fig. 2.29. Substituting R/A for R in the electrical equivalent circuit of the passive beam current transformer in Fig. 2.25 and again neglecting C_L leads to the time constant

$$\tau = \frac{L}{\frac{R}{A} + R_L} \approx \frac{L}{R_L} \,. \tag{2.47}$$

Since $L/R_L \gg L/R$, the time constant is increased considerably and in consequence the number of windings N can be reduced to achieve higher sensitivity. Because the resistor R_L is usually in the order of only some ohms or even less, the number of windings N can be reduced to 10–20. Referring to the example of the passive transformer, this would result in a considerable gain in sensitivity. Of course, the reduction of N also results in a decrease of the stray capacitances and inductances L_s, C_L (see Fig. 2.26), which can improve the rise times down to nanoseconds. This is illustrated in Fig. 2.30

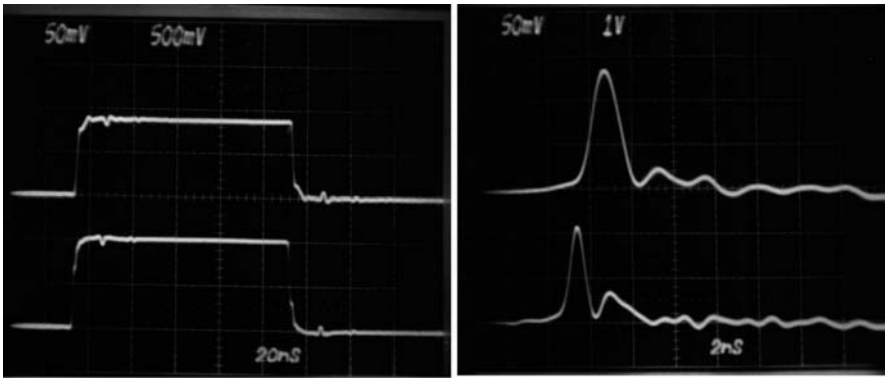

Fig. 2.30. Response (upper traces) of a fast beam transformer to ns- test pulses (lower traces) [79]

for a transformer with 10 windings [79], showing the response to nanoseconds test pulses. To achieve a high bandwidth, spurious oscillations are damped by small resistors across each winding. The fast transformer has been installed in the high energy line behind the SIS to monitor the length during plasma physics experiments. Figure 2.31 shows a bunch signal, displayed on a digital oscilloscope with a bandwidth of 500 MHz. In a very special accelerator experiment, four SIS bunches of a N^{7+} beam with an energy of 350 MeV/u were merged to one bunch. After that procedure, the remaining single bunch was shortened in time by bunch rotation. Due to the high intensity of about

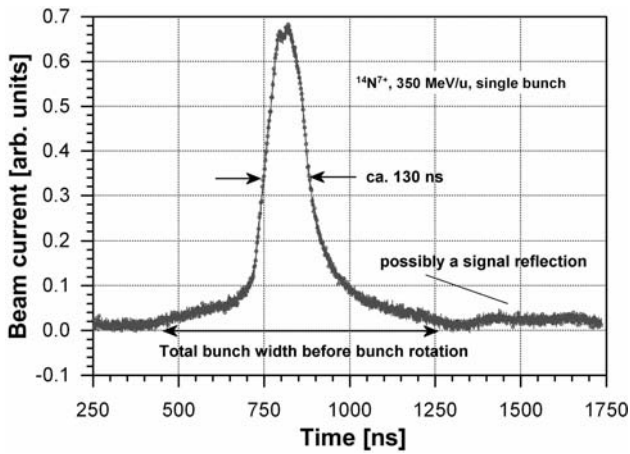

Fig. 2.31. Bunch signal behind the SIS measured with a fast beam transformer [79]. See text for details

Table 2.5. Specifications of a fast beam current transformer

Inner diameter	140 mm
Outer diameter	180 mm
Transfer factor on 50Ω	0.23 A/V
Droop	2.5 % / ms
L/R-time constant	≈ 80 ms
Low frequency limit (−3dB)	≈ 2 kHz
Rise time (10–90%)	< 1.5 ns
Upper frequency limit (−3dB)	300 MHz
Error due to not centered beam	< 0.2 % / mm
Max. $i \times t$ product	10 mA × s
Desired load impedance	50 Ω (BW=1GHz)
Resolution with appropriate amplifier BW = 500 MHz, $F < 2$ dB, S/N=1	≈ 35 μA_{pp}

3×10^{10} particles within the bunch, the transformer output signal could be transmitted without additional amplification via a 50- Ω cable (RG214) over a distance of about 120 m directly to the oscilloscope. The specifications of the transformer are given in Table 2.5 [79].

For noise and detection limits, as discussed very briefly for the passive transformer, one has to consider the noise figures of the individual electronic stages of amplification for an active transformer. In most cases, the noise figure of a complex electronic circuit is determined by the first stage [87]. This follows immediately from an example given in [87], considering three stages of amplification with noise figures F_1, F_2, F_3 and amplifications V_1, V_2, V_3. The resulting total noise figure f_g is given by

$$f_g = F_1 + \frac{F_2 - 1}{{V_1}^2} + \frac{F_3 - 1}{{V_1}^2 {V_2}^2} \; . \tag{2.48}$$

In the literature and data sheets on electronic circuits, the noise figure is given in dB (see for example [88]). To calculate the equivalent noise at the input of an electronic circuit for a given noise figure F, one has to perform the following steps:

$$f = 10^{\frac{F}{10}} \tag{2.49}$$

$$N_P = f \, k_b T \Delta f \; , \quad \text{noise power [W]} \tag{2.50}$$

$$i_{min} = \sqrt{\frac{N_P}{R_A}} \tag{2.51}$$

$$u_{min} = \sqrt{N_P \, R_A}. \tag{2.52}$$

With R_A as the input impedance of the circuit, i_{min} and u_{min} give the required input current and input voltage to obtain a signal-to-noise ratio of 1. Referring to Fig. 2.26, one needs an amplifier, having a bandwidth of about 1 GHz.

Taking a noise figure $F = 3.5$ and an impedance of $50\,\Omega$, which is somehow typical for the frequency range considered [88], one gets $i_{\min} = 0.30\,\mu\text{A}$ and $u_{\min} = 15.1\,\mu\text{V}$.

The introduction of new techniques such as complex electronic circuits, operational amplifiers, charge amplifiers, filters, and active feedback loops in beam current transformer technology results in manifold highly sophisticated solutions to improve bandwidth, resolution, and accuracy [76]. Especially the introduction of an active feedback loop through a separate feedback winding (Hereward feedback), improves the low frequency response considerably and was a first step to the development of dc-transformers.

2.3.3 The DC-Transformer

The principles of dc-current measurement applied in beam diagnostics are similar to methods used to detect very weak magnetic fields such as the earth vs field. But the principle is also known from telecommunication. A device for measuring weak magnetic fields is known as a fluxgate sensor, also known as Foerstersonde [89, 90]. In telecommunication, the principle is used for pulse phase modulation (PPM) of signals [36, 91]. Furthermore, the principle is also well known in the magnetic amplifier technique. Figure 2.32 shows the scheme of a pulse phase modulator which changes the width of an output pulse proportional to the dc-current. The scheme is the right one to explain the principle of dc-current measurement and to discuss the improvements, resulting from applications in beam diagnostics. With the modulator, the core is driven into saturation, as shown in Fig. 2.33. Replacing the detector of Fig. 2.32 with a narrowband spectrum analyzer or a similar device, the dc-current can be measured by detecting the second harmonics arising.

Remark. In the application of pulse phase modulation, the core is driven much more into saturation, which results in nearly square pulses that change their lengths proportional to the dc-component.

The scheme of Fig. 2.32 has some drawbacks:

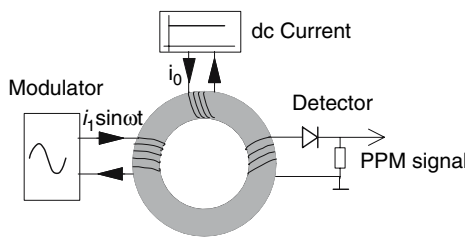

Fig. 2.32. Scheme of a pulse phase modulator. See text for details

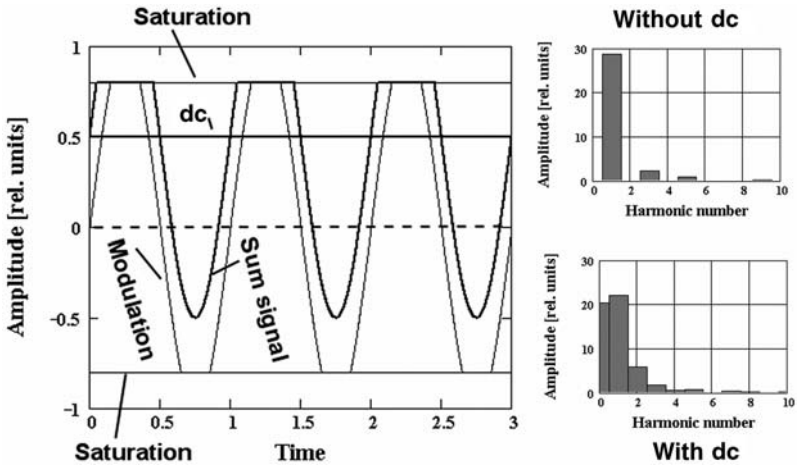

Fig. 2.33. Principle of dc-current measurement. Left: Analog signals cropped by saturation (saturation level at 0.8, dc-current = 0.5 in the units used). Right: Fourier spectra of the signals without and with the dc-component

- The relation between the dc-current, which has to be measured, and the amplitude of the second harmonics depends on many factors and, therefore calibration and accurate absolute determination of current are difficult.
- Due to the large first harmonic, the first stages of the electronics have to process relatively large signals without any information about the beam current.
- On the other hand, total suppression of the first harmonic requires complex filters.
- Changes in the core temperature have a strong direct effect on the output signal.

The further development of dc-beam current transformers was very much influenced by the operation of storage rings, especially the proton synchrotron (CERN) (PS) and the old intersecting storage ring (CERN) (ISR) [62, 92, 93].

As a first consequence, the scheme of Fig. 2.32 has been improved by adding a second core modulated opposite to the modulation, of the first one. With this modification, the scheme can be further extended to a zero detector, as shown in Fig. 2.34. Referring to Fig. 2.33, the resulting analog signal as well as the expected Fourier spectrum are shown in Fig. 2.35.

From the working principle of the dc-transformer, based on a strong modulation of the magnetic material and the shift of the hysteresis curve by the external beam, it becomes clear that the Barkhausen noise produced by wall-jumps of magnetic regions is a limiting factor with respect to achievable performance. To achieve high sensitivity and resolution, there are extremely specific requirements with respect to identity of the magnetic characteristics for the

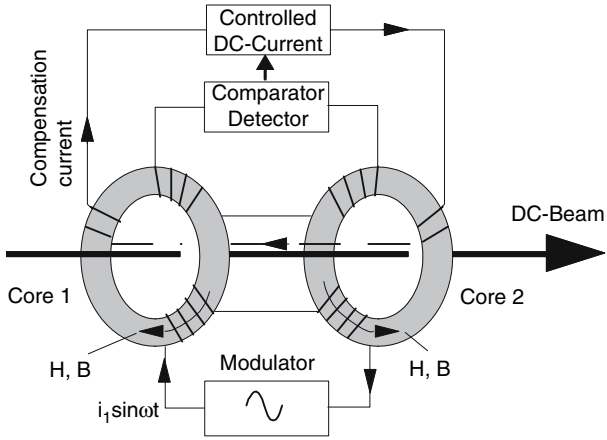

Fig. 2.34. Scheme of a dc-transformer based on two cores, modulated in the opposite sense. See text for details

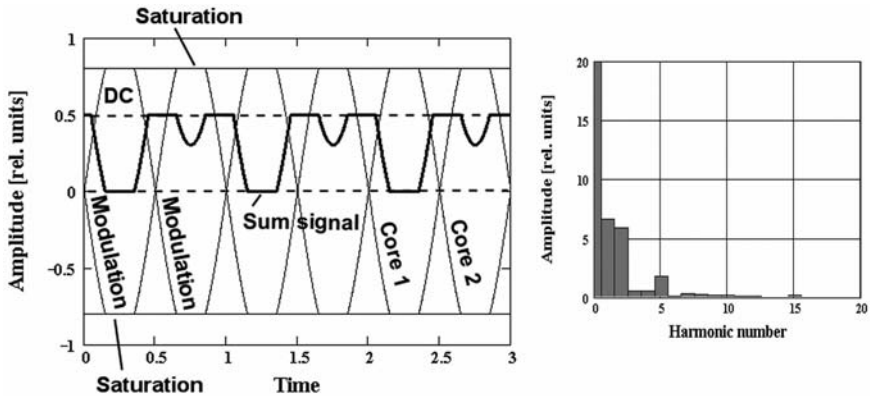

Fig. 2.35. Principle of dc-current measurement using two cores. Left: Analog signals cropped by saturation (saturation level at 0.8, dc-current = 0.5 in the units used). Right: Fourier spectra of the signals with the dc-component. Due to the modulation of the two cores in the opposite sense, there is no output signal in the absence of dc-current

pair of cores. Thus, selection and treatment of the core material require much effort and have to be done with care as described in more detail in [93].

2.3.4 Combined Systems

The manifold operating modes of modern computer-controlled synchrotrons with respect to possible time structures gave impetus to further developments.

To monitor the beam current, the number of particles during one machine cycle requires a large bandwidth, determined by

- the injection, usually multiturn injection. Thus, to observe the increase in current per turn, the rise time of the measuring transformer has to be smaller than the revolution time, usually in the order of microseconds;
- the acceleration cycle (mostly of the order of microseconds), where the increasing beam current has to be measured and compared with the values obtained from the so-called β normalization;
- the flattop and slow extraction which may last up to 10 s and even longer.

As a consequence, combined beam transformer systems have been developed, consisting of a number of toroidal cores [93, 94]. Figure 2.36 shows the hardware of such a combined transformer system installed in the SIS. The transformer is a combination of three types of transformers. The fast one (arranged on the right-hand side) has a rise time of less than 0.5 µs and is provided to observe the steps in current during multiturn injection. The response of this fast transformer to a test pulse, simulating the stepwise current increase during multiturn injection, is shown in Fig. 2.37. The dc-part, arranged on the left-hand side, consists of two cores modulated with a frequency of 1 kHz. The specifications of this part are summarized in Table 2.6).

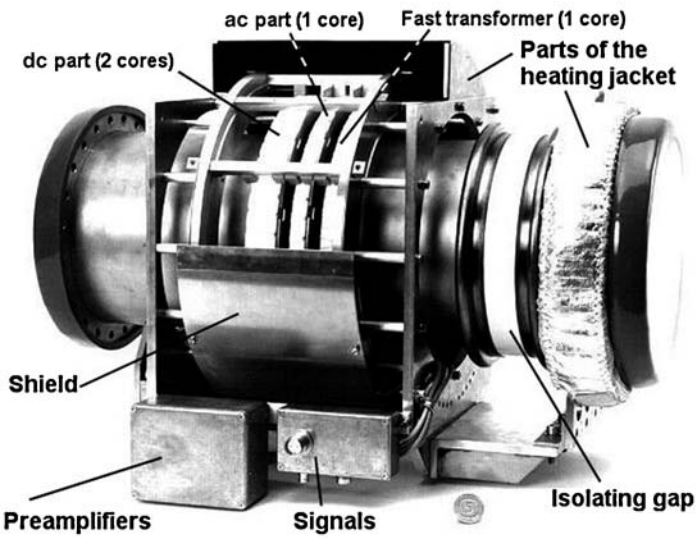

Fig. 2.36. Picture (GSI Foto) of a combined beam current transformer system (a part of the heating jacket and shielding removed). The transformer is installed in period 9 of the SIS

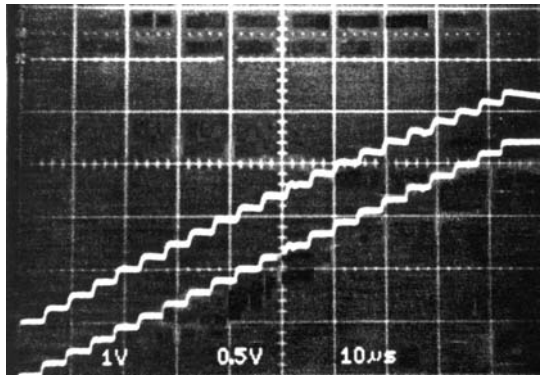

Fig. 2.37. Test of the fast transformer (see Fig. 2.36). Lower trace = test signal; upper trace = transformer response. From [69]

Table 2.6. Specification of the dc-transformer installed in the SIS [79]. Note: The bandwidth of 200 kHz does not hold in the most sensitive range.

Aperture	$\gtrsim 200\,\mathrm{mm}$
Core material	Vitrovac 6025 F, [83]
Core radii	$r_\mathrm{i} = 135\,\mathrm{mm}, r_\mathrm{a} = 145\,\mathrm{mm}$
Permeability	$\simeq 10^5$
Number of windings	16 for modulation and sensing 12 for feedback
Isolating gap	Al_2O_3
Ranges (full scale)	$300\,\mu\mathrm{A} \ldots 1\mathrm{A}$, bipolar
Steps	$1 \ldots 3 \ldots 10$
Resolution	$2\,\mu\mathrm{A_{pp}}$, S:N = 1, full bandwidth
$1/f$ noise threshold	$\simeq 2\,\mathrm{Hz}$
Bandwidth	dc to 20 kHz (200kHz)
rise time	$\simeq 20\,\mu\mathrm{s}$
Overshoot	$< 1\%$
Gain error	$< 3\%$
Linearity error	$< 0.1\%$
Offset compensation	$\pm 2.5\,\mu\mathrm{A}$ in auto mode $< 15\,\mu\mathrm{A/day}$ in free run mode
Temperature coeff.	$1.5\,\mu\mathrm{A}\,/^\circ\mathrm{C}$

The core in the middle has an intermediate rise time and is provided for β normalization. The fast transformer is electronically separated from the dc- and ac-parts, whereas these are connected together to an amplifier and phase correction network. A simplified block diagram of the network and the corresponding Bode plot are shown in Figs. 2.38 and 2.39. A system with similar characteristics was developed and discussed more in detail earlier by

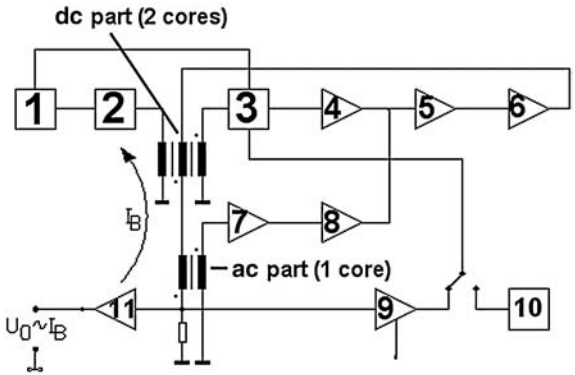

Fig. 2.38. Simplified block diagram of the combined dc-ac-current transformer [79]. 1=Modulator (1000 Hz), 2=Power amplifier, 3=Phase sensitive detector (PSD), 4=Integrator, 5=Adding amplifier, 6=Compensation amplifier (zeroing beam current), 7=$di/dt-$ detector, 8=Amplifier, 9=Amplifier, 10=Automatic zeroing (during pause), 11=Signal output

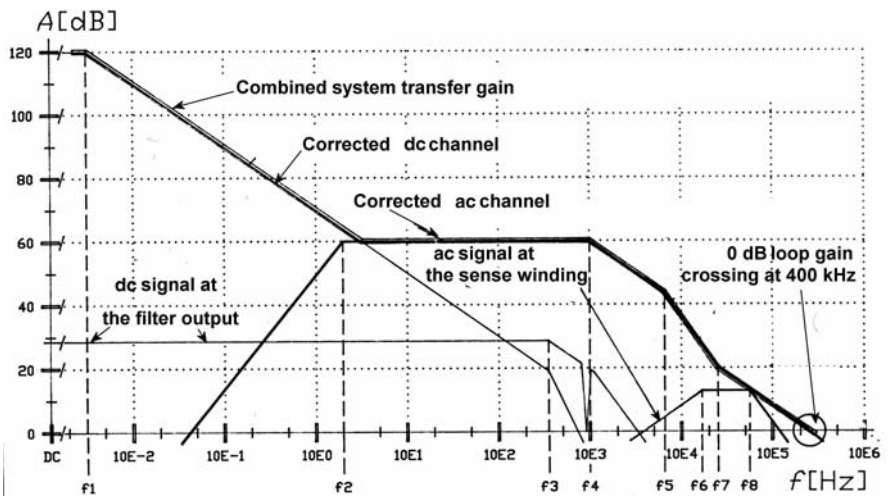

Fig. 2.39. Bode plot [79], corresponding to the amplifier and phase correction network of Figure 2.38. Note the dip at1 kHz due to the suppression of the modulation frequency

Unser [62]. A measurement over one cycle of the SIS, shown in Fig. 2.40, illustrates the usefulness of the combined system. The observed losses due to bad capture (see Fig. 2.40) could be minimized by improvements in hardware and software involved in rf capture.

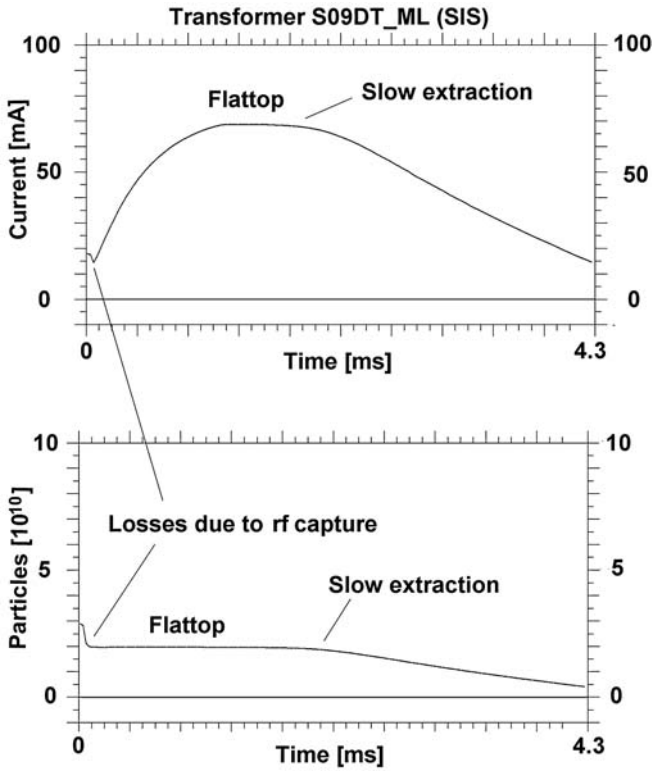

Fig. 2.40. Beam intensity measurement over one cycle of the SIS [79] with a combined dc- and ac-transformer system. Note the loss due to bad rf capture during the injection phase and the constancy of the number of particles (obtained from β normalization) during acceleration and on the flattop

2.3.5 The Integrating Current Transformer

Replacing the resistor in the feedback loop of the first stage by a capacitance C leads to integrating the beam current signal according to

$$U_{\text{out}} = \frac{1}{N\,C}\int i_{\text{beam}}\,dt \quad \rightarrow U_{\text{out}} = \frac{i_{\text{beam}}\Delta t}{N\,C} = \frac{Q}{N\,C} \quad \text{for square pulses.} \tag{2.53}$$

With this special application of a beam current transformer, it is possible to measure the charge within beam pulses. The integrating current transformer (ICT) is commercially available [95] and even integrates pulses with rise times < 1 ps. The charge sensitivity goes down to 1 pC. Supplementing the integrator by a sample and hold circuit, the output voltage can be digitized by an ADC with a readout by the control computer. Clearing the integrating capacity after the readout by a reset pulse allows continuous monitoring during routine

machine operation. Of course, the time structure of the beam pulse will be lost by applying this principle.

2.3.6 The Resonant Current Transformer

A simple approach to measuring the beam current intensity of short beam pulses refers to the well-known principle of the "ballistic galvanometer." Designing the secondary winding on a ferrite toroid as a resonant $L-C$ circuit, a short beam pulse, which acts as the primary winding, will force the system to damped oscillations. If the period of the resonance frequency T_{LC} is large compared to the primary pulse duration Δt, the initial amplitude of the oscillation is proportional to the charge that has passed the toroid and does not depend on the time structure of the beam pulse. A prototype was assembled in the beam diagnostic laboratory of GSI [96] to study the characteristics and achievable sensitivity dependent on the design parameters. Because the system was developed for intensity measurements during fast extraction from the SIS, the design is determined by the requirement $T_{\mathrm{LC}} \gg 1.5\,\mu\mathrm{s}$. A simple approximation for the initial amplitude of the resonant circuit at the end of the primary impact of duration Δt leads to [97]

$$U(\Delta t) = \frac{Q}{N\,C}\left(1 - \frac{\omega^2 \Delta t^2}{24}\right) \tag{2.54}$$

$$Q = \int_0^{\Delta t} i_{\mathrm{beam}} \Delta t \quad \text{charge within the beam pulse} \tag{2.55}$$

$$\omega = \frac{2\pi}{T_{LC}} \qquad \text{resonance frequency,} \tag{2.56}$$

holding for $T_{\mathrm{LC}} > 10\,\Delta t$ and a damping time constant larger than T_{LC}. Comparing (2.54) and (2.53), the integration error can be defined as $\delta = \omega^2 \Delta t^2 \,/\, 24 \simeq 1.6(\Delta t / T_{\mathrm{LC}})^2$. Thus, the resonance circuit's period T_{LC} is determined by the tolerable value of δ. For the prototype of such a resonant current transformer (RCT), the following parameters have been chosen [96]:

$T_{\mathrm{LC}} = 54.05\ \mu\mathrm{s} \rightarrow \delta = 1.6\,(1.5/54.05)^2 < 0.15\%$
$L = 8.6\ \mu\mathrm{H},\ N = 100, C \simeq 1\mathrm{nF}$

A beam pulse of $i_{\mathrm{beam}} = 1\,\mu\mathrm{A}$ having a length of $\Delta t = 1\,\mu\mathrm{s}$ gives 1 pC. Passing the resonant current transformer (RCT) leads to an output voltage of $U(\Delta t) = 10\,\mu\mathrm{V}$, which is well above the noise level of narrowband amplifiers or oscilloscopes. On the other hand, an output voltage of 10 V seems to be a useful maximum considering typical signal processing electronics. This leads to a maximum beam current $i_{\mathrm{beam}} = 1$ A which is more than a factor of 10 above the current that can be handled in the SIS due to space charge limitations. In practice, electronic signal processing consists of the following components [96]:

- the resonant current transformer (RCT) itself;

- an operational amplifier with a relatively high input impedance and a gain of 20, whereby frequencies below 2 kHz are suppressed by a high-pass filter;
- an operational amplifier with programmable gain (G) between $1 < G < 100$, having a bandwidth between 1–70 kHz;
- a peak detector;
- a differential output push-pull stage;
- a trigger and synchronization unit, including electronic switches to clear the charge on the capacitance after a measurement.

2.3.7 Some Hints for the Design of Beam Current Transformers

In addition to the aspects discussed above, the following points are also important for the design of a beam current transformer system:

- The shortcomings of a beam transformer are its high sensitivity to mechanical vibrations, as well as to stray electric and magnetic fields. Therefore, the location of the installation along the beam line should be selected very carefully. Furthermore, the mechanical layout has to take these aspects into account, too. One has to keep in mind that the magnetic flux density produced by a 1-μA beam current is of the order of 10^{-11} tesla, which is about five orders of magnitude below that of the earth's magnetic field.
- The measured current may be falsified, if electrons are moving with or against the ions. Those electrons may be generated by residual gas ionization or emitted from the beam pipe wall by ions of the beam halo hitting the beam pipe wall. Due to the high mass ratio between heavy ions end electrons of about $2000\,A : 1$, electrons with much lower energy can have the same velocity as accelerated ions or protons.
- Differential signal transmission is essential, if line interference lies inside the signal passband.
- To minimize microphonic effects, use of ferromagnetic cores with low magnetostriction and reduced remanent induction should be preferred.
- Since the metallic beam pipe has to be interrupted by an isolating gap, the mechanical design has to provide an external bypass for the image currents, taking into account the required bandwidth, determined by the beam pulse structure.
- With respect to the mechanical layout of the isolating gap and the specified vacuum, it is also important to decide on the type of vacuum seal at the connection between the gap and beam pipe.

2.4 The Cryogenic Current Comparator

The classification of beam intensity measuring devices in Table 2.1 shows that all properties required are fulfilled only by the beam transformer. With respect to the absolute calibration of more or less relative methods of beam intensity

measurements, such as the secondary electron emission monitor (SEM) or ionization chamber (IC), it becomes very clear from Fig. 2.1 that there is no overlap on the beam current transformer (BCT). To get an overlap in this intensity region, it is worthwhile to look for an extension of the beam transformer principle down to about 5×10^9 charged particles per second to cover the dc-current region from about 10 nA to some microamperes. Extension of dc-current measurements down to this region requires reduction of noise, which can be achieved by

- reduction of the Barkhausen noise. This has the consequence that modulation of the core material is not allowed.
- cooling down the detector to reduce the thermal noise. A cryogenic current comparator (CCC) was first developed as a standard for calibration of current measuring devices [98].
- Use of a superconducting quantum interference device (SQUID), in this case, a dc-SQUID as a zero indicator.

Figure 2.41 shows the principle of a CCC in a very simplified scheme. The magnetic flux of the two currents I_1 and I_2 is coupled to the SQUID, which measures the strength in units of the flux quantum $\phi_0 = h/2e = 2.07 \times 10^{-15} Vs = 2.07 \times 10^{-11}\,\mathrm{T\,cm^2}$. Of course, this simple arrangement cannot be adapted to measure nanoamperes current in the environment of accelerators. Time dependent magnetic stray fields would affect the measurement, preventing any SQUID operation. Furthermore, the signal would be a function of the beam location and of the coil geometry. The drawbacks have been overcome by changing to a toroidal geometry and introducing complex superconducting shields [99–101]. As a consequence, the design of a CCC becomes rather complex. The main part is a special liquid helium bathcryostat with a "warm hole" through which the beam goes. Figure 2.42 shows schematically the parts of a prototype, developed at GSI [31, 32] to measure

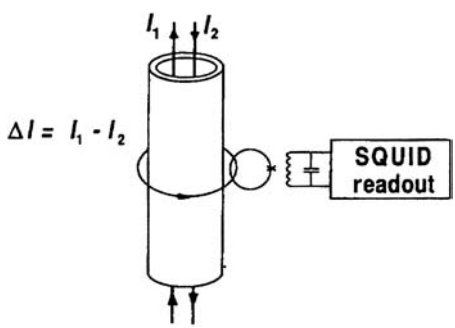

Fig. 2.41. Principle of dc-current measurement with a Cryogenic Current Comparator. (From: Peters, A., et al., *AIP* Conference Proceedings 451, (1998), p. 166. With permission)

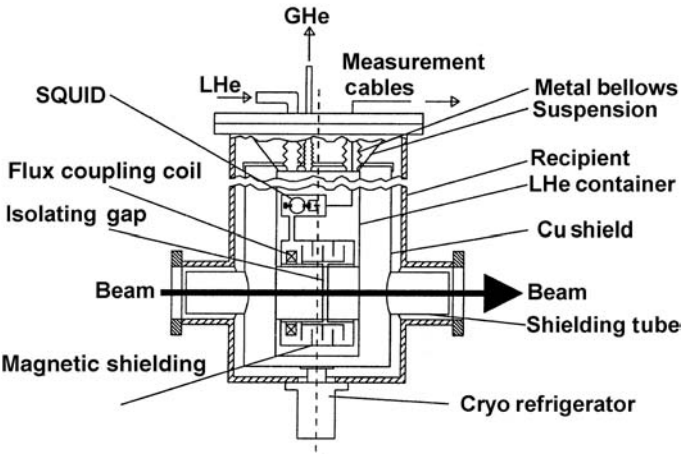

Fig. 2.42. The main parts of a Cryogenic Current Comparator (CCC) [31]

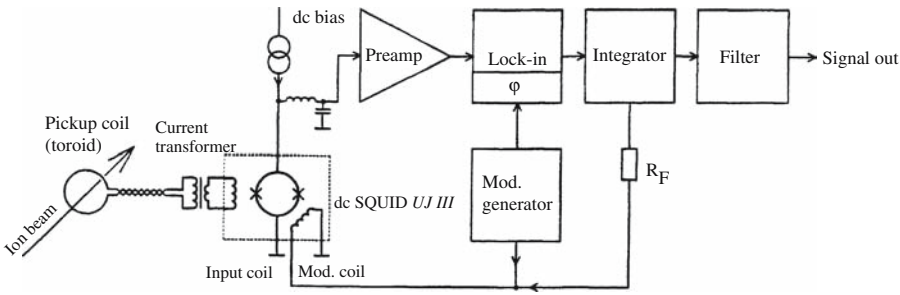

Fig. 2.43. Scheme of a dc-SQUID's electronics (From: Peters, A., et al., *AIP* Conference Proceedings 451, (1998), p. 170. With permission.)

the current during slow extraction from the SIS. The cryostat has a height of about 1.2 m and a diameter of about 0.66 m. The calculated attenuation factor for external background fields (nonazimuthal) has been calculated at about 2×10^{-9} using a meander-shaped shielding made from lead plates and tubes isolated by Teflon® foils. The toroid consists of a Vitrovac® [83] core with a single-turn input coil made from niobium. The scheme of the dc-SQUID electronics in shown in Fig. 2.43. First tests have given promising results:

- The minimum boil-off rate has been determined at 5.61 LHe/day.
- The current sensitivity has been measured at $181\,\mathrm{nA}\,/\,\phi_0$ which leads to an output signal of about 2.5 V/180 nA with a bandwidth of 500 Hz.
- The linearity error was $< 0.5\%$.
- After cooling down time of 100 h, the zero drift was below 0.5 mV/s.

- Depending on the measuring frequency, the current resolution was between 0.006 and 0.065 nA $/\sqrt{\text{Hz}}$.
- In the small signal mode, the cutoff frequency was found at about 10 kHz.

The system has been used to analyze the structure of extracted ion beams. It is planned [102] to improve the system in the following aspects:

- Extension of the dc-SQUID electronics to a higher dynamic range in connection with a higher slew rate and an increased bandwidth.
- Addition of an automatic offset correction.
- Replacement of the refrigerator used by a so-called pulse tube cooler to reduce the disturbances due to vibrations by about a factor of 1000.
- Development of a small and cheap helium liquefier.

Some of the proposed improvements are already realized during the development of a new high performance SQUID based measurement system for detection of dark currents generated by superconducting cavities. Such a system is in development for the TESLA project (X-FEL) at DESY Hamburg [103]. It uses the CCC principle. In the first test measurements, a current sensitivity of 167 nA$/\phi_0$ and a noise limited current resolution of 13 pA$/\sqrt{\text{Hz}}$ were achieved.

2.5 Secondary Electron Monitors

Referring to Fig. 2.1, the usable current ranges of the CCC and the secondary electron emission monitor (SEM) overlap each other in the nanoamperes region, which offers the possibility of covering this current range with SEMs, by performing the necessary absolute calibration of the SEMs with a CCC or a well-designed Faraday cup.

The principle of a SEM is shown in Fig. 2.44. An arrangement of thin foils (typical some micrometers) is passed by the beam. Secondary electrons are generated from the surfaces of the foils and are collected by appropriate voltages between the foils. The foils are slightly curved to increase the mechanical strength and reduce the microphonic noise signal. The accompanying electromagnetic field of the charged particle, passing the thin foils, interacts with the peripheral electrons of the foil surface atoms as well as with the free electrons of the metal. If the transfer of energy to the electrons is sufficiently high, they can be ejected from the atoms and escape from the surface. Emission from the foils takes place if the energy E_i transferred to the electrons fulfills the relation [104]

$$E_\mathrm{i} > E_\mathrm{r} + W \ , \tag{2.57}$$

where W is the work function of the foil. Assuming the process takes place at a depth Δx below the surface, then the remaining energy E_r, respectively, the range of electrons with that energy must be large enough to penetrate a foil of thickness Δx. Measurements of the foils with variable bias have shown that the

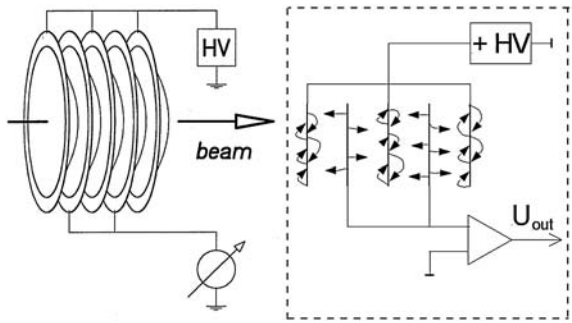

Fig. 2.44. Construction principle (left) and electrical connections (right) of a SEM. The foil is nearly pure aluminum ($\simeq$ 99.5 %). The foils have an active surface of $80 \times 80\,\mathrm{mm}^2$, a thickness of 100 µm, and a spacing of 3 mm

most probable energy of escaping electrons is in the range from 5−10 eV and Δx is of the order of about 100 Å [104]. There is a small (some %) contribution from other processes such as production of δ electrons due to Rutherford scattering or even from nuclear processes. Neglecting these processes, the secondary emission process has to be considered as a surface phenomenon, which is independent of foil thickness. To compare different foils with respect to their efficiency, a yield factor Y defined by

$$I_{\mathrm{sec}} = Y \frac{dE}{dx} i_{\mathrm{beam}} \tag{2.58}$$

has been introduced. Yields have been determined by experiments [105] with a precision of about 5%. The actual value of the yield is very much influenced by the surface structure of the material and depends on the production process as well as the cleaning procedures applied. Furthermore, yield Y can change considerably due to irradiation, which causes modification of the surface; and, in consequence changes the work function. Significant degeneration has been observed after irradiation with 450-MeV protons [106]. Since SEMs are used at CERN not only for beam intensity measurements but also for beam profile monitoring, the question of degeneration becomes of essential importance. The authors [106] investigated various materials and came to the results given in Table 2.7.

The percentages given in Table 2.7 are based on the definition of the secondary emission efficiency ρ_{e} defined by [104]

$$\rho_{\mathrm{e}} = \frac{N_{\mathrm{e}}}{N_{\mathrm{cp}}} \times 100\% \tag{2.59}$$

$$N_{\mathrm{e}} = \text{Number of emitted electrons} \tag{2.60}$$

$$N_{\mathrm{cp}} = \text{Number of incident charged particles.} \tag{2.61}$$

Table 2.7. Measured secondary emission efficiencies for 450-MeV protons dependent on the charge density. [106]. Note: The combination Al/Au stands for a gold-coated aluminum foil

	Ti	Al	Al/Au	Au
New	3.5%	6.8%	6.7%	$\sim 7.2\%$
10^{18} p/cm^2	3.6%	6.5%	7.0%	$\sim 7.1\%$
10^{20} p/cm^2	3.8%	4.0%	4.9%	

Comparing the definition of ρ_e with the definition of Y in (2.58), it becomes clear that the efficiency also depends on the charged particle properties and possibly on the incident angle of the charged particles. Considering the definition of Y, these dependencies have been included in the term dE/dx. Of course, both definitions can be related to each other. Taking the specifications of a typical ion beam facility for cancer therapy [107,108,110,114–117], typical beam intensities are 5×10^8 (oxygen ions) $<$ pps $< 4\times10^{10}$ (protons), assuming a spill of 1 s. Thus, to reach flux densities of the order of 10^{20} particles / cm^2 will take some years. But the situation changes if one considers high intensity machines with 10^{14} pps. In this case, SEM monitors have to be recalibrated within a suitable time.

2.6 Ionization Chambers

Figure 2.1 shows that ionization chambers (ICs) cover the medium intensity range with an overlap on diamond and scintillation counters at the low intensity side, which allows absolute calibration of the IC. Due to the big overlap with the SEM on the high intensity side, indirect absolute calibration against a beam transformer (BT) or cryogenic current comparator (CCC) via a SEM is possible. Figure 2.45 shows the scheme of an IC installed in the external high energy beam lines of the SIS. The ionization chamber of 5 mm length in the beam direction with two 1.5-µm Mylar® windows is filled with a mixture of 80% Ar and 20% CO_2 at $\sim$1 bar or less. To protect the high vacuum system of the beam transport system, the gas-filled IC is separated from the vacuum pipe by a metallic foil about 100 µm thick. The Mylar windows forming the electrodes have an active surface of $\simeq 64 \times 64\,\mathrm{mm}^2$ and are coated with 100 µg/cm^2 silver. Due to the energy loss of ions passing the detector, electrons are created in the gas volume. To separate the charges from the ionization of the gas, a high voltage between 500 and 2000 V is applied to one of the electrodes. The other electrode measures the secondary charges arising from the ionization using an appropriate current measuring device such as a current to voltage converter. The so-called proportional region is reached at about 500 V, corresponding to a collecting field of 1 kV/cm. Since gas amplification starts at about 10 kV/cm, there is no gas amplification and therefore

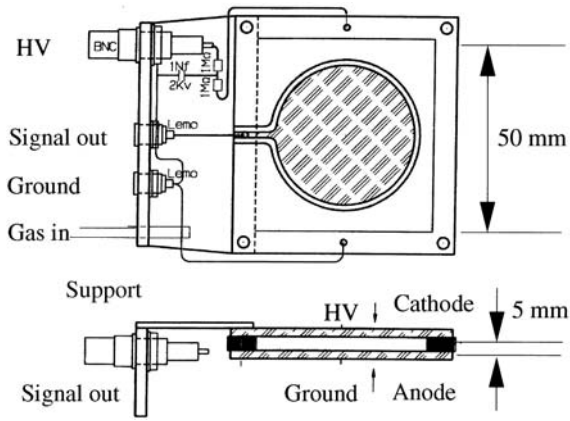

Fig. 2.45. Principle of an ionization chamber (IC) [118–120]

the output of the ionization chamber is proportional to the energy loss of the charged particles. Since the "target thickness" is about $1\,\mathrm{mg}/\mathrm{cm}^2$, the number of electrons created in the gas volume is of the order of 10^4/particle (considering heavy ions), and therefore secondary electrons from the two foils can be neglected. Furthermore, supposing that losses by recombination and escaping electrons can be neglected, the current output from the chamber should be calculable using energy loss data [121–124] and the well-known W values [125, 126] of gases ($\mathrm{Ar} \rightarrow W = 26.3\,\mathrm{eV}$, $\mathrm{CO_2} \rightarrow W = 33.0\,\mathrm{eV}$). The results from a series of calibration measurements are shown in Fig. 2.46 [105], using a particle counter (see next Sect.) for absolute calibration. The straight line, corresponding to $y = x$, shows good linearity and excellent agreement with the calculated values.

Referring to Fig. 2.1, the lower detection limit of an IC is determined by the minimum secondary current of about 1 pA. The upper limit is caused by a decrease in the efficiency due to recombination of the liberated electrons with the positive gas ions. Due to the risk of sparks, this decrease in efficiency cannot be compensated for by applying higher voltages. Because the collision frequency of electrons and ions is proportional to their concentration, it turns out that the recombination rate is $\sim$ to i^2_{beam} [120, 126]. For the ionization chamber of Fig. 2.45, the secondary current should be below $\sim 1\,\mu\mathrm{A}$ to avoid saturation effects. The corresponding upper limit for the primary current, as shown in Fig. 2.1, can be verified from calculations of the energy loss or from the values given in Fig. 2.46. To get a large upper threshold, gases with high electron affinity, such as O_2 and H_2O, should not be used. In particular, an IC should not contain any air. Another restriction concerns the maximum size of the active area. Due to electrostatic forces acting on the thin foil, the target thickness changes. Therefore, for good performance, the maximum size is limited to about $200 \times 200\,\mathrm{mm}$.

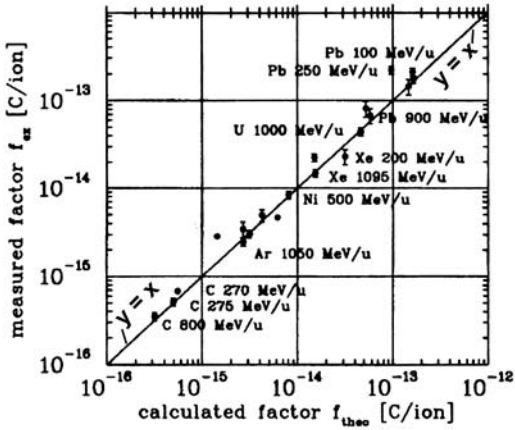

Fig. 2.46. Measured calibration factor in coulombs per ion for the ionization chamber versus calculated values. The straight line corresponding to $y = x$ shows excellent agreement. (From: Forck, P., Heeg, P., Peters, A., *AIP* Conference Proceeding 390, (1996), p. 425. With permission)

2.7 Particle Counting

Referring again to Fig. 2.1, there is a comfortable overlap between the IC and particle counting by scintillation counters or newly developed counters, using diamonds as detectors.

2.7.1 Scintillation Counters

If the counting rate is well below 10^6/s, scintillation counters are suitable for measuring particle fluxes precisely. Particles hitting and penetrating a scintillation material create fluorescent photons due to collisions with target electrons. These photons are guided by special light pipes to the photocathode of an electron multiplier, as shown schematically in Fig. 2.47. The amplified output signal of the photomultiplier tube(PMT) is shaped by a discriminator and fed to a scaler. The high gain of the PMT allows counting each single particle. Of course, there are some special requirements concerning the properties of the scintillating material as well as the material of the light guide used [126, 127]:

- The light output should be linear with respect to the energy loss in the material.
- To achieve a high counting rate, the so-called decay time should be as short as possible.
- The scintillator material has to be transparent to fluorescent light, and the index of refraction should be around $n \simeq 1.5$ for optimal further transmission through a light guide.

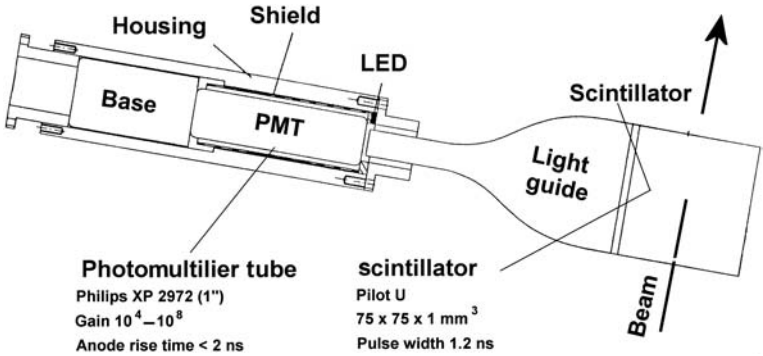

Fig. 2.47. Scheme of a plastic scintillator counter connected to a photomultiplier (PMT) via a plastic light guide [118]

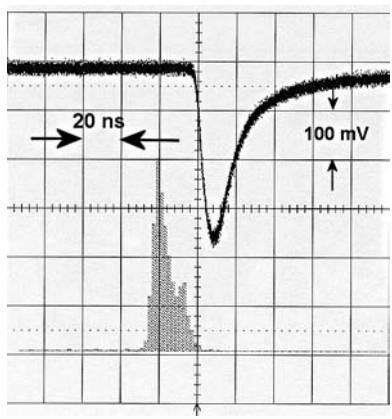

Fig. 2.48. Output pulses from a plastic scintillator recorded [120] from 300-MeV/u Kr ions. The lower trace shows the pulse-height distribution.

- The wavelength λ of the light generated should be in the range $350\,\text{nm} < \lambda < 500\,\text{nm}$ to achieve high efficiency at the photo-cathode, which converts the light into electrons.
- The material should be easy to form and available in sufficiently large sizes to cover larger beam sizes, too.
- Last, but not least, the material should be radiation hard for long lifetimes.

In most cases, plastic scintillators are used that have a decay time in the nanoseconds range. Typical output pulses are displayed in Fig. 2.48. Due to the dispersion in several 100-m long cables between detector and signal processing electronics, the pulses are broadened and show the typical shape of fast pulses transmitted over long dispersive cables. Figure 2.49 shows the combination of a particle scintillation counter and an ionization chamber of the type shown in

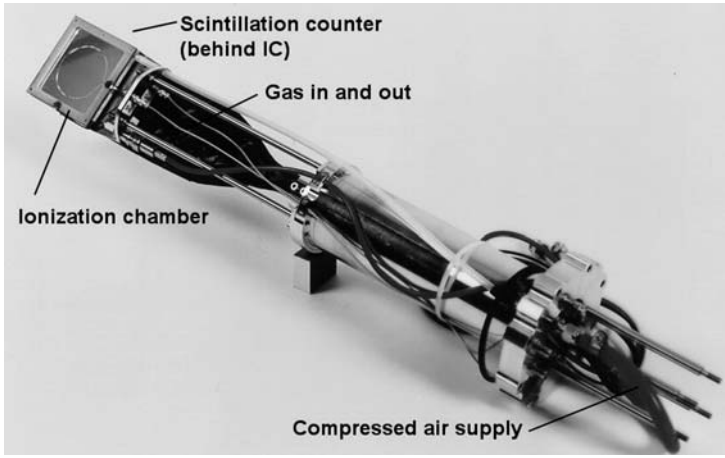

Fig. 2.49. Combination of an ionization chamber and a scintillation counter (arranged behind the IC, wraped in black tape to shield against stray light)

Fig. 2.45. The scintillation counter is arranged behind the ionization chamber, allowing absolute calibration of the IC at intensities below about 10^6/pps. To avoid damaging the scintillator by irradiation at higher beam intensities, the scintillator can be moved out of the beam by a separate compressed air drive.

2.7.2 The Scintillation Current Monitor

By collecting the light of a plastic scintillator, it is possible to readout the scintillation light intensity, operated in current mode by photodiodes [128–130]. In contrast to the pulse counting mode, in this mode, the dependence of the light output on the deposited energy becomes important. Calibration of such a scintillation current monitor (SCM) is simple because of the linear relation between energy loss and light output. The energy loss of incident ions can be calculated easily from tables of stopping powers. A series of measurements has been performed [131], using a round plastic scintillator sheet of NE108 surrounded by 15 photodiodes SFH100 to minimize the position dependence of the output by summing up the signals. For ions of C, Ne, Ar, Kr, Xe, and U in the energy range between 200 and 1800 MeV/u, the authors found good linearity up to 10^5/pps comparing the results with counted pulses.

2.7.3 Comparison of the SEM, IC, and SCM

Obviously, for this kind of beam intensity monitor, the detector response, defined as the output charge per incident ion, is a function of energy loss. This holds also in case of the SEM where the output signal is independent of the foil thickness. The response of these three types of monitors is shown in

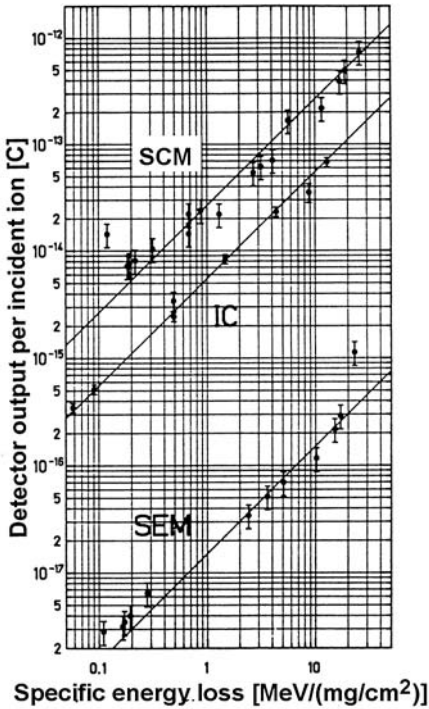

Fig. 2.50. Response of the SEM, IC, and SCM as a function of calculated specific energy loss. (From: Heeg, P., Peters, A. Strehl, P., *AIP* Conference Proceedings 333, 1994, p. 290. With permission)

Fig. 2.50 [131] as a function of the specific energy loss taken from tables given in [122]. The straight line through the data of the SEM results from a fit and corresponds to 23 electrons /[MeV/(mg/cm^2)].

2.7.4 Radiation-Hard Counters

An important drawback of scintillation counters and scintillation current monitors, based on organic plastic material, is their low radiation hardness. Much higher radiation hardness can be expected from inorganic crystals, often Ce-activated materials [126]. But these inorganic scintillators are rather difficult to produce in larger sizes because they are made of single crystals. Relatively new in the field of particle counting is the use of cadmium telluride (CdTe) photoconductor material and polycrystalline diamonds, manufactured by chemical vapor deposition (CVD). An ionizing particle passing such a detector produces electron–hole pairs along its track. The electrons and holes are

Table 2.8. The most important physical properties of diamond and silicon

Property [at 300K]	Diamond	Silicon
Thermal conductivity [W / mm K]	2	0.13
Resistivity [Ω cm]	$> 10^{13}$	2.3×10^5
Breakdown field [V/m]	10^7	3×10^5
Band gap [eV]	5.45	1.12
Electron mobility [cm^2/Vs]	2200	1500
Hole mobility [cm^2/Vs]	1600	600
Energy to remove an atom from the lattice [eV]	80	28
Energy to create an electron-hole pair [eV]	13	6

separated by an applied electric field. In combination with a modern broadband signal processing system, particles can be counted up to some 10^8/s.

CdTe Detectors

Radiation-hard polycrystalline CdTe detectors were newly developed at CERN [132] to monitor the luminosity of the large hadron collider (LHC). The material is often used as detector for nuclear radiation and in optoelectronics. Test measurements on prototype detectors, consisting of discs of polycrystalline CdTe discs about 16 mm in diameter are very promising for signal response, maximum counting rate, sensitivity, and radiation hardness [132]. The authors report the following results:

- Counting rates up to 40 MHz and even higher should be possible without problems from fast signals with rise times below 10 ns.
- A minimum ionizing particle produces more than 10.000 electrons, which, in combination with a fast 50-Ω preamplifier, results in an excellent signal-to-noise ratio.
- No significant loss in sensitivity and signal rise time has been observed after irradiation with 10^{15} neutrons/cm^2.

Diamond Detectors

The use of semiconductors having a p-n junction made mostly of silicon for particle counting is also well known from nuclear physics and leads also to applications in beam diagnostics [133–140]. The advantages of diamond become obvious by looking at the most relevant parameters of a CVD diamond, compared to silicon in Table 2.8.

The high energy of 80 eV needed to remove an atom from the diamond lattice results in excellent radiation hardness [141]. Since diamond produces very short pulses during the passage of a charged particle, counting them can be extended to counting rates up to some 10^8/s. The short pulses with a rise time

of about 100 ps are a consequence of the high mobility of electrons and holes in diamond. Of course, to preamplify and process such fast pulses, sophisticated broadband electronics is essential. Figure 2.51 shows a typical detector system [140, 142]. As marked by the gray box on the left-hand side, the coupling of the diamond detector to the broadband amplifier via a microstrip line and a 50-Ω coaxial transmission line allows location of the active electronics outside the area of irradiation. To process the very fast pulses from the detector to the broadband preamplifier without remarkable reflections back to the detector, the preamplifier input has to be carefully matched to the impedance of the transmission line. A series of Diamond Broadband Amplifier (DBA) systems has been developed and successively improved at GSI [140, 143, 144], using modern GaAs two- or three-stage monolithic modular integrated circuits (MMICs). The electrical properties of the newest version DBA-IV are given in Table 2.9 [143].

Beside the DBA-IV series, a modified version DBA-IV/R exists, where the input attenuator is omitted. Thus the input has no protection, but the input noise factor is reduced considerably. Referring to Table 2.9, the result is a change "Gain max." from +50 dB (DBA-IV) to +53 dB (DBA-IV/R), "Gain min." from +10 dB (DBA-IV) to +23 dB (DBA-IV/R), and a reduction of the noise factor from 5 dB (DBA-IV) to 3 dB (DBA-IV/R). In both systems, the gain can be remotely controlled by applying a control voltage from 0–5 V.

Spill Analysis

The excellent time resolution of diamond detectors is illustrated in Fig. 2.52. A particle spill analysis at the SIS has been performed with a CVD-diamond

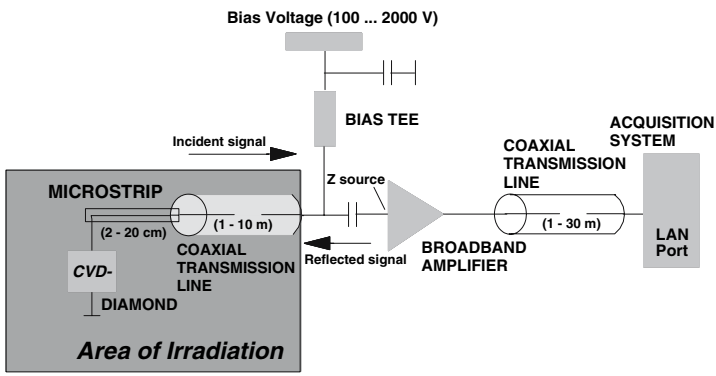

Fig. 2.51. Detector system arrangement showing the basic elements and analog signal transmission [142]

Table 2.9. Specifications of the DBA-IV amplifier series

Type	**DBA-IV**
Description	GaAs 3-stage MMIC, noninverting broadband amplifier
Bandwidth (−3dB)	0.003−2.0 GHz
Gain max.	+50 dB
Gain min.	+10 dB, Remote Controlled 0–5 V, dc
Input impedance	50Ω, SWR < 1.5
Output impedance	50Ω, SWR < 1.5
Noise fig. (input terminated)	5 dB
Max. input voltage at min. gain	$1\,V_{peak}$
Max. output power level	+18 dBm / $2V_{peak}$
Max. bias voltage	± 2000 V, No damage at detector input shorts
for detector	for −600/ + 100 V bias range
Power supply	+12 V, 150 mA
Dimensions	Length × Width × Height 95 mm × 47 mm × 25 mm
Connectors	rf in/out, bias: SMA, power/remote gain: LEMO 4-pole

330 µm thick [142]. The measurement with about 10^8 pps in the spill also demonstrates the extreme radiation hardness of the diamond detector. Plastic scintillators hit at this rate would be destroyed within a very short time.

The excellent time resolution is also demonstrated in a time of flight (TOF) reported in [140]. The energy of 200-MeV/u U^{73} single ions has been measured with a setup of two diamond detectors with a spacing of only 3 cm. A nine-strip diamond was used as the first detector, whereas the second detector, located 3 cm downstream, was a 16- pixel diamond. At 200 MeV/u, the time of flight is of the order of 175 ps, which could be recorded with a Tektronix TDS694C at 10 GS/s.

A further application of diamond counters for measurements in the longitudinal phase plane is discussed in Chap. 6, Sect. 7.

Beam Surveillance in Medical Applications (Veto-Counters)

As already mentioned, a relatively new application of high energy proton- and heavy ion beams is the treatment of cancer by irradiation [107, 108, 110, 114–117]. Two different beam delivery systems are in use:

- The passive system, where a broad uniform beam profile is generated by wobbling magnets in front of a collimator system, shaping the beam according to the projected area of the cancer. The beam energy and therefore the penetration depth of the particles is adjusted by so-called "range

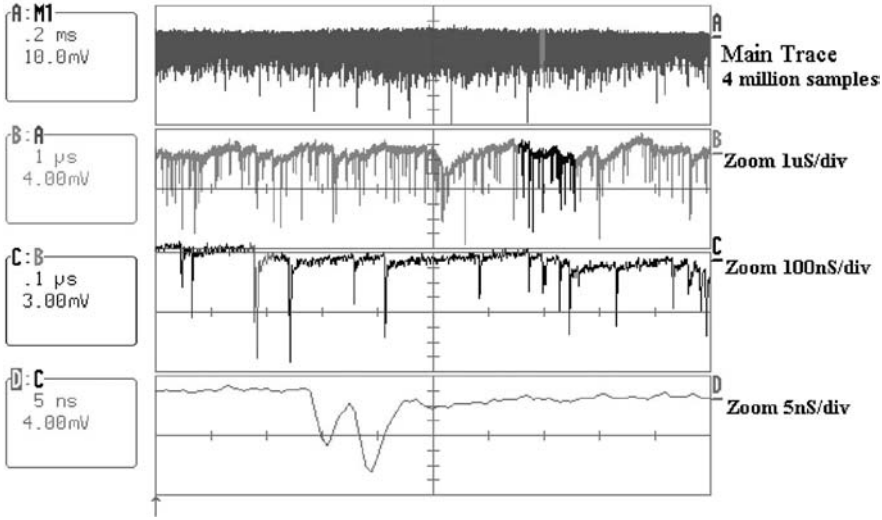

Fig. 2.52. Spill analysis at the SIS with a diamond detector [142]. Upper trace (main trace): Sampling diamond output signals with 2 GS/s. The measured data correspond to a spill with about 10^8 pps. The lower traces correspond to increasing zooming. On the lowest trace, the zoom shows single particles

shifters." The range shifters may consist of a set of solid plates or more complex devices which are often used in material research by irradiation. Figures 2.53 and 2.54 show two examples provided for well-defined attenuation of a particle beam.

- The active system uses a beam of very small transverse dimensions (typical 5 mm FWHM), which is moved by fast vertical and horizontal scanning systems [113] over the projected area of the cancer. Systems applying three-dimensional raster scanning techniques adapt the required penetration depth by active, computer-controlled variation of the beam energy [110].

It is evident that the application in radiotherapy requires an extremely stable beam with respect to beam profile, beam position, beam intensity, and beam energy. A halo detector was designed for the surveillance of beam stability during irradiation of patients [109, 110]. The so-called veto-counter system is based on four single particle detectors such as scintillation counters or diamond detectors, arranged at the edges of the beam. A system based on a four-segment ionization chamber has been developed for the PROSCAN medical facility at the PSI [111], and the design and construction of a coronagraph for observation of the beam halo and tail are reported in [112]. Figure 2.55 shows schematically the proposed GSI arrangement of the detectors, signal processing, and storing of counts, measured in specific time segments.

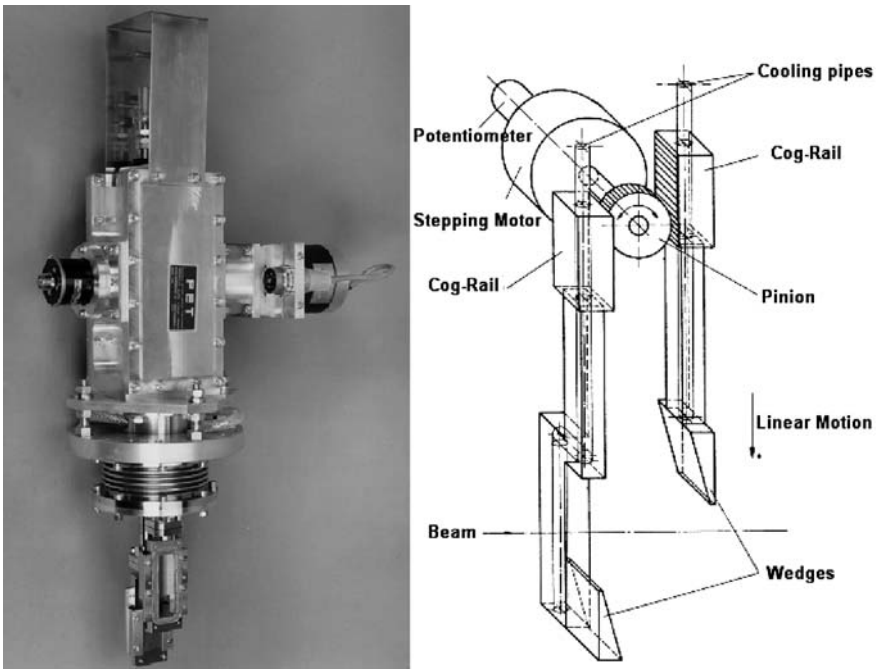

Fig. 2.53. Left: picture of a "range shifter" of the wedge type [33]. Right: working principle of the device

Assuming beam profiles of Gaussian shape, sufficient sensitivity with respect to a change in the relevant beam parameters can be achieved, if the detectors are located at the edge of the beam. Due to the high radiation hardness of diamond counters discussed, this type of detector should be preferred for this application. To derive fast, potential free interlock signals, the data can be evaluated from various viewpoints, as shown schematically in Fig. 2.56. Taking advantage of modern PCI-systems data processing as well as data evaluation, according to Figs. 2.55 and 2.56, can consist of a mix between hardware and software implementation. Assuming beam profiles with a Gaussian intensity distribution in both transverse directions, the expected counting rates are easily derived, if the relevant beam parameters are known. But, finally, the positions of the detectors as well as the specification of reference values (see Fig. 2.56) should be determined experimentally before irradiation of patients takes place. In routine operation of a machine dedicated to radiotherapeutic applications, approved data sets should be available from a data bank. To give an example of expected system performance, let us assume the following beam parameters:

Beam dimensions in the x-direction (horizontal): $\sigma_{\mathrm{x}} = 4.19 \rightarrow R_{\mathrm{x}}(10\%) \simeq 9\,\mathrm{mm}$

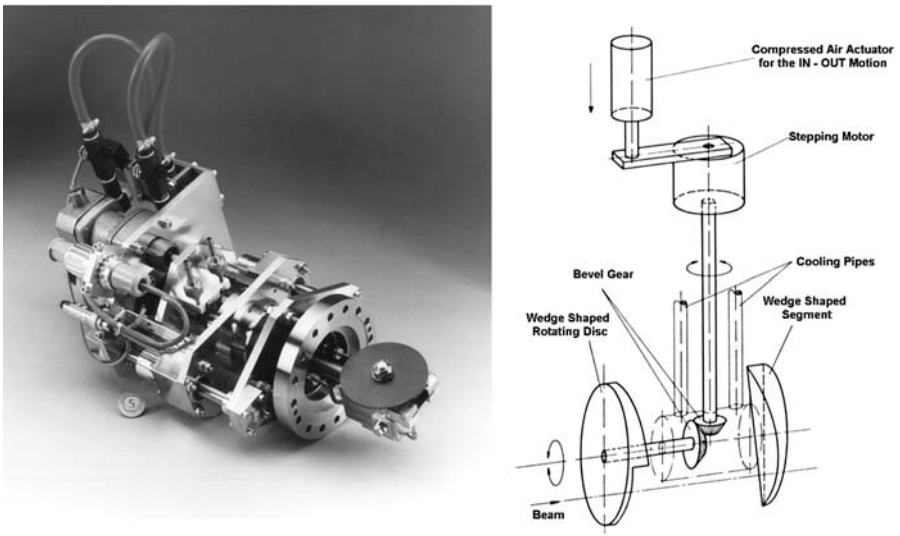

Fig. 2.54. Left: "range shifter" on the base of two rotating discs [33]. Right: Working principle of the device. Possible variation in target thickness 0.25–5 mm, target material graphite or others, maximum beam power loss 500 W/disc, maximum revolution frequency 5 Hz, computer controlled

Beam dimensions in the y-direction (vertical): $\sigma_\mathrm{y} = 2.33 \rightarrow R_\mathrm{y}(10\%) \simeq 5\,\mathrm{mm}$
Number of C^{6+} ions delivered to the patient: $N = 10^8/\,\mathrm{spill}$
Proposed counts on one of the four veto counters: $N_0 = 2000/\mathrm{spill}$

The counting rates can be calculated from the two-dimensional Gaussian distribution:

$$F(x, a, \sigma_\mathrm{x}, y, b, \sigma_\mathrm{y}) = \frac{1}{2\pi\sigma_\mathrm{x}\sigma_\mathrm{y}} e^{-\frac{1}{2}\left[\frac{(x-a)^2}{\sigma_\mathrm{x}^2} + \frac{(y-b)^2}{\sigma_\mathrm{y}^2}\right]} \tag{2.62}$$

with x, y as the position of the veto counter (beam sided edge of the detector) and a, b as the displacement of the beam from the position $x = 0$, $y = 0$. The proposed reference counts of $N_0 = 2000/\mathrm{spill}$ lead to $x_0 \simeq 17.2\,\mathrm{mm}$ and $y_0 \simeq 9.6\,\mathrm{mm}$. Figure 2.57 gives the expected counts/spill dependent on beam displacement. From the derivation of (2.62), the change in counts/spill for $x_0 = 17.2\,\mathrm{mm}$ and $y_0 = 9.6\,\mathrm{mm}$ comes out to about 207 counts per 1/10 mm beam displacement in the x-direction. Due to the smaller vertical dimensions of the beam, the corresponding change is about 372 counts for the y-direction. The sensitivity which can be achieved becomes clearer from Fig. 2.58 that shows the change in counts/spill for sum and difference values.

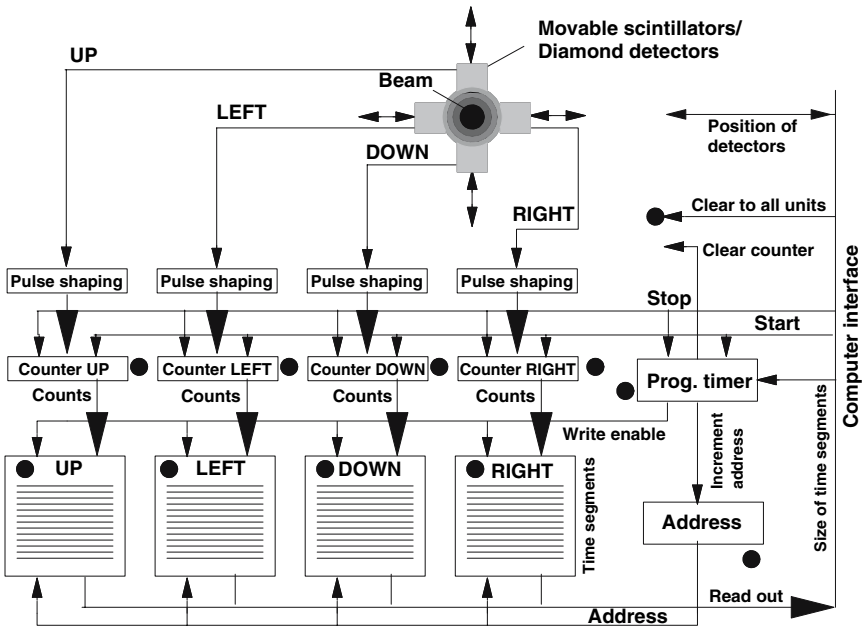

Fig. 2.55. Scheme of a veto-counter system provided for surveillance of beams in radiotherapeutic applications

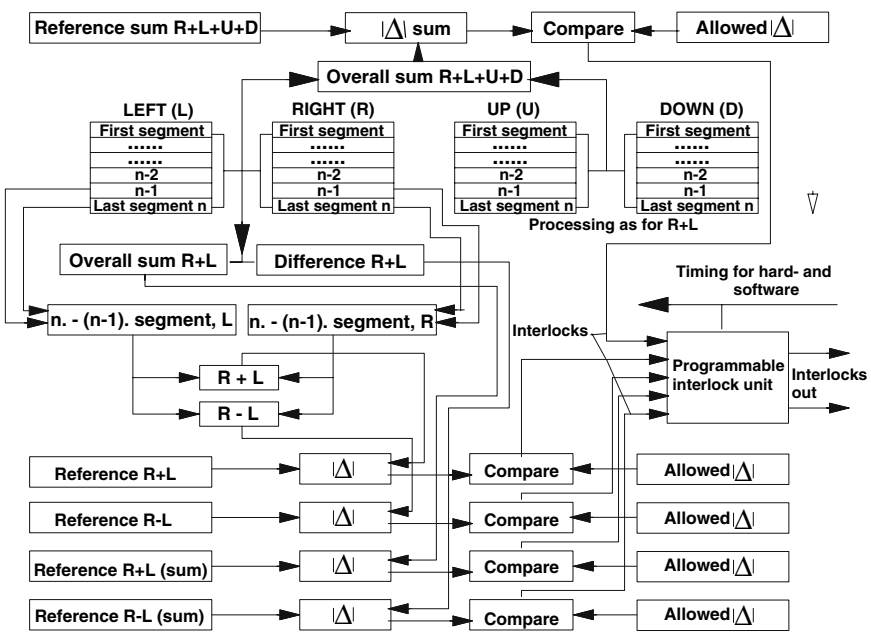

Fig. 2.56. Possible evaluation of data collected with four veto counters to derive interlock signals relevant beam parameters change during irradiation of patients

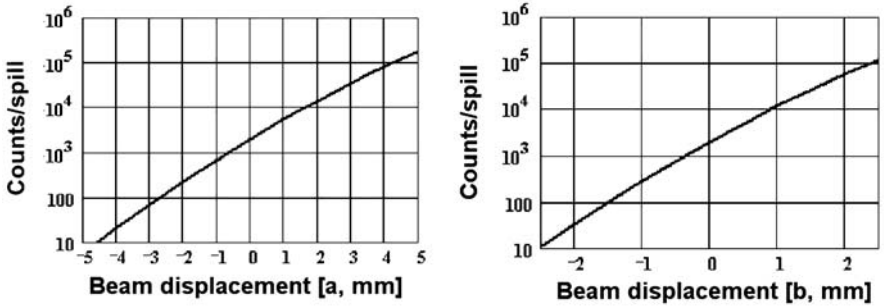

Fig. 2.57. Expected counts/spill for one veto counter dependent on beam displacement. The horizontal veto counter (left diagram) is positioned at $x_0 = 17.2\,\text{mm}$, the vertical one is positioned at $y_0 = 9.6\,\text{mm}$

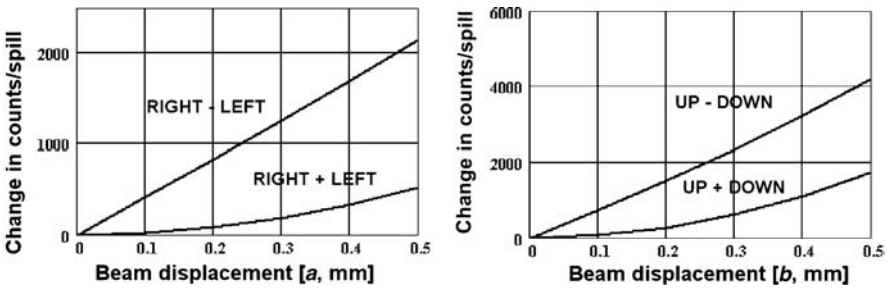

Fig. 2.58. Expected change in counts/spill for sum and difference values dependent on beam displacement. The horizontal veto counter (left diagram) is positioned at $x_0 = 17.2\,\text{mm}$, the vertical one is positioned at $y_0 = 9.6\,\text{mm}$

Conclusion

The example shows that the use of veto counters for beam surveillance is a nearly non-destructive, very sensitive possibility for monitoring the stability of a particle beam for changes in profile, intensity, and position. Taking advantage of the radiation hardness of diamond detectors, counting rates of the order of some thousands per spill are moderate for the lifetime of a diamond detector.

3

Thermal Aspects

Many diagnostic devices such as Faraday cups, simple beam stoppers, slit systems, scrapers, wire scanners, profile grids, and stripping foils stop a particle beam completely or lead to partial interception. Therefore, in the worst case, the total beam power has to be handled by a device hit by the beam. For highly intense beams, this can even result in destroying devices, if one does not take care of the thermal effects. Also loss of a beam, which is one of the most severe concerns in the operation of high intensity accelerators requires attention. Lost particles produce radioactivity in construction materials, sputter their surfaces and, in the worst case, can melt holes in the walls of beam pipes, in thin bellows, or in synchrotron magnet chambers. To avoid such problems, estimation and calculation of thermal effects is essential for the design and use of beam intercepting devices.

3.1 Relevant Formulas

When a beam is completely stopped, the beam power is given by

$$P = \frac{\mathrm{d}W}{\mathrm{d}t} = \frac{N}{\delta t} AW \ , \tag{3.1}$$

where $N/\delta t$ is the number of impinging particles per time interval δt, A is the mass number of the ions and W[eV/u] is their kinetic energy. $N/\delta t$ can be replaced by $i/\zeta e$, with $e = 1.602$ As, ζ as the charge of the ions. As briefly discussed in the introduction, i is related to the time interval δt, respectively, pulse length. Replacing $N/\delta t$ in (3.1) by $i/\zeta e$, one obtains for the beam power during the time interval δt,

$$P = \frac{A}{\zeta} \frac{i}{e} W \tag{3.2}$$

$$P[kW] = \frac{A}{\zeta} i\,[\mathrm{mA}] W\,[\mathrm{MeV/u}] \ . \tag{3.3}$$

If the beam is pulsed with a macropulse length of T_p, the deposited beam energy per pulse is

$$W_\mathrm{p} = P\delta t = \frac{A}{\zeta}\frac{i}{e}W \quad \rightarrow \tag{3.4}$$

$$W_\mathrm{p}\,[Ws] = \frac{A}{\zeta} i\,[\mathrm{mA}]\,T_\mathrm{p}\,[\mathrm{ms}]\,W\,[\mathrm{MeV/u}]\ . \tag{3.5}$$

Thermal effects, efficiency of cooling, and maximum ratings for materials are related to the basic laws of heat transfer [145–149].

For simple estimations of thermal effects [150, 151], the required energy ΔW_V to melt a given volume V is of interest. ΔW_V has to be calculated in two steps:

$$\Delta W_\mathrm{V} = \Delta W_\mathrm{h} + \Delta W_\mathrm{m} \tag{3.6}$$

$$\Delta W_\mathrm{h} = mc_\mathrm{p}(T_\mathrm{m} - T_0) = \rho V c_\mathrm{p}(T_\mathrm{m} - T_0) \tag{3.7}$$

$$\Delta W_\mathrm{m} = mw_\mathrm{m} = \rho V\, w_\mathrm{m}\ , \tag{3.8}$$

where c_p is the specific heat, ρ is the mass density, w_m is the heat of fusion, T_0 is the environment temperature, and T_m is the melting temperature.

Thermal effects in materials depend very much on

- the thermal characteristics of the stopping material;
- the duty-factor of the beam;
- the size of the beam; and
- the penetration depth p_d of the impinging particles, which in turn depends on the kind of ions and their energy.

Especially for dependence on the duty factor, a classification distinguishing between dc-beams and intense pulsed beams has proven useful.

For dc-beams and beams with a high duty cycle, one has to consider the stationary temperature distribution $T(x, y, z)$ given by the solution of

$$\Delta T(x, y, z) = -\frac{1}{\lambda} P_\mathrm{V}(x, y, z)\ , \tag{3.9}$$

where Δ is the Laplace operator ($\Delta = d^2/dx^2 + d^2/dy^2 + d^2/dz^2$), $\lambda[\mathrm{W/(mm\,K)}]$ is the heat conductivity, and $P_\mathrm{V}(x, y, z) = \mathrm{d}W_\mathrm{p}(x, y, z)/dt$ (e.g., in $[\mathrm{W/mm^3}]$) is the power deposited in the volume element V.

For intense pulsed beams, one has to take the time dependence into account, which means solving the partial equation of heat transfer:

$$\frac{\partial T}{\partial t} = \frac{\lambda}{c\rho}\Delta T(x, y, z) + \frac{1}{c\rho} P_\mathrm{V}(x, y, z)\ . \tag{3.10}$$

Here $\lambda/c\rho$ describes the time dependence of heat transfer; the larger values result in faster transfer.

Table 3.1. Relevant thermal characteristics of materials

	Z	A	ρ	λ	T_m	w_m	c_p25	c_p2000	W_mg	W_mm
Be	4	9	1.85	0.20	1278	1350	1.83	3.28	4213	7.79
C∗	6	12	2.25	0.09	3650	–	0.71	1	3579	8.05
Mg	12	24	1.74	0.16	649	362	1.02	1.34	1034	1.80
Al	13	27	2.7	0.24	660	388	0.90	1.09	983	2.65
Si	14	28	2.34	0.1	1410	1650	0.70	0.91	2727	6.38
Ti	22	48	4.5	0.02	1660	365	0.52	0.79	1401	6.31
V	23	51	6.1	0.31	1890	345	0.49	0.87	1587	9.68
Cr	24	52	7.1	0.09	1857	260	0.52	0.94	1567	11.1
Fe	26	56	7.87	0.08	1535	272	0.44	0.83	1163	9.15
Cu	29	64	8.96	0.37	1083	205	0.39	0.50	645	5.78
Zr	40	91	6.49	0.02	1852	211	0.28	0.35	783	5.08
Mo	42	96	10.2	0.14	2617	290	0.25	0.37	1176	12.0
Ag	47	108	10.5	0.43	962	103	0.24	0.29	337	3.54
Ta	73	181	16.6	0.06	2996	174	0.14	0.17	660	11.0
W	74	183	19.3	0.17	3410	192	0.13	0.17	751	14.5
Au	79	197	19.3	0.32	1064	64.9	0.13	0.15	205	3.96
Pb	82	208	11.4	0.04	328	23.2	0.16	0.14	71.7	0.81

In Table 3.1, the relevant characteristics of some typical construction materials are listed. The symbol C* stands for an isotropic graphite composition. The dimensions in the table are chosen from a practical point of view: ρ[g/cm^3], λ[W/(mm K)], T_m[C], w_m[Ws/g], c_{p25}, c_{p2000}[Ws/(g K], W_mg[Ws/g], W_mm[Ws/mm^3]. The values in the last two columns correspond to the sum of required energies for melting 1g (W_mg), respectively, 1mm^3 (W_mm) according to (3.6–3.8), inserting a mean value of c_p25 (specific heat at 25°C) and c_p2000 (specific heat at 2000°C). The results hold for $T_0 = 20$°C.

3.2 DC-Beams

The stationary temperature distribution for dc-beams and beams with a high duty factor is determined by the solution of (3.9). In principle, there are three possibilities:

- an analytical solution for the given geometry, considering the deposition of power by the beam $P_\mathrm{V}(x, y, z)$,
- a numerical solution applying the finite-element (FE) method (see, e.g., [152–158]),
- a numerical solution by the finite-difference (FD) method.

Due to the complex formulas of energy loss in matter, analytical solutions exist only in some very special cases. Many FE programs exist for the solution of differential equations of the kind discussed. However, in the special case under consideration, the generation of finite elements is time-consuming because

the deposited power/element has to be calculated or taken from known tables of energy loss. The FD method also requires complex calculations but offers the physicists and engineers the possibility of implementing their own programs, adapted to the very special problem of energy loss in matter. Various algorithms applying the FD method to solve the Poisson equation (3.9) are described in the literature of numerical mathematics (see, e.g., [159–161]). Nevertheless, the problem requires special treatment with respect to

- the size of the beam spot in comparison to the geometrical dimensions and shape of the stopping device;
- the intensity distribution within the transverse coordinates;
- the very strong varying energy loss along the path of the particles in the material, especially the enhanced "Bragg peak";
- increase of the beam spot size along the path due to multiple scattering; and
- use of various materials in the composition of a stopping device.

To implement a numerical program, the following steps are essential:

- Calculation of the maximum dc-beam power to estimate if cooling of the intercepting device becomes necessary. A maximum of ≈100 W dc-power or even below that value may be considered critical in this respect, taking into account that inside a vacuum system, no cooling by convective heat transfer takes place and heat conduction is very low due to the electrical insulation.

  Remark: It's evident that for beams with a high duty factor, the average power $P_{\mathrm{av}} = P_{\mathrm{pulse}} \times \mathrm{duty}$ has to be considered. This also holds for the calculation of the P_{V} values in (3.9).
- Selection of the stopping material, whereby the choice can be influenced by
  - Geometrical constraints, requiring, for example, a material with a high Z value to minimize the penetration depth p_{d} and, therefore the length of the device in the beam direction. The penetration depth can be determined from available "Range and Stopping Power Tables" ([121–124]).
  - The requirement to minimize the production of dangerous radiation, which would give preference to a low Z value of the stopping material.
  - The necessity for high heat conductivity λ, which for highly intense beams is the dominating criterion.
- Determination of the specific energy loss along the longitudinal z-coordinate for the selected material. Figures 3.1 and 3.2 show an example of 350-MeV/u carbon ions stopped in a tungsten block.
- Definition of parameters, fixation of geometrical dimensions and materials, provided for the final construction design in a schematic layout, as shown, for example, in Fig. 3.3. Here a 350-MeV/u carbon beam is stopped in a

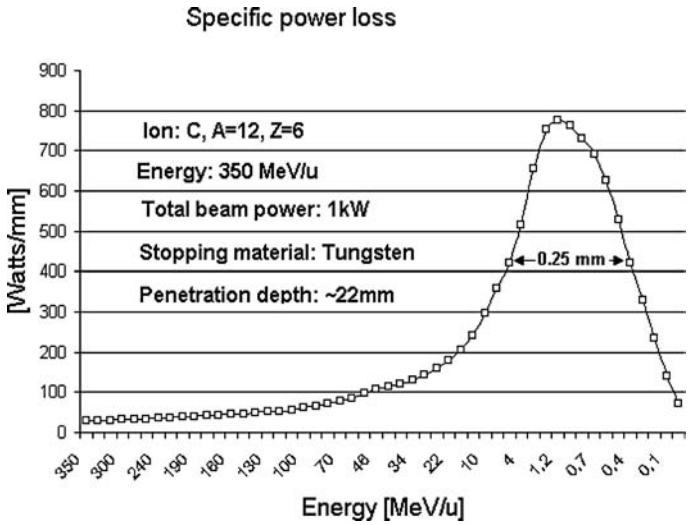

Fig. 3.1. Example of power loss calculation

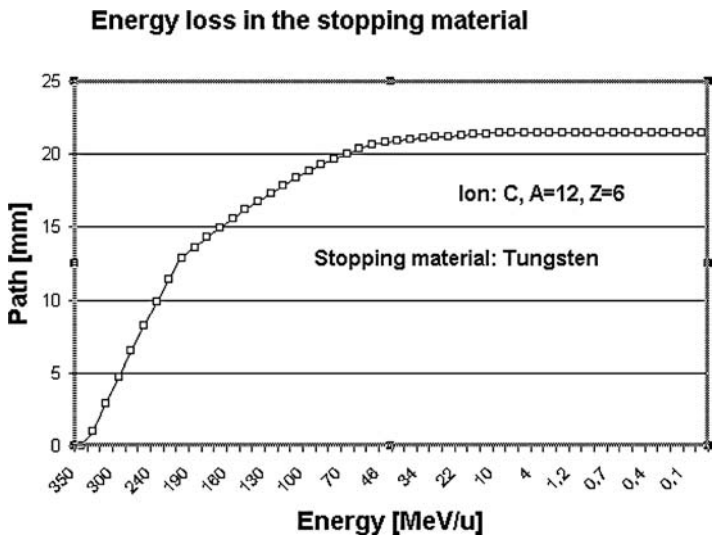

Fig. 3.2. Energy degradation in a tungsten stopper

block of tungsten with a backing of a cooled copper body, which requires special attention at the boundary between two materials having different λ values. Because the stopper has rotational symmetry, only two indexes I and J are required. As becomes very clear from the example shown in Figs. 3.1 and 3.2, the extension of the "Bragg peak" can be very small

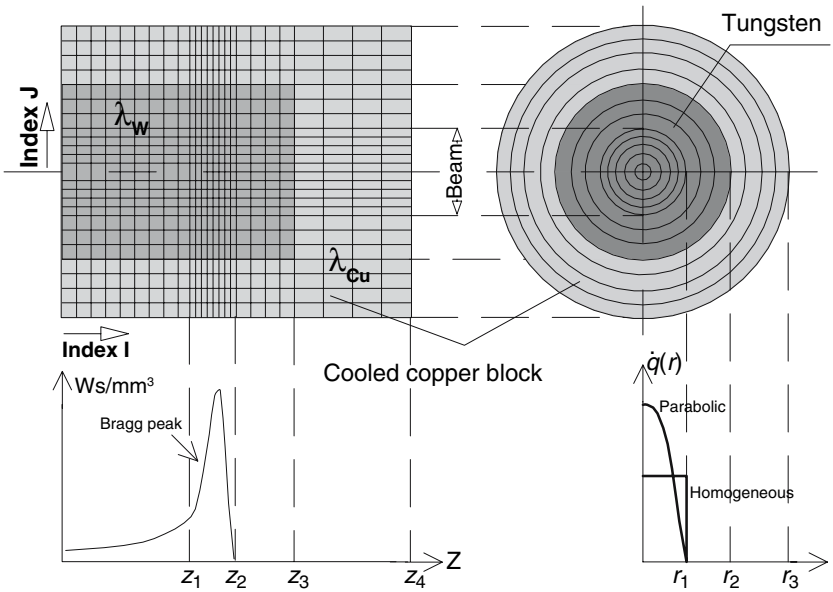

Fig. 3.3. Example for the numerical solution of equation 3.9

in comparison to the dimension of the stopper along the z-axis. Therefore, it is useful to choose a mesh having a variable width along the axial coordinate. Assuming, for example, 10-mesh lines in the z-direction over the Bragg peak would require a spacing of about 0.05 mm, which results in more than 450 lines over the total length of about 22 mm. Considering the relatively plain curve of power loss in the higher energy region, such a tight spacing is absolutely unnecessary. Variable spacing of mesh lines should also be implemented, if the beam spot size is small versus the radial stopper dimensions. Of course, this complicates the equations with respect to

- the necessary conversion of the power loss data to the mesh points,
- the determination of the coefficients in the numerical equations given below in (3.12) and (3.19).

On the other hand, it saves memory and diminishes the time of iteration. This becomes even more important considering geometries, that require at least three indexes.

- Evaluation of $P_{\mathrm{V}}(x, y, z)$ defined in (3.9) as the power loss per volume at the mesh points, which consists of the following steps:
  - Conversion of the calculated power loss along the path to the z-coordinate points which coincide with the mesh points. This is necessary because the tables with stopping power data are given dependent

on the energy and not just exactly at the z-coordinates of the mesh points. (See the example given in Figs. 3.1 and 3.2). The conversion results in one-dimensional power losses for example in [watts/mm] at each mesh point with the coordinates $z,\ x = 0,\ y = 0$.
  - Estimation of the contribution of multiple scattering along the path within the stopping material, which increases the transverse size of the beam and as a consequence reduces the specific power loss (watts/mm^3) along the path.
  - Distribution of one-dimensional power losses over the cross section of the beam at the mesh points, taking the effect of multiple scattering into account and assuming an appropriate intensity distribution over the transverse coordinates.
- Fixing of all boundary conditions to perform the numerical solution of (3.9) by the FD method.

Further steps, the required formulas, the boundary conditions, and the iteration algorithm for this numerical calculation are discussed referring to the example of Fig. 3.3.

3.2.1 Determination of the Coefficients

The Laplace operator Δ in cylindrical coordinates is given by

$$\Delta = \frac{\partial^2}{\partial z^2} + \frac{\partial^2}{\partial r^2} + \frac{1}{r}\frac{\partial}{\partial r} + \frac{1}{r^2}\frac{\partial^2}{\partial \varphi^2}\ . \tag{3.11}$$

Due to the rotational symmetry of the example considered the last term on the right-hand side of (3.11) can be dropped. Referring to Fig. 3.4 and applying a Taylor series expansion, the second derivatives are obtained:

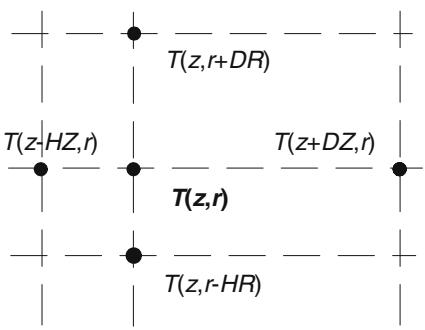

Fig. 3.4. Relevant points for the determination of $T(z, r)$

$$\frac{\partial^2}{\partial z^2}T(z) = A_{2z}T(z+DZ) + B_{2z}T(z-HZ) + C_{2z}T(z) \tag{3.12}$$

$$A_{2z} = \frac{2}{DZ(DZ+HZ)} \tag{3.13}$$

$$B_{2z} = \frac{2}{HZ(HZ+DZ)} \tag{3.14}$$

$$C_{2z} = -\frac{2}{DZ\,HZ}\ . \tag{3.15}$$

From $T''(z) = \frac{\partial^2}{\partial z^2}T(z)$, the second derivative $T''(r) = \frac{\partial^2}{\partial r^2}T(r)$ follows immediately by substitution of $DZ \to DR$ and $HZ \to HR$ in (3.12–3.15). The first derivative $\partial/\partial r$ can be expressed in terms of T and T'' from the Taylor series:

$$T(r+DR) + T(r) = DR\,T'(r) + \frac{DR^2}{2}T''(r) \tag{3.16}$$

$$T(r-DR) - T(r) = -HR\,T'(r) + \frac{HR^2}{2}T''(r)\ . \tag{3.17}$$

The result is

$$T'(r) = \frac{\partial}{\partial r}T(r) = \frac{T(r+DR) - T(r-HR)}{DR+HR} - \frac{DR-HR}{2}T''(r)\ . \tag{3.18}$$

Using (3.18), the term $\frac{1}{r}\frac{\partial}{\partial r}$ of the Laplace operator in (3.11) leads to

$$\frac{1}{r}\frac{\partial}{\partial r}T(r) = A_{1r}T(r+DR) + B_{1r}T(r-HR) + C_{1r}T(r) \tag{3.19}$$

$$A_{1r} = \frac{1}{DR+HR}\frac{HR}{DR} \tag{3.20}$$

$$B_{1r} = \frac{-1}{DR+HR}\frac{DR}{HR} \tag{3.21}$$

$$C_{1r} = \frac{DR-HR}{DR\,HR}\ . \tag{3.22}$$

Referring to Fig. 3.3, (3.9) can be solved numerically by successive iteration of all possible ensembles of five points in the mesh. Of course, this does not include points located at the borders. Furthermore, mesh points located on the border between materials with different λ values require special treatment. Since the mesh points at $T(z, r+DR), \ldots$ in a numerical computer program are represented by $T(I, J+1)$, $T(I, J-1)$, $T(I+1, J)$, $T(I-1, J)$, and $T(I, J)$, this notation is used in the following. Therefore, the coordinates $z_1 \ldots z_4$ and $r_1 \ldots r_3$ can be represented by the indexes $I_1 \ldots I_4$ and $J_1 \ldots J_3$.

3.2.2 Estimation of Multiple Scattering

Before determination of the $P_V(z, r)$ values, respectively, $P(I, J)$ in the notation of the mesh coordinates, the effect of multiple scattering on the beam spot

size along the path in the stopping material should be estimated. This can reduce the specific thermal load especially at the end of the path, where the Bragg peak leads to a high specific power loss. To take this into account, an estimate of the root-mean-square (rms) scattering angle $\langle\theta\rangle$ given by Rossi [162] is useful:

$$\langle\theta\rangle = \frac{21\,MeV}{\beta pc}\sqrt{\frac{\rho\Delta x}{X_0}}\,, \tag{3.23}$$

where p is the momentum of the impinging particles and $\rho\Delta x/X_0$ is the thickness in units of the so-called radiation length, also given in [162]:

$$X_0[\mathrm{g/cm^2}] = \frac{A}{4\alpha\, Z(Z+1)\, r_\mathrm{e}^2\, N_\mathrm{A} \ln(183\sqrt[3]{Z})} = \frac{716.4\,A}{Z(Z+1)\ln(183\sqrt[3]{Z})}, \tag{3.24}$$

with the fine structure constant $\alpha = 1/137.04$, the classical electron radius $r_\mathrm{e} = 2.82 \times 10^{-13}\,\mathrm{cm}$, and Avogadro's number $N_\mathrm{A} = 6.022 \times 10^{23}\,\mathrm{mole}^{-1}$.

Although the interested reader will find various definitions of the radiation length in the literature (for a discussion see [53]), the differences are in general small and not relevant in the connection considered. To take corrections to (3.24) into account, a table given in reference [53] is recommended. Referring to Fig. 3.2, estimated the multiple scattering effect on the beam spot size can be as follows:

- Starting with the initial energy E_0 ($E_0 = 350\,\mathrm{MeV}$ in the example) $(\beta pc)_\mathrm{n}$ can be determined for each energy value E_n along the abscissa. The target thickness Δz relevant for the calculation of $\langle\theta\rangle_\mathrm{n}$ is given by the path difference. In Fig. 3.2, Δz can be calculated from the ordinates belonging to E_n and E_{n+1}.
- Then, approximating $\Delta z \cos(\langle\theta\rangle_\mathrm{n}) \approx \Delta z$, the deviation of the particle from a straight line due to multiple scattering in each small target section is $\Delta r_\mathrm{n} = \Delta z \sin(\langle\theta\rangle_\mathrm{n})$. Of course, the Δr_n of successive sections have to be summed up, which results in a function $\Delta r(z_\mathrm{n})$.
- In general, the z_n-values do not coincide with the mesh points. Therefore, one needs a continuous function $\Delta r(z)$. Experience has shown that an approximation can be performed by

$$\Delta r(z) = Az + Bz^2 + Cz^3\,, \tag{3.25}$$

  applying a least squares fit to $\Delta r(z_\mathrm{n})$ for the determination of A, B, C. In the example of Figs. 3.1, 3.2, and 3.3 discussed, the maximum Δr value at the end of the path 0.16 mm, which can be neglected. But considering, for example, 350-MeV protons stopped in tungsten, the penetration depth p_d goes up to about 64.5 mm and Δr max sums up to about 9.5 mm, reducing the specific thermal load considerably.

3.2.3 Determination of the $P_V(z, r)$ Values

The calculated specific power loss (see, e.g., Fig. 3.1) to the mesh points, located along the $J = 0$ line, can be converted by applying an appropriate spline fit or similar fit to the data and interpolation to the points located on the mesh. This results in a vector $P(z_I)$, respectively, $P(I)$ using the indexes I along the z-axis with $r = 0$. The dimension is in [watts/mm]. Due to multiple scattering, the beam spot size increases along the path in the stopping material. Referring to (3.25), this can be taken into account by a quadratic addition as follows:

$$R_I = \sqrt{R_{beam}^2 + \Delta r(z_I)^2} \; . \tag{3.26}$$

Since the mesh width in the z-coordinate can be variable, as shown in Fig. 3.3, one has to be careful in determining the correct z_I and I values.

Experience has shown that a parabolic intensity distribution over the radial coordinate is a good and simple approach. Assuming a mesh width of Δr_1 in the region $0 \le r \le R_I + \delta r$, the vector $P(I)$ can converted to the array $P(I, J)$ according to

$$P(I, J) = \frac{2P(I)}{\pi R_I^2} \left[1 - \left(\frac{J \Delta r_1}{R_I} \right)^2 \right] \tag{3.27}$$

$$P(I, J) = 0, \text{ if } P(I, J) < 0 \; . \tag{3.28}$$

A small margin δr has been introduced to remain inside the mesh width of Δr_1 up to the penetration depth. A less realistic homogeneous distribution leads to $P(I, J) = P(I)/\pi R_I^2$. Comparing this with (3.27) shows that the power density of the parabolic distribution at the center of the beam with $J = 0$ is just a factor of 2 higher than the homogeneous one.

3.2.4 Determination of the Boundary Conditions

From the theory of differential equations, it is well known that fixing appropriate boundary conditions is very important. Furthermore, treatment of particular points, like the change in the λ value in Fig. 3.3, requires special attention.

To begin with, the boundary conditions for cooling the stopper body have to be introduced. Referring to Fig. 3.3, there are for three possibilities cooling:

- Cooling of the end face at $I = I_4$, which can be considered by setting $T(I_4, J) = 0$ for all J. In this case, the fact that no heat can be transported through the cylindrical mantle can be taken into account by setting $T(I, J_3) = T(I, J_3 - 1)$ for all I with the exception of I_4.
- Cooling of the mantle at $J = J_3$, setting $T(I, J_3) = 0$ for all I and $T(I_4, J) = T(I_4 - 1, J)$ for all J with the exception of J_3.
- Cooling end face and mantle, which, of course, results in $T(I_4, J) = 0$ for all J and $T(I, J_3) = 0$ for all I.

The cooling water temperature T_w can be taken into account by adding T_w to all calculated T values. All points located on the boundaries discussed are not included in the iteration procedure. Due to cylindrical symmetry, the points along the axis with $J = 0$ also require special treatment by setting $T(I, -1) = T(I, 1)$ during the iteration. The treatment of the points located at the front face with $I = 0$ depends on the definition of $P(I = 0)$. From the physical point of view, the power loss $P(0) = 0$. A reasonable approach is to split the calculated power loss $P(1)$ into $P(0)/2$ and $P(1)/2$. In this case, $T(-1, J)$ has to be substituted by $T(1, J)$ in the iteration of the $T(0, J)$ values. From the practical point of view, it is simpler to start with $P(I = 1, J)$ and set the points on the front face $T(0, J) = T(1, J)$, without iteration of $T(0, J)$. Experience has shown that the differences in the results are marginal.

When the stopper is composed of various materials, as in the example of Fig. 3.3, the discontinuity in λ has to be considered in the numerical iteration procedure. As shown schematically in Fig. 3.5, three cases must be considered.

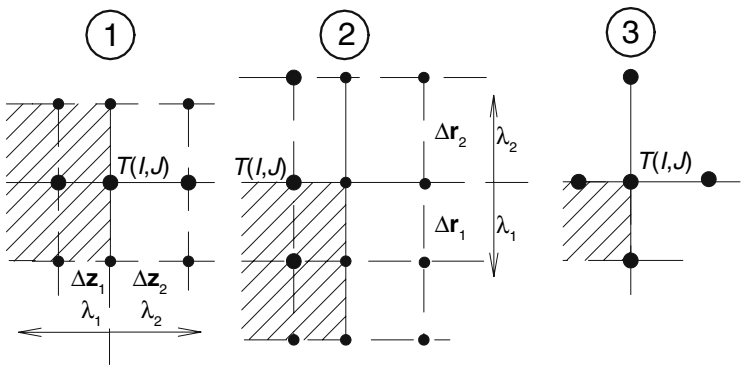

Fig. 3.5. Special points located on the borders between different λ values

The problem of determines the $T(I, J)$, belonging to one of the three cases shown in Fig. 3.5, can be solved by taking advantage of the well-known equation of heat transfer:

$$\frac{\dot{Q}}{A_\mathrm{n}} = -\lambda \,\mathrm{grad}\, T \;, \tag{3.29}$$

where $\dot{Q}/A_\mathrm{n}$ is the power flow through a given cross section A_n and $\mathrm{grad}\, T$ describes the increase in temperature along the power flow. Obviously, continuity requires

$$\lambda_\mu \,\mathrm{grad}\, T(I, J) = -\frac{\dot{Q}}{A_\mathrm{n}} \tag{3.30}$$

$$\mu = 1, 2 \;. \tag{3.31}$$

From this, it follows immediately that

$$\lambda_1 \frac{T(I,J) - T(I-1,J)}{\Delta z_1} = \lambda_2 \frac{T(I+1,J) - T(I,J)}{\Delta z_2} \; . \tag{3.32}$$

For the three cases of Fig. 3.5,

$$T(I,J)_1 = \frac{1}{\lambda_1/\Delta z_1 + \lambda_2/\Delta z_2} \left[\frac{\lambda_1}{\Delta z_1} T(I-1,J) + \frac{\lambda_2}{\Delta z_2} T(I+1,J) \right] , \tag{3.33}$$

$$T(I,J)_2 = \frac{1}{\lambda_1/\Delta r_1 + \lambda_2/\Delta r_2} \left[\frac{\lambda_1}{\Delta r_1} T(I,J-1) + \frac{\lambda_2}{\Delta r_2} T(I,J+1) \right] , \tag{3.34}$$

$$T(I,J)_3 = \frac{1}{2} \left[T(I,J)_1 + T(I,J)_2 \right] \; . \tag{3.35}$$

Of course, the indexes I, J in (3.35) are not the same as in (3.33) and (3.34).

3.2.5 Initial Temperature Distribution

Before starting the iteration, the question of a reasonable initial distribution $T(I,J)$ arises. Starting the iteration with an ensemble $T(I,J)$, close to the final result, will shorten the computing time. However, experience has shown that the choice of the initial distribution is not very critical. One possibility is to consider (3.29) to derive the initial values of $T(I,J)$ from a simple model adapted to the geometry under discussion.

To give an example: Referring to Figs. 3.1, 3.2, and 3.3, let us assume that the total power $P_{\mathrm{total}} = 1\,\mathrm{kW}$ is deposited in a cylinder, determined by the beam radius R_{b} and a length L determined by the penetration depth $p_{\mathrm{d}} = 22\,\mathrm{mm}$. Neglecting the Bragg Peak, we define the specific power loss along the z-coordinate as $\dot{Q}/L$. Assuming a parabolic intensity distribution $\dot{q}(r)$ over the radial coordinate, one obtains

$$\dot{q}(r) = \frac{2\dot{Q}/L}{\pi R_{\mathrm{b}}^2} \left[1 - \frac{r^2}{R_{\mathrm{beam}}^2} \right] \tag{3.36}$$

$$\dot{q}_{\mathrm{total}}(r = r_{\mathrm{i}}) = \int_0^{r_{\mathrm{i}}} 2\pi r \dot{q}(r) dr = \frac{4\dot{Q}}{L} \frac{r_{\mathrm{i}}^2}{R_{\mathrm{b}}^2} \left[\frac{1}{2} - \frac{r_{\mathrm{i}}^2}{4R_{\mathrm{b}}^2} \right] . \tag{3.37}$$

Now, using 3.29, it is straightforward to determine the temperature difference along the r-coordinate:

$$-\int_{T(r=0)}^{T(r)} = T(0) - T(r) = \int_0^r \frac{\dot{q}_{\mathrm{total}}(r_{\mathrm{i}})}{2\pi\lambda r_{\mathrm{i}}} dr_{\mathrm{i}} \tag{3.38}$$

$$T(0) - T(r) = \frac{\dot{Q}}{2\pi\lambda L} \frac{r^2}{R_{\mathrm{b}}^2} \left[1 - \frac{1}{4} \frac{r^2}{R_{\mathrm{b}}^2} \right] \tag{3.39}$$

$$T(0) - T(R_{\mathrm{b}}) = \frac{3\dot{Q}}{8\pi\lambda L} \; . \tag{3.40}$$

On the other hand, the temperature difference outside the beam follows from

$$T(R_\mathrm{b}) - T(r_\mathrm{o}) = \frac{\dot{Q}}{2\pi\lambda L}\ln\left(\frac{r_\mathrm{o}}{R_\mathrm{b}}\right) \tag{3.41}$$

$$T(R_\mathrm{b}) - T(R_\mathrm{mantle}) = \frac{\dot{Q}}{2\pi\lambda L}\ln\left(\frac{R_\mathrm{mantle}}{R_\mathrm{b}}\right) . \tag{3.42}$$

Now, if the cylinder mantle is cooled by setting $T(R_\mathrm{mantle}) = 0$, the initial temperatures along the r-coordinate are defined in the section $0 \leq z \leq L$, taking the different λ values and the geometric dimensions into account. A reasonable approach to defining the initial values for the rest of the body is a simple linear decrease in the temperatures determined at the border of the cylinder to the remaining cooled surfaces with $T = 0$. Of course, there are other possibilities for arriving at reasonable initial conditions, which also depends last but not least on the cleverness of the engineers and programmers. Experience has shown that the simplest way is to set all initial values to zero.

3.2.6 Proposed Iteration Algorithm

The last and most important step in the numerical calculation of the temperature distribution is the iteration procedure. Although skilled programmers surely have their own ideas, a short description of a procedure which has been tested and compared with the FE method may be helpful. Defining

$$I_\mathrm{plus} = \lambda A_{2z} \tag{3.43}$$

$$I_\mathrm{minus} = \lambda B_{2z} \tag{3.44}$$

$$J_\mathrm{plus} = \lambda\left(A_{2r} + \frac{1}{r}A_{1r}\right) \tag{3.45}$$

$$J_\mathrm{minus} = \lambda\left(B_{2r} + \frac{1}{r}B_{1r}\right) \tag{3.46}$$

$$A_{00} = \lambda\left(C_{2z} + C_{2r} + \frac{1}{r}C_{1r}\right) \tag{3.47}$$

$$r = J\Delta r_1 \tag{3.48}$$

$$r = J_1\Delta r_1 + (J - J_1)\Delta r_2, \quad \text{if} \quad J > J_1 \ , \tag{3.49}$$

the iteration procedure can be performed, setting

$$DL = I_\mathrm{plus}T(I+1,J) + I_\mathrm{minus}(T(I-1,J) + \ldots \tag{3.50}$$

$$+ \ J_\mathrm{plus}T(I,J+1) + J_\mathrm{minus}T(I,J-1) + \ldots \tag{3.51}$$

$$+ \ A_{00}T(I,J) + P(I,J) \tag{3.52}$$

$$T(I,J) = T(I,J) - C_\mathrm{k}DL/A_{00}, \text{ iterative correction} \tag{3.53}$$

$$DI = DI + ABS(DL/A_{00}). \tag{3.54}$$

C_k is a convergence factor, which has to be optimized according to the problem. Experience has shown that $1 < C_\mathrm{k} < 2$. The iteration correction is applied to all $T(I, J)$, with exception of the substitutions defined by the boundary conditions and other special cases. To value the convergence, the quantity DI can be referred to, which has to be summed up from $DI = 0$ in each pass over all mesh points. DI has the dimension of a temperature and represents a measure of the quality and convergence of the numerical solution. Experience has shown that in most cases the iteration can be stopped if DI is of the order of 1.

Remark. In the equations discussed and the iteration algorithm described, it has been assumed that the heat conductivity λ is independent of temperature. For the most suitable materials, one finds a slight decrease with temperature. Keeping a constant λ value, this can be taken into account by using an average value for heat conductivity. On the other hand, the dependence of λ on T can be included very easily in the iteration procedure by fetching the appropriate values from a table. Including an analytical dependency of the type $\lambda(T) = f(T)$ from a fit to available data in the iteration procedure is another way. In this case, the temperature at a certain point in the mesh has to be taken from the preceding pass through the iteration procedure.

3.2.7 Check of Consistency

Referring once more to (3.29), there is a possibility of checking the consistency of the results. Because there is nearly no heat transfer by convection in a vacuum, the power deposited by the beam has to flow over the cooled surfaces. Therefore, summing up the power flow through these surfaces should be about the same as the total deposited power.

$$P_\mathrm{total} \approx A_\mathrm{n} \lambda \,\mathrm{grad}\, T \tag{3.55}$$

In the example discussed the gradient of T along the end face of the cylinder is determined by grad $T \approx T(J, I_4-1) - T(J, I_4)$ divided by the mesh spacing Δz, along the mantle grad $T \approx T(J_3-1, I) - T(J_3, I)$ divided by the mesh spacing Δr. Summing up all contributions, one has to consider that $\Delta A_\mathrm{n} = 2\pi r \Delta r_\mu$ at the end face with r according (3.48), (3.49), and $\Delta A_\mathrm{n} = 2\pi R_\mathrm{mantle} \Delta z_\mu$ along the mantle. The evaluation of the power flow through the cooled surfaces is also important in optimizing the heat flow to the cooling water, which is discussed in the next example.

3.2.8 Some Examples

Figure 3.6 shows the calculated temperature distribution within a graphite stopper hit by 1000-MeV/u uranium ions of 10-kW dc-beam power. The penetration depth is about 46.4 mm in this case. Taking this and the beam radius of $R_\mathrm{beam} = 10$ mm into account, in a first approximation, a cylinder radius

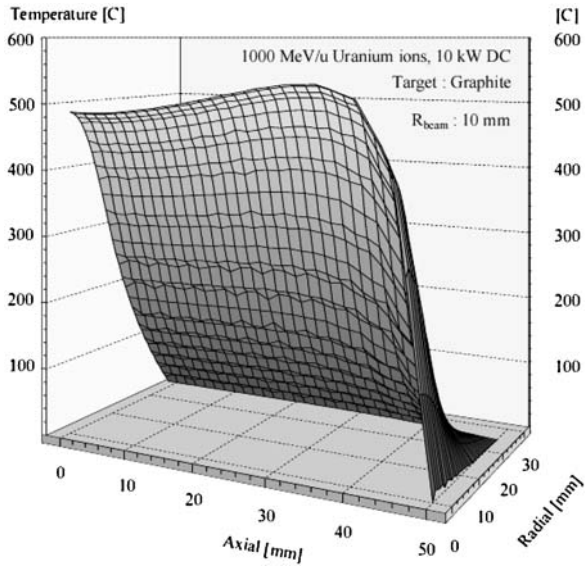

Fig. 3.6. Example of the numerical calculated temperature distribution applying the FD method

of $R_{\text{mantle}} = 25\,\text{mm}$ and a length of $z = 50\,\text{mm}$ was chosen for the stopper dimensions.

Although the calculated maximum temperatures came out well below the melting point of graphite, looking at the power flow through the cooled mantle and end face, the designer was confronted with a serious problem. Normally, water flow is laminar, and therefore the maximum power flow to the cooling water should be below about $120\,\text{watt/cm}^2$ to avoid so-called film boiling [145, 146], which would destroy the cooling water pipes as well as the stopper device by overheating. Figure 3.7 shows that this condition is fulfilled just at the mantle. However, it becomes very clear from Fig. 3.8 that the power flow through the cooled end face is much too high. Destroying a water-cooled device in the UHV system of an accelerator can have dramatic consequences. Thus, this example demonstrates clearly the importance of thermal calculations as a first step in the design of beam intercepting devices. In the example, the design engineer has the following options to end up with a safe device:

- Increasing the length z results in decreasing power flow through the end face. However, at the same time, the maximum temperature will increase. As a consequence, this preventive measure has to go along with new calculations of the expected temperature distribution.
- Choice of another material having better heat conductivity ($\lambda_{\text{Graphite}} = 0.09\,\text{W/mm K}$). In this case, even a new determination of $P(I, J)$ has to be performed.

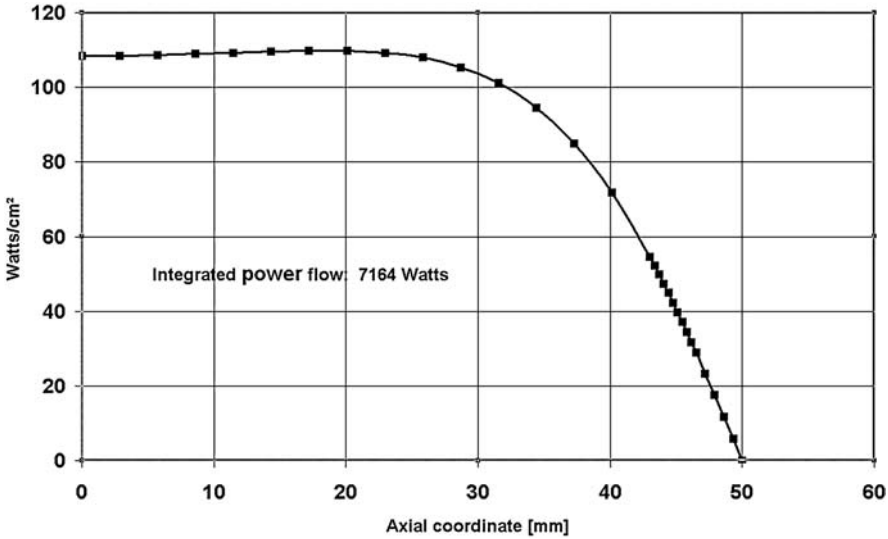

Fig. 3.7. Power flow through the cylinder mantle dependent on the axial coordinate

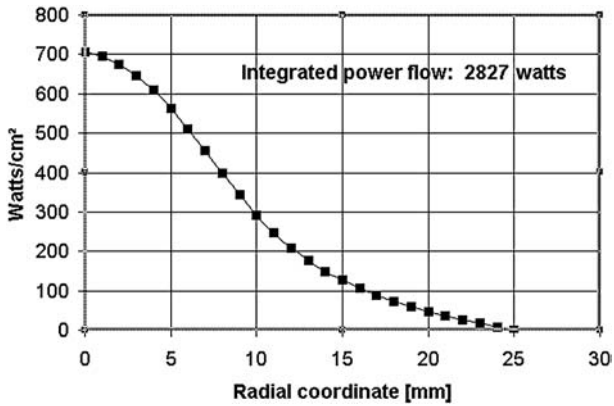

Fig. 3.8. Power flow through the cooled end face dependent on the radial coordinate

- Change to turbulent cooling water flow, which would allow higher power flow to the cooling water. But this requires considerable effort in the construction design, as well as the dimensioning of the cooling system. In Figs. 3.9–3.11, a solution of the problem discussed is proposed. Here the stopper consists of a copper block with $R_{\mathrm{mantle}} = 50\,\mathrm{mm}$ and $z = 50\,\mathrm{mm}$. Although p_{d} goes down to only 15.3 mm, by increasing the specific thermal load near the front face, the maximum temperature is slightly reduced, and the power flow through the end face remains within acceptable values. This results from the much better heat conductivity of $\lambda = 0.37\,\mathrm{W/mm\,K}$.

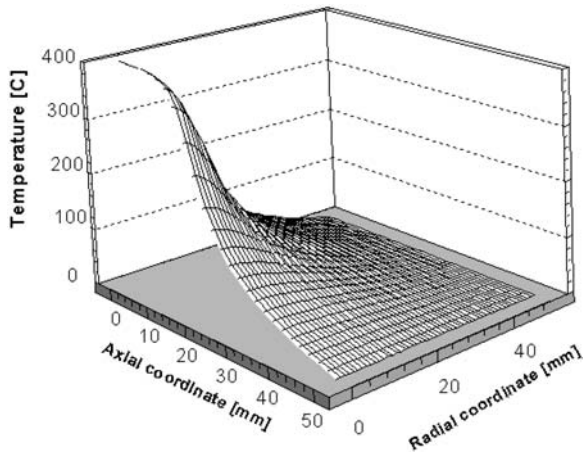

Fig. 3.9. The 1000-MeV/u beam (see also Fig. 3.6) hits a cooled copper stopper instead of graphite

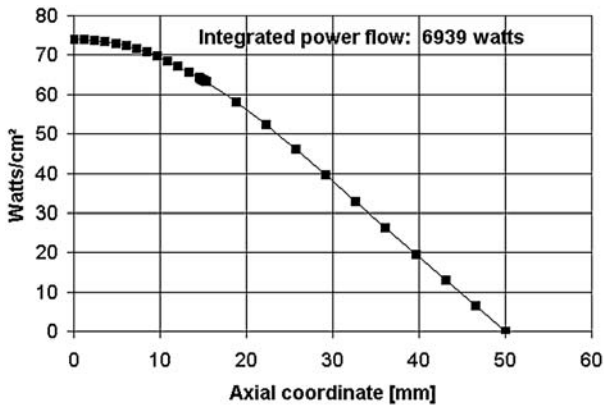

Fig. 3.10. Power flow through the cylinder mantle dependent on the axial coordinate

Remark: Summing up the power flow through the cooled surfaces (see Figs. 3.7, 3.8 and 3.10, 3.11) the check of consistency discussed is confirmed.

3.2.9 Comparison with the FE Method

Although the consistency of the FD method discussed has been proven in many examples, a comparison with the more modern FE method is worthwhile. As expected, the agreement is excellent, as demonstrated in Fig. 3.12 for a 100-MeV proton beam with a power of 20 kW dc.

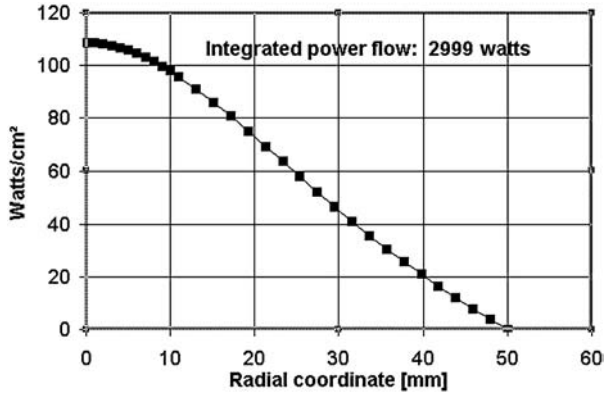

Fig. 3.11. Power flow through the cooled end face dependent on the radial coordinate

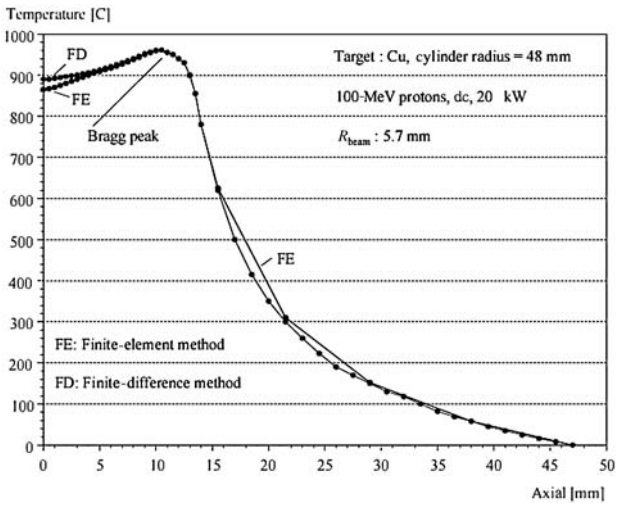

Fig. 3.12. Comparison of the FE and FD methods. The FE calculations were performed [166] using the DOT program described in [156]

3.2.10 The Special Case of Very Small Penetration Depth

In some cases, especially for heavy ions of low energy, the penetration depth p_d can be the order of only some micrometers, and therefore of $p_\mathrm{d} \ll$ stopper length. This reduces the numerical effort because the deposition of power can be simply derived from (3.29) as follows:

$$T(I=0,J) = T(I=1,J) + \Delta z_1 \frac{P(J)}{A_\mathrm{n}\,\lambda}\,, \tag{3.56}$$

with $P(J)/A_n$ [watt/mm^2] as the radial power density of the beam at the mesh points along the index J. Of course, referring to Fig. 3.3, the width Δz_1 of the mesh in the axial direction has to be approximately p_d in the section $0 < z < z_1$. As a consequence of the small penetration depth, the maximum temperature will be found at the front face with $I = 0$. Because the beam power is deposited within a very small volume, this can result in rather high temperatures in this region, requiring careful design of the intercepting device. The designer has the following options:

- Tilting the intercepting surface to reduce the incident power density. This option is the one mostly used for Faraday cups or slit systems. Figure 3.13 shows the scheme of a Faraday cup, provided to stop 25-MeV protons with a dc-power of 25 kW and a maximum power density of 10 kW/cm^2. Figure 3.14 is a picture of a high-power slit system with tilted slit jaws.

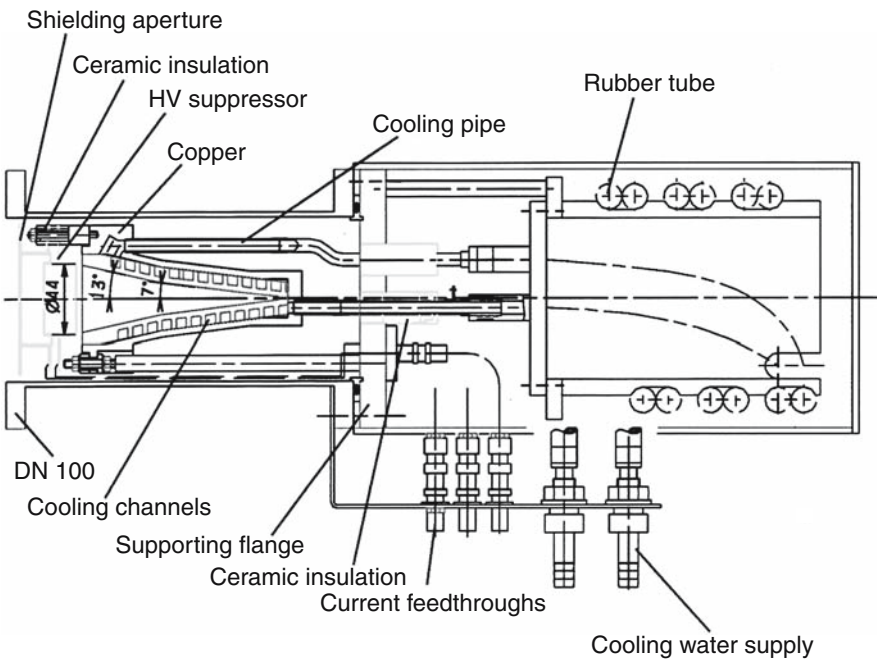

Fig. 3.13. High-power beam stopper in kind of a Faraday cup

- Stopping the highly intense beam in a thin layer of material with a high melting point, in combination with a cooled backing, consisting of a material with high heat conductivity such as copper. This can be a practicable solution for slit constructions, as shown in the example of Fig. 3.15. Figure 3.16 shows the numerical results for a combination of a 2-mm tantalum plate with a cooled copper backing hit by a 10-MeV/u uranium beam.

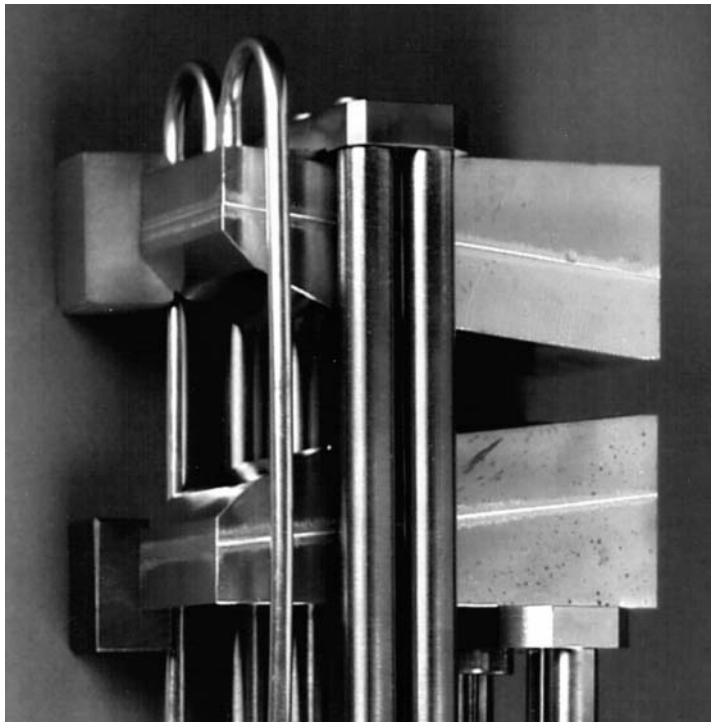

Fig. 3.14. High-power slit system. The linear feedthrough to vary the slit width is not shown. The beam comes from the left-hand side. GSI Foto

Since the penetration depth is only about 40 µm, the power deposited has been determined according to (3.56) choosing $z_1 = 0.4\,\mathrm{mm}$, with a mesh width of $\Delta z_1 = 0.04\,\mathrm{mm}$. The discontinuity in λ, which occurs at $z = 2\,\mathrm{mm}$ has been considered according to (3.33). Due to the very different λ values of tantalum with $0.055\,\mathrm{W/mm\,K}$, and copper with $0.372\,\mathrm{W/mm\,K}$, the change in $\mathrm{grad}\,T$ is rather high and becomes clearly visible in the diagram. For the design engineer, the expected temperature at the connection between the two materials is of great importance when selecting an appropriate solder.

3.2.11 Cooling by Radiation

Equation 3.56 offers the possibility of introducing a term for the power loss by radiation from the hot front face. Referring to the well-known Stefan-Boltzmann radiation law in a practical form [145],

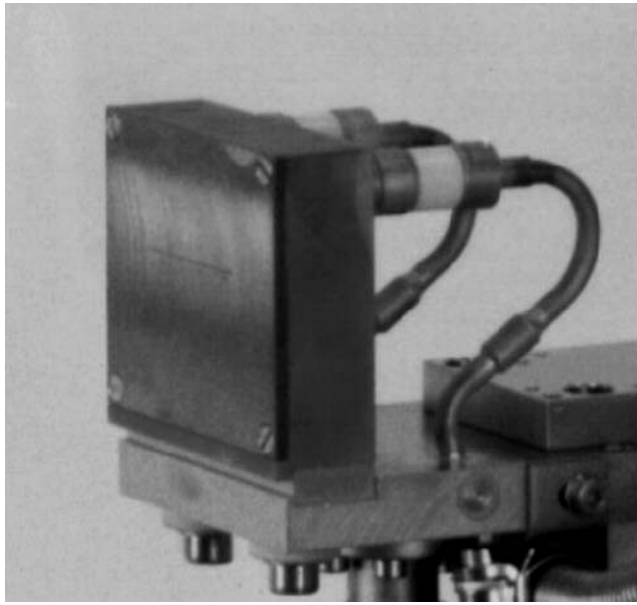

Fig. 3.15. Cooled slit system consisting of a tantalum stopper plate 2 mm thick and a cooled copper backing. The slit is provided for emittance measurements on highly intense particle beams with penetration depths of the order of some ten micrometers. The slit is 0.1 mm wide. GSI Foto

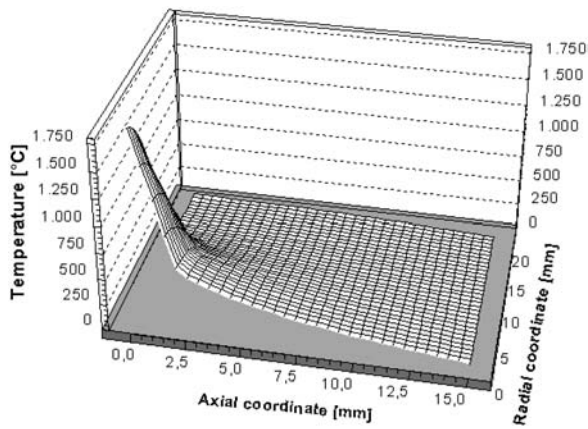

Fig. 3.16. A beam of 10-MeV/u uranium ions with a radius of 10 mm and a power of 6 kW dc hits a tantalum stopper plate with a cooled copper backing

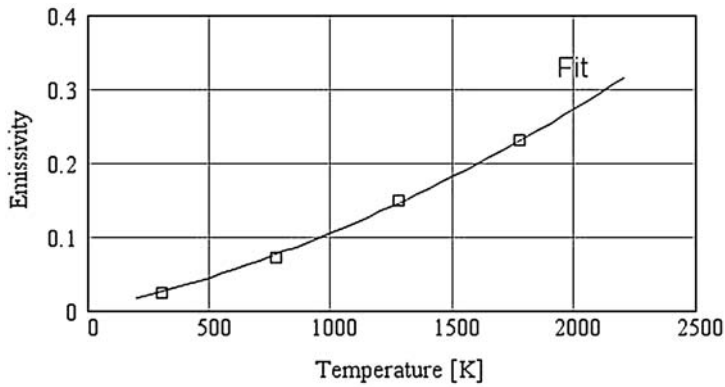

Fig. 3.17. Dependence of the emissivity ϵ of tungsten on temperature. *Boxes*: Data taken from [163], *solid line*: least squares fit to the data

$$P_{\mathrm{r}} \left[\frac{W}{\mathrm{cm}^2} \right] = \epsilon \, C_{\mathrm{s}} \left(\frac{T\ [K]}{100} \right)^4 \tag{3.57}$$

$$C_{\mathrm{s}} = 5.67 \times 10^{-4} \left[\frac{W}{\mathrm{cm}^2} \right] . \tag{3.58}$$

Equation 3.56 may be supplemented in the following way:

$$T(0, J) = T(1, J) + \Delta z_1 \left[\frac{P(J)}{F\lambda} - \frac{5.67 \times 10^{-6} \, \epsilon}{\lambda} TE4 \right] \tag{3.59}$$

$$TE4 = \left(\frac{T(0, J)^* + T_0}{100} \right)^4 , \tag{3.60}$$

where $T(0, J)^*$ is the calculated temperature at the front face from the preceding pass through the iteration. Here λ has to be inserted with the dimension [W/mm K] and $T_0 = 273$ K. The emissivity ϵ depends on temperature and the composition of the material surface. Because the contribution to the power loss from radiation is $\sim T^4$, the additional term becomes only of interest for materials like tungsten or tantalum with melting points above about 2000 K. The emissivities of both materials are similar. Figure 3.17 gives the dependence of $\epsilon(T)$ for tungsten, applying a fit $\epsilon(K) = a\,K + b\,K^2$ to the data [163]. To illustrate the effect of cooling by radiation, a numerical calculation has been performed for a beam of 10 MeV / u with a radius of $R_{\mathrm{beam}} = 7.5$ mm that hits a plate of tantalum with $R_{\mathrm{mantle}} = 20$ mm and $L = 10$ mm. The differences in the temperatures determined at the front face ($J = 0$) are shown in Fig. 3.18.

Remark. In some special cases, the radiated power can be in equilibrium with the power deposited by the beam in a thin layer of material. In this case, no additional cooling is necessary. An example is given by the W-Re

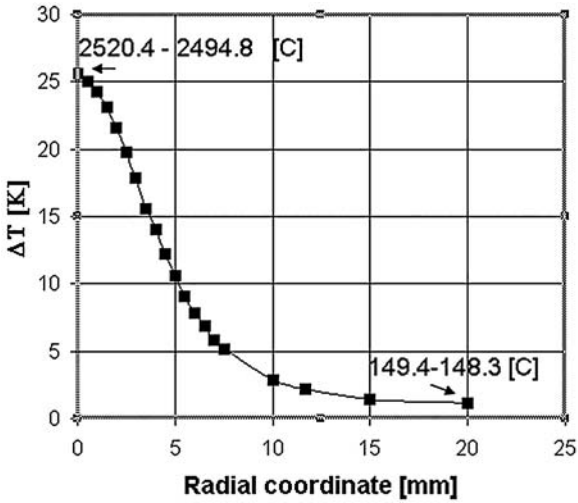

Fig. 3.18. Effect of cooling by radiation at the front face of a tantalum stopper plate, assuming only cooling of the end face results in $T \neq 0$ along the mantle. The calculation holds for $\epsilon = \text{const.} = 0.22$

wires of a profile grid or harp, as described in Chap. 4, Sect. 4.1. A more detailed discussion, as well as a short description of a program algorithm for the calculation of the steady state is given in Chap. 3, Sect. 3.4.

3.2.12 Rectangular Geometries

For rectangular geometries, the iteration procedure has to be performed on a three-dimensional array $T(I, J, K)$, where the corrections to the mesh point with the indexes I, J, K have to be determined from the six points $T(I-1, J, K)$, $T(I+1, J, K)$, $T(I, J-1, K)$, $T(I, J, K-1)$, $T(I, J, K+1)$. With (3.12–3.15), determination of the coefficients in the extended versions, of (3.50), (3.53), and (3.54) is straightforward. Due to the third dimension, the number of variables increases, requiring much more memory space, with the consequence of increasing calculation time. Experience has shown that a reasonable approach to get the temperature distribution can be achieved by an approximation in two dimensions with cylindrical symmetry. In this approximation, one sets RE as the equivalent of R_{mantle} to $RE = \sqrt{4x_{\max}y_{\max}/\pi}$, with $-x_{\max} \leq x \leq x_{\max}$ and $-y_{\max} \leq y \leq y_{\max}$ as the transverse borders of the geometry considered. Such a approximation may even be applied to tilted rectangular plates, where a circular beam of radius R_{b} deforms to an ellipse with the half axes $a = R_{\text{b}}/\sin\alpha$ and $b = R_{\text{b}}$ with α as the angle of the tilted plate against the z-axis. Therefore, the equivalent of R_{b} is given by $RB = \sqrt{ab}$.

3.3 Intense Pulsed Beams

3.3.1 Short Pulses and Low Penetration Depth

Special attention is required by very short intense pulsed beams with low penetration depth p_d. In this case, cooling by heat conduction will not help, since heat cannot be transported fast enough to cold regions and especially to cooled surfaces. Neglecting the Bragg Peak by supposing that energy deposition is constant over the range and setting $T_0 = 0$, the temperature rise of the "range volume" $V_\mathrm{range} = \pi R_\mathrm{b}^2 p_\mathrm{d}$ is

$$T(t) = \frac{P_\mathrm{F}}{\rho\, c\, p_\mathrm{d}} t \;, \tag{3.61}$$

where P_F is the beam power density $P/\pi R_\mathrm{b}^2$ within the pulse and $c\,[\mathrm{Ws/g\,K}]$ is the heat capacity, as given, for example, in Table 3.1. Therefore, the material melts if $T(T_\mathrm{p}) > T_\mathrm{m}$, with T_m as the melting temperature given in Table 3.1.

However, in [164], it is shown that this linear rise of the temperature with t holds only in the very first moment, because on this short timescale, the heat conductivity λ can be neglected. After a very short time, heat conduction into cooler regions starts. According to (3.29), this transfer of heat is proportional to the area over which the transfer can take place. Therefore, tilting of the material surface against the beam axis, as already discussed for highly intense dc-beams will increase the heat transfer to other regions, lowering the temperature. Because the maximum temperature occurs at the front face, a practical formula derived in [164] can be very useful for determining the required tilt angle α dependent on the stopping material and the beam pulse length. The temperature rise at the surface is given as a function of time:

$$T(z = 0, t) = \frac{2 P_\mathrm{F} \sin\alpha}{\sqrt{\pi \lambda \rho c}} \sqrt{t} \;. \tag{3.62}$$

It shows, that the rise in temperature from heat transfer by conduction is proportional only to $\sqrt{t}$. This holds for $t \gg c\,\rho\, p_\mathrm{d}^2 \sin^2\alpha/\lambda T$.

Remark: Equation (3.62) has been derived by supposing a homogeneously distributed power loss over the beam cross section. Remembering that in general, the beam power at the center will be higher, a factor of 2 should be applied to estimate the maximum temperature at $r = 0$, $z = 0$, because it holds for a parabolic distribution of the intensity over the beam cross section (see 3.27).

To save space, one wants a tilt as large as possible. Furthermore, the designer tends to select a material which is suitable from the technological point of view. Keeping in mind the very different melting temperatures T_m of materials (see Table 3.1) and the factors $\lambda\rho c$ in (3.62), a "figure of merit" Q has been defined [164], composed of material constants:

$$Q = T_{\mathrm{m}} \sqrt{\lambda \rho c}\,. \tag{3.63}$$

If the pulse length $T_{\mathrm{p}} \gg c\,\rho\,p_{\mathrm{d}}^2 \sin^2\alpha/\lambda T$, (3.62) and the "figure of merit" can be very useful for determining the expected maximum temperature at the end of the beam pulse for optimizing the tilt angle and for selecting a suitable material.

Table 3.1 gives the "figures of merit" Q and the values of Q/T_{m} for some often used construction materials.

Table 3.2. Figures of merit

Material	$\boldsymbol{Q/T_{\mathrm{m}}}$ [$\mathrm{Ws^{\frac{1}{2}}/K\,cm^2}$]	$\boldsymbol{Q}$ [$\mathrm{Ws^{\frac{1}{2}}/cm^2}$]
Fe	2.0	3071
Al	2.5	1667
Ta	1.2	3649
W	2.2	7643
Cu	3.8	4149
Ag	3.4	3301
Au	2.9	3109
Graphite	1.3	4807
Diamond	6.4	23230

For the designer, the dependence $T(z,t)$ may also be of interest. A practical formula can be derived from a solution of the one-dimensional partial differential equation given by Smirnow [165], who considers the special case of an infinite rod with the deposition of heat in a very small region at one end. Although the formula derived, adapted to the problem discussed, looks rather complicated, evaluation is straightforward with an appropriate PC program [84–86]. Setting the initial temperature $T_{\mathrm{o}} = 0$, one gets

$$T(z,t) = \frac{P_{\mathrm{F}}}{\sqrt{\lambda c \rho \pi}} \frac{1}{2p_{\mathrm{d}}} \int_{-p_{\mathrm{d}}\sin\alpha}^{p_{\mathrm{d}}\sin\alpha} \left[\int_0^t \frac{1}{\sqrt{t'}} e^{-\frac{c\rho(z'-z)^2}{4\lambda t'}} dt' \right] dz'. \tag{3.64}$$

First of all, we use this correct solution to check the approximation of (3.62). Figure 3.19 compares both solutions for a copper target hit by a beam of $P_{\mathrm{F}} = 4\,\mathrm{kW/mm^2}$ with a penetration depth of $p_{\mathrm{d}} = 40\,\mu\mathrm{m}$ and a tilt angle $\alpha = 11.5°$. The exact solution according to (3.64) and the approximation according to (3.62) show a nearly constant difference of about 8.4°C, which will not be relevant in most cases. Nevertheless, a correction factor has been derived in [164] leading to

$$T(z=0,t) = \frac{2P_{\mathrm{F}} \sin\alpha}{\sqrt{\pi\lambda\rho c}} \left(\sqrt{t} - \frac{\sqrt{\pi\rho c}\, p_{\mathrm{d}} \sin\alpha}{4\sqrt{\lambda}} \right)\,. \tag{3.65}$$

The approximations (3.62) and (3.65) do not hold in the neighborhood of $t = 0$. In the example considered, the correction results in $\Delta T = -8.6°$ C.

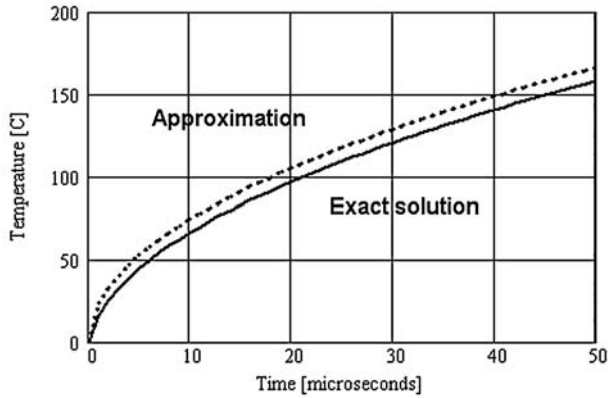

Fig. 3.19. Comparison of the results according to the approximation of (3.62) (dotted line) with the exact solution given in (3.64) (solid line)

The solution for $T(z,t)$, given by (3.64) is a very useful formula for studying the influence of material constants on the maximum temperature at the front face as well as the heat transfer into cooler regions over time. This is illustrated in Fig. 3.20 for seven selected materials, where diamond has been included for comparison with standard construction materials. Hence, calculating similar diagrams for given beam parameters, the design engineer should be able to select a suitable material considering the maximum temperature at the front face as well as the desired material thickness up to the cooled surface. Because, usually the heat transfer in the radial direction is smaller than in the beam direction, the one-dimensional equations (3.62), (3.64) and (3.65), also give good estimations of the thermal effects in various materials in higher dimensional problems. Figure 3.20 clearly confirms: The heat transfer into cooler regions is faster

- as the heat conductivity λ is larger,
- as the specific weight ρ is smaller, and
- as the specific heat c is smaller.

3.3.2 Numerical Solution of the Partial Equation of Heat Transfer

The specific energy loss of high energy particles along their path in a stopping material is considered in the distribution $P_{\mathrm{V}}(x,y,z)$ or $P_{\mathrm{V}}(r,z)$, respectively. Due to the complex specific energy loss of charged particles in materials, this results in rather complex distributions P_{V}, with the consequence that analytical solutions of the partial equation of heat transfer (3.10) can be found only in some very special cases. On the other hand, based on the solutions given above for dc-beams, the implementation of a numerical iteration procedure

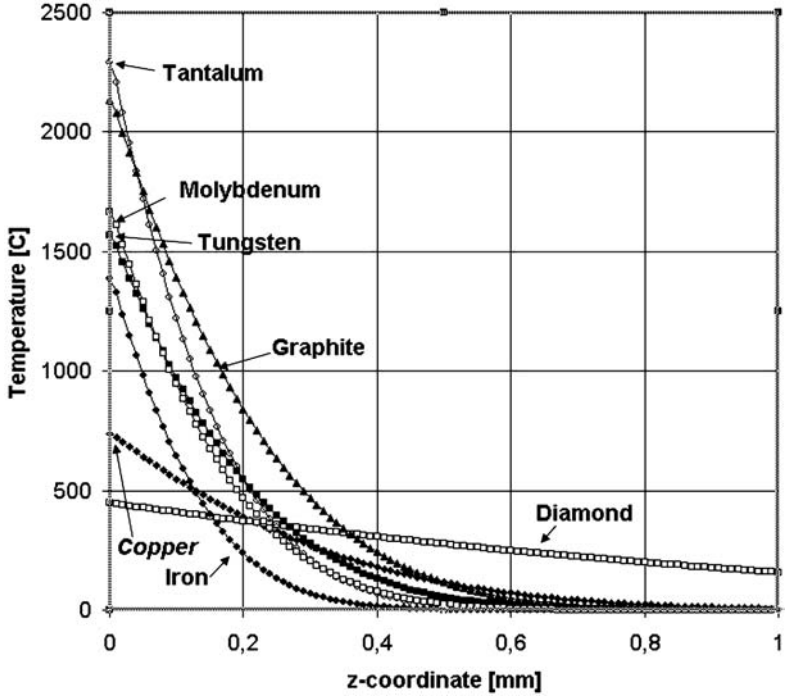

Fig. 3.20. The diagram shows calculated temperatures at the end of a beam pulse. It holds for the following parameters: $P_{\mathrm{F}} = 4\,\mathrm{kW/mm^2}$, $p_{\mathrm{d}} = 40\,\mu\mathrm{m}$, $\alpha = 11.5°$, $T_{\mathrm{p}} = 1\,\mathrm{ms}$

is straightforward. Some hints for the implementation of a program may be helpful:

- Referring to (3.50) for the iteration, the DL value which has to be minimized by iteration is given by

$$DL = \lambda \Delta T(x,y,z,t) - P_{\mathrm{V}}(x,y,z,t) - \rho c \frac{\partial T}{\partial t} \; . \tag{3.66}$$

- $\partial T/\partial t$ should be approximated by $\left[T(x,y,z,t) - T(x,y,z,t-\Delta t)\right]/\Delta t$, where the step width in Δt can be different during pulse and pause.
- $P_{\mathrm{V}}(x,y,z,t)$ should be multiplied by the step function of Heaviside, switched on during the pulse and switched off during pause. The most external loop should be the loop over time, as shown in the simplified scheme of Fig. 3.21, assuming cylindrical symmetry. Because we consider a periodically pulsed beam, the last time slice of the nth iteration has to be inserted as the first time slice of the $(n+1)$th pass through the iteration procedure. Iteration can be stopped when the changes in the last time

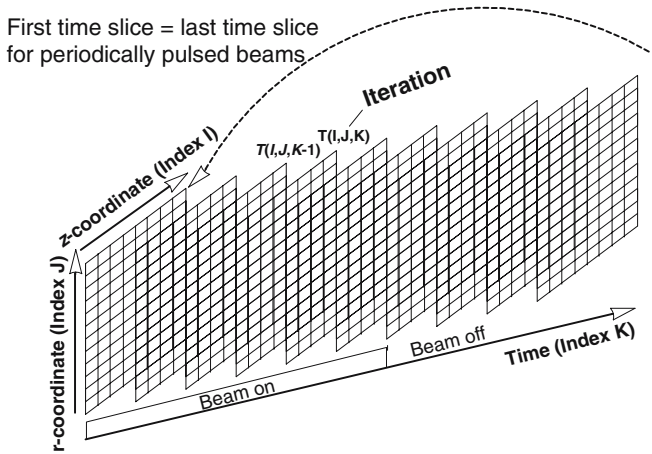

Fig. 3.21. Simplified scheme to illustrate iteration in time

slice are below an acceptable level. The treatment of a periodically pulsed beam includes two simpler cases:

- heating up the material during only one beam pulse,
- Cooling down when the beam is switched off (pause).

- Because the number of variables can be very large in a four-dimensional array, computing time can increase considerably. To reduce required memory and computing time finding an approximation in cylindrical symmetry is recommended.
- Referring to Fig. 3.21 and (3.66), the iteration procedure, analogous to 3.50, looks like

$$DL = I_{\text{plus}}T(I+1,J,K) + I_{\text{minus}} \ldots + J_{\text{plus}} \ldots$$
$$+ J_{\text{minus}} \ldots + K_{\text{minus}}T(I,J,K-1) \quad (3.67)$$
$$+ A_{000}T(I,J,K) + P(I,J,K) \quad (3.68)$$
$$T(I,J,K) = T(I,J,K) - C_{\text{k}}DL/A_{000}, \text{ iterative correction} \quad (3.69)$$
$$DI = DI + ABS(DL/A_{000}), \quad (3.70)$$
$$K_{\text{minus}} = c\rho/\Delta t(K), \; K \text{ is the index of time} \quad (3.71)$$
$$A_{000} = A_{00} - c\rho/\Delta t(K), \; A_{00} \text{ see (3.47)} \quad (3.72)$$

- For low penetration depth $P_{\text{V}}(x,y,z,t)$ can be replaced by the heat flow at the front face, as discussed for dc-beams (see 3.56).

3.3.3 Some Examples

For comparison with the example of a dc-beam shown in Fig. 3.6, a calculation for a single pulse has been performed. Figure 3.22 holds at the end of the

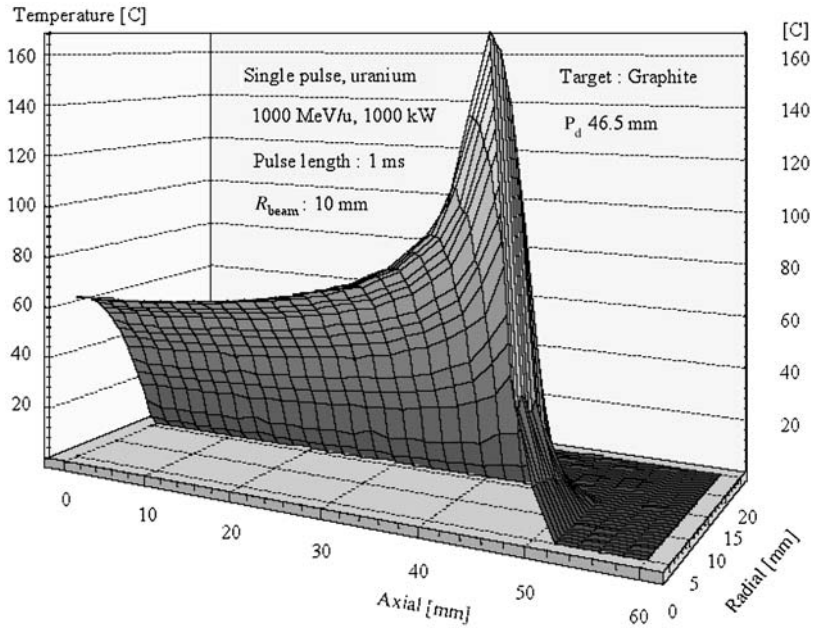

Fig. 3.22. Numerical solution of the partial differential equation of heat for the parameters given in the diagram (single pulse)

beam pulse, showing the Bragg peak very clearly and illustrating the time dependence of heat transfer. The next example of Fig. 3.23 holds for a very highly intense periodically pulsed beam heating up a tungsten stopper plate of a Faraday cup to a rather high temperature of nearly 1800°C. Due to the high temperature, the material is extremely stressed in this case. The temperature decreases with increasing duty cycle.

The last example is taken from the field of "heavy-ion-driven fusion" [167, 168], where very intense beams of heavy ions are required to drive fusion pellets to low gain fusion burn. In various scenarios, mostly Bi^{1+} ions have been discussed. Since the envisaged linac beam pulse power is of the order of more than 1000 MW, even a beam loss of less than 1% can damage the beam pipe, slits, or other parts of the accelerator structure. This is demonstrated in Fig. 3.24 for a 200-mA Bi^{1+} beam with an energy of 50 MeV/u and a pulse length of 1 ms. The resulting pulse power is about 2100 MW and, as the example shows, even a loss of only some 10^{-3} would melt an iron beam pipe or similar material when hit by the beam.

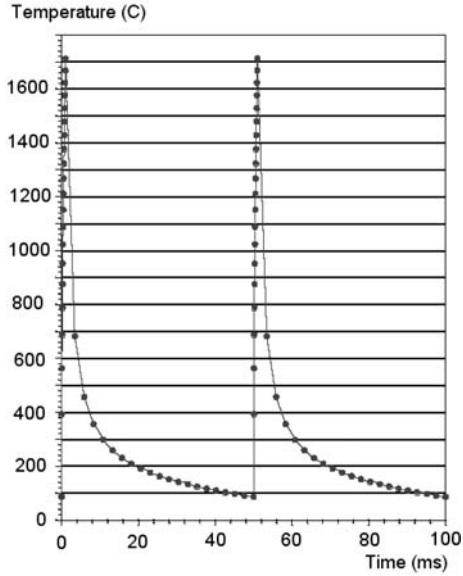

Fig. 3.23. A 200 µs beam pulse of U^{4+}-ions with an energy of 1.4 MeV/u, an pulse power of 1.25 MW and a power density of about 2.5 kW/mm^2 hits a Tungsten stopper plate every 50 ms (20 Hz repetition frequency). The diagram holds for the maximum temperature at the front face in the center of the beam

3.4 Cooling by Radiation

In some cases, a beam intercepting device can be driven into an equilibrium between radiated thermal power and deposited beam power. This holds especially if the beam power is deposited within a very thin layer at the front face of the intercepting device. In such cases, no additional cooling is necessary. However, due to the proportionality of radiated heat to T^4 (see 3.57), cooling by thermal radiation requires rather high surface temperatures of the radiating body. Figure 3.25 gives the radiated power from a tungsten surface, taking the temperature dependence of the emissivity ε according to Fig. 3.17 with $a = 7.5 \times 10^{-5}\,\mathrm{K}^{-1}$, $b = 3.1 \times 10^{-8}\,\mathrm{K}^{-2}$ into account.

3.4.1 DC-Beams

For dc-beams, it is relatively simple to find the steady state, where the radiated thermal power is equal to the deposited power. In most cases, one has to determine the maximum allowed power loss for a given maximum temperature. Taking as a reasonable maximum allowed temperature $\approx 3/4 \times T_{\max}$ with $T_{\max} = T_{\mathrm{m}} + 273$ (T_{m} from Table 3.1 +273), one gets $T_{\max} \simeq 2750\,\mathrm{K}$ for tungsten and $T_{\max} \simeq 2450\,\mathrm{K}$ for tantalum. Assuming radiation only into

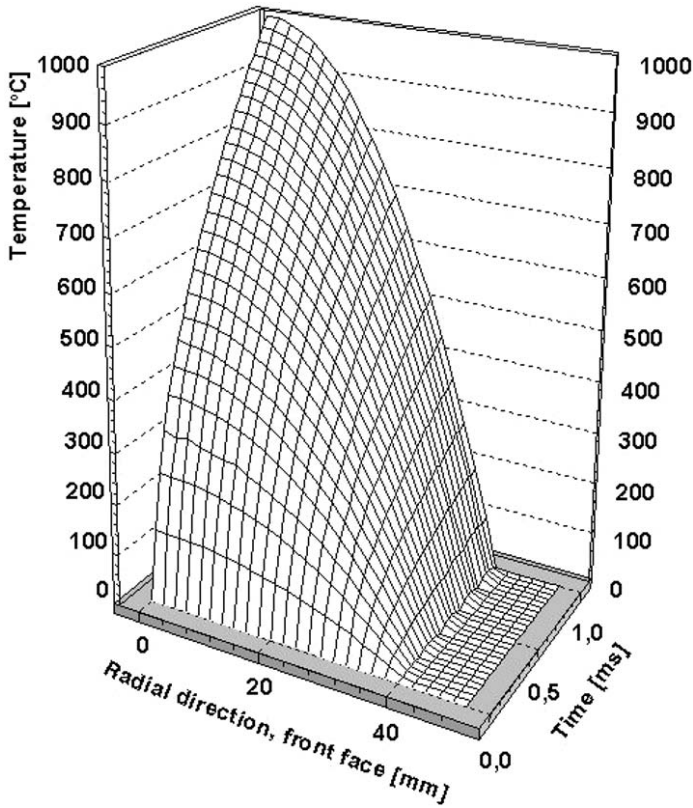

Fig. 3.24. Lost Bi^{1+} ions with a total beam power of 2100 kW hit an iron plate (beam pipe, ...) in an area of 50 cm^2. To simplify the calculations, a circular cross section of 40 mm radius has been assumed, and the lost particles were parabolically distributed over the hit area

one hemisphere, this leads to a maximum allowed specific power deposition of $P_{\max} \approx 1.5 \mathrm{W/mm^2}$ (tungsten) and $P_{\max} \approx 0.75 \mathrm{W/mm^2}$ (tantalum). The values can be estimated from Fig. 3.25 or from a numerical solution of (3.57). The maximum ratings have to be multiplied by a factor of 2 for thin targets radiating into both hemispheres. Scaling to other parameters can be performed according to the dependencies given in (3.57).

3.4.2 Pulsed Beams

For pulsed beams, one expects a swing in temperature between a maximum achieved at the end of the beam pulse and a minimum at the end of the pause. To find the steady state is much more complicated and requires the solution of the partial equation of heat. We use a solution given in [169–171] and define

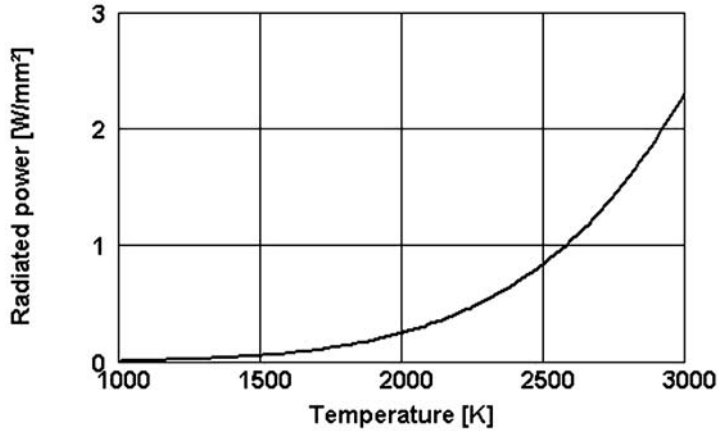

Fig. 3.25. Radiated power from a tungsten surface in dependence of the surface temperature

$$As(T) = \frac{P_\mathrm{p} + 2\varepsilon(T)\sigma T_\mathrm{e}^{\,4}}{c_\mathrm{m}\rho\Delta x} \tag{3.73}$$

$$Ap(T) = \frac{2\,\varepsilon(T)\,\sigma\,T_\mathrm{e}^{\,4}}{c_\mathrm{m}\rho\Delta x} \tag{3.74}$$

$$Cs(T) = \left[\frac{2\,\varepsilon(T)\,\sigma}{P_\mathrm{p} + 2\varepsilon(T)\sigma T_\mathrm{e}^{\,4}}\right]^{\frac{1}{4}} \tag{3.75}$$

$$Cp = \frac{1}{T_\mathrm{e}}\ . \tag{3.76}$$

Definitions (3.73) and (3.75) hold during the pulse (see 3.77), and (3.74) and (3.76) holds during the pause, when the beam is switched off (see 3.78). P_p is the deposited beam pulse power; $\sigma = 5.67 \times 10^{-8}[\mathrm{W/m^2K^4}]$ is the Stefan-Boltzmann constant, related to C_s (see 3.57) with $C_\mathrm{s} = 10^8\sigma$; c_m is the mean of the specific heat (see Table 3.1), $\varepsilon(T)$ is the emissivity (see Fig. 3.17), T_e is the temperature of the environment (mostly 300 K), ρ is the specific weight, and Δx is the target thickness. Assuming square beam pulses, a solution of the partial differential equation of heat has been obtained by stepwise integration [169] and the results are

$$t - t_0 = \frac{1}{4\,As(T)\,Cs(T)} \left[\begin{array}{c} \ln\frac{[1+Cs(t)T(t)][1-Cs(t)T(t_0)]}{[1-Cs(t)T(t)][1+Cs(t)T(t_0)]} + \ldots \\ +2\arctan Cs(T)T(t) - 2\arctan Cs(T)T(t_0) \end{array}\right], \tag{3.77}$$

valid during "beam on" (pulse) and

$$t - t_0 = \frac{1}{4\,Ap\,Cp} \left[\begin{array}{c} \ln\frac{[1+CpT(t)][1-CpT(t_0)]}{[1-CpT(t)][1+CpT(t_0)]} + \ldots \\ +2\arctan CpT(t) - 2\arctan CpT(t_0) \end{array}\right], \tag{3.78}$$

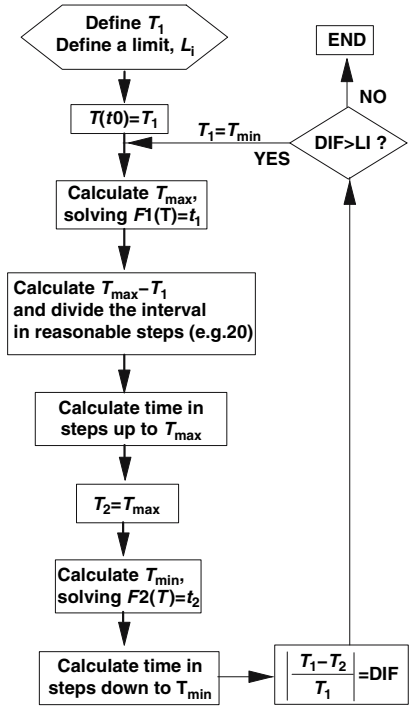

Fig. 3.26. Proposed algorithm for calculating temperature as a function of time, according to (3.77) and (3.78)

holding during "beam off" (pause). The time t_0 is the time at the begining of the beam pulse (3.77), respectively, at the end, which coincides, of course, with the beginning of the "beam off" time (3.78). $T(t_0)$ is the corresponding temperature of the target. The solution holds for a thin material radiating into both hemispheres.

With (3.77) and (3.78), the time dependence of temperature is given in a relatively complex connection. To determine the target temperature as a function of time, a numerical procedure can be implemented. A simplified algorithm is shown in Fig. 3.26. The following definitions and abbreviations have been introduced in the flow diagram:

- $F1(T)$ as the right-hand side of (3.77),
- $F2(T)$ as the right-hand side of (3.78),
- $t1$ as the beam pulse length (beam on), and
- $t2$ as the length of the pause (beam off).

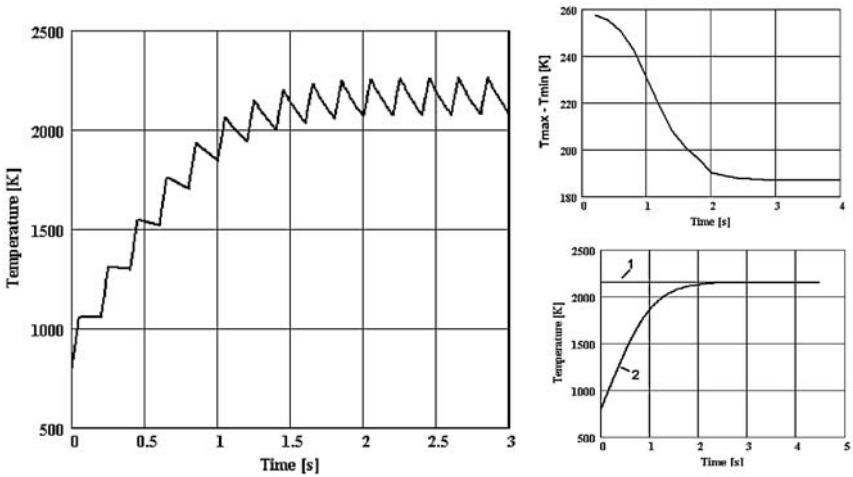

Fig. 3.27. Calculation of the steady state for a thin tungsten target, cooled only by thermal radiation. Left: calculation according to (3.77) and (3.78), applying an numerical algorithm as shown simplified in the flow diagram of Fig. 3.26. Right, top: calculated swing in temperature. Right, bottom: curve, marked **1** calculated temperature from the dc-calculation taking the average power P_{DC} over one cycle. Curve marked **2** calculated heating up with P_{DC} according to (3.77)

Example

Tungsten, $\Delta x = 0.2\,\mathrm{mm}$
Environment temperature, $T_{\mathrm{e}} = 300\,\mathrm{K}$
Pulse length (beam on): $t1 = 50\,\mathrm{ms}$
Pause (beam off): $t2 = 150\,\mathrm{ms}$
Beam pulse power: $P_{\mathrm{p}} = 3\,\mathrm{W}\,/\,\mathrm{mm}^2$
Equivalent dc-power: $P_{\mathrm{dc}} = 0.75\,\mathrm{W/mm}^2$

Figure 3.27 shows the results. The swing between $Tmax$ and $Tmin$ increases with decreasing duty factor. The example is typical for the maximum power ratings on a tungsten wire of a profile grid. Similar calculations have been performed for SiC fibers [172].

Conclusion

The connections discussed between thermal effects, the relevant parameters of highly intense particle beams, and the physical-mathematical properties of construction materials should enable a designer of beam intercepting beam diagnostic devices to solve even more complex problems concerning this matter.

4

Beam Profile Measurements

In accelerator physics, the density distributions of particles over the two transverse coordinates x (horizontal) and y (vertical) are called beam profiles. As discussed in Chap. 6, beam profiles can be derived from the two-dimensional transversal subspaces of six-dimensional phase space, occupied by the ensemble of all particles. Hence, emittance measurements in the transverse phase planes automatically deliver also the beam profile (see Chap. 6).

Beam profile measurements and their continuous monitoring are important during routine machine operation as well as for accelerator experiments to optimize parameters settings and study space charge effects. Determination of the beam width from a profile measurement is important for matching different parts of an accelerator facility in the transverse phase planes. On the other hand, dependency of the beam width on beam intensity may indicate space charge effects. Furthermore, separation of isotopes by analyzing magnets as well as determination of the charge numbers in complex stripper spectra require beam profile measurements. There is a great variety of measuring devices, depending on the kinds of particles, intensity, and energy. Devices can be classified into

- non-destructive or nearly non-destructive devices, such as harps, profile grids, SEM grids, residual gas ionization monitors, viewing screens (holds only if the penetration depth is large in comparison to the screen thickness), and wire scanners,
- destructive devices, such as segmented Faraday cups, Faraday cup - scanning slit combinations, and sandwich detectors used for emittance measurements (see Chap. 6).

4.1 Profile Grids, Harps

One can classify these types of detectors according to the following criteria:

- The penetration depth of the particles is small in comparison to the thickness of the grid wires or strips. This is typical for protons or heavy ions with relatively low energies delivered mostly by linacs. In this case, the electric current signal from a wire or strip is the sum of the charge of the stopped particle itself and the escaping secondary electrons (assuming there is no secondary electron suppression). Therefore, the profile signal will gain from the secondary electrons, if positive ions hit the wires/strips, and the signal will be lowered if negative ions hit the wires/strips. When charged particles are completely stopped, thermal heating due to the energy loss has to be considered, since it may be the limiting factor with respect to the maximum allowed beam intensity on the grid. Typically, about 10% of the beam area is covered by wire grids and, therefore the transparency is of the order of 90%. For grids consisting of thin detector strips, transparency is lower.
- On the other hand, if the thickness of the grid wires/strips is small in comparison to the penetration depth of the particles, the particles will go through, and the signal from the grid is generated only from escaping secondary electrons. As a consequence, the signals are in general much smaller than when the particles are stopped, especially if one considers highly positive charged heavy ions. Therefore, in many cases, so-called SEM strips having a larger cross section perpendicular to the beam are used, which improves the yield of secondary electrons. For energies above about 1GeV/u, the specific energy loss is relatively small and therefore thermal heating may be neglected in most cases.

Typical specifications of profile grids are given in Table 4.1.

Thermal protection (see Table 4.1) by a light-sensitive diode can be used to trigger a fast device to attenuate or even stop the beam in front of the grid. Figure 4.1 shows some construction details of a typical profile grid. If

Table 4.1. Typical parameters of profile grids

Diameter of wires	0.05–0.5 mm
Spacing	0.5−5 mm
Length of wires	40−100 mm
Number of wires	15−127
Material	W-Re alloy (typical)
Material of tension springs	Duratherm® 600
Tension	$\approx 0.5-0.6$ N
Signal wires	Kapton® isolated
Insulation (frame)	Glass ceramics, Al_2O_3, peek
Vacuum performance	$\simeq 10^{-7}$ mbar
Maximum power rating (dc)	$\lesssim 0.5\,\mathrm{W/mm^2}$
Maximum power rating (pulse)	Depends on many parameters; see text
Thermal protection	Light-sensitive diode

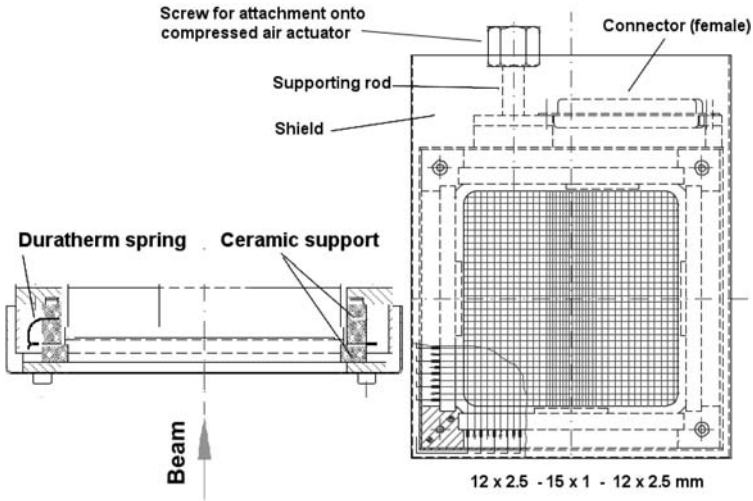

Fig. 4.1. Construction drawing (overview from the front side) of a typical profile grid [33]. To reduce the number of required signal processing channels, a larger spacing outside the center has been chosen

the thermal load on the wires can be neglected, tensioning of the wires is not necessary, which results in a simpler and cheaper design. The grid itself can be completely dismantled from the compressed air actuator by releasing only one screw. All signal cables from the grid to the vacuum-tight connector are fed via a second internal connector mounted on the grid frame, usually made from vacuum compatible plastics (up to 10^{-7} mbar) but may be also made from ceramics, which can be baked. Figure 4.2 is a photo of a prototype with 96 wires per plane and 0.5-mm spacing. The frame consists of machinable ceramic and each wire is tightened up by a Duratherm® spring. From the prototype, it follows that 0.5-mm spacing seems to be the minimum for this type of grid.

4.1.1 Signal Processing

As discussed in the context of emittance measuring systems in Chap. 6, signals can be amplified by current to voltage conversion (I/U converter) or by applying the switched integrator principle (see Fig. 6.7 in Chap. 6). The performance of both types is determined mainly by the time structure of the beam current. In Fig. 4.3, the current required to obtain an output signal of 1 V is compared for both types, assuming a conversion rate of 2 nA/V in the most sensitive range of the I/U converter [173] and a conversion rate of $Q_{\mathrm{U}} = Q/U = 10^{-10}$As/V for the switched integrator type ACF2101 (integrated circuit). Figure 4.4 shows a computer display of three measured profiles from an 11.45-MeV/u $^{12}C^{6+}$-carbon beam in the transfer channel from the

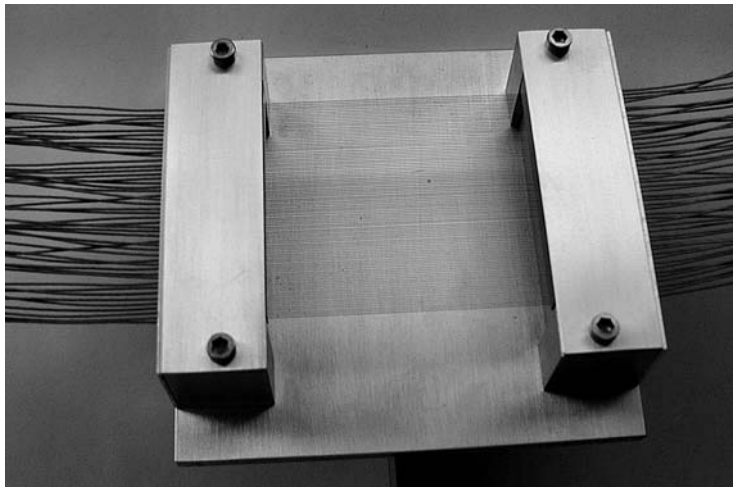

Fig. 4.2. Prototype [33] of a profile grid with 96 wires/plane and 0.5-mm spacing of the wires. Each wire is tightened up by a *Duratherm*® spring. The prototype shows only one plane. The *Kapton*®-isolated wires on the right and left-hand sides are connected to two 55-pin connectors

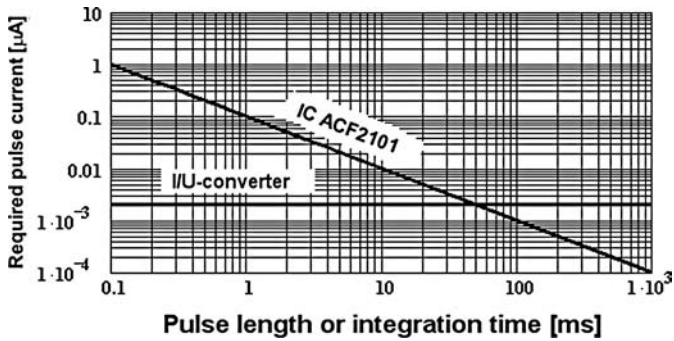

Fig. 4.3. Comparison of an I/U converter with a switched integrator (IC ACF2101) with respect to the required pulse current dependent on the pulse length or integration time, respectively

UNILAC to the SIS. Since the pulse length in the transfer channel is below 1ms in this operating mode of the UNILAC, signal processing is based on the I/U converter principle. An integration time of 500 µs has been chosen for the sample and integrator stages following the I/U converters. To smooth the profiles, a spline fit is applied to the measured raw data, which also allows mathematical localization of the peak centers. Taking advantage of such fitting procedures also gives the possibility of increasing the spacing of the wires outside the center, which reduces the number of required signal processing channels and therefore the costs of mechanics and electronics.

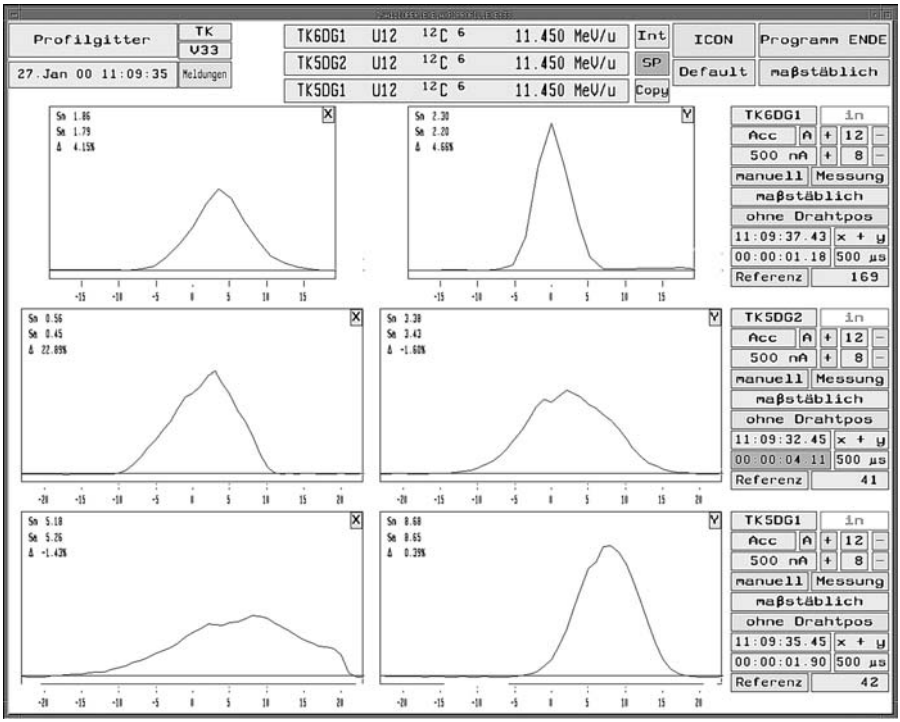

Fig. 4.4. Three measured profiles in the transfer channel from the UNILAC to the SIS of GSI. The horizontal profiles are displayed on the left; the vertical ones are displayed on the right. The abscissa is scaled in millimeters

Remark. Attempts to simplify the electronics by multiplexing the signals from the wires sequential to only one signal processing channel have shown that the effort is comparable to a system with one channel for each wire. This is caused by the requirement to ground all unconnected channels to avoid charging the wires to relatively high potentials in a short time. Another drawback of this method, especially for many channels and rather fast changes in the beam intensity, can be the time delay between signals.

4.1.2 Minimum Current Required per Wire

For the I/U converter, the output does not depend on integration time. Therefore, it may be worthwhile to estimate the minimum current required per wire. Experience has shown that a current leading to 50-mV output voltage from the wire at the center of the profile is about the detection limit. Taking the conversion rate of 2 nA/V, this corresponds to a current of 100 pA. Of course, the corresponding total beam current depends on the beam size. Assuming a

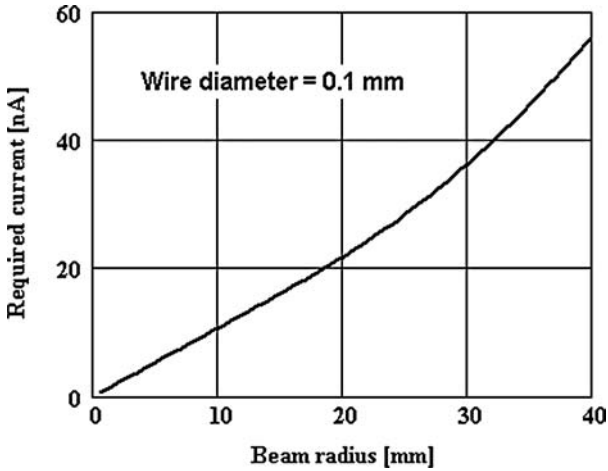

Fig. 4.5. Minimum beam current required to collect 100 pA on the wire at the center of the beam

round beam with a symmetric Gaussian intensity distribution in both transverse directions, the required minimum is given in Fig. 4.5. In the calculation, only the primary beam current has been considered. The contribution of secondary electrons may be estimated from Fig. 4.6.

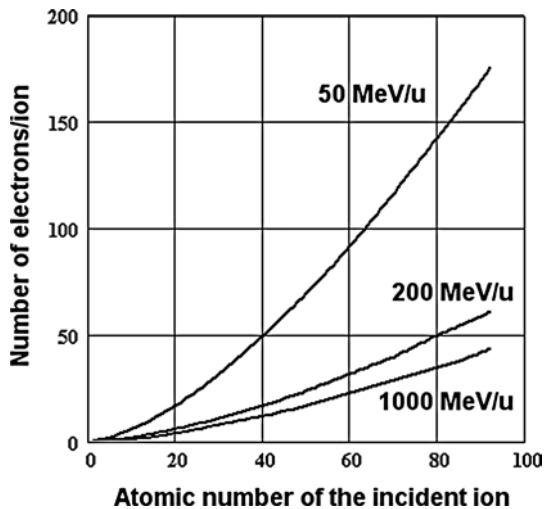

Fig. 4.6. Roughly estimated number of secondary electrons per incident ion with the energy of the incident ion as a parameter. The data have been scaled $\sim z^{1.5}$ from various data found in the literature (e.g., [203])

4.1.3 Maximum Current on a Wire

The maximum current on a wire is limited

- due to thermal heating, leading to break of the wires,
- by too high thermal emission of electrons according to the Richardson - Dushmann law (see Chap. 6, Sect. 7 for more details). In this case, the measured profile peak is strongly enhanced in the center of the beam. From this point of view, a maximum temperature of about 1900–2000 K seems to be tolerable. Test measurements in the laboratory [174] have shown that the wires break at about 2200 K.

Due to the very small cross section of the wires and the rather low heat conductivity of the W-Re alloy, heat transfer along the thin wire can be neglected. Because there is also no convection in a vacuum, cooling of the wires takes place only via radiation. For a pulsed beam maximum, minimum as well as swings in temperature depend very much on pulse length and duty cycle. A more detailed discussion of this thermal problem as well as description of a program algorithm for the calculation of the steady state is given in Chap. 3, Sect. 3.59. Assuming a maximum temperature of 2000 K at the end of each beam pulse, the allowed maximum power density P_d deposited on a wire is given in Table 4.2 for some typical macropulse lengths T_p and duty factors $D = T_\mathrm{p}/(T_\mathrm{p} + T_\mathrm{pause}) = T_\mathrm{p}\, f_\mathrm{p}$ (f_p is the repetition frequency of macropulses). In the last column of the table, the swing in temperature after reaching the steady state is given, too. The P_d values for $D = 16.7\%$ compare well with the value of about 0.5 W/mm^2, given in Table 4.1 for a dc-beam.

Table 4.2. Calculated maximum power density deposited on a W-Re wire in dependence of the time structure of the beam pulses. In the last column, the calculated swing in temperature is given. The data hold for a maximum temperature of 2000 K in the steady state.

T_p	T_pause	D	P_d [W/mm^2]	T_swing[K]
200 µs	0.5 s	3.998×10^{-4}	500	438
200 µs	0.1 ms	1.996×10^{-3}	190	166
200 µs	10 ms	0.02	27	24
200 µs	1 ms	0.167	3.2	2.8
1 ms	2.5 s	3.998×10^{-4}	190	832
1 ms	0.5 s	1.996×10^{-3}	102	437
1 ms	50 ms	0.02	22	94
1 ms	5 ms	0.167	3	11
5 ms	12.5 s	3.998×10^{-4}	53	1160
5 ms	2.5 s	1.996×10^{-3}	38	828
5 ms	0.25 s	0.02	14.5	310
5 ms	25 ms	0.167	2.8	51

4.1.4 Algebraic Reconstruction Techniques

When monitoring beam profiles with profile grids, consisting of two planes of wires (horizontal, vertical), one has to keep in mind that an integration of the intensity distribution along a wire takes place. This integration can result in misinterpretations, if one deals with "strange" profiles (for example, from a hollow beam). To improve the performance of standard profile grids in resolving such "strange" profiles, integration over one direction (over the wire length) has to be avoided [mathematically, $I(x, y) \neq I(x) \times I(y)$]. A solution of the problem can be the rotation of a so-called harp around the beam axis and applying the multiplicative algebraic reconstruction technique (MART) to data, measured at various angles. With this method, very complex beam profiles can be reconstructed. The method is well known in medical applications as computer tomography (CT), but one also finds applications in electron microscopy and accelerator physics [175–184]. Of course, the computer-controlled rotation of a harp inside the vacuum system complicates the construction design. On the other hand, it also halves the number of required signal processing channels, which saves costs.

Short Description of the Mathematical Problem

To determine is the intensity distribution $I(x, y)$ defined by the beam in a limited region G, but, instead to have the information about the function $I(x, y)$ at any x, y, one has only the integral along a straight line g (the wire) through the region G. Assuming that the function $I(x, y)$ does not change very much in certain subregions of G, one divides the region G into m subregions where $I(x, y)$ is approximated by piecewise constant functions. This simplifies the problem because the integral along g can be replaced by the sum,

$$\int_g I(x, y)ds \rightarrow \sum_{i=1}^{m} s_\mathrm{i} L_\mathrm{i} \ , \tag{4.1}$$

with s_i as the approximated constant value of $I(x, y)$ within the subregion i and L_i as the length along g bounded by the subregion i. Obviously, $L_\mathrm{i} = 0$ if the path along g does not cross the subregion i. Having a harp with k wires, one measures k intensity values T_k:

$$T_\mathrm{k} = \int_{g_\mathrm{k}} I(x, y)ds \approx \sum_{i=1}^{m} s_\mathrm{i} L_\mathrm{ik} \tag{4.2}$$

with unknown subintensities s_i. Hence, the approximation results in a system of linear equations which can be solved unequivocally, if there are $i = n \times k$ measured values, where n is the required number of different viewing angles of the harp. To achieve good resolution, the number of subregions should be $\gg k$ or, in other words, the integral along a wire should be approximated by a

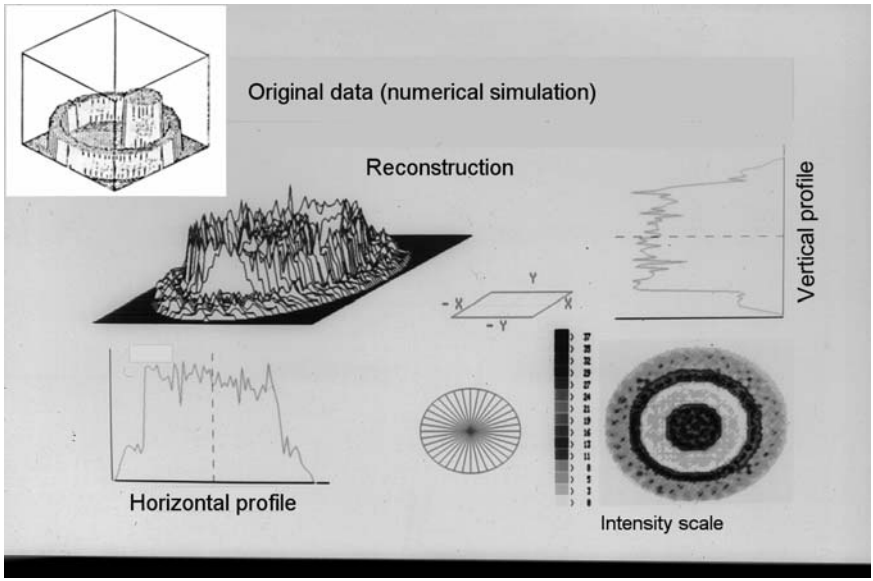

Fig. 4.7. Reconstruction of simulated data using the an extended MART - technique [185]. 18 different viewing angles between 0° and 180° have been used to reconstruct the cylinder in the hollow cylinder

sufficiently large number of short pieces. In general, the number of measured values is smaller than required, and, therefore numerical solutions are introduced. The MART algorithm [185] is based on maximization of the entropy, defined by the number of subregions, their shapes, the measured values of T, and the L values. This algorithm uses subregions in the shape of hexagons, which are formed when the harp is positioned at $0°, 120°$, and $240°$. An advantage of this method is that the lengths of all L's are equal. To improve the solution, the algorithm has been extended to an arbitrary number of view directions and quadratically shaped subregions [185]. A drawback of this method is that the lengths L differ along the lines, but taking advantage of computer programs, this problem is easily solved. The results from a simulation with numerically generated data describing a cylinder inside a hollow cylinder are displayed in Fig. 4.7. From the figure, it becomes clear that, due to the integration over one coordinate, the cylinder in the hollow cylinder cannot be observed in the one-dimensional profiles. On the other hand, the algebraic reconstruction of the contour plot (bottom right) shows it very clearly. Due to increasing medical applications of tomographic techniques, the reconstruction algorithms have been refined considerably in recent years. A method, described as the filtered-back projection technique [184], has been developed at the Brookhaven National Laboratory (BNL). The technique is applied to signal evaluation of a residual gas ionization monitor in the Relativistic Heavy Ion Collider (RHIC). It is based on a mathematical sequence,

consisting of one- and two-dimensional Fourier transforms, convolution, and back-projection by inverse Fourier transforms. The procedure has been applied to reconstruct contour plots in two-dimensional transverse phase planes from about 40 beam profile measurements.

4.2 Profile Grids with Gas Amplification (MWPC)

In case of higher beam energies, particles go through wires/stripes with the following consequences:

- There is no direct contribution from the charge of the passing ion to the electrical signal. Then the signal comes only from the emitted secondary electrons. Considering, for example, the SIS, where uranium ions are stripped before injection at 11.5 MeV/u to charges around 70^+ this results in a considerable loss in signal strength.
- As discussed in Chap. 2 for SEM monitors, the emission of secondary electrons decreases with increasing energy of incident particles due to lower specific energy loss and increasing penetration depth. This causes a further reduction in signal strength at higher energies.

Increasing medical applications in the field of cancer therapy [117] require precise beam profile measurements. For this application, the energies are of the order of some 100 MeV/u, and the required intensities for protons or ions with rather low atomic numbers such as $^{12}C^{6+}$ ions are relatively low. Thus, the signals from conventional profile grids and harps are too small. The same arguments hold for proton machines, provided for high energy physics experiments, delivering energy of the order of some GeV.

As a consequence, multistep avalanche chambers known as multiwire proportional chambers (MWPC), first described by Breskin et al. [186] are coming more and more into use for beam monitoring. A schematic layout of a MWPC is shown in Fig. 4.8. There are three planes with thin wires inside a vacuum-tight case: two cathode planes, one with vertical wires to measure the horizontal profile and another one with horizontal wires to measure in the vertical direction. On the anode plane which is located between both cathode planes, the thin wires are arranged diagonally. The anode plane is held at a positive potential of 2–2.5 kV. The case is sealed against the vacuum pipe by two very thin foils (typically 25 µm) and filled with a mixture of Ar and CO_2 (ratio around 90 : 10) at atmospheric pressure. An impinging ionizing particle liberates electrons in the gas, which are multiplied in the high electric field between cathodes and anode. The gain due to this multiplication is of the order of 10^3–10^4 and can be easily controlled by changing the high voltage. In the current readout mode, each wire of the cathode plane is at virtual ground via an operational amplifier. Depending on the beam pulse a length, respectively, integration time, the operational amplifier works as a current to voltage converter or switched integrator (see Fig. 6.8 in Chap. 6). In this operating mode,

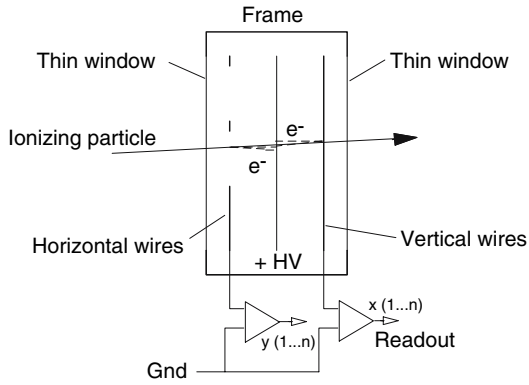

Fig. 4.8. Scheme of a MWPC for beam profile measurements

one obtains global information on the spatial distribution of the particles in the detector planes. The current readout mode is appropriate for beam profile measurements in the high energy lines of large machines. In medical applications for cancer therapy by protons or heavy ions, large MWPCs are arranged outside the vacuum system in front of patients. Figure 4.9 shows an exploded view of a chamber [187] with an active area of $400 \times 400\,\mathrm{mm}^2$, provided for beam profile monitoring at the so-called ISO-center of a cancer therapy facility working with protons. In this chamber, the amplification gap between the anode and each cathode is 5 mm. Therefore the localization of highly misaligned beams, strongly focused or defocused beams differ. To reduce this effect, gaps will be reduced to 3 mm in an improved new version [188].

In experimental applications, physicists are often interested in the positional information, event-by-event, and the device can be supplemented by a so-called preamplifier gap in front of the cathode/anode planes [189]. This leads to two-stage gas amplification with an overall gain of the order of 10^5–10^6. Due to the very high gain in the avalanche, the width of the Gaussian shaped charge distribution on cathode planes is of the order of 20 mm (FWHM, [189]). Hence, more than one cathode wire (e.g., 5) are connected to an amplifier and analog-to-digital converter (ADC). The data are processed to a computer to determine the position by a center of gravity (COG) calculation. This method is rather complex and expensive. An alternative method is based on the delay line technique, converting the information about the position via commercially available delay lines into time differences, which are analyzed by a time to digital converter (TDC) [189].

4.3 Wire Scanners

Profile signal generation from a wire scanner is comparable to that from a profile grid. However, instead of many wires covering the beam cross section,

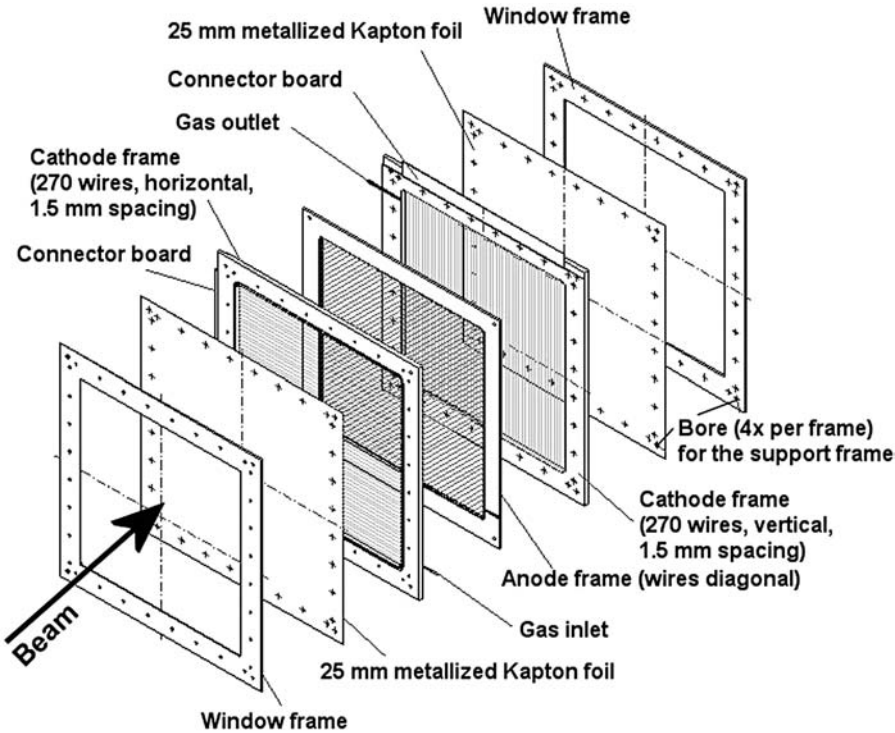

Fig. 4.9. Exploded view of a large MWPC [33, 187] for beam profile measurements outside a vacuum system

only one wire is moved through the beam. Referring to the remark concerning multiplexing signals from the wires of a grid to only one signal processing electronic circuit, the motion of the wire overtakes this function. There is a great variety of devices in use [190–200]. Most popular are scanners performing a linear motion through the beam and rotating wire scanners. Figure 4.10 shows the head of a wire scanner provided for moving under 45° through the beam by a motor driven UHV feedthrough. The scanning speed is typically in the range of 10–20mm/s. Due to the motion under 45°, the profiles in both directions (horizontal and vertical) can be monitored at the same time. The required displacement, the wire length, and the aperture of the fork have to be scaled by $\sqrt{2}$ to cover the beam cross section. Tension springs made from Duratherm® 600 are provided on both sides of the scanning wires.

Another scanning mode takes advantage of two wires, mounted at an angle of 90° onto a vibrating support [191]. The vibrating motion is performed by an electromagnet. The device has to be mounted onto a 45° port of a vacuum chamber to perform profile measurements in both transverse directions at the same time.

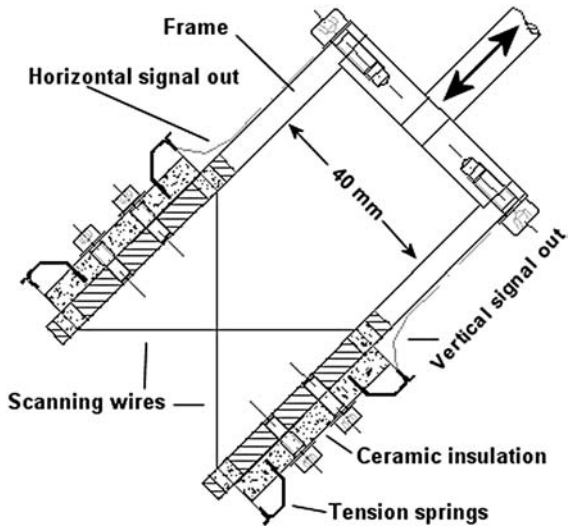

Fig. 4.10. Head of a wire scanner [33] moved under 45° through the beam

The so-called Hortig scanner [190] uses a rotating wire, which allows scanning speeds of the order of some millimeters/milliseconds. Figure 4.11 shows the head of such a scanner. The shape of the spiral allows scanning in both transverse coordinates, if the scanner is mounted on a 45° vacuum chamber port. To avoid deformation of the spiral due to fast rotation and/or thermal heating, the scanning wire is driven from both ends. The achievable resolution is limited to about 1mm by the diameter of the scanning tantalum wire. The scanner rotates at 750 rpm, which corresponds to a scanning speed of 1.34 mm/ms. The maximum measurable beam spot size is ≈ 35 mm.

4.3.1 Wire Scanner Versus Profile Grids

When deciding between profile grids or scanners, the following points should be taken into account:

- With a profile grid, the beam intensity is always sampled at the same time, whereas a moving wire will sample the profile at different locations at different times. Therefore longitudinal variations of the beam intensity are mixed with transverse intensity variations. This holds especially during the rise time of a beam pulse caused by the finite response time of pulsed ion sources.
- For pulsed beams, exact synchronization of an electromechanical system such as a scanning device is complicated.
- For a profile grid system, the signal-to-noise ratio can be enhanced by integration of the acquired signal. This is not possible for a fast scanner.

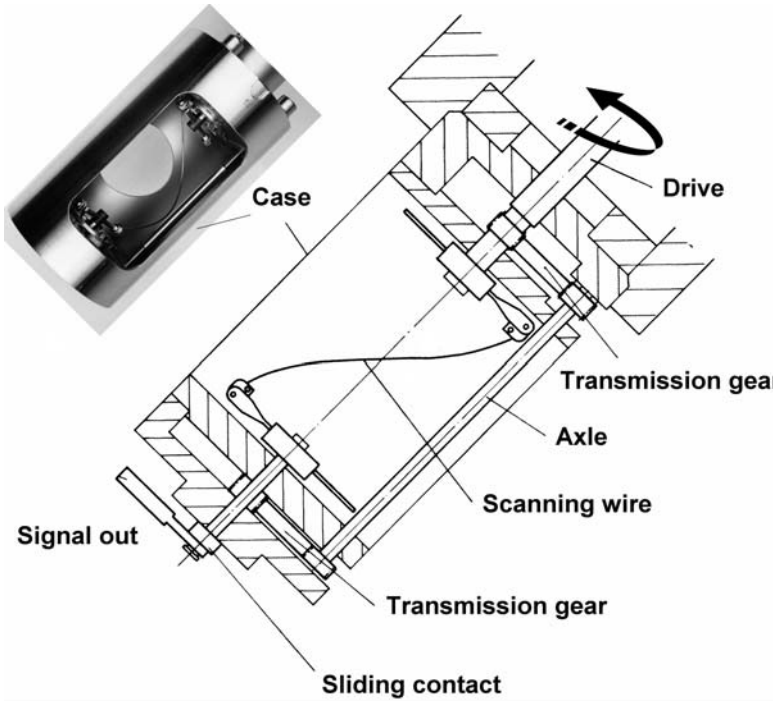

Fig. 4.11. Head of a rotating wire scanner, according, to Hortig [190]

- Considering a rotating wire scanner, as for example shown in Fig. 4.11, the geometric duty factor, caused by the rotation, reduces the thermal load and therefore allows a higher beam power loss than a static grid.
- Changes of the secondary emission efficiency, caused by high beam power and/or long operating time, have a smaller effect on the measured profiles if a scanning wire is used.
- Considering especially, the electronics for signal processing is much cheaper for a scanner than for a profile grid system.

4.3.2 Flying Wire

Profile grids, harps, and scanners, as discussed above, cannot be used in circular machines (synchrotrons, cyclotrons, storage rings) because the beam will be destroyed due to the large number of repetitive passes. For beam profile and emittance measurements in the proton synchrotrons of CERN, a very fast scanner sometimes called a "flying wire" was developed [194]. Taking advantage of pneumatic or spring-loaded drive systems, scanning speeds up to 20 m/s can be achieved. Since the energy loss dE/dx in the scanning wire is proportional to $\rho Z/A$, the scanning wire should be made of a material with low specific weight and a low atomic number such as carbon, SiC, or Be. The

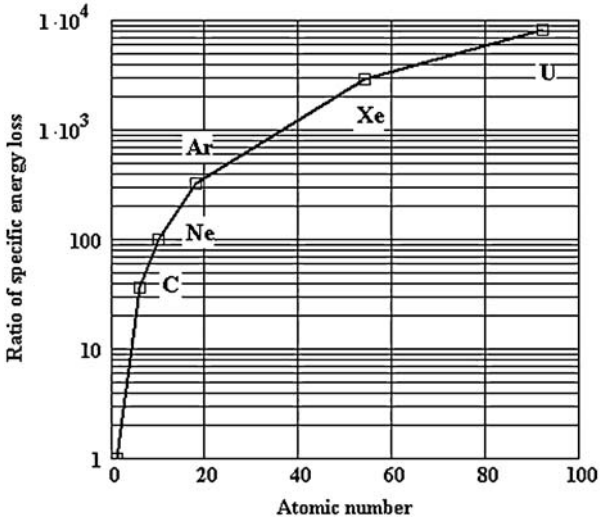

Fig. 4.12. Specific energy loss in a beryllium target normalized to the loss of protons. See text for details

wire thickness can be as low as 10 µm. But, keeping in mind the relatively short revolution times of circular machines of the order of microseconds, the measured profile results from a mix of transverse-intensity distribution and longitudinal variations of the beam intensity. Nevertheless, the flying wire has proven itself versatile tool for probing the steady-state transverse-intensity distributions in circular proton machines. However, considering circular machines for acceleration or storage of heavy ions, the use of flying wires is limited due to the much higher specific energy loss of heavy ions. This is demonstrated in Fig. 4.12, comparing the specific energy loss of C, Ne, Ar, Xe and U ions with the specific energy loss of protons in the energy range between 100 and 2000 MeV/u. The data hold for a beryllium target and are the average from calculated specific energy losses [122] at 100, 500, 1000, and 2000 MeV/u. As a consequence, flying wires cannot be used in heavy ion synchrotrons.

Example
Scanning wire: Beryllium with a diameter of $\delta x = 50 \times 10^{-3}\,\mathrm{mm}$
Specific weight of Be: $\rho_{\mathrm{Be}} = 1.848\,\mathrm{g/cm^3}$
Scanning speed: $v = 20\,\mathrm{m/s}$
Beam radius: $R_{\mathrm{beam}} = 10\,\mathrm{mm}$
Beam energy: $W = 1000\,\mathrm{MeV/u}$
Ion species: $^{238}\mathrm{U}^{73+}$
Specific energy loss (U→Be) *at* 1000 MeV/u*:* $\simeq 15.2\,\mathrm{MeV/(mg/cm^2)}$
Number of ions: $N_{\mathrm{U}} = 5 \times 10^{10}$ *(about the space charge limit)*
Revolution time: $T_{\mathrm{rev}} = 825\,\mathrm{ns}$

With the specific weight of beryllium, the maximum target thickness comes out to $\rho\delta x = 9.24\,\mathrm{mg/cm^2}$. The part of the beam that hits the scanning wire,

is about $p = 0.003$. This gives a power loss in the scanning wire of

$$P_{\text{wire}} = \frac{15.2\, p\, N_{\text{u}}\, \rho \delta x}{T_{\text{rev}}} \simeq 4.1\,\text{kW} \tag{4.3}$$

during the movement through the beam within about 1ms. Taking the same number of protons with 1000 MeV, one gets $P_{\text{wire}} \simeq 0.5\,\text{W}$. As a consequence of the much higher energy loss for the uranium beam, the wire will be destroyed in a short time, and also the beam will be lost due to the high energy loss per turn.

4.4 Scintillation Screens

The combination of a scintillation screen with a CCD camera for observation of the light spots is a very simple, reliable profile monitor. This combination does not require computer control or computerized signal processing, such as more sophisticated monitors. Thus viewing screens can be very useful during commissioning periods and for troubleshooting. This implies that viewing screens should be installed in addition to other monitors at all critical points along a beam transport system. Figure 4.13 shows a compact unit, consisting of an electromagnetic lifting system, which drives a simple flipping mechanism to move the viewing screen in and out of the beam. The electromagnetic lifter has a stroke of 10 mm and operates at 24V/ 0.85 A. A quartz window, mounted onto the supporting CF flange allows observation of the beam spot by a CCD camera. The window also allows illumination of the screen by an external light source. If a graticule is provided on the screen, a factor of $\sqrt{2}$ has to be taken into account for the spacing of the lines due to the 45° mounting. Furthermore, it may be advantageous for the operators to mark the screen with signs such as U = Up, D = Down, L = Left, and R = Right. To avoid charging the

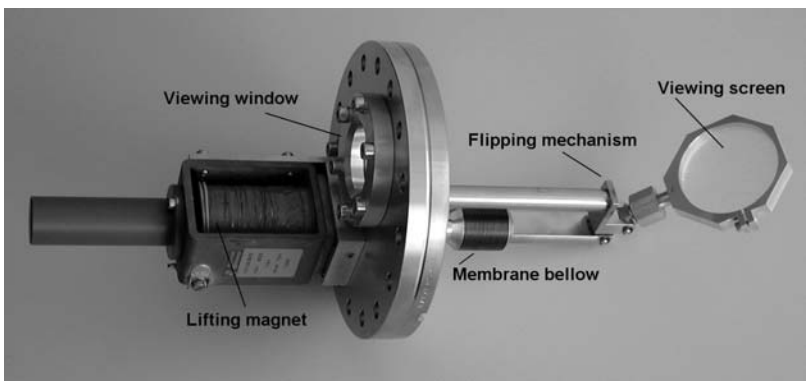

Fig. 4.13. Picture of a viewing screen mounted onto an electromechanically driven flipping mechanism [33]

non-conducting screen material, coating of the screen with a thin conductive layer is essential. Of course, the scintillation material has to be matched to the kind of ions and their energy, as well as to the expected beam currents. Additionally, the beam power deposited on the screen has to be considered to avoid thermal damage to the screen. The most important criteria for selecting a scintillation material are [120]

- The wavelength of the emitted light should be in the range $300\,\text{nm} < \lambda < 700\,\text{nm}$ to match the optical properties of commercial CCD cameras.
- High intensity of the emitted light, a high dynamic range, and good linearity between the incident particle flux and the light output are of importance. Saturation effects will lead to falsifications of the recorded profile signals.
- The absorption of the emitted light by the screen material itself should be as low as possible to prevent artificial broadening by stray light.
- To observe transients and fast variations in the beam profile, a fast decay time is essential.
- To produce large screens, the material should have good mechanical properties for machining and mechanical strength.
- To achieve long operating times, the material should have high radiation hardness, which automatically excludes plastic scintillators.

Table 4.3 summarizes the relevant properties of most used scintillation materials [201], [126].

Chromolux [202] (also named Chrolox6$^{\text{R}}$) is a very robust ceramic, which is very often used to measure beam profiles in the external beam lines of synchrotrons with slow extraction. Most of the tests of lifetime and sensitivity were performed with minimally ionizing protons, and, therefore, scaling to low energies and to various ion species is difficult. Assuming a minimal number of 2×10^6 protons/mm^2, required within the decay time of Chromolux ([203],

Table 4.3. Chemical composition and relevant optical properties of some often used inorganic scintillation materials

Name	Material	Activator	λ_{max}	Decay time
Quartz	SiO_2	None	Optical	$< 10\,\text{ns}$
	CsI	Tl	550 nm	1 µs
	ZnS	Ag	450 nm	0.2 µs
Chromolux	Al_2O_3	Cr	700 nm	100 ms
	Li glass	Ce	400 nm	0.1 µs
P43	Gd_2O_2S	Tb	545 nm	1 ms
P46	$Y_3Al_5O_{12}$	Ce	530 nm	0.3 µs
P47	$Y_2Si_5O_5$	Ce	400 nm	50 ns

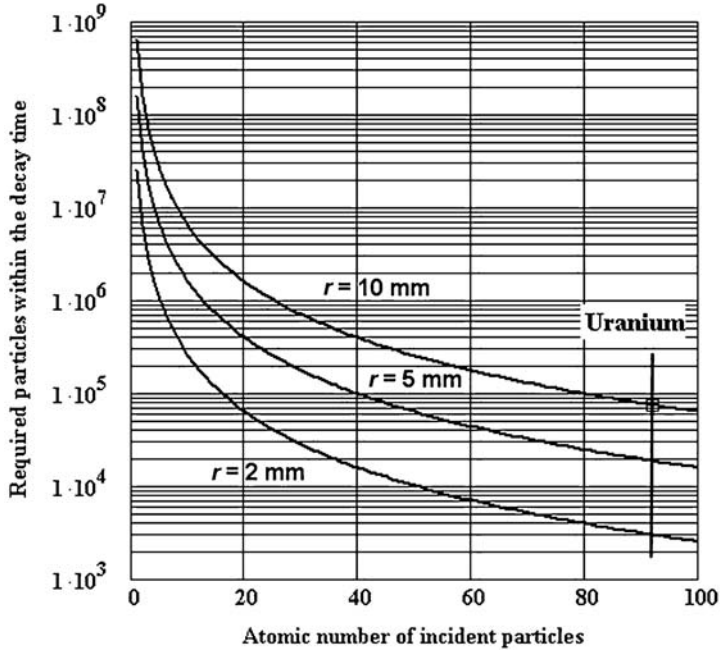

Fig. 4.14. Required number of particles hitting a Chromolux viewing screen within the decay time. The data have been scaled from measured data for protons. See text for details

[202]), a rough estimation for other particles is possible by scaling the data $\sim Z^2$ [204] (Z is the atomic number of the incident ion). Figure 4.14 shows the results of such scaling for ions up to uranium assuming beam radii of 2, 5, and 10 mm.

The materials named P43, P46, P47 are scintillation phosphor screens, where a powder is deposited on glass or metal plates. The best optical properties use Ce-activated materials, which are also used for analog oscilloscopes, electron microscopes, and image intensifiers. Due to the rapid development of digitizing circuits, most CCD cameras are equipped with a digital output of the CCD-pixel signals, which allows completely computer-aided evaluation of beam profiles dependent on time.

4.4.1 Scintillation Screens Versus Profile Grids

Comparing scintillation screens with profile grids, one should keep in mind the following points:

- Usually the beam losses are lower for a profile grid. Therefore, the emittance growth caused by multiple scattering is smaller for a grid system.

- At low energies, particles are completely stopped in the screen material and therefore the viewing screen acts as completely destructive beam intercepting device. On the other hand, the transparency of a grid is determined only by the spacing and diameter of the wires. This allows the observation of more than one profile at the same time along a beam line. Only at very high beam energies will this be possible with viewing screens, too.
- The response of various scintillation materials depends on many parameters, such as energy, ion species, and time structure of the beam. Therefore, different scintillation materials may be required at large, universal accelerator facilities.
- The separation of horizontal and vertical profile projections, which is characteristic for grids, can be advantageous for beam alignment by operators. Of course, this separation can be performed for a scintillation screen by applying appropriate computer algorithms.
- The dynamic range is higher and linearity is better for profile grid electronics. This can be important in view of the diversity of heavy ion accelerator facilities.

Although most of the summarized points favor grid systems, viewing screens offer the most direct way of beam observation and are installed in nearly all accelerator facilities from the source up to the target.

4.5 Residual Gas Ionization Monitors

A highly ionizing particle, passing a certain volume ΔV in a beam transport system, generates ion-electron pairs due to collisions with the atoms or molecules of the residual gas within ΔV. The fact that the number of liberated ion-electron-pairs is directly proportional to the beam intensity within ΔV allows nearly non-destructive beam profile measurements by collecting the ionized particles. The first devices using this technique were developed for proton machines in 1967 [205,206]. Many similar devices based on this principle have been developed since that time [207–218], including a sophisticated device, the so-called ionization beam scanner [210]. Although the number of electrons liberated by the ionization process is exactly equal to the number of positive charges generated, the collection of positively charged ions is preferred for beam profile measurements with high resolution, due to the following facts:

- The momentum transfer to the electrons and ions perpendicular to the collecting electric field caused by the space charge field of the beam is much larger for electrons, which reduces the achievable resolution if electrons are collected [215,216,218,223].
- The same argument holds considering the recoil caused by the ionization process itself [215,218,224].

Nevertheless, there are some special applications based on the collection of electrons. A rather complex device, provided for measurement of the longitudinal intensity distribution is described in Chap. 6, Sect. 7. A device, which

collects the electrons as well as the ions to measure horizontal and vertical profiles at the same time with only one electrode system, is discussed in [215].

The designer of a residual gas ionization monitor has to take into account some important differences between devices provided for linacs and transfer systems, on the one hand, and devices provided for circular machines delivering or storing particles at high energies, on the other hand:

- Typical pressures in linacs and transfer lines are of the order of 10^{-6}–10^{-8} mbar, whereas the pressure in synchrotrons and storage rings, is mostly of the order of 10^{-9}–10^{-11} mbar.
- Due to the different vacuum pumps in linacs and transfer lines, the residual gas is composed mainly of N_2,O_2 and only 10–20% H_2, in circular machines H_2 makes the highest contribution (up to 90%).
- In many cases, the velocity of the accelerated/transported ions in linacs and transfer lines is well below relativistic values, and, therefore, the specific energy loss is much higher than that for circular machines, operated mostly at relativistic energies. As a consequence, the number of liberated electron-ion pairs differs very much in both cases.
- low particle energies, the deflection of the particles by the collecting field is much higher and if not tolerable, has to be compensated by additional steering devices.
- Last, but not least, the different time structure of the beam has to be considered in the design of a monitor, too.

4.5.1 Example for the Linac Case

Due to the high ionization cross sections, it can be sufficient to collect the liberated ions (electrons) on metal strips and feed the signals to conventional profile grid electronics of the type of I/U converters or switched integrators. Figure 4.15 shows a monitor, which can be rotated around the beam axis to perform tomographic data evaluation, as discussed above. The monitor is equipped with 15 collector rods having a diameter of 1 mm and covering a width of 30 mm.

Signal Calculation

Experience has shown that the expected signals can be calculated within an accuracy of about 30% from energy loss data in N_2 and H_2 gas (see Fig. 7.16, Chap. 6, Sect. 7). In the energy range between 2.2 keV/u and 11.5 MeV/u, the ratio between the primary beam current and the expected electron current collected on all detector strips has been calculated, assuming the following parameters:

Diameter of the collector rods: 1 mm
Spacing between the rods: 1 mm
Length of the rods: 100 mm

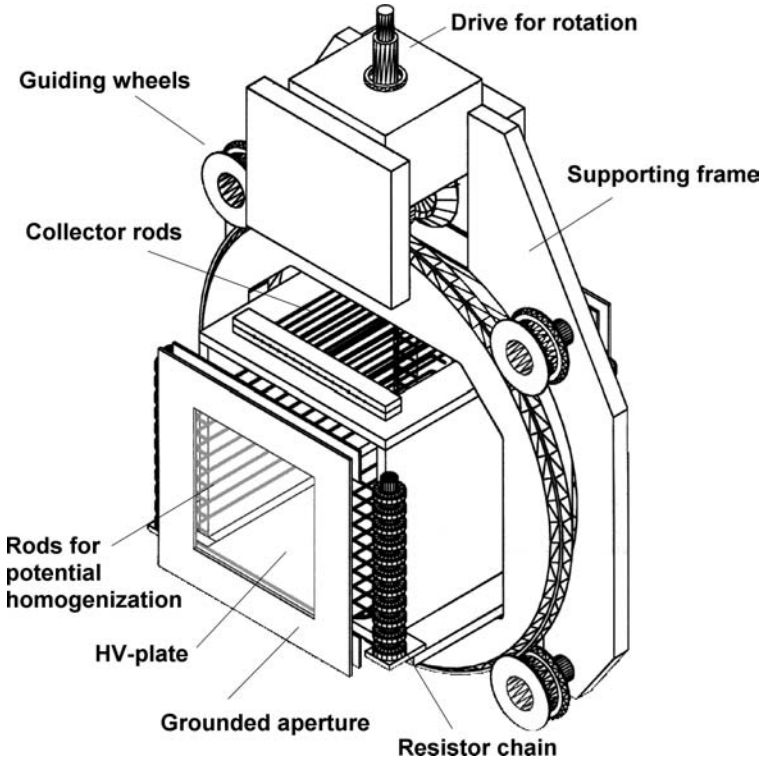

Fig. 4.15. Study of a rotatable residual gas ionization monitor [33]

Vacuum pressure: 10^{-7} mbar
Residual gas composition: 80% N_2, 20% H_2
W value: 36.5 eV (assumed to be the same for N_2 and H_2 [120])

Since the example is from the UNILAC with two strippers, one at 1.4 MeV/u and one at 11.5 MeV/u, the current ratio has been calculated for the energies, ion species, and charge states given in Table 4.4.

Table 4.4. Energies, ion species, and their charge states used for the calculation of expected ion currents from residual gas ionization, shown in Figure 4.16

Beam energy [MeV/u]	Ne	Ar	Xe	U
0.0022	1+	1+	2+	4+
0.5	1+	1+	2+	4+
1.4	1+	1+	2+	4+
5	7+	10+	20+	28+
11.5	10+	18+	46+	72+

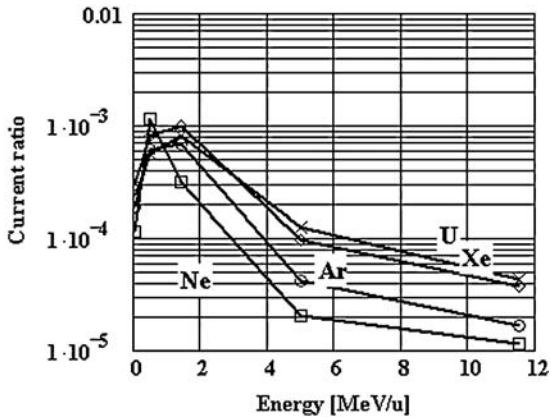

Fig. 4.16. Expected total current from residual gas ionization. See text for the parameters

The results are shown in Fig. 4.16, taking energy loss data from [122, 225]. Assuming primary currents in the range between μA and mA leads to acceptable signals, using I/U converters with conversion rates between nA/V and μA/V. In an experiment, calculated signals were compared with measured signals for $W = 2.2\,\mathrm{keV/u}$. The result is shown in Fig. 4.17. For signal calculation, a parabolic intensity distribution in both transverse directions (centered around zero) 17.7 mm wido (FW) was assumed. The agreement within about 30% confirms the approximative calculability based on energy loss data and W values.

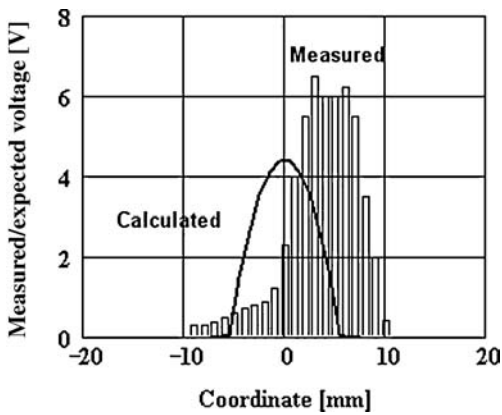

Fig. 4.17. Comparison of expected profile signals from a residual gas ionization monitor with measured data. Relevant data: pressure 4×10^{-7}mbar, beam current 6mA Ar^{1+} ions, I/U-conversion rate 0.2 μA/V, collecting field 50 V/mm

The Steering Effect

Due to the collecting field of the order of ∼500 V–1 kV/cm, considerable deflection of the primary beam at low beam energies has to be taken into account. The deflecting angle is given by

$$x' = \frac{\dot{x}}{\dot{z}} = \frac{\zeta\, e\, E\, L}{A\, m_0 c^2\, \beta^2}\ , \tag{4.4}$$

where ζ is the charge state of the ion; $e = 1.602 \times 10^{-19}$As; E is the collecting field strength; L is its extension in the beam direction, including the fringing fields on both sides; A is the mass number of the ion, $m_0 c^2 = 931.5016$ MeV; and $\beta = v/c = \dot{z}/c$. Depending on the beam energy and the tolerable x', the deflection may be compensated for by steerers behind, or in front of and behind the monitor.

Space Charge Effects

There are two monitors, based on residual gas ionization, installed in the stripper section of the UNILAC: one to measure the transverse beam profiles, collecting ions, and the other one to monitor the longitudinal intensity distribution within the bunches, collecting electrons. The measured data from both monitor systems are influenced by space charge forces from the electromagnetic bunch fields, which are discussed in Chap. 8. The space charge effects on the bunch shape monitor, collecting electrons, are studied in Chap. 7.

Due to the higher mass, the momentum transfer to ions liberated from the residual gas is much smaller than that for electrons. On the other hand, the acceleration of the ions in the collecting field is much smaller. This fact, in turn leads to a longer interaction time between the space charge of the bunch and the ion. Therefore, for bunched beams, the fast accelerated electrons may "see" only the space charge force from the bunch in which they are created, whereas the ions can experience the forces of many bunches, depending mainly on their velocity βc and their spacing $\beta\lambda$. The problem is illustrated in Fig. 4.18. At $t = 0$, the center of one bunch passes the center of the monitor. The bunch shape is approximated by a sphere, which is a good approximation for the stripper section of the UNILAC with typical bunch length of the order of 0.5–1ns and a β value of 5.5% ($W = 1.4$ MeV/u). The small inset at top left shows the shape of the electric field strength, assuming a parabolic charge density distribution inside the spherical bunch. Due to the integration of the signals over the collector strips, which are aligned parallel to the z-coordinate, displacements of the ions in the z-direction have no effect on the measured profile. The same holds for changes in velocity in the x-direction, since this leads only to differences in the arrival time of the ions at the collector strips.

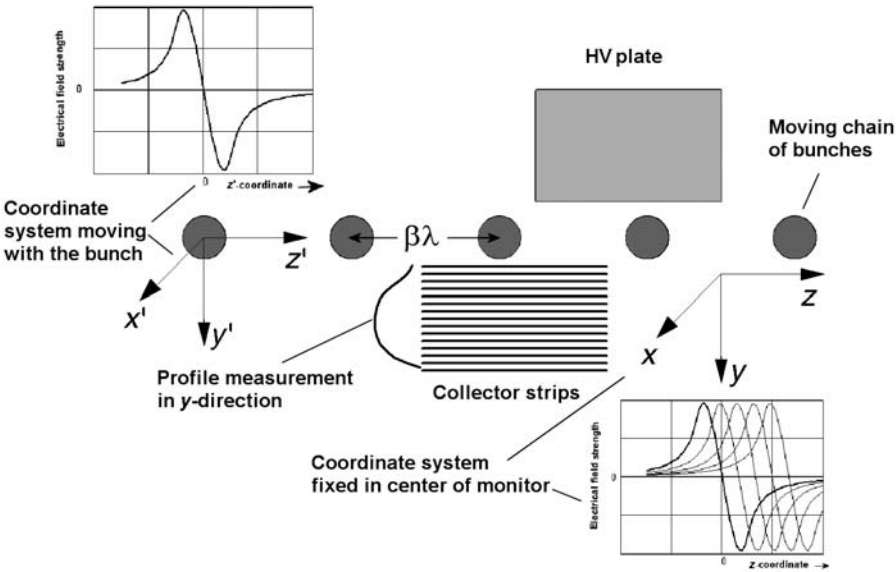

Fig. 4.18. Scheme to illustrate the estimation of space charge effects from moving bunches on the ions driven to the collector strips by an external electrical field in the x-direction. λ is the wavelength of the accelerating rf

To study the space charge effect with respect to measured profiles, one has to consider the action of the field components $E_\mathrm{x}, E_\mathrm{y}, E_\mathrm{z}$ caused by the space charge and the external field component E_{ext} on the ions. Due to the movement of the bunch chain as well as the movement of the ions, the field components are changing permanently. The numerical procedure, which has been applied to calculate the field components, velocity components and coordinates dependent on time and the initial conditions, is described in more detail in Chap. 7.

Radius of the spherical bunch: $\mathrm{R_{bunch}} = 10\,\mathrm{mm}$
Ion species in the bunch: U^{4+}
Number of ions within one bunch: 10^9
Charge density distribution in the spherical bunch: parabolic
$\beta = 0.055$
$E_\mathrm{ext} = 100\,\mathrm{V/mm}$
Distance from the center of the beam line to the collector strips: 25 mm
Bunches considered in the numerical calculation: 25
Step width in time: 0.1 ns (0.01 ns for electrons; see Fig. 4.22)

Various calculations have been performed with different sets of initial conditions for ions from residual gas. Assuming the ions ($\mathrm{H_2}$,$\mathrm{N_2}$) start at $t = 0$ at the center of the bunch with initial coordinates $x = \dot{x} = 0$, $y = \dot{y} = 0$,

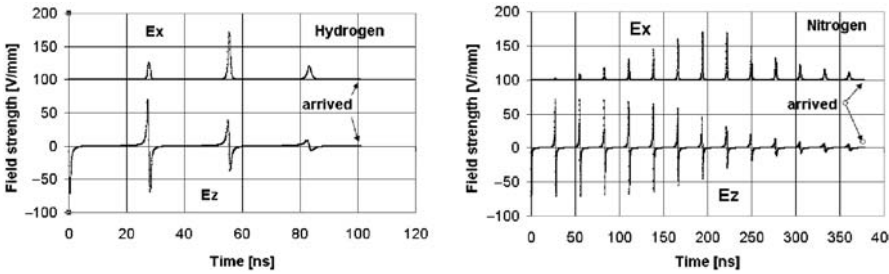

Fig. 4.19. Electrical field strength "seen" by hydrogen, respectively, nitrogen ions moving toward the collector strips. Note that the external field $E_{\text{ext}} = 100\,\text{V/mm}$

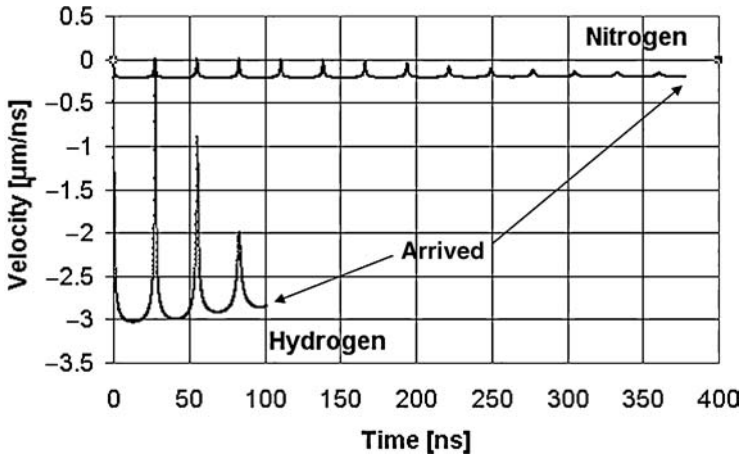

Fig. 4.20. Illustration of the repulsive space charge forces acting on the positive ions during the flight time to the collector strip

$z = \dot{z} = 0$, Fig. 4.19 shows that the space charge of more than one bunch acts on the ions. Figure 4.20 shows the actions of repulsive space charge forces.

Figure 4.21 demonstrates the influence of space charge forces on measured profiles. It shows the deviations between the required arrival coordinate (which is just the start coordinate $y(0)$) and the calculated one. For the parameters of the example, the maximum space charge force occurs at about $r = 7\,\text{mm}$ (see Chap. 8). For this reason, in one set of the initial coordinates, $x(0) = -7\,\text{mm}$ has been considered. In addition, an initial velocity $\dot{y}(0)$ of the ions in the y-direction, corresponding to the thermal energy of $1/40\,\text{eV}$ has been assumed in this set (all remaining initial coordinates are given in the figure). Due to the lower speed of N_2 ions, the space charge force acts a longer time (compare Figs. 4.19 and 4.20), and, therefore the effect on both ion species is nearly the same. From Fig. 4.21, it follows that the resolution of the monitor is better than 1mm, which is tolerable in most cases.

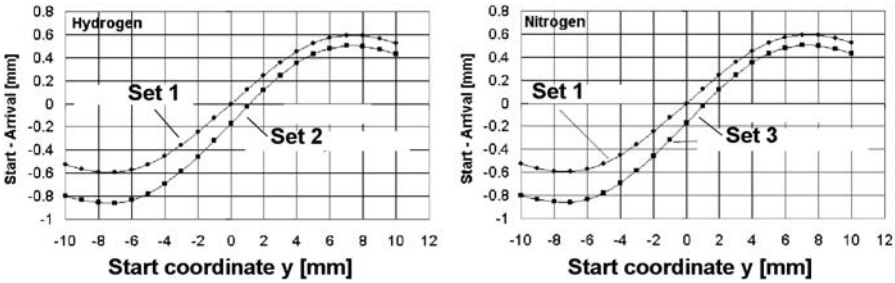

Fig. 4.21. Deviations between the required arrival coordinate and the calculated one. Left: hydrogen, right: nitrogen. Set **1** corresponds to the initial coordinates $x(0) = z(0) = \dot{x}(0) = \dot{y}(0) = \dot{z}(0) = 0$. Set **2:** $x(0) = -7\,\mathrm{mm}$, $z(0) = 0$, $\dot{x}(0) = z(0) = 0$, $y(0) = 4.15 \times 10^{-4}\,\mathrm{mm/ns}$. Set **3:** $x(0) = -7\,\mathrm{mm}$, $z(0) = 0$, $\dot{x}(0) = z(0) = 0$, $y(0) = 1.55 \times 10^{-4}\,\mathrm{mm/ns}$

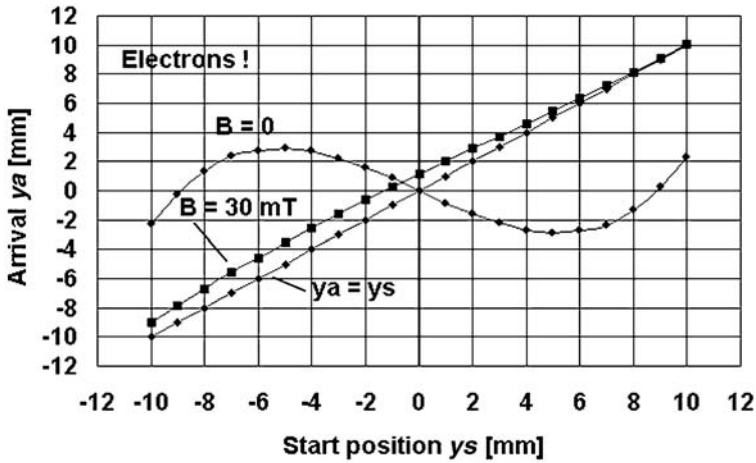

Fig. 4.22. For comparison: start coordinate (ys) versus arrival coordinate (ya) if electrons would be collected. See text. The diagram holds for $x(0) = z(0)$ and $\dot{x}(0) = \dot{y}(0) = \dot{z}(0)$

The situation changes drastically if electrons would be collected as shown in Fig. 4.22 for comparison. From the figure, it becomes very clear that there is a focusing action of the attractive space charge force, which results in too small measured profiles. During the flight time of the electron to the collector in about 1.73 ns, the bunch itself moves 28.5 mm. Thus, the distortion results from the action of only one bunch.

It is well known that the deviations due to space charge forces can be diminished by an appropriate magnetic field parallel to the electric one. From the mathematical point of view, it is very easy to consider a homogeneous B_x field in a numerical algorithm, but it complicates the mechanical design

of the monitor considerably. As shown in Fig. 4.22, a rather small magnetic field of 30 mT (= 300 G) can diminish the deviations to a tolerable level for electrons. To reduce the calculated deviations for nitrogen and hydrogen (see Fig. 4.21) remarkable below 1 mm, much higher B fields would be required.

4.5.2 Residual Gas Fluorescence Monitor

A completely non-destructive method of beam profile monitoring is residual gas fluorescence, previously applied at the continuous wave (CW) proton linac of Los Alamos [226] and the CERN superproton synchrotronsynchrotron [227]. For a pulsed linac with relatively short pulse lengths, the emitted light intensities are rather low, requiring high amplification. The emitted fluorescent light comes mainly from excited N_2 molecules and covers the blue wavelength range. In an application at the UNILAC [228], the captured photons are converted to electrons by a special photocathode, which has enhanced sensitivity to UV light with a quantum efficiency of 25−30%. The photocathode is coupled to a double multichannel plate (MCP) MCP of the Chevron type with a maximum gain of about 10^6. For further signal enhancement, a moderate pressure bump can be easily applied. The amplified electron current hits a P46 screen. The light pattern generated is observed with a CCD camera which is coupled to the image intensifier system via a tapered light guiding system. Figure 4.23 shows a comparison between profile data measured with the fluorescence monitor and a residual gas ionization monitor installed about 1m behind the UNILAC in the transfer channel of the UNILAC to the SIS. A very useful property of this image intensifier system is the possibility of switching

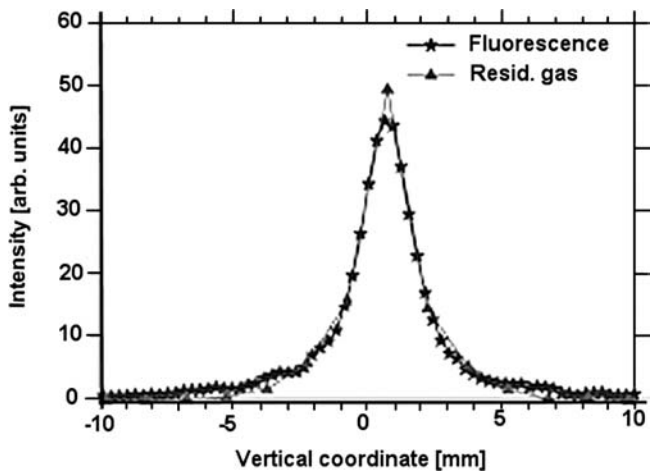

Fig. 4.23. Comparison of beam profiles measured at 11.4 MeV/u with a fluorescence monitor and a residual gas ionization monitor [228]. Both curves are normalized to the same integral over the intensity distribution

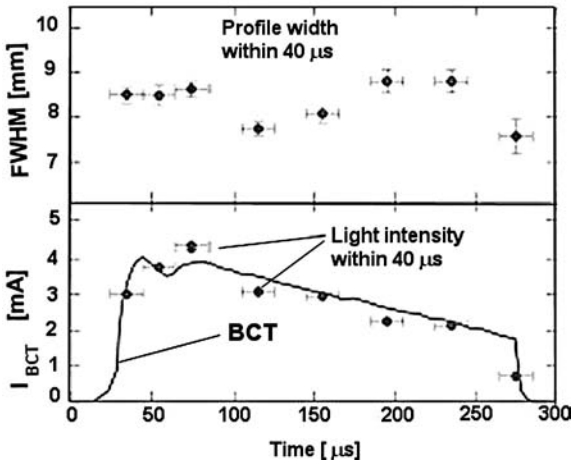

Fig. 4.24. Top: Measured beam width of the macropulse within segments of 40 μs. Bottom: Comparison of the measured light intensity with the beam transformer signal (BCT) [228]

the voltage between the photocathode and the first stage of the MCP from the transfer mode to the block mode. The relatively fast mode change within only 100 ns offers the observation of segments within the macropulse by controlling the exposure time. In the example of Fig. 4.24, the beam width has been measured within segments of 40 μs over one macropulse. Additionally, the intensity within the segments has been determined and compared with the signal from a beam current transformer (BCT).

4.5.3 Residual Gas Ionization Monitors for Circular Machines

Due to the much lower pressure in circular machines such as synchrotrons and storage rings and the small cross sections for ionization at higher energies, much higher amplification is required. Taking advantage of two-stage multichannel plates (MCP) of the Chevron-type, an additional gain of the order of 10^6–10^7 can be achieved. To detect the amplified secondary electrons at the MCP output dependent on position, the designer has a choice among the following methods:

- Arranging a harp detector behind the MCP, which may consist of thin wires ($\varnothing < 0.5$ mm) or more stable rods ($\varnothing \simeq 1$mm). But, in contrast to profile grid or harp designs, the collectors have to be spaced equidistant in this application. Although the spatial resolution will be limited by the harp characteristic, the achievable performance is sufficient in most practical applications. This holds, especially if one considers that beam profile

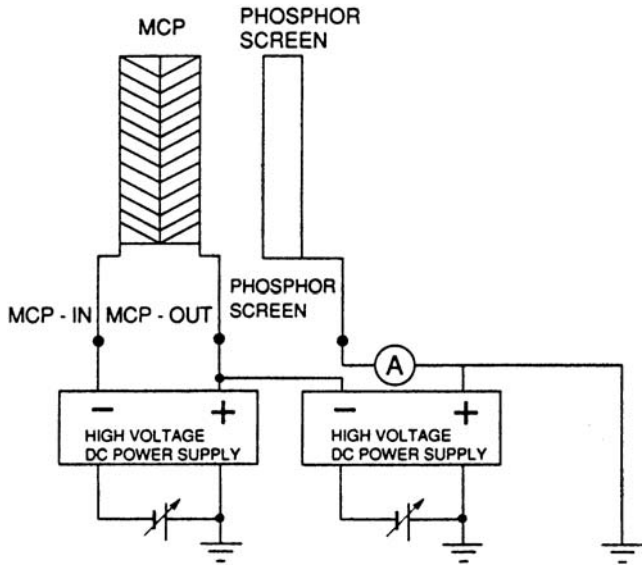

Fig. 4.25. Scheme of a MCP-fluorescent screen arrangement, taken from [230]

monitors based on residual gas ionization are rarely used in electron machines due to the extremely small beam widths in those machines. The advantage of the method is that standard profile grid electronics can be used for further signal processin.

- Use of anodes in wedge and strip anodes or resistive anodes [229], [222], based on the detection of single particles, which can improve the resolution considerably by collecting data with high statistics.
- Use of a so-called delay line anode and measuring time differences to localize the creation of single ions after signal amplification by the MCP. The design of such a delay line is rather complicated, especially if one has to consider fast signals requiring high bandwidth in the delay line.
- Installation of a phosphor screen directly behind the MCP, as shown schematically in Fig. 4.25, and observing the light pattern created by the secondary electrons from the MCP output. Obviously, in this case the most cheap and simple method is to use a CCD camera for image processing. An advantage is the high achievable resolution. A further advantage may be the supply of standard interfaces as well as corresponding software together with commercial CCD cameras. A drawback is the relatively low time resolution and the limited image rate. Replacing the CCD camera by a photomultiplier or an avalanche diode [231] improves the time resolution and image rate.

The characteristics of some examples are discussed in the following.

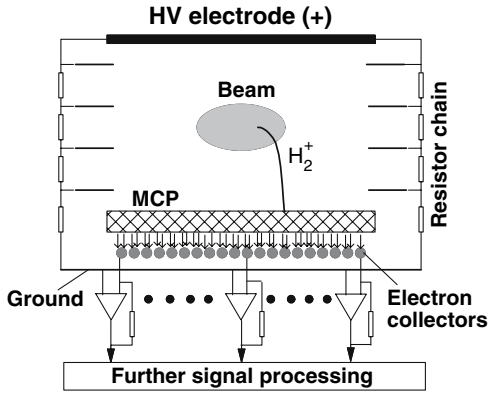

Fig. 4.26. Simplified scheme of a beam profile monitor using a MCP in front of a harp for signal amplification

Example 1

Typical Layout

Figure 4.26 shows the simplified scheme of a monitor, using collector rods on the back side of a MCP. Due to the very high vacuum as well as the necessity to back out the beam pipe system, the design of such a monitor requires experience in construction technique as well as excellent knowledge in material science. Figure 4.27 shows part of a monitor developed for the SIS. The MCP, not shown, is arranged directly above the collector rods. To measure both transverse beam profiles, two monitors are installed in a vacuum chamber, which is equipped with two sets of deflecting plates to compensate for steering by the collecting fields.

Signal Estimation

Assuming that the residual gas consists mainly of hydrogen, the expected H_2^+-ion current has been estimated from measured cross sections [232] given in Table 4.5 for uranium ions.

Table 4.5. Measured cross section for the creation of electron-H_2 pairs by uranium ions

Energy [MeV/u]	10	20	50	100	200	500	1000
σ_U $\left[10^{-14}\,\mathrm{cm}^2\right]$	1.8	1	0.4	0.2	0.13	0.06	0.045

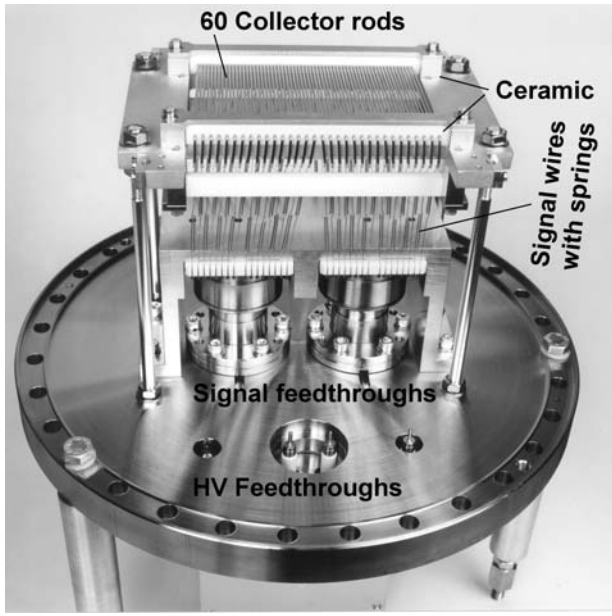

Fig. 4.27. Part of a residual gas monitor, showing the 60 collector rods (⌀1 mm, spacing 0.5 mm). GSI Foto

For a collecting length L, the total rate R_t of H_2^+ ions results from

$$R_\mathrm{t} = n \frac{N_\mathrm{U}}{T_\mathrm{rev}(W)} L\, \sigma_\mathrm{U} \tag{4.5}$$

$$n = \frac{6.022 \times 10^{23}\, \rho_\mathrm{H}}{2} \frac{p}{p_\mathrm{n}}\,, \tag{4.6}$$

where n is the number of H_2 molecules per cm^3 at pressure p, N_U is the number of uranium ions in the machine, and T_rev is their revolution time dependent on energy W. For the SIS, the revolution time varies between 4.63 µs at the injection energy (11.5 MeV/u) and 822 ns at the maximum achievable energy of $\simeq$ 1000 MeV/u for uranium ions. Figure 4.28 gives the calculated rates per millimeters of collecting length and µs assumes $N_\mathrm{U} = 10^9$ U^{73+} ions in the machine, a beam radius of 10 mm, and a pressure of 5×10^{-11} mbar. Although, according to Table 4.5, the cross sections vary by about a factor of 40 between 10 and 1000 MeV/u, the expected rates vary only by about a factor of 6.6 in the energy range considered. Obviously, the decreasing cross section is partly compensated for by the increasing revolution frequency. For comparison, the rates have been calculated from energy loss data assuming a W value of 36.5 eV. At low energies (<20 MeV/u), the values agree within about a factor of 2; at higher energies, the values from the energy loss data are about a factor of 5 higher than the values from the measured cross sections.

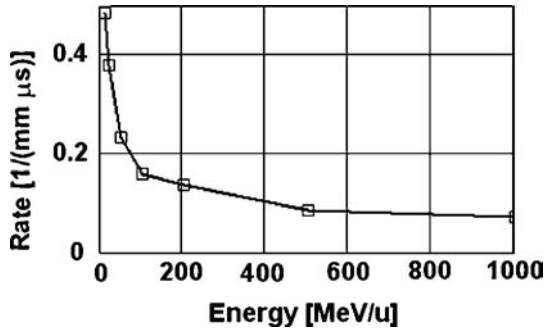

Fig. 4.28. Calculated total number of H_2^+ ions per mm of collector length and μs. The data hold for 10^9 U^{73+} ions in the SIS

But to specify the design parameters of a monitor, these differences should not be relevant.

Keeping in mind that the collector length can be of the order of 100 mm and the collecting time may be extended up to microseconds, the output of electrons on the back of a MCP with a gain of $10^6 - 10^7$ is more than sufficient as input for I/U converters. But, due to the universality of the SIS, a dynamic range of 1 : 8 has to be taken into account, depending on the ion species, the number of particles in the machine, and their energy. The largest signals are expected for very heavy ions at rather low energy, as, for example, uranium ions at the space charge limit ($N_U \simeq 4 \times 10^{10}, \sim 20\,\mathrm{MeV/u}$). On the other hand, very low signals are expected for few light ions at high energy, as, for example, neon ions with $N_{Ne} = 10^4$ and $W = 1\,\mathrm{GeV/u}$. Considering these two extreme cases, the expected rate will differ by about a factor of 10^8. Adaptation of this broad range of rates to the MCP and the following signal processing electronics can be performed by

- changing the gain of the MCP,
- mounting a variable slit in front of the MCP,
- varying the collecting time,
- applying a moderate pressure bump, and
- taking advantage of the dynamic range of suitable I/U converter electronics, which can be of the order of 1–10^6.

Aging of the MCP

To avoid fast degradation of a MCP at the highest rates, the monitor should not be used for continuous monitoring. It has been found [212, 233] that the gain of a MCP halves after emission of about $0.1\,\mathrm{C/cm^2}$. Assuming a rate of $R_t = 0.3/\mathrm{mm\,\mu s}$ (see Fig. 4.28), this results in 30×10^6 H_2^+ ions per $\mathrm{cm^2 \mu s}$ at the front side of the MCP. With a gain of 10^6, this corresponds to an output current of about $4.8\,\mu\mathrm{A}$ leading to a half-life of $T_{1/2} = 0.1\,\mathrm{C}/4.8\,\mu\mathrm{A} \simeq 2 \times 10^4\,\mathrm{s}$.

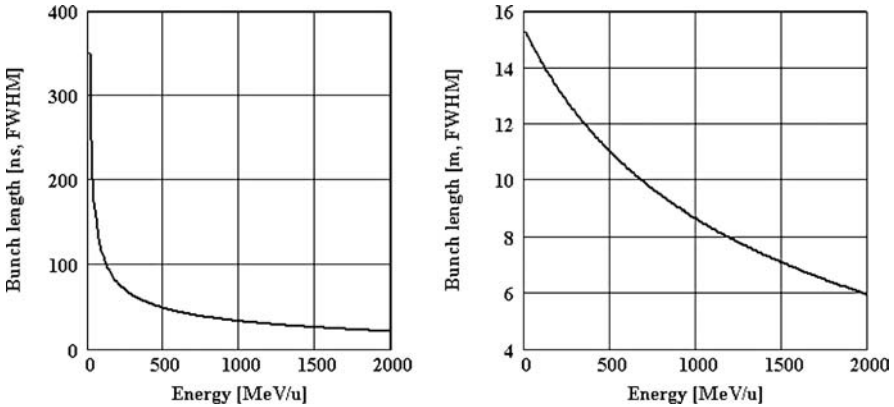

Fig. 4.29. FWHM-bunch length (left in ns, right in m) in the SIS in dependence of the energy. The data hold for the standard mode working at the 4th harmonics

Resolution

The achievable resolution is influenced by the following parameters [234]:

- The strength and homogeneity of the collecting field,
- The recoil energy of the H_2^+ ions,
- The density of the residual gas ions,
- The linearity and homogeneity of the MCP.
- The spacing and voltage between the MCPs,
- The spacing and voltage between the last MCP and the collecting anode,
- The spacing and dimensions of the collector strips,
- The parallelism between the beam and the collector strips, and
- The action of space charge forces on H_2^+ ions.

Considering the action of space charge separately, a resolution better than 1 mm can be achieved by careful design of the mechanics and optimized electronic parameters.

Space Charge Effects

For the SIS, the space charge limit of U^{73+} ions is about 4×10^{10}. Referring to Fig. 4.18 and the estimation of space charge effects for the bunched beam of the UNILAC with 10^9 U^{4+} ions in one bunch, the space charge effect has to be considered in more detail. Although the charge density and therefore the space charge force will be smaller due to the distribution over long bunches, the momentum transfer $\sim$ force $\times$ time can be much higher. Figure 4.29 gives the bunch length in the SIS dependent on energy. Potential and electric field strength within and outside of long bunches may be calculated in two ways:

- by approximating the long bunch by a dc-beam
- by approximating the bunch shape by a rotational symmetrical ellipsoid.

Potentials as well as electric fields for homogeneous and parabolic charge density distributions within spherical and elliptical bunches are derived in Chap. 8. From the mathematical point of view, the estimation of the space charge effect on the resolution achievable with the approximation by a dc-beam is much simpler. The estimations given in the following are based on this approximation.

1. Long Bunch, Low Beam Energy Referring to Fig. 4.29, the bunch length in the SIS at injection energy is about 15 m (FWHM). On the timescale, this corresponds to about 325 ns. Now, if H_2^+ ions arrive at the collector within a time less than 325 ns, we deal with the action of only one bunch. Assuming a collecting field strength of $E_x = 50\,\mathrm{V/mm}$, the flight time over a distance of 80 mm is roughly 260 ns, and therefore the condition is fulfilled. The electric field strength inside a dc-beam with radius R and a parabolic charge distribution along the radial coordinate $\rho^p(r)$ is given by (non relativistic, see Chap. 8)

$$\rho(r) = \rho_0 \left(1 - \frac{r^2}{R^2}\right) \tag{4.7}$$

$$E(r)_{r \le R} = \frac{1}{2\,\varepsilon_0}\rho_0 \left(r - \frac{r^3}{2\,R^2}\right) . \tag{4.8}$$

In the example considered, the "length" of the dc-beam is $L = 2\,\beta\,c\,\Delta t$ ($\beta = 0.156, \Delta t = 325\,\mathrm{ns} \rightarrow L \simeq 2 \times 15\,\mathrm{m}$) giving

$$\rho_0 = 2\frac{N_\mathrm{U}\zeta e}{\pi R^2 L} . \tag{4.9}$$

N_U is the number of uranium ions in the long bunch, and ζ is their charge state. Outside the beam, the field strength shows the well-known $1/r$ slope:

$$E_\mathrm{r}(r)_{r \ge R} = \frac{1}{4\,\varepsilon_0}\rho_0 \frac{R^2}{r} . \tag{4.10}$$

Figure 4.30 shows the calculated electric field strength at the space charge limit with $N_\mathrm{U} = 10^{10}$ and $\zeta = 73$. Assuming the collecting field in the x-direction, the resolution of the monitor is diminished by the deflection of the H_2^+ ions in the y-direction. With $r = \sqrt{x^2 + y^2}$, the action of the fields on the H_2^+ ions can be separated:

$$m\ddot{x} = E_\mathrm{x} + E_\mathrm{r}(r)\cos\vartheta \tag{4.11}$$

$$m\ddot{y} = E_\mathrm{r}(r)\sin\vartheta \tag{4.12}$$

$$\vartheta = a\tan\frac{y}{x} . \tag{4.13}$$

The trajectories shown in Fig. 4.31 have been calculated by piecewise integration of (4.11) and (4.12). From the figure, it becomes very clear that the achievable resolution is around 1 mm at moderate beam currents, whereas deviations due to the very high beam current at the space charge limit are not tolerable.

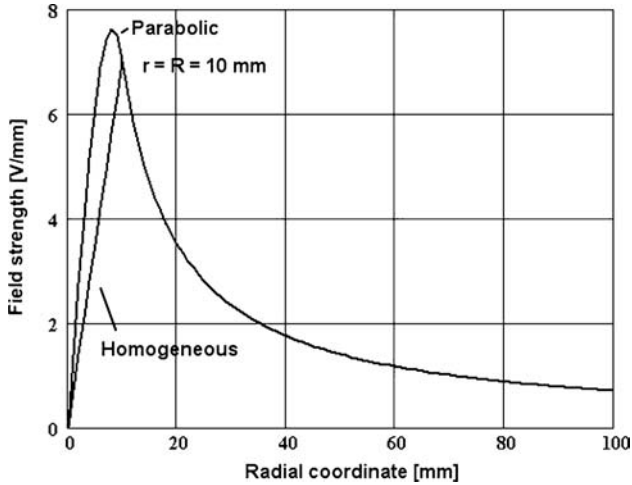

Fig. 4.30. Electrical field strength for a dc-beam with parabolic intensity distribution over the radial coordinate. For comparison, the result for a homogeneous charge distribution is shown, too. Note: The corresponding potential $V(r)$ fulfills the boundary condition at the beam pipe, i.e., $V(r = R_{\mathrm{p}}) = 0$

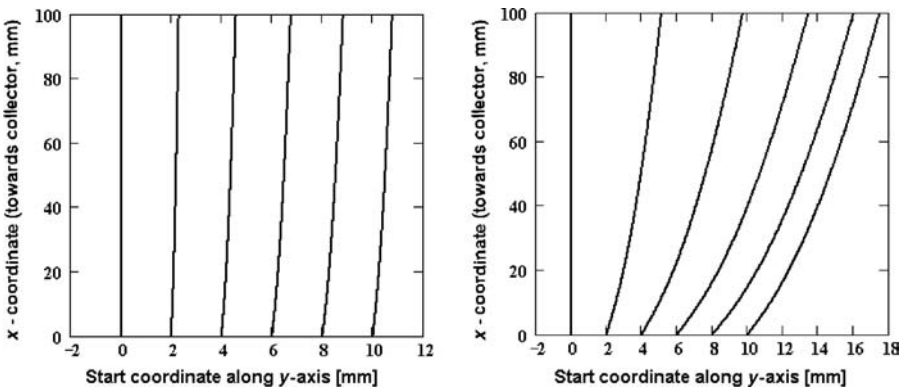

Fig. 4.31. Trajectories of H_2^+ ions in a residual gas ionization profile monitor dependent on the starting position along the y-axis. The data hold for a collecting field strength of 50 V/mm, bunches with a length of $L = 30\,\mathrm{m}$, $N_{\mathrm{U}} = 10^9$ U^{73+} ions (left), and $N_{\mathrm{U}} = 10^{10}$ U^{73+} ions (right). All H_2^+ ions start at $\dot{x}(0) = \dot{y}(o) = 0$

2. Short Bunch, High Energy Considering the use of the monitor at the highest energy ($\simeq 1000\,\mathrm{MeV/u}$ for U^{73+} ions in the SIS) does not remarkably change the effect of the space charge force. Due to the shorter bunch of $L \simeq 8.5\,\mathrm{m}$, $\Delta t = 33\,\mathrm{ns}$, and a revolution time of 825 ns, the space charge is higher, acts for a shorter time, but after about 140 ns between the bunches, the H_2^+ ions experience the force of a second bunch. This is illustrated in Fig. 4.32 showing the velocity of the H_2^+ ions gained transverse to the beam in the y-direction.

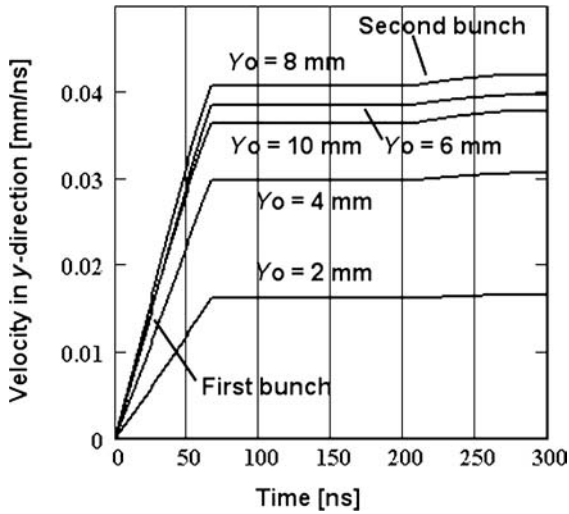

Fig. 4.32. Velocity of H_2^+ ions gained transverse to the beam in the y-direction as a function of time. The parameters are the initial parameters y_0. The diagram holds for $\dot{x}(0) = \dot{y}(0) = 0$

Because the maximum field strength occurs at $r = \sqrt{2/3}R = 8.2\,\text{mm}$, an H_2^+ ion starting at $x = 0, y = 8\,\text{mm}$ gains the highest velocity.

Example 2

A Proposed New Residual Gas Ionization Monitor

It is easy to show (see Chap. 4) that the space charge effect on the resolution of a residual gas ionization monitor can be nearly compensated for by providing a homogeneous magnetic field in parallel to the electric collecting field. To use the principle of residual gas ionization for beam profile measurements on a beam with high space charge, an advanced high performance monitor has been proposed and is now under development [235, 236]. Because electrons have much smaller bending radii in moderate magnetic fields, it is proposed to collect electrons. The main features of the new monitor are

- The collecting field strength will be of the order of 50 V/mm.
- The proposed MCP is of the Chevron-type with a size of 100×30 mm^2.
- To achieve the specified resolution of 0.1 mm, a magnetic field strength of $\approx$0.1 T (1 kG) is foreseen, realized by rare earth permanent magnets of a rod type dipole [237]. The magnetic alloy consists of Nd-Fe-B with a remanent induction $B = 1.2\,\text{T}$. Although the working range in the z-direction ($\rightarrow$ beam direction) is limited by the MCP to 30 mm, the rod dipole will have a length of about 300 mm to achieve the required homogeneity in the working region. This sums to a total weight of about 92 kp for the magnet.

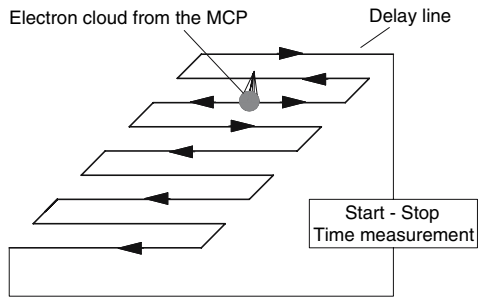

Fig. 4.33. Simplified scheme to illustrate the function of a delay line anode for beam profile determination

- A resolution of 0.1 mm cannot be achieved with an ensemble of collecting rods or wires on the back of a MCP. The same holds for a delay line anode. Therefore, a phosphor screen will be arranged on the back of the MCP.
- There is the intent to operate the monitor in two modes:
  - A high-resolution mode, provided for precise beam monitoring with a spatial resolution down to 0.1 mm. In this mode, the measuring time will be within the 0.1–100 ms range. A digital CCD camera can fulfill the requirements for exposure time and frame rate up to 100 fps (frames per second).
  - To estimate the emittance blow-up due to space charge and to control the matching conditions during and after injection within the first few hundred turns in the SIS, a fast readout mode is proposed. In this mode, a photodiode array is proposed to provide about 1 mm resolution in a turn-by-turn readout within about 1μs. A phosphor screen of the P47-type (see Table 4.3) with a short decay time of about 70 ns is proposed. To use the same phosphor screen in both modes, a rotatable mirror above the phosphor screen is foreseen.
- To increase the amount of residual gas electrons, a moderate pressure bump has to be applied in the fast readout mode.

Example for a Delay Line Design

Using a delay line anode, the profile information is extracted by measuring time differences on a delay anode as explained very simply in the scheme of Fig. 4.33. Although the principle looks very simple, the design of the delay line itself as well as further signal processing and extraction of profile information by appropriate software tools is rather complex. A delay line with high bandwidth can be designed as a strip line or microstrip line with well-defined impedance. To achieve high spatial resolution, the width of the strips and their spacing should be minimized, with the consequence of increasing coupling between strips. Therefore, the design requires careful optimization of the dimensions shown in Fig. 4.34. To perform an optimization, the following parameters are the most important:

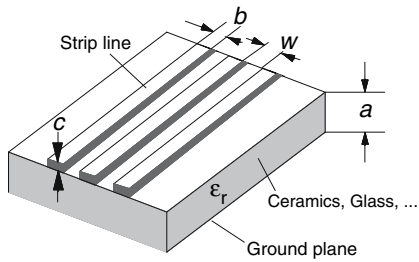

Fig. 4.34. Scheme of a microstrip line with the relevant design parameters

- The impedance, mostly between 50 and 100 Ω. There are many formulas given in the literature, e.g., [36–38], differing only slightly. A practical formula given in the "MECL Design Handbook" [37] is

$$Z\,[\Omega] = \frac{87}{\sqrt{\varepsilon_\mathrm{r} + 1.4}} \ln\left(\frac{5.98\,a}{0.8\,b + c}\right) . \tag{4.14}$$

- For a delay line, consisting of many strips in parallel and connected according to the scheme of Fig. 4.33, the capacitive coupling between the strips has to be considered, too. If this coupling is not small in comparison to the coupling of the strips to the ground plate; a fast signal will travel across the strips instead of along the striplines. Therefore, the ratio between these capacitances has to be optimized. Keeping in mind the other conditions such as required impedance, required number of strips, and last but not least, sufficient mechanical stability, the optimization procedure may require some compromises. The capacity between one strip of length L and the ground plane is given by [250]

$$C_0\,[\mathrm{pF}] \approx L\,[\mathrm{cm}] \left[\frac{0.09\varepsilon_\mathrm{r} b}{a} + \frac{0.56\,(\varepsilon_\mathrm{r} - 1)}{\ln\left(\frac{2a}{c} + \sqrt{\frac{a^2}{c^2} - 1}\right)}\right] . \tag{4.15}$$

  This has to be compared with the capacity between two strips [250]:

$$C_\mathrm{mn}(\mathrm{pF}) \approx 0.064\,L[\mathrm{cm}]\;(1 + \varepsilon_\mathrm{r})\,\frac{b}{w} . \tag{4.16}$$

- The achievable delay time t_d can be estimated from [38]

$$t_\mathrm{d}\,[\mathrm{ns/cm}] \approx 33.4 \times 10^{-3}\sqrt{0.48\varepsilon_\mathrm{r} + 0.7} . \tag{4.17}$$

In most cases, a given impedance – possibly also in a certain range – will determine the first set of parameters $\varepsilon_\mathrm{r}, a, b, c$. The remaining parameter w has to be determined to maximize the ratio of C_0/C_mn keeping in mind the desired spatial resolution. This may result in a later change of the first set.

Example
Impedance: $50\,\Omega$
Length of one strip: $L = 10\,\text{cm}$
Substrate material: Al_2O_3*-ceramic,* $\varepsilon_r = 9.8$
Substrate thickness: $a = 0.3\,\text{mm}$
Width of the strips: $b = 0.265\,\text{mm}$
Height of conducting strips: $c = 50\,\mu\text{m}$
Spacing between strips: $w = 0.5\,\text{mm}$

With $b + w = 0.765\,\text{mm}$, the spatial resolution of the delay line is better than 1 mm. The ratio C_0/C_{mn} is $23.31/3.66 = 6.37$. This ratio can be improved in a second step of optimization by looking at the dependencies of the parameters. Figures 4.35–4.37 give the dependencies of the relevant parameters. For the height of the conducting strips, the skin effect has to be taken

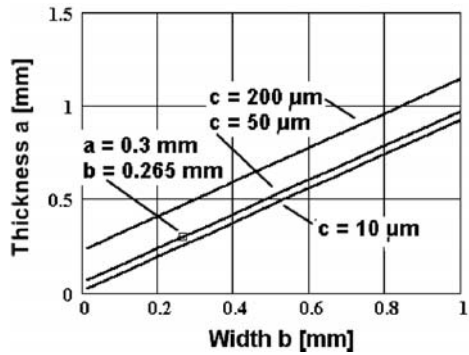

Fig. 4.35. Required substrate thickness a in dependence of the strip width b. The diagram hold for stripline with an impedance of $50\,\Omega$

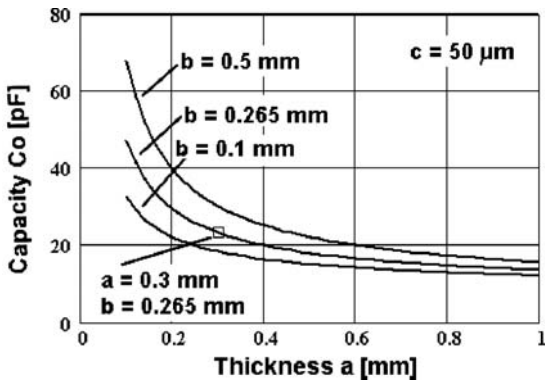

Fig. 4.36. Capacity of a strip to the ground plane in dependence of the substrate thickness. The diagram holds for a stripline with an impedance of $50\,\Omega$

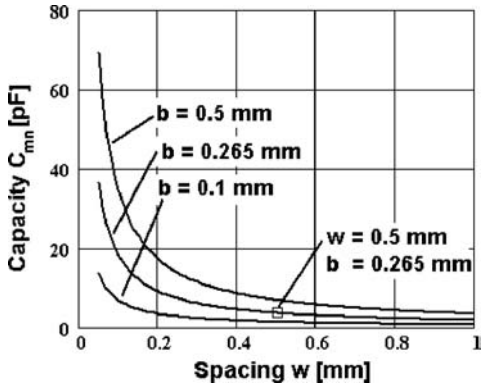

Fig. 4.37. Coupling capacity dependent on the strip spacing. The diagram holds for a stripline with an impedance of 50 Ω

into account, too. In practical units, the skin depth α is given by [38]

$$\alpha\,[\mathrm{mm}] = \sqrt{\frac{\rho[\Omega\,\mathrm{mm}^2/\mathrm{m}]}{\mu_\mathrm{r}\, f\ [\mathrm{MHz}]}}\ . \tag{4.18}$$

4.6 Evaluation of Charge States and Mass Spectra from Beam Profile Measurements

4.6.1 Spectra Produced by Ion Sources

In contrast to electron or proton machines, universal heavy ion accelerators deliver all kinds of ion species to the target. A typical ion source, such as a sputtering ion source of the PIG-type will produce a spectrum of charge states for each isotope. Therefore, the very first separation and optimization of a certain ion species starts in the injection behind the ion source. In most cases, the separation is performed by measuring the beam profile behind a slit dependent on a magnetic or/and electric deflecting field. Magnetic separation is based on the relation (relativistic)

$$\frac{m\,v^2}{\rho} = \zeta\, e\, v\, B \quad \rightarrow \tag{4.19}$$

$$B\rho = \frac{m\,v}{\zeta\, e} = \frac{A\,\gamma m_0\, c^2 \beta\, c}{\zeta e\, c^2} \tag{4.20}$$

$$B\rho\,[\mathrm{Tm}] = 3.10715\,\frac{A}{\zeta}\beta\,\gamma\ , \tag{4.21}$$

whereas the electrostatic rigitidy is related to $B\rho$ according to $E\rho = \beta c\, B\rho$. Figure 4.38 is a spectrum of ^{68}Zn from an electron cyclotron resonance (ECR)

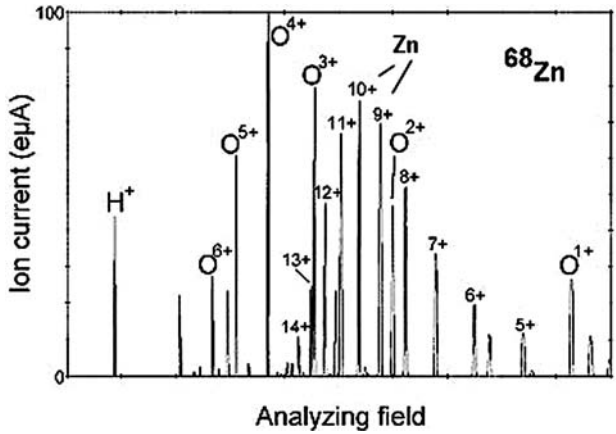

Fig. 4.38. Spectrum from an ECR ion source [251]. The charge states of Zn are classified from 5^+ to 14^+

ion source [251]. The correct classification of all peaks requires a skilled operator or ion source expert. After classification, the optimum peak has to be selected with respect to intensity and required rf power.

Figure 4.39 shows the charge state and mass spectrum of lead produced by a sputtering PIG [238]. The charge state spectrum has been obtained by scanning the extraction voltage of the ion source. To measure the mass spectrum, the mass separation magnet has been scanned and the beam profile was measured with a Faraday cup behind a very small slit ($\approx 0.2 - 0.3\,\mathrm{mm}$); the extraction voltage was adjusted to the 9^+ charge state. Since the energy in the injection area is well known, identification and separation of a certain charge state is straightforward. To identify a certain isotope, a high-resolution $M/\Delta M > 200$ is required. It may be helpful for the identification, if the relative isotopic abundance – the natural one or from an enrichment – is known. Nevertheless, due to an unfavorable combination between required metal ion, the auxiliary gas, and the material of other parts such as the cathode and anode, strange ions with nearly the same charge over mass ratio ζ/A as the required one are produced. An example where separation is nearly impossible is the combination of $^{207}\mathrm{Pb}^{9+}$ ($\zeta/A = 22.9973$) and $^{184}\mathrm{W}^{8+}$ ($\zeta/A = 22.9939$). In addition, there are other W^{8+} and Ta^{8+} isotopes with similar ζ/A ratios just around the Pb^{9+} isotopes [239]. Therefore, if $^{207}Pb^{9+}$ ions are required at the target, the use of tungsten in the ion source has to be avoided. Other combinations with nearly identical charge over mass ratio are $^{96}\mathrm{Mo}^{4+}$ and $^{144}\mathrm{Sm}^{6+}$, $^{40}\mathrm{Ar}$ and $^{40}\mathrm{Ca}$, $^{76}\mathrm{Ge}^{4+}$, and $^{38}\mathrm{Ar}^{2+}$ and $^{57}\mathrm{Fe}^{3+}$ [239].

In most of these cases, operators will not be able to separate or even analyze the contents of a beam in the magnetic and/or electric analyzing systems of standard accelerator equipment. One possibility for analyzing the contents of the beam is X-ray spectroscopy. A thin carbon foil is moved into the beam,

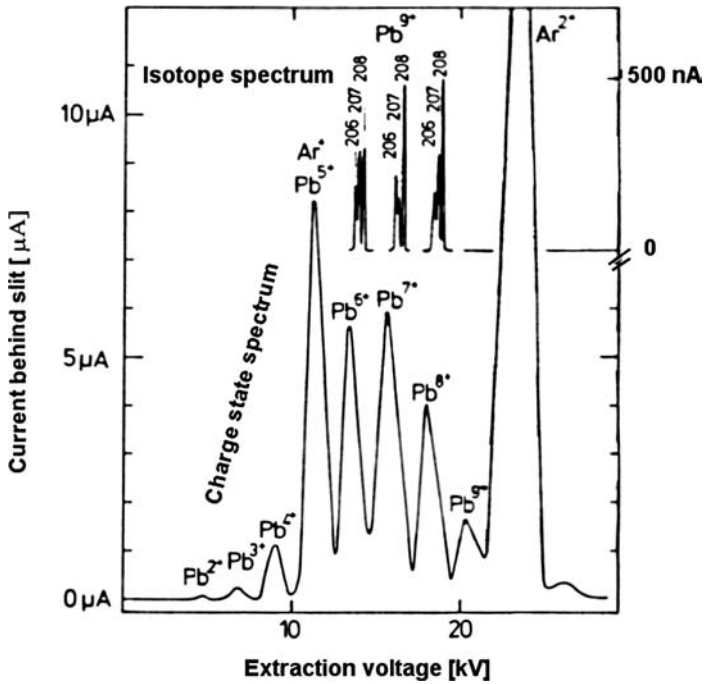

Fig. 4.39. Charge state and mass spectrum (inset) of lead from a sputtering PIG ion source [238]. The three mass spectra shown in the inset correspond to different settings of the parameters to optimize the intensity of a certain isotope. Since Ar gas has been used as burning gas, the very large peak of Ar^{2+} coincides with the small Pb^{10+} peak

the accelerated ions are excited by the foil, and the emitted characteristic X rays are analyzed with a commercial detector system. Identification and, in turn, optimization of the composition of the beam can be performed easily by the K lines emitted in the keV region. Modern analyzer systems deliver appropriate software in combination with X ray energy tables for all isotopes. The energy of the ions in the beam must be high enough to produce X rays in the keV region, which means that the position of the detector system along the machine has to be selected with respect to this point.

4.6.2 Stripper Spectra

Due to the proportionality of the required accelerating rf power to $1/\zeta^2$, stripping in a gas target or a thin foil is a common method for reducing the required rf power. There are two strippers at the UNILAC; one in the so-called prestripper section behind the IH_2- accelerator section ($W = 1.4\,\mathrm{MeV/u}$); the other in the poststripper section in front of the SIS ($W = 11.4\,\mathrm{MeV/u}$, typical).

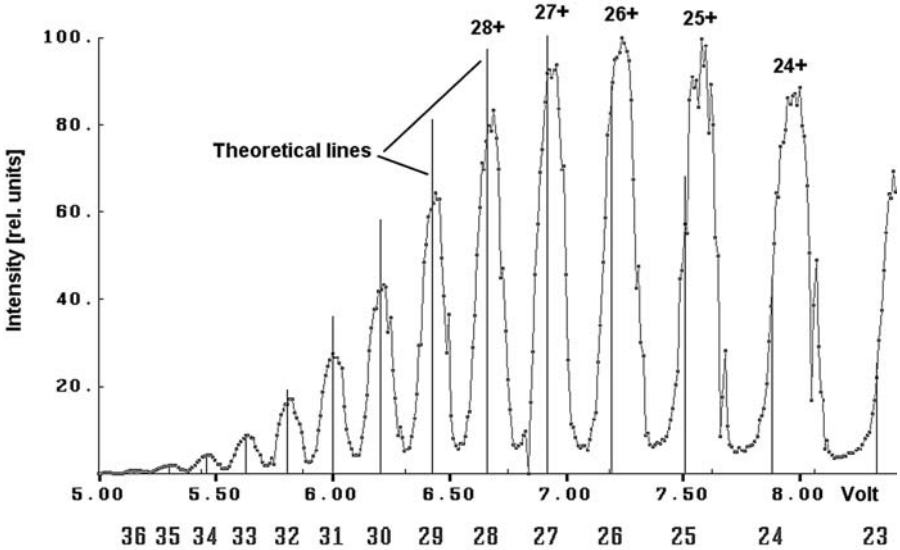

Fig. 4.40. Charge state spectrum [240] behind a N_2 gas stripper with a "target thickness" $\rho_{N_2}\Delta x$ corresponding to the equilibrium charge state distribution ($dN_\zeta/\rho_{N_2}\Delta x = 0$). The scale of the abscissa in volts is normalized to the maximum B field

Due to the high beam power and high energy loss, foils would be destroyed in the 1.4-MeV position. Therefore, a gas stripper is used in the high current mode of operation. Figure 4.40 shows a spectrum of uranium ions from the gas stripper at this location. In the poststripper at 11.4 MeV/u, a foil stripper is in use, leading to much higher charge states due to better foil efficiency and higher energy. Figure 4.41 is a display of the corresponding spectrum, again for uranium ions. To estimate the expected equilibrium charge state distribution, an empirical formula [239] may be used:

$$\zeta = Z\left(1 - C\,e^{-137\,\beta\,Z^{-\gamma}}\right) . \tag{4.22}$$

From many spectra for all kinds of ion species measured over a long period, the parameters C and γ have been optimized by a least squares fit in the range from $1.4 - 20$ MeV/u, resulting in $C = 1.0285 + 140/Z^2$, $\gamma = 0.56$ for the foil stripper, and $\gamma = 0.65$ for the gas stripper. Figure 4.42 shows the expected charge distributions based on these parameters.

Although the charge states behind the strippers differ in the ζ/A ratio up to some percent, correct assignment can be difficult due to the following uncertainties:

- Uncertainty in the beam energy, which may happen, if the stripper is located in a straight section behind an accelerator section.

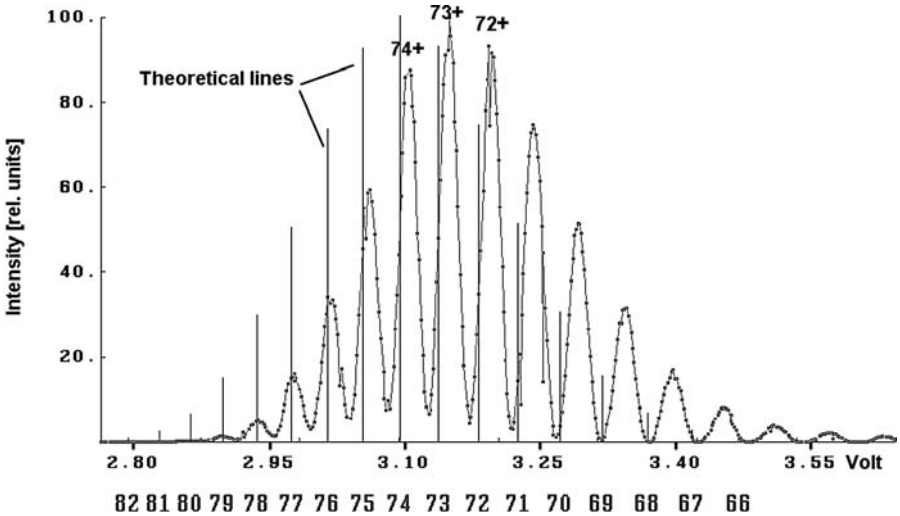

Fig. 4.41. Charge state spectrum behind a carbon foil stripper in the injection line to the SIS (W =11.4 MeV/u). A foil thickness of 0.5 mg / cm^2 has been chosen to get the equilibrium charge state distribution. For detailed specification and especially the estimated maximum ratings of the carbon foil see [241]. The scale of the abscissa in volts is normalized to the maximum B field

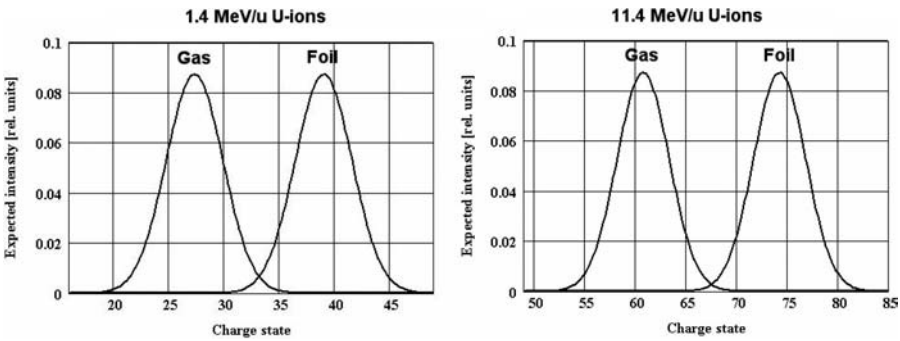

Fig. 4.42. Expected charge state distribution according to the empirical equation for uranium ions with 1.4 MeV/u and 11.4 MeV/u. The spectra are taken with a foil and gas stripper, having a target thickness corresponding to the equilibrium charge state distribution

- Uncertainties concerning the correct entrance of the ions into the charge state analyzing system. This can be an offset with respect to the center of the system as well as an unaligned beam.
- Effects of fringing fields and magnetic hysteresis.
- Not exactly known absolute calibration for the relation between required magnetic field strength and the setting via a ADC-DAC control loop.
- Overlap of the peaks due to insufficient resolution of the analyzing system.

Therefore mathematical procedures for exact localization of the lines within the measured spectra as well as fit procedures for the correct assignment of ζ values to the peaks become essential. In this connection, the following relations are helpful:

$$\frac{B_1}{B_2} = \frac{\zeta_2}{\zeta_1}, \quad \text{if } \beta = \text{const.} \tag{4.23}$$

$$\frac{B_1}{B_2} = \sqrt{\frac{\zeta_2}{\zeta_1}}, \text{ if } W = \text{const.} \tag{4.24}$$

Beam Energy Known

Assuming the stripper spectrum is analyzed via a magnet system, then a least squares fit of the type of

$$\sum_{\mathrm{i}} \left[B_{\mathrm{i}} - \frac{3.10715\, A\, \beta\, \gamma,}{\rho\, \zeta_{\mathrm{i}}} \right]^2 = \text{Minimum} = S(J) \tag{4.25}$$

can be applied. Because $\Delta\zeta = 1$ for two lines next to each other, the charge states of all peaks are known, if the correct charge state can be assigned to only one of them. Therefore, a corresponding computer algorithm can start with a guess, let's say J, for the assignment to the peak with the highest magnetic field. For the next peak, the assignment is $J + 1$ and so on. Summing up the values according to (4.25) to $S(J)$ is the next step. This procedure has to be repeated changing J as long as a minimum can be detected. The charge state assignments shown in Figs. 4.40 and 4.41 have been obtained by this procedure.

Energy Not Known

The procedure is a little bit more complex. If the beam energy is not known or known within limits, it allows different assignments to the peaks. In this case, (4.25) can be replaced by

$$\sum_{\mathrm{i}} \left[B_{\mathrm{i}} - \left(\frac{a}{\zeta_{\mathrm{i}}} + b \right) \right]^2 = \text{Min.} = S(J, a, b)\ . \tag{4.26}$$

The fit variable a leads to the kinetic energy W via the relation

$$\beta\, \gamma = \frac{a\, \rho}{3.10715\, A}, \tag{4.27}$$

$$\beta = \sqrt{\frac{(\beta\gamma)^2}{1 + (\beta\gamma)^2}} \tag{4.28}$$

$$\gamma = \sqrt{\frac{1}{\left(1 - \beta^2\right)}} \tag{4.29}$$

$$W = m_0 c^2\, (\gamma - 1)\ . \tag{4.30}$$

The other fit variable b considers a possible magnetic field offset, which may result from various effects, such as incorrect injection or fringing fields. The fit procedure can be performed similarly to that described for (4.25), with the exception that for each J, the variables a and b have to be determined from the relations,

$$\frac{\partial S(J,a,b)}{\partial a} = 0 \tag{4.31}$$

$$\frac{\partial S(J,a,b)}{\partial b} = 0, \tag{4.32}$$

with the results,

$$a = \frac{\begin{bmatrix} [B/\zeta] & [1/\zeta] \\ [B] & N \end{bmatrix}}{DET} \tag{4.33}$$

$$b = \frac{\begin{bmatrix} [1/\zeta^2] & [B/\zeta] \\ [1/\zeta] & [B] \end{bmatrix}}{DET} \tag{4.34}$$

$$DET = \begin{bmatrix} [1/\zeta^2] & [1/\zeta] \\ [1/\zeta] & N \end{bmatrix}, \tag{4.35}$$

where $[\ldots]$ stands for the sum over all lines with the assignment determined by the corresponding J value for each pass. N is the number of peaks included in the summing procedure.

Referring to (4.23), two other least squares fits may be applied to determine the correct charge state assignments:

$$\sum_{i,k} \left[\frac{B_\mathrm{i}}{B_\mathrm{k}} - \frac{\zeta_\mathrm{k}}{\zeta_\mathrm{i}} \right]^2 = S(J) \tag{4.36}$$

$$\sum_{i,k} \left[\frac{B_\mathrm{i} - B_{i+k}}{B_\mathrm{i} + B_{i+k}} - \frac{\zeta_{i+k} - \zeta_\mathrm{i}}{\zeta_{i+k} + \zeta_\mathrm{i}} \right]^2 = S(J). \tag{4.37}$$

Of course, the beam energy and any offset cannot be determined in these two cases.

4.7 Beam Alignment Based on Beam Profile Measurements

Beam alignment becomes essential for the following reasons:

- A misaligned beam diminishes the effectiveness of transverse optimization procedures due to the well-known steering effects of focusing elements such as quadrupoles and sextupoles.

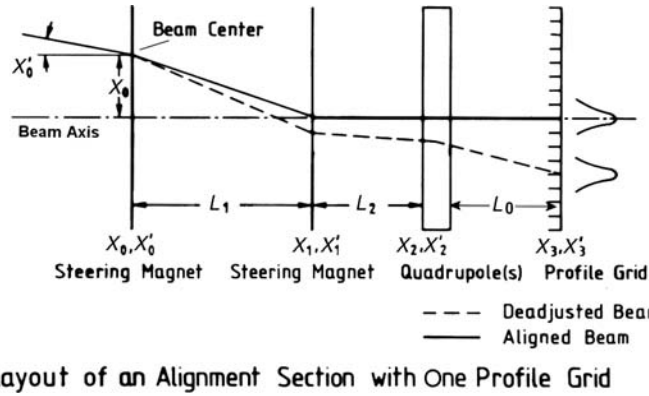

Fig. 4.43. Ideal layout of an alignment section [243]. The profile grid may be replaced by another profile measuring device

- Emittance defining collimator systems, consisting, e.g., of three collimators with well-defined spacing and well-defined apertures require aligned beams in both transverse directions.
- A misaligned beam can hit parts of the beam transport system, accelerator components, or even the beam pipe which, in the case of high intensity, can be destroyed. As a further consequence of beam loss, dangerous radiation can be produced.

A misalignment can be detected by beam position measurements (see Chap. 5). The beam offset from the axis as well as the steering angle can be determined with two position monitors along a drift space. Taking advantage of the steering effect of quadrupoles requires only one position measuring device. The layout of an ideal beam alignment section is shown schematically in Fig. 4.43. By changing the quadrupole setting and observing the beam profile at the same time, a skilled operator will be able to align the beam within a short time. But, for machines with a low duty cycle, this procedure can be very time-consuming and troublesome. Therefore, automatic computer-controlled alignment procedures can be very helpful. Assuming that the deflection of the steering magnets is determined by the product of a known constant k and the current I supplied through the coils, theoretically two different quadrupole settings and profile measurements are necessary to calculate the beam center x_0 and slope x_0' at the entrance of the first steering magnet (see Fig. 4.43). The whole alignment procedure consists of the following steps [243]:

- Determination of the beam center as the center of gravity from the measured profile. This can be performed by
  - Applying a spline fit to the measured profile.
  - Fitting Gaussian functions to the profile curves. Since in general the profiles will not be symmetrical, the left and right sides of the profile peaks should be described separately by two Gaussian functions.
  - Determination of the rms value from the raw data.

- Calculation of x_2 and x_2' from two profile measurements with different quadrupole settings and the known transfer matrix T between quadrupole and grid. Let

$$T = \begin{bmatrix} a_{11}^n & a_{12}^n \\ a_{21}^n & a_{22}^n \end{bmatrix} , \tag{4.38}$$

where $n = 1, 2$ stands for the two different settings. Then, from

$$\begin{bmatrix} x_3^n \\ x_3'^n \end{bmatrix} = T \begin{bmatrix} x_2^n \\ x_2'^n \end{bmatrix} , \tag{4.39}$$

it follows immediately that

$$x_2 = \frac{\left(a_{12}^2\, x_3^1 - a_{12}^1\, x_3^2\right)}{D} \tag{4.40}$$

$$x_2' = \frac{\left(a_{11}^1\, x_3^2 - a_{11}^2\, x_3^1\right)}{D} \tag{4.41}$$

$$D = a_{11}^1 a_{12}^2 - a_{11}^2 a_{12}^1 \,. \tag{4.42}$$

- With the known products $k_1\, I_1$ for the first steerer and $k_2\, I_2$ for the second, determination of the beam offset x_0 and the slope x_0' is straightforward, giving

$$x_0 = x_2 - x_2'(L_1 + L_2) + k_2 I_2 L_1 \tag{4.43}$$

$$x_0' = x_2' - k_1\, I_1 - k_2\, I_2 \,. \tag{4.44}$$

- The correct current I_1^* for the first steerer results from the condition

$$x_1 = x_0 + L_1 x_0' + k_1 I_1^* L_1 = 0 \quad \rightarrow \tag{4.45}$$

$$I_1^* = -\frac{x_0 + L_1 x_0'}{k_1 L_1} \,. \tag{4.46}$$

- Finally, with the correct current I_2^* for the second steerer, the remaining slope $x_0' = -x_0/L_1$ has to be compensated for; hence

$$I_2^* = \frac{x_0}{k_2 L_1} \,. \tag{4.47}$$

The reliability of the procedure can be improved by performing more than two quadrupole variations and profile measurements, applying least squares fits to the resulting equations.

Another nearly ideal configuration is the arrangement of two profile grids (or profile measuring devices) in front of a pair of steerers. Obviously, off-set x_0 and slope x_0' at the position of the first steerer can be calculated from the measured offsets at both grids and the spacing between them.

Of course, due to spatial limitations as well as other restrictions, ideal layout sections as discussed may not occur often enough along a beam transport system. In this case, one can include the steering of quadrupoles in a statistical procedure, as described in [243]. The method is very useful for transport lines and does not require changes in focusing or defocusing by the quadrupoles after the alignment procedure.

5

Measurements with Capacitive or Inductive Pickups

5.1 Principles of Signal Extraction

Signals from the electromagnetic fields of moving charged particle bunches to gain information about several beam parameters can be extracted without any significant distortion of the beam itself. The principle of inductive signal extraction was already discussed in Chap. 2, Sect. 2.3 because beam current measurements by all kind of beam transformers are based on this principle.

The equivalent (2.30) in Chap. 2 for a capacitive monitor is given by

$$i\,(t) = \frac{d}{dt}\int_{\text{area}} \epsilon_0\,\overrightarrow{E}\,\overrightarrow{dA} = \frac{d}{dt}\int_{\text{area}} \overrightarrow{D}\,\overrightarrow{A}\;, \tag{5.1}$$

where E is the electric field of the moving charged particles and the "electric displacement" is given by $\overrightarrow{D} = \epsilon_0\,\overrightarrow{E}$. In the field of beam diagnostics, the radial component E_r is the most interesting one.

Equations 5.1 and 2.30 are two of the four famous Maxwell equations [39, 244, 245] and are well known as the "law of induction" (2.30), also known as "Faraday's law" and the so-called "displacement current" (5.1), so defined by Maxwell. Figures 5.1 and 5.2 show schematically the two methods of signal extraction from beam.

Remark:
Considering the influenced current according to (5.1), there is another possibility of extracting a signal from the beam by measuring the so-called image current flowing through the vacuum pipe, oppositely directed to the beam current. Inserting a small isolated break into the beam pipe, bridged by small resistors, results in a measurable voltage, proportional to the beam current (e.g. [6, 246–248]). But, caused by the small resistors, the voltages are in general very small. From the construction point of view, the design of such a gap is rather complex and will not be considered here.

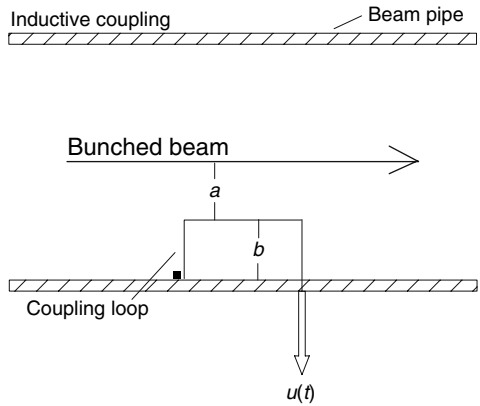

Fig. 5.1. Scheme of inductive signal extraction

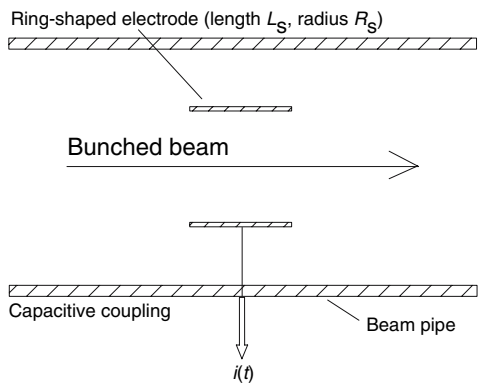

Fig. 5.2. Scheme of capacitive signal extraction

5.1.1 Comparison of Inductive and Capacitive Signals

The schemes of both monitor types look similar and both can be used to extract the same information. Therefore an estimate of the signal ratio can be helpful. Remembering the well-known relation $B_\Theta = \beta/c\, E_\mathrm{r}$ (see [39, 245]), the ratio between capacitive and inductive signals can be estimated dependent on the β value:

$$\left|\frac{i(t)}{u(t)}\right| = \frac{c\epsilon_0}{\beta}\,\frac{\frac{d}{dt}\int_{\mathrm{cylinder}} E_\mathrm{r} dF}{\frac{d}{dt}\int_{\mathrm{loop\ area}} E_\mathrm{r} dF}\ . \tag{5.2}$$

For the most practical designs, the ratio of both integral terms is very near one. Taking this into account and assuming broadband signal processing with an impedance of $R = 50\,\Omega$, one gets

$$\left|\frac{i(t)\,R}{u(t)}\right| = \left|\frac{u_\mathrm{cap}}{u_\mathrm{ind}}\right| \approx \frac{c\epsilon_0 R}{\beta} \approx \frac{0.133}{\beta}\ . \tag{5.3}$$

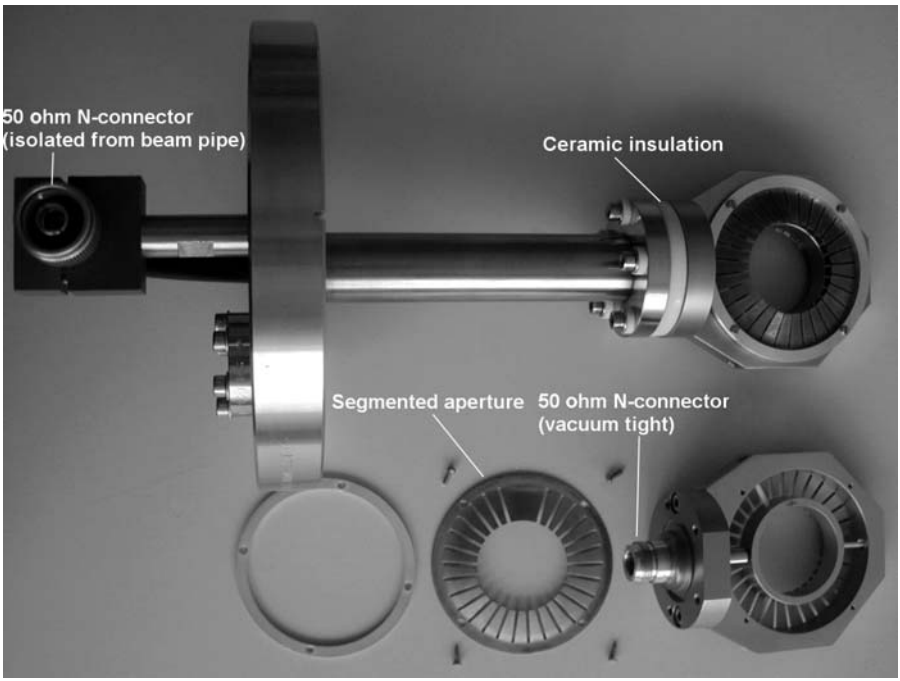

Fig. 5.3. Capacitive pickup in 50-Ω geometry

As expected, the induced signal is higher for low β values, which becomes clear, if one considers the well known relation $i \cdot l = q \cdot v$. Because simple loop monitors are very sensitive to rapidly changing magnetic fields always present in the environment of rf accelerators, capacitive pickups are preferred in general.

5.2 Capacitive Pickups, Basics

Figure 5.3 is a picture of a pickup in 50-Ω geometry for broadband measurements [249]. The segmented aperture in front and behind the pickup electrode is provided for impedance matching. The ground potential of the probe has been separated from the ground potential of the beam pipe to reduce noise coming along the beam pipe.

5.2.1 Design Hints

Supposing $2\pi R_\mathrm{s} \gg L_\mathrm{s}$ (see Fig. 5.2) and imagining that the capacitive pickup is a strip line bent around the beam pipe axis, the designer can take advantage of formulas given in the literature for the design of strip lines and microstrip

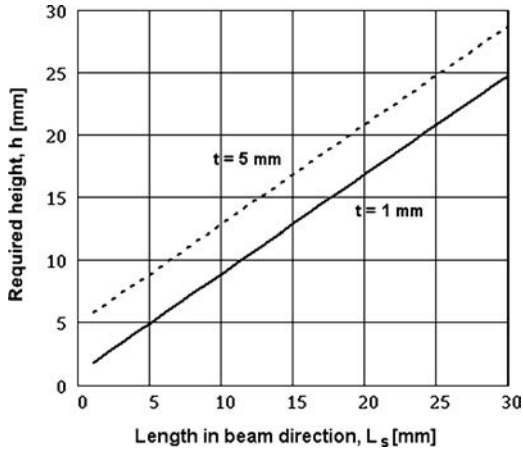

Fig. 5.4. Required height h dependent on length L_s, according to (5.4). See text for details

lines. The design of the pickup shown in Fig. 5.3 is based on a formula taken from [37]:

$$Z_0(L_\mathrm{s}) = \frac{87}{\sqrt{\varepsilon_\mathrm{r} + 1.4}} \ln\left(\frac{5.89\,h}{0.8\,L_\mathrm{s} + t}\right) , \tag{5.4}$$

[36–38, 250] where ε_r is the relative permeability, h is the distance between inner and outer conductor, and t is the thickness of the inner ring. Because the influenced signal can travel along two paths to the output, which corresponds to a parallel circuit of two transmission lines, the pickup is designed in 100-Ω geometry. Figure 5.4 gives the required height h dependent of L_s for two different values of material thickness h. The diagram holds for $Z_0 = 100\ \Omega$ and $\varepsilon_\mathrm{r} = 1$

5.2.2 Simplified Electric Circuit Diagram

The differences between low impedance and high impedance signal processing can be derived from the simplified electric circuit diagram of Fig. 5.5.

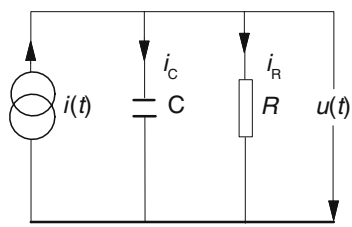

Fig. 5.5. Simplified electric circuit diagram according to Fig. 5.2

Here, C is the capacity of the pickup electrode against the beam pipe. A general relation can be derived for $i(t)$, considering the image current, generated by the motion of a charged particle. Because this image current changes sign by passing the center of the pickup, a current according to the scheme of Fig. 5.6 flows into the external circuit. For small Δt, $f(t+\Delta t) - f(t) = \frac{d}{dt} f(t)\,\Delta t$. Thus, the current $i(t)$ flowing from the pickup into the external circuit is proportional to $\frac{d}{dt} i_{\mathrm{B}}(t)$.

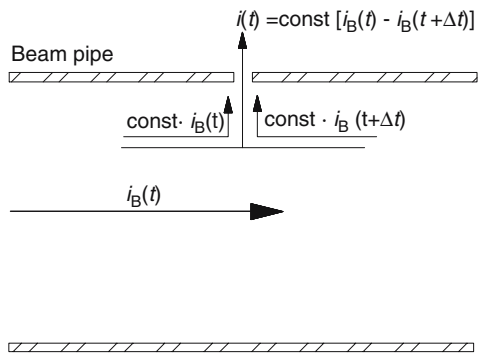

Fig. 5.6. Simplified scheme to explain the generation of a signal on a capacitive pickup

Considering the electric circuit diagram of Fig. 5.5, the ratio of the cutoff frequency of this simple circuit $f_{\mathrm{c}} = 1\,/\,2\pi RC = \omega_{\mathrm{c}}\,/\,2\pi$, to the frequencies f_{s}, which have to be processed, determines how the output voltage $u(t)$ looks like. Applying a Laplace transformation, one gets

$$u(s) = i(s)\,\frac{R}{1+RCs}\ . \tag{5.5}$$

The exact solution for $u(t)$ is

$$u(t) = \frac{1}{C}\int_0^t i(u) e^{-\frac{(t-u)}{RC}}\,du\ . \tag{5.6}$$

For $RCs \ll 1$, corresponding to $f_{\mathrm{s}} \ll f_{\mathrm{c}}$, it follows immediately from (5.5) that $u(s) \approx R\,i(s)$ and $u(t) \approx R\,i(t)$. Then, because $i(t)$ is proportional to $\frac{d}{dt} i_{\mathrm{B}}(t)$, the output voltage is proportional to $R\,\frac{d}{dt} i_{\mathrm{B}}(t)$. In this case, the main part of the current $i(t)$ flows through R. On the other hand, if $RCs \gg 1$, corresponding to $f_{\mathrm{s}} \gg f_{\mathrm{c}}$, one obtains $u(s) = R\,\frac{i(s)}{s}$ with the solution:

$$u(t) = \frac{1}{C}\int_0^t i(u)du = \frac{q(t)}{C}\ , \tag{5.7}$$

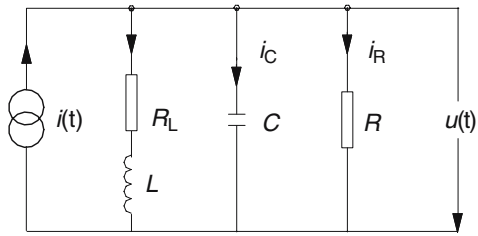

Fig. 5.7. Simple parallel resonance circuit

which follows also immediately from (5.6), since the exponential function goes to 1. Thus, $u(t)$ is proportional to the collected charge $q(t)$ and the output signal becomes directly proportional to $i_{\mathrm{B}}(t)$. In this case, the main part of the influenced current $i(t)$ flows into the capacity.

5.2.3 Resonant Circuit

In the circuit diagram of Fig. 5.5, the capacity C, determined by the geometric design of the pickup, can be supplemented by a small inductance to a resonant circuit, as shown in Fig. 5.7. The resistor R_{L} takes account of the ohmic losses in the inductance coil and, in general is small versus R. The resonant circuit can be tuned to a harmonic of the accelerating frequency f, which results in high sensitivity to the selected frequency. Neglecting first R_{L}, the complex impedance $Z = |Z|\, e^{i\varphi}$ is given by

$$|Z| = \frac{R/Q}{\sqrt{(\omega_0/\omega - \omega/\omega_0)^2 + 1/Q^2}} \tag{5.8}$$

$$\tan(\varphi) = Q(\omega_0/\omega - \omega/\omega_0) \tag{5.9}$$

with $\omega_0 = 1/\sqrt{LC}$ and the quality factor $Q = \omega_0 RC$. At resonance $|Z| = R$, $\varphi = 90^\circ$ and the induced current flows only through the load resistor R. Therefore, it is possible to obtain high sensitivity by using a high load impedance R. Due to the small bandwidth of the circuit, the signal-to noise-ratio will improve considerably. But any information about the bunch shape is lost, and even the phase of the output signal depends on the bunch shape.

Taking the resistor R_{L} (see Fig. 5.7) into account results in damping and, in consequence in a shift of the resonance frequency (ω_{D}). Furthermore, it causes a change of the impedance at resonance (R_{D}) and leads to a decrease in the Q value (Q_{D}):

$$\omega_{\mathrm{D}} = \omega_0 \sqrt{1 - R_{\mathrm{L}}^2 \frac{C}{L}} \tag{5.10}$$

$$\frac{1}{Q_{\mathrm{D}}} = \frac{1}{R}\sqrt{\frac{L}{C}} + R_{\mathrm{L}}\sqrt{\frac{C}{L}} \tag{5.11}$$

$$R_{\mathrm{D}} = \frac{L}{R_{\mathrm{L}} C + L/R} \,, \tag{5.12}$$

which can easily be verified from the complex admittance of the circuit. By setting the imaginary part of the admittance to zero, the resonance frequency can be determined.

5.2.4 Signal Estimation

Let us assume that a bunch of charged particles with geometric length Δz moves with βc along the z-axis. Then $\Delta z = \beta c \Delta t$ holds, with Δt as the bunch length in time (FWHM). Replacing d/dt in (5.1) by $1/\delta t$, where δt represents approximately the rise time of the longitudinal charge density distribution within the bunch, leads to a useful estimation of the expected signal amplitude:

$$i_{\mathrm{ring}} \approx \frac{160 \text{ pA}}{\delta t \ \ [\mathrm{ns}]}\, k\, \frac{L_{\mathrm{s}}}{\beta c \Delta t} \frac{2\pi R_{\mathrm{s}} L_{\mathrm{s}}}{2\pi R_{\mathrm{s}} L_{\mathrm{s}} + 2\pi R_{\mathrm{s}}^2} = \frac{160 \text{ pA}}{\delta t \ \ [\mathrm{ns}]}\, k\, \frac{L_{\mathrm{s}}}{\beta c \Delta t} \frac{1}{1 + R_{\mathrm{s}}/L_{\mathrm{s}}} \,. \tag{5.13}$$

The meaning of the separated terms is evident; the last term considers that the cylindrical probe is not closed on both sides, and the term $L_{\mathrm{s}}/\beta c \Delta t$ is the ratio between bunch length and probe length L_{s} (see Fig. 5.2). The factor k has been introduced to consider the influence of particles yet outside of the probe volume. Experience leads to $k \approx 2$ for bunch length $\beta c \Delta t \gg L_{\mathrm{s}}$. On the other hand, for very short bunches $\beta c \Delta t \ll L_{\mathrm{s}}$, the product of $k L_{\mathrm{s}}/\beta c \Delta t$ has to be replaced by one. Whereas (5.13) gives an estimate low impedance signal processing ($RC \ll \Delta t$), the corresponding estimation for high impedance signal processing ($RC \gg \Delta t$) leads to an expected voltage of

$$u \approx \frac{Q_{\mathrm{bunch}}}{C}\, k\, \frac{L_{\mathrm{s}}}{\beta c \Delta t} \frac{1}{1 + R_{\mathrm{s}}/L_{\mathrm{s}}} \,, \tag{5.14}$$

where Q_{bunch} is the sum of all charges within the bunch and C is the capacity of the pickup, according to Fig. 5.5.

5.2.5 One-Dimensional Signal Calculation

Idealized Square Bunch, Ring-Shaped Pickup

To calculate $i(t)$ according to Figs. 5.2 and 5.5 dependent on the bunch shape and β value, it is sufficient to consider only the longitudinal z-coordinate. In

this approximation, a moving charge distribution (bunch) of the type of a square pulse can be described as follows [249]:

$$\rho(x,y,z,t) = \delta(x)\delta(y)\frac{N\zeta e}{\beta c\Delta t}\left\{\Theta\left[z-\beta c\left(t-\frac{\Delta t}{2}\right)\right]-\Theta\left[z-\beta c\left(t+\frac{\Delta t}{2}\right)\right]\right\}. \tag{5.15}$$

In (5.15), $\delta(x)$ and $\delta(y)$ are the well-known δ functions of Dirac; N is the number of particles in the bunch; ζ is their charge; Δt is the bunch length, as already introduced in (5.13), and $\Theta(z-a)$ is the step function of Heaviside. The bunch moves along the z-axis and its center passes the observation point $z=0$ at time $t=0$. Taking the relativistic correction (see, e.g., [245]) with $\gamma = 1/\sqrt{1-\beta^2}$ into account, the potential $\varphi(r,z,t)$ is given by

$$\varphi(r,z,t) = \frac{\gamma}{4\pi\varepsilon_0}\frac{N\zeta e}{\Delta t}\int_{t'=t-\frac{\Delta t}{2}}^{t'=t+\frac{\Delta t}{2}}\frac{dt'}{\sqrt{[\gamma(z-\beta ct')]^2+r^2}}, \tag{5.16}$$

where r is the distance of the observation point from the beam axis ($x=0,\ y=0$). Substituting $\gamma(z-\beta ct')/r$ for Z, the solution is straightforward and leads to

$$\varphi(r,z,t) = \frac{1}{4\pi\varepsilon_0}\frac{N\zeta e}{\beta c\Delta t}\left\{\begin{array}{c} Arsinh\left[\frac{\gamma(z-\beta c)(t-\Delta t/2)}{r}\right] \\ ... - Arsinh\left[\frac{\gamma(z-\beta c)(t+\Delta t/2)}{r}\right]\end{array}\right\}. \tag{5.17}$$

The electric field strength follows from $E_\mathrm{r} = -\frac{\partial}{\partial r}\varphi(r,z,t)$:

$$E_\mathrm{r}(r,z,t) = \frac{1}{4\pi\varepsilon_0}\frac{N\zeta e}{\beta c\Delta t}\frac{1}{r}\left\{\begin{array}{c} \frac{\gamma(z-\beta c)(t-\Delta t/2)}{\sqrt{[\gamma(z-\beta c(t-\Delta t/2)]^2+r^2}} \\ ... - \frac{\gamma(z-\beta c)(t+\Delta t/2)}{\sqrt{[\gamma(z-\beta c)(t+\Delta t/2)]^2+r^2}}\end{array}\right\} \tag{5.18}$$

For the cylindrical pickup shown in Fig. 5.2, the influenced current $i(t)$ is given by (5.1), integrating over the surface of the cylinder:

$$i(t) = \varepsilon_0 2\pi R\frac{d}{dt}\int_{z=-L/2}^{z=L/2}E_\mathrm{r}(r=R,z,t)dz. \tag{5.19}$$

This can be solved very easily without integrating, keeping in mind that $E_\mathrm{r} = f(z-\beta ct)$. Therefore, d/dt can be replaced by $-\beta cd/dt$, and the result follows immediately from (5.18)

$$i(t) = \frac{\gamma N\zeta e}{2\Delta t}\left[T_1 - T_2 + T_3 - T_4\right], \tag{5.20}$$

with the abbreviations ($L_\mathrm{s} \to L$):

$$T_1 = \frac{[L/2 - \beta c(t + \Delta t/2)]}{\sqrt{\{\gamma[L/2 - \beta c(t + \Delta t/2)]\}^2 + R^2}} \tag{5.21}$$

$$T_2 = \frac{[L/2 - \beta c(t - \Delta t/2)]}{\sqrt{\{\gamma\,[L/2 - \beta c(t - \Delta t/2)]\}^2 + R^2}} \tag{5.22}$$

$$T_3 = \frac{[L/2 + \beta c(t + \Delta t/2)]}{\sqrt{\{[L/2 + \beta c(t + \Delta t/2)]\}^2 + R^2}} \tag{5.23}$$

$$T_4 = \frac{[L/2 + \beta c(t - \Delta t/2)]}{\sqrt{\{\gamma[L/2 + \beta c(t - \Delta t/2)]\}^2 + R^2}}\,. \tag{5.24}$$

From the solution, it is clear that the shape of the signal will depend very much on the ratio between the bunch length $\beta c\Delta t$ and the length of the pickup. In Fig. 5.8, two cases with $\beta = 0.1$ are considered. Curve 1 shows the signal of a long bunch with $\Delta t = 8\,\text{ns}$ with $\beta c\Delta t/L \approx 240\,\text{mm}/50\,\text{mm}$. Because there is no change d/dt while the long bunch is inside the pickup, the signal becomes zero at this time. The two peaks, corresponding to the entrance, respectively, to the exit of the bunch, are separated exactly by 8 ns, which is just the bunch length. The second curve represents a signal from a bunch with $\Delta t = 1$ ns and $\beta c\Delta t/L \approx 30\,\text{mm}/50$ mm. In this case, the bunch length compares with the length of the pickup, and thus the distance between the two peaks is determined by the time of flight (TOF) through the probe, which is 1.67 ns.

The relativistic effect enhances the transversal field component with increasing β value, whereas the longitudinal component becomes smaller. One expects sharper peaks in this case. Figure 5.9 demonstrates this for $\beta = 0.9$ and the same bunch lengths in time as for Fig. 5.8. The higher β value results in a larger geometric bunch length and therefore, even for curve 2,

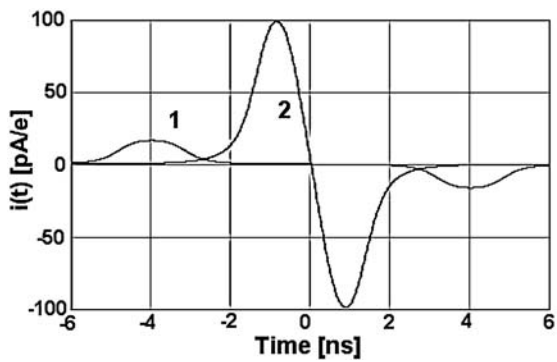

Fig. 5.8. Comparison of the signals from two square bunches of different lengths for $\beta = 0.1$. The length of the pickup is $L = 50\,\text{mm}$. Curve 1: Bunch length $\Delta t = 8\,\text{ns}$. Curve 2: Bunch length $\Delta t = 1\,\text{ns}$

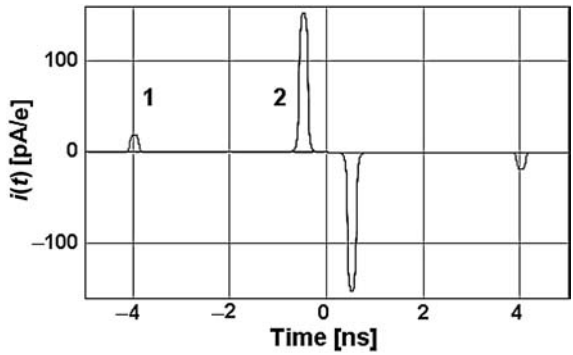

Fig. 5.9. Comparison of the signals from two square bunches of different lengths for $\beta = 0.9$. Parameters: Length of the pickup = 50 mm, radius = 17.5 mm length of the square bunches $\Delta t = 8$ ns (curve 1), $\Delta t = 1$ ns (curve 2)

$\beta c \Delta t / L \gg 1$. The charges in the bunches are normalized to $N\zeta e = 1e = 1.602 \times 10^{-19}$ As, thus the signal of the very long bunch (curve 1 in Fig. 5.9 with $\Delta t = 8$ ns and $\Delta z = 2.16$ m is much smaller than for the shorter bunch of curve 2. Because the rise time of the idealized square bunch is zero, the signal estimation (5.13) should not be used in this special case.

5.2.6 Bunches of Arbitrary Shape, Ring-Shaped Pickup

The one-dimensional density distribution within a bunch is more complex than the idealized homogeneous density distribution, representing a bunch with a square shape. Better approximations are given by a Gaussian, a $\cos^2$-like or a parabolic distribution. In each case, the analytical solutions for $i(t)$ according to (5.19) become rather complex and even impossible for the Gaussian distribution. But numerical signal calculation for bunches of arbitrary shape can be performed very easily by summing up the weighted contributions of a point charge. To derive the equivalent of (5.16–5.20) for a point charge, one can take advantage of the fact that each of the terms $T_1 - T_4$ in (5.20) is a function of $(t \pm \Delta t/2)$:

$$i\,(t) = \frac{\gamma N\,\zeta e}{2\Delta t}\left[f\,(t + \Delta t/2) - f\,(t - \Delta t/2)\right]\ . \tag{5.25}$$

From this relation, the final result for a point charge follows immediately from $\lim_{\Delta t \to 0}$ and therefore the result is given by

$$i\,(t) = \frac{\gamma N \zeta e}{2\,\Delta t}\Delta t\,\left[\frac{d}{dt}\left[T_{12}(t) + T_{34}(t)\right]\right] \tag{5.26}$$

$$T_{12}(t) = \frac{L/2 - \beta ct}{\sqrt{\left[\gamma(L/2 - \beta ct)\right]^2 + R^2}} \tag{5.27}$$

$$T_{34}(t) = \frac{L/2 + \beta ct}{\sqrt{\left[\gamma(L/2 + \beta ct)\right]^2 + R^2}}\ . \tag{5.28}$$

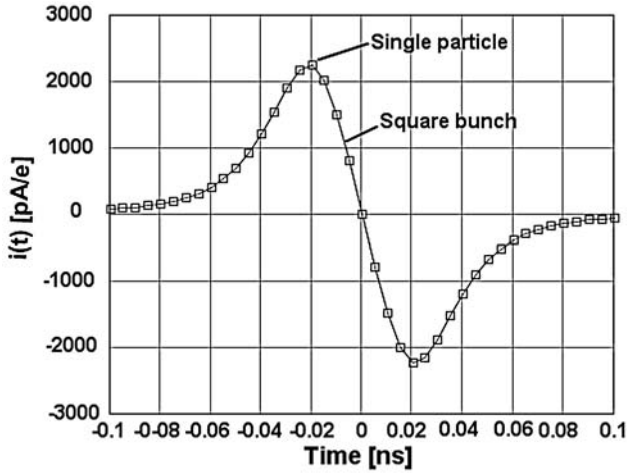

Fig. 5.10. Signal of one electron in comparison with the signal of a very short square bunch. Parameters: Lengths of the pickup = 10 mm, radius = 17.5 mm; length of the square bunch $\Delta t = 1$ps, $\beta = 0.9$

This leads to

$$i\,(t) = \frac{e\gamma\beta c R^2}{2}\left[\frac{1}{[[\gamma(L/2+\beta ct)]^2+R^2]^{3/2}} - \frac{1}{[[\gamma(L/2-\beta ct)]^2+R^2]^{3/2}}\right]. \tag{5.29}$$

Remembering the relation $B_\Theta = \beta/c\,E_\mathrm{r}$ a similar expression can be derived for the voltage, induced on an inductive monitor. From (5.29), it becomes clear that even the signal of a point charge will be broadened by two effects:

- The advanced electric field, which, with increasing β, becomes more and more peaked in the transversal direction,
- the integration (convolution) over the length of the pickup.

To demonstrate the effect of signal broadening, Fig. 5.10 shows an example for $\beta = 0.9$. For comparison, the signal for a very short square bunch with $\Delta t = 1$ ps is also shown (continuous line).

Equation 5.29 gives the base for numerical signal calculation $i(t)$, assuming arbitrary bunch shapes. In a first step, a normalized density distribution has to be determined, which means that the point charge has to be distributed over the selected bunch shape. This results in an ensemble of weights, normalized to one. Applying this procedure, it is simple to compare various models of bunch shape by calculating the $P(m)$ weights. The $P(m)$ values for some typical density distributions, having all the same FWHM-widths Δt are various:

$\cos^2$ – like charge density distribution

With Δt as the half width of the bunch (FWHM), $T_0 = 2\Delta t$, where T_0 is the full width of the bunch at the baseline. Then, N_s sample points over time

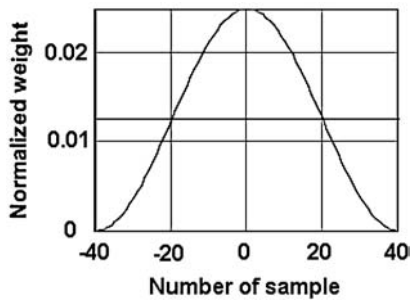

Fig. 5.11. Weights defined for a $\cos^2$-like intensity distribution

T_0 lead to $\delta t = T_0/N_\mathrm{s}$. The normalized density distribution is

$$P(m) = \frac{\cos^2(m\,\delta t \frac{\pi}{T_0})}{P_0} \tag{5.30}$$

$$P_0 = \sum_{m=-N_\mathrm{s}/2}^{m=N_\mathrm{s}/2} \cos^2\left(m\,\delta t \frac{\pi}{T_0}\right) . \tag{5.31}$$

Figure 5.11 shows the distribution assuming $N_\mathrm{s} = 80$; the line at $P(-20)$ marks FWHM. The composition of the signal $i\,(t)$ is straightforward and gives

$$i(t) = \frac{e\gamma\beta c R^2}{2} \sum_{m=-N_\mathrm{s}/2}^{m=N_\mathrm{s}/2} P(m)(T_\mathrm{A}(t,m) - T_\mathrm{B}(t,m) \tag{5.32}$$

$$T_\mathrm{A}(t,m) = \frac{1}{(\{\gamma[L/2 + \beta c(t + m\,\delta t)]\}^2 + R^2)^{3/2}} \tag{5.33}$$

$$T_\mathrm{B}(t,m) = \frac{1}{(\{\gamma[L/2 - \beta c(t + m\,\delta t)]\}^2 + R^2)^{3/2}} . \tag{5.34}$$

Figure 5.12 shows the calculated signal for the $\cos^2$-shaped bunch, setting all other parameters identical to the parameters for the single particle in Fig. 5.10.

Parabolic bunch shape: The full width is $T_0 = \sqrt{2}\Delta t$, $\delta t = T_0/N_\mathrm{s}$

$$P_\mathrm{P}(m) = \frac{\left[1 - (\frac{m\,\delta t}{T_0/2})^2\right]}{p_0} . \tag{5.35}$$

Gaussian shape: Since the Gaussian distribution extends to $-\infty < t < \infty$, one needs a cutoff. Setting the cutoff at $P(T_0/2) = s\,P(0)$ $(s \ll 1)$, one obtains $T_0 = \sqrt{\ln(1/s)/\ln 2}$, $\delta t = T_0/N_\mathrm{s}$, and

$$P_G(m) = \frac{e^{-\left[\frac{2\sqrt{\ln 2} m\,\delta t}{\Delta t}\right]^2}}{P_0} . \tag{5.36}$$

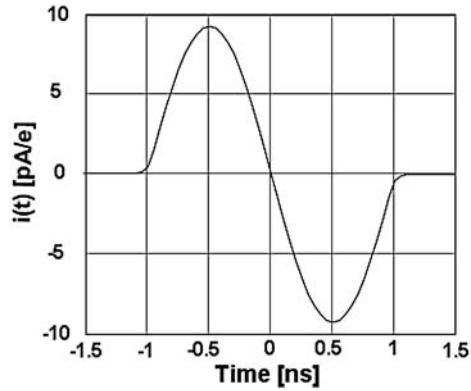

Fig. 5.12. Numerical calculated signal for a $\cos^2$ distribution. Parameters Length of the pickup = 10 mm, radius = 17.5 mm length of the bunch $\Delta t = 1$ ns, (FWHM) $\beta = 0.9$

Triangular bunch shape: Here the full width is $T_0 = 2\Delta t$, $\delta t = T_0/N_\mathrm{s}$, and

$$P_\mathrm{T}(m) = \frac{\left[1 - \frac{|m|\,\delta t}{\Delta t}\right]}{P_0} \ . \tag{5.37}$$

In each case, P_0 is the normalization given by the sum over all $P(m)$ from $m = -N_\mathrm{s}/2$ to $m = +N_\mathrm{s}/2$.

5.2.7 Pickup Plates

In practice, signal calculation for rectangular plates is of special interest for beam position measurements. In this case, the electric field components have to be determined in the Cartesian coordinate system. Assuming dimensions and orientation of the Cartesian coordinate system, as shown schematically in Fig. 5.13, the y-component is relevant. Signal calculation for a square bunch shape has been performed in [252].To perform signal calculation by summing up weighted point charges, it is sufficient to derive the influenced current $i\,(t)$ for one plate and a point charge e. The electric potential and the y-component of the electric field are given by

$$\varphi(x,y,z,t) = \frac{e\gamma}{4\pi\varepsilon_0} \frac{1}{\sqrt{[\gamma(z-\beta ct)^2 + x^2 + y^2]}} \tag{5.38}$$

$$E_\mathrm{y} = -\frac{\partial}{\partial y}\varphi = \frac{e\gamma}{4\pi\varepsilon_0} \frac{y}{\sqrt{[\gamma(z-\beta ct)]^2 + x^2 + y^2}^3} \tag{5.39}$$

$$i\,(t) = \varepsilon_0 \int_{\mathrm{x}=-b}^{x=b} \left[\int_{z=-a}^{z=a} E_\mathrm{y}(y=h)dz \right] dx \ . \tag{5.40}$$

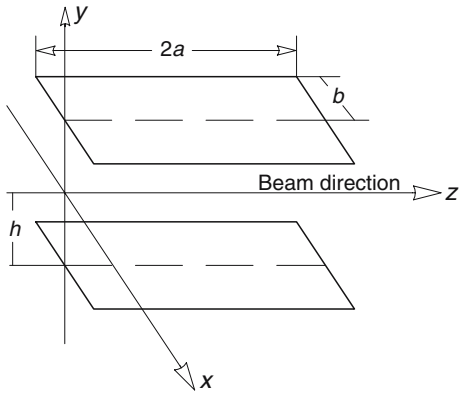

Fig. 5.13. Definitions for signal calculation of a rectangular pickup

Remembering that $d/dt = -\beta c\, d/dz$, only the integration over the x-coordinate is left:

$$i\,(t) = \frac{e\gamma}{4\pi}\beta\, c\, h \int_{-b}^{b} \left[\frac{1}{\left(A^2 + x^2\right)^{3/2}} - \frac{1}{\left(B^2 + x^2\right)^{3/2}} \right] dx \tag{5.41}$$

$$A^2 = \left[\gamma(a + \beta ct)\right]^2 + h^2 \tag{5.42}$$

$$B^2 = \left[\gamma(a - \beta ct)\right]^2 + h^2\ . \tag{5.43}$$

The remaining integral is of the kind $\int dx/R_{\mathrm{x}}^3$ with $R_{\mathrm{x}} = \sqrt{A^2 + x^2}$, respectively, $R_{\mathrm{x}} = \sqrt{B^2 + x^2}$. The solution is straightforward (see, e.g., [84, 253]):

$$i\,(t) = \frac{e\,\gamma\beta\, c\, h\, b}{2\,\pi}\left[TP_1(t) - TP_2(t)\right] \tag{5.44}$$

$$TP_1(t) = \frac{1}{\left[h^2 + C(t)^2\right] W_1(t)} \tag{5.45}$$

$$C(t) = \gamma(a + \beta ct) \tag{5.46}$$

$$W_1(t) = \sqrt{b^2 + h^2 + C(t)^2} \tag{5.47}$$

$$TP_2(t) = \frac{1}{\left[h^2 + E(t)^2\right] W_2(t)} \tag{5.48}$$

$$E(t) = \gamma(a - \beta ct) \tag{5.49}$$

$$W_2(t) = \sqrt{b^2 + h^2 + E(t)^2}\ . \tag{5.50}$$

The composition of the signal can be performed by replacing $t \rightarrow m\,\delta t$ and summing up over all weighted terms, as demonstrated in (5.32–5.34).

5.2.8 Comparison of Charge Density Distributions

Due to the advanced electric field of moving charged particle bunches, it is to be expected, that it will be very difficult to decide between the discussed

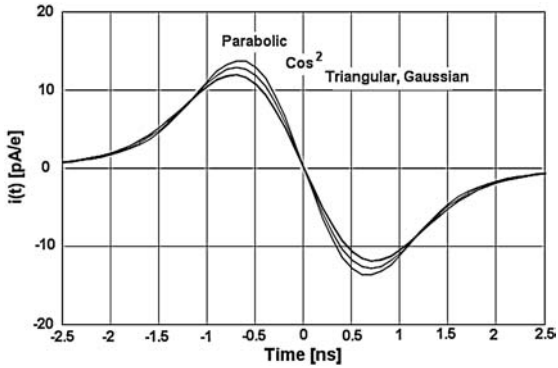

Fig. 5.14. Comparison of various bunch shape models for low β value. Parameters: Plate length = 30 mm, plate width = 30 mm, spacing between the plates = 40 mm, $\beta = 0.1$, $\Delta t = 1$ns (FWHM)

models in case of low β values. This is demonstrated in Fig. 5.14, showing calculated signals for a plate with dimensions of $2a = 30$ mm, $2b = 30$ mm, and $h = 20$ mm (see Fig. 5.13 for the definition of plate dimensions). For a bunch with $\Delta t = 1$ns (FWHM), moving with $\beta = 0.1$, the geometric bunch length is $\Delta z = 0.1 \cdot 300\,\text{mm/ns} \cdot 1\,\text{ns} = 30$ mm. The differences in the influenced signals are below any detection limit. The picture changes for highly relativistic charged particle bunches with $\beta = 0.95$, as shown in Fig. 5.15. The data hold for a bunch length of $\Delta t = 0.5$ ns which results in $\Delta z = 142.5$ mm. The differences between the models are evident. Especially the proportionality of the signal $i(t)$ to the derivative of the charge density distribution comes out very clearly.

5.2.9 Detection Limits

Broadband Signal Processing

To determine the signal-to-noise ratio at the output of a signal processing circuit, which in the simplest case can be a high quality broadband amplifier, the noise factor F of the circuit has to be known. In data books of amplifiers and electronic circuits, it is usual to specify the so-called noise number F_{dB}, related to the noise factor by $F = 10^{F_{\text{dB}}/10}$. For a bandwidth δf of the signal processing circuit, an environment temperature T_o, and an input impedance of R_{L}, the required minimum input current $i_{\min}$ to get a signal-to-noise ratio of $S\!:\!N = 1$ is determined from

$$i_{\min} = \sqrt{\frac{F\, k_{\text{B}} T_0\, \delta f}{R_{\text{L}}}} \tag{5.51}$$

$$k_{\text{B}} = 1.38 \cdot 10^{-23}\,\text{Ws/K, the Boltzmann constant .} \tag{5.52}$$

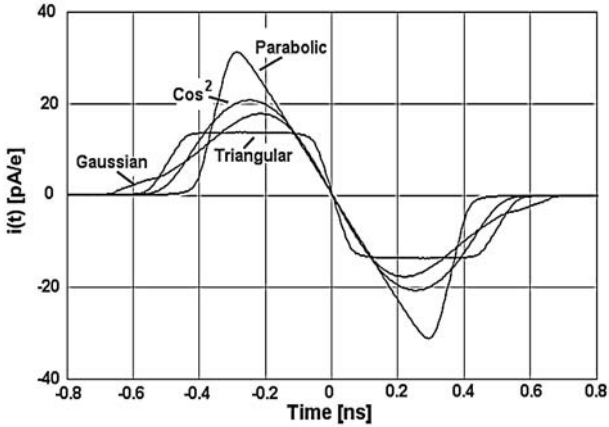

Fig. 5.15. Comparison of various bunch shape models for high β values. Parameters: Plate length = 30 mm, plate width = 30 mm, spacing between the plates = 40 mm, $\beta = 0.95$, $\Delta t = 0.5$ ns (FWHM)

The required bandwidth follows immediately from the well-known relation δf [GHz] $= 0.35/t_{\mathrm{rise}}$ [ns]. Because all signal calculations in this chapter are normalized to $1e$, the required number of charges $N\,\zeta$ within a bunch is easily calculated from

$$[N\,\zeta]_{\mathrm{min}} = \frac{i_{\mathrm{min}}}{i(t)_{\mathrm{max}}}\ , \tag{5.53}$$

where $i(t)_{\mathrm{max}}$ is the maximum current in pA/e, taken from the calculations for $i(t)$. Referring to Fig. 5.12, a value of $i(t)_{\mathrm{max}} = 9$ pA/e seems reasonable. Assuming a bandwidth of 500 MHz with a typical noise number $F_{\mathrm{dB}} = 3.2$, an impedance of 50 Ω, and room temperature, (5.51) and (5.53) lead to $[N\,\zeta]_{\mathrm{min}} = 0.29\,\mu\mathrm{A}\,/\,9$ pA $= 3.2 \times 10^4$. Of course, to observe amplified bunch signals on an oscilloscope or to perform measurements described in the following, the signal-to-noise ratio has to be significantly larger than one. Experience has shown that in most cases either the macro-pulse current i_{p} or the dc-current, respectively, mean current i_{m} are known. Keeping in mind that $[N\,\zeta\,e]_{\mathrm{min}}\,/\Delta t$ corresponds to the bunch current i_{b} the expected signal-to-noise ratio is easily derived from these parameters.

A very similar estimation of the required current or voltage to obtain a signal-to-noise ratio, is based on the noise power of a resistor, which does not depend on its value and is given by $P_R = 4\,k_{\mathrm{B}}T_0\delta f$ [38]. Keeping in mind $P = u^2/R = i^2\,R$, the required charge within a bunch for $S : N = 1$ can be figured out in the same way as described above. If the signal is processed according to (5.7), $u_{\mathrm{noise}} = \sqrt{R\,P_R}$ has to be used for estimation of $[N\,\zeta]_{\mathrm{min}}$.

Resonant Signal Processing

Estimation of the signal-to-noise ratio, respectively, of the required $[N\,\zeta]_{\min}$ value becomes more complicated for a resonant circuit, according to Fig. 5.7. In this case, the magnitude of the processed harmonic component has to be determined by a Fourier analysis. A fast Fourier transformation (FFT) can be performed directly on the signal, calculated in the time domain. However, due to different definitions, of normalization in the programs as well as in the literature, special attention has to be given to this point. A good recommendation is to transform, as a test, a simple square pulse of the type of

$$i(t) = \left\{ \Theta \left[\beta c \left(t - \frac{\Delta t}{2} \right) \right] - \Theta \left[\beta c \left(t + \frac{\Delta t}{2} \right) \right] \right\}, \tag{5.54}$$

having an amplitude of one and a length of Δt. For a repetition frequency f, the duty factor D is given by $D = f\,\Delta t = \Delta t/T$, with T as the period of f ($T = 1/f$). With the definition of $i(t)$ by the Heaviside function, the average dc-current is $i_{\mathrm{m}} = i(t) \cdot D$. Therefore, the correct normalization can be checked by comparing this with the dc-component of the Fourier-transformed signal. Assuming correct normalization, the amplitude of the harmonics with frequency $f_{\mathrm{n}} = n\,f$ is given by $|C_{\mathrm{n}}|$, with C_{n} as the coefficients of the FFT.

Another possibility is to perform a FFT directly on a measured signal, taking advantage of modern digital oscilloscopes, as shown in Fig. 5.16 for an accelerator frequency $f = 108$ MHz. But also in this case, one has to be careful concerning normalization.

To give an example, we compare resonant signal processing with broadband signal processing for an input signal $i(t)$, according to Fig. 5.12 for a

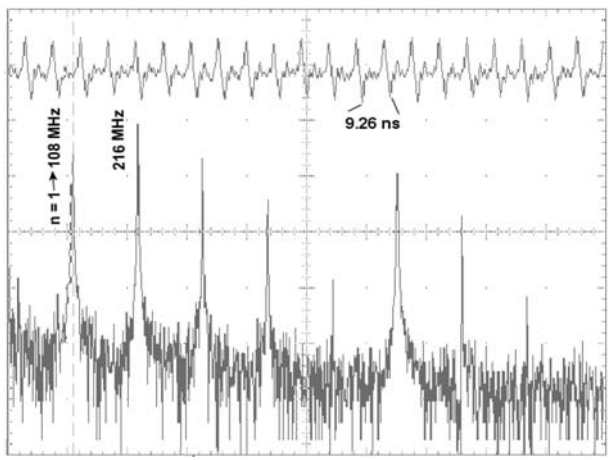

Fig. 5.16. FFT of a measured bunch signal (upper trace) performed with a digital *Tektronix* oscilloscope. Data taken with 2.5 Gs/s in the main control room of GSI

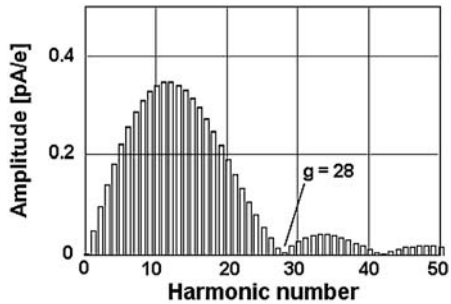

Fig. 5.17. FFT of the signal $i(t)$ according to Fig. 5.12. The frequencies of the harmonics are given by $f_\mathrm{n} = 36\,\mathrm{MHz} \times$ harmonic number

bunch repetition frequency $f = 36\,\mathrm{MHz}$. To perform a FFT, the signal $i(t)$ has to be sampled. The number of sampling points N has to be a power of 2. Taking $N = 2048$, the signal $i(t)$ is described by a data vector with N components according to

$$I_g = i\left[\frac{g - S_\mathrm{N}}{(N-1)\,f}\right] = i\left[\frac{g - 1023}{2047\,f}\right] \tag{5.55}$$

$$g = 0, 1, \ldots N-1 \tag{5.56}$$

$$S_\mathrm{N} = (N-2)/2\,. \tag{5.57}$$

The coefficients C_n are given by

$$C_\mathrm{n} = \frac{1}{N}\sum_g I_g\, e^{i(2\,\pi\, n\,/\,N)\,g}, \qquad i = \sqrt{-1}\,. \tag{5.58}$$

Figure 5.17 gives the result for the signal of Fig. 5.12. Because the bunch length $\Delta t = 1\,\mathrm{ns}$ and $f = 36\,\mathrm{MHz}$, corresponding to $T = 27.8\,\mathrm{ns}$, the first minimum in the Fourier spectrum occurs at $g = 28$ (see Sect. 7.1.2 for more details). Tuning the electronics, for example, to the sixth harmonic with $f = 216\,\mathrm{MHz}$, the resulting amplitude of about 0.26 pA/e is very small in comparison to the maximum of 9 pA/e (see Fig. 5.12) for the signal in the time domain. However, the signal-to-noise ratio can be improved considerably by

1. Reducing the bandwidth (BW) to a very small value in comparison to broadband signal processing. The noise goes down $\sim \sqrt{\mathrm{BW}}$.
2. Increasing the load resistor R_L to a higher value, keeping in mind that the main current flows through R_L in resonance.

In the example, the noise voltage is determined from $u_\mathrm{N} = \sqrt{4R_\mathrm{L}k_\mathrm{B}T_0\delta f}$, which gives $u_\mathrm{N} = 4.02\ \mu\mathrm{V}$, assuming $R_\mathrm{L} = 10^5\ \Omega$ and $\delta f = 10\,\mathrm{kHz}$. On the other hand, the signal voltage on R_L is $u_\mathrm{S} = i_6\,R_\mathrm{L} = 0.26\ \mathrm{pA/e} \times 10^5\ \Omega = 26\ \mathrm{nV}$. The required number of charges $[N\,\zeta]_\mathrm{min}$ for S:N = 1 follows immediately from $[N\,\zeta]_\mathrm{min} = u_\mathrm{N}/u_\mathrm{S} = 155$, which is much better than 2.3×10^4,

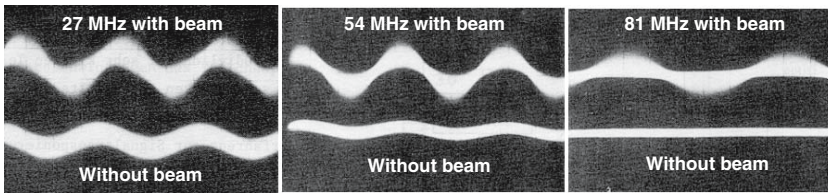

Fig. 5.18. Observed distortions from the accelerating frequency $f = 27\,\mathrm{MHz}$ at three different harmonics. The pictures are taken in the main control room of GSI

evaluated for broadband signal processing. But, as already mentioned, any information concerning the bunch shape will be lost using narrowband signal processing.

Special attention should be given to the selection of the harmonic number. Beside the white noise, according to the formulas given above, distortions from the high-power rf transmitters, which are always present in the environment of rf accelerators, have to be considered. Optimizing the selection of the harmonic number by measuring those distortions, with a tunable narrowband amplifier is recommended. Figure 5.18 shows an example from the UNILAC with $f = 27\,\mathrm{MHz}$. Although the signal amplitudes of the harmonic increase up to about the 10th harmonic, in this case as a compromise, the third harmonic $f = 27$ MHz has been selected because the poststripper is operated at $f = 108\,\mathrm{MHz}$, which is the fourth harmonic of the prestripper accelerating frequency.

5.2.10 Sensitivity of Position Measurements

The difference signal from two plates, respectively, two electrodes of a segmented ring-shaped pickup, positioned on opposite sides of the beam, is often used to determine the beam position. Therefore, it might be of interest to determine the sensitivity which can be achieved using this so-called proximity effect. In both cases – segmented ring shaped pickups or rectangular plates – the signal amplitude for a given displacement can be estimated from the signal, induced by a point charge.

Segmented Ring-Shaped Electrodes

The signal from one segment (see Fig. 5.19) is given by (5.29) as $i\,(t) = i_{\mathrm{SP}}(t)/k$. A good approximation of the difference signal from two opposite plates, assuming a displacement δr of the beam is $-\delta i(t, \delta r) = i\,(t, R - \delta r) - i\,(t, R + \delta r)$. For small δr, this is just proportional to the derivation of the sum signal, giving

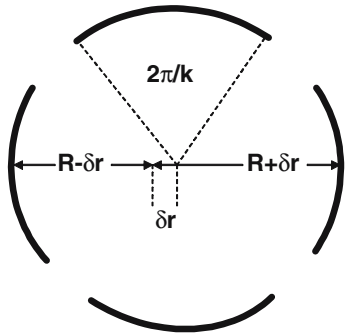

Fig. 5.19. Simplified scheme to define the parameters of a segmented pickup provided for determining beam position

$$\delta i\,(t,\delta r) = -2\,\delta r\,\frac{d}{dR} i\,(t,R) \tag{5.59}$$

$$\delta i\,(t,\delta r) = -\frac{e\,\gamma\,\beta\,c\,R\,\delta r}{k}\,(T_{\mathrm{A}} - T_{\mathrm{B}}) \tag{5.60}$$

$$T_{\mathrm{A}} = \frac{[\gamma(L/2+\beta ct)]^2 - R^2/2}{\{[\gamma(L/2+\beta ct)]^2 + R^2\}^{5/2}} \tag{5.61}$$

$$T_{\mathrm{B}} = \frac{[\gamma(L/2-\beta ct)]^2 - R^2/2}{\{[\gamma(L/2-\beta ct)]^2 + R^2\}^{5/2}}\,. \tag{5.62}$$

Pickups of the Plate Type

The difference signal from two rectangular pickups, positioned according to Fig. 5.13, can be derived in the same way by calculating the derivative d/dh. One obtains

$$\delta i\,(t,\delta r) = -2\,\delta r \frac{d}{dh} i\,(t,h)\,. \tag{5.63}$$

The differentiation of (5.44) with the definitions (5.45–5.50) is straightforward. However, it results in rather long expressions and therefore the result is not given here. The results for both versions, the ring-shaped monitor and the plate type, are similar, if the relevant parameters are scaled as follows: $2a \approx L,\ 2b \approx 2\pi R/k,\ h \approx R$. As an example, sum and difference signals for both types are displayed in Fig. 5.20 for a point charge.

Therefore, instead of calculating the difference signal for a pickup of the plate type from (5.63), it can be estimated from the sum signal (5.44) and the ratio for the segmented ring-shaped pickup, according to (5.29) and (5.59). The required number $[N\zeta]_{\min}$ to achieve a signal-to-noise ratio S:N = 1 can be scaled with the ratio Δ/Σ (Δ is the difference signal and Σ is the sum signal).

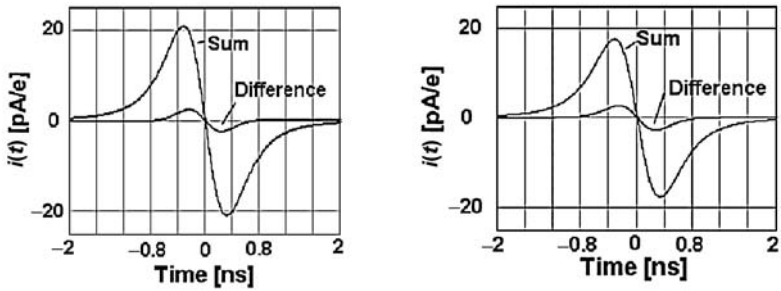

Fig. 5.20. Sum and difference signal for a point charge with $\beta = 0.1$. Left: Ring-shaped pickup with $2\pi/k = 60°$, pickup radius = 17.5 mm pickup length = 10 mm. Right: Plate type pickup with $2b = 18$ mm, $2a = 10$ mm, and $h = 17.5$ mm. The difference signals hold for a displacement of 1 mm in both cases

5.2.11 Linearity of Position Measurements

To be independent of changes in beam intensity during beam position measurements, the Δ signal has to be normalized with the Σ signal. Keeping in mind the dependencies of the equations given in this section, the linearity of Δ/Σ should be calculated for the selected probe dimensions and beam parameters to consider corrections in the evaluation software. Figure 5.21 shows a calculation for a plate-type pickup according to (5.44):

$$\Sigma = i\left(\frac{-TOF}{2}, h - \delta h\right) + i\left(\frac{-TOF}{2}, h + \delta h\right) \tag{5.64}$$

$$\Delta = i\left(\frac{-TOF}{2}, h - \delta h\right) - i\left(\frac{-TOF}{2}, h + \delta h\right) \tag{5.65}$$

with $t = \mathrm{TOF}/2$ and TOF as the time of flight through the pickup, which corresponds about to the positive signal maximum.

From the calculation, one can conclude that the normalized difference signal is linear up to a displacement of about one-half of the aperture.

Conformal Mapping

The position sensitivity for circularly shaped pickups can be determined, taking advantage of the bilinear transformation

$$w = R\,\frac{i - z}{i + z} \tag{5.66}$$

$$z = i\,\frac{R - w}{R + w} \tag{5.67}$$

which maps the upper half of the z-plane ($z = x + iy$) into a circle with radius R into the w-plane ($w = u + iv$). The point $z = i$ is mapped into $w = 0$.

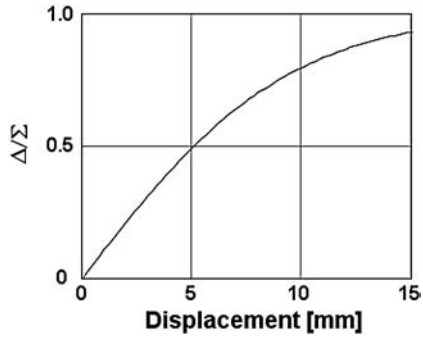

Fig. 5.21. Linearity of position signals for a plate-type pickup. Parameters: Single particle of charge e with $\beta = 0.5$. Plate dimensions: $2b = 25\,\mathrm{mm}$, $2a = 20\,\mathrm{mm}$, $h = 25\,\mathrm{mm}$

A point moving on the real axis in the w-plane moves along the imaginary axis in the z-plane. In the z-plane, the potential of a line charge q, located at $z = z_0$ is given by

$$\phi(z) = -\frac{q}{2\pi\varepsilon_0}\ln\frac{z - z_0}{z + z_0}\ . \tag{5.68}$$

For a dc-beam, q is given by $i/\beta c$. The solution holds for $\phi(y = 0, x) = 0$ and is easily derived by placing a second line charge at $z = -z_0$. In the w-plane, $z_0 = i$ corresponds to a centered line charge. With (5.67), we obtain the potential $\phi(z)$ for a line charge located at position $w = r_\mathrm{i}$:

$$\phi(z) = -\frac{q}{2\pi\varepsilon_0}\ln\frac{z - i\,\frac{R-r_\mathrm{i}}{R+r_\mathrm{i}}}{z + i\,\frac{R-r_\mathrm{i}}{R+r_\mathrm{i}}}\ . \tag{5.69}$$

Mapping to the w-plane results in

$$\phi(w) = -\frac{q}{2\pi\varepsilon_0}\ln\frac{r_\mathrm{i} - w}{R - \frac{r_\mathrm{i} w}{R}}\ . \tag{5.70}$$

In connection with the problem discussed, the real part of $\phi(w)$ is of interest. The observation point is at $w = r$. Thus, $r_\mathrm{i} - r$ and $R - r_\mathrm{i} r/R$ can be replaced, applying the law of vector multiplication. For the real part of the potential, we arrive at

$$\phi(r) = -\frac{q}{2\pi\varepsilon_0}\ln\frac{\sqrt{r_\mathrm{i}^2 + r^2 - 2r_\mathrm{i} r\cos\theta}}{\sqrt{R^2 + \left(\frac{r_\mathrm{i} r}{R}\right)^2 - 2r_\mathrm{i} r\cos\theta}}\ . \tag{5.71}$$

Here the parameters are defined as follows:

- r is the radial distance from the center of the pickup to the observation point on the segmented electrodes.
- θ is the angle between the u-axis (abscissa) and the vector to the observation point.

- R is the radius of the grounded beam pipe.
- r_i is the displacement of the beam along the positive u-axis.

To calculate the influenced signals on the electrodes dependent on the displacement r_i, the radial component of the electric field must be determined from $E_\mathrm{r} = -d\phi(r)/dr$. One ends up with

$$E_\mathrm{r}(r, r_\mathrm{i}, \theta) = \frac{q}{2\pi\varepsilon_0} \left(T_1(r, r_\mathrm{i}, \theta) + (T_2(r, r_\mathrm{i}, \theta)\right. \tag{5.72}$$

$$T_1(r, r_\mathrm{i}, \theta) = \frac{r - r_\mathrm{i}\cos\theta}{r_\mathrm{i}^2 + r^2 - 2r_\mathrm{i} r\cos\theta} \tag{5.73}$$

$$T_2(r, r_\mathrm{i}, \theta) = \frac{r_\mathrm{i}\left(r_\mathrm{i} r - R^2\cos\theta\right)}{R^4 + r_\mathrm{i}^2 r^2 - 2r_\mathrm{i} r R^2\cos\theta}\ . \tag{5.74}$$

The influenced signal on one segment located at r with the extension $\theta_1 \le \theta \le \theta_2$ has to be figured out from

$$u = \frac{L}{C}\int_{\theta_1}^{\theta_2} \varepsilon_0\, E_\mathrm{r}(r, r_\mathrm{i}, \theta) r\, d\theta\ , \tag{5.75}$$

with L as the length of the electrode in the beam direction and C as the capacity of the pickup electrode against ground.

Example 1. $L = 10\,\mathrm{mm}$, $C = 10\,\mathrm{pF}$, $R = 17.5\,\mathrm{mm}$, $\theta_1 = -30°$, $\theta_2 = 30°$ (electrode on the right), $\theta_2 = -150°$, $\theta_2 = 210°$ (electrode on the left).

Example 2. $L = 10\,\mathrm{mm}$, $C = 10\,\mathrm{pF}$, $R = 17.5\,\mathrm{mm}$, $\theta_1 = 15°$, $\theta_2 = 75°$ (electrode on the right), $\theta_2 = -195°$, $\theta_2 = 255°$ (electrode on the left).

Figure 5.22 shows the normalized difference signal Δ/Σ for both examples dependent on the displacement r_i against the electrode on the right. Obviously, due to the normalization by the sum signal, specification of L and C is irrelevant. Because the estimations given by (5.59) and (5.60) hold only for small displacements, the method of conformal mapping delivers more precise results. Using the manifold of conformal mappings described in the literature [254], it is possible to solve more complex problems of this kind, too.

5.2.12 Examples for Design and Signal Processing

Figures 5.23 and 5.24 show two examples of capacitive pickups with electrode systems, provided for additional position measurements. About 30 pickups of the type shown in Fig. 5.23 are installed along the UNILAC and in the experimental beam lines of GSI to perform measurements as discussed in the next section. The pickup shown in Fig. 5.24 has been designed [33] for installation between two superconducting accelerator sections, which requires a very short insertion length of about 10 mm, a small aperture of 12 mm, and

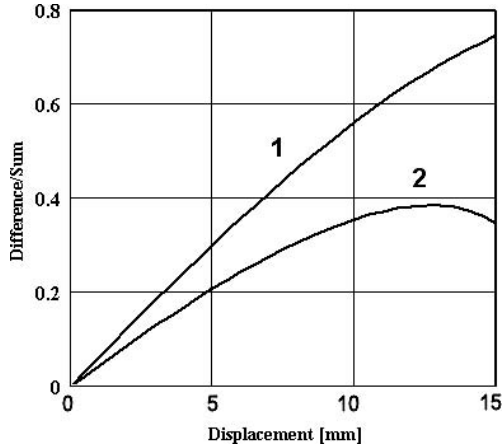

Fig. 5.22. Normalized difference signal dependent on the beam displacement. Curve 1: Electrodes centered at 0° and 180°. Curve 2: Electrodes centered at 45° and 225°. See text for details

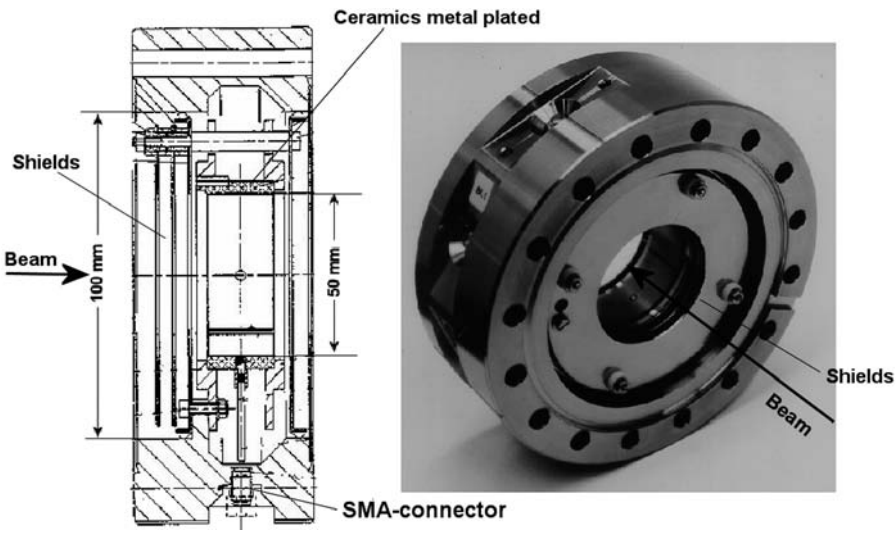

Fig. 5.23. Segmented capacitive pickup for measurements in the longitudinal phase plane, including position measurements. The picture on the right-hand side is a GSI Foto

qualification with respect to a cryogenic environment. The scheme of signal processing for the pickups, according to Fig. 5.23, is shown in Fig. 5.25. The most relevant specifications are given in Table 5.1. To take advantage of the higher sensitivity of narrowband signal processing, the position measurement is based on the extraction and detection of the eighth harmonic, which is 216 MHz in this case. To allow comparison of bunch signals with rf tank signals

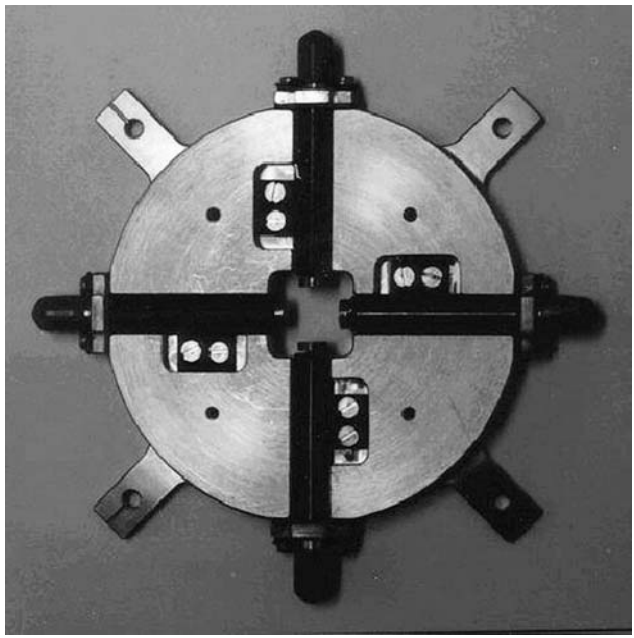

Fig. 5.24. Capacitive pickup, design [33], and manufaturing [255], provided for the installation between two superconducting accelerator sections. See text for the specifications

with respect to phase differences, all rf tank signals are also fed into the system. This enables the operator to adjust and monitor the powering of the accelerator sections with the correct rf phase setting. Beside evaluation of the Δ/Σ signals by the computer, the beam position is displayed to the operator in a bar diagram (see Fig. 5.23), too.

The most important parameters of the pickup shown in Fig. 5.24 are given in Table 5.2.

5.3 Examples of Application

5.3.1 Beam Energy Determination by Time of Flight

Taking advantage of the periodic bunch structure, very precise time of flight (TOF) measurements can be performed to determine the beam. In this case, the energy is determined directly by two of the basic units [m, s] of the International Unit System (SI) [256]. Figure 5.26 shows schematically two typical schemes. Energy is determined on the basis of the arrangement shown on top by two measurements: the first to determine the number of bunches between pickups P1 and P2 by measuring the time of flight from P1 to P2 and the

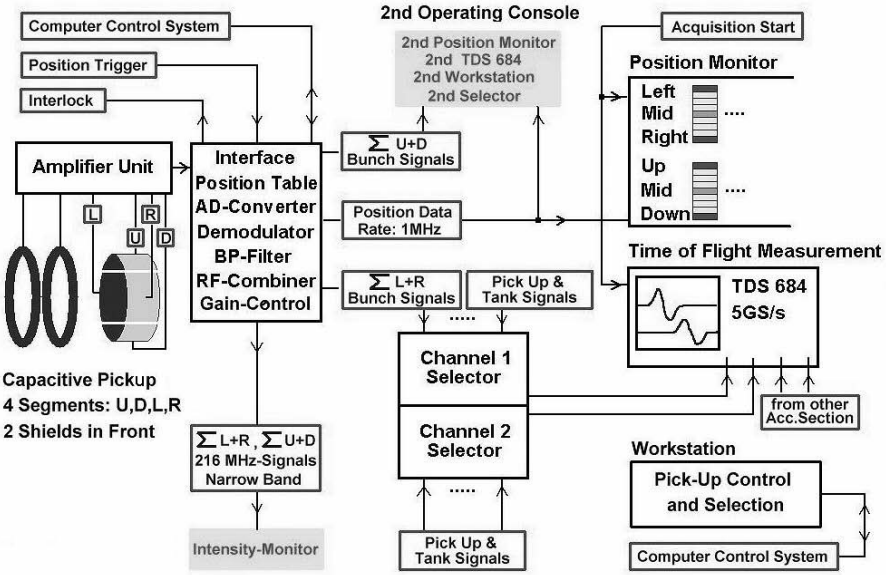

Fig. 5.25. Scheme of the signal processing [40] for capacitive pickups shown in Figure 5.23. (Taken from Forck, P., Peters, A., Strehl, P., AIP Conference Proceedings 546, (2000), p. 606. With permission)

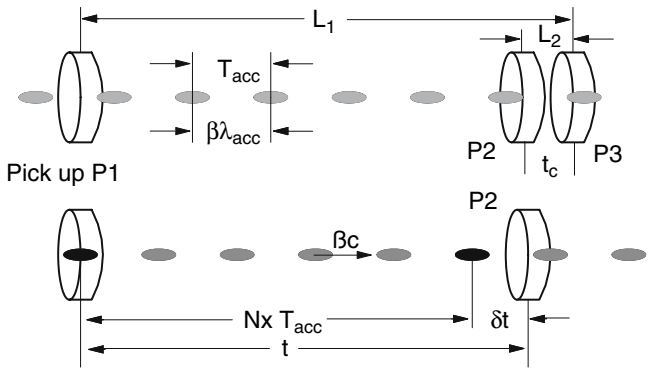

Fig. 5.26. Arrangement of capacitive pickups to perform time of flight measurements. See text for details

second to determine the time of flight $t = NT_{\mathrm{acc}+\delta t}$. Similar systems have been installed in the experimental lines of the Super-HILAC (LBL) [257].

If the beam energy is known within certain limits, the arrangement shown at the bottom of Fig. 5.26 can be used. Only one measurement is required in this case. In both schemes, the precision in the time of flight measurement is increased considerably by taking advantage of the high accuracy and stability of the accelerating rf period.

Table 5.1. Most important specifications of the capacitive pickups shown in Figure 5.23 [40]

Electrode length	20 mm
Aperture	50 mm
Number of electrodes	4
Insertion length	55 mm
Sealing	DN 100 CF
Impedance	50 Ω
Bandwidth	1 GHz
Processed signals	2 ×Σ, 2 ×Δ
Σ, broadband, 2×	L+R,U+D
Σ, narrowband, 216 MHz, 2×	L+R,U+D
Δ, digital from narrowband, 2×	L-R,U-D
Required charges/bunch holds for S:N = 1 and 1 mm displacement	2×10^7, (Δt =1 ns, β =1.6 %)
	4×10^6, (Δt =1 ns, β = 4 %)
	2.5×10^6, (Δt =1 ns, β = 5.5 %)
	2×10^6, (Δt = 0.5 ns, β = 5.5 %)
	3×10^6, (Δt =1.5 ns, β = 5.5 %)

Table 5.2. Most important specifications of the capacitive pickups shown in Figure 5.24 [33]

Aperture	12 mm
Shape of the electrodes	4 discs
Size of the discs	7 mm ∅
Impedance	50 Ω
Bandwidth	≈ 2 GHz
Σ-signal	≈ 20−40 pA / e
Δ-signal	≈ 3−5 pA / e·mm
Connectors	4 SMA-coax
Material of the housing	Copper
Insulation	Vespel

Scheme with Three Pickups

To determine the unknown number N of bunches between pickups $P1$ and $P2$, the time of flight is measured between $P2$ and $P3$. Obviously, the distance $P2$ and $P3$ has to fulfill the condition $L_2 < \beta\lambda_{\mathrm{acc}}$ to avoid ambiguity. After the time of flight t_{c} (see Fig. 5.26) has been measured, N has to be determined from

$$\beta_{\mathrm{c}} = \frac{1}{c}\frac{L_2}{t_{\mathrm{c}}} \tag{5.76}$$

$$N = INT\left(\frac{L_1}{\beta_{\mathrm{c}}\,\lambda_{\mathrm{acc}}}\right). \tag{5.77}$$

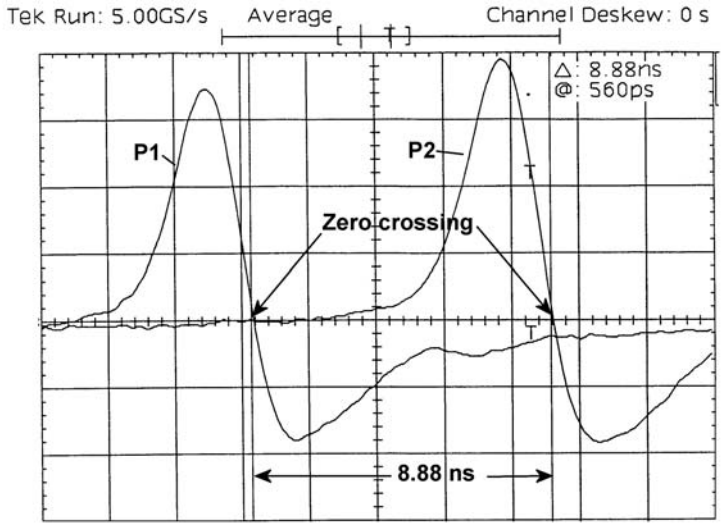

Fig. 5.27. Example for determination of t_c, t from the crossover points of both signals. Note: The asymmetry of the positive and negative parts of the signals is due to cable dispersion via more than 40 m and not the result of an asymmetric bunch. The picture was taken in the main control room of GSI

With the condition $\Delta N < 1$, the required accuracy in the determination of t_c can be estimated from the relation $N\,\Delta t_c\,/\,t_c < 1$. In the second step, the measurement of the time difference between the arrival of a bunch at pickup $P1$ and the first bunch in the chain arriving at $P2$ leads to δt and, finally to the time of flight $t = NT_{acc} + \delta t$ (see Fig. 5.26). With $\beta = L_1\,/\,ct$, the kinetic beam energy follows immediately from (relativistic)

$$W\ [\mathrm{MeV/u}] = m_0c^2\ [\mathrm{MeV/u}] \left(\frac{1}{\sqrt{1-\beta^2}} - 1 \right) \tag{5.78}$$

$$W\ [\mathrm{MeV/u}] = m_0c^2\ [\mathrm{MeV/u}]\,(\gamma - 1) \tag{5.79}$$

$$\gamma = \frac{1}{\sqrt{1-\beta^2}}\,. \tag{5.80}$$

Because the signal, delivered from a pickup in 50-Ω geometry and broadband signal processing is proportional to the derivative of the density distribution within the bunch, a zero crossing of the signals occurs. Therefore, in most cases, determining t_c and t from the two crossover points will be more accurate than determining them from the two signal maxima. Figure 5.27 gives an example from a TOF measurement behind the IH2 section ($\approx 1.4\,\mathrm{MeV/u}$) of the UNILAC. To minimize errors due to different signal transmission times from the pickups to the measuring device (oscilloscope), the signal transmission systems via preamplifier, possibly coaxial relays, and long high quality

cables, must be trimmed to equal overall transmission times. Using a modern time domain reflectometer (TDR) or network analyzer, this is possible within a Δ of 10 ps.

Remark. Depending on the expected steps in energy due to different operating modes of an accelerator facility, a larger spacing $L_2 < n\beta\lambda_{\mathrm{acc}}$ $(n > 1)$ is a possible alternative for improving the accuracy of N determination.

Scheme with Two Pickups

Beam energy may be known within certain limits from the setting of a deflecting magnet, from the status of the machine in the accelerator sections involved in the accelerating process, or even from the results of an experiment. In this case, coarse measurement can be omitted. Then, only two pickups are involved in the energy determination, which then corresponds to the second step of the procedure described above. Assuming an uncertainty in N as ± 1, the separation of the corresponding energies belonging to $N = N_0$, $N = N_0 + 1$, and $N = N_0 - 1$ can be estimated very roughly (nonrelativistic) from

$$\beta = \frac{L_1}{c\,(NT_{\mathrm{acc}} + \delta t)} \approx \frac{L_1}{c\,N\,T_{\mathrm{acc}}} \tag{5.81}$$

$$\frac{\Delta\beta}{\beta} \approx -\frac{\Delta N}{N} \approx -\frac{\Delta N}{L_1/\beta\lambda_{\mathrm{acc}}} = -\frac{\Delta N\,\beta\,\lambda_{\mathrm{acc}}}{L_1} \tag{5.82}$$

$$\frac{\Delta W}{W} = 2\frac{\Delta\beta}{\beta} \approx -\frac{2\,\beta\,\lambda_{\mathrm{acc}}}{L_1}, \quad \Delta N = 1\,. \tag{5.83}$$

Two Examples

The accelerator sections of the high current linac of GSI, one radio-frequency quadrupole RFQ section and two IH structures [258], have been commissioned, using a versatile test bench [259]. Time of flight measurements could be performed with two capacitive pickups separated by exactly $L_1 = (3249 \pm 0.5)$ mm. In a measurement, the IH_2 section was operated with a certain amplitude and rf phase setting. A δt of 8.88 ns, as shown in Fig. 5.27, was measured in this case. From the data shown in Table 5.3, presented to the operators, the decision about the correct energy, $W = 1.351$ MeV/u, was very clear, even considering that the set-values of the rf ($f_{\mathrm{acc}} = 36.136$ MHz) were not yet optimal with respect to the design value of 1.4 MeV/u.

The expected separation according to the rough estimation given in (5.83) for $N_0 = 7$ is $\Delta W/W = -2 \cdot 446.326/3249 = -27.5\%$; $\Delta W/W$ is figured out from the table to $(1.351 - 1.814)/1.351 = -34.3\%$, respectively, $(1.045 - 1.351)/1.351 = -22.6\%$.

In the second example, the output energy of the first prestripper section, the RFQ, has been measured dependent on the rf voltage. Due to the low design value of 120 keV/u, the spacing between the bunches is only about 133 mm, and, therefore the separation of energies belonging to $N, N \pm 1$ is

Table 5.3. Calculated beam energy dependent on N. The correct energy is given with $N = 7$.

N	t [ns]	β [%]	$\beta\lambda_{\mathrm{acc}}$ [mm]	W [MeV/u]
5	147.246	7.402	614.089	2.562
6	174.919	6.231	516.937	1.814
7	**202.593**	**5.38**	**446.326**	**1.351**
8	230.266	4.733	392.686	1.045
9	257.939	4.225	350.557	0.833

rather small. Nevertheless, as shown in Fig. 5.28, even changes of more than 30% in the rf amplitude did not result in crossovers of the three lines with $N = 23, 24$, and 25.

5.3.2 Achievable Accuracy

The accuracy of a TOF measurement can be estimated for not to high β-values from the well-known nonrelativistic relation

$$W = \frac{m}{2}v^2 = \frac{m}{2}\left(\frac{L}{t}\right)^2 \quad \rightarrow \tag{5.84}$$

$$\left|\frac{\Delta W}{W}\right| = 2\left|\frac{\Delta L}{L}\right| + 2\left|\frac{\Delta(\delta t)}{NT_{\mathrm{acc}} + \delta t}\right| , \tag{5.85}$$

which, of course is the worst case estimation. This can be compared with the quadratic error addition, leading to

$$\frac{\Delta W}{W} = 2\sqrt{\left(\frac{\Delta L}{L}\right)^2 + \left[\frac{\Delta(\delta t)}{NT_{\mathrm{acc}} + \delta t}\right]^2} . \tag{5.86}$$

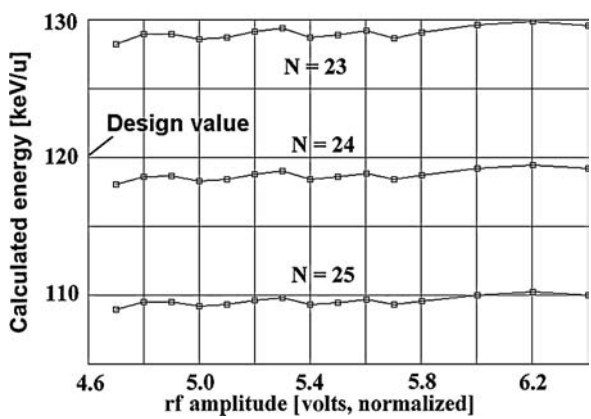

Fig. 5.28. Measured energy (TOF) of the RFQ (UNILAC) dependent on the rf amplitude [259]. The parameter is the assumed number of bunches N between the pickups of the test bench

Due to the dependencies on accelerator characteristics and on the spacing between the pickups, and the accuracy of time measurements, the achievable accuracy has to be considered in each case separately. In practice, $\Delta W/W$ is of the order of $1-5 \times 10^{-3}$.

5.3.3 Determination of Distances by TOF

Applying the time of flight technique, the distances between two pickups can be determined precisely, if the energy of the particles, respectively, their β values and the rf wavelengths are known. Supposing that the distance L is known with an uncertainty $< \beta\lambda_{\mathrm{acc}}$, then L follows from a measurement of δt according to Fig. 5.26:

$$L = N\beta\lambda_{\mathrm{acc}} + \Delta L \tag{5.87}$$

$$\Delta L = \frac{\delta t}{T_{\mathrm{acc}}}\beta\lambda_{\mathrm{acc}} \; . \tag{5.88}$$

This method is advantageous, if a direct precise determination of L is not possible. A typical constellation is given, if one of the pickups is installed directly in front of a large accelerator section, and the second one is located behind it.

5.3.4 Fine-Tuning of Beam Energy

Let us assume that after an energy determination by TOF, a small, but very precise change in energy ΔW is required. Supposing that a single gap resonator or a buncher is located upstream of the TOF arrangement, fine-tuning of the energy can be performed with the following steps:

- Adjusting the phase of the rf to $\varphi_{\mathrm{s}} = -90°$. This can be easily realized by monitoring the bunch signal on an oscilloscope, while the rf on the single gap resonator or buncher is switched from ON to OFF and vice versa. Because $\varphi_{\mathrm{s}} = -90°$ corresponds to the zero crossing of the rf sine wave (phase convention in accelerator physics), the bunch signal does not shift in time if the phase is correctly adjusted to $-90°$.
- Replacing the nonrelativistic (5.84) by the relativistic one leads to the relation between $\Delta W/W$ and $\Delta\beta/\beta$:

$$\frac{\Delta W}{W} = (\gamma + 1)\,\gamma\frac{\Delta\beta}{\beta} \; . \tag{5.89}$$

  Assuming $\gamma = \mathrm{const}$ for small changes of $\Delta W/W$, the change in the time of flight Δt is given by

$$\Delta t = -\frac{1}{\gamma(\gamma+1)}\frac{\Delta W}{W}\frac{L_0}{\beta\, c} \; , \tag{5.90}$$

  with L_0 as the spacing between the rf cavity and the capacitive pickup.

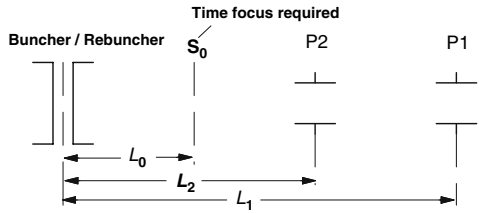

Fig. 5.29. Setup to optimize a rebuncher. See text for details

- Now the shift in the arrival time according to (5.90) can be observed on the oscilloscope, changing the phase of the rf to acceleration or deceleration and adjusting the rf amplitude.

Example 3. $L_0 = 50\,\mathrm{m}$, $\beta = 0.5 \rightarrow W = 144.104\,\mathrm{MeV/u} \rightarrow \gamma = 1.155$

$\Delta W = +100\,\mathrm{keV/u} \rightarrow \Delta W/W = 6.94 \times 10^{-4} \rightarrow \Delta t = -93\,\mathrm{ps}$.

5.3.5 Optimization of Bunchers

Due to the energy spread of particles within a bunch, the bunch width Δt increases continuously in a drift space behind a waist. Most rf accelerators use bunchers, rebunchers and, in some cases debunchers to shape the density distribution in the longitudinal phase plane. In practice, mostly the generation of a focus at a given location is required. The correct set-values of the corresponding buncher or rebuncher can be easily determined from a measurement of the bunch width at two capacitive pickups located downstream of the buncher/rebuncher. For an arrangement as shown in Fig. 5.29, the procedure is as follows:

- In the first step, a time focus is generated at pickup P1 by varying the rf amplitude of the buncher/rebuncher. Let the corresponding rf amplitude be U_1.
- The second step with the time focus at P2 leads to the set-value U_2 with $U_2 > U_1$, assuming a divergent beam at the buncher/rebuncher location.
- Then the correct set-value U_0 to produce the focus at location S_0 is given by

$$U_0 = (1 - Q)U_2 + Q\,U_1 \tag{5.91}$$

$$Q = \frac{(L_0 - L_2)\,L_1}{(L_1 - L_2)L_0}\,. \tag{5.92}$$

The time focus can be detected on an oscilloscope in the time domain or more sensitively in the Fourier spectrum of the bunch signal, as illustrated in Fig. 5.30. Since the bunch width itself is not relevant for this optimizing procedure, the determination of the time focus by the Fourier spectrum should be preferred.

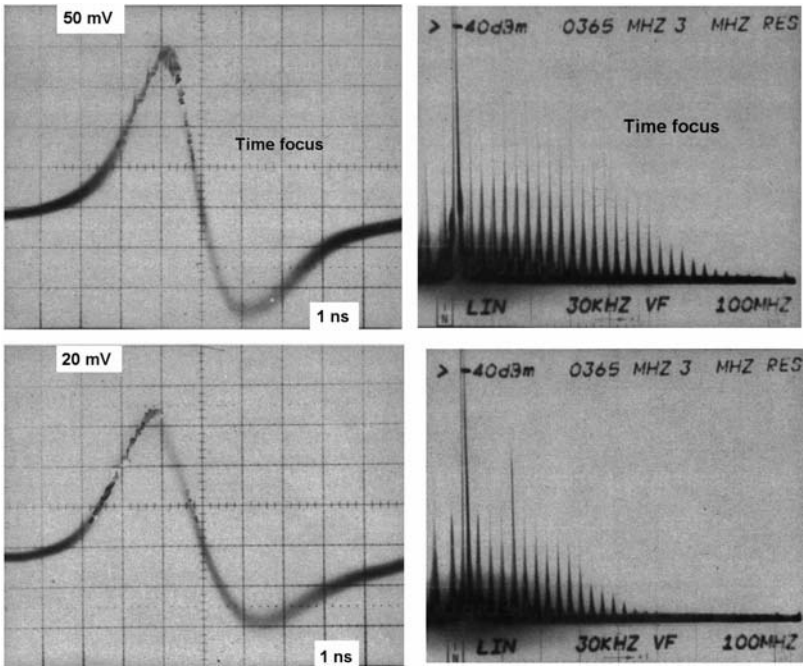

Fig. 5.30. Detection of a time focus at a capacitive pickup by observing the signals in the time domain as well as in the frequency domain using a spectrum analyzer. The pictures are taken in the main control room of GSI

5.3.6 Stopping Power Measurements

The TOF technique can be used to determine energy losses in thin targets [260]. This method has higher accuracy than measurements with semiconductor detectors and is free from the pulse height defect of these detectors. Figure 5.31 shows a typical setup with two capacitive pickups, which can be supplemented by a third pickup if there is an uncertainty in the number of bunches between P1 and P2. The relevant formulas are already discussed in Sect. 5.3.1. In the example of Fig. 5.31, the stopping power has been measured dependent on particle energy, taking various accelerator sections in front of the target successively in operation. This leads to a change of the mean charge state of the particles due to stripping in the dE/dx target. Therefore, different settings for the focusing quadrupoles between the two pickups would be necessary for the unattenuated and attenuated beams, which can change the path length between the two pickups. To avoid this effect, a thin charge-exchange foil was installed permanently in front of the target. The counting rate was adjusted by the rate divider (RD) to the maximum ratings of the time to amplitude converter (TAC) and multichannel analyzer (MCA) boards in the PCI system. Evaluation of the time of flight spectra by fitting Gaussians to

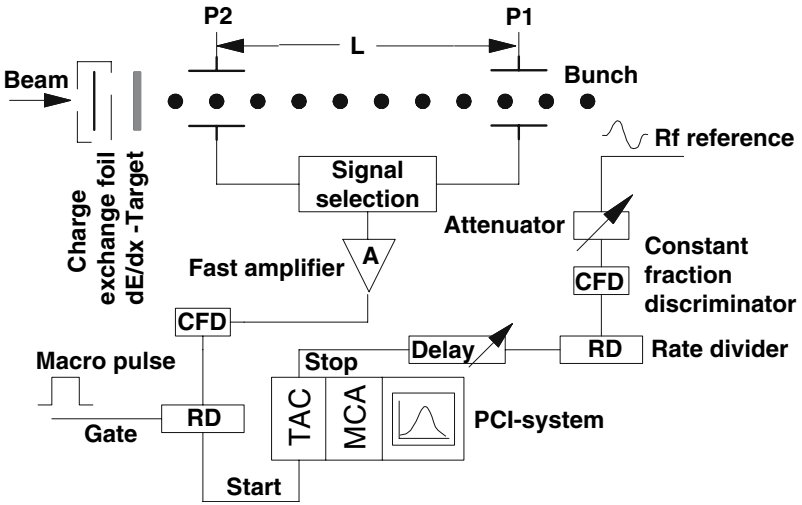

Fig. 5.31. Scheme for precise stopping power determination taking advantage of the TOF technique

the measured data can reduce the error in $\Delta(\delta t)$ [see (5.85) and (5.86)] to about 10 ps, which leads to very precise determination of the energy loss in the target. The main contribution to the error estimation may come from the determination of the target thickness. Results for a series of dE/dx values with Kr-projectiles and various targets, obtained with this method and reported in [260], show excellent agreement with data published by other authors. The method can also be applied to determine energy loss and energy straggling very precisely in gas- and foil-strippers.

5.3.7 Determination of the Correct Injection Energy and Prebuncher Settings

Figure 5.32 shows a practical injection scheme, consisting of two prebunchers in front of a capacitive pickup and the first accelerator section of a rf accelerator. During routine operation or changes of the injector scheme in the commissioning phase of a new machine, precise determination of the injection energy, as well as the correct phase setting of the prebunchers becomes essential. Taking advantage of the TOF technique, this problem can be solved easily by a skilled operator performing the following steps:

- In a first step, the rf phase of both prebunchers is set to exactly the same value, which is normally done by rf experts.
- Supposing that the potential of the ion source terminal, respectively, the gap-voltage of the first accelerating gap behind the ion source is settled to nearly the correct values, the integral and nonintegral part of bunches N (N_i, n) between PB1 and PB2 are known from

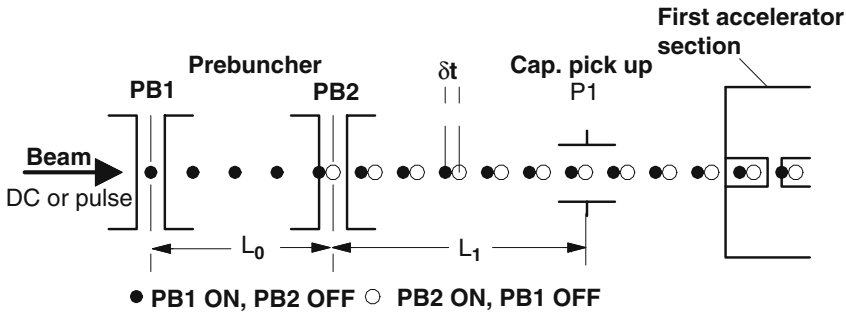

Fig. 5.32. Typical layout in the injection area of a rf accelerator

$$N_{\mathrm{i}} = INT\left(\frac{L_0}{\beta\,\lambda}\right) \tag{5.93}$$

$$n = \frac{L_0}{\beta\,\lambda} - N_{\mathrm{i}}\,, \tag{5.94}$$

with λ as the wavelength of the rf.

- Therefore, the arrival time of bunches with PB1=ON, PB2=OFF and PB1=OFF, PB2=ON differs with a time difference

$$\Delta t = nT\,, \tag{5.95}$$

where T is the period of the rf. This can be detected and adjusted very easily – by change of the gap-voltage – observing Δt with the capacitive pickup P1. Due to relatively low energies in the injection areas, in general, $\beta\lambda$ will be small and, therefore the accuracy, which can be achieved is high, even for moderate spacing between PB1 and PB2. The error in energy can be estimated from

$$\frac{\Delta W}{W} \simeq 2\frac{\delta\Delta t}{N_{\mathrm{i}}T_{\mathrm{acc}} + \Delta t}\,, \tag{5.96}$$

neglecting an error in the spacing PB1–PB2.

- The next step concerns the correct phase setting of PB1 and PB2. Because the ion source is operated either in the dc-mode or in a macropulse mode, the phase of PB1 is irrelevant and only the phase of PB2 has to be adjusted for optimal action of both prebunchers. Obviously, the required change is determined from

$$\varphi(\mathrm{PB2}) = \varphi(\mathrm{PB1}) + \Delta\varphi \tag{5.97}$$

$$\Delta\varphi = \frac{\Delta t}{T}360^{\circ}\,. \tag{5.98}$$

- The correct setting can be controlled by observing the bunch signals at P1. No shift of the bunch signals should be observed if both prebunchers are switched ON, one after the other.

Example 4. $L_0 = 1074\,\text{mm}$, which has been determined and fixed very precisely by a massive stainless steel rod between the two prebunchers in the injection area of the UNILAC-injector section. The accelerator frequency $f = 27.1015\,\text{MHz}$ gives $T = 36.8983\,\text{ns}$ and $\lambda = 11061\,\text{mm}$. A required β value of $\beta = 0.005$ leads to $N_\text{i} = 19, n = 0.4196$, and $\Delta t = 15.48\,\text{ns} \rightarrow \Delta\varphi = 151°$. The achievable accuracy in $\Delta W/W$ is about 0.028%, assuming a $\delta\Delta t$ of 100 ps.

Remark. The scheme shown in Fig. 5.32 can be used to detect wrong masses, after correctly setting U for a certain ion species. In this application, one takes advantage of the nonrelativistic relation

$$\frac{m}{2}v^2 = \zeta eU \rightarrow \tag{5.99}$$

$$\frac{\Delta m}{m} + 2\frac{\Delta L}{L} - 2\frac{\Delta t}{t} = 0 \quad \text{because } U = \text{const} \tag{5.100}$$

$$\frac{\Delta m}{m} = 2\frac{\Delta t}{t}\,, \tag{5.101}$$

again neglecting the error ΔL. Evidently, the highest accuracy can be achieved by switching PB1 ON, PB2 OFF and with $L = L_0 + L_1$ as the drift space of the bunches, formed by the action of PB1. For the example, one gets high resolution with

$$\Delta t\ [\text{ns}] \simeq 772\frac{\Delta m}{m}\,. \tag{5.102}$$

5.3.8 Estimation of Bunch Lengths

Due to the advanced field of the moving bunches and the integration over the probe length as well as a possible limitation of the oscilloscope, direct determination of the bunch width is not possible. On the other hand, it is useful to estimate the bunch width very quickly and non-destructively from a displayed pickup signal. Taking advantage of the algorithm for numerical signal calculation (see Sect. 5.2.6), a relation between the bunch width Δt (FWHM) and the time between signal maximum and signal minimum Δk can be calculated for a given β and known pickup dimensions. Figure 5.33 shows a numerical calculation for a pickup with $L = 10\,\text{mm}$, $R = 17.5\,\text{mm}$, $\beta = 0.055$ and a $\cos^2$-like bunch shape. Neglecting the final bandwidth of the oscilloscope, the measured $\Delta k = 1.6\,\text{ns}$ ($= 2 \cdot 0.8\,\text{ns}$; see Fig. 5.33) leads to a bunch width $\Delta t = 1.36\,\text{ns}$.

The diagram in Fig. 5.33 also shows the limits very clearly. No Δk value exists below a certain value on the abscissa, which, of course, is a consequence of integration over the length of the pickup. The asymptotic value for $\Delta t = 0$ (single particle) tends toward $\Delta k \approx 2L/\beta c$ for low β values caused by the advanced field. For higher β values, $\Delta k \rightarrow L\,/\,\beta c$. The broadening of the signal, caused by the advanced field and the integration also becomes very clear from the Fourier spectrum of the original $\cos^2$ distribution and the convoluted one. Figure 5.34 shows a comparison of the Fourier spectra.

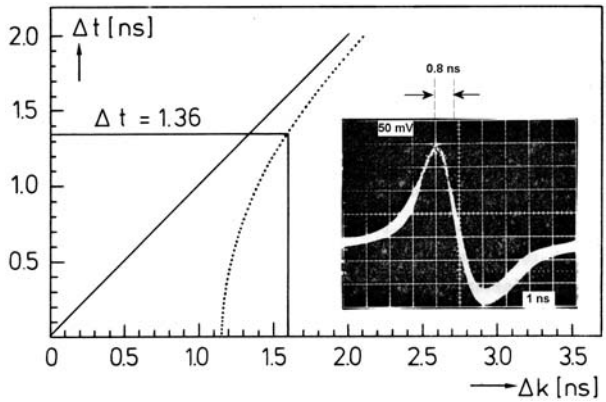

Fig. 5.33. Left: Numerical calculated relation between bunch width Δt (FWHM) and the measured time diference between the signal maximum and signal minimum Δk. Right: Measured signal. Note: Due to cable dispersion, determining Δk from the time difference between the positive maximum and zero crossing is recommended

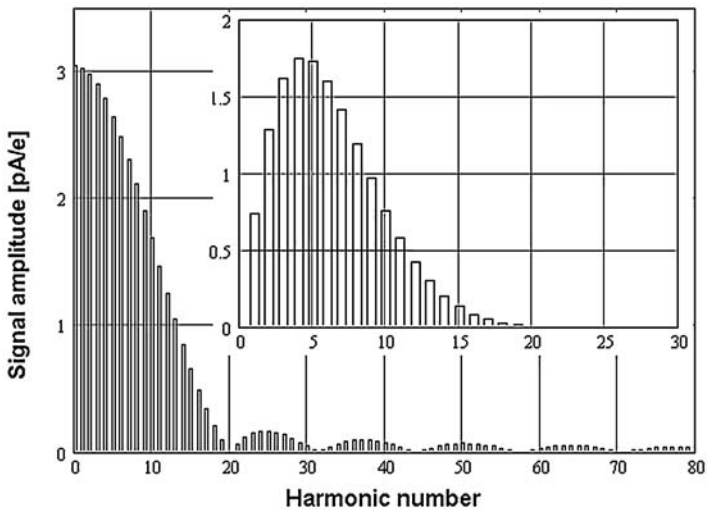

Fig. 5.34. Fourier spectrum of a $\cos^2$ distribution with width $\Delta t = 1.36\,\text{ns}$ (FWHM) and a repetition frequency of 36 MHz. Inset: Fourier spectrum of the bunch signal after passing a capacitive pickup with $L = 10\,\text{mm}$, $R = 17.5\,\text{mm}$, and a β value of 0.055

In accelerator laboratories around the world, a great variety of devices for bunch length determination with better accuracy have been developed [261–268]. Nevertheless, non-destructive bunch length monitoring with a capacitive pickup is a very useful tool during routine operation of rf accelerators.

5.3.9 Monitoring of Low Beam Currents

Non-destructive absolute beam intensity measurement and monitoring of pulsed beams with beam transformers goes down to some microamperes, as discussed in Chap. 2, Sect. 2.3. But, in many applications, only a surveillance of the beam current with respect to a reference value or observation of the beam current constancy over time is required. For this application, the absolute value of the beam current is not of great relevance and, therefore the non-destructive bunch signals from capacitive pickups can be used. Furthermore, for dc-beams with rf structure, non-destructive beam current monitoring based on capacitive pickups will be very sensitive and much cheaper than the installation of dc-beam current transformers. There are two methods for processing the pickup signals for this application:

- Broadband amplification of the original fast bunch signals. Splitting the amplified output signals into two branches: One of them can be used to observe the bunch structure, the other one is fed on a bandpass filter, tuned to a harmonic of the accelerating rf. Further narrowband amplification and demodulation of the resulting rf signal delivers the envelope of the bunches. The signal-to-noise ratio, which can be achieved by this method, is determined by the relatively high input noise of the first broadband stage.
- To improve the signal-to-noise ratio, one may give up the bunch shape observation. Then the first amplifier stage can be tuned to a harmonic and the signal-to-noise ratio is determined by the first narrowband amplifier stage. Although the amplitude of the harmonic is lower than the maximum amplitude of the signal itself, a net gain in sensitivity can result, depending on the bandwidth and the amplitude of the harmonic selected.

Example 5. Taking the analog signal of Fig. 5.12 and the corresponding Fourier spectrum of Fig. 5.17, the relevant parameters are summarized in Table 5.4 for a pulsed beam with a repetition frequency of 50 Hz and a duty cycle of 10%. For narrowband signal processing, a bandwidth of 10 kHz is assumed, which responds in a time constant of about 100 µs. Depending on the application, this may be further reduced. The data, for a signal-to-noise ratio of 5, demonstrate clearly, that this method of non-destructive beam current surveillance competes very well with beam current transformers if the absolute values are not relevant.

Figure 5.35 shows the signal, generated from the demodulation of the first harmonic of the bunch chain. The signal marked “rf envelope” in Fig. 5.35 is a distortion from the accelerating rf. Because the first harmonic of the bunch signal corresponds just to the accelerating rf, the bunch signal adds to the envelope. The electronics has been improved by

- demodulation of another harmonic (third),

Table 5.4. Comparison of demodulated bunch signals in broadband and narrowband signal processing, n is the harmonic number. See text for details.

Parameter	Broadband	Narrowband
β value	0.9	
Δt(FWHM)	1ns	
rf	36 MHz	
Bandwidth (1-stage)	500 MHz	10 kHz
Impedance	50 Ω	50 Ω
Noise voltage at the input	≈ 15 µV	≈ 67nV
Corresponds to	≈ 0.3 µA	1.35 nA
I_{max} (signal)	≈ 9 pA/e	≈ 0.14 pA/e ($n = 3$) ≈ 0.26 pA/e ($n = 6$)
Required $N\zeta$ (S:N = 5)	$\approx 1.7 \times 10^5$	$\approx 4.8 \times 10^4$ ($n = 3$) $\approx 2.6 \times 10^4$ ($n = 6$)
Bunch current with $N\zeta$	≈ 27 µA	≈ 7.7 µA ($n = 3$) ≈ 4.2 µA ($n = 6$)
Macropulse current with $N\zeta$	≈ 970 nA	≈ 277 nA ($n = 3$) ≈ 151 nA ($n = 6$)
Mean dc-current with $N\zeta$	≈ 97 nA	≈ 28 nA ≈ 15 nA

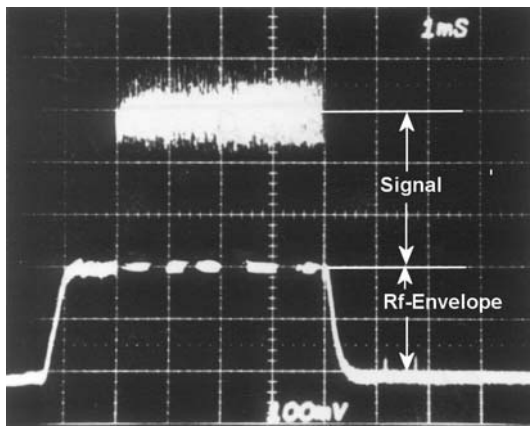

Fig. 5.35. Signal from an electronic-prototype based on demodulation of the first harmonic of the bunch signal. The signal corresponds to a macropulse current of 16 nA. See text for details

- use of tunnel diodes with a relatively high threshold voltage, and
- use of narrowband filters.

Nevertheless, the signal from the prototype demonstrates the sensitivity of the method.

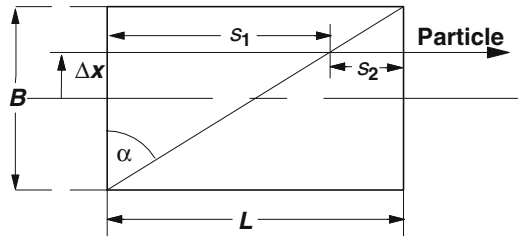

Fig. 5.36. Scheme to derive the position sensitivity of a "linear cut"

5.4 Beam Position Monitors (BPM) in Circular Machines

5.4.1 Basics

All kinds of capacitive pickups, discussed above, including variations in design and signal processing, can be used in circular machines. The beam position is determined from the difference of the influenced signals of opposite electrodes (see, e.g., Figs. 5.23 and 5.24). For electron machines with relatively short bunches, the most frequently used electrode systems are buttons [1, 269, 270], which can be arranged in various schemes around the beam. In most cases, such monitors have nonlinear transfer functions.

For machines with long bunches and relatively large apertures in the beam pipe, especially proton and heavy ion synchrotrons, position determination is based on the so-called linear cut. Figure 5.36 illustrates the principle. A single particle moving above the plate influences a signal proportional to the plate length at that position. Therefore, the signal difference between the left triangular part, and the right one is a linear function of the displacement Δx that is independent of the intensity distribution within a real beam. With $G = C_1 B\, L$ ($C_1 = \text{const.}$) as the sum signal, the ratio S between the difference signal D and the sum signal G is given by

$$S = \frac{D}{G} = \left(\frac{s_1}{s_1 + s_2} - \frac{s_2}{s_1 + s_2} \right) \tag{5.103}$$

$$s_1 + s_2 = L,\ \frac{s_1}{\frac{B}{2} + \Delta x} = \frac{L}{B} = \frac{s_2}{\frac{B}{2} - \Delta x} \rightarrow \tag{5.104}$$

$$S = \frac{2\,\Delta x}{B}\ . \tag{5.105}$$

Other linear cut configurations have been developed and discussed in the literature [1, 6, 271]. Some of them allow combination of the vertical and horizontal planes, but vertical and horizontal electrode sets should be separated to achieve good performance. If full separation is not possible due to spatial limitations, a guard ring should be provided between the two electrode sets.

When designing a BPM system, a question arises about the required precision in manufacturing and alignment. For manufacturing, let us assume the extreme case that the two triangular plates are machined with the dimensions $L_2 = L_1 - \epsilon$ and $B_2 = B_1 + \delta$. The beam position is determined from a measured S by $\Delta x = S\,B/2$ if $L_2 = L_1 = L$ and $B_2 = B_1 = B$. With the assumed differences in L and B, one obtains

$$\Delta x = \frac{SB}{2} \frac{1 + \frac{\epsilon}{2L}\left(\frac{1}{S} - 1\right)}{1 + \frac{\epsilon}{2L}(S-2) + \frac{\delta}{2B}(S-2)} \,. \tag{5.106}$$

Example 6. $B = 200\,\text{mm}, L = 120\,\text{mm}, \Delta x = 1\,\text{mm}$ gives $S = 0.01$ for the perfectly machined pickup. It is reasonable to assume $\epsilon = \delta = 0.1\,\text{mm}$, which leads with $S = 0.01$ to $\Delta x = 1.043\,\text{mm}$.

To estimate the required accuracy for alignment of the BPM, let us assume that the two plates are rotated by a small angle $\Delta\alpha$ around the center (see Fig. 5.36 for the definition of α). One gets

$$\tan\alpha = L/B \tag{5.107}$$

$$\tan(\alpha - \Delta\alpha) = (\tan\alpha - \tan\Delta\alpha)/(1 + \tan\alpha\tan\Delta\alpha) \tag{5.108}$$

$$\tan\Delta\alpha \approx \Delta\alpha \tag{5.109}$$

$$\Delta x = \frac{SB}{2} \frac{1 + \frac{L}{B}\Delta\alpha}{1 - \frac{B}{L}\Delta\alpha} \,. \tag{5.110}$$

For the example considered and $\Delta\alpha = 0.01745$ (1°), $\Delta x = 1.041$. Irreversible misalignments in the order discussed may also result from the bake-out procedure performed on BPMs.

5.4.2 Signal Calculation

In most circular machines, the bunch length $\beta c\Delta t$ is large in comparison to the length of the BPMs. This holds especially for heavy ion machines that accelerate heavy ions to maximum β values < 1. As a consequence of the longer bunches, the required bandwidth can be lower as mostly required for pickups in rf linacs, which in turn allows high impedance signal processing. To compare the expected signals for high and low impedance signal processing, we calculate the expected sum signal for one plate with the dimensions given in the example above. Furthermore, let us assume a distance $H = 35\,\text{mm}$ of the plate to the beam center, $\beta = 0.75$ ($\approx 500\,\text{MeV/u}$) and a bunch length of $\Delta t = 50\,\text{ns}$. The expected signal for a low impedance system, according to (5.41), assuming a $\cos^2$-like bunch shape, is shown in Fig. 5.37. On the other hand, the signal for a high load impedance can be estimated from (5.7), taking advantage of the approximation given in (5.14), which has to be changed to

$$u \approx \frac{Q_{\mathrm{bunch}}}{C}\, k\, \frac{L}{\beta c \Delta t}\, \frac{1/2}{1 + 2H/B + 2H/L}\ . \tag{5.111}$$

Assuming that $C = 100\,\mathrm{pF}$, $Q_{\mathrm{bunch}} = 1e$, and $k = 2$ leads to

$$u \approx 2\, \frac{1.6 \times 10^{-19}\mathrm{As}}{100 \times 10^{-12}\mathrm{As\,/V}}\, \frac{120\,\mathrm{mm}}{11240\,\mathrm{mm}}\, \frac{1/2}{1 + 0.35 + 0.58} \tag{5.112}$$

$$\approx 8.9\,\mathrm{pV/e}\ . \tag{5.113}$$

Equation (5.111) gives only a time independent, rough estimation for a bunch with square shape. To compare the time dependence of the signal for high load impedance with the low impedance case (see Fig. 5.37), we replace $k\, Q_{\mathrm{bunch}}\, L\,/\beta c \Delta t$ in (5.111) by

$$Q(t) = \frac{\int_{-\mathrm{TOF}}^{\mathrm{TOF}} \cos^2\left[\frac{\pi(x-t)}{2\Delta t}\right] dx}{\int_{-\Delta t}^{\Delta t} \cos^2\left[\frac{\pi t}{2\Delta t}\right] dt}\ , \tag{5.114}$$

with $\mathrm{TOF} = L/\beta c$ as the time of flight through the pickup. The factor k, introduced in the estimation of (5.111) has been considered here by performing the integration from $-\mathrm{TOF}$ to $+\,\mathrm{TOF}$ instead of from $-\mathrm{TOF}/2$ to $+\,\mathrm{TOF}/2$. Equation (5.114) is an estimation of the part within the pickup. The integral in the denominator of (5.114) is the normalization and leads just to Δt. With this replacement of Q_{bunch} by $Q(t)$, the time-dependent signal comes out as

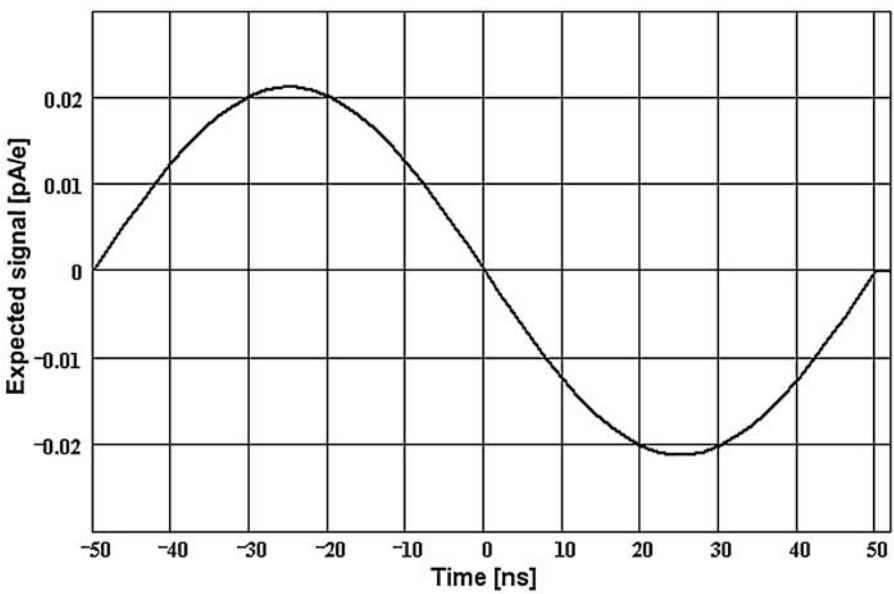

Fig. 5.37. Calculated signal for one plate with $L = 120\,\mathrm{mm}$, $B = 200\,\mathrm{mm}$, $H = 35\,\mathrm{mm}$, $\beta = 0.75$, $\Delta t = 50\,\mathrm{ns}$ (FWHM), assuming a $\cos^2$-like bunch shape and low impedance signal processing

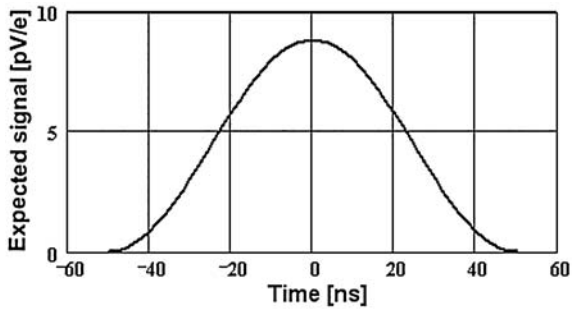

Fig. 5.38. Calculated signal for one plate with $L = 120\,\text{mm}$, $B = 200\,\text{mm}$, $H = 35\,\text{mm}$, $\beta = 0.75$, $\Delta t = 50\,\text{ns}$ (FWHM), assuming a $\cos^2$-like bunch shape and high impedance (1-MΩ) signal processing

$$u(t) = \frac{Q(t)}{C} \frac{1/2}{1 + 2H/B + 2H/L} \,. \tag{5.115}$$

Figure 5.38 is a display of the expected signal according to (5.114) and (5.115). The maximum of the signal in Fig. 5.38 shows good agreement with the estimation given in (5.113). Assuming a 50-Ω load in the low impedance system, one obtains from Fig. 5.37 a voltage of about $0.02\,\text{pA/e}{\cdot}50\,\text{V/A} = 1\text{pV/e}$, which has to be compared with about $9\,\text{pV/e}$ for high load impedance.

5.4.3 Calibration of BPMs

To maximize the signal, the proportionality of $u(t)$ to $1/C$ for high impedance systems requires minimizing the capacity . Because the capacity of the cables between the pickup and the head amplifiers adds to C, the front-end electronics has to be located as near as possible to the pickups. This may be require careful shielding against irradiation by lost particles or γ-rays. Furthermore, to avoid systematic errors in position measurements, the capacity of each plate has to be measured very precisely and considered in the calibration constant k, introduced in the equation for the determination of beam position P of the type of $P = k \times (U_\text{A} - U_\text{B})/(U_\text{A} + U_\text{B})$. Some BPM designs also allow fine-tuning of the capacities. Independent from the mode of signal processing, in general, the required measurement accuracy will be high, which in turn may demand a reliable test setup. A versatile and solid construction [272], provided for the calibration of at least 28 BPMs for the SIS and the experimental storage ring (ESR), is shown in Fig. 5.39. The main parts are two granite blocks and a cross sliding carriage with a stroke of $30 \times 30\,\text{cm}$, driven by two stepping motors. The carriage supports a framework with a 0.2 mm diameter wire stretched vertically in its center. The pulling force on the wire is nominally 20 N but can be varied from 0–30 N. The BPM under test is mounted in a fixed position on a support bolted to the upright granite block.

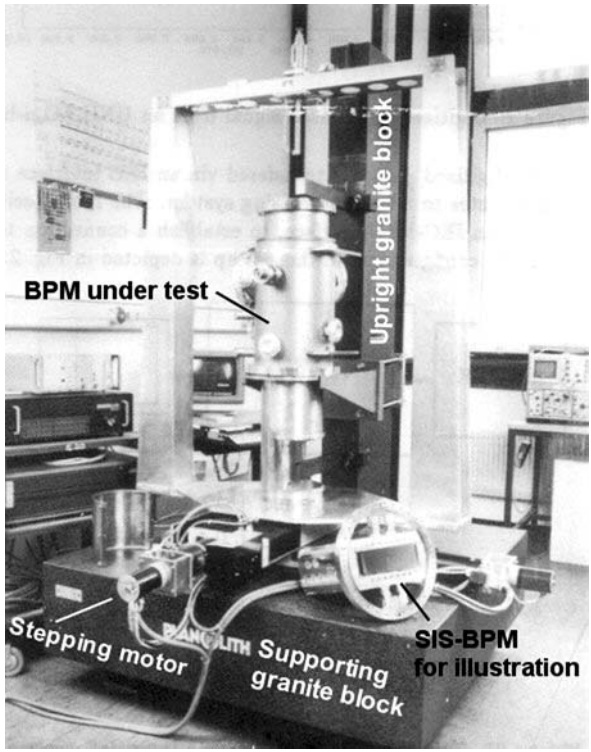

Fig. 5.39. Test set-up for the calibration of beam position monitors. GSI Foto

The wire is fed through the BPM and moved by the sliding carriage in a programmed pattern inside the aperture. Two absolute angular encoders give a resolution of ± 0.01 mm, and the overall accuracy is 0.03 mm for each axis. To avoid framework tilting, a "top centered" check is provided at the top of the frame using magnetic sensors with an accuracy better than ± 0.05 mm. The wire, isolated from ground at the top end by a rigid glass fiber rod, is fed with a rf signal of 10V rms at 2 MHz. Control of the stepping motors according to the programmed pattern for data collection, data storage, evaluation of the data, and their display are computer controlled. Of course, fine-tuning of the capacitances has to be done before the calibration measurement, using a capacity measuring bridge with a resolution of the order of 1 pF.

5.4.4 Signal Processing

The mathematical procedures discussed for calculating expected signals, including approximations for rough signal estimations, hold for all kind of capacitive BPMs. However, there are various demands on the overall performance of a BPM system for signal processing and signal evaluation. A very

detailed comparison of signal processing systems is given in [273]. It includes a schematic representation of the different families of systems as well as a description of the operating principles for many implemented systems. Focusing the attention on heavy ion synchrotrons, one has to take the following additional facts into account:

- Heavy ion synchrotrons differ from e-and p-machines with respect to the relation between accelerating frequency and particle velocity. For light particles such as electrons or protons, $\beta \simeq 1$ is mostly achieved after some turns (or are even injected with $\beta \simeq 1$). As a consequence, the accelerating frequency remains constant over nearly the whole acceleration cycle. On the other hand, for heavy ion synchrotrons, the relativistic mass increase has to be taken into account over the whole accelerating process, leading to a rather complex relation between revolution time and correct rf.
- The great variety of the charge ζ of accelerated ions $1 \leq \zeta \leq 92$, as well as the strong change in bunch length during acceleration, require an extremely high dynamic range for the amplifier systems. In the SIS, the total dynamic range for broadband signal processing covers 140 dB (−80 dBm to +60 dBm, [274, 275]).

5.4.5 Broadband Signal Processing

Monitoring single bunches, turn-by-turn, in a heavy ion synchrotron requires broadband signal processing. In most cases, a bandwidth up to about 100 MHz will be sufficient; it can be achieved with a load of up to 1 MΩ. Therefore, the expected signals can be calculated from (5.114) and (5.115). Using modern broadband amplifiers, the input noise voltage for a bandwidth of 100 MHz is of the order of some 10 μV. To reduce noise, the front-end electronics should be gated in coincidence with the bunch signal. Due to the change in particle velocity and the bunch shrinking process of the bunch length during acceleration, the generation of gate pulses requires rather complex electronics, which may be realized by

- use of programmable counters, deriving the clock frequency from the rf acceleration;
- use of shift registers arranged in a ring counter and shifting the bits with a rf-related clock;
- setting up a fast RAM-table, whereby addressing is performed also by a rf-related clock frequency, and
- use of modern DSPs.

Figure 5.40 shows a simplified scheme of gate pulse generation, which can be used additionally to derive trigger signals for the kickers. In the SIS, operating normally on the fourth harmonic of the revolution frequency, there are four bunches in the machine, shown in the inset at the top right of Fig. 5.40. The gate generator allows selection of one or two bunches, caused by the limited length of the kicker pulses. The implementation of such a timing system

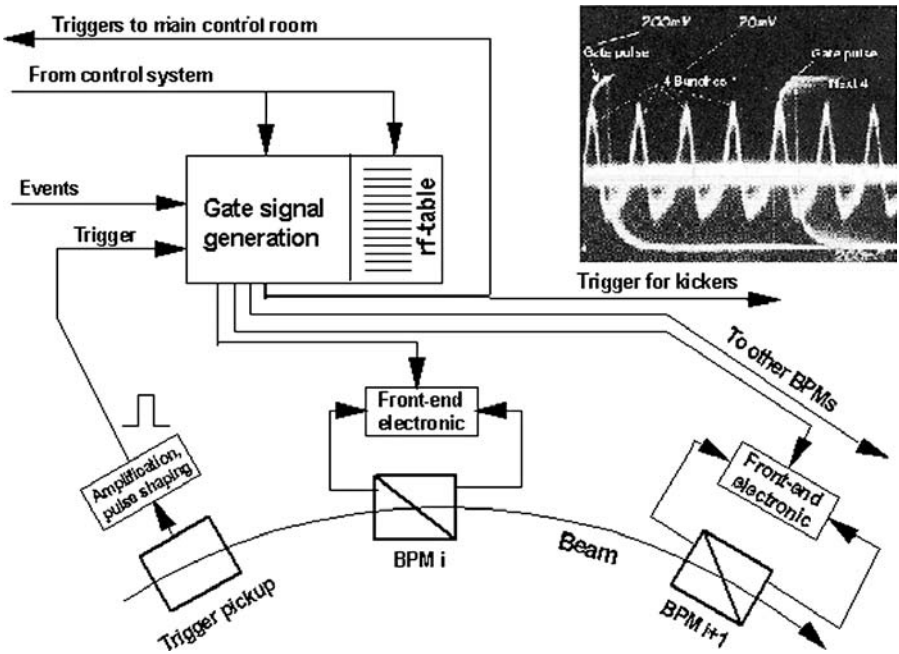

Fig. 5.40. Scheme of gate pulse generation for BPM electronics. The inset at top right shows a typical sum signal from a BPM, measured from a 30 µA Bi-beam at the end of acceleration in the SIS to about 200 MeV/u. The picture was taken in the main control room of GSI

requires additionally exact determination of all cable lengths and consideration of all signal transmission times in programming the timing system. To realize the scheme shown in Fig. 5.40, the following specific times have to be considered:

- Time of flight of the particles from the trigger probe to the selected pickup numbered i;
- time for the transmission of the pickup signals through the cables;
- transmission time of the signal from the trigger probe to the gate generator;
- transmission time for the gate pulse from the gate generator to the point of coincidence;
- delay times within the electronics;
- dynamic change of the bunch length; and
- advance of the gate pulse, changing during acceleration, too.

Of course, a BPM system with broadband signal processing allowing turn-by-turn measurements is not limited to orbit and trajectory measurement but can give information about betatron and synchrotron oscillations, tune, transfer functions, and many other static and dynamic beam parameters. Further-

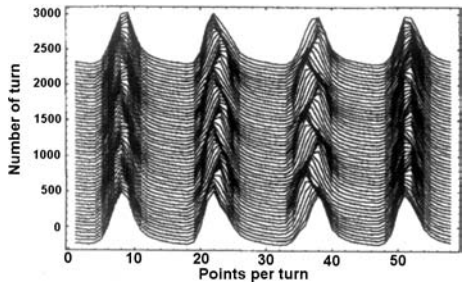

Fig. 5.41. Bunch oscillations observed [9] at the flattop of the SIS with a broadband BPM signal processing system

more, BPMs arranged around a circular machine can be used for active beam correction, establishing a feedback loop to kicker systems (see, e.g., [276–278]).

Some Examples

Observation of Bunch Oscillations

The advantage of single bunch observation is demonstrated impressively in Fig. 5.41 showing bunch oscillations observed at the flattop of the SIS.

Closed Orbit and Beam Trajectory Measurements

- The ideal trajectory of particles in a circular machine coincides with the center of the focusing devices.
- Since the field is zero there, this idealized trajectory, the so-called closed orbit is solely determined by the bending magnets (dipoles).
- But imperfections, misalignment, stray fields and, as a consequence, arising betatron oscillations require a more realistic definition of the closed orbit.
- Therefore, the closed orbit is defined by the paths of the particles along the machine, taking all the unavoidable imperfections into account.
  The closed orbit can be measured by bunch synchronous monitoring of the beam position at various locations along the circular machine. In a broadband system, it is possible to measure the closed orbit for even one turn. Figure 5.42 shows a measurement performed in the horizontal plane of SIS, to control the efficiency of six horizontal correction coils [280]. Without corrections, the beam orbit shows oscillations with maximum amplitudes of about ± 15 mm. Three different settings for the correction magnets were gradually tested, leading to a reduction of oscillations to about ± 7 mm.

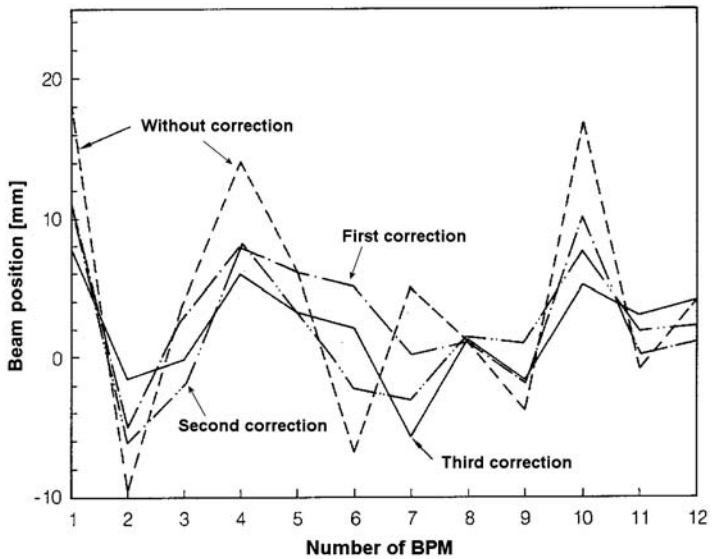

Fig. 5.42. Closed orbit measurements with various settings of six horizontal correction magnets [280]

Q-Value Determination in the Time Domain

A direct method for the determination of the tune Q is illustrated schematically in Fig. 5.43. A betatron oscillation with wavelength λ is excited by the Q kicker. Immediately after excitation, position measurements, synchronous with the kicked bunch, are performed at all N BPMs along the path of the particles. Assuming a suitable number of BPMs around the machine, the displacement y_i at a certain pickup with index i can be described by

$$y_\mathrm{i} = y_0 \sin\left[\frac{Q}{\overline{R}}(s_\mathrm{i} - s_0)\right] . \tag{5.116}$$

Now, a least squares fit can be applied to determine the unknown parameters $Q = 2\pi\overline{R}/\lambda$, y_0 and s_0. However, due to the complexity of the resulting equations, no analytical solution will be found. An alternative method to determine first the Q value and afterward to estimate y_0 and s_0 is based on the following procedure:

- Determination of the number of zero crossings, which means to find the couples of BPMs where the sign of the y signal changes from $+ \longleftrightarrow -$.
- Approximation of the zero crossings in the s-coordinate system by a straight line between the corresponding y-values. This leads to the locations of the zero crossings:

$$S(i, i+1) = \frac{y_{i+1}s_\mathrm{i} - y_\mathrm{i}s_{i+1}}{y_{i+1} - y_\mathrm{i}} . \tag{5.117}$$

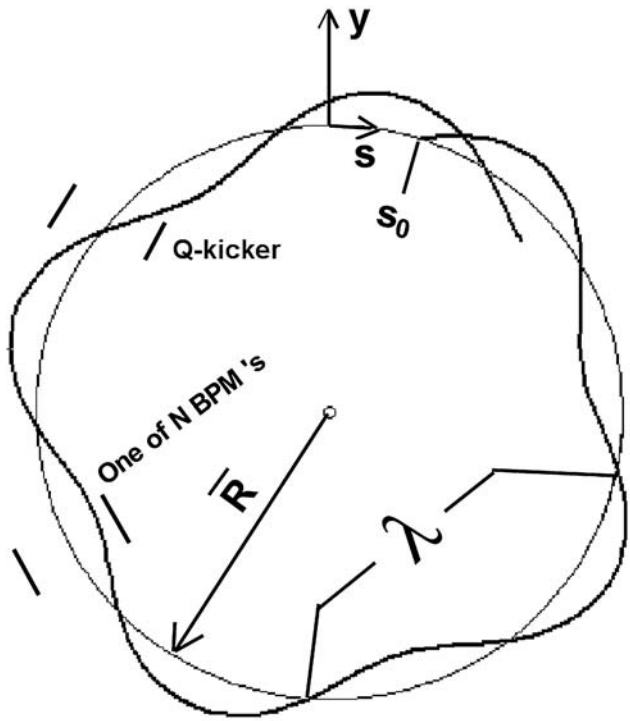

Fig. 5.43. Scheme to illustrate the Q-value determination by a kick and synchronous measurement of the beam position

- Determination of the Q value from the arithmetic average over all possible differences between two zero crossings. For a number of m zero crossings, $\binom{m}{2}$ combinations exist, determined by

$$S(i, i+1) - S(k, k+1) = \frac{(i-k)\,\pi\overline{R}}{Q}\ . \tag{5.118}$$

- After the Q value is determined, an approximation for s_0 can be obtained from the average of all zero crossings because $s_{01} = S(1,2)$, $s_{02} = S(2,3) - \pi\overline{R}Q$, $s_{03} = S(3,4) - \pi\overline{R}Q$, ...
- Then, with known Q and s_0, the amplitude of the excited betatron oscillation can be determined from a least squares fit or from the arithmetic average of the measured amplitudes.
  - From the least squares fit

$$\sum_{i=1}^{N} \left\{ y_{\mathrm{i}} - y_0 \sin\left[\frac{Q}{\overline{R}}\,(s_{\mathrm{i}} - s_0)\right]\right\}^2 = \mathrm{Min}\ , \tag{5.119}$$

    one obtains

Table 5.5. Maximum Q value which can be determined with a relative accuracy of 0.1% dependent on the number of BPMs installed. The data hold for a random error distribution of ± 15% for the positions measured

Number of BPMs	Qmax zero-crossing method	Qmax gradient procedure
8	2.8	3.3
12	4.0	5.6
16	6.2	7.0
20	7.0	7.0

$$y_0 = \frac{\sum_{i=1}^{N} y_\mathrm{i} \sin\left[\frac{Q}{\overline{R}}\left(s_\mathrm{i} - s_0\right)\right]}{\sum_{i=1}^{N} \sin^2\left[\frac{Q}{\overline{R}}\left(s_\mathrm{i} - s_0\right)\right]} \,. \tag{5.120}$$

– The arithmetic average is

$$y_0 = \frac{1}{N} \sum_{i=1}^{N} \frac{y_\mathrm{i} \sin\left[\frac{Q}{\overline{R}}\left(s_\mathrm{i} - s_0\right)\right]}{\sin^2\left[\frac{Q}{\overline{R}}\left(s_\mathrm{i} - s_0\right)\right]} \,. \tag{5.121}$$

The procedure described to determine the Q value can be used to estimate the minimum number of BPMs, which have to be installed in a machine to achieve a given accuracy in the determination of the Q value. This has been studied in the range $2.8 \leq Q \leq 7$ for $8, 12, 16$, and 20 BPMs considering a random distribution of errors for the measured positions y_i. An error of ±15% has been assumed in a program using the algorithms described above. Alternatively, an improved numerical fit procedure (gradient procedure) has been applied for comparison. Requiring an accuracy of 0.1% for $\Delta Q/Q$, the results are given in Table 5.5 [282].

Remark. The zero-crossing method is very simple and delivers acceptable values for unknown parameters, especially for Q values.

Q-Value Determination in the Frequency Domain

The coherent pickup signal, measured at a BPM after a kick, is damped as a consequence of the decoherence of the individual motion of particles, caused by the spread in the betatron frequency. The damping mechanism is described in the frame of Landau damping (see, e.g., [283, 284] and further literature given there). Nevertheless, applying a well-defined kick with a strength that the particles are not lost, results in damped oscillation, which endures several revolutions. Thus, a FFT (fast Fourier transform) can be performed on the measured data, taken from a single BPM. An example of excited oscillations in the SIS is shown in Fig. 5.44. Referring to (5.116) and keeping in mind that $s/\overline{R} = 2\pi s/2\pi\overline{R} = 2\pi t/T_0$, $2\pi/T_0 = \omega_0$, the time dependence of the signal at a certain pickup can be written as

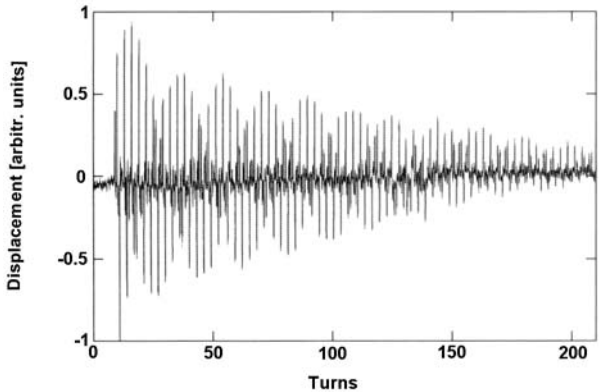

Fig. 5.44. Excited oscillations observed at one BPM in the SIS [120]

$$y(t) = y_0 \sin(Q\omega_0 t)\ \delta(t - nT_0) \tag{5.122}$$

with T_0 as the period for one revolution. In this simplified representation, the signal at the pickup is a pulse train. The frequency spectrum of such a signal is a series of harmonics with sidebands at $\pm q\, f_0$ given by $f_\mathrm{m} = f_0\ |m \pm q|$, where q is the nonintegral part of Q. Obviously, the FFT then gives the fractional part of Q and the width of the line gives the tune spread with $\Delta q = \Delta Q$. The total number of oscillations determined by Q cannot be seen by this method, but normally the integral part of Q is known from the machine setting. A drawback of the method is that the damping limits, the observation time, and the kick may blow up the transverse emittance.

Remark. The Q value, respectively, the nonintegral part q can also be determined from signals, as discussed in more detail in Chap. 7, Sect. 7.1.3. For (5.122), a more detailed mathematical description of the expected signals is given there.

Beam Transfer Function Measurements

An alternative method uses the measurement of the so-called beam transfer function (BTF). The method uses a beam excitation, driven by a continuous sine wave, generated by a network analyzer. The excitation is swept over a certain band and the response of the beam, the Δ/Σ signal from one BPM, is measured in coincidence with the excitation, feeding the signal into the network analyzer. Another BPM can be used as an exciter. A typical setup for Schottky and BTF measurements is shown in Fig. 7.36 (Chap. 7, Sect. 7.1.3).

As a result, amplitude and phase relative to the excitation are displayed, representing the transfer function. This gives the betatron frequency and the tune spread in units of the betatron frequency [285]. The results of a BTF measurement performed on a cooled beam in the experimental storage ring (ESR)

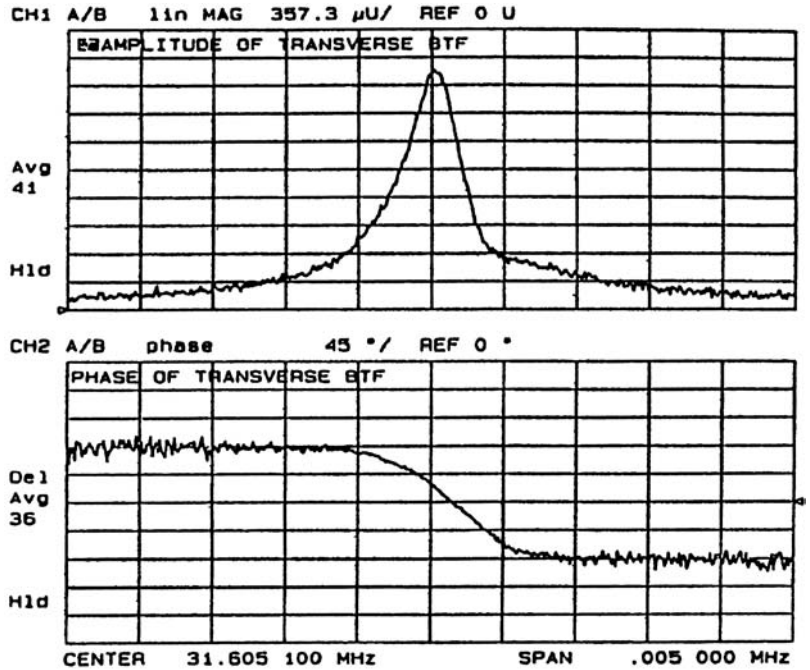

Fig. 5.45. Display of the results from a BTF measurement on a cooled ion beam in the ESR, recorded with a scan around the 22nd harmonic [120]. The amplitude is shown on top in a linear scale, the phase, shown on bottom, is scaled with 45°/div. Picture taken in the main control room of GSI

are displayed in Fig. 5.45. Applying this method, precision in the determination of Q of the order of 10^{-4} can be achieved. On the other hand, it takes some time because the frequency has to be swept slowly around f_0.

Q Measurement on the Ramp

With the broadband BPM, electronics of the SIS, sum and difference signals of each BPM are digitized with a fast ADC and stored in a 4 kRAM, which means 1 kRAM for sum and difference signals of the horizontal and vertical plate systems. In the so-called function mode, the 1 kRAM can be divided into N blocks with $1024/N$ data in each block. Because data acquisition is always related and synchronized to the revolution of one bunch, the stored data blocks represent measured values with very precise time stamps. Taking advantage of this feature, Fig. 5.46 shows a series of Q measurements on the ramp of the SIS, using the data from a single BPM. Every point in the plot represents the result of a discrete Fourier transform, with about 100 position measurements per data block.

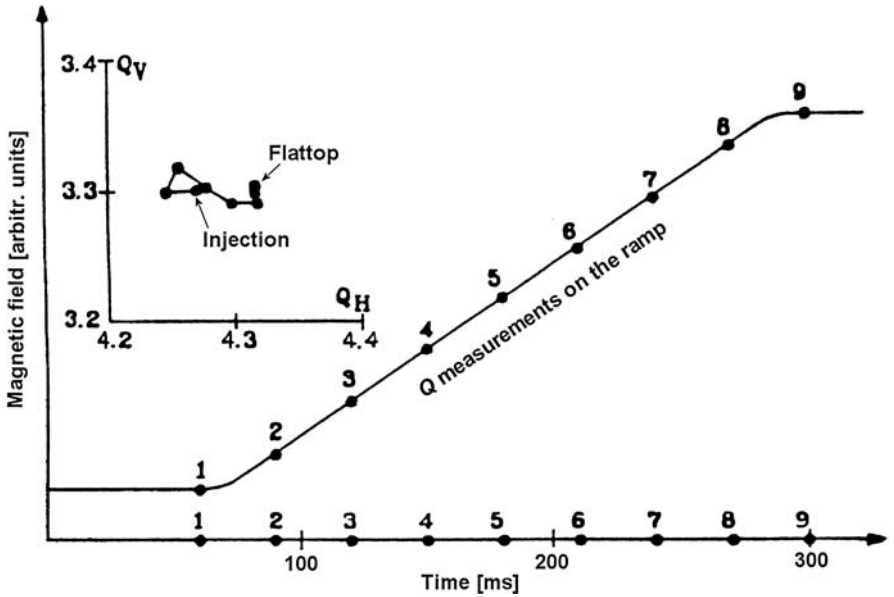

Fig. 5.46. Q measurements during acceleration in the SIS [280]

5.4.6 Narrowband Signal Processing

Narrowband analysis of BPM signals for a beam revolving with constant frequency can be performed simply by connecting the analog outputs of the head amplifiers to a spectrum analyzer, setting the analyzer to the zero-span mode with a resolution of some kHz. Many much more sophisticated narrowband processing systems are described in the literature [273, 281]. Most systems transform the beam signal into a constant intermediate frequency, but, due to the frequency swept signal during acceleration in a heavy ion accelerator like the SIS, most methods would work only for observation of injected bunches or on the flattop. To transform the frequency swept beam signal into a constant IF, one needs an additional circuit, which is controlled by the accelerating rf. Figure 5.47 shows one possibility of realizing such a transformation [275]. The signals IN A and IN B are derived from the buffered analog outputs of the 100-MHz broadband head amplifiers. Thus, the features of broadband signal processing are still available.

The voltage-controlled oscillator (VCO) tracks the accelerator rf via a phase-locked loop (PLL). A quartz oscillator (XO) generates the intermediate frequency (IF), which results in a frequency offset inside the loop. The two multichannel mixers are fed with the resulting oscillator signal at their local oscillator ports, while the bunch signals from the two plates LEFT,RIGHT or UP,DOWN (A and B in Fig. 5.47) are fed to the mixer input ports. As a result, the BPM signals are converted to a constant IF signal.

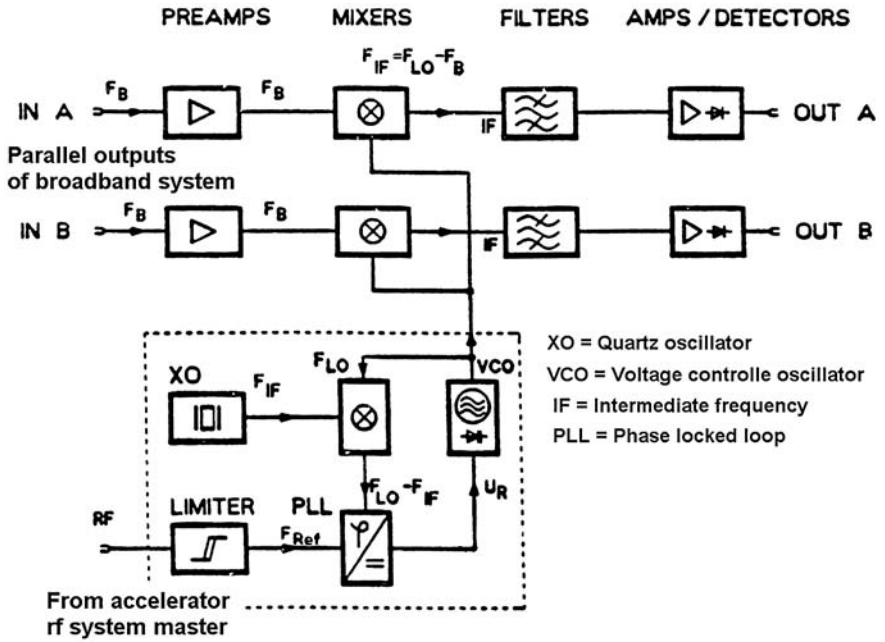

Fig. 5.47. Narrowband signal processing system provided for beam position measurement and beam intensity display [275]

To illustrate the gain in sensitivity by narrowband signal processing, let us take the signal shown in Fig. 5.38 which shows a maximum of about 9 pV/e. The lower straight line in Fig. 5.48 gives the required number of charges within a bunch to obtain a signal-to-noise ratio of 1 for the sum signal. The upper straight line gives the corresponding number of particles to measure a beam displacement of 1 mm with S:N = 1. The data are based on an input noise voltage of 30 μV for a bandwidth of 100 MHz, which is a conservative value. A sensitivity of $S = 2\,\Delta x\,/B = 0.01$ results in a factor of 100 between the number of particles required for the difference signal in comparison to the sum signal. The dBm values given in the figure correspond to the power output for a 50-Ω system and are based on the convention 0 dBm → 1 mW.

Some Examples

Real-Time Beam Intensity and Beam Position Monitor

Feeding the two mixer output signals to a matched sum and difference amplifier system [286] connecting the sum and difference output to a spectrum analyzer delivers a very sensitive real-time beam intensity and beam position display. The spectrum analyzer has to be tuned to the IF and operated in a two-channel receiver mode. An example from the SIS is shown in Fig. 5.49.

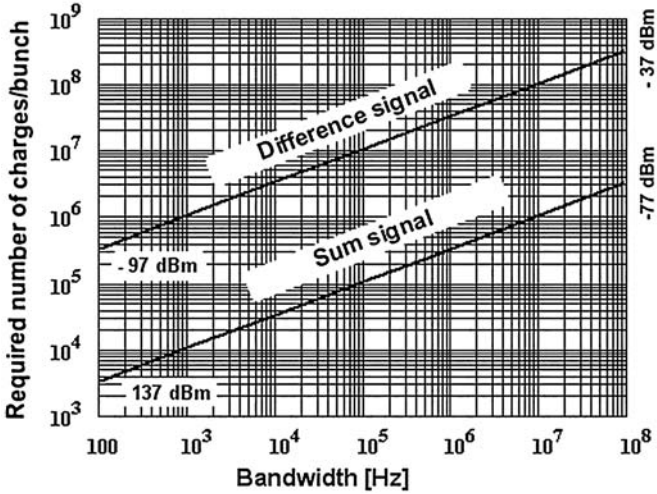

Fig. 5.48. Required number of particles to obtain a signal-to-noise ratio of 1 for the sum and difference signals of the BPM system in the SIS. See text for details

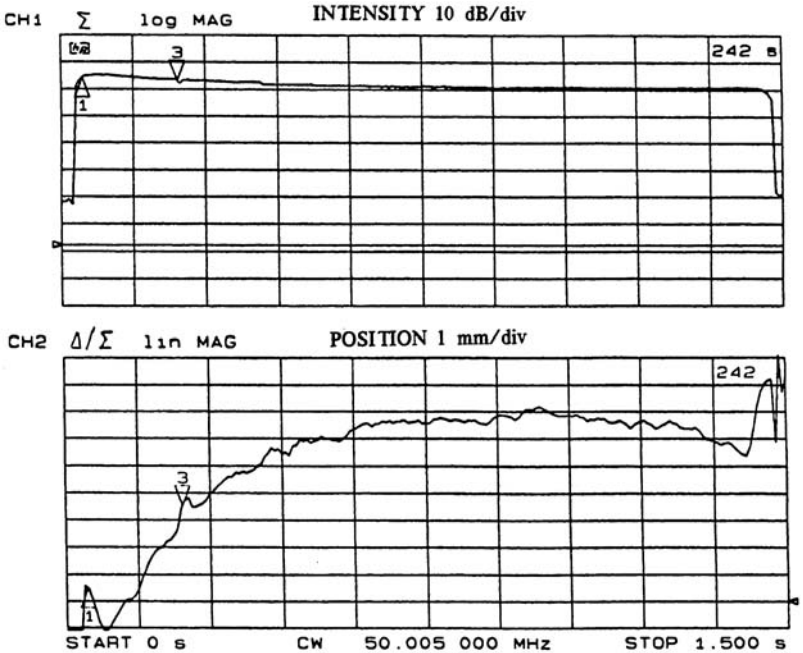

Fig. 5.49. Display of beam intensity (upper trace) and beam position during a complete machine cycle of the SIS [275]

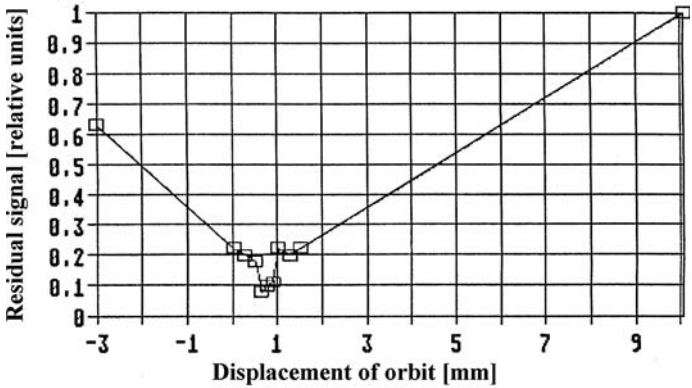

Fig. 5.50. Application of the k-modulation method at the SIS [142]. The abscissa gives the displacement of the beam in millimeters

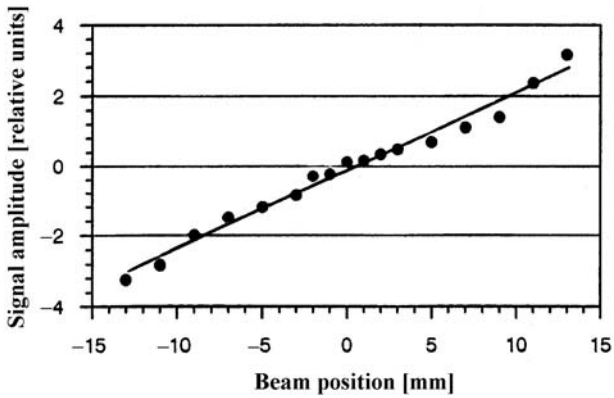

Fig. 5.51. Demonstration of the linearity of the k-modulation method [142]

The K-Modulation Method

A very efficient and precise method for determining the center of magnetic quadrupoles in a circular machine by position measurements is the so-called k-modulation method [287, 288]. It is well known that a beam passing the center of a quadrupole is deflected (steering additional to focusing). Hence, modulation of a quadrupole at a low frequency (10–45 Hz) and shifting the orbit results in position signals proportional to the misalignment of the beam. Because the bandwidth of the signal detection circuit must be only of the order of some hertz, the achievable sensitivity is very high. An example from a measurement performed at the SIS by [142] is shown in Fig. 5.50. The linearity of the method is excellent, as demonstrated in Fig. 5.51.

Conclusion

Although bunch shape determination and turn-by-turn measurements are excluded due to the longer response time of a narrowband system, similar measurements as described in the examples for broadband systems can be performed [275], taking advantage of the much higher sensitivity. Of course, the examples, discussed here cannot cover the whole spectrum of possible measurements performed with a BPM system (see, e.g., [6, 7, 28].

6

Measurements in Phase Spaces

In general, the motion of particles can be described by the Hamiltonian formalism based on the well-known Hamiltonian equations. Assuming an ensemble of N identical, non-interacting particles, the Hamiltonian of a particle depends only on six coordinates in so-called phase space. Here the assumption of non-interacting may be a particular case, but it is a very common one. Therefore, the N particles will occupy a six-dimensional volume in the phase space, determined by their distribution over the six coordinates. For the following reasons, measurement of phase space distributions are important for the accelerator designer, physicist, operator, and, last but not least also for the experimentalist:

- The ease with which a particle beam can be transported depends mainly on the distribution of particles in phase space.
- The minimum spot size that can be achieved at a given target location is determined by this distribution.
- The accuracy with which the beam energy can be measured depends also on this distribution.
- The bunch microstructure in time, for example, the half width (FWHM) of bunches and the bunch shape can be derived from measured phase space distributions.
- Also the precision with which scattering angles in physics experiments can be determined depends on the distribution of the particles in phase space.
- Furthermore, the so-called emittances which are defined in phase space influence all aspects of accelerator design and operation.

In the Hamiltonian formalism [289], the three conjugate coordinate pairs $(x; p_{\mathrm{x}})$, $(y; p_{\mathrm{y}})$, $(z; p_{\mathrm{z}})$ of each particle determine the distribution in phase space. In this phase space, a point, which characterizes a single particle, describes a curve in phase space determined by the Hamiltonian function and the initial coordinates. The ensemble of N identical particles, representing the ion beam, is characterized by a set of points in phase space

and, in general, can be represented at one instant, by a density distribution function $I_6(x, p_x, y, p_y, z, p_z, t)$. The integral over all particles defines the six-dimensional phase space volume V_6:

$$V_6 = \int\int\int\int\int\int dx\, dp_x\, dy\, dp_y\, dz\, dp_z\,. \tag{6.1}$$

In the Hamilton formalism, the continuity equation in phase space [290–292], $dV_6/dt = 0$, leads, to the well-known theorem of Liouville [293, 294] which states:

For Hamiltonian systems, the density of the representative points – or particles – in the appropriate phase space is invariant along the trajectory of any given point.

Obviously, this means that, due to $dV_6/dt = 0$, the six-dimensional hypervolume that encloses the whole ensemble of particles remains constant. Now, if one or more components of the motion in one phase space are decoupled from the motion in the other phase planes, as often happens in beam transport systems, Liouvilles theorem also holds for certain subspaces, resulting from various projections of six-dimensional phase space. Therefore the projected phase space areas,

$$A_x = \int\int dx\, dp_x, \qquad A_y = \int\int dy\, dp_y, \qquad A_z = \int\int dz\, dp_z, \tag{6.2}$$

may all be maintained, which has very useful practical consequences in accelerator physics. Usually, in accelerator physics, the direction of motion is assigned to the z-coordinate, and therefore, the three projected phase spaces are subdivided into two transverse phase planes A_x and A_y and the longitudinal phase plane defined by A_z. Measurements in the longitudinal phase space are postponed to Chap. 7.

6.1 Transverse Phase Planes

In general, motions in the transverse directions $\dot{x}$ and $\dot{y}$ are small in comparison to the longitudinal motion $\dot{z}$, and, therefore relativistic effects in transverse motions can be neglected, which leads immediately to the relations,

$$p_x = m\dot{x} = m_0\gamma\frac{dx}{dz}\frac{dz}{dt} = m_0\gamma\beta c\frac{dx}{dz} = m_0\gamma\beta c x' \tag{6.3}$$

$$p_y = m\dot{y} = m_0\gamma\frac{dy}{dz}\frac{dz}{dt} = m_0\gamma\beta c\frac{dy}{dz} = m_0\gamma\beta c y'\,. \tag{6.4}$$

Here, the relativistic mass increase is taken into account by $m = \gamma m_0$ with m_0 as the rest mass and $\gamma = 1/\sqrt{1-\beta^2}$, where $\beta = v/c = (dz/dt)/c$ is determined by the well-known velocity of light ($c = 2.993 \times 10^8\,\mathrm{m/s} = 299.3\,\mathrm{mm/ns}$).

Applying (6.3), and (6.4) to the two projected transverse phase planes of (6.2), one gets immediately

$$A_{\mathrm{x}} = m_0\gamma\beta c \int\int dx\, dx' \quad \text{and} \quad A_{\mathrm{y}} = m_0\gamma\beta c \int\int dy\, dy' \,. \tag{6.5}$$

Obviously, in a two-dimensional coordinate system with horizontal and vertical directions as transversal coordinates, an individual particle in one of the two transverse phase planes is characterized by its coordinate x, respectively, y, and the angle of motion dx/dz, respectively, dy/dz, referred to the beam axis. Thus, the N particles considered, representing the ion beam, occupy a certain area in the x, x'-plane as well as in the y, y'-plane and, referring to (6.5), according to the theorem of Liouville, these areas scale only with $1/\beta\gamma$. Because these areas can be well described for most beams by ellipses and the area of an ellipse contains the factor π, it is convenient to define

$$\varepsilon_{\mathrm{x}} = \frac{\int\int dx\, dx'}{\pi} \tag{6.6}$$

as the horizontal emittance and accordingly

$$\varepsilon_{\mathrm{y}} = \frac{\int\int dy\, dy'}{\pi} \tag{6.7}$$

as the vertical emittance. Taking the scaling with $1/\beta\gamma$ into account, it follows immediately that the so-called normalized emittances $\varepsilon_{\mathrm{x}}^n = \beta\gamma\varepsilon_{\mathrm{x}}$ and $\varepsilon_{\mathrm{y}}^n = \beta\gamma\varepsilon_{\mathrm{y}}$ are conserved. In general, phase planes, bounded by ellipses or straight lines may be transformed by a linear transformation, mapping the initial coordinates in phase space within their final values. Furthermore, straight lines are transformed into straight lines, parallel lines remain parallel, and ellipses transform into ellipses, changing only shape and orientation.

6.2 Emittance Measurements in Transverse Phase Planes

Measurement of transverse emittances becomes essential

- for the valuation of newly developed; ion sources, including electron guns;
- during the commissioning of a new accelerator facility;
- for the elaboration of data sets, provided for routine operation of a machine;
- for matching acceptances of various sections of a transport system, respectively, accelerator sections to the beam emittances; and
- for planning experiments, especially with respect to the beam spot size and divergence angles that can be achieved at a given target position.

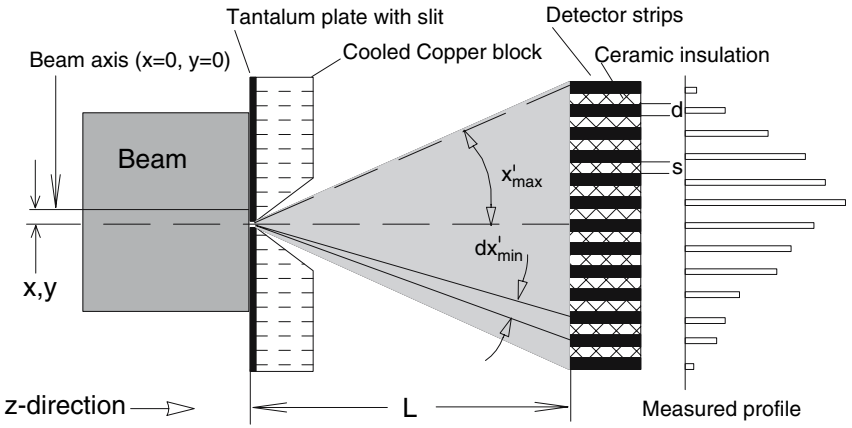

Fig. 6.1. Simplified scheme of an emittance measuring system showing a slit-detector system. Typical parameters for the sandwich detector are 32–64 collector strips with $d = 0.05$–$0.2\,\mathrm{mm}$ and $s = 0.2\,\mathrm{mm}$

To determine, for example, the emittance in the horizontal phase plane, the distance x from the beam axis and the corresponding angle of motion dx/dz for each particle has to be determined. It is evident that this will not be possible except in very special cases. But, due to the large number of particles within a realistic charged particle beam, it is sufficient to perform the measurement successively on small well-defined parts of the beam.

6.2.1 Description of a Typical Measuring System

A great diversity of devices have been developed to measure transverse emittances. A comparison of different methods is given in [295]. To start with a description of various devices, perhaps the classical scheme shown schematically in Fig. 6.1 will be most suitable to illustrate the complexity of an emittance measuring system, requiring tight collaboration of the constructor, accelerator physicist, electronic engineer, and software expert. A narrow slit, mounted together with a detector sandwich onto a supporting bar, is moved stepwise across the beam. The two mechanical units, slit-detector sandwich and a high precision UHV feedthrough, to perform the movement through the beam are shown in Fig. 6.2. The completely mounted unit is very compact but has some drawbacks:

- Once the distance L between slit and detector as well as the parameters of the sandwich detector have been fixed, the relevant physical parameters cannot be changed. For this reason in the example of Fig. 6.2, the sandwich detector can be mounted at three different positions on the supporting bar $(100, 200, 300\,\mathrm{mm})$.

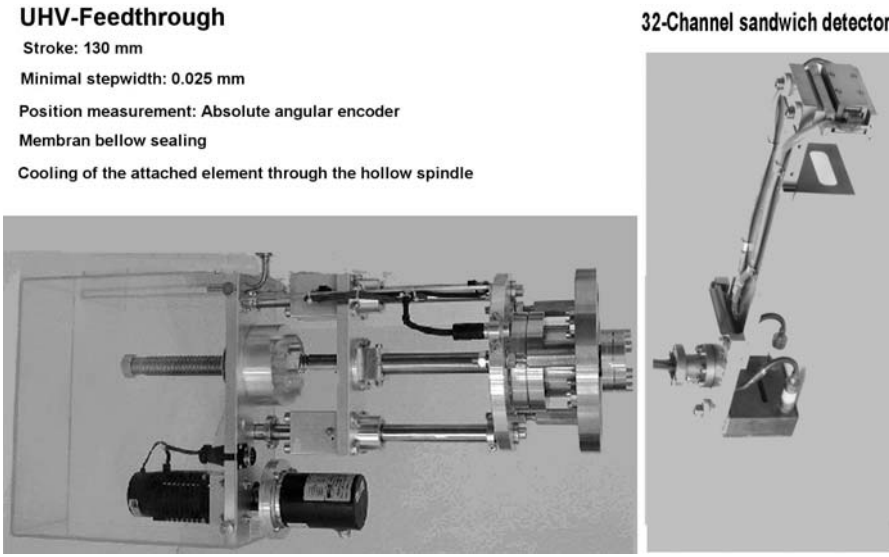

Fig. 6.2. Mechanical components of an emittance measuring system. See Appendix 6.A for the dimensioning of motor driven feedthroughs

- Since the slit width is also fixed, the part of the beam distributed over the collector strips may be very small, which reduces the achievable signal-to-noise ratio.
- The insulation between the collector strips can break down due to sputtering and implantation effects. Experience has shown that degradation of the detector quality in general will be a slow process, depending of course on the beam intensity and the frequency of measurements.
- Since the unit has to be mounted onto only one flange of a vacuum chamber in the beam line, the length L is limited, resulting in limitation of the achievable resolution in divergence.

A very flexible scheme, which avoids most of this drawbacks, uses a harp as shown in Fig. 6.3 instead of the detector sandwich. Mounting the harp onto a separately driven UHV feedthrough offers the following advantages:

- Because the feedthrough with the harp can be installed in a separate vacuum chamber, there is nearly no limitation on L.
- The movement of the two feedthroughs can be controlled independently; thus more than one position of the harp detector (so-called intermediate steps) for each slit position are possible. This improves the achievable resolution in divergence considerably.
- Positioning the harp detector with an offset measured against the slit position allows the measurement of very large emittances or extremely misaligned beams.

Fig. 6.3. Harp detector [33], shown from the back, provided for emittance measurements. The detector consists of 60 W-Re wires with a diameter of 0.1 mm having a spacing of 1 mm

Of course, performing intermediate steps and/or measurements in offset, positions increases the measuring time accordingly. Although an emittance measurement with the sandwich system lasts typically 40–60 s, this time may go up to some minutes depending on the parameters of the measurement.

Remark. Due to the $1/\beta\gamma$ scaling, the measurable emittance ε becomes smaller with an increasing β value. Especially the divergence of a highly relativistic beam may become very small, due to the compensation of space charge defocusing effects by magnetic focusing forces. For two reasons, measurements of emittances on high energy particles require special treatment:

- The emittances may become so extremely small that the resolution of schemes discussed above will not be sufficient to measure a phase space distribution.
- The penetration depth of the high energy particles can be very large, which also requires special methods of emittance measurement.

Furthermore, also the determination of emittances for circular machines requires special treatment, since destructive schemes cannot be applied.

For low particle energies and heavy ion accelerators, emittance measurements, based on schemes similar to those discussed, are extremely important for the following reasons:

- Due to space charge effects and the low stiffness of low energy beams, the design and operation of the corresponding transport system requires knowledge of emittances along the machine.
- Considering accelerator facilities provided for acceleration and transport of all kind of ions up to uranium, there is a great diversity of ion sources with different characteristics, delivering the required beams. It is self-explanatory that changes of the ion species as well as the use of various ion sources, require knowledge of emittances to retune the machine.

6.2.2 The Relevant Parameters of an Emittance Measuring System

From the examples, it is evident that the design of an emittance measuring system requires clear specifications to meet the demands on the system. In consequence, a detailed design study to fix and optimize the parameters with respect to the mechanical parts and signal processing is very important. This holds for all schemes of destructive emittance measurement systems. The most important steps for the design of a system are discussed in the following, supposing x and x' are the two independent variables of the phase plane.

Resolution and Range in x and x'

Clearly, the achievable maximum range $x_{\max}$ in the x-coordinate is determined by the stroke of the feedthrough, but is determined ultimately by the beam size at the slit position. On the other hand, the resolution in x- coordinate δx is fixed by the width of the slit (typically 0.1 mm). Assuming a stepping motor driven feedthrough, the Δx of measured points in x-direction is given by $\Delta x = N_{\text{slit}}\, \delta S_{\text{slit}}$, with δS_{slit} as the displacement of the feedthrough per step of the motor (typically $0.02-0.05$ mm) and N_{slit} as the number of steps (typically 10–20). To achieve high accuracy in the absolute determination of the x-coordinates, the use of absolute angular encoders, instead of linear potentiometers or incremental encoders is recommended. The use of stepping motors with a small angle of rotation per step is recommended to minimize the overshoot effect and achieve more flexibility in the separation Δx of measured points.

On the other hand, referring to Fig. 6.1, the maximum measurable divergence $x'_{\max}$ is determined by the total width of the detector system divided by L. Referring to Fig. 6.1, this results in $1/2\, N\, (d+s)/L$ for the sandwich detector but can be extended to much larger values for the harp detector, taking advantage of offset positions. From experience, the range form 30–200 mrad will cover most applications. Obviously, the resolution achievable in divergence is given by d/L, typically $(0.05-0.2\,\text{mm})/(100\text{–}300\,\text{mm}) \rightarrow 0.15-2$ mrad. The separation in $\Delta x'$ is $(d+s)/L$ for the sandwich and can be reduced to very small values for a harp detector, considering intermediate positions.

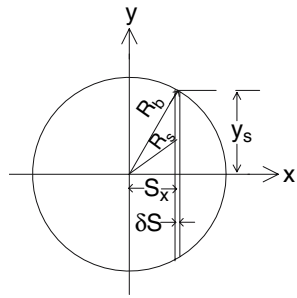

Fig. 6.4. Scheme to derive the current density distribution over an emittance measuring slit. See text for details

Signal Estimation

From the principle of measurement, it becomes very clear that signal processing electronics has to cover a high dynamic range and has to handle very low currents. Therefore, an estimation of the expected signals is essential. Although one does not know the exact size and orientation of the emittance pattern, some simple geometric considerations can lead to usable results. The estimation of the expected intensity on a certain collector strip can be performed in two steps:

- First, determining the part of the beam going through the slit, dependent on the slit and beam parameters.
- Distribution of this part over the collector strips, taking into account a presumed divergence.

Referring to Fig. 6.4, assuming a parabolic intensity distribution over the radial coordinate, the current density is given by

$$i(R_\mathrm{s}) = \frac{2I_0}{\pi R_\mathrm{b}^2}\left(1 - \frac{R_\mathrm{s}^2}{R_\mathrm{b}^2}\right) = \frac{2I_0}{\pi R_\mathrm{b}^2}\left(1 - \frac{S_\mathrm{x}^2 + y_\mathrm{s}^2}{R_\mathrm{b}^2}\right), \tag{6.8}$$

and in a good approximation, the current I_s passing the slit at position S_x is

$$I_\mathrm{s}(S_\mathrm{x}) \approx 2\,\delta S \frac{2I_0}{\pi R_\mathrm{b}^2}\int_0^{\sqrt{R_\mathrm{b}^2 - S_\mathrm{x}^2}}\left(1 - \frac{S_\mathrm{x}^2 + y_\mathrm{s}^2}{R_\mathrm{b}^2}\right) dy_\mathrm{s} \tag{6.9}$$

$$I_\mathrm{s}(S_\mathrm{x}) \approx \frac{8}{3}\frac{\delta S}{R_\mathrm{b}}\frac{I_0}{\pi}\left(1 - \frac{S_\mathrm{x}^2}{R_\mathrm{b}^2}\right)^{3/2}. \tag{6.10}$$

Defining $V = S_\mathrm{x}/R_\mathrm{b}$ with $0 \le V \le 1$, the percentage passing the slit is approximately

$$P(V) \approx 100\,\frac{8}{3}\frac{\delta S}{\pi R_\mathrm{b}}(1 - V^2)^{3/2}. \tag{6.11}$$

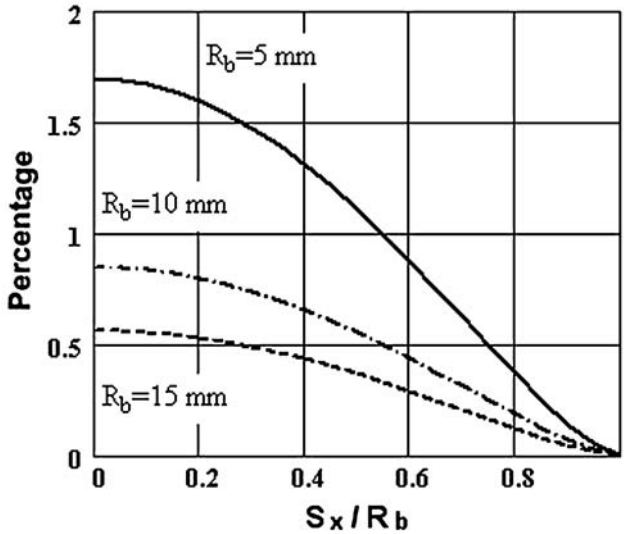

Fig. 6.5. Percentage of total beam current passing a slit 0.1 mm wide (according to 6.11). $V = S_x/R_b = 0$ corresponds to the center position of the slit; for $V = 1$, the slit is at the boundary of the beam

In Fig. 6.5, $P(V)$ is plotted for three different radii R_b, taking a slit width of 0.1 mm. According to (6.11), $P(V)$ scales linearly with δS. The approximations (6.10) and (6.11) may be used to estimate the current on profile grids, harps, and other detectors, provided for beam profile measurements. In emittance measurements, the percentage of the beam that passes the slit is distributed over the detector system. The resulting percentage hitting a collector strip depends on the width of the strips, the divergence in the beam, and the distance between slit and detector. The approximation of phase plane distributions by ellipses offers the possibility of estimating the divergences in the beam. There are different representations of the relevant ellipse parameters marked as points 1–4 in Fig. 6.6. In a PSI Report by Joho [296], the parametric representation defined by x_{max}, x'_{max}, and χ, the so-called correlation phase describing the orientation of the ellipse, is compared with the well-known Courant-Snyder representation [297], defined by the Twiss parameters α, β, γ and the emittance parameter $\varepsilon = \text{Area}/\pi$. As it becomes very clear from Fig. 6.6, points 1–4 define the shape, size, and orientation of the emittance ellipse in both representations. Furthermore, they also play important roles, in the behavior of a particle under the action of quadrupoles, steerers, magnets, and drift spaces. Therefore, a table given in [296] is helpful for further discussions.

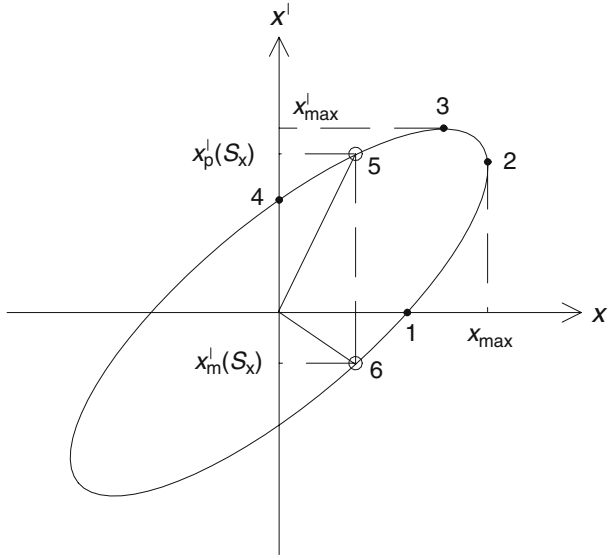

Fig. 6.6. Typical ellipse to approximate distributions in the phase plane. The meaning of the four points marked 1–4 is explained in the context of this chapter (see also [296]). The points marked 5 and 6 are relevant to the estimation of the current on the detectors

Table 6.1. Coordinates of the points marked 1–4 of Figure 6.5 in the two representations discussed

	Parametric		Twiss	
Nr.	x	x'	x	x'
1	$x_{\max}\cos\chi$	0	$\sqrt{\varepsilon/\gamma}$	0
2	$x_{\max}$	$x'_{\max}\sin\chi$	$\sqrt{\varepsilon\beta}$	$-\alpha\sqrt{\varepsilon/\beta}$
3	$x_{\max}\sin\chi$	$x'_{\max}$	$-\alpha\sqrt{\varepsilon/\gamma}$	$\sqrt{\varepsilon\gamma}$
4	0	$x'_{\max}\cos\chi$	0	$\sqrt{\varepsilon/\beta}$

In the parametric representation, the correlation phase χ is determined by $\chi = \arctan(x_3/x_1) = \arctan(x'_2/x'_4)$; the Twiss parameter α, describing the orientation of the ellipse, is determined from $\alpha = -x_3/x_1 = -x'_2/x'_4$. In the parametric representation, a point on the boundary of the ellipse is given by x, $x' = x_{\max}\cos\delta$, $x'_{\max}\sin(\delta + \chi)$ with $0 \leq \delta \leq 2\pi$, which simplifies plotting the ellipse considerably in comparison to the Courant-Snyder representation. Furthermore, although the emittance parameter ε is defined as one of the Twiss parameters, $\varepsilon = x_{\max}\, x'_{\max}\cos\delta$ in the parametric representation. In the following context, it becomes clear that both representations have their advantages and disadvantages. Therefore, both representations are used, depending on the problem under discussion.

Remark: In the well-known TRANSPORT program [298], a representation of the so-called σ-matrix is used, which differs only slightly from the Courant-Snyder representation:

$$\sigma = \begin{bmatrix} \sigma_{11} & \sigma_{12} \\ \sigma_{12} & \sigma_{22} \end{bmatrix} = \varepsilon \begin{bmatrix} \beta & -\alpha \\ -\alpha & \gamma \end{bmatrix} . \tag{6.12}$$

Setting $t = \arccos(S_\mathrm{x}/R_\mathrm{b})$ and taking advantage of the parametric representation, the points marked 5 and 6 of Fig. 6.6 determine the maximum divergence behind the slit, located at position S_x:

$$x'_\mathrm{p}(S_\mathrm{x}) = x'_\mathrm{max}\sin(t+\chi) \tag{6.13}$$
$$x'_\mathrm{m}(S_\mathrm{x}) = x'_\mathrm{max}\sin(-t+\chi) \tag{6.14}$$
$$\chi = -\arctan(\alpha) . \tag{6.15}$$

In the notation of this book, $\alpha < 0$ describes a divergent beam as shown, for example, in Fig. 6.6; $\alpha > 0$ describes a convergent beam and $\alpha = 0$ represents a waist. Obviously, the maximum width of the partial beam behind the slit is given by

$$x_\mathrm{max}(S_\mathrm{x}) = L\,\left|x'_\mathrm{p}(S_\mathrm{x}) - x'_\mathrm{m}(S_\mathrm{x})\right| . \tag{6.16}$$

Clearly, $x_\mathrm{max}(0)$ holds for the center position of the slit and results in the maximum width, defining the required size of the detector array. To estimate the part of the total beam on a certain collector strip, a parabolic intensity distribution over the x-coordinate leads to

$$i(x) \approx I_\mathrm{s}(S_\mathrm{x})\frac{3}{2x_\mathrm{max}(S_\mathrm{x})}\left(1 - 4\frac{x^2}{x_\mathrm{max}(S_\mathrm{x})}\right), \quad 0 \le x \le \frac{x_\mathrm{max}(S_\mathrm{x})}{2} . \tag{6.17}$$

For a detector width δ_x, the current i_c on a collector comes out to

$$i_\mathrm{c}(S_\mathrm{x}, \delta_\mathrm{x}) \approx i(x)\delta_\mathrm{x} . \tag{6.18}$$

Example. The ellipse shown in Fig. 6.6 is somehow typical for the shape and orientation of a divergent beam. Therefore, we assume the following parameters:

$\varepsilon = 120$, area of the ellipse/π [mm mrad]
$R_\mathrm{b} = 10$, beam radius [mm]
$\beta = 0,833$, Twiss parameter, $\beta = R_\mathrm{b}^2/\varepsilon$, [mm/mrad]
$\alpha = -1$, Twiss parameter, determines the orientation of the ellipse, [–]
$\gamma = 2.4$, Twiss parameter, $\gamma = \left(1+\alpha^2\right)/\beta$, [mrad/mm]
$x'_\mathrm{max} = 17$, maximum divergence, $x'_\mathrm{max} = \sqrt{\varepsilon\gamma}$, [mrad]
$\chi = 0.785$, correlation phase in the parametric representation [–]
$\delta s = 0.1$, slit width, [mm]
$\delta_\mathrm{x} = 0.1$, width of the collector strips, [mm]
$L = 300$, distance slit-detector array, [mm]

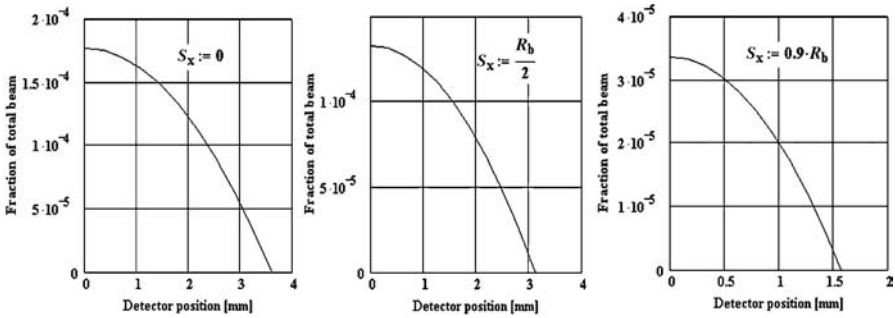

Fig. 6.7. Fraction of total beam on the detectors dependent on the slit and detector positions. For parameters, see text

First of all, the required width of the detector array is of interest. From (6.13), (6.14), and (6.16), we obtain $x_{\max}(0) = 7.2\,\mathrm{mm}$, a size which can be realized easily with a sandwich detector. The expected part of beam, estimated from (6.10), (6.17), and (6.18) is shown in Fig. 6.7 for three positions of the slit: $S_\mathrm{x} = 0$ (centered), $S_\mathrm{x} = R_\mathrm{b}/2$, and $S_\mathrm{x} = 0.9R_\mathrm{b}$ (near the boundary).

Signal Processing

For further evaluation of emittance data, the measured collector currents I have to be converted into reasonable voltages U provided for digitization. There are two suitable methods of I/U conversion:

- Conversion based on the simplified scheme, shown at the left-hand side of Fig. 6.7.
- Conversion based on the principle of a switched integrator, shown at the right-hand side of the Fig. 6.7

The output voltages using operational amplifiers of very high gain are given by

$$(a) \qquad U(t) = -I(t)R \tag{6.19}$$

$$(b) \qquad U(T) = -\frac{1}{C}\int_0^T I(t)\,dt \tag{6.20}$$

Both schemes have their advantages and disadvantages:

- Scheme (a), the classical I/U converter, also converts the time dependence of the input current with a certain smoothing due to the time constant of the operational amplifier. Replacing R by an array of resistors, each in series with remotely controllable switches, offers the possibility of covering a large dynamic range required by emittance measurements. Due to increasing problems of noise from very large resistors, the conversion rate

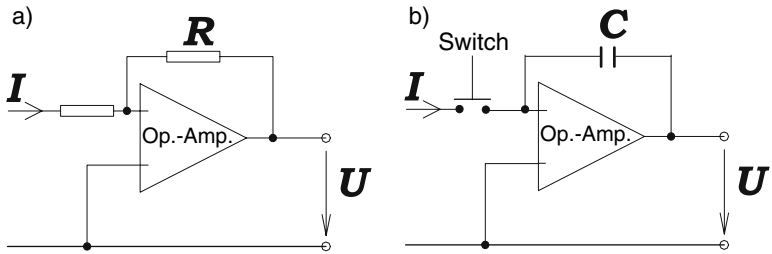

Fig. 6.8. Simplified schemes of I/U conversion

is limited to about 1–10 nA/V from the practical point of view, depending also on the required accuracy.

- Scheme (*b*) is the so-called "switched integrator type" and, due to the integration over time, the output voltage of this type does not show any time dependence. Variation of the integration time as well as the size of the switched capacity (optional also in the type of an array) offers the possibility of covering a very large dynamic range. Taking as an example the data of the integrated circuit ACF 2101, having a conversion rate of $Q_{\mathrm{U}} = Q/U = 10^{-10}$As/V, it becomes evident that the I/U converter should be preferred for short beam pulses. On the other hand, the switched integrator shows advantages in long beam pulses, resulting for example, from slow extraction of synchrotrons or dc-beams. Taking for comparison the most sensitive range of commercial [173] I/U converter electronics with $I_{\mathrm{U}} = I/U$ =2 nA/V, the crossover point with respect to the integration time T_{int} is $T_{\mathrm{int}} = Q_{\mathrm{U}}/I_{\mathrm{U}} = 50$ ms (see also Fig. 4.3 in Chap. 4).

Of course, the electronics of an emittance measuring system has to cover many more functions than the discussed conversion of collector current into voltage. This becomes very clear from the schematic system overview in Fig. 6.9 and the simplified block diagram based on the I/U converter scheme, shown in Fig. 6.10. Since measurements in the horizontal, respectively, vertical phase planes have to be performed sequentially, a relay switching unit has been added in front of the I/U converter system to reduce the costs of the system. To reduce the influence of changes in beam intensity during a measurement, one channel of the 32 I/U converters is provided to measure the current on the isolated slit, allowing normalization of the measured data to the total current. Taking the higher expected current on the slit into account, the ranges of this channel are shifted by a factor of 100 to lower conversion rates in comparison to the detector channels.

In the scheme, the output signals of the I/U converters are fed into an integrator system which has the following advantages:

- Fast fluctuations during the measurement are averaged over the integration time.

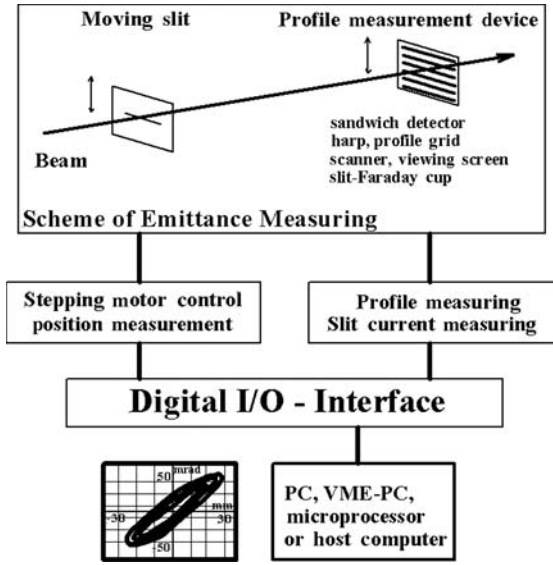

Fig. 6.9. Schematic system overview showing the most important parts of an emittance measuring system

- The start point of the integration with respect to the front edge of the beam pulse as well as the width of the integration window T_{int} can be varied in wide ranges.
- The integration can be performed with an additional amplification of the signal according to

$$U_{\mathrm{out}} = \frac{1}{RC} \int_0^{T_{\mathrm{int}}} U_{\mathrm{in}} dt \; . \tag{6.21}$$

  Assuming a square beam pulse, this results in an additional amplification of T_{int}/RC ($= 5$ in the example of Fig. 6.10).
- For dc-beams, synchronous integration over exactly one period of the network frequency can reduce distortions synchronous to the network frequency considerably.

In the example of Fig. 6.10, the ranges of I/U converters cover five decades (1 nA/V, 10 nA/V; 10 µA/V), selected by the controlling computer based on the comparator system providing a "gain to high" or "gain to low" signal, respectively. A change of range takes place to a higher I/U-conversion rate when all 31 detector channels are below a certain threshold (80 mV in the example), whereas change to lower I/U conversion is performed if only one of the detectors is above a certain threshold (1.2 V in the example).

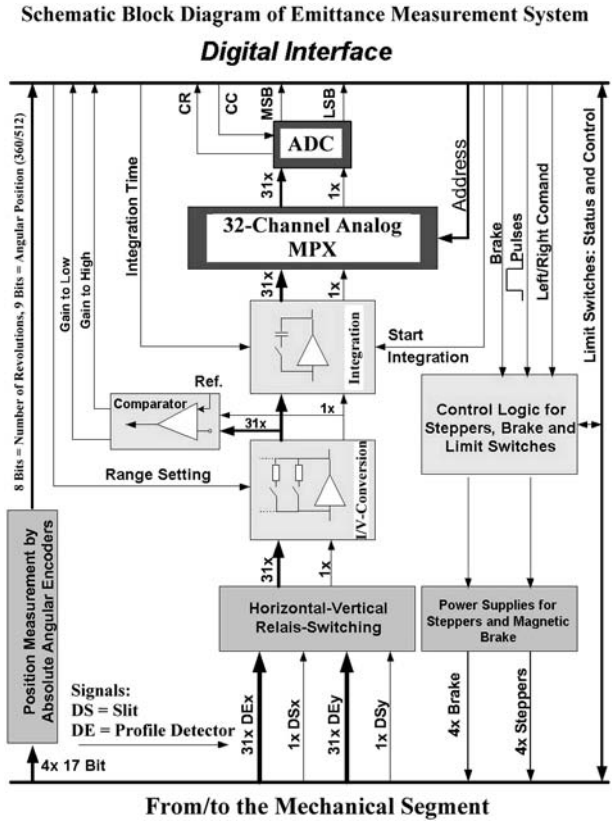

Fig. 6.10. Simplified block diagram of control and signal processing electronics based on the I/U-converter scheme

Typical Example of a Complete System

The great variety of possible modes of measurement as well as the parameters, which have to be specified and controlled may be illustrated by referring to a system [299], designed for development of ion sources for highly intense beams and study of space charge effects. To start with the mechanical components, the system consists of

- Two UHV feedthroughs such as shown in Fig. 6.1 on the left-hand side. Due to the demand for very high precision, both feedthroughs are equipped with stepping motors of low step width (0.72°/step). The stepping motors drive ball bearing spindles, having a pitch of 5 mm. With a gear ratio of 2:1 between motor drive and spindle, a displacement of 500 µm per step results. To determine the position of the spindle with adequate precision, absolute angular encoders with 512 bit/revolution have been installed. From that, the absolute resolution comes out to 4.883 µm/bit. The stepping motors

are equipped with magnetic brakes to avoid moving the feedthroughs when the power on the motors is switched off or in case of power failure.
- One of the feedthroughs has been equipped with a cooled slit to withstand the expected high beam power, especially for dc-beams.
- A 60-wire harp detector shown in Fig. 6.3 is mounted onto the second feedthrough.

The electronic signal processing system has been designed to measure pulsed beams as well as dc-beams of positive or negative ions. The relevant specifications are

- number of ranges of current measurement: six decades
- conversion rates of the ranges: $100\,\mathrm{nA/V}, 1\mu\mathrm{A/V}, \ldots 10\,\mathrm{mA/V}$.
- selectable integration times: $50\,\mu\mathrm{s} - 20\,\mathrm{ms}$ in steps of $50\,\mu\mathrm{s}$
- adjustable delay times against a delivered trigger pulse: $10\,\mu\mathrm{s} - 20\,\mathrm{ms}$ in steps of $10\,\mu\mathrm{s}$.

The signal processing electronics is based on the scheme of the switched integrator. Combining the six decades with the great variety of integration times results in nearly eight decades in the dynamic range. Because this could not be realized with only one capacitor, an array of three capacitors with $10\,\mathrm{nF}$,$100\,\mathrm{nF}$, and $1\mu\mathrm{F}$ has been used to cover low, medium, and high beam currents.

The system is very versatile with respect to the modes of measurementes that can be performed.

Control Software

Two complex program packages had to be implemented to control the measurement as well as evaluate and visualize data. The control software can be considered as an interface between the operator, who has to specify the parameters of a measurement, and the computer, accomplishing the measurement. Since the system may be operated by scientists and operators, who can be more or less familiar with the system parameters, the control software implemented displays a table (see Fig. 6.11), showing the relevant parameters in a simplified scheme to explain their meaning.

To start a measurement, many parameters have to be specified. First of all, the operator has to select one of four different measuring modes:

- **Profile 1 – mode:** The slit and harp move together in parallel through the beam. The slit position as well as the measured profile behind the slit are displayed on the screen. The mode is provided to get a first rough estimation of the beam characteristics. This mode has to be applied in case of high beam currents because it does not allow moving the harp through the beam without protection by the slit jaws.

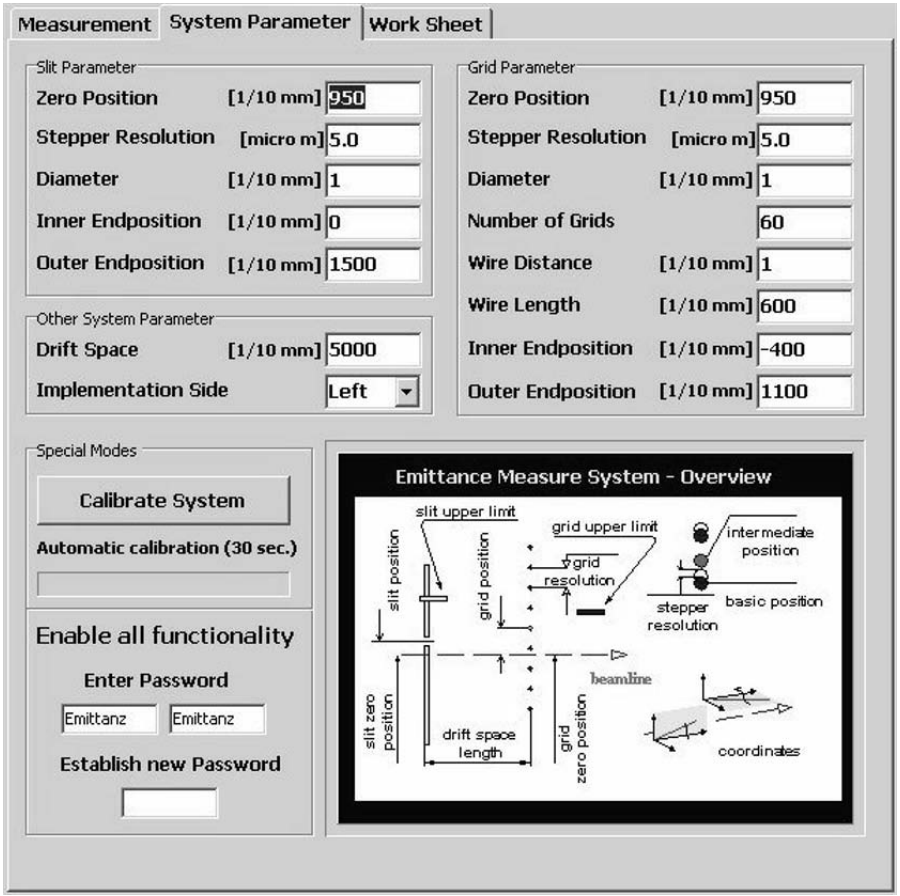

Fig. 6.11. Computer display, explaining the relevant system parameters of an emittance measuring system [300]

- **Profile 2 – mode:** Only the harp moves into the beam to estimate the beam size or observe the change in profile due to the action of beam transport elements or manipulations of the ion source.
- **Emittance 1:** In principle as **Profile 1 – mode,** but performing an emittance measurement.
- **Emittance 2:** Sophisticated emittance measuring program, allowing intermediate steps as well as offset positions of the harp. Due to the large amount of different settings for slit and harp position, the amount of collected data as well as the measuring time can increase considerably in this mode.

To specify the measuring mode with the corresponding parameters, a PC menu, shown in Fig. 6.12, is presented to the operator. Here, in the outer

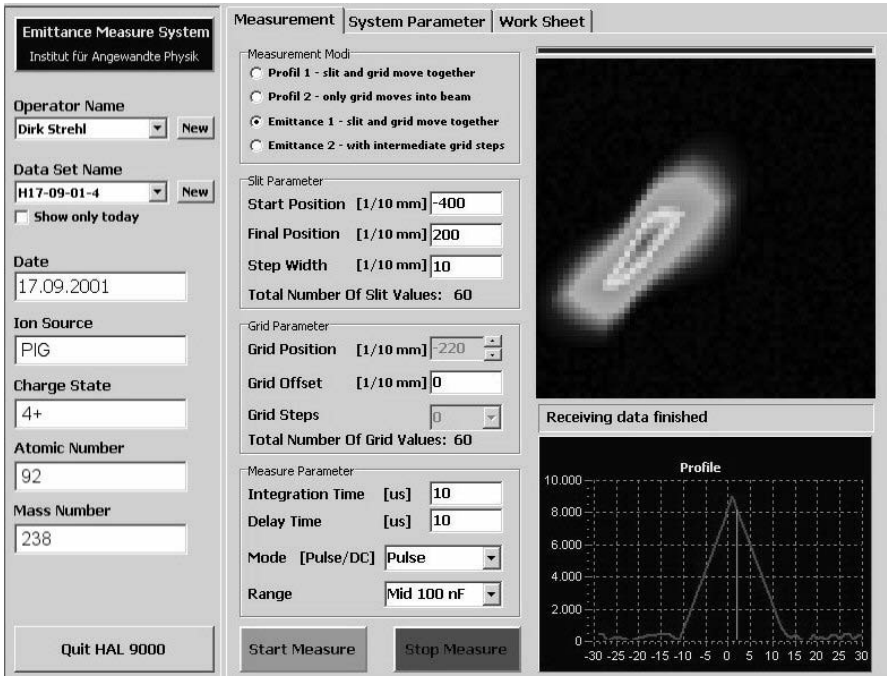

Fig. 6.12. PC menu displayed to the operator to specify parameters and set up the emittance measuring system [300]

left-hand side, some important data such as operator's name, date of measurement, name of the corresponding data set, kind of ion, and type of ion source used have to be inserted. After the measurement has been started, the operator can observe the collection of the rough data on the two displays on the right-hand side of the menu (colored).

Evaluation Software

On the basis of the known setup parameters, the evaluation program first converts and stores the measured rough data in a matrix such as shown in the example of Fig. 6.13. Here each number gives the normalized intensity, measured in a small area of the phase plane defined by Δx, the step width of the slit movement, and $\Delta x'$, the divergence determined by the detector positions behind the slit, considering intermediate steps and/or offset positions, if necessary. Depending on the measuring mode, the matrix may contain some thousands of numbers, where some cells can be filled up with very small numbers, generated by electronic noise instead of representing a real emittance pattern. Therefore, an evaluation program should offer possibilities for removing those strange points. Obviously, the simplest method is to set all numbers in the matrix below a given threshold to zero. More sophisticated

Divergence ----->

	12	13	14	15	16	17
10	0.447	0.521	0.553	0.564	0.543	0.512
11	0.596	0.662	0.708	0.705	0.68	0.608
12	0.704	0.814	0.845	0.838	0.777	0.71
13	0.799	0.885	0.934	0.913	0.852	0.723
14	0.794	0.94	0.979	0.959	0.843	0.74
15	0.837	0.94	0.999	0.966	0.878	0.703
16	0.821	0.955	1.001	0.982	0.862	0.745
17	0.838	0.913	0.965	0.941	0.865	0.695
18	0.781	0.857	0.891	0.876	0.78	0.682
19	0.723	0.76	0.78	0.757	0.708	0.583
20	0.594	0.637	0.645	0.633	0.569	0.508

$E =$

----> x-coordinate of slit position

Fig. 6.13. Arrangement of measured emittance data for further evaluation. The numbers in the matrix represent the measured intensities in the phase plane

programs offer graphical solutions, having the advantage of examining the data by visualization before any manipulation. The program implemented in the example presents two different solutions to the operator, which are illustrated in Fig. 6.14. Using method (a), the program converts the mouse pointer into a pencil, giving the operator the option to define an area inside a closed boundary, provided for further processing. Points outside of the boundary are set to zero in the matrix after saving the original data in a separate file. Method (b) converts the mouse pointer into a "rubber" which gives flexibility to erase individual points (deep black areas) in the diagram, respectively, to set them to zero in the data matrix.

After applying corrections like that, the data can be evaluated according to options available in the evaluation algorithms. Practice has shown that the following algorithms should be implemented in a versatile program:

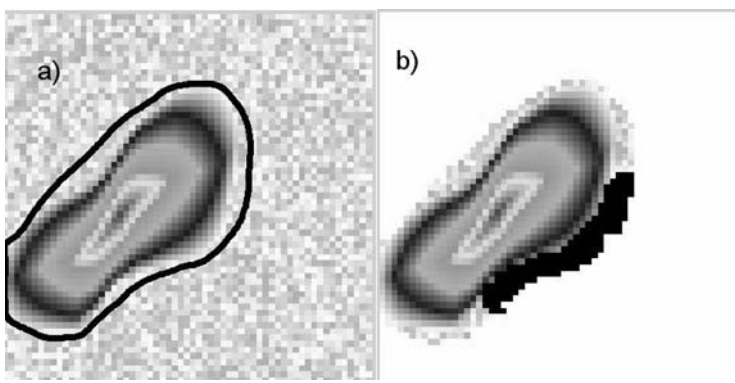

Fig. 6.14. Illustration (colored in reality) of the two methods for removing "strange" points from the data matrix. See text for details

- determination of size and shape of emittances ε dependent on given percentages of the beam inside an area determined by $\pi\varepsilon$.
- determination of beam profiles.
- determination of angular profiles.
- determination of rms values and Twiss parameters.
- transformation of ellipses over a drift space.
- conversion of data into formats used by ray-tracing programs, such as Parmila, Parmt, Parmtra [304–306] for design and evaluation of beam transport systems.

There are three different algorithms for extracting the size and shape of the emittance dependent on a given percentage from the original data. The results can differ considerably. Naming the three modes of processing "**Emittance Mode**," "**Intensity Mode**," and "**Minimum Subtraction Mode**," the accompanying algorithms can be described as follows.

Emittance Mode

Summing up all intensities $I_{\mathrm{x},x'}$ of the corrected data matrix defines the maximum intensity $I_{\max}$, taken as reference to calculate the percentages. Therefore, to calculate, for example, the so-called 80% emittance, a value of $S = 0.2\ I_{\max}\ /n_{\mathrm{x}}\, n_{\mathrm{x}'}$ (n_{x} = number of rows, $n_{\mathrm{x}'}$ = is number of columns) has to be subtracted from each element with $I_{\mathrm{x},x'} > 0$ in the data matrix. No subtraction takes places if $I_{\mathrm{x},x'} = 0$. Furthermore, since $I_{\mathrm{x},x'} < 0$ is not allowed, the subtraction has to be performed successively in much smaller steps as defined by S (for example $S/100$). Elements below zero are set to zero. The procedure is repeated until the required value of $S\, n_{\mathrm{x}} n_{\mathrm{x}'}$ is achieved within a given threshold. An example of the corresponding program algorithm using MATHCAD is shown in Fig. 6.15. It can be easily converted to any other suitable programming language. Figure 6.16 illustrates the effect, comparing the original data with the reduced data in a 3-D display as well as in the corresponding projection onto the phase plane. In the example, the base of each column represents an area of $dx\, dx' = 1.167\,\mathrm{mm} \times 0.354\,\mathrm{mrad} = 0.413\,\mathrm{mm} \times \mathrm{mrad}$. After correction for noise ($\sim 1\%$), the original matrix contains 544 elements > 0, corresponding to an emittance of $\varepsilon(100\%) = 544{\cdot}0.413/\pi = 71.58\,\mathrm{mm} \times \mathrm{mrad}$. On the other hand, in the 80% matrix, reduced according to the emittance mode algorithm, only 432 elements > 0 are left, which leads to an emittance of $\varepsilon(80\%) = 56.85\,\mathrm{mm} \times \mathrm{mrad}$. Therefore, in this mode, the size of the emittance corresponds to about the chosen percentage ($56.85/71.58 = 0.794$).

Intensity Mode

In this mode, the maximum intensity gives the reference for the percentages. In the corresponding algorithm, the value calculated for a chosen percentage is subtracted from each element. Elements below zero are set to zero. In Fig. 6.17, the corresponding MATHCAD program code is listed. The resulting

$$I100 := \sum_{ix} \sum_{iy} E_{ix,iy} \qquad I100 = 139.805 \qquad = 100\% \qquad PERCENT := 80$$

$$TOTALSUBTRACT := I100 \cdot \frac{100 - PERCENT}{100} \qquad TOTALSUBTRACT = 27.961$$

$$ELEMENTSUBTRACT := \frac{TOTALSUBTRACT}{nx \cdot ny} \qquad ELEMENTSUBTRACT = 0.031$$

$$STEPNUMBER := 100 \qquad SUBTRACTPERSTEP := \frac{ELEMENTSUBTRACT}{STEPNUMBER}$$

$$SUBTRACTPERSTEP = 3.107 \times 10^{-4} \qquad \text{Subtraction per iteration step}$$

```
NEWMATRIX :=
    SUBTRACT ← 0
    for i ∈ 0.. nx − 1
        for j ∈ 0.. ny − 1
            NEW_{i,j} ← E_{i,j}
    while |(SUBTRACT − TOTALSUBTRACT) / TOTALSUBTRACT| > 5·10^−3
        for i ∈ 0.. nx − 1
            for j ∈ 0.. ny − 1
                S ← NEW_{i,j} − SUBTRACTPERSTEP
                if S < 0
                    SUBTRACT ← SUBTRACT + NEW_{i,j}
                    NEW_{i,j} ← 0
                if S > 0
                    SUBTRACT ← SUBTRACT + SUBTRACTPERSTEP
                    NEW_{i,j} ← S
    NEW
```

$$\max(E) = 1 \qquad \max(NEWMATRIX) = 0.941$$

Fig. 6.15. Programming example in MATHCAD to determine size and shape of emittances dependent on a given percentage. In the example, the 80% emittance is evaluated in the so-called "Emittance Mode." **Remark:** In the program *ny* stands for $n_{x'}$, see text

data are presented in Fig. 6.19, together with the results from the "Minimum Subtraction Mode" (see below).

Minimum Subtraction Mode

In this mode, the reference value for the percentage is again the sum over all intensities as in the "Emittance Mode." But, to subtract the calculated amount from each element, the smallest values are removed (set to zero) as long as the required value is achieved. The corresponding program algorithm is shown in Fig. 6.18. No subtraction takes place from large elements in the matrix. This is shown at the end of the program (see Fig. 6.18) where the maximum of $I_{xx'}$ is displayed before [max(E) = 1] and after [max(ENEW) = 1] treatment of the data. Because it can happen, that the last subtraction step is larger than that required, the resulting difference is added to the last processed element at the end of the program.

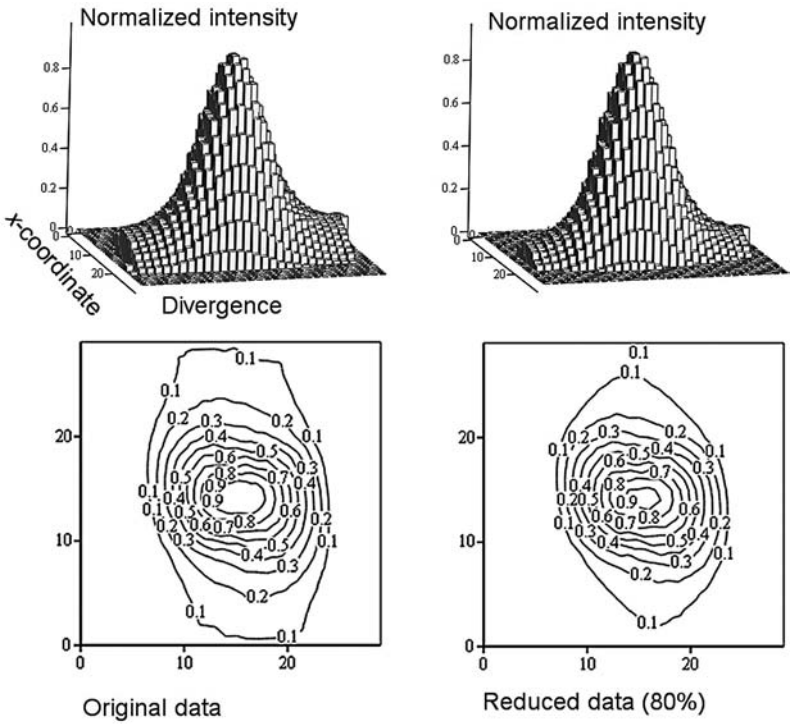

Fig. 6.16. Comparison of the original emittance data with an 80% emittance evaluated in the "Emittance Mode." In the example, a matrix of 30×30 values represents the measured data. Keep in mind that the surface plots at the bottom have to be rotated 90° to the right to compare with the 3-D plots on top. The numbers on the x- and y-axes in all plots present the index $(1 \ldots 30)$ of the data matrix

The 3-D displays as well as the contour plots are compared in Fig. 6.19. Obviously, the two modes last discussed lead to considerable changes in the shape of the emittance as well as to a large reduction of their size. Ultimately, which evaluation method has to be applied depends on the problem of beam transport, respectively, beam manipulation, studied. It should be clear that an algorithm based on the subtraction of a given percentage from each element in the matrix does not change the shape and size of the pattern measured. A complex measured emittance pattern may look like that illustrated in Fig. 6.20

Evaluation of Beam and Angular Profiles

From the example shown in Fig. 6.13, it is clear that a summation over all columns of the data matrix will result in a distribution of the intensity over the x-coordinate $I(x)$, which is the beam profile. On the other hand, a summation over the rows results in a distribution $I(x')$, representing the measured

$\max(E) = 1 \qquad PERCENT := 80$

$$SUBTRACT := \max(E) \cdot \frac{100 - PERCENT}{100} \qquad SUBTRACT = 0.2$$

```
ENEW := | for i ∈ 0 .. nx − 1
        |   for j ∈ 0 .. ny − 1
        |     | NEW_{i,j} ← E_{i,j}
        |     | NEW_{i,j} ← 0  if  E_{i,j} < 0
        | for i ∈ 0 .. nx − 1
        |   for j ∈ 0 .. ny − 1
        |     | S ← NEW_{i,j} − SUBTRACT
        |     | NEW_{i,j} ← 0  if  S < 0
        |     | NEW_{i,j} ← S  if  S > 0
        | NEW
```

$\max(E) = 1 \qquad \max(ENEW) = 0.8$

Fig. 6.17. Programming example in MATHCAD to determine size and shape of emittances dependent on a given percentage. In the example, the 80% emittance is evaluated in the so-called "Intensity Mode." **Remark:** *ny* stands for $n_{x'}$; see text for details

divergences in the beam. Processing the original data of the example, shown on the left of Fig. 6.16, results in the profiles shown in Fig. 6.21.

Determination of rms Values and Twiss Parameters

There are various methods for determining the Twiss parameters from the measured data. Using rms values, determined from $I(x)$ and $I(x')$ in the description of a two-dimensional Gaussian normal distribution, is one of the most applied methods. The relevant formulas are

$$\text{Sum} = \sum_{n_x} \sum_{n_{x'}} E_{n_x, n_{x'}} \tag{6.22}$$

$$X_0 = \frac{1}{\text{Sum}} \sum_{n_x} \sum_{n_{x'}} n_x \, E_{n_x, n_{x'}} \tag{6.23}$$

$$X_c = X_0 \, dx + x_{\min} \tag{6.24}$$

$$X'_0 = \frac{1}{\text{Sum}} \sum_{n_x} \sum_{n_{x'}} ny \, E_{n_x, n_{x'}} \tag{6.25}$$

$$X'_c = X'_0 \, dx' + x'_{\min} \tag{6.26}$$

$$\text{SUBTRACT} := \text{I100} \cdot \frac{100 - \text{PERCENT}}{100} \qquad \text{SUBTRACT} = 27.961$$

```
ENEW := | SUBTRACTED ← 0
        | for i ∈ 0 .. nx − 1
        |   for j ∈ 0 .. ny − 1
        |     NEW_{i,j} ← E_{i,j}
        | while SUBTRACT − SUBTRACTED > 0
        |   | MIN ← max(NEW)
        |   | for i ∈ 0 .. nx − 1
        |   |   for j ∈ 0 .. ny − 1
        |   |     | S ← NEW_{i,j}
        |   |     | if S < MIN  if S > 0
        |   |     |   | MIN ← S
        |   |     |   | l ← j
        |   |     |   | k ← i
        |   | NEW_{k,l} ← 0
        |   | SUBTRACTED ← SUBTRACTED + MIN
        | NEW_{k,l} ← SUBTRACTED − SUBTRACT
        | NEW
```

$$\max(E) = 1 \qquad \max(ENEW) = 1$$

Fig. 6.18. Programming example in MATHCAD to determine the size and shape of emittances dependent on a given percentage. In the example, the 80% emittance is evaluated in the so-called "Minimum Subtract Mode." **Remark:** *ny* stands for $n_{x'}$; see text

Here X_c and X'_c are the center of the x-coordinates and x'-coordinates, respectively. They are derived from the corresponding index X_0, X'_0. The rms values σ_x, σ_y, and ρ of the Gaussian distribution

$$f(x,x') = S_0\, e^{S_1\left[\left(\frac{x-X_0}{\sigma_x}\right)^2 - \frac{2\rho\,(x-X_0)(x'-X'_0)}{\sigma_x\,\sigma x'} + \left(\frac{x'-X'_0}{\sigma_{x'}}\right)^2\right]} \tag{6.27}$$

$$S_0 = \frac{1}{\sigma_x \sigma_{x'} 2\pi\sqrt{1-\rho^2}} \tag{6.28}$$

$$S_1 = \frac{-1}{2\,(1-\rho^2)}, \tag{6.29}$$

are determined from

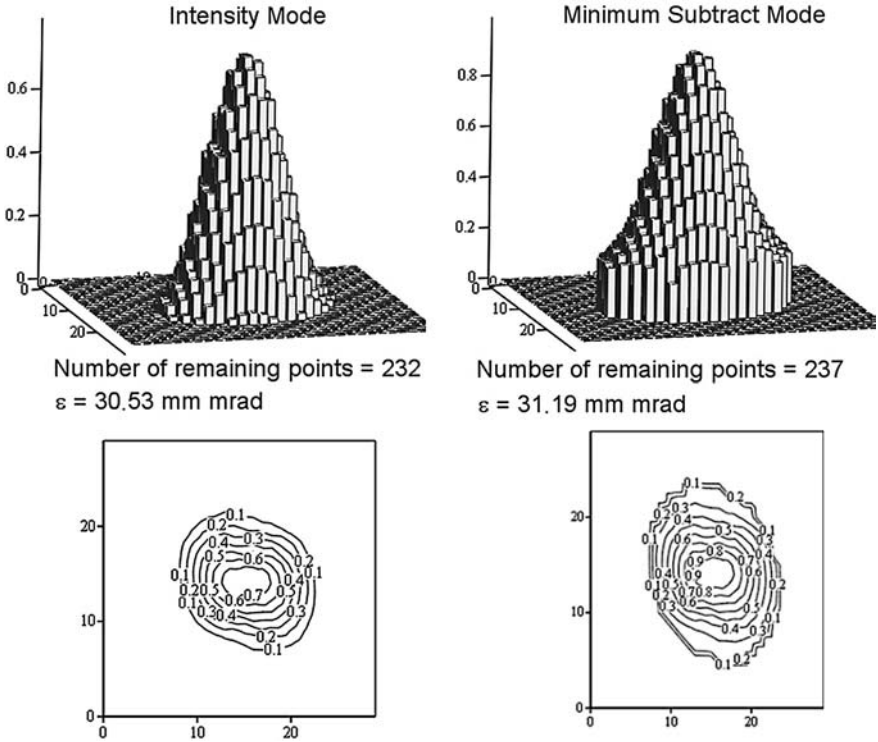

Fig. 6.19. Comparison of the 80% emittances evaluated in the "Intensity Mode" (left) and "Minimum Subtract Mode" (right). See also Fig. 6.16 for further explanations and comparison with the original data

$$D_{\mathrm{x}} = \frac{1}{\mathrm{Sum}} \sum_{n_{\mathrm{x}}} \sum_{n_{\mathrm{x}'}} \left[n_{\mathrm{x}} - X_0\right]^2 E_{n_{\mathrm{x}},\, n_{\mathrm{x}'}} \tag{6.30}$$

$$D_{\mathrm{x}'} = \frac{1}{\mathrm{Sum}} \sum_{n_{\mathrm{x}}} \sum_{n_{\mathrm{x}'}} \left[n'_{\mathrm{x}} - X'_0\right]^2 E_{n_{\mathrm{x}},\, n_{\mathrm{x}'}} \tag{6.31}$$

$$M_{\mathrm{x}x'} = \frac{1}{\mathrm{Sum}} \sum_{n_{\mathrm{x}}} \sum_{n_{\mathrm{x}'}} \left[n_{\mathrm{x}} - X_0\right] \left[n'_{\mathrm{x}} - X'_0\right] E_{n_{\mathrm{x}},\, n_{\mathrm{x}'}} \tag{6.32}$$

$$\sigma_{\mathrm{x}} = \sqrt{D_{\mathrm{x}}} \qquad \sigma_{\mathrm{x}'} = \sqrt{D_{\mathrm{x}'}} \qquad \rho = \frac{M_{\mathrm{x}\mathrm{x}'}}{\sigma_{\mathrm{x}}\, \sigma_{\mathrm{x}'}} \,. \tag{6.33}$$

Of course, the representation by the normalized Gaussian distribution results in smoothing the measured data in the three-dimensional representation as well as in the two-dimensional display of the beam profile and angular profile.

To evaluate the rms values of the Twiss parameters, σ_{x}, $\sigma_{\mathrm{x}'}$, and in consequence ρ have to be converted as follows:

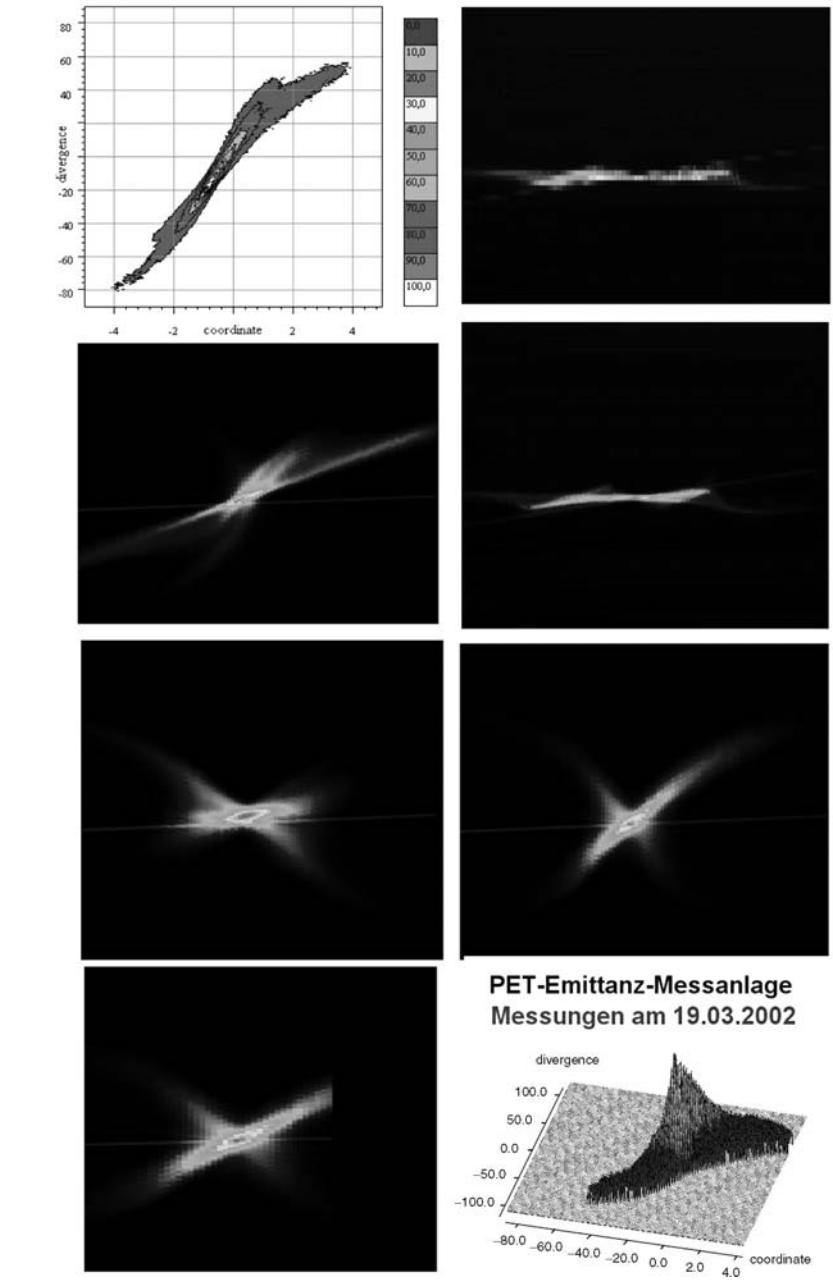

Fig. 6.20. Computer display (colored) of measured emittance data studying space charge effects and as well as quadrupole lens aberrations on a test stand for development of highly intense ion sources. The pictures were taken at the Institut für Angewandte Physik der Universität Frankfurt, Germany [299, 300]

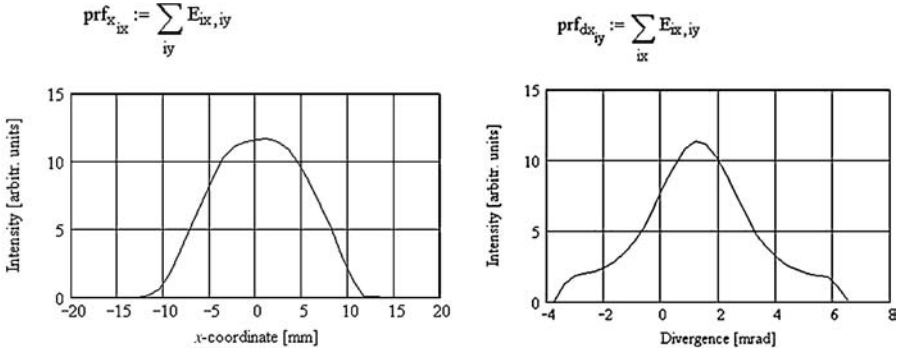

Fig. 6.21. Beam profile $I(x)$ and angular profile $I(x')$ derived from the original data matrix of the example under discussion

$$\sigma_{\mathrm{x}} \rightarrow \frac{x_{\max} - x_{\min}}{n_{\mathrm{x}}}\,\sigma_{\mathrm{x}} \tag{6.34}$$

$$\sigma_{\mathrm{x}'} \rightarrow \frac{x'_{\max} - x'_{\min}}{n_{\mathrm{x}'}}\,\sigma_{\mathrm{x}'}\ , \tag{6.35}$$

leading immediately to the rms values of the Twiss parameters:

$$\varepsilon = 4\,\sigma_{\mathrm{x}}\,\sigma_{\mathrm{x}'}\sqrt{1-\rho^2} \tag{6.36}$$

$$\beta = \frac{\sigma_{\mathrm{x}}}{\sigma_{\mathrm{x}'}}\,\frac{1}{\sqrt{1-\rho^2}} \tag{6.37}$$

$$\gamma = \frac{\sigma_{\mathrm{x}'}}{\sigma_{\mathrm{x}}}\,\frac{1}{\sqrt{1-\rho^2}} \tag{6.38}$$

$$\alpha = -\rho\,\sqrt{\beta\,\gamma}\ ,\ \text{with}\ \beta\gamma - \alpha^2 = 1. \tag{6.39}$$

It is of interest to compare the dependency of the Twiss parameters, representing the original data as well as the 80% values of the example discussed above. Figure 6.22 compares the 100% values of the original data with the 80%-values, evaluated according to the modes discussed. Referring

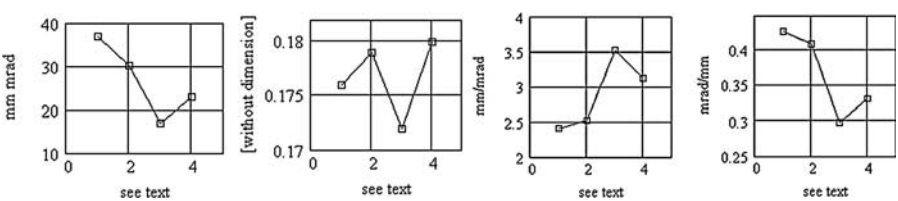

Fig. 6.22. Left: rms emittance, point 1 = 100% value; point 2 = 80% value according to the "Emittance Mode"; point 3 = 80% value in the "Intensity Mode"; point 4 = 80% value in the "Minimum Subtract Mode." The next diagrams show α, β, γ in the same order

to Figs. 6.16 and 6.19, the rms emittances are significantly smaller than the values from the direct evaluation of the data matrix. The ratio depends on the model of the density distribution, used as an approximation for describing a realistic beam. The dependency of this ratio is discussed in detail in [309], studying five different models of distribution functions. As a consequence, the authors conclude:

"... Of the different types considered, the truncated Gaussian distribution represents undoubtedly the closest approximation to a laboratory beam."

Beside the dependencies of the Twiss parameters on the distribution function, the dependency on the percentage is also of interest. The "Emittance Mode" is the most used mode for data evaluation, and the Gaussian distribution function seems to be the most realistic. Figure 6.23 presents the data obtained from the example.

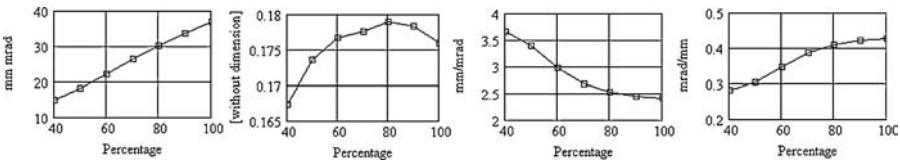

Fig. 6.23. Left: rms emittance dependent on the percentage, next three from the left in this order: α, β, γ. The data evaluation is performed in the "Emittance Mode" for a Gaussian distribution

Conversion of Data for Ray-Tracing Programs

Although the description of intensity distributions by the Twiss parameters is very useful for studying the action of beam transport elements such as quadrupoles, magnets, and steerers, more refined studies will require the application of programs. Therefore, the evaluation software of an emittance measuring system should offer an output of data, adapted to the format of the corresponding ray-tracing program. Thus, the evaluation software of the system referred to in [299,300] can convert the data in the PARMTRA format. In the example of Fig. 6.24, the operator has to specify the number of particles (here 5000) as well as the mode of data evaluation (here "Emittance Mode") to generate a file in the PARMTRA format.

6.2.3 Other Emittance Measuring Systems

Fast Emittance Measuring System

Fast measurement and continuous monitoring of emittances, in connection with on-line calculation and visualization of beam envelopes, during operation of an accelerator can be very efficient for the following reasons:

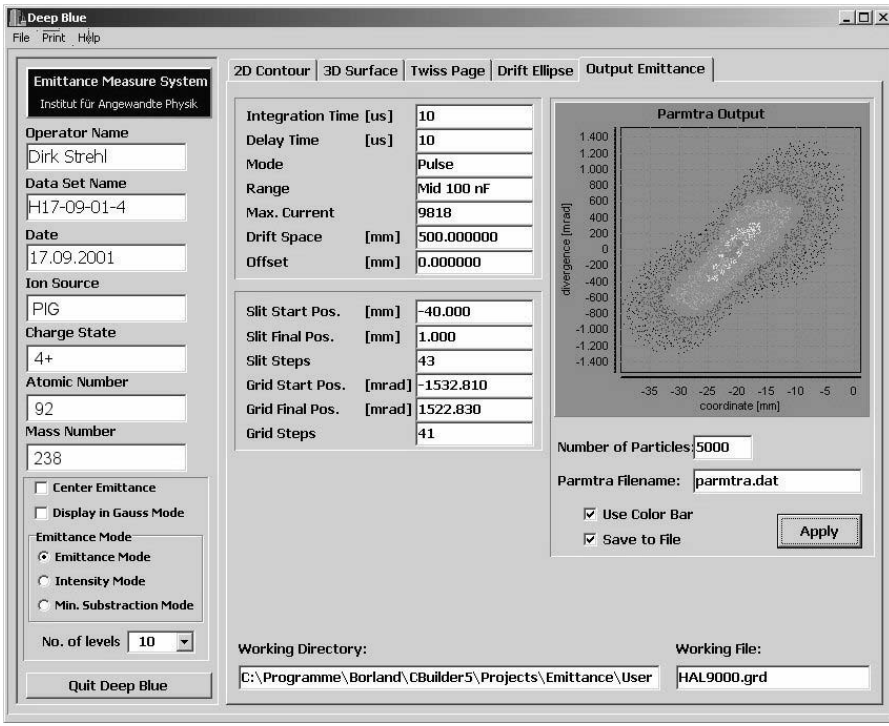

Fig. 6.24. Computer display to specify the output data file in PARMTRA format [299,300]

- The ion source may change characteristics during its lifetime, which holds especially for sputtering ion sources of the PIG type. As a consequence the flow of charged particles through a machine can decrease. Thus, continuous monitoring of emittance during routine operation of a machine can be very helpful and efficient.
- The same arguments hold with respect to frequent changes in the kinds of ions, typical for universal heavy ion accelerators.
- Last but not least, a fast emittance measuring system, in connection with an appropriate fast display of relevant data, can be very helpful for ion source development and accelerator experiments, provided for the development of optimization procedures.

Experience has shown that the installation of such a fast measuring system in the injection, respectively, low energy area, can be very effective. The low beam energy offers the possibility of sweeping a part of the beam over a slit detector system instead of moving the mechanics through the beam. Figure 6.25 shows schematically a system [310,311] that combines a very fast, nearly, non-destructive emittance scan with the total destructive system, moving through the beam. In the conventional method, the slit-sandwich detector

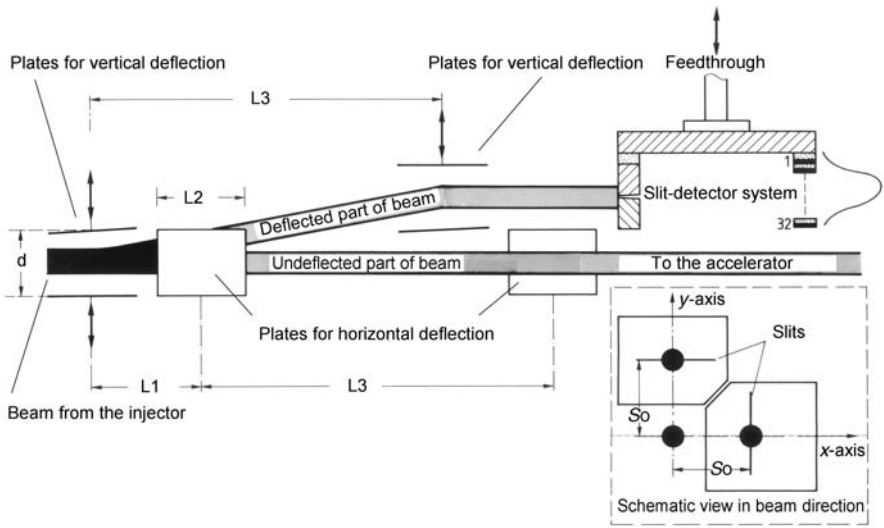

Fig. 6.25. Scheme of a fast emittance measuring system based on a slit - sandwich-detector system. See text for details

systems can be moved sequentially through the beam, performing high precision emittance measurements. For continuous monitoring, both devices are positioned near the boundaries outside the beam, parallel to the beam line. To sweep the beam over the slit-detector units, two sets of horizontal and vertical deflecting plates are installed in front of the measuring systems. The sweep is performed by an electric field, modulated by a staircase function. Taking the x-direction to derive the required voltage, the angle of deflection α is given by

$$\tan\alpha = \frac{S_0}{L_3} = \frac{\dot{x}}{\dot{z}} = \frac{\dot{x}}{\beta c} \; . \tag{6.40}$$

Proposing low β values, $\dot{x}$ can be calculated in a nonrelativistic approximation from the well-known formula,

$$m\ddot{x} = \zeta e E_{\mathrm{x}} \; , \tag{6.41}$$

with $m = A\,m_0$ the mass of the ions, ζ their charge, and $E_{\mathrm{x}} = U/d$ as the electric deflecting field strength ($e = 1.6 \times 10^{-19}$ As). From (6.41), $\dot{x} = \zeta e E_{\mathrm{x}} t/m$ with $t = l/\dot{z}$ as the time of flight through the plates. This leads immediately to the required deflecting voltage U:

$$U = \frac{A}{\zeta}\,\frac{S_0 d}{L\,l}\,m_0 c^2\,\beta^2 \; . \tag{6.42}$$

Referring to Fig. 6.25, it is evident that there are two free parameters due to the possibility of changing the width d as well as the distance from the slit to

Table 6.2. Characteristic parameters of the fast emittance measuring system

Minimum deflecting voltage	9.200 V
Maximum deflecting voltage	18.500 V
Increment in voltage	300 V
Minimum time per increment	1 ms
Covered range in x, y-coordinates	$\pm$ 7.5–25 mm
Covered range in divergence	$\pm$ 16 mrad
Current range	10 nA–100 µA
Resolution in x , y-coordinates	0.1 mm
Resolution in divergence	1 mrad
Step width in position	0.5–1.6 mm

the beam axis S_0. Taking advantage of this mechanical flexibility, the power supply to generate the required deflecting voltages has been designed to sweep between two fixed values $U_{\min}$ and $U_{\max}$ dividing the stroke $U_{\max} - U_{\min}$ into 31 steps to realize staircase modulation. Referring to [310], the mechanical design parameters $40\,\text{mm} \leq S_0 \leq 75$ mm, $31\,\text{mm} \leq d \leq 60\,\text{mm}$, $L_3 = 552\,\text{mm}$, $l = 110\,\text{mm}$ lead to the system parameters, given in Table 6.2, for a β value of 0.5%.

A picture of the large vacuum chamber, equipped with all parts, provided for emittance measurements in both transverse phase planes is shown in Fig. 6.26.

A System to Handle High Beam Power

As discussed in Chap. 3, it can be necessary to tilt the surface of stopping devices to avoid melting the material due to high beam power density in connection with low penetration depth of particles. Figure 6.27 shows a slit-detector system for emittance measurements for very intense beams (≈20 kW dc), with low penetration depth (of the order of mm). Since the power density behind the slit would melt tungsten wires or tantalum collector strips, a second cooled slit in front of a small Faraday cup is used as a detector. Of course, scanning the profile for each position of the slit increases the measuring time up to some minutes.

Crossed Slit Systems

In the examples discussed up to now, determination of emittances in both transverse phase planes requires the installation of two complete systems, measuring one plane after the other one. In some cases, it may also be sufficient to use only one system installed either on the horizontal ports or on the vertical ones. This, of course, requires some effort and a lot of time. Using a cross-like slit with an appropriate detector, instead of a harp, offers the possibility of measuring simultaneously in both planes. Two types of suitable detectors

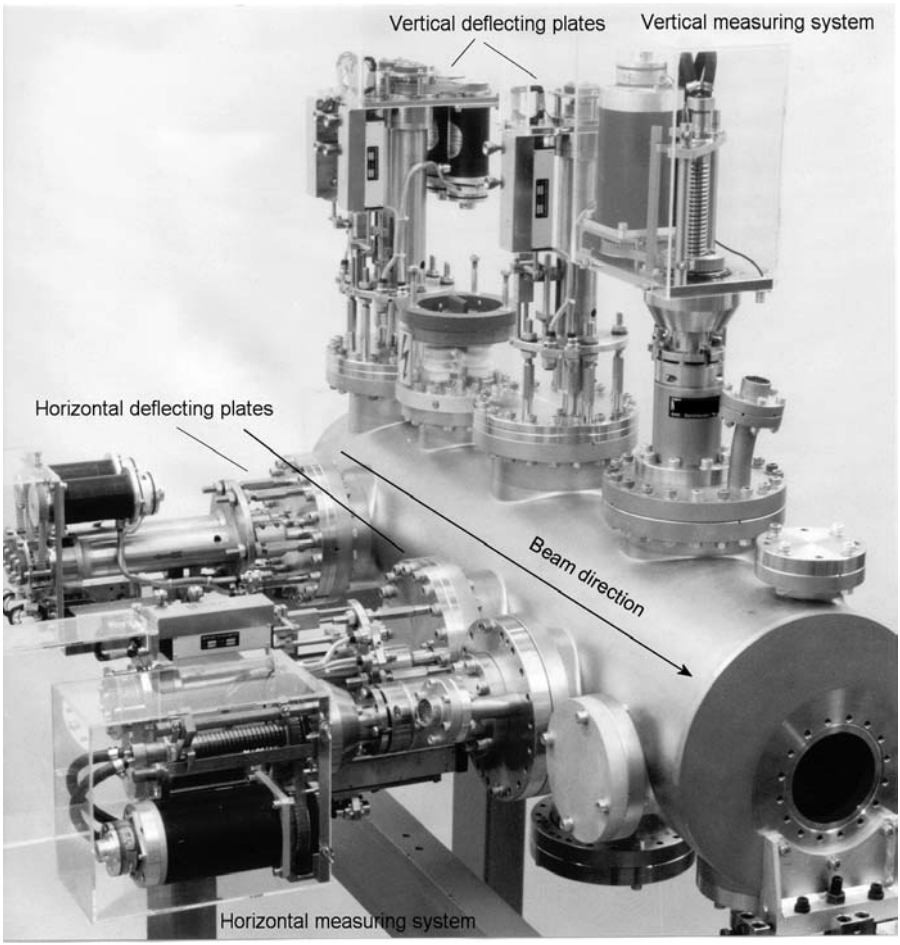

Fig. 6.26. Large beam diagnostic chamber, housing deflecting plates and emittance measuring systems. GSI Foto

are shown in Fig. 6.28. The detector shown on the left-hand side is a special profile grid, which has to be moved together with the cross-like slit in a 45° direction through the beam. The detector, shown schematically on the right-hand side of Fig. 6.28, consists of two thin scanning wires which are driven by an eccentric motion of a fork connected to two rotating disks.

The system using scheme (a) of Fig. 6.28 as a detector offers all options for intermediate steps as well as offset positions. Of course, a factor of $\sqrt{2}$ has to be considered in the system design as well as in the evaluation of data. On the other hand, a system based on the detector scheme (b) of Fig. 6.28 requires only one feedthrough, which results in compact mechanics. Figure 6.29 shows a complete unit (the scanning wires are not mounted). Two motors are provided

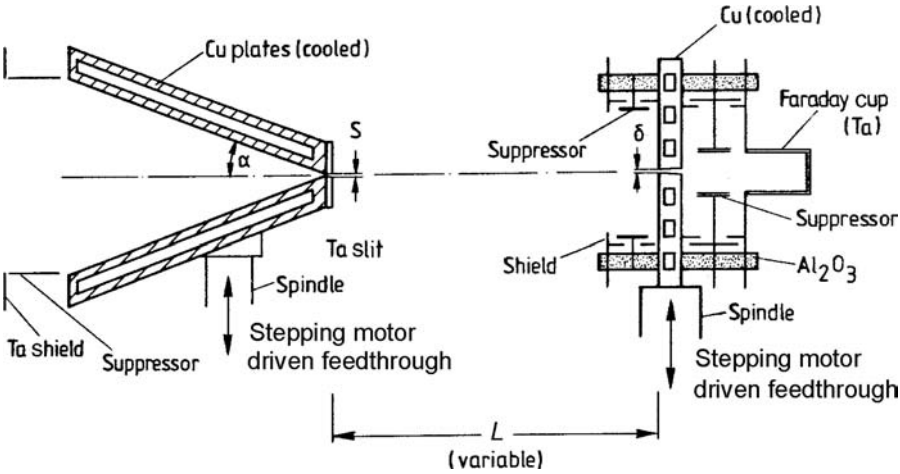

Fig. 6.27. Slit detector system, provided for emittance measurements of very high beam power and low penetration depth

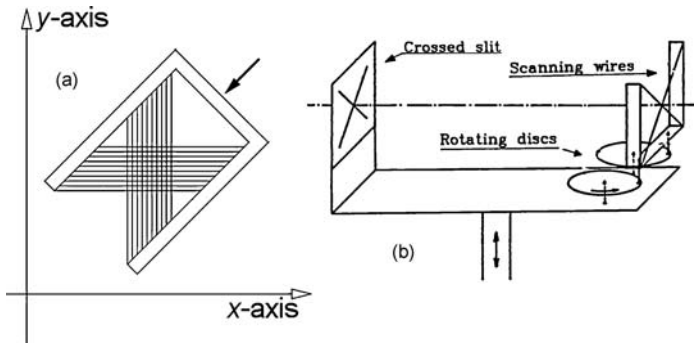

Fig. 6.28. Two schemes of detectors suitable for measuring profiles in x- and y-directions at the same time. Left (a): profile grid, right (b): scanning wires

to perform the translation of the crosslike slit as well as the scanning motion of the detector wires. A stepping motor is used for the translation; the rotating disks are driven by a dc-motor.

Because the movement of the crosslike slit is slow in comparison to the speed of the scanning wires, the unit can be moved continuously through the beam, taking advantage of fast ADCs to determine synchronously the position of the slit, the position of the scanning wires, and the measured profiles. Due to the difficulty of synchronizing the scanning motion of the detector wires with a pulsed beam, the measuring system is not suitable for pulsed beams. In the evaluation of the data, the variable distance between slit and detector wires due to the eccentric motion has to be taken into account. In the example considered, this distance is determined by the simple geometric

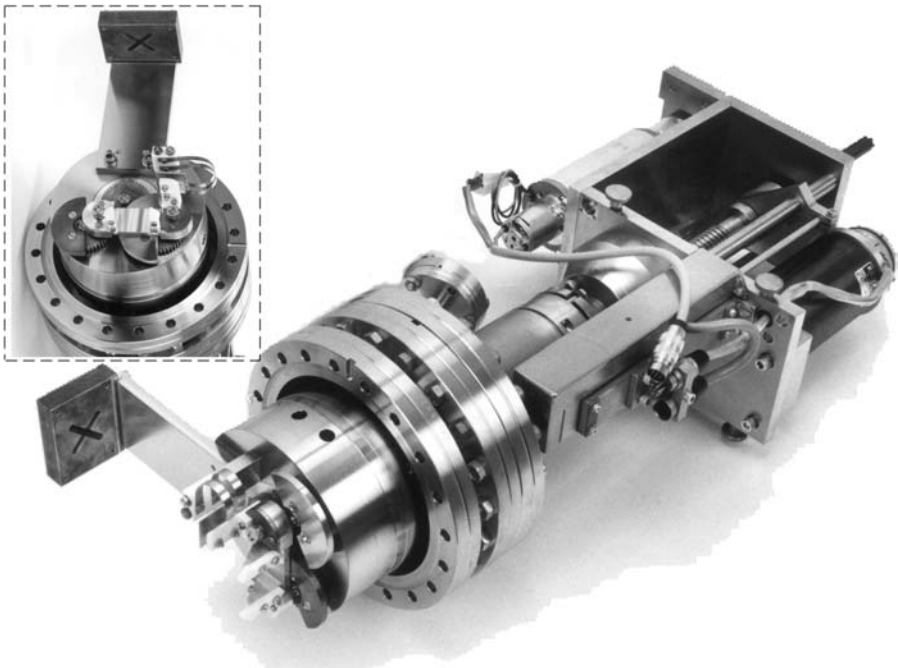

Fig. 6.29. Mechanics of an emittance measuring system moving a crosslike slit together with two scanning wires according to scheme (*b*) of Fig. 6.28 through the beam. The picture shows the crosslike slit seen against the beam direction. The scanning wires are not yet mounted into the supporting fork. The inset shows the rotating disks with the eccentrically mounted supporting fork. GSI Foto

relation $L(\varphi) = l_0 - r_0 \cos(\varphi)$, where l_0 is the distance between the slit and the line through the axes of the two driving disks and r_0 is the offset of the eccentrically mounted supports. The most important specifications of the emittance measuring system shown in Fig. 6.29 are summarized in Table 6.3:

The relatively low specified beam power of 400 W did not lead to any relevant restrictions, since the system has been developed for the study of ion sources [312], where the relatively short measuring time of about 13 s can be advantageous.

Error Estimation

Using systems with a crosslike slit results in a contribution to the detector from the second cross arm, which falsifies the profile measurements. This is illustrated, simplified in Fig. 6.30, with a profile grid as a detector. An estimation of the error in emittance determination is very complex, since the relative contribution from the crossed slit to the measured profile depends very much on

Table 6.3. Characteristic parameters of the emittance measuring system, shown in Figure 6.29.

Stroke of the feedthrough	100 mm
Displacement per step of 1.8°	0.003 mm
Maximum acceleration	400 mm/s^2
Maximum speed of translation	15 mm/s
Resolution of position measurement	0.1 mm
Dimension of the crosslike slit	2 × 0.1 mm × 30 mm
Material of the crosslike slit	Tantalum
Backing (without water cooling)	Copper
Maximum allowed beam power	400 W
Distance l_0	205 mm
Dimensions of the scanning wires	0.05 × 42 mm
Material of the scanning wires	Tungsten
Maximum measurable divergence	± 50 mrad
Resolution in divergence	< 0.7 mrad
Measuring time per position of the slit	≈ 31 ms
Total measuring time	≈ 13 s

- the position of the crosslike slit;
- the shape of the emittance patterns, determined mainly by the beam extensions and the maximum divergences in both phase planes;
- the slit and detector dimensions; and
- the distance between slit and detectors.

Referring to Fig. 6.30 and considering, for example, the profile measurement in the horizontal direction, it is evident that the relative contribution

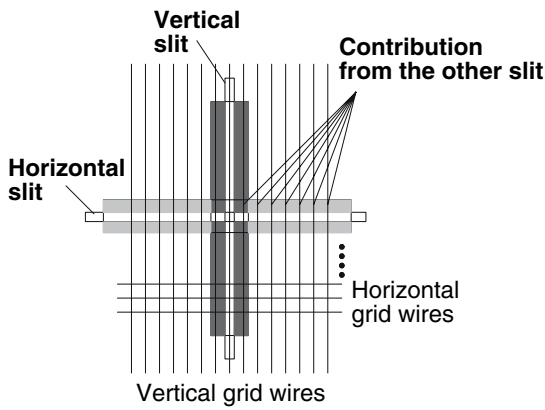

Fig. 6.30. Simplified scheme to illustrate the falsification of the measured profile behind a crosslike slit. The black and gray areas indicate the extension of the beam on the detector wires behind the slit

from the horizontal slit increases with increasing displacement x_d of the detector wire from the position centered behind the vertical slit. Corrections measured data should be possible after the measurement. The ratio V_i between the currents from the two arms of the crosslike slit can be very roughly estimated by approximating the intensity behind the two slits $f^{\,x}(x,y)$, $f^{\,y}(x,y)$, by parabolic distributions:

$$f^{\,x}(x,y) = \frac{9}{16\, x^y_\mathrm{max}\, y^y_\mathrm{max}} \left[1 - \left(\frac{x}{x^y_\mathrm{max}}\right)^2\right] \left[1 - \left(\frac{y}{y^y_\mathrm{max}}\right)^2\right] \tag{6.43}$$

$$f^{\,y}(x,y) = \frac{9}{16\, x^y_\mathrm{max}\, y^y_\mathrm{max}} \left[1 - \left(\frac{x}{x^y_\mathrm{max}}\right)^2\right] \left[1 - \left(\frac{y}{y^y_\mathrm{max}}\right)^2\right] . \tag{6.44}$$

Here x^x_max, y^x_max are the maximum extensions behind the vertical slit and x^y_max, y^y_max behind the horizontal slit, respectively. Assuming the same geometries for both directions, as well as a round beam with radius R_b, the ratio V_i is independent of the beam current and, therefore can be normalized as follows:

$$\int_{-y^x_\mathrm{max}}^{y^x_\mathrm{max}} \int_{-x^x_\mathrm{max}}^{x^x_\mathrm{max}} f^{\,x}(x,y)\, dx\, dy = \int_{-y^{\,y}_\mathrm{max}}^{y^{\,y}_\mathrm{max}} \int_{-x^y_\mathrm{max}}^{x^y_\mathrm{max}} f^{\,y}(x,y)\, dx\, dy = 1 \, .$$

Considering the profile measurement behind the vertical slit (means that the emittance is measured in the horizontal phase plane), x^x_max, y^x_max in (6.43) can be approximated by

$$x^x_\mathrm{max} \approx \frac{\delta_\mathrm{s}}{2} + L\, x'_\mathrm{max} \tag{6.45}$$

$$y^x_\mathrm{max} \approx R_\mathrm{b} + L\, y'_\mathrm{max} \, . \tag{6.46}$$

The parameters x'_max and y'_max depend on the slit position, as discussed for (6.13–6.16). The normalized contribution from the vertical slit is given by

$$i(x) = \int_{-y^x_\mathrm{max}}^{y^x_\mathrm{max}} \int_{\mathrm{x_d}-\delta_\mathrm{x}/2}^{x_\mathrm{d}+\delta_\mathrm{x}/2} f^x(x,y) dx\, dy \, , \tag{6.47}$$

where δ_x is the width of the detector and x_d is its position, measured against the center of the slit. On the other hand,

$$x^y_\mathrm{max} \approx R_\mathrm{b} + L\, x'_\mathrm{max} \tag{6.48}$$

$$y^y_\mathrm{max} \approx \frac{\delta_\mathrm{s}}{2} + L\, y'_\mathrm{max} \, , \tag{6.49}$$

and the normalized contribution of "false current" from the horizontal slit is given by

$$i(y) = \int_{-y^y_\mathrm{max}}^{y^y_\mathrm{max}} \int_{\mathrm{x_d}-\delta_\mathrm{x}/2}^{x_\mathrm{d}+\delta_\mathrm{x}/2} f^{\,y}(x,y)\, dx\, dy \, . \tag{6.50}$$

The ratio $V_\mathrm{i} = i(y)/i(x)$ can be determined in analytical form by solving the integrals of (6.47) and (6.50), leading to

$$V_\mathrm{i} = \frac{\left(x^x_\mathrm{max}\right)^3 \left(x^y_\mathrm{max}\right)^2 - 12\,x_\mathrm{d}^2 - \delta_\mathrm{x}^2}{\left(x^y_\mathrm{max}\right)^3 \left(x^x_\mathrm{max}\right)^2 - 12\,x_\mathrm{d}^2 - \delta_\mathrm{x}^2}\ . \tag{6.51}$$

The approximation (6.51) does not consider that the contribution from the region, where both slit arms cross each other, does not lead to a falsification of the horizontal profile and, therefore gives only a very rough estimation of the errors arising. Furthermore, due to the parabolic approximations of profiles behind the slits, $V_\mathrm{i} \to \infty$ for $xd \to x^x_\mathrm{max}$. Replacing the parabolic distributions by Gaussian ones shows very similar results, if the necessary numerical integrations are performed. Since the ratio V_i can be of the order of some 10%, the application of crosslike slits cannot be recommended for precise emittance measurements.

The Pepper-Pot System

The measuring systems described up to now have some drawbacks:

- Due to the relatively slow movement of slit-detector systems through the beam, the measuring time becomes rather long. Although this time will be of the order of some $10s$ up to about 1 minute for dc-beams, this can extend to some minutes for pulsed beams with a low repetition rate, due to the necessary synchronization. Therefore, fluctuations of beam intensity and, possibly emittance, cannot be observed during the measuring time. However, this can be very important, for example, to assess the performance of new types of ion sources. Furthermore, highly intense pulsed beams with a low repetition rate and very low penetration depth can require a measurement within one beam pulse to avoid thermal destruction of the materials.
- Due to the integration over one phase plane, coupling effects between both transverse phase planes cannot be observed.

A possible solution offers the so-called "pepper-pot method" as analyzed and discussed in [292]. The principle is illustrated in Fig. 6.31.

The beam hits a plate with an appropriate number of small holes, arranged in the x, y-plane like the elements of lines and columns in a matrix. The sample beamlets, defined by this pattern, fall on a viewing screen, where the light spots are observed by a fast PC-controlled CCD-camera system. It is evident that the design of the hole pattern has to be adapted to the expected emittances to avoid overlap of beamlets. Taking this into account, the pattern of light spots will represent a four-dimensional "hyperemittance" (see also [292]), which, according to (6.1), (6.6), and (6.7), is derived from

$$V_4 = \int\int\int\int dx\,dp_\mathrm{x}\,dy\,dp_\mathrm{y}\ . \tag{6.52}$$

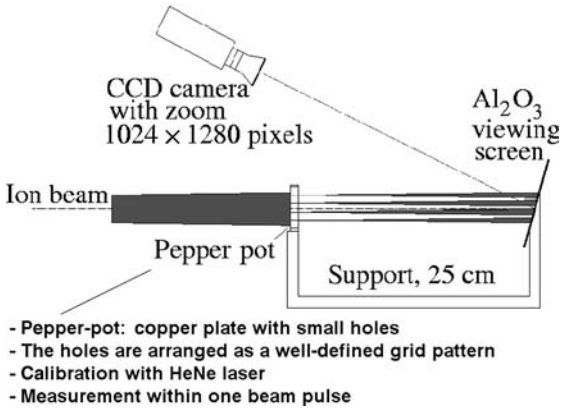

Fig. 6.31. Scheme of the "Pepper-Pot Method" to perform emittance measurements within one beam pulse [120]

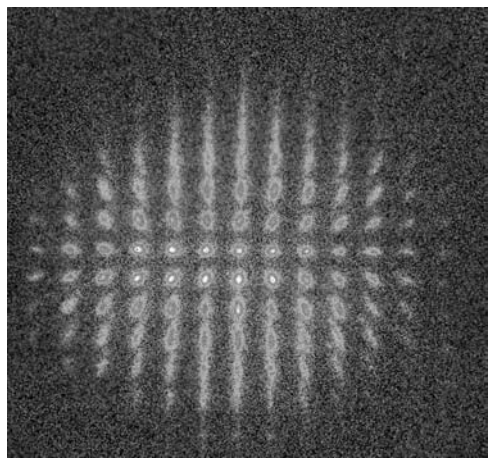

Fig. 6.32. Example of observed light spot pattern on the viewing screen of a pepper-pot emittance measuring system. See text for a more detailed description of the system. The picture was taken in the main control room of GSI

From a measured light spot pattern, as shown in the example of Fig. 6.32, a determination of the four-dimensional hyperemittance defined by

$$\varepsilon_4 = \frac{1}{\pi^2} \iiint dx\, dx' dy\, dy' \tag{6.53}$$

is possible [292]. However, in practice, determination of the two-dimensional emittances defined by (6.6) and (6.7) is of more interest.

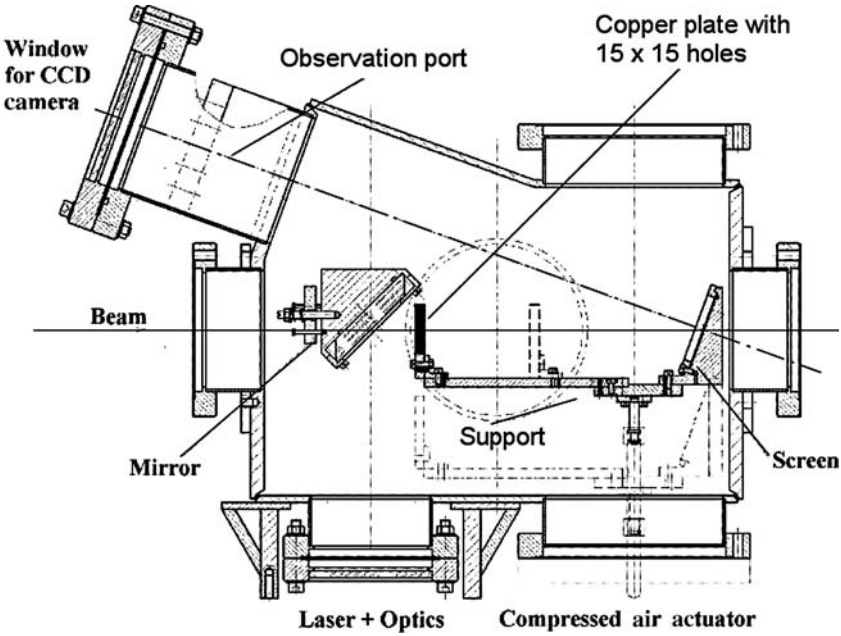

Fig. 6.33. Schematic drawing of the mechanics of a pepper-pot measuring system installed in the stripper section of the UNILAC

Example of a Pepper-Pot System

As an example, the relevant design parameters as well as appropriate evaluation procedures are discussed, referring to a system [313,315,316], to measure emittances of highly intense pulsed heavy ion beams. The complete system has been integrated into a compact measuring chamber, shown schematically in Fig. 6.33. The system is installed in the prestripper section of the UNILAC high current injector.

Alignment The achievable resolution in phase space coordinates depends very much on the alignment of the system. The alignment procedure consists of three steps:

- Alignment of the measuring chamber against the beam axis, which has to be performed only once when the chamber is installed into the beam line. For this purpose, the mirror and the pepper-pot plate are moved out of axis by two compressed air actuators (not shown in Fig. 6.33). Installing the He-Ne laser with a spot size of 0.8 mm in front of the system, the chamber is aligned exactly with beam axis.
- After this procedure, the pepper-pot plate and viewing screen are moved in and the laser beam is enlarged with a telescope lens system to a parallel beam, covering the pepper-pot plate. The pattern of light spots is observed on the PC display and stored in the computer.

- Afterward, the laser with the telescope lens is installed in a fixed position opposite the mirror. Then the mirror is moved in front of the pepper-pot plate and adjusted as long as the light spot pattern of the laser beam corresponds exactly to the stored one. Since the two compressed air actuators always move the mirror as well as the support bearing the pepper-pot plate and viewing screen exactly to the same position, alignment can be checked remotely at any time. Because the parallel laser beam has no divergence, the light spots, generated by the laser-mirror combination and observed on the PC display, guarantee exact calibration in the course of data evaluation.

Thermal Aspects Due to a maximum beam pulse power up to 1.4 MW, thermal aspects, as discussed in Chap. 3, had to be investigated very carefully. Taking the very low penetration depth of about 10 µm into account, it is evident that the beam at normal incidence will produce vapor and plasma instantaneously at the surface of the pepper-pot plate. Cooling will not help and tilting of the material surface against the beam axis (see Chap. 3) would complicate the mechanical design and evaluation of measured data very much. There are two possibilities to avoid melting the pepper-pot plate:

- reduction of the power density by enlarging the beam spot size.
- With a fast chopper installed in front of the high current injector, the beam pulse length can be shortened during an emittance measurement.

As a compromise, a beam spot size of 1200 mm^2 and a maximum beam pulse length of 200 µs was proposed to dimension the pepper-pot plate from the thermal point of view. Taking into account the "figures of merit" Q, as discussed in Chap. 3, copper was selected as the material for the pepper-pot plate. Assuming a parabolic intensity distribution over the beam spot with a size of 1200 mm^2, an increase in the temperature at the surface at the center of the beam of $\Delta T \simeq 800$ C for a beam pulse length of 200 µs has been calculated [313]. The rise in temperature, as shown in Fig. 6.34, shows the typical proportionality to $\sqrt{t}$, as discussed in Chap. 3.

Due to the pour thermal characteristics of Al_2O_3, which was selected as the screen material, thermal heating of the screen had to be investigated, too. The holes have a diameter of 0.1 mm and are arranged in a mesh 2.5 mm wide. Although only a small part of particles goes through the small pepper-pot holes, the power density, which is the relevant parameter, is diminished only a little by the divergence of the beamlets and the small tilt of the screen (see Fig. 6.33). Because heat transfer in the radial direction can be neglected completely on the timescale under consideration, the maximum temperature is determined only by the maximum power density at the position of the corresponding hole. Neglecting enlargement of the beam spot sizes, Fig. 6.35 shows the calculated maximum temperatures at the center of the small beam spots on the screen, reducing the beam pulse length to 50 µs. Although the calculation represents the worst case, it shows very clearly, that the viewing

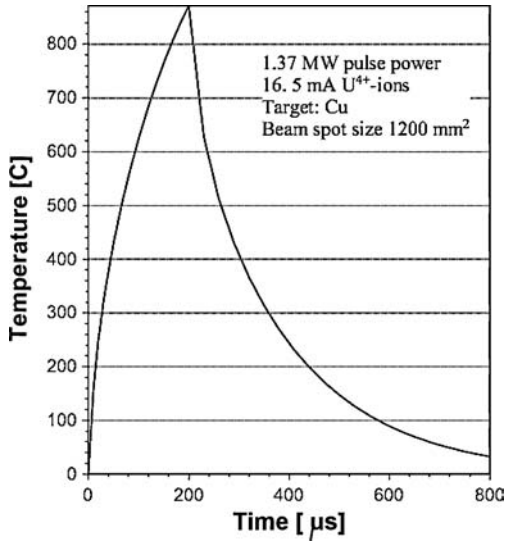

Fig. 6.34. Temperature as a function of time for one beam pulse, hitting the Cu pepper-pot plate

screen as the critical part in thermal heating determines the allowed beam pulse length during a measurement.

CCD Camera and Optics Fortunately, the required limitation in measuring time was not a problem in the exposure time required for the selected CCD-camera type, whose main characteristic data are given in Table 6.4 [314]. To extend the focal width into the macroregion, a remote control and some additional lenses improve the performance of the monitoring system. For example, having a magnification of 5:1, the spacing of the light spots on the PC display is enlarged to about 1.25 cm.

Determination of the Most Important Geometric Dimensions The maximum divergence that can be measured depends mainly on the spacing of the holes and the distance L between copper plate and viewing screen. For the following reasons, the distance L should not be too large:

- In most cases, there will be limitations on the allowed insertion length. This was also the case for the GSI system discussed.
- The necessary condition that the light spots of the beamlets are not allowed to overlap requires a small distance.
- A shorter distance L minimizes broadening of the beamlets due to the space charge.

Because the pepper-pot device has also been used to measure emittances behind the first accelerator section of the prestripper, enlargement of the small

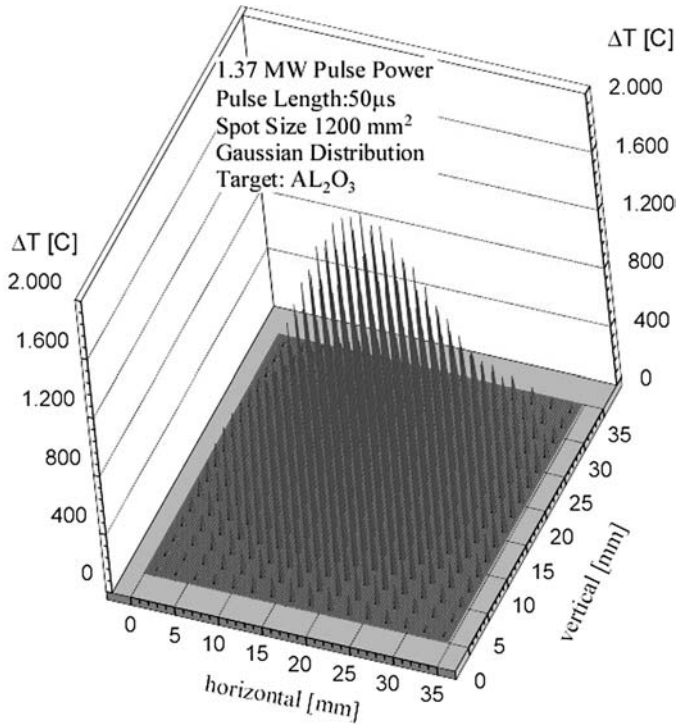

Fig. 6.35. Maximum temperature at the center of the beam spots behind the holes in the copper plate

partial beams has been estimated for a bunched beam of 120 keV/u U^{4+} ions using the formula [317]

$$r(z) = r_0 + \frac{\zeta i_{\text{hole}}\, z^2}{2.09^2\, \pi\, r_0\, c\, \varepsilon_0\, A\, m_0\, (\beta\gamma)^3}\ . \tag{6.54}$$

Here r_0 is the initial beam radius in a double waist; ζ is the charge state of the ions; z is the drift space; c is the velocity of light, $\varepsilon_0 = 8.8542 \cdot 10^{-12}$As/Vm; A is the number of the ions, and m_0 is the rest mass in [eV/c^2]. Figure 6.36 shows the calculated relative broadening $(r(z) - r_0)/r_0$ in percent. The two boxes have been calculated using a formula given in [318]:

$$r(z) = r_0 + 0.46 \left[\frac{\Delta U}{U} \left(\frac{z^2}{r_0} \right) \right] \tag{6.55}$$

$$\Delta U = \frac{i_{\text{hole}}}{4\pi\varepsilon_0 \beta\gamma c} \tag{6.56}$$

$$U = W \frac{A}{\zeta}\ . \tag{6.57}$$

Table 6.4. Main characteristics of the CCD camera

Name	**SensiCam**
Sensor type	CCD-Interline
Resolution	Super-VGA
Number of pixels	1280 (H) × 1024 (V)
Pixel size	6.7 µm × 6.7 µm
Sensor format	$2/3''$
Scan area	8.6 mm × 6.9 mm
Response (monochrome)	280–1000 nm
Response (color)	RGB primary colors
Trigger	TTL, external, BNC
Exposure time setting	Fast shutter
Exposure times	0–10 ms
Step width	100 ns
Multiple exposure	Free programmable
Link to the PC	high speed serial
Type	Fiber optic, 200 m

The formulas hold for a dc-beam; therefore, to consider the much higher bunch current, a bunching factor BF= 20 has been introduced.

Because the beam spot size has to be enlarged during measurement by defocusing to avoid thermal destruction of parts, the expected divergences are below 10 mrad. A distance of $L = 250$ mm and a spacing of 2.5 mm was chosen for the 15×15 holes with 0.1 mm in diameter. This leads to overlapping of the light spots for divergences > 10 mrad. Assuming a rather low maximum divergence of ± 1 mrad, the increase in the light spot size due to the beam divergence is about ± 0.25 mm and therefore, referring to Fig. 6.36, broadening by space charge forces can be neglected.

The geometric parameters chosen have been tested by transformation of 100.000 single particles, occupying an area of $10\,\pi$ mm× mrad in each transverse phase plane [319]. To improve the statistics, the diameter of the holes was increased to 0.2 mm. Figure 6.37 shows the calculated distribution of the 520 particles going through the holes in the horizontal and vertical phase planes as well as the resulting pattern in the x, y-plane.

Data Processing The set of light spots on the viewing screen that have different brightness levels, shapes, and sizes represents the intensity distribution in four-dimensional phase space V_4. If the emittances of the two transverse phase planes can be considered independent of each other, the same information about the density distribution in the horizontal phase plane should be contained within each row. The same holds for the vertical phase plane, considering the columns. Taking advantage of this assumption, a simplified algorithm, based on the slit-detector measurement approach, allows a skilled operator fast data evaluation. Figure 6.38 illustrates the evaluation of light spot intensities along a row. Due to the vanishing divergence of the laser beam,

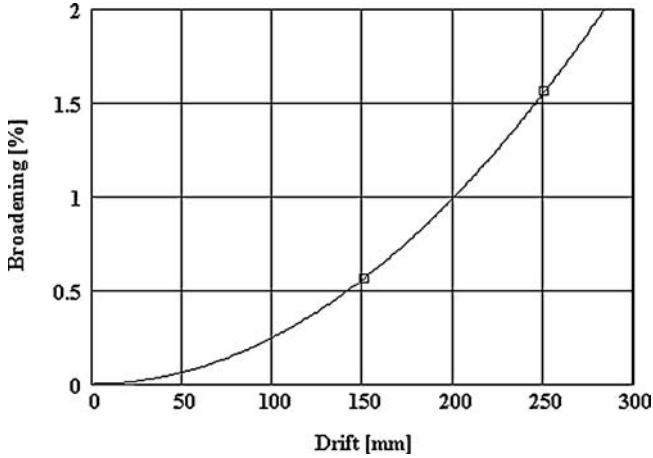

Fig. 6.36. Broadening of the beamlets behind holes of 0.1 mm diameter in percent. The solid line corresponds to a formula given in [317], and the two boxes are calculated using a formula given in [318]. Parameters: $W = 120\,\mathrm{keV/u}$ U^{4+} ions, $i_{\mathrm{dc}} = 16.5\,\mathrm{mA}$, BF= 20 (bunching factor, see text), $i_{\mathrm{hole}} = 5.2\,\mu\mathrm{A}$

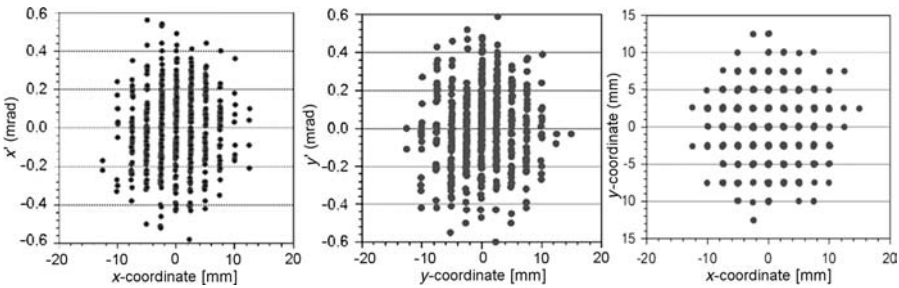

Fig. 6.37. Single particle transformation of 100.000 particles hitting the pepper-pot plate. The diagrams show the expected distributions on the viewing screen for the 520 particles going through the holes

the spacing between the laser peaks is constant. The scale on the PC display considers the magnification of the optical system as well the scaling, resulting from graphics software. Due to the finite ion beam, no regular grid fits the corresponding light spot pattern.

A nonlinear grid can be generated by an interactive graphic procedure. This is illustrated in Fig. 6.39, where the ticks on top and bottom of the figure represent the position of the light spots from the laser beam. Once a skilled operator has manually adjusted the nonlinear grid, represented by the long lines, to the peaks, the divergences along each row or column of the pepper-pot holes can be determined, as shown in the example of Fig. 6.38. Obviously, the extracted data are comparable to the profile measurements in a conventional slit-detector system. As a consequence, the software for further data processing

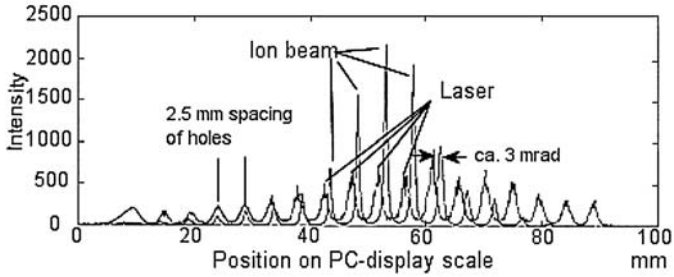

Fig. 6.38. Example showing the light peaks from the laser calibration procedure and the peaks from the ion beam. The data hold in the horizontal direction and are extracted from the light spots along a row behind the holes

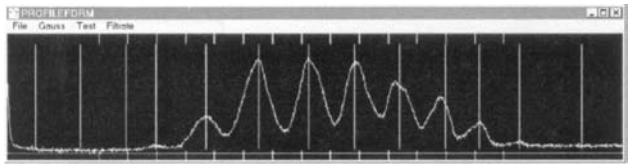

Fig. 6.39. Generation of a nonlinear grid (long lines) by manual adjustment of the grid lines

and display of the results can be similar to the software implemented in the frame of a conventional slit-detector system. A detailed description of the implemented software, the visualization possibilities, as well as possible import of data, obtained by other emittance measurement devices, is given in [320]. It should be mentioned that the exploitation of the experimental data has been tried also in a somewhat different way, resulting in the implementation of some additional mathematical routines, including

- A fit to the observed light spots assuming Gaussian shapes of the peaks. This results in automatic generation and adjustment of a nonlinear grid instead of the manually adjusted one.
- Implementation of a mathematical algorithm for exploitation of the experimental results. Interesting features of the corresponding software tools are
  - Performing a smoothing process along all pixels in each line of the total image by applying a least squares fit with Legendre polynomials as a basis.
  - A routine to detect each spot automatically and, assuming no overlap, definitive assignment of each detected spots to a corresponding hole.
  - Furthermore, a routine has been implemented to determine the vertical and horizontal size of all spots resulting in a set of four coordinates $(-x_{\max}, x_{\max}, -y_{\max}, y_{\max})$ representing the borders of each spot.
  - Another routine derives the horizontal and vertical projected peaks.

- In a next step, the projected spot curves are approximated by two Gaussian functions to take the nonsymmetrical shape into account. As a result, each spot is described by four Gaussian functions (two for each transverse phase plane).
- Once the mathematical description of the peaks is available, further evaluation and display of relevant data are straightforward; especially rms values and Twiss parameters can be determined, as already discussed in Sect. 6.2.2.

The mathematical tools are described in more detail in [315]. They also allow the investigation of coupling effects between the two transverse phase planes.

The usefulness of the pepper-pot system, respectively, of emittance measurements in general, is illustrated in Fig. 6.40. The data were taken during the commissioning of the high current injector at GSI [258]. The three-dimensional display (top left) and the corresponding projection onto the horizontal phase plane show two nearly separated parts of the beam, caused by a wrong phase setting between RFQ and a so-called "superlens" behind the RFQ. The pictures on the right-hand side, corresponding to the correct setting of the phase, impressively demonstrate the usefulness of emittance measurements with the pepper pot.

The Multislit System

A variation based on the pepper-pot system is the combination of a plate with a series of horizontal or vertical slits and a viewing screen behind. Depending on the inserted slit pattern, the emittance in one of the transverse phase planes can be determined in a similar way as described for the pepper-pot system. The relevant criteria to optimize the design parameters of such a system can be adapted from the discussion of the pepper-pot design. The "multislit" technique was used for the first time at CERN [321] to check the pulse to pulse stability of the heavy ion injector. A design study for the SPARC photon injector (INFN) is reported in [322].

6.2.4 Determination of Emittances by Beam Profile Measurements

All examples of measuring schemes discussed up to now allow the determination of intensity distributions of arbitrary shape in transverse phase planes. This will be necessary

- to study aberrations as well as higher order effects of beam transport elements, such as quadrupoles, sextupoles, and magnets and, in some cases also complete accelerator sections;
- to investigate and improve; ion sources;

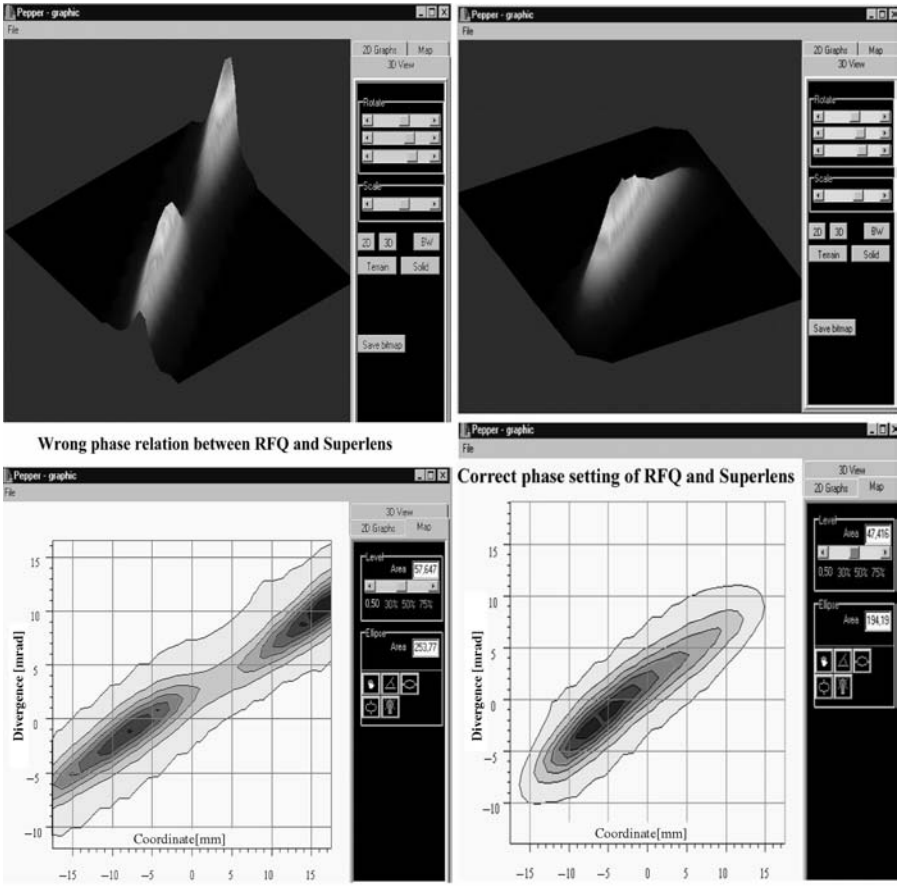

Fig. 6.40. Emittance measurements performed with the pepper-pot system to search the correct setting of phase between a RFQ-accelerator section and a superlens provided for matching to the following IH-accelerator section in the prestripper of the UNILAC. The pictures were taken in the main control room of GSI

- to study space charge effects; and
- during commissioning of a new machine.

On the other hand, the measured emittance patterns in most cases are approximated by ellipses applying more or less sophisticated fit procedures to the data. Experience has shown that even for strange patterns, the core of those beams will be included in appropriately fitted ellipses. Figure 6.41 shows an extremely deformed emittance area, but even in this case the fitted ellipse contains about 60% of the beam intensity.

Emittances, characterized by the Twiss parameters, are much easier to handle with respect to

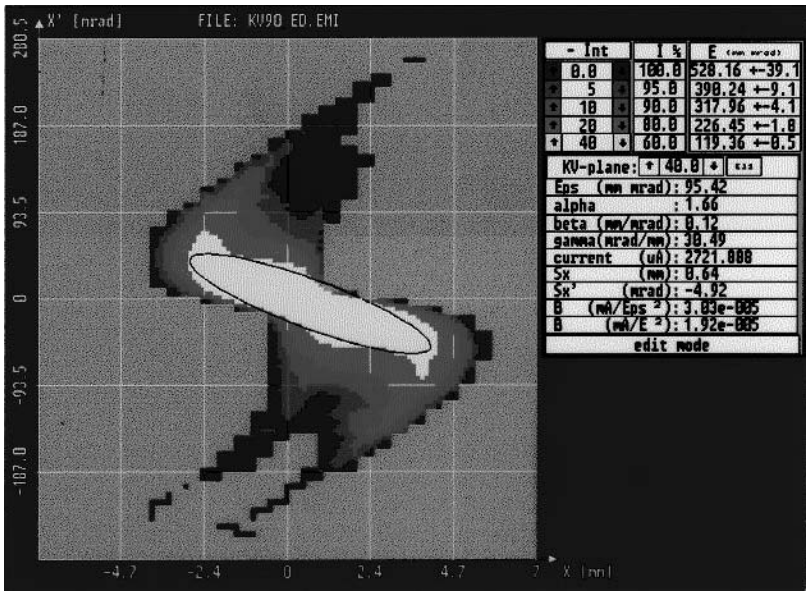

Fig. 6.41. Measured emittance [323] showing extreme aberrations.The fitted ellipse contains about 60% of the beam intensity and corresponds roughly to 50% emittance if evaluated in the intensity mode

- the transformation of a beam through a channel of various beam transport elements;
- the comparison of emittances and acceptances, including correct matching of accelerator sections; and
- the elaboration and storage of data sets for computer-aided routine operation, including optimization procedures.

Emittance Measurements in Circular Machines

The approximation of emittance patterns by ellipses allows the determination of ε in circular machines. The schemes discussed of emittance measuring systems cannot be applied here, since the beam would be destroyed instantaneously. But, remembering that the $\beta(s)$ function should be well known, ε can be determined from only one measurement of the beam profile. Assuming a Gaussian intensity distribution

$$f(x,\sigma) = \frac{1}{\sigma\sqrt{2\pi}} e^{-\frac{x^2}{2\sigma^2}} \tag{6.58}$$

where σ is the rms value of the measured profile data, determined according to (6.30) and (6.33), the percentage emittances can be figured out from the integration over the normalized function $f(x,\sigma)$. The result is displayed in

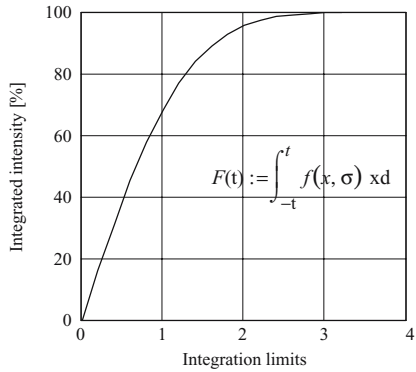

Fig. 6.42. Integrated Gaussian normal distribution [%]. The integration limits have been normalized to σ; therefore, the abscissa shows t/σ

Fig. 6.42. An alternative procedure to fit a Gaussian function by a noniterative method has been described in [324]. A very rough first estimation can be obtained from the relation $\varepsilon = x_{\max}/\beta$ (see Fig. 6.6).

One method for determining the beam width in a circular machine is by scrapers, which are normally installed in circular machines

- to remove particles in the halo of the beam,
- to define the beam pipe aperture at critical locations, and
- to stop the beam at a definitive location in case of emergency.

To perform a beam profile measurement in the horizontal direction, one scraper jaw is positioned near the edge of the beam (see, e.g., [325]), as shown schematically in Fig. 6.43. Then, at a well-known time, the accelerating rf is switched off, while the magnetic ramp continues. As a consequence, the beam will be swept over the scraper jaw. The beam profile can be extracted from a measurement of the current $i(t)$ on the jaw or by using a dc-transformer. In both cases, the beam profile has to be derived from the current measured as a function of time. The relevant relationships are

$$\frac{dN}{dR} \simeq \frac{dN}{dx} = \frac{i(t)}{e\,\zeta}\frac{1}{dR/dt} \tag{6.59}$$

$$\frac{\Delta p}{p} = \frac{\Delta B}{B} \tag{6.60}$$

$$\Delta R = D_{\mathrm{x}}(s)\frac{\Delta p}{p}\,. \tag{6.61}$$

In (6.59), dN/dx represents the beam profile sought, R is the mean radius of the central trajectory, p is the nominal momentum at time t, and $D_{\mathrm{x}}(s)$

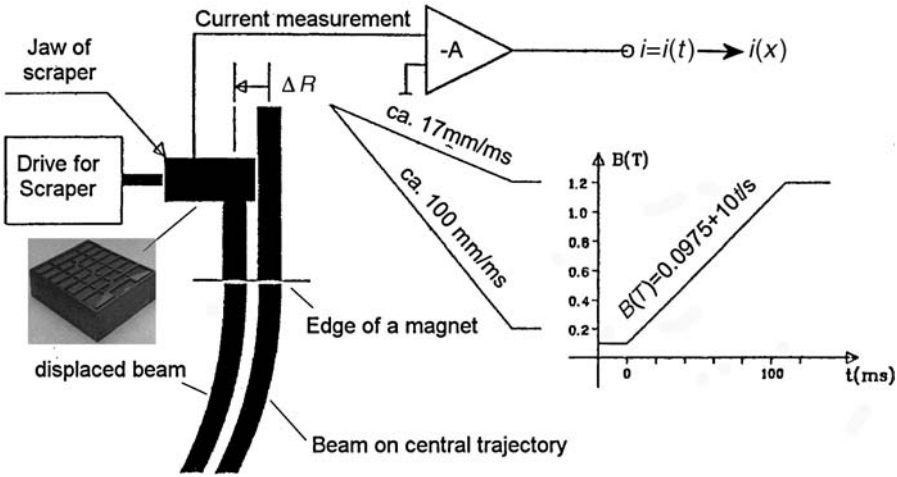

Fig. 6.43. Schematic illustration of beam profile measurement in a circular machine by scrapers. The diagram showing the magnetic field B as a function of time t holds for the SIS and especially for Ne^{10+} ions injected with 11.5 MeV/u. See text for details

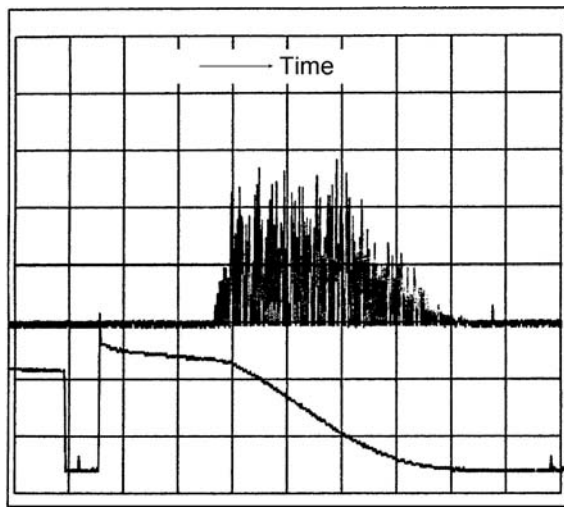

Fig. 6.44. Current measurement during displacement of the beam to determine the emittance in the SIS. Upper curve: current measured on the jaw of the scraper. Lower curve: intensity measured with a dc-transformer

is the well-known periodic dispersion function along the central trajectory s. Switching off the accelerating rf at time t leads immediately to $\Delta B(t)/B(t) = -\Delta R(t)/R$. Figure 6.44 gives an example of a measurement performed on the SIS.

Determination of the Twiss Parameters from Beam Profile Measurements

The simple method to determine ε from only one beam width measurement possible in circular machines cannot be applied in general, since normally the Twiss parameter β is not known. Furthermore, beside ε and β, γ and α also have to be determined to characterize the corresponding emittance ellipse with respect to size, shape, and orientation. According to the theorem of Liouville, the area of an emittance ellipse $\pi\varepsilon$ remains constant along the trajectory of the particles, whereas shape and orientation will change under the action of quadrupoles, magnets, and along drift spaces. The transformation laws applying the matrix formalism are given in various books (e.g., [326–329]. Referring to (6.12), the ellipse is described by

$$S(\alpha_0, \beta_0, \gamma_0) = \begin{bmatrix} \beta_0 & -\alpha_0 \\ -\alpha_0 & \gamma_0 \end{bmatrix} , \tag{6.62}$$

and the propagation of the Twiss parameters along a transport line is given by the transformation

$$S(\alpha_1, \beta_1, \gamma_1) = M\, S(\alpha_0, \beta_0, \gamma_0)\, M^T , \tag{6.63}$$

where M represents the 2×2 matrix of the single-particle transformation:

Drift space (length L):

$$D(L) = \begin{bmatrix} 1 & L \\ 0 & 1 \end{bmatrix} . \tag{6.64}$$

Thin lens (focal length F):

$$L(F) = \begin{bmatrix} 1 & 0 \\ -1/F & 1 \end{bmatrix} . \tag{6.65}$$

Focusing quadrupole (k = quadrupole constant, l = effective length):

$$QF(k) = \begin{bmatrix} \cos(k\,l) & \frac{1}{k}\sin(k\,l) \\ -k\sin(k\,l) & \cos(k\,l) \end{bmatrix} . \tag{6.66}$$

Defocusing quadrupole:

$$QD(k) = \begin{bmatrix} \cosh(k\,l) & \frac{1}{k}\sinh(k\,l) \\ k\sinh(k\,l) & \cosh(k\,l) \end{bmatrix} . \tag{6.67}$$

In practice, customarily the maximum current allowed through the coils of the quadrupoles, which determines the maximum of the quadrupole constant, is normalized to a reference voltage U_{ref} (mostly $U_{\mathrm{ref}} = 10\,\mathrm{V}$). Setting a well-defined k value then requires transmission of the digital set-value (S_{V}) from

the control computer to the DAC, mostly integrated in the power supply. In this case, the quadrupole constant k is determined by

$$k = \sqrt{\frac{k_\mathrm{r} S_\mathrm{V}}{B\rho}}\,, \tag{6.68}$$

where $k\,[\mathrm{T/V\,m}]$ is defined by the normalization and $0 \le S_\mathrm{V} \le U_\mathrm{ref}$ is the set-value. $B\rho$ is the magnetic rigidity of the ions

$$B\rho\,[\mathrm{Tm}] = 3.10715\,\frac{A\,\beta\,\gamma}{\zeta}\,. \tag{6.69}$$

Deflecting magnet (ρ = bending radius, n = field gradient, φ = deflecting angle, [330]):

Horizontal plane:

$$\mathrm{MMH} = \begin{bmatrix} \cos(\sqrt{1-n}\varphi) & \frac{\rho}{\sqrt{1-n}}\sin(\sqrt{1-n}\varphi) \\ -\frac{\sqrt{1-n}}{\rho}\sin(\sqrt{1-n}\varphi) & \cos(\sqrt{1-n}\varphi) \end{bmatrix}\,. \tag{6.70}$$

Vertical plane:

$$\mathrm{MMV} = \begin{bmatrix} \cos(\sqrt{n}\varphi) & \frac{\rho}{\sqrt{n}}\sin(\sqrt{n}\varphi) \\ -\frac{\sqrt{n}}{\rho}\sin(\sqrt{n}\varphi) & \cos(\sqrt{n}\varphi) \end{bmatrix}\,. \tag{6.71}$$

Let us assume that the transformation matrix from a location "0" to a location "1" can be represented by

$$M = \begin{bmatrix} a_{11} & a_{12} \\ a_{21} & a_{22} \end{bmatrix} \rightarrow M^T = \begin{bmatrix} a_{11} & a_{21} \\ a_{12} & a_{22} \end{bmatrix}\,, \tag{6.72}$$

which can be a drift space, or a drift space + quadrupole.

Taking advantage of the proportionality between $\sqrt{\varepsilon\beta}$ and the profile width (see Fig. 6.6) and keeping in mind that $\beta\gamma - \alpha^2 = 1$, the Twiss parameters can be determined from at least only three measurements of the profile width $\sim \sqrt{\varepsilon\beta}$. Therefore, referring to (6.63), only the transformation of β is relevant in this connection:

$$\beta_1 = \left(a_{11}^2 - 2a_{11}a_{12} + a_{12}^2\right) \begin{pmatrix} \beta_0 \\ \alpha_0 \\ \gamma_0 \end{pmatrix}\,. \tag{6.73}$$

Multiplying both sides by $\varepsilon = \mathrm{const}$ leads to the profile width $\sqrt{\varepsilon\beta_1}$ at location "1":

$$\sqrt{\varepsilon\beta_1} = \sqrt{a_{11}^2\,\varepsilon\beta_0 - 2\,a_{11}a_{12}\,\varepsilon\alpha_0 + a_{12}^2\,\varepsilon\gamma_0}\,. \tag{6.74}$$

Long-term experience has shown that the procedure is very sensitive to the accuracy of the transfer matrices as well as to the achievable precision of

profile determination. Thus, even small errors in the matrix elements or in the measured profiles sometimes lead to negative square roots, which of course are impossible from the physical point of view. This does not happen, if more than three (let's assume m) profile measurements are performed. This leads to a set of m equations,

$$P_{\mathrm{m}} = \sqrt{[a_{11}^2]_{\mathrm{m}}\ \varepsilon\beta_0 - 2\,[a_{11}a_{12}]_{\mathrm{m}}\ \varepsilon\alpha_0 + [a_{12}^2]_{\mathrm{m}}\ \varepsilon\,\gamma_0}\ , \tag{6.75}$$

where the index m represents the different transformation matrices and the $P_{\mathrm{m}} = \sqrt{[\varepsilon\beta]_{\mathrm{m}}}$ represent the accompanying measured profile widths. Setting $x = \varepsilon\beta_0$, $y = \varepsilon\alpha_0$, $z = \varepsilon\gamma_0$, $a_{\mathrm{m}} = \left[a_{11}^2\right]_{\mathrm{m}}$, $b_{\mathrm{m}} = -2\,[a_{11}a_{12}]_{\mathrm{m}}$, $c_{\mathrm{m}} = \left[a_{12}^2\right]_{\mathrm{m}}$, and applying a least squares fit [331] to the relation

$$S = \sum_{\mathrm{m}} \left[P_{\mathrm{m}}^2 - (a_{\mathrm{m}}x + b_{\mathrm{m}}y + c_{\mathrm{m}}z)\right]^2\ , \tag{6.76}$$

x, y, z can be determined from the requirements

$$\frac{\partial S}{\partial x} = \frac{\partial S}{\partial y} = \frac{\partial S}{\partial z} = 0 \tag{6.77}$$

giving immediately,

$$\left[a_{\mathrm{m}}P_{\mathrm{m}}^2\right] - \left[a_{\mathrm{m}}^2\right]\ x - [a_{\mathrm{m}}b_{\mathrm{m}}]\ y - [a_{\mathrm{m}}c_{\mathrm{m}}]\ z = 0 \tag{6.78}$$

$$\left[b_{\mathrm{m}}P_{\mathrm{m}}^2\right] - [a_{\mathrm{m}}b_{\mathrm{m}}]\ x - \left[b_{\mathrm{m}}^2\right]\ y - [b_{\mathrm{m}}c_{\mathrm{m}}]\ z = 0 \tag{6.79}$$

$$\left[c_{\mathrm{m}}P_{\mathrm{m}}^2\right] - [a_{\mathrm{m}}c_{\mathrm{m}}]\ x - [b_{\mathrm{m}}c_{\mathrm{m}}]\ y - \left[c_{\mathrm{m}}^2\right]\ z = 0\ , \tag{6.80}$$

where $[\ldots]$ stands for the sum over all m. The system of equations can be written as

$$[CM] \begin{bmatrix} x \\ y \\ z \end{bmatrix} = \begin{bmatrix} \left[a_{\mathrm{m}}P_{\mathrm{m}}^2\right] \\ \left[b_{\mathrm{m}}P_{\mathrm{m}}^2\right] \\ \left[c_{\mathrm{m}}P_{\mathrm{m}}^2\right] \end{bmatrix} \tag{6.81}$$

with CM as the 3×3 coefficient matrix. The solution for x, y, z, $\varepsilon = \sqrt{xz - y^2}$, $\beta_0 = x/\varepsilon$, $\alpha_0 = y/\varepsilon$ and $\gamma_0 = z/\varepsilon$ is straightforward. For example, $x = \varepsilon\beta_0$ is determined from

$$x = \frac{\begin{bmatrix} \left[a_{\mathrm{m}}P_{\mathrm{m}}^2\right] & [a_{\mathrm{m}}b_{\mathrm{m}}] & [a_{\mathrm{m}}c_{\mathrm{m}}] \\ \left[b_{\mathrm{m}}P_{\mathrm{m}}^2\right] & \left[b_{\mathrm{m}}^2\right] & [b_{\mathrm{m}}c_{\mathrm{m}}] \\ \left[c_{\mathrm{m}}P_{\mathrm{m}}^2\right] & [b_{\mathrm{m}}c_{\mathrm{m}}] & \left[c_{\mathrm{m}}^2\right] \end{bmatrix}}{DET\ [|CM|]}\ . \tag{6.82}$$

When a weighted least squares fit is applied, the weight factors are determined from the measured beam sizes and their errors. An expression for the errors in the determination of ε is derived in [331].

Measurement Procedures

Two variants of schemes are discussed in the literature [310,332,333,335–341, 343]:

- **The multigrid method:** Performing profile measurements (≥ 3) with profile grids at various positions along the beam line. Of course, the profile grids may be replaced by other profile measuring devices, such as scanners, and viewing screens, and residual gas ionization monitors
- **The gradient variation method:** Using different settings of a quadrupole in front of one profile measuring device.
- A combination of both methods.

Independent of the method applied, the accuracy that can be achieved depends very much on the precision of the profile measurement as well as on the evaluation of the profile data. This holds especially if the measured profiles cannot be well approximated by a single Gaussian function. A better characterization of such more complex intensity distributions by "asymmetrical Gaussian" fits has been described in [28] and compared with a series of wire-scan profile measurements. The fitting function,

$$f(x) = f_0 + f_{\max}\, e^{\left\{ -\frac{(x-\langle x\rangle)^2}{2\langle x^2\rangle\{1+\alpha[\mathrm{sign}(x-\langle x\rangle)]\}} \right\}} \tag{6.83}$$

approximates the profile by an offset (f_0) and two Gaussians. The asymmetry parameter is α (do not confuse with the Twiss parameter α), which vanishes for a perfect Gaussian profile. The σ values for the left- and right-hand sides are $\sigma = \langle x^2 \rangle (1 \pm \alpha)$. The authors use the average of both values for the reconstruction of the ellipses. A more sophisticated algorithm, developed at KEK [342], does not assume that the measured profiles have a special form, as, for example, Gaussian. The only assumption is that each percentage emittance area can be described by an ellipse with a uniform particle distribution. The algorithm is rather complex but described in detail by the authors. A comparison with the usual method (based on a Gaussian profile approximation) shows deviations of the order of some percent up to some 10%, depending on the percentage level under consideration.

The Multigrid Method

Assuming very high precision in the profile determination, the method can be performed with only three profile measurement devices along a drift space. As shown in [295,343], best accuracy is achieved if a waist can be transformed to the profile measuring device in the middle, and the spacing L to the upstream and downstream measuring devices is just $L = \sqrt{3}\beta_{\mathrm{waist}}$. To improve the accuracy, profile measurements at five equidistant positions should be preferred. In this case, a spacing of $L = 0.73\,\beta_{\mathrm{waist}}$ has been figured out [333,334,343]. But the optimal conditions, mentioned above, will probably not often be found at

an accelerator facility, if not especially foreseen for emittance determination by this method. Applying the method in a section, containing quadrupoles between unequally spaced profile measuring devices, a waist must occur within the section.

The Gradient Variation Method

Due to the possibility of varying profile widths in a wide range, this method is more flexible and results mostly in higher accuracy. Before varying the transfer matrix, the beam should be aligned carefully to avoid steering effects that can falsify the results. The scheme of a typical section suitable for beam alignment is shown in Fig. 4.43 and the equations for setting of the steerers are given in Chap. 4, Sect. 4.7 (4.38–4.47).

After the beam has been aligned, the emittance can be measured. Experience has shown that the implementation of a semiautomatic algorithm offers more control for the operators and physicist than a fully automatic procedure. This holds, for example, with respect to the range of profile variation, to prevent too large profiles from covering the range of the profile measuring device. With a semiautomatic algorithm, the operator can determine the range of gradient variation by a first inspection of the profiles. This can be performed by setting the quadrupoles manually via potiboard, which usually is available for manual fine-tuning of beam transport elements. Once the range of gradient variation has been fixed and the number of quadrupole settings has been specified, measurement and evaluation of data can be performed automatically by an appropriate computer program. Taking advantage of advanced techniques to describe the measured profile by mathematical functions, as discussed above, the evaluation of emittance data is straightforward. Figure 6.45 shows two examples of profiles, measured at the UNILAC. In the large picture, the solid curve results from the least squares fit and shows excellent agreement with the measured profiles. But, as shown in the small inset, such an excellent agreement does not always occur by far. The deviations increase in case

- of very low beam currents diminishing the accuracy of profile determination,
- of strongly asymmetric profiles, and

of strange emittances resulting from aberrations and higher order effects by the action of beam transport elements.

The examples of Fig. 6.45 show that the location of the minimum profile width with respect to the corresponding quadrupole gradient (scale on the abscissa) can give one more independent equation for the determination of the Twiss parameters. The location of the minimum can be obtained by inspection of the $P_{\mathrm{m}} = f(k_{\mathrm{m}})$ diagram or even by manual variation of the quadrupole gradient observing the displayed profiles. In the waist position, $\partial P/\partial k = 0$. From (6.76), it follows immediately that

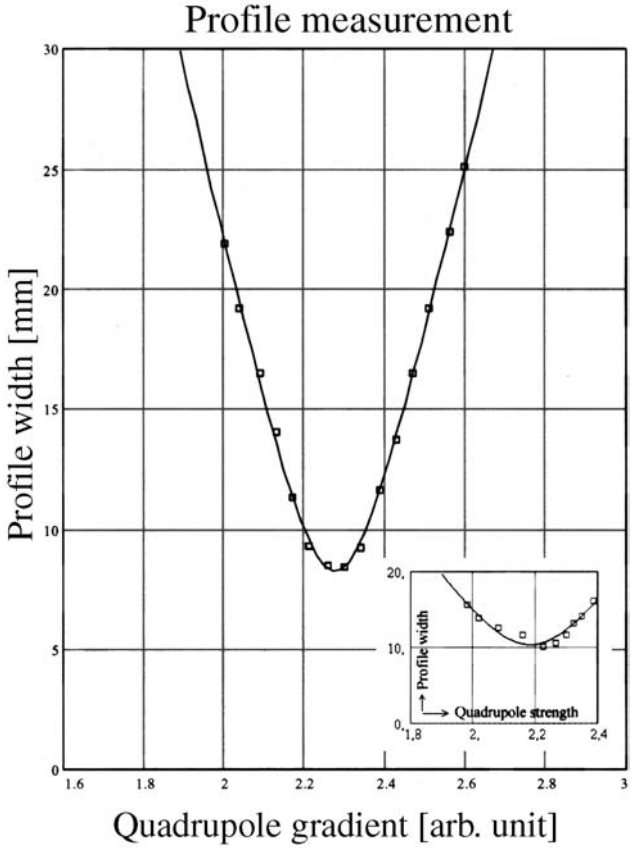

Fig. 6.45. Two examples of measured profile widths applying the gradient variation method. The solid curves in the large picture and the small inset are determined from the least squares fit according to (6.78–6.80)

$$\left[a_{11}\frac{\partial a_{11}}{\partial k}\right]\beta_0 - \left[a_{12}\frac{\partial a_{11}}{\partial k} + a_{11}\frac{\partial a_{12}}{\partial k}\right]\alpha_0 + \left[a_{12}\frac{\partial a_{12}}{\partial k}\right]\gamma_0 = 0\,. \qquad (6.84)$$

Assuming the waist is generated by a focusing quadrupole in front of the profile measuring device with a drift space of length D between leads to

$$\frac{\partial a_{11}}{\partial k} = -l\sin(k\,l) - D\sin(k\,l) - D\,k\,l\cos(k\,l) \qquad (6.85)$$

$$\frac{\partial a_{12}}{\partial k} = -\frac{1}{k^2}\sin(k\,l) + \frac{l}{k}\sin(k\,l) - D\,l\sin(k\,l)\,. \qquad (6.86)$$

Inserting $\partial a_{11}/\partial k$ and $\partial a_{12}/\partial k$, as given in (6.85) and (6.86), into (6.84) and the k value, known from the location of the waist, one of the three unknown parameters α_0, β_0, or γ_0 can be determined and removed from (6.76). Because the success of the procedure depends on many parameters, it is difficult to

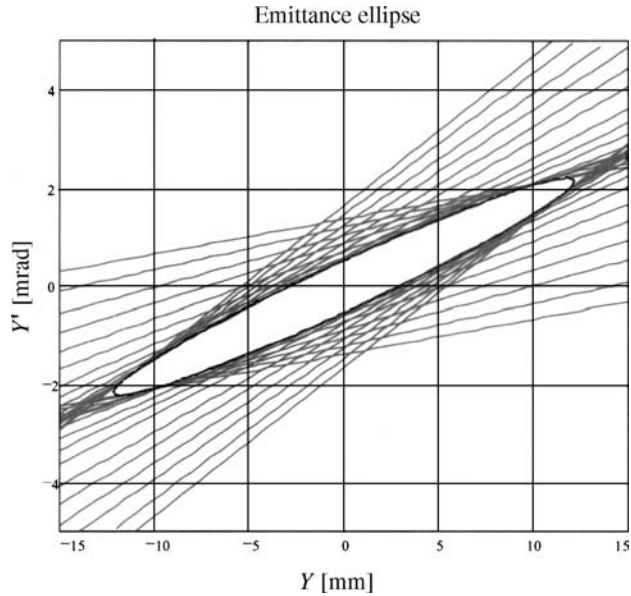

Fig. 6.46. Graphical determination of the emittance ellipse by inverse mapping to the reference point (located at the front of the quadrupole)

decide on the best choice of this parameter. The best recommendation is to apply the well-known "trial and error" strategy.

In some cases, a graphical method for the determination of the emittance ellipse, as discussed in the literature [6, 28, 295] can also be useful. Figure 6.46 illustrates the method taking the relevant data belonging to the example shown in Fig. 6.45. Here the straight lines, generated from the inverse mapping of the points $[\sqrt{\varepsilon\beta}]_{\mathrm{m}}$ and x'_{m}, form the boundary of the ellipse. Whereas $[\sqrt{\varepsilon\beta}]_{\mathrm{m}}$ is determined by the m_{th} profile measurement, the divergence angle x'_{m} is unknown and has to be considered as a parametrization of the corresponding straight lines in Fig. 6.46.

Combination of Both Methods

A transport channel, equipped with some quadrupoles, magnets, and profile measuring devices, offers the possibility of combining the multigrid method with the gradient variation method. Figure 6.47 gives an example from the transfer channel UNILAC → SIS. Applying a least squares fit according to (6.76), the extracted emittance ε and the Twiss parameters correspond to an average over the whole channel, as demonstrated impressively by the calculated envelopes.

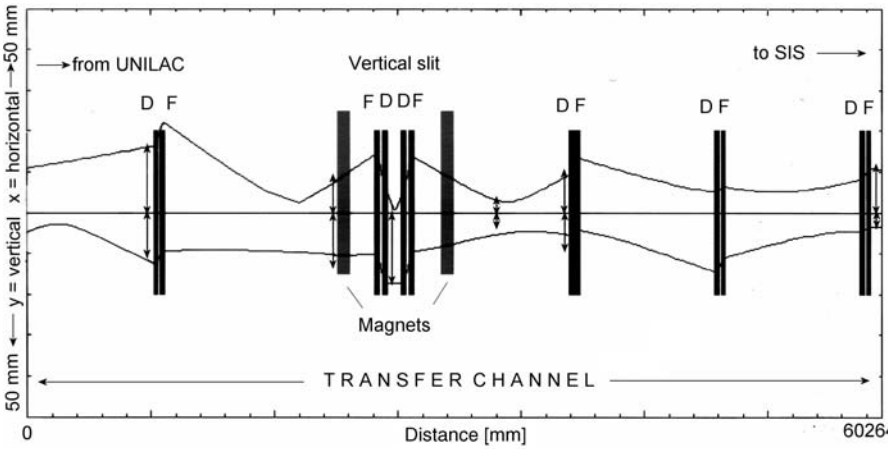

Fig. 6.47. Combination of the two emittance measuring methods discussed in the transfer channel from the UNILAC to the SIS [240]. The emittance and the calculated envelope have been determined from six profile measurements and the readout of the transfer matrices by the computer. The arrows indicate the position of the profile grids as well as the measured profiles. As usual, F and D mark the focusing and defocusing elements in the horizontal plane. The routine for emittance determination was implemented as a subroutine of the *MIRKO* program [345]

6.3 Computer-Aided Optimization and Operation

Modern accelerators are operated setting calculated data or stored data from earlier runs to the beam transport elements and accelerating structures. However, these settings hardly ever result in sufficient beam transmission, mass separation, or charge state separation. The reasons are manifold: nonreproducible emittances from different ion sources, respectively, different settings of ion source parameters, tolerances of geometrical dimensions, disabled elements, and misalignments. With regard to the various types of accelerator facilities in operation around the world, the required effort for subsequent optimization differs from machine to machine. From the long-term experience of operators, shift leaders, and supervisors at GSI, who have operated, the UNILAC, the heavy ion synchrotron SIS, the experimental storage ring ESR, as well as numerous complex beam lines, some admittedly subjective, comments may be given for further discussions and scrutiny of the arguments.

- Linear accelerators can deliver a beam to a target, even when there are considerable losses in the machine.
- The same holds for beam transport lines, where the beam can go through with considerable losses along the line.
- This does not hold for circular machines, such as synchrotrons, and storage rings. Due to the large number of revolutions, normally all particles are lost, if there is only a small beam loss at one location.

- The elaboration of optimum data sets for accelerator facilities provided for acceleration and delivery of a limited species of light particles such as electrons, protons, deuterons converges faster than for universal machines delivering all kind of ions with various energies. This is proved by the rather high number of different ions and also by the great variety of emittances from various ion sources that inevitably have to be used.
- The correct determination and separation of undesirable masses and isotopes, as well as charge state identification and separation, requires additional effort in operating heavy ion accelerators.
- It is much more cumbersome to optimize the performance of very slowly pulsed machines in comparison to dc-machines or machines with high duty cycles.

An important postulate for the application of computer-aided optimization and operation is that the transport system is computable. That can require time-consuming activities to bring all the components to their design status. The effort has to include checkup of calibration curves for all magnets, steerers, and quadrupoles. Precise and reproducible reaction of the corresponding power supplies to the command signals transmitted from the control computer has to be proved, too. Furthermore, the geometric distances between all components, including the beam diagnostic elements, have to be determined precisely. Based on this work, either fully automatic programs [243, 346–349] for beam optimization in the transverse phase planes or programs for on-line manipulations of the beam transport elements during accelerator experiments can be implemented. Computer-aided manipulations are done mostly by skilled operators or with the support of accelerator physicists to improve the performance of a machine. Figure 6.48 shows part of an interactive graphic display, provided for on-line optimization of the displayed beam transport section.

Two emittance measuring devices of the slit-sandwich detector type were installed at that time within this section. The envelopes, calculated from emittance measurements at both places, show excellent agreement, confirming the computability of this section. The same holds with respect to the measured beam profile widths, marked as stars. The program package offers various options for interactive manipulations, which can be activated by a cursor (the corresponding command fields are not shown in the Figure). The actions and subroutines, which can be activated by a skilled operator, are illustrated in the schematic diagram of Fig. 6.49. The box "subroutines for options" contains the command fields mentioned that are available in the interactive graphic display. As illustrated in the diagram, the subroutines for options are divided into three classes: on-line only, on-line or off-line, off-line only. Some of the features implemented may stimulate physicists and programmers to develop similar tools for transverse beam optimization. Therefore, a short description of the actions, triggered by cursor movement in the corresponding command fields, may be helpful.

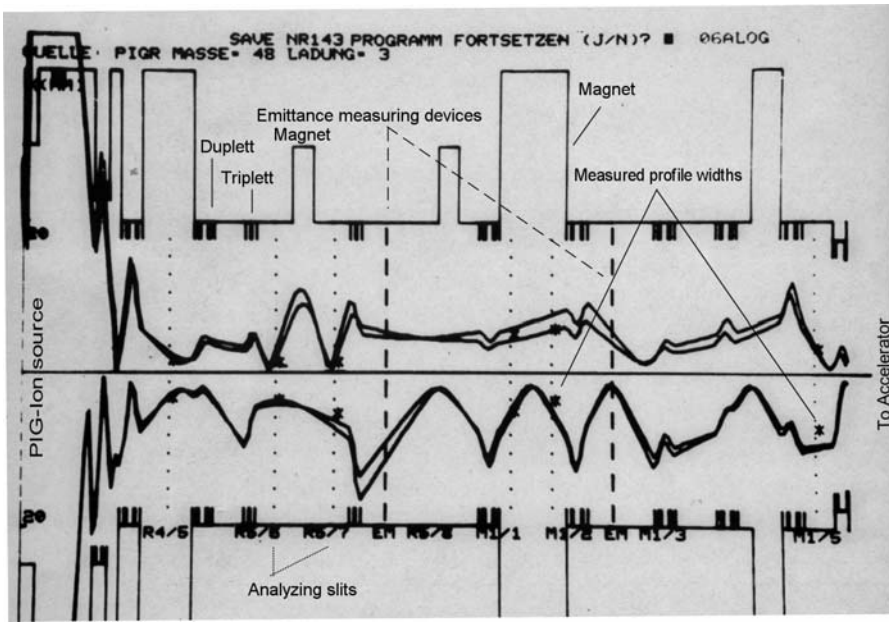

Fig. 6.48. Interactive graphic display provided for computer-aided optimization. The picture shows the section between ion source and the first Wideroe section of the UNILAC. The picture was taken in the main control room of GSI. See text for details

On-line only:

1 × L	Readout of actual quadrupole gradients, calculation of envelopes and their display
AUTO	same as 1 × L, refresh time ca. 1–3 s (depending on the length and complexity of the displayed section)
STOP	Stops AUTO-mode, done by an independent program
SOLL/IST (toggle)	Switching between real quadrupole gradients (IST) and data transmitted to the power supplies by computer (SOLL)

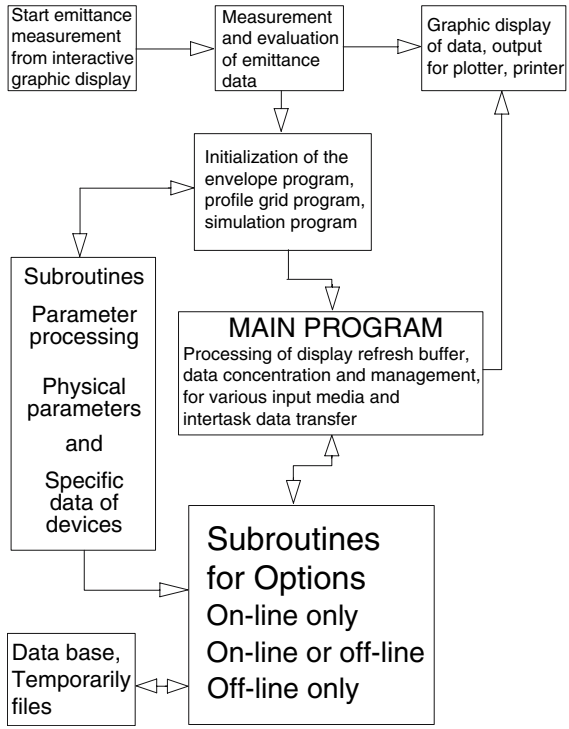

Fig. 6.49. Simplified scheme of a computer program [348] for computer-aided transverse beam optimization. See text for detailed explanations of the available subroutines and options

On-line or Off-line:

SAVE	Start of savefile-handling program offering the possibility for save-allocation, file read-back and printout of file data
PRINT	Printout of all data from beam transport elements on a line printer
ELLIP	Calculation of emittance ellipses at a selected position along the displayed section and display of the results as an insert
BETA	Update of $\beta = v/c$ by readout of relevant devices (terminal voltage, extraction voltage...) Additionally: Possibility for change of β by direct input from the keyboard
UPDT	Readout of actual quadrupole gradients and save on a temporary file. This function is automatically done when the program is started
ENVD	Return to last SAVE or SET-values on temporary file

RESET	Return to data before a fit procedure has taken place
KURZ	ZOOM function to shorten the displayed section
ORIG	Return to original beam transport section (PAN function)
PROF	Measurement and display of beam profile width (FWHM of profile grid data)
SLIT	Measurement of slit positions
ERROR	Error diagnostic on demand from the operator, explaining combinations of options not allowed
ENABLE	Security switch for options such as SET, PROF,

Off-line only:

SET	Setting of quadrupole gradients after manipulation on the envelopes
QUVA	Variation of quadrupole gradients by cursor (percentage of change $\sim$ to distance of cursor from the beam center line) or direct input of quadrupole gradients from the potiboard
CFIT	Manipulation on the envelope by cursor using a special mathematical procedure [345]
SFIT	Optimization of larger sectors using "TRANSPORT"
INTG	Numerical integration of measured quadrupole gradients $[B'(s)]$ instead using hard-edge model
HELP+option	Explanations of the specified option (menu-filed, dedicated areas on display etc.) on a separate display

Taking advantage of a database, containing

- all beam transport elements and their characteristics (mostly called "properties"),
- the relevant apertures determined by those elements, vacuum chambers, and limiting apertures, and
- the exact location of all relevant elements with respect to reference point, optimization programs, such as the example discussed, can be applied at different locations along the machines, including beam lines in the experimental halls. Once a skilled operator has selected a certain section, the computer can automatically display the arrangement of the elements.

6.A Dimensioning Motor Driven Feedthroughs

Motor driven UHV feedthroughs and compressed air actuators are often used to move detectors and other components , such as emittance detectors, slits, Faraday cups, and scrapers controlled inside a vacuum system. Compressed

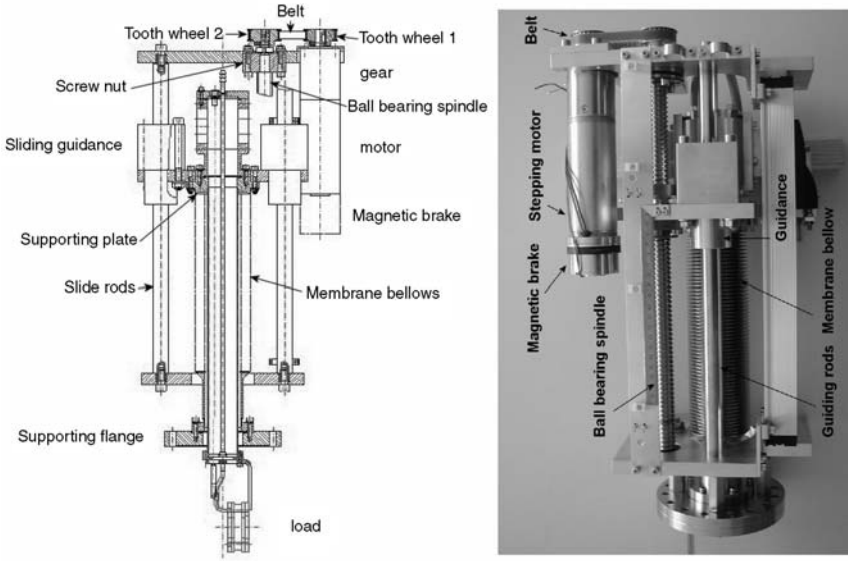

Fig. 6.50. Schematic drawing and picture of a motor driven feedthrough [299]

air actuators are used mostly for a pure IN/OUT motion and are available commercially in great variety. Motor driven feedthroughs are more flexible, and special demands can result designing such a device.

For the system designer as well as the user, the following questions are of interest:

- maximum load and their maximum size that have to be moved in a vertical or horizontal motion;
- required stroke and accuracy of positioning;
- required acceleration and speed for the specified load, respectively, the total time to move the load with a given stroke;
- the required torque (M) and power ($M\,\omega$) of a motor to fulfill the specifications.

It is the aim of this Appendix, to give the designer some hints, which can be helpful for the design of other moving mechanical systems, too.

Consider a feedthrough as shown in Fig. 6.50, provided to displace a load in vertical direction. That means that the load has to be moved against the force of gravity, when it has to be lifted. An important part of the feedthrough is a ball bearing spindle, with the load attached at its end. The spindle is displaced by a stepping motor or a dc-motor, outside the vacuum, via tooth wheels and a belt. A membrane bellows seals the spindle against the vacuum. A magnetic brake prevents movement of the load due to the vacuum counterpressure in case of power failure or the power on the motor is switched off.

Because there are parts that move in a linear axial motion as well as parts that rotate at various angular velocities, it is advantageous to apply the Lagrange formalism (see e.g. [350], [351]) to find the corresponding differential equation of motion. To determine the Lagrange function $L = T - U$, with T as the sum of all kinetic energies and U as the sum of all potential energies, the following contributions to L have to be considered (see Fig. 6.50):

- Axial movement of
  - the load itself;
  - the supporting plate, driven by the ball screw nut; and
  - diverse small parts such as the slider of the linear potentiometer, cooling pipes, and connectors; and
- Rotary motion of
  - the rotor of the motor;
  - the moving part of the magnetic brake, attached to the motor;
  - tooth wheel 1 on the gear;
  - the belt, coupling this tooth wheel to the driving screw nut on the ball bearing spindle;
  - tooth wheel 2 on the screw driving nut; and
  - the ball bearing spindle itself.
- Furthermore, the counterpressure of the vacuum has to be considered. Because it acts like an additional mass, it can be taken into account by $m_{\mathrm{V}} = A_{\mathrm{eff}\times 1\,\mathrm{kg/cm^2}}$, with A_{eff} as the effective area $\left[\mathrm{cm}^2\right]$ of the membrane bellows, resulting in a force $F_{\mathrm{V}} = m_{\mathrm{V}}\, g = [\mathrm{N}]$.
- Moreover, the force of the membrane bellows, acting like a spring, has to be taken into account. This force is defined by $F_{\mathrm{m}} = k_{\mathrm{m}}\, x$, with
  - k_{m} as the spring constant, normally given in the data sheets for the bellows, and
  - x as the coordinate, describing the axial displacement, with $x = 0$ defined by the so-called "free length" (B_{FL}) of the bellows, as illustrated schematically in Fig. 6.51.

6.A.1 Estimations

Required Motor Power

Referring to a feedthrough, as shown in Fig. 6.50, one can neglect the rotating parts and estimate the required motor power P from

$$P = \sum_{\mu} F_{\mu}\, \dot{x}_{\mathrm{nom}}\ , \tag{6.87}$$

where $\dot{x}_{\mathrm{nom}}$ is the specified nominal velocity for the movement of the load and F_{μ} are the main forces, acting against the motion. Assuming a lifting, vertical motion, the most important contributions are

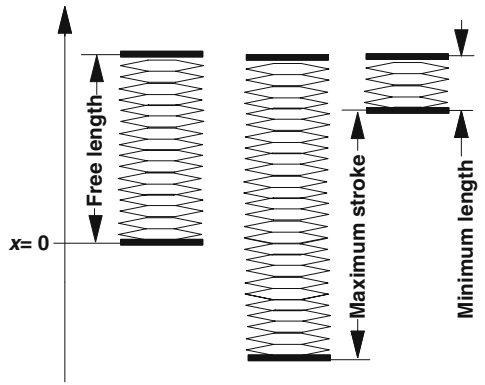

Fig. 6.51. Definition of the origin of the axial x-coordinate system by the so-called free length of the membrane bellows

- The mass of the load itself, given by $F_1 = m_\mathrm{L}\, g$ ($g = 9.81\mathrm{m/s}^2$).
- The counterpressure of the vacuum caused by the membrane bellows sealing and given by $F_2 = m_\mathrm{V}\, g$. In many cases, this will be the largest contribution.
- The maximum counterforce of the membrane bellows given by $F_3 = k_\mathrm{m} x_\mathrm{max}$. For the lifting motion, x_max is determined by the free length (B_FL) and the minimum length of the membrane bellows B_m to $x_\mathrm{max} = B_\mathrm{FL} - B_\mathrm{m}$ (see Fig. 6.51).

For the feedthrough shown in Fig. 6.51, the relevant parameters are given in Table 6.5

Table 6.5. Relevant parameters of the motor driven feedthrough, as shown in the example of Figure 6.51

$m_\mathrm{L} = 5$	kg	Moving load
$S = 0.2$	m	Stroke of the feedthrough
$B_\mathrm{FL} = 0.140$	m	Free length of the membrane bellows
$B_\mathrm{m} = 0.03$	m	Minimum length of the membrane bellows
$k_0 = 49 \times 10^3$	N/m	Spring constant per membrane pair
$N_\mathrm{m} = 50$		Number of membrane pairs
$k_\mathrm{m} = 49/50 \times 10^3$	N/m	Resulting total spring constant of the bellows
$A_\mathrm{eff} = 28$	cm^2	Relevant area of the membrane bellows
$m_\mathrm{V} = 28$	kg	Mass related to the vacuum counterpressure

Summing up the contributions to F_μ, as defined in (6.87), one gets for the example ($g \simeq 10\,\mathrm{m/s}^2$):

$$\sum_\mu F_\mu = F \simeq 50 + 280 + 108 = 438\,\mathrm{N}\,. \tag{6.88}$$

The velocity was specified as $\dot{x} = 8\,\mathrm{mm/s}$, which leads immediately from (6.87) to the required motor power $P \simeq 438 \cdot 8 \times 10^{-3}\,\mathrm{Nm/s} \simeq 3.5\,\mathrm{W}$.

Required Torque, Revolution Frequency, and Gear Ratio

For a motor rotating at an angular frequency $\omega_\mathrm{N} = 2\pi f_\mathrm{N}$ (f_N is the nominal revolution frequency), the power is given by $P = M_\mathrm{N}\,\omega_\mathrm{N}$ (M_N is the torque at frequency f_N). Because parts, are rotating at different revolution frequencies, we define

- $\varphi_0(t)$, which describes the rotation of the driving motor with $\dot{\varphi}_0(t) = d\varphi_0(t)/dt = \omega_0(t) = 2\pi f_0$, with f_0 as the frequency of revolution in [1/s].
- $\varphi_1(t)$ describes the rotation of the belt driving tooth wheel 1 (see Fig. 6.50) on the gear box, attached to the motor.
- $\varphi_2(t)$ is the angle of rotation of tooth wheel 2 (see Fig. 6.50) driven by the belt and driving the screw nut on the ball bearing spindle.

Of course, $\omega_1(t)$ and $\omega_2(t)$ are related to $\varphi_1(t)$ and $\varphi_2(t)$, and this holds for the relation between $\omega_0(t)$ and $\dot{\varphi}_0(t)$. To determine the required nominal torque of the motor, the law of conservation of energy $F\ \delta x = M_\mathrm{N}\,\delta\varphi$ leads to $M_\mathrm{N} = F\,\delta x/\delta\varphi$. The ratio $\delta x/\delta\varphi$ can be determined from $x(\varphi_0) = p_\mathrm{s}\varphi_0/2\pi G$ giving $\delta x/\delta\varphi = p_\mathrm{s}/2\pi G$. Here p_s is the displacement per revolution of wheel 2 and G is the total gear ratio, determined by the ratio of the teeth on the two wheels N_1, N_2, and the gear box.

For the example (see Fig. 6.50), $p_\mathrm{s} = 5\,\mathrm{mm}$ and $G = G_\mathrm{r}/S$, with $G_\mathrm{r} = 20.25$, $S = 25/40$. With $G \simeq 32$, this leads to the required torque $M_\mathrm{N} = 438 \cdot 5 \times 10^{-3}/64\pi$ [Nm] $\simeq 0.011\,\mathrm{Nm}$. To achieve the required speed of $\dot{x} = 8\,\mathrm{mm/s}$, the required nominal revolution frequency from $f_\mathrm{N} = G\dot{x}/p_\mathrm{s} \simeq 51/\mathrm{s}$.

In the example, a motor with $M_\mathrm{N} = 0.02\,\mathrm{Nm}$ and $f_\mathrm{N} = 50/\mathrm{s}$ was selected to take friction and the efficiency $\eta = 0.81$ of the gear box into account. The estimations given here are confirmed by the solution of the corresponding differential equation applying the Lagrange formalism.

6.A.2 The Lagrange Function

Determination of Potential Energies (U)

Summing up all masses to m_g, including m_V and considering the contribution to the potential energy from the membrane bellows:

$$U(x) = U_g(x) + U_\mathrm{b}(x) = m_g g x + \frac{k_\mathrm{m}}{2} x^2\ . \tag{6.89}$$

Determination of Kinetic Energies (T)

The kinetic energy from axial motion is given by

$$T(\dot{x}) = \frac{m_\mathrm{g}}{2}\left(\frac{dx}{dt}\right)^2 = \frac{m_\mathrm{g}}{2}v^2 = \frac{m_\mathrm{g}}{2}\dot{x}^2 \ . \tag{6.90}$$

On the other hand, the kinetic energy of all rotating parts has to be determined from $I/2\ \dot{\varphi}^2$, where I is the moment of inertia, defined as $I = \int r^2 dm$. Keeping in mind the various angular velocities of the rotating parts, one has to sum up the moments of inertia with respect to the angular velocities $\dot{\varphi}_0, \dot{\varphi}_1, \dot{\varphi}_2$.

$$T(\dot{\varphi}_0) = \frac{I_0}{2}\dot{\varphi}_0^2, \text{ with } I_0 = \sum I(\varphi_0) \tag{6.91}$$

$$T(\dot{\varphi}_1) = \frac{I_1}{2}\dot{\varphi}_1^2, \text{ with } I_1 = \sum I(\varphi_1) \tag{6.92}$$

$$T(\dot{\varphi}_2) = \frac{I_0}{2}\dot{\varphi}_2^2, \text{ with } I_2 = \sum I(\varphi_2) \ . \tag{6.93}$$

For the Lagrange function $L = T - U$,

$$L(x, \dot{x}, \dot{\varphi}_0, \dot{\varphi}_1, \dot{\varphi}_2) = T(\dot{x}) + T(\dot{\varphi}_0) + T(\dot{\varphi}_1) + T(\dot{\varphi}_2) - U(x) \ . \tag{6.94}$$

Now a differential equation can be derived from the well-known relation:

$$\frac{d}{dt}\frac{\vartheta L}{\vartheta \dot{q}_\mathrm{k}} - \frac{\vartheta L}{\vartheta q_\mathrm{k}} = F_\mathrm{qk} \ , \tag{6.95}$$

where $q_\mathrm{k}, \dot{q}_\mathrm{k}$ represent all relevant coordinates and F_qk represents the external forces in the corresponding coordinates. In the case considered, the external force is the torque of the driving motor. Performing the procedure according to (6.95), one obtains a system of differential equations in the coordinates $x, \varphi_0, \varphi_1, \varphi_2$. However, from the practical point of view, it is of much more interest to know the movement of the load as a function of time in the x-coordinate. This means that the solution should be determined for $x(t)$. This can be done in different ways, the simplest is to transform $L(x, \dot{x}, \dot{\varphi}_0, \dot{\varphi}_1, \dot{\varphi}_2)$ to $L(x, \dot{x})$.

Transformation of Coordinates

With $S = N_1/N_2$ and G_r as the gear ratio of the gear box, one obtains

$$x(\varphi_0) = \frac{S}{G_\mathrm{r}}\frac{p_\mathrm{s}}{2\pi}\varphi_0 \tag{6.96}$$

$$x(\varphi_1) = S\frac{p_\mathrm{s}}{2\pi}\varphi_1 \tag{6.97}$$

$$x(\varphi_2) = \frac{p_\mathrm{s}}{2\pi}\varphi_2 \ . \tag{6.98}$$

The kinetic energy of the rotating parts becomes

$$T_{\mathrm{I}}(\dot{\varphi}_\mu) = \frac{I_0}{2}\dot{\varphi}_0^2 + \frac{I_1}{2}\dot{\varphi}_1^2 + \frac{I_2}{2}\dot{\varphi}_2^2, \quad \mu = 1\ldots 3, \rightarrow$$

$$T_{\mathrm{I}}(\dot{x}) = \frac{1}{2}\left[I_0 \left(\frac{2\pi}{p_{\mathrm{s}}}\frac{G_{\mathrm{r}}}{S}\right)^2 + I_1 \left(\frac{2\pi}{p_{\mathrm{s}}}\frac{1}{S}\right)^2 + I_2 \left(\frac{2\pi}{p_{\mathrm{s}}}\right)^2 \right] \dot{x}^2 \tag{6.99}$$

$$T_{\mathrm{I}}(\dot{x}) = \frac{m_{\mathrm{I}}}{2}\dot{x}^2 \tag{6.100}$$

where a fictitious mass m_{I} has been introduced, defined by

$$m_{\mathrm{I}} = \left[I_0 \left(\frac{2\pi}{p_{\mathrm{s}}}\frac{G_{\mathrm{r}}}{S}\right)^2 + I_1 \left(\frac{2\pi}{p_{\mathrm{s}}}\frac{1}{S}\right)^2 + I_2 \left(\frac{2\pi}{p_{\mathrm{s}}}\right)^2 \right]. \tag{6.101}$$

Remark. Because the kinetic energy of relatively fast rotating masses is now determined by a velocity of the order of mm/s, the fictitious mass can become very large.

Transformation of Torque M

Usually the torque of a motor depends on the revolution frequency and is specified as torque M_{N} at the nominal frequency f_{N} and the so-called "start torque" M_{S} at $\omega_0 = 0$, which in general is higher than M_{N}. In a good approximation, the dependency of M on the angular velocity $\omega_0 = \dot{\varphi}_0$ can be assumed to be linear in the range $0 \le \dot{\varphi}_0 \le 2\pi f_{\mathrm{N}}$. Thus, we set

$$M(\dot{\varphi}_0) = M_{\mathrm{S}}^* - b\dot{\varphi}_0, \qquad \text{with } b = \frac{M_{\mathrm{S}}^* - M_{\mathrm{N}}^*}{2\pi f_{\mathrm{N}}}\ . \tag{6.102}$$

Remark. To consider the efficiency of the gear box η in (6.102), the specified motor torques $M_{\mathrm{S}}, M_{\mathrm{N}}$ are replaced by $M_{\mathrm{S}}^* = \eta M_{\mathrm{S}}$ and $M_{\mathrm{N}}^* = \eta M_{\mathrm{N}}$.

To transform torque M in the x-coordinate system, the work $F\,\Delta x$ of a force F in the x-coordinate system can be compared with the work $M\,\Delta\varphi_0$ done by M in the φ_0-coordinate system. From $F\,\Delta x = M\,\Delta\varphi_0$ and (6.96), it follows immediately

$$F_{\mathrm{M}} = \frac{2\pi}{p_{\mathrm{s}}}\frac{G_{\mathrm{r}}}{S}M_{\mathrm{S}}^* - b\frac{2\pi}{p_{\mathrm{s}}}\frac{G_{\mathrm{r}}}{S}\dot{x} = F_{\mathrm{MS}} - \gamma\dot{x}\ , \tag{6.103}$$

with the definitions $x_\varphi = 2\pi G_{\mathrm{r}}/p_{\mathrm{s}}S$, $F_{\mathrm{MS}} = x_\varphi M_{\mathrm{S}}^*$, and $\gamma = x_\varphi^2 b$.

The Differential Equation of Motion

With $m = m_{\mathrm{g}} + m_{\mathrm{I}}$, the transformed Lagrange function is

$$L(x,\dot{x}) = \frac{m}{2}\dot{x}^2 + \frac{k_{\mathrm{m}}}{2}x^2 - m_{\mathrm{g}}g\,x\ , \tag{6.104}$$

and the differential equation results from

$$\frac{d}{dt}\frac{\vartheta L}{\vartheta \dot{x}} - \frac{\vartheta L}{\vartheta x} = F_{\mathrm{M}}\,, \tag{6.105}$$

leading to

$$m\ddot{x} + k_{\mathrm{m}}x + m_{\mathrm{g}}g = F_{\mathrm{MS}} - \gamma\dot{x}. \tag{6.106}$$

It is practical to set this second-order differential equation in a mathematical standard form:

$$\ddot{x}(t) + p\dot{x}(t) + qx(t) = k \tag{6.107}$$

with

$$k = \frac{F_{\mathrm{MS}} - m_{\mathrm{g}}g}{m} \tag{6.108}$$

$$p = \frac{\gamma}{m} \tag{6.109}$$

$$q = \frac{k_{\mathrm{m}}}{m}\,. \tag{6.110}$$

The homogeneous part of (6.107) $\ddot{x}(t) + p\dot{x}(t) + qx(t) = 0$ is typical for damped oscillations, and the "Ansatz" $x(t) = e^{-\lambda t}$ leads to the characteristic equation

$$\lambda^2 - p\lambda + q = 0\,, \tag{6.111}$$

with the solutions

$$\lambda_1 = \frac{p}{2} + \frac{1}{2}\sqrt{p^2 - 4q} \tag{6.112}$$

$$\lambda_2 = \frac{p}{2} - \frac{1}{2}\sqrt{p^2 - 4q}\,. \tag{6.113}$$

As it is well known from the damped oscillator, there are three possible modes of movement:

- damped oscillation when $p^2 - 4q < 0$,
- "creeping motion" when $p^2 - 4q > 0$,
- "aperiodic limited case" if $p^2 - 4q = 0$.

In the first two cases, the solution of the homogeneous equation is

$$x(t) = C_1 e^{-\lambda_1 t} + C_2 e^{-\lambda_2 t}. \tag{6.114}$$

Keeping in mind the well-known relation $e^{ix} = \cos(x) + i\sin(x)$, we arrive at two expressions for damped oscillation:

$$x_1(t) = C_1 e^{-\frac{p}{2}x}\sin\left(\frac{1}{2}\sqrt{p^2 - 4q}x\right) \tag{6.115}$$

$$x_2(t) = C_2 e^{-\frac{p}{2}x}\cos\left(\frac{1}{2}\sqrt{p^2 - 4q}x\right)\,. \tag{6.116}$$

For the aperiodic case with $p^2 - 4q = 0$ and $\lambda_1 = \lambda_2$, the solution is

$$x(t) = C_1 e^{-\lambda t} + C_2 t e^{-\lambda t} \; . \tag{6.117}$$

For the first two cases, which are the probable ones, a solution of the inhomogeneous equation is $x(t) = k/q$. Therefore, the solution of (6.107) is given by

$$x(t) = C_1 e^{-\lambda_1 t} + C_2 e^{\,-\lambda_2 t} + \frac{k}{q} \; . \tag{6.118}$$

The constants C_1 and C_2 have to be determined from the initial conditions $x(0)$ and $\dot{x}(0)$. Assuming $x(0) = P_0$ and $\dot{x}(0) = 0$,

$$C_1 = \frac{P_0 - \frac{k}{q}}{1 - \frac{\lambda_1}{\lambda_2}} \tag{6.119}$$

$$C_2 = \frac{-\lambda_1}{\lambda_2} C_1 \; . \tag{6.120}$$

For the example of Fig. 6.50, $p^2 - 4q \simeq 4.7 > 0$ and, therefore the solution represents a "creeping motion," described by the coordinate $x(t)$, the velocity $\dot{x}(t)$, and the acceleration $\ddot{x}(t)$ as follows:

$$x(t) = C_1 e^{-\lambda_1 t} + C_2 e^{-\lambda_2 t} + \frac{k}{q} \tag{6.121}$$

$$\dot{x}(t) = -\left(C_1 \lambda_1 e^{-\lambda_1 t} + C_2 \lambda_2 e^{-\lambda_2 t}\right) \tag{6.122}$$

$$\ddot{x}(t) = C_1 \lambda_1^2 e^{-\lambda_1 t} + C_2 \lambda_2^2 e^{-\lambda_2 t} \; . \tag{6.123}$$

Because the solutions do not "know" the limitation $\dot{\varphi}_0 \leq 2\pi f_\mathrm{N}$ coming from (6.102), they hold only up to the time t_N, when the nominal frequency f_N is achieved. Normally, the revolution frequency is electronically controlled afterward to hold the nominal revolution frequency for all times $t > t_\mathrm{N}$. Movement then takes place at constant velocity determined by $\dot{\varphi}_0 = 2\pi f_\mathrm{N}$, corresponding to $\dot{x}_\mathrm{nom} = S\, p_\mathrm{s}\, f_\mathrm{N}/G_\mathrm{r}$ (7.7 mm/s in the example). The time t_N, where the frequency achieves f_N, can be determined from the relation $f(t) = \dot{x}(t) G_\mathrm{r}/S\, p_\mathrm{s}$.

Some Results from the Example

Figure 6.52 shows the main characteristics of motion during the first two seconds. From the plot of $f(t)$ versus t, one obtains $t_\mathrm{N} \simeq 1.2\,\mathrm{s}$.

Of course, the initial position of $P_0 = -90\,\mathrm{mm}$ chosen has an influence on the time t_N, because this starting position results in a force on the membrane bellows, which tries to lift the load. The direction of this force changes, when the load passes the position $x = 0$, related to the so-called "free length" (see Table 6.5). This can be demonstrated by calculating the value of t_N for a positive initial position. Taking, for example, $P_0 = +90\,\mathrm{mm}$ results in $t_\mathrm{N} = 1.47\,\mathrm{s}$.

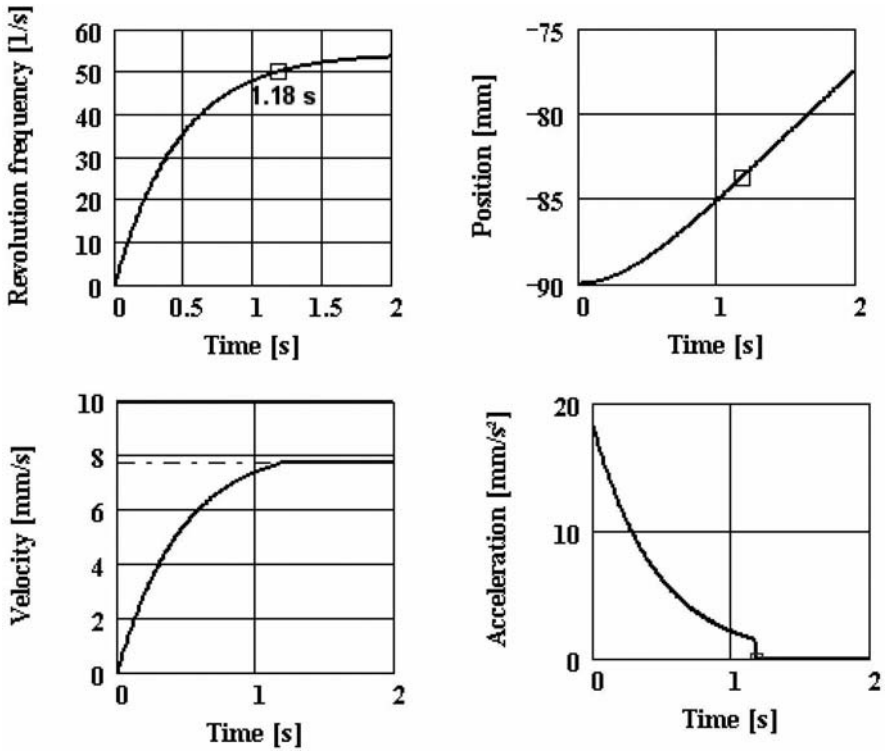

Fig. 6.52. Top left: Revolution frequency dependent on time. After 1.18 s, the nominal revolution frequency of 50/s is reached and further acceleration is stopped. Top right: Position of the load starting at $P_0 = -90$ mm. Bottom left: Velocity versus time, taking into account the limitation in the revolution frequency at $f_N = 50/s$. Bottom right: Acceleration versus time, stopped at $t = t_N$

Conclusion

The estimations given in the first part of this appendix are confirmed by the equations of movement. Therefore, in most cases, the dimensioning of similar mechanical systems can be based on the given estimations. On the other hand, the application of the Lagrange formalism may be helpful for dimensioning more complex mechanical systems.

7

The Longitudinal Phase Plane

Referring to (6.2) (Chap. 6) and keeping in mind that the particles are moving along the z-axis, the longitudinal phase plane is defined by $A_\mathrm{z} = \int\int dz\, dp_\mathrm{z}$. But, because the longitudinal coordinate z itself does not give very much practical information, it is usual to define a fictitious reference particle moving at $v = \beta\, c$, which corresponds to a kinetic energy of $W = m_\mathrm{u} c^2(\gamma{-}1)$. Inserting $m_\mathrm{u} = 931.5016\,\mathrm{MeV/c^2}$ for ions and $m_\mathrm{u} = 0.511\,\mathrm{MeV/c^2}$ for electrons leads to the energy per mass unit in MeV/u. Therefore, the total energy of the reference particle is $A\,W$ with A as the mass number of the ion and $A = 1$ for electrons. Considering rf accelerators, particles moving in a bunch along the z-axis

- can have the correct kinetic energy but may be a small time Δt ahead of or behind the reference particle,
- can be in phase with the reference particle but have a deviation in energy ΔW,
- or may even have deviations in Δt and ΔW.

Because $\phi = \omega t$ and $dz = \beta c \Delta t = \beta c \Delta\phi/\omega$, Δt or $\Delta\omega$ can be taken as the abscissa in the longitudinal phase plane, where $\omega = 2\pi f$ (f, accelerating frequency). Because $d\,p_\mathrm{z}/p_\mathrm{z} \sim \mathrm{d}W/W$, it has proven very practical to define the longitudinal emittance as

$$\varepsilon_\mathrm{z} = A_\mathrm{z}/\pi = \frac{1}{\pi}\int\int d\phi\,\mathrm{d}W\ . \tag{7.1}$$

However, accelerator physicists are mostly interested in the energy or momentum spread of particles, and therefore it is usual to take $\Delta W/W$ (or sometimes $\Delta p/p$) as the ordinate in the phase plane diagram. Of course, the reference particle is always located at the origin of the $\Delta\phi - \Delta W/W$, respectively, $\Delta t - \Delta W/W$ diagram. Thus, assuming an elliptical shape of the intensity distribution in the longitudinal phase plane and referring to Fig. 6.5, point 2

represents the bunch width, and point 3 is determined by the maximum energy or momentum spread. Obviously, for dc-beams, the definition of a phase deviation does not make sense.

Remark. For practical reasons, some computer codes for the design of accelerator structures and beam transport systems use the same dimensions for the longitudinal emittance as for the transverse ones, e.g. mm·mrad. Because $p_z = \gamma m_u \beta c$ and $\Delta p_z/p \sim \Delta p/p$ can be expressed in the dimensionless unit "mrad," one finds for the normalized longitudinal emittance,

$$\epsilon_n\,[kev/u \cdot ns] = m_0 c \cdot \epsilon_n\,[\mathrm{mm \cdot mrad}] = 3.107 \cdot \epsilon_n\,[\mathrm{mm \cdot mrad}] \qquad (7.2)$$

with $m_u = 931.5016$ MeV/c^2 and $c = 299.7925$ mm/ns; the factor 3.107 can be easily determined from $m_0 c^2/c$ (see also [352]).

7.1 Emittance Measurements in the Longitudinal Phase Plane

7.1.1 Destructive Measurements

Determination of density distributions in the longitudinal phase plane is more complicated than those for transverse planes. A sophisticated scheme to determine the longitudinal emittance of a H^- beam has been described in [353]. Negatively charged ions are deflected by a bending magnet. A laser installed in front of the magnet delivers very short (30 ps) strobe pulses. The H^- ions hit by the laser pulses are neutralized and therefore go straight ahead through the magnet. The short neutralized pulses are analyzed with respect to their energy by a semiconductor detector installed behind the magnet. Moving of the bunches through the mode-locked laser pulse results in sampling the bunch in 30-ps time slices. Referring to the slit-detector method applied in the transverse phase planes, this can be compared with the movement of the slit through the beam (see also Fig. 7.2).

A simplified scheme of a destructive measurement is shown in Fig. 7.1. Here a slit-magnet-slit combination defines a small momentum spread Δp around the momentum p, determined by the setting of the bending magnet. The particles going through the second slit are deflected by a rf-synchronous sweep of the deflecting device (cavity, deflecting plates), installed behind the slit. Therefore, the intensity profile in time is transformed into a transverse profile that can be detected with a profile measuring device. By changing the magnetic field strength, the density distribution in the $\Delta t - \Delta p/p$, respectively, $\Delta t - \Delta W/W$ diagram can be determined. In this scheme, a change in the magnetic field strength moves a small window of width $\Delta p \sim \Delta W \sim \Delta W/W$ along the $\Delta W/W$-axis parallel to the $\Delta\phi, \Delta t$ - axis. The two schemes discussed are illustrated and compared in Fig. 7.2.

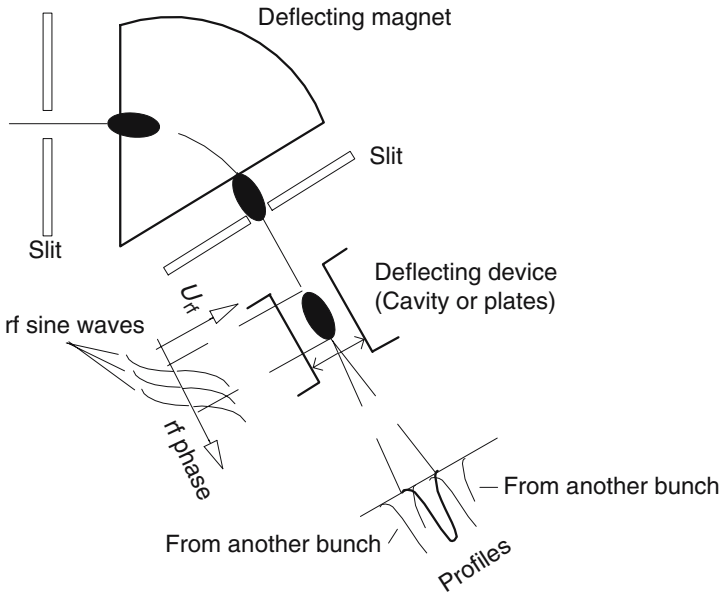

Fig. 7.1. Simplified scheme to measure longitudinal emittance

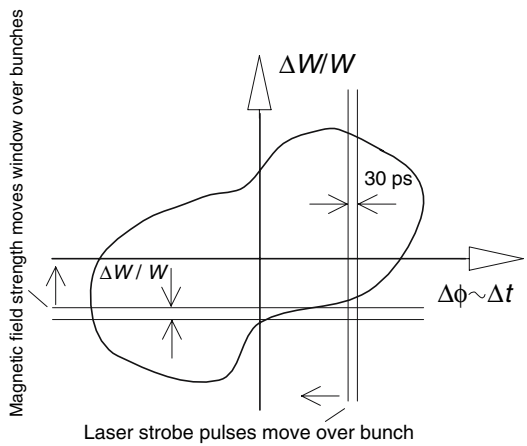

Fig. 7.2. The figure explains two methods of longitudinal emittance measuring. In one scheme, a small "window" in time is moved along the t-axis (abscissa). In the other scheme, a small "window" in W or $\Delta W/W$ is moved along the ordinate

Modern particle detectors, such as scintillation counters, semiconductor devices, multichannel plates (MCP) with anodes in 50-Ω geometry, and diamond detectors [133,138,143,267,354] can deliver fast signal pulses if hit by a particle. The scheme of a versatile setup is shown in Fig. 7.3. The system has been developed to study the influence of space charge on bunch shape and

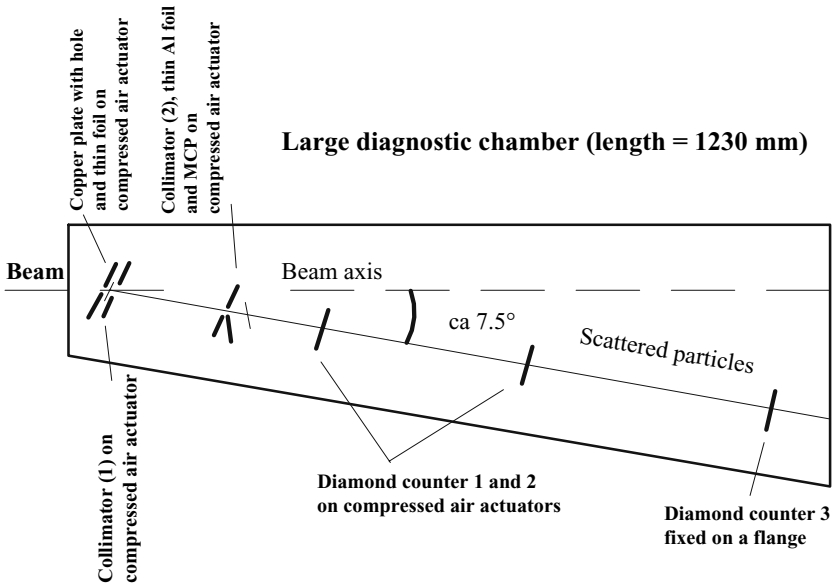

Fig. 7.3. Schematic sketch showing the arrangement of components in an experimental setup to measure intensity distributions in the longitudinal phase plane. See text for details

longitudinal emittance at high currents [258, 267]. A long experimental chamber is equipped with three diamond counters and one MCP to generate fast pulses. Due to saturation effects and pile-up, the counting rates have to be limited to some hundred kHz. This reduction in counting rate can be achieved by Rutherford scattering in a thin foil. There are two possible modes for using the system:

- Measurement of bunch shape along a drift space. This corresponds to a projection of the density distribution in the phase plane onto the time axis.
- Measurement of the longitudinal emittance.

Bunch Shape Measurement

In this application, the MCP and the second thin foil are moved out of the beam. The bunches hit the first thin foil. A small part of particles is scattered by Rutherford scattering in a small solid angle $\Delta\Omega_{\mathrm{lab}}$, well defined by the collimator system. The scattered particles hit the first diamond counter generating a fast signal. The signal is amplified and shaped by a discriminator, shown schematically in Fig. 7.4. The signal from the discriminator starts (start 1) a time to digital converter (TDC) with a resolution of at least 25 ps (least significant bit, LSB). Since the stop signal for the TDC is derived from

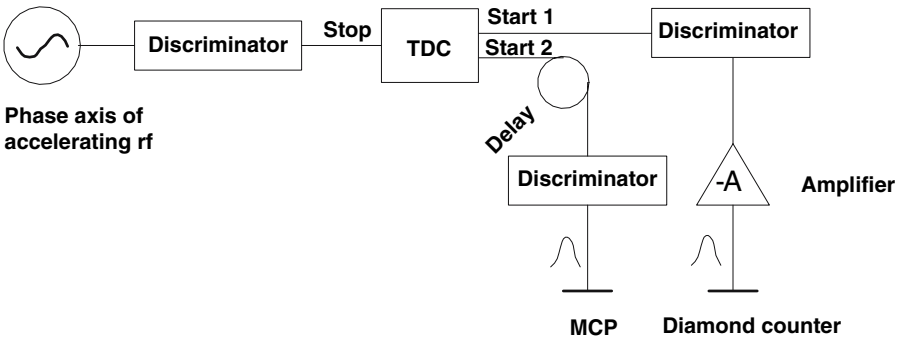

Fig. 7.4. Scheme of signal processing to determine intensity distributions in the longitudinal phase plane. In bunch shape measurements, only the signal generating start 1 is relevant (see text)

the accelerating rf, the measured counting rate reflects the bunch shape along the time axis. Repeating the measurement with the second and third diamond counter allows visualization of the dispersion of the bunches along the drift spaces of about 400 mm between each of them. Figure 7.5 shows the results from commissioning [267] a 120-keV/u RFQ. A thin gold foil has been used as a target for Rutherford scattering. The resolution achieved was 48 ps per bin. The three diagrams on the left-hand side of the picture correspond about to the shapes expected from numerical simulations [355]. The two side peaks observed at diamond 1 are smeared out due to the energy spread after a drift of about 800 mm. The usefulness of bunch shape measurements is demonstrated in the three diagrams on the right-hand side of Fig. 7.5, measuring the dependency of the bunch shape on the rf amplitude of the RFQ with one diamond detector.

Measurement of Longitudinal Emittance

In this case, a second thin aluminum foil ($15\,\mu g/cm^2 \sim 50\,nm$) and the MCP are moved in, and diamonds 1 and 2 are moved out. A scattered particle hits the aluminum foil behind the collimator. The secondary electrons arising are accelerated by a 1-kV/cm electric field toward the MCP with a 50-Ω anode, delivering fast output signals, shaped to the start 2 signal of the TDC. The same particle is stopped in diamond detector 3 located about 800 mm behind the MCP. Therefore, the time of flight of the particle between the MCP and the diamond detector determines the energy of that particle. This leads to the density distribution in the longitudinal phase plane. In an accelerator experiment, the system was installed in the stripper section of the UNILAC to study space charge effects on the size and shape of the longitudinal emittance of the high current injector. An example of a measurement is given in Fig. 7.6. Here the phase space plot on the left-hand side corresponds to a low current

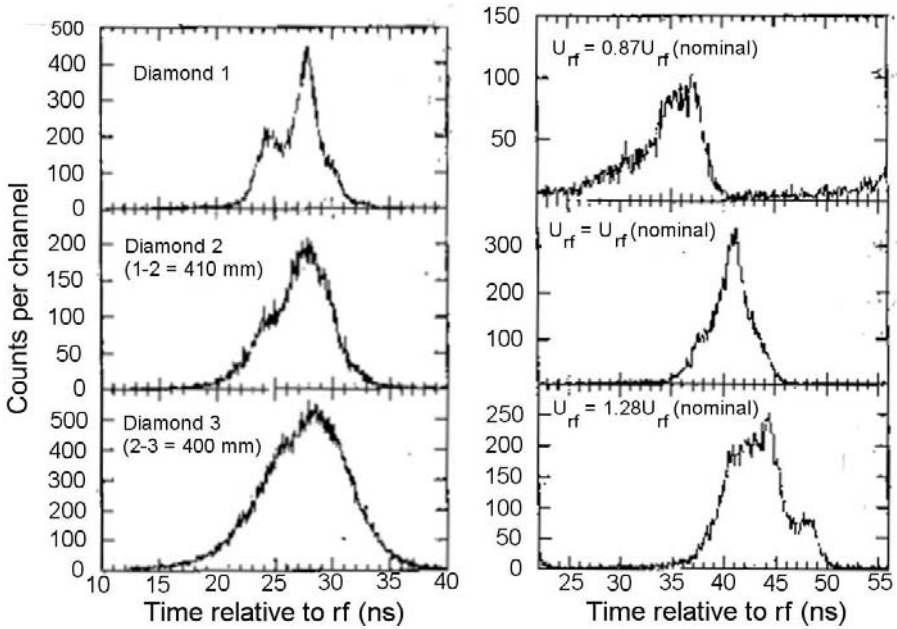

Fig. 7.5. Observed bunch shapes during commissioning [267] of a RFQ section with 120-keV/u output energy. The measurements on the left-hand side show the dispersion of the bunches along a drift space of about 800 mm. The bunch shape signals on the right-hand side, measured with only one diamond detector, show the dependency of bunch shape on the rf amplitude

Ar beam of 0.1 mA; the diagram on the right-hand side corresponds to a high current beam of 5 mA. The emittance is asymmetrically broadened due to the action of space charge forces. In the diagrams, the abscissa gives the arrival time of a scattered particle at the MCP, measured relative to a certain phase of the accelerating rf (see Fig. 7.4). The ordinate shows the time of flight (TOF) between the MCP and the diamond detector. Taking into account the rather low energy $W = 1.4\,\mathrm{MeV/u}$ of the particles in this section, which corresponds to $\beta = v/c = 0.055$, the energy spread of each particle can be determined from the nonrelativistic relation

$$\frac{\Delta W}{W} = 2\frac{\Delta t}{t} \tag{7.3}$$

$$t = \frac{800\ [\mathrm{mm}]}{0.055 \cdot 300\ [\mathrm{mm/ns}]} = 48.5\,\mathrm{ns} \tag{7.4}$$

$$\frac{\Delta W}{W} = 2\,\frac{0.42}{48.5} = 1.73\% \quad \text{(FWHM, diagram on left)} \tag{7.5}$$

$$\frac{\Delta W}{W} = 2\,\frac{0.68}{48.5} = 2.80\% \quad \text{(FWHM, diagram on right).} \tag{7.6}$$

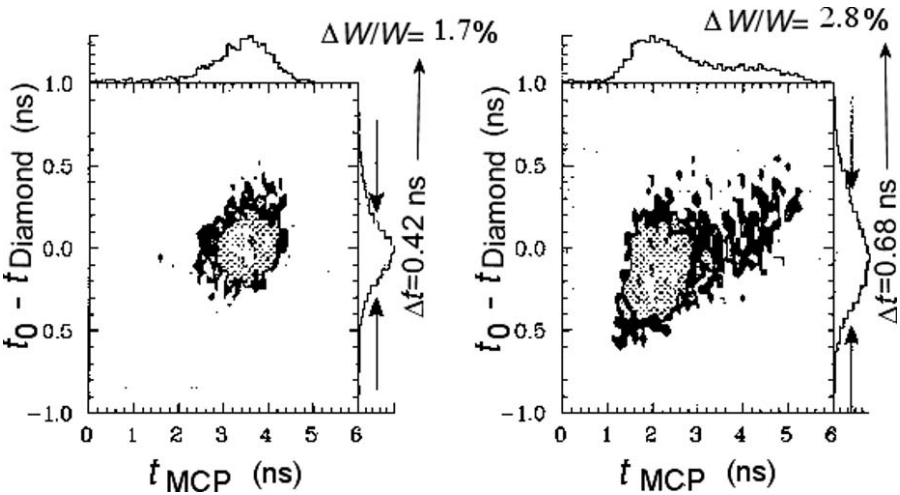

Fig. 7.6. Phase space plots measured at low (left) and high (right) beam current in the stripper section of the UNILAC [356]. Note that the measured energy spread might be too large. See text for details

The measured values are larger by about a factor of 2 in comparison to tracking calculations [356]. Several reasons are discussed:

- errors due to imperfections in the measuring system,
- possible problems inside the stripper [357] due to inhomogeneity of the gas jet.

In fact, considering the complexity of the system, the design parameters have to be studied very carefully to achieve the expected performance.

Study and Discussion of the Design Parameters

When designing such a system, the following points have to be considered:

- required attenuation by Rutherford scattering with respect to the maximum counting rates of the detectors, as well as the limitations from the TDC;
- transfer of energy in the elastic scattering process, leading to uncertainties in time of flight measurements that take the finite solid angle into account;
- thermal effects, considering the energy loss of the particles in the scattering foil;
- energy spread due to the energy loss in the foils;
- achievable accuracy in time determination, due to the limited drift space between various detectors;
- achievable time resolution with the TDC.

Rutherford Scattering

The Rutherford scattering formula has been derived to determine the deflection of protons, considering a heavy nucleus as scatterer. In the original version [46], the formula is nonrelativistic and refers to a fixed center, neglecting the finite mass of the scatterer. The differential scattering cross section for the number of protons deflected through an angle between θ and $\theta + d\theta$ has been determined by [45]

$$\frac{d\sigma}{d\omega} = \frac{1}{4}\left(\frac{e^2 Z}{mv^2}\right)^2 \frac{1}{\sin^4(\theta/2)} \,. \tag{7.7}$$

Here $d\omega$ is the solid angle, included between the two cones of aperture θ and $\theta + d\theta$, Z is the atomic number of the scatterer, and m and v are the mass and velocity of a proton. The concept of cross section σ was introduced in nuclear physics as a very practical proportionality factor for calculating the number of events in a certain nuclear reaction:

$$\frac{\mathrm{NE}}{\mathrm{Time}} = \frac{\mathrm{NP}}{\mathrm{Area} \times \mathrm{Time}} \sigma \, \mathrm{NT} \tag{7.8}$$

with

NE = number of events
NP = number of projectiles
NT = number of nuclei (scatterer) in the target.

To apply (7.7) to the problem under consideration, two important corrections have to be made:

- consider projectiles of any type,
- take the finite mass of the target nuclei into account.

The extension to other particles beside the proton can be done by replacing Z with Zz, where z is the atomic number of the projectile. Of course, m then stands for the mass of the projectile instead of the mass of the proton. To consider the finite mass of the target, one has to transform (7.7) to center of mass coordinates. This can be performed by replacing the laboratory angle θ by the angle Θ defined in the center of mass system. To calculate the kinetic energy in the center of mass frame, the concept of reduced mass is introduced. The transformation of (7.8) gives

$$\frac{\mathrm{NE}}{\mathrm{NP}} = \mathrm{NT} \, d\sigma(\Theta) \, \Delta\omega \, \frac{\Delta\Omega}{\Delta\omega} \,. \tag{7.9}$$

Introducing practical units and taking the corrections discussed into account, $d\sigma(\Theta)$ is given by

$$d\sigma(\Theta) = FAC \left(\frac{Z\,z}{A_{\mathrm{red}}\,m_{\mathrm{u}}c^2}\right)^2 \frac{1}{\beta^4}\frac{1}{4\,(\sin\frac{\Theta}{2})^4} \tag{7.10}$$

$$FAC = \frac{e}{4\pi\varepsilon_0} = 1.44 \times 10^{-13}\,\mathrm{MeV\,cm} \tag{7.11}$$

$$A_{\mathrm{red}} = \frac{A_{\mathrm{P}}\,A_{\mathrm{T}}}{A_{\mathrm{P}} + A_{\mathrm{T}}}, \text{ reduced mass number.} \tag{7.12}$$

In (7.12), A_{P} stands for the mass number of the projectile, and A_{T} is the mass number of the target nuclei. Using these units, $m_{\mathrm{u}}c^2$ has to be inserted in MeV. As usual, the number of target nuclei NT is determined from

$$\mathrm{NT}[1/\mathrm{cm}^2] = \rho\,\Delta x\,N_{\mathrm{A}} = \rho\,\Delta x\,\frac{6\times10^{23}}{A_{\mathrm{T}}}\,, \tag{7.13}$$

where N_{A} is Avogadro's number (also Loschmidt's number).

The solid angle in the laboratory system $\Delta\omega = \sin\theta\,d\theta\,d\phi$ is defined by the limiting aperture of the collimator system, which simplifies to $\Delta\omega = \pi R^2/D^2$ for a round hole with radius R, located at distance D behind the target.

The transformation $\Delta\Omega/\Delta\omega$ between the solid angles in the center of mass system and the laboratory system remains, which is a classical exercise in nuclear physics [45, 358]:

$$\frac{\Delta\Omega}{\Delta\omega} = \frac{\sin^3\Theta}{\sin^3\theta}\frac{1}{\left(1+\frac{A_{\mathrm{P}}}{A_{\mathrm{T}}}\cos\Theta\right)}, \quad \text{with} \tag{7.14}$$

$$\theta = \arctan\left(\frac{\sin\Theta}{\frac{A_{\mathrm{P}}}{A_{\mathrm{T}}}+\cos\Theta}\right). \tag{7.15}$$

Equation (7.15) gives the transformation of the scattering angle Θ into the scattering angle of the laboratory system, which is more relevant for the design of a system. This is shown at the left-hand side of Fig. 7.7 for small angles; the diagram on the right gives the ratio of the solid angles $\Delta\Omega/\Delta\omega$, according to (7.14).

The rf-accelerating frequency of the GSI high current linac is 36 MHz. Therefore, to reduce the counting rate to less than one event per rf period, rather high attenuation is required. Due to the proportionality of the cross section to $1/\sin^4(\Theta/2)$, increasing the scattering angle is most effective in this respect. Furthermore, taking the proportionality of the cross section to Z, the atomic number of the target nuclei into account, at first glance, the designer may prefer targets with low Z. But, beside the attenuation factor, one also has to consider the energy spread from the finite solid angle.

Energy Spread from Scattering

In nonrelativistic approximation, the total energy of the projectile and the recoil energy of the target nucleus after the collision are given by

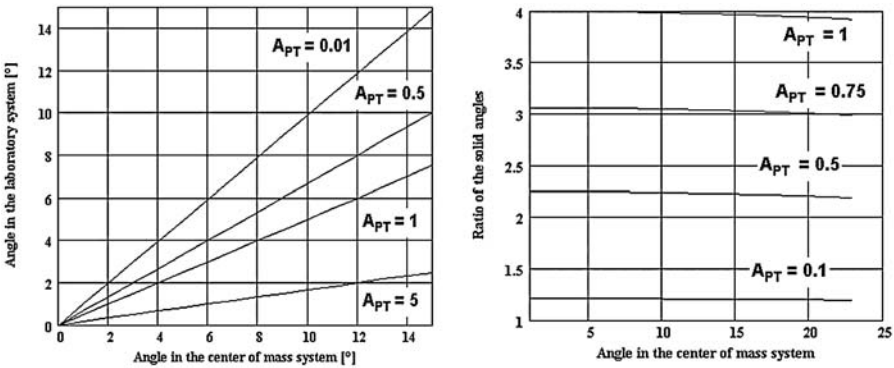

Fig. 7.7. Left: Angle in the laboratory system as a function of the angle in the center of mass system. The parameter A_{PT} is the mass ratio of the projectile to the target ($A_{\mathrm{P}}/A_{\mathrm{T}}$ in 7.15). Right: Ratio of the solid angles $\Delta\Omega/\Delta\omega$, according to 7.14

$$W_{\mathrm{P}} = W_{P_0}\left[1 - 4\sin^2\left(\frac{\Theta}{2}\right)\frac{A_{\mathrm{red}}}{A_{\mathrm{P}}+A_{\mathrm{T}}}\right] \tag{7.16}$$

$$W_{\mathrm{T}} = W_{P_0}\frac{A_{\mathrm{T}}}{A_{\mathrm{P}}}\left(\frac{A_{\mathrm{red}}}{A_{\mathrm{T}}}\right)^2 4\sin^2\left(\frac{\Theta}{2}\right), \tag{7.17}$$

with $W_{P_0} = \frac{1}{2}A_{\mathrm{P}}m_0c^2\beta^2$ as the kinetic energy before the collision. The energy spread due to the finite solid angle follows immediately from

$$\mathrm{d}W_{\mathrm{P}} = \frac{\mathrm{d}W_{\mathrm{P}}}{d\Theta}\frac{d\Theta}{d\theta}\delta\theta \tag{7.18}$$

$$\frac{\mathrm{d}W_{\mathrm{P}}}{d\Theta} = -4W_{P_0}\sin\frac{\Theta}{2}\cos\frac{\Theta}{2}\frac{A_{\mathrm{red}}}{A_{\mathrm{P}}+A_{\mathrm{T}}} \tag{7.19}$$

$$\frac{d\Theta}{d\theta} = \frac{1+\left(\frac{A_{\mathrm{P}}}{A_{\mathrm{T}}}\right)^2 + 2\frac{A_{\mathrm{P}}}{A_{\mathrm{T}}}\cos\Theta}{\frac{A_{\mathrm{P}}}{A_{\mathrm{T}}}\cos\Theta + 1}. \tag{7.20}$$

The quantity $\delta\theta$ is determined by the finite solid angle in the laboratory system. The distribution of particles over $\Delta W/W$ is derived from time of flight measurements, with Δt referenced to the particle having energy W_{P} [see (7.3)]. Therefore, the relative energy spread due to the finite solid angle

$$\frac{\Delta W_{\mathrm{P}}}{W_{\mathrm{P}}} = -\frac{4\sin\frac{\Theta}{2}\cos\frac{\Theta}{2}\frac{A_{\mathrm{red}}}{A_{\mathrm{P}}+A_{\mathrm{T}}}}{1-4\sin^2\left(\frac{\Theta}{2}\right)\frac{A_{\mathrm{red}}}{A_{\mathrm{P}}+A_{\mathrm{T}}}}\frac{1+\left(\frac{A_{\mathrm{P}}}{A_{\mathrm{T}}}\right)^2+2\frac{A_{\mathrm{P}}}{A_{\mathrm{T}}}\cos\Theta}{\frac{A_{\mathrm{P}}}{A_{\mathrm{T}}}\cos\Theta+1}\delta\theta \tag{7.21}$$

should be small in comparison to the required resolution in $\Delta W_{\mathrm{P}_0}/W_{\mathrm{P}_0}$. Contrary to the arguments for large scattering angles and low mass targets, this requires small scattering angles θ and high mass targets.

Example: To illustrate the dependencies, we assume the following parameters:

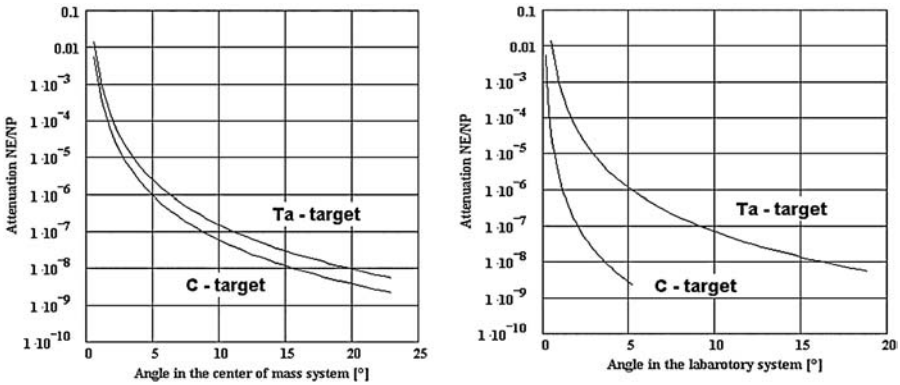

Fig. 7.8. Attenuation factor NE/NP. Left: dependence on Θ, the angle in the center of mass system. Right: dependence on θ, the angle in the laboratory system

Projectile: Ar ($A_{\mathrm{P}} = 40$, $z = 18$, $W_{P_0} = 1.4\,\mathrm{MeV/u}$, $\beta = 5.5\%$)
Target 1: C-foil ($A_{\mathrm{T}} = 12$, $Z = 6$, thickness 25 nm, $\rho = 2\,\mathrm{g/cm^3}$)
Target 2: Ta-foil ($A_{\mathrm{T}} = 181$, $Z = 73$, thickness 126.5 nm, $\rho = 16.6\,\mathrm{g/cm^3}$)
Scattering angle: $2.5°$ *in the laboratory system*
Limiting aperture: hole of 0.25 mm *radius in a distance of* 160 mm
Resulting $\Delta\theta$: 1.56×10^{-3}
Resulting solid angle $\Delta\omega$: 7.7×10^{-6}

Target 1 gives $\rho\Delta x = 5\,\mu\mathrm{g/cm^2}$ and NT$= 2.5 \times 10^{17}/\mathrm{cm^2}$, Target 2 gives $\rho\Delta x = 210\,\mu\mathrm{g/cm^2}$ and NT$= 3.66 \times 10^{17}/\mathrm{cm^2}$. Figure 7.8 shows the attenuation factor NE/NP for both targets dependent on the scattering angles in the center of mass system (left), as well as in the laboratory system (right). Figure 7.9 shows the energy spread due to the finite solid angle, demonstrating the advantage of the target with the larger mass. Comparing the energy spread for the chosen scattering angle of $\theta = 2.5°$ leads to $\Delta W/W_{\mathrm{C}} \approx -0.046\%$ and $\Delta W/W_{\mathrm{Ta}} \approx -0.003\%$, which is a factor of 15.25 in favor of the Ta target.

Remark. The finite solid angle also leads to an uncertainty in θ ($\delta = 0.25\,\mathrm{mm}/160\,\mathrm{mm} = 1.56 \times 10^{-3} \approx 0.09°$, in the example), which results in a spread of the time of flight. In the nonrelativistic approximation, one finds $\Delta L/L = 1/2\ \Delta\theta^2$ and $\Delta W/W = \Delta\theta^2$, which can be neglected.

Energy Spread from Electronic Stopping in the Foil

On the other hand, considering the contributions to the energy spread from electronic stopping in the foil, the C target shows much lower values of energy straggling. The energy distribution of transmitted particles for both targets has been calculated with the well-known and practical TRIM program [359]. Tracking about 10.000 argon ions with a total energy of 56 MeV ($\approx$1.4 MeV/u) through the $210\,\mu\mathrm{g/cm^2}$ Ta foil, the remaining energy of each particle is one

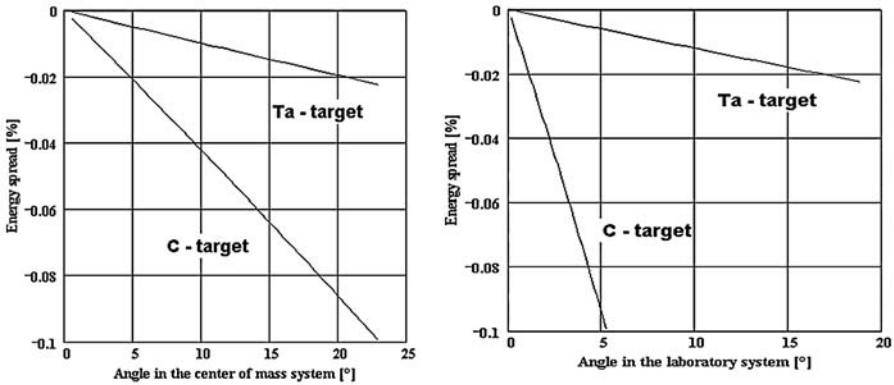

Fig. 7.9. Energy spread from the finite solid angle. Left: dependent on Θ, the scattering angle in the center of mass system. Right: dependent on θ, the scattering angle in the laboratory system

option in the program outputs. Collecting the particles in bins with a width of 0.01 MeV leads to the distribution shown on the left-hand side of Fig. 7.10: the new peak energy at 54.33 MeV has a half-width (FWHM) of about 0.155 MeV, resulting in a relative energy spread of about 0.28%. This is confirmed in the diagram on the right-hand side of Fig. 7.10, where the particles are sorted in bins of 0.1% width referenced to the mean value of energy loss.

Remark. Sorting the particles in bins of an appropriate width in energy and refering the percentages to the mean value of energy loss gives results, which differ slightly from calculation of the rms values of the original data. Due to the high weights of large deviations from the average, the rms values tend to be somewhat larger (see Table 7.1).

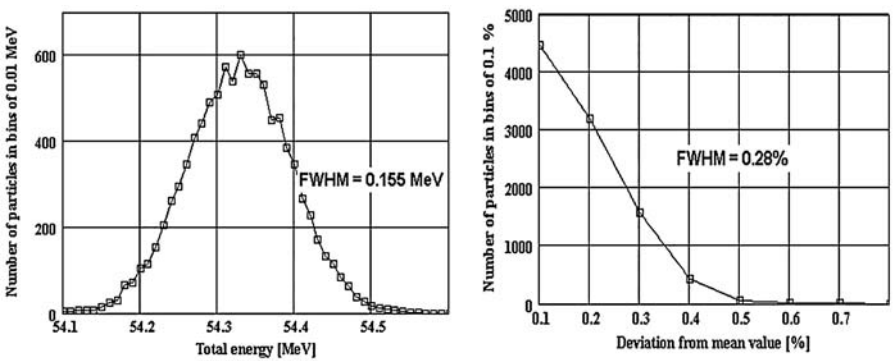

Fig. 7.10. Calculated energy spread from electronic stopping of 1.4-MeV/u Ar-ions passing a 210-µg/cm^2 Ta foil. Left: energy distribution. Right: relative energy spread referenced to the new peak energy of 54.3 MeV

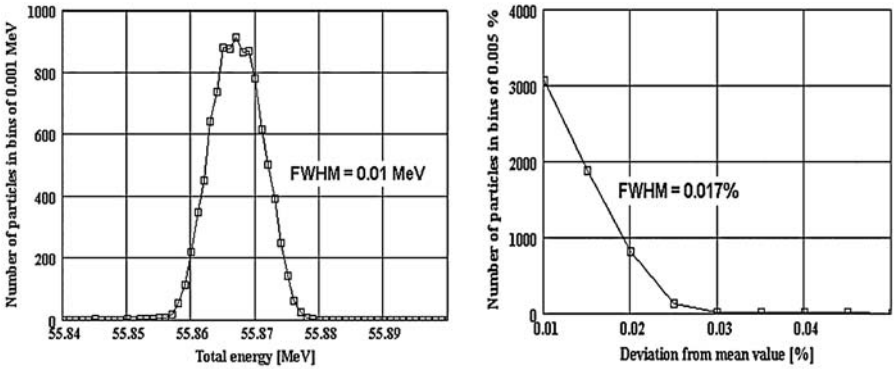

Fig. 7.11. Calculated energy spread from electronic stopping of 1.4-MeV/u Ar-ions passing a 5-μg/cm^2 C foil. Left: energy distribution. Right: relative energy spread referenced to the new peak energy of 55.867 MeV

The results for the 5 μg/cm^2 C foil are displayed in Fig. 7.11. The peak energy after passing the C foil is 55.87 MeV, leading to a relative energy spread of about 0.017%. Taking the much lower values of energy loss and straggling into account, the bin widths have been changed in Fig. 7.11 to 0.001 MeV and 0.005%, respectively. Clearly, considering the energy spread due to straggling in the foil, one would prefer a lower mass target. On the other hand, inhomogeneities in the foil thickness can lead to a larger contribution to the energy spread for the very thin C target.

The numerical calculation with the TRIM program can be compared with an analytical formula given by Bohr [360]:

$$\sigma(t) = 10^{-3}\sqrt{4\pi\,\mathrm{FAC}\,z\,Z^2\,t\,\frac{N_\mathrm{A}}{A_\mathrm{T}}\,\frac{1-\beta^2/2}{1-\beta^2}} \tag{7.22}$$

where t is the target thickness in units of μg/cm^2. Table 7.1 shows the results in comparison to the evaluation of the TRIM data.

Table 7.1. Comparison of calculated energy spread, applying various methods. Method 1: rms-values and FWHM directly from the TRIM output energies. Method 2: FWHM and σ determined from sorting into bins (see text for details). Method 3: rms values and FWHM calculated from (7.22).

Target	Ta	210 μg/cm^2	C	5 μg/cm^2
Method	σ [MeV]	FWHM [%]	σ [MeV]	FWHM [%]
1	0.076	0.33	0.0057	0.024
2	0.065	0.28	0.004	0.017
3	0.132	0.56	0.011	0.046

Thermal Heating of Scattering Foils

Although the Al foil provided to deliver the start signal via the MCP (see Fig. 7.3) is hit only by scattered particles, the scattering foils have to withstand the full power density of the beam. Thermal heating of thin foils arises in many experimental setups of nuclear and high energy physics. Because of very poor heat conductivity in the radial direction and nearly no heat transfer by convection in a vacuum, cooling of thin foils takes place exclusively by radiation. Due to the manifold parameters such as foil thickness, foil material, beam power density, beam energy, kind of ions hitting the target, duty cycle if pulsed, the problem is very complicated. Although cooling by radiation is discussed in Chap. 3, some simple estimations will be discussed with respect to the example discussed.

Let's assume the following beam parameters additionally to those already known (some parameters are repeated for the sake of review):

Beam energy: $W = 1.4\,\mathrm{MeV/u}$, Ar^1-ions ($A_\mathrm{P} = 40$, $z = 18$, $\zeta = 1$)
rf accelerating frequency: $f = 36\,\mathrm{MHz}$
Macropulse length: $T_\mathrm{p} = 200\ \mu\mathrm{s}$
Macropulse current: $I_\mathrm{p} = 5\,\mathrm{mA}$
Beam spot size: $R_\mathrm{b} = 5\,\mathrm{mm}$
Repetition frequency of the macropulse: $f_\mathrm{p} = 2/\mathrm{s}$

The energy loss is well defined by the TRIM calculation, but it may be of interest to compare this with data on electronic stopping power (ESP), available in the literature. For the projectile–target combination, argon ($W = 1.4\,\mathrm{MeV/u}$)–carbon, one gets from the TRIM-calculation

$$\mathrm{ESP}_{\mathrm{A}\to\mathrm{C}} = \frac{56-55.867\ [\mathrm{MeV}]}{5\,\mu\mathrm{g/cm}^2} = 26.6\,\frac{\mathrm{MeV}}{\mathrm{mg/cm}^2}\,, \tag{7.23}$$

and the combination argon–tantalum leads to

$$\mathrm{ESP}_{\mathrm{A}\to\mathrm{Ta}} = \frac{56-54.326\,\mathrm{MeV}}{210\,\mu\mathrm{g/cm}^2} = 7.971\,\frac{\mathrm{MeV}}{\mathrm{mg/cm}^2}\,. \tag{7.24}$$

Programming formulas given in the "Handbook of Stopping Cross Sections for Energetic Ions in All Elements" [122], taking also into account nuclear stopping, lead to $\mathrm{ESP}_{\mathrm{A}\to\mathrm{C}} = 24.552\,\mathrm{MeV/mg\,cm^{-2}}$ and $\mathrm{ESP}_{\mathrm{A}\to\mathrm{Ta}} = 8.078\,\mathrm{MeV/mg/cm^{-2}}$.

From the tables given in [124], one finds $\mathrm{ESP}_{\mathrm{A}\to\mathrm{C}} = 24.6\,\mathrm{MeV/mg/cm^{-2}}$ and $\mathrm{ESP}_{\mathrm{A}\to\mathrm{Ta}} = 7.41\,\mathrm{MeV/mg/cm^{-2}}$. Keeping in mind the complexity of the problem, as well as the manifold processes involved, the agreement is respectable and in each case sufficient, considering the example under discussion.

To estimate the thermal load on scattering foils, the energy deposited in the foil within one macropulse should be compared with the required energy

for melting the volume, where the energy is deposited. The deposited energy W_d follows immediately from the following relations:

$$N_\mathrm{m}\, e = \frac{I\,T}{\zeta_\mathrm{Ar}} = 5\ \times 10^{-3} \cdot 200\ \times 10^{-6} = 1\ \times 10^{-6} \tag{7.25}$$

$$W_{\mathrm{Ar}\to\mathrm{C}} = N_\mathrm{m} e\, \Delta W_{\mathrm{Ar}\to\mathrm{C}} = (56 - 55.867) = 0.133\,\mathrm{Ws} \tag{7.26}$$

$$W_{\mathrm{Ar}\to\mathrm{Ta}} = N_\mathrm{macro}\, \Delta W_{\mathrm{Ar}\to\mathrm{Ta}} = (56 - 54.326) = 1.674\ \mathrm{Ws}. \tag{7.27}$$

The volumes where the energy is deposited are $V_\mathrm{C} = \pi\, R_\mathrm{b}^2 \times 25\,\mathrm{nm} = 1.96 \times 10^{-3}\,\mathrm{mm}^3$ and $V_\mathrm{Ta} = \pi\, R_\mathrm{b}^2\ \times 126.5\,\mathrm{nm} = 9.94 \times 10^{-3}\,\mathrm{mm}^3$. From Table 3.1 in Chap. 3, the energy required to melt a volume of $1\mathrm{mm}^3$ of carbon is $W_\mathrm{C} = 8.05$ Ws and for tantalum it is $W_\mathrm{Ta} = 10.95$ Ws. Therefore, the energy required to melt V_C within only one macropulse is 0.016 Ws and to melt V_Ta it is 0.109 Ws. In both cases the deposited energy per macropulse is much higher. Thus, the foils will not withstand the total beam power density. Use of thinner foils does not solve the problem due to the linear proportionality of target thickness and energy loss in the target. One possibility of reducing the power density is transverse defocusing of the beam. However, because the measuring system was provided to study space charge effects in the longitudinal phase space, this has to be considered in more detail.

Counting Rates

Due to the disadvantageous mass ratio Ar–C, the experiment has been performed with the Ta target. Assuming all particles hit the scattering foil results in a counting rate CR of

$$\mathrm{CR} = f_\mathrm{m}\, N_\mathrm{macro} \left(\frac{\mathrm{NE}}{\mathrm{NP}}\right)_{\theta=2.5^0} \tag{7.28}$$

$$= 2 \cdot 6.25\ \times 10^{12} \cdot 1.69\ \times 10^{-5} = 2.113\ \times 10^{8}, \tag{7.29}$$

which of course is too high. A factor of 100 in the reduction of the counting rate results from the small aperture in front of the target to define the scattering angle with the required accuracy. Figure 7.3 shows schematically this limiting aperture consisting of a copper plate with a small hole ($\varnothing = 0.5\,\mathrm{mm}$). Of course, this does not solve the thermal problems arising with a beam radius of 5 mm. The defocusing required to avoid melting the foil can be estimated from the ratio of the deposited energy to the required energy. This requires a defocusing factor $>1.674/0.109 \approx 15$. Taking a factor of 20 results in a beam radius between 22 and 23 mm. As a consequence, the expected counting rate goes down to about 100 kHz.

Conclusion

The measuring system can be a powerful tool for studying intensity distributions in longitudinal phase space. It has been discussed in detail. But, it is

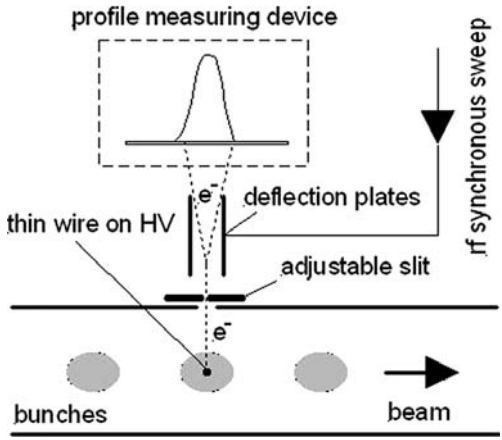

Fig. 7.12. Scheme to use secondary electrons emitted from a thin wire to observe bunch structure [361, 362]

suitable to discuss manifold physical problems as well as to derive important relations, which are also relevant for the design of other beam diagnostic devices. On the other hand, based on the parameters and problems discussed, it should be possible to design and optimize similar systems, provided for measurements with completely other parameters, as discussed in the example.

7.1.2 Non-destructive Measurements

Detection of Secondary Electrons

A nearly non-destructive device for bunch structure observation, reported in [361, 362] is based on the scheme of Fig. 7.12. It is used in several low energy proton and heavy ion linacs. The beam hits a thin wire (⌀ ca. 0.1 mm) and generates secondary electrons. The wire is at a potential of about −10 kV. In consequence, electrons are accelerated perpendicularly to the beam pipe, pass a slit and, are deflected rf-synchronously by a rf deflector. This results in transformation of the longitudinal density distribution within the bunch into a profile distribution (in principle, it compares to an analog oscilloscope). The profile can be detected with a SEM or a particle counter. To focus the electrons onto the detector, a constant dc-voltage applied to the deflector plates acts as an electrostatic lens. The sweep over the bunch length is performed by shifting the phase of the deflecting rf. If the HV wire is mounted onto a movable feedthrough, the bunch shape can be measured at different positions across the bunch. Because the emission of secondary electrons is a fast process, the resolution of the device is of the order of some pecoseconds. Thus the method can be applied to various linac types. For the two-dimensional longitudinal phase plane, the device is a powerful tool for determining the one-dimensional

projection on the time axis. By combining the device with a bunch length detector [363, 364], the energy spread of the particles in the beam can also be obtained. On the other hand, by proposing elliptically shaped emittances in the longitudinal phase plane, procedures similar to the methods for emittance determination in transverse phase planes by beam profile measurements can be performed.

Three effects can restrict the application of the device to intense beams:

- Heating of the wire, leading to strong deformations and even melting of the wire.
- As a consequence of heating, the electron current arising from emission according to Richardson-Dushmann's law [365] can be comparable or even larger than the current from secondary electron emission.
- Strong space charge forces of the moving bunch can deflect the electrons considerably, diminishing the resolution of the device. The effects of space charge for the monitor type under discussion have been considered in [366]. A more general study of space charge effects is postponed to a later section in this chapter.

To estimate the electron emission according to the Richardson-Dushmann law, calculation of wire heating is desired. As in case of thin scattering foils discussed above, cooling of the wire takes place mainly by radiation. Referring to Chap. 3, where the relevant tools for performing such calculations are discussed, heating of the wire is illustrated, taking the beam parameters of the previous example:

Beam energy: $W = 1.4\,\mathrm{MeV/u}$, Ar^{1+}-ions ($A_\mathrm{P} = 40$, $z = 18$, $\zeta = 1$)
rf accelerating frequency: $f = 36\,\mathrm{MHz}$
Macropulse length: $T_\mathrm{p} = 200\ \mu\mathrm{s}$
Macropulse current: $I_\mathrm{p} = 5\,\mathrm{mA}$
Beam spot size: $R_\mathrm{b} = 5\,\mathrm{mm}$
Repetition frequency of the macropulse: $f_\mathrm{p} = 2/\mathrm{s}$

In a wire with a diameter of 0.1 mm, most Ar-ions are stopped because the range at 1.4 MeV/u is only the order of some μm. The total macropulse power is 280 kW ($WA_\mathrm{P}I_\mathrm{macro}/\zeta$). To calculate the steady state (deposited power equal to the radiated power), one needs the power density on the wire. Supposing $R_\mathrm{beam} = 5\,\mathrm{mm}$ is the FWHM value of a Gaussian distribution, the maximum power density at the center of the beam is $9.84\,\mathrm{kW/mm^2}$. A first calculation shows that even a tungsten wire 0.1 mm in diameter does not withstand this high power density, although the duty cycle is very low ($T_\mathrm{p} = 200\,\mu\mathrm{s}$, $f_\mathrm{p} = 2/\mathrm{s}$). Fortunately, power density can be reduced by defocusing or by positioning the wire at the beam edge. Figure 7.13 shows a calculation of the steady state (see Chap. 3, Sect. 3.4), assuming a power density of $1.5\,\mathrm{kW/mm^2}$. Although a temperature of about 3000 K is well below the melting temperature of tungsten, the electron emission according to

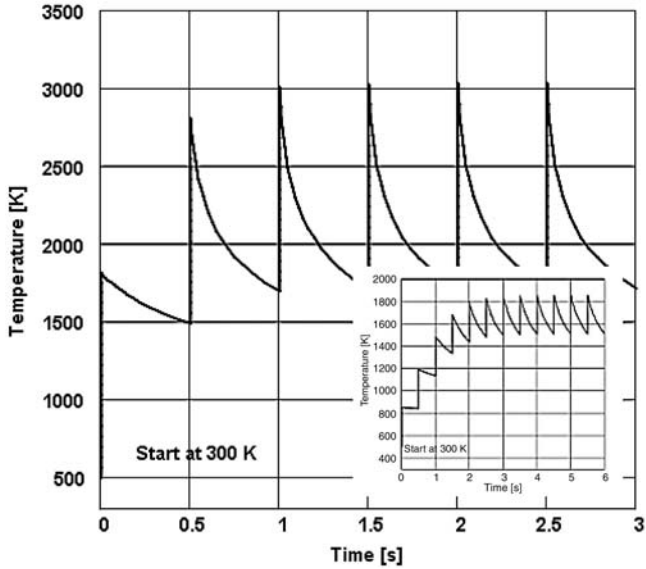

Fig. 7.13. Estimation of the maximum steady-state temperature below the melting temperature of tungsten. In the calculation, a power density of $1.5\,\mathrm{kW/mm^2}$ was assumed. The small inset shows a calculation assuming a reduced power density of $400\,\mathrm{W/mm^2}$ to end up with a maximum temperature of about 1800 K. See text for details

Richardson-Dushmann's law is much too high at this temperature and, therefore does not allow operating the device at this level of power density. To estimate the electron current from the wire from the emission of secondary electrons, one needs the efficiency, defined in the literature as

$$\eta_{\mathrm{se}} = \frac{\text{Number of emitted electrons}}{\text{Number of incident charged ions}} \times 100\,\% \tag{7.30}$$

The efficiency η_{se} is a function of many factors, mainly,

- the nature of the emitting material;
- the surface conditions;
- the characteristics of the incident ion such as atomic number, mass number, and energy; and
- the angle of incidence.

One way to estimate η_{se} is to measure the beam current with a Faraday cup consisting of a similar material dependent on the suppression voltage, as illustrated in Chap. 2. Experience has shown that for heavy ions of relatively low energies ($\approx 0.1-15\,\mathrm{MeV/u}$), the efficiency can be some 100% which means that more than one electron per incident ion will be emitted. Let us define $\mathrm{SE} = \eta_{\mathrm{se}}/100$ which is just the number of emitted electrons per incident ion.

Then, coming back to the example discussed, the electron current within one macropulse from secondary electron emission I_{SE} is given by

$$I_{\mathrm{SE}} = \mathrm{SE}\frac{1}{2\pi\sigma_{\mathrm{x}}\sigma_{\mathrm{y}}}\int_{-0.05}^{0.05}\int_{-20}^{20} I_{\mathrm{macro}}\, e^{\frac{1}{2}\left[\left(\frac{x}{\sigma_{\mathrm{x}}}\right)^2+\left(\frac{y}{\sigma_{\mathrm{y}}}\right)^2\right]}\, dy\, dx \qquad (7.31)$$

$$I_{\mathrm{SE}} = 93.7\,\mu A \times \mathrm{SE} \qquad (7.32)$$

for a wire of 0.1mm ⌀ and 40 mm long. On the other hand, the thermal emission can be figured out from the Richardson-Dushmann law

$$J_{TE} = B\,T^2\, e^{-\frac{A}{kT}} \qquad (7.33)$$

with $B = 60.2\,\mathrm{A/cm^2K^2}$. A is the electronic work function and the Boltzmann constant $k = 8.614\times10^{-5}\mathrm{eV/K}$. Figure 7.14 gives the results for tantalum and tungsten as the emitting materials. Based on these data, the determination of the electron current emitted from a tungsten wire 0.05 cm in radius and 2 cm long is straightforward. Taking the maximum temperature $T = 3000\,\mathrm{K}$ (see Fig. 7.13), one obtains $I_{\mathrm{TE}} = 804\,\mathrm{mA}$, which of course is much too high. Therefore, to end up well below I_{SE} given by (7.31) and (7.32), only some microamperes can be accepted. This requirement limits the maximum temperature of the wire to less than about $T = 1900\,\mathrm{K}$, as shown in the small inset of Fig. 7.14. Due to the strong dependency of radiation on temperature in the Stefan-Boltzmann law (Chap. 3, Sect. 3.4), it is not trivial to determine

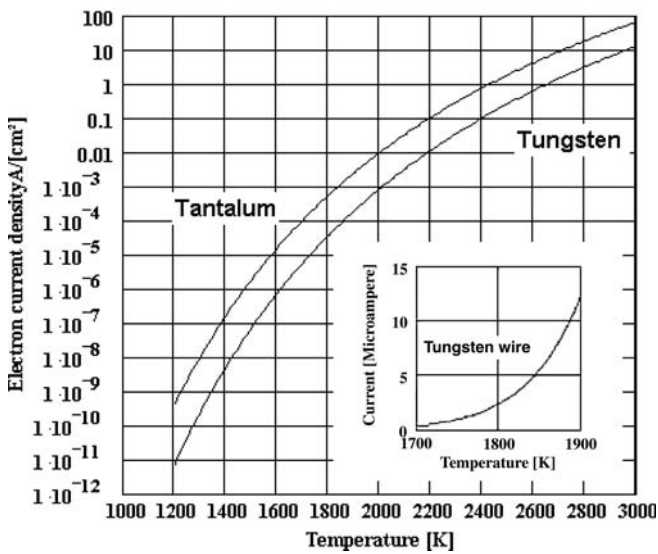

Fig. 7.14. Thermal electron current according to the Richardson-Dushmann law dependent on temperature. The inset shows the electron current in the temperature range of interest. See text for details

the power density allowed on the wire. A new calculation leads to a value of about $400\mathrm{W/mm^2}$ (see the small inset in Fig. 4.2). Therefore, comparing this with the maximum power density of $9.84\,\mathrm{kW/mm^2}$ at the center of the beam, considerable reduction of the beam power density is required.

Remark. The calculated electron currents due to secondary electron emission and thermal emission are reduced by the small aperture of about 0.1 mm in front of the deflecting system (see Fig. 7.12). However, the reduction holds for both and, therefore, is not relevant in the estimation of the ratio between them.

Detection of Electrons from Residual Gas Ionization

A drawback of all methods inserting material, such as thin foils and thin wires, in a beam is the required attenuation of highly intense beams. At GSI, a system is in development [367, 368], which adapts the principle of the monitor according to the scheme of Fig. 7.12, but detects electrons freed from the residual gas. The layout of such a system is shown schematically in Fig. 7.15. Electrons from residual gas ionization within the moving bunch are extracted by an electric field. After passing a fixed aperture, they pass a variable slit of width Δz=0.1–2 mm, moving then into an electrostatic analyzer system. The reason to install two 90° systems is to come away from the beam pipe with the required installations behind the analyzer systems. Especially the $\lambda/4$- resonator deflecting system requires roughly 800 mm ($\lambda/4$ of 108 MHz $\approx$ 750 mm). The resolution of the analyzing system determines the range Δx within the bunch, from which the electrons can be collected. Due to synchronization between deflection and accelerating rf, the moment of creation of a certain electron is transformed into a spatial profile. The phase shifter is used only at the beginning of the measurement to adjust the phase of the third harmonic with respect to a reference electron, passing the resonator without deflection. In the example, the detector consists of a multichannel plate (MCP), a viewing screen, and a CCD camera. Although the device consists of components that are often used at accelerator facilities, the design of each component requires careful optimization of the parameters of the physical processes involved. Similar systems and ideas were already discussed by Zieher in 1971 [369].

Considering the system, shown schematically in Fig. 7.15, the physical and technical questions arising during the design of the system can illustrate the variety of accelerator physics and techniques. Therefore, it may be of interest to discuss the physical questions and problems in the layout of such a versatile, but complex measuring system. Let us start with a summary of the relevant parameters:

Beam energy: $W = 1.4\,\mathrm{MeV/u}$ *(*$\rightarrow \beta = 0.055$*)*
Accelerating frequency: $f = 36\,\mathrm{MHz}$
Repetition frequency: $f_\mathrm{p} = 2/\mathrm{s}{-}50/\mathrm{s}$

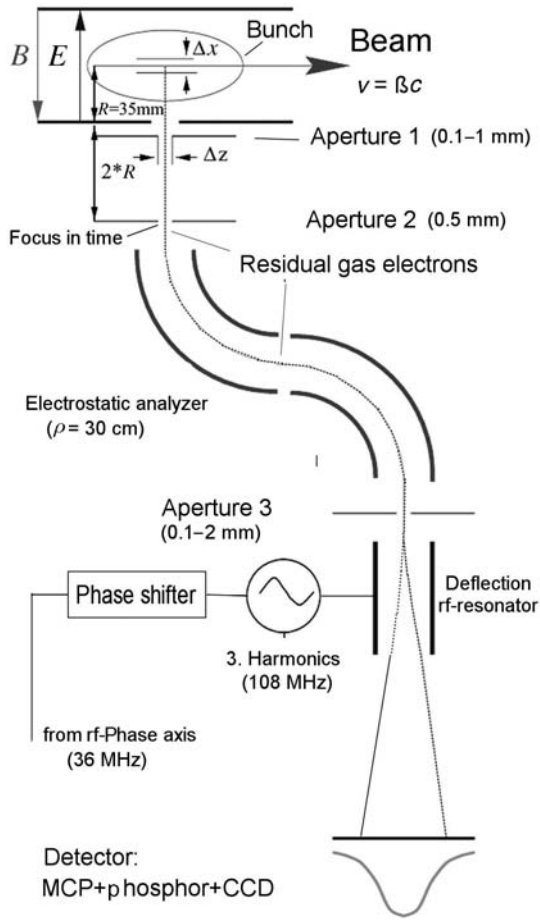

Fig. 7.15. Scheme of a device analyzing bunch shapes by detection of electrons arising in the bunch by residual gas ionization

Macropulse length: $T_\mathrm{p} = 200\ \mu\mathrm{s}$–$10\,\mathrm{ms}$
Bunch length: $\Delta t \sim 0.5$–$1\,\mathrm{ns}$ (FWHM)
Required resolution: $\Delta t < 100\,\mathrm{ps}$
Beam radius: $R_\mathrm{b} = 5\,\mathrm{mm}$
Vacuum pressure: $p = 10^{-7}\,\mathrm{mbar}$

Expected Number of Electrons

From the required resolution of 100 ps and the velocity of the moving bunch, it follows immediately that $\Delta z = 0.1 \cdot 0.055 \cdot 300\,\mathrm{mm} = 1.65\,\mathrm{mm}$. Thus, to achieve a resolution better than 100 ps, electrons have to be collected on a distance of about 1–1.5 mm along the z-axis. Beside ionization, other complex processes are involved in the emission of electrons from the [370–372]

- ionization of the target atoms by
  - binary encounter electron emission due to collisions between the nuclei of the projectile and the electrons of the target atom;
  - electron emission due to collisions between the nuclei of the projectile, the nuclei of the target, and the electrons of the target atom;
- Auger electron emission of the multiple excited target atoms;
- Auger electron emission from the projectile; and
- ionization of the projectile.

It is important to notice that the emission is not isotropic. The liberated electrons escape with different energies and different angles, where energies in the electronic Volts – region and angles $\vartheta = 0°$ are preferred. The expected electron current can be estimated by applying the concept of the cross section. Residual gas analysis has shown that the residual gas in the stripper section of the UNILAC consists mostly of N_2 and H_2. The ratio of the partial pressures of N_2/H_2 varies from 80/20 to 50/50. For target combinations of N_2 and H_2 and heavy ions with β in the percentage– region, the total cross sections σ_e are of the order of some 10^{-16}cm^2, and the differential cross sections $d^2\sigma_e / dE\, d\Omega$ are around some $10^{-17}\text{cm}^2/\,\text{eV sr}$ [372]. On the other hand, there are detailed tables and diagrams about the stopping power of various ions of H_2 and N_2 available in the literature [122] ($W = 200\,\text{keV/u}-100\,\text{MeV/u}$), [225] ($W = 1$–$15\,\text{keV/u}$). Taking advantage of such diagrams and tables, it is more practical to estimate the number of electrons collected by a sufficiently high electric field in the following way:

- determination of the loss in the gas target;
- taking into account a mean energy $\Delta_e \approx 36.5\,\text{eV}$ required to generate one electron–ion pair (for H_2 and N_2 about the same, [206]);
- calculation of the total number of electrons generated within one macropulse;
- calculation of the number of electrons generated within a single bunch;
- determination of the limitations of Δz and Δx (see Fig. 7.15) with respect to the time required; and
- determination of the number of electrons collected, assuming a three-dimensional Gaussian density distribution of the ions in the bunch.

This estimation neglects the nonisotropic angular distribution of electrons, as well as the dependency of the differential cross section on the energy of the emitted electrons. On the other hand, a strong electric collecting field reduces the errors arising from both effects. For the system designer, this rough estimation should be sufficient to fix the relevant system parameters.

Taking over the proposed procedure, calculation of electrons freed from the residual gas is straightforward. The stopping power of H_2 and N_2 for Ar and U ions taken from diagrams given in [122] is displayed in Fig. 7.16 in the energy range from $W = 0.5 - 100\,\text{MeV/u}$.

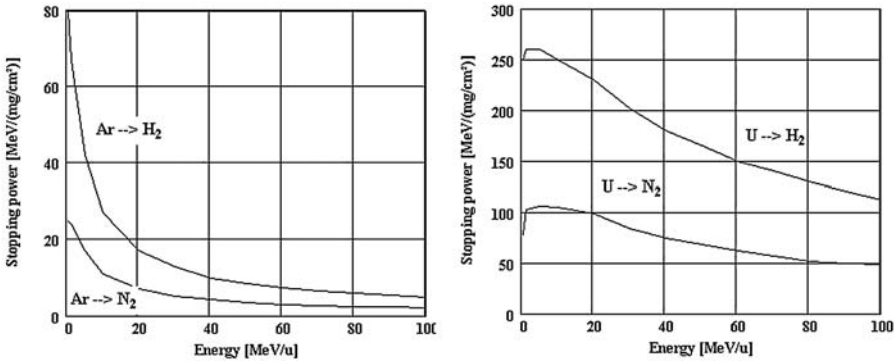

Fig. 7.16. Stopping power of H_2 and N_2 for Ar and U ions in the energy range from 0.5–100 MeV/u. Taken from diagrams given in [122]

Taking the parameters from the previous example (secondary electrons from a wire in the beam, see Fig. 7.12), we deal with Ar^{1+}-ions and a macropulse length of 200 µs. From the diagrams of Fig. 7.16, one obtains the stopping powers $[\Delta W/\rho\Delta z]_{\mathrm{Ar}\to\mathrm{H_2}} = 67\,\mathrm{MeV/(mg/cm^2)}$ and $[\Delta W/\rho\Delta z]_{\mathrm{Ar}\to\mathrm{N_2}} = 24\,\mathrm{MeV/(mg/cm^2)}$. The target thickness is

$$[\rho\,\Delta z]_{\mathrm{H,N}} = \rho_{H,N}\,\Delta z\,\frac{p}{p_{\mathrm{n}}} \tag{7.34}$$

$$\rho_{\mathrm{H}} = 0.08989\,\mathrm{mg/cm^3}\ \text{at}\ p = P_{\mathrm{n}} \tag{7.35}$$

$$\rho_{\mathrm{N}} = 1.2506\ \mathrm{mg/cm^3}\ \text{at}\ p = P_{\mathrm{n}} \tag{7.36}$$

$$p_{\mathrm{n}} = 1013\,\mathrm{mbar} \tag{7.37}$$

$$[\rho\,\Delta z]_{\mathrm{H}} = 8.874\times10^{-13}\,\mathrm{mg/cm^2} \tag{7.38}$$

$$[\rho\,\Delta z]_{\mathrm{H}} = 1.235\times10^{-11}\,\mathrm{mg/cm^2}\,. \tag{7.39}$$

Due to the required resolution, the target thickness has to be limited to $\Delta z = 1\,\mathrm{mm}$. Taking $\Delta_{\mathrm{e}} = 36.5\,\mathrm{eV}$ as the average energy to create one electron-ion pair and the total number of Ar-ions within one macropulse $N_{\mathrm{m}} = 6.25\,x\,10^{12}$ (equation 7.25) leads immediately to the total number of electrons freed in a single macropulse:

$$N^e_{\mathrm{H}} = N_{\mathrm{m}}\,\frac{[\Delta W\,/\,\rho\Delta z]_{\mathrm{Ar}\to\mathrm{H_2}}\,[\rho\,\Delta z]_{\mathrm{H}}}{\Delta_{\mathrm{e}}} = 1.02\times10^{7} \tag{7.40}$$

$$N^e_{\mathrm{N}} = N_{\mathrm{m}}\,\frac{[\Delta W\,/\,\rho\Delta z]_{\mathrm{Ar}\to\mathrm{N}}\,[\rho\,\Delta z]_{\mathrm{N}}}{\Delta_{\mathrm{e}}} = 5.07\times10^{7}\,. \tag{7.41}$$

Because the ratio N_2/H_2 does not influence the final result very much, it is reasonable to continue the estimation with $N^e_{\mathrm{m}} = 0.6\,N^e_{\mathrm{N}} + 0.4\,N^e_{\mathrm{H}} = 3.45\times10^7$. Finally, we are interested on the number of Ar^{1+}-ions and electrons per bunch $N^{\mathrm{Ar}}_{\mathrm{b}}$, $N^{\mathrm{e}}_{\mathrm{b}}$. This follows immediately from the number of bunches within one macropulse:

$$N_\mathrm{b} = T_\mathrm{m}\, f = 200 \times 10^{-6} \cdot 36 \times 10^6 = 7.2 \times 10^3 \tag{7.42}$$

$$N_\mathrm{b}^\mathrm{Ar} = \frac{N_\mathrm{m}}{N_\mathrm{b}} = 8.68 \times 10^8 \tag{7.43}$$

$$N_\mathrm{b}^\mathrm{e} = \frac{N_\mathrm{m}^{\simeq e}}{N_\mathrm{b}} = 4.79 \times 10^3\,. \tag{7.44}$$

Thus, $\simeq 4.8 \times 10^3$ electrons would reach the resonant deflector within a time just corresponding to the time of flight over one bunch length, if all particles would gain the same energy in the E^ext field. Evidently, that's not true. Otherwise, one would not need the electrostatic analyzer. To estimate the fraction of electrons reaching the detector, a reference electron is defined. It starts at a potential $V_\mathrm{ref} = V/2$ in the middle ($\Delta x = 0$) of the deflecting condenser with a width of $2 \times 35\,\mathrm{mm} = 2\,R$ (see Fig. 7.15). Furthermore, we assume that the reference electron starts at $v_\mathrm{x} = 0$ and does not experience any space charge force. In the chosen right - handed coordinate system, the positive x-axis points in the direction of the accelerated electrons, and the positive z-axis points in the direction of the moving bunches. Hence, electrons starting at $\Delta x < 0$ will gain more energy but have to travel a longer way down to the grounded plate of the extraction condenser at $x = R = 35\,\mathrm{mm}$ (see Fig. 7.15). On the other hand, electrons with $\Delta x > 0$ are accelerated over a shorter distance, resulting in lower energy gain, but having a shorter path. After passing the small slit in the grounded plate, all electrons travel without any acceleration. As a consequence, there must be a distance s_f (time focus), where the faster particles pass the slower ones. To find s_f dependent on the parameters, it is practical to work in the following units:

$c = 300\,\mathrm{mm/ns}$ (velocity of light, correct would be 299.7925)
$m_\mathrm{e}c^2 = 511 \times 10^3\mathrm{eV}$ (m_e is the rest mass of the electron)
$b = e\,E_\mathrm{x}^\mathrm{ext}/m$ (acceleration by the electric field, $E_\mathrm{x}^\mathrm{ext}[\mathrm{V/mm}] \rightarrow b\,[\mathrm{mm/ns^2}]$)

In a nonrelativistic approximation, $\ddot{x}(t)$, $\dot{x}(t)$, and $x(t)$ follow immediately from Newton's famous formulas:

$$\ddot{x} = bx \tag{7.45}$$

$$\dot{x}(t) = b\,t + \dot{x}_0 \tag{7.46}$$

$$x(t) = \frac{b}{2}t^2 + \dot{x}_0\,t + x_0\,. \tag{7.47}$$

For the reference particle ($\dot{x}_0 = x_0 = 0$), the time of flight down to the grounded plate is $t_0 = \sqrt{2R/b}$ and its velocity is $v_0 = \sqrt{2\,b\,R}$. The design value for the voltage between the plates is $V = 30\,\mathrm{kV}$, leading to the following values:

$$\left|E_{\mathrm{x}}^{\mathrm{ext}}\right| = 428.6\,\mathrm{V/mm} \tag{7.48}$$

$$b = 75.5\,\mathrm{mm/ns^2} \tag{7.49}$$

$$t_0 = 0.96\,\mathrm{ns} \tag{7.50}$$

$$v_0 = 72.69\,\mathrm{mm/ns} \tag{7.51}$$

$$\beta_0 = \frac{v_0}{c} = 0.242\,. \tag{7.52}$$

From (7.46) and (7.47), the difference in the flight time of an electron, starting at $\Delta x < 0$ and an electron starting at $\Delta x > 0$ is given by

$$\Delta t(s) = \Delta t_{0s} + \Delta t_{\mathrm{s}} \tag{7.53}$$

$$\Delta t_{0s} = \sqrt{\frac{2}{b}}\left[\sqrt{R+\Delta x} - \sqrt{R-\Delta x}\right] \tag{7.54}$$

$$\Delta t_{\mathrm{s}} = \frac{s}{\sqrt{2b}}\left[\frac{1}{\sqrt{R+\Delta x}} - \frac{1}{\sqrt{R-\Delta x}}\right], \tag{7.55}$$

where s counts from the grounded plate of the extractor. Arriving at this point, the electrons move with constant velocity. Looking for the focus in time, we expand $\Delta t(s)$:

$$\Delta t(s) \approx \sqrt{\frac{2R}{b}}\left[\frac{\Delta x}{R} - \frac{1}{4}\left(\frac{\Delta x}{R}\right)^2\right] - \frac{s}{\sqrt{2bR}}\frac{\Delta x}{R} \tag{7.56}$$

$$\Delta t(s) \approx \sqrt{\frac{2}{b}}\left[\sqrt{R}\left(\frac{\Delta x}{R} - \frac{1}{4}\left(\frac{\Delta x}{R}\right)^2\right) - \frac{s}{2\sqrt{R}}\frac{\Delta x}{R}\right] \tag{7.57}$$

and find s_{f} from

$$0 = \sqrt{R}\left(\frac{\Delta x}{R} - \frac{1}{4}\left(\frac{\Delta x}{R}\right)^2\right) - \frac{s_{\mathrm{f}}}{2\sqrt{R}}\frac{\Delta x}{R} \tag{7.58}$$

$$s_{\mathrm{f}} = 2R - \frac{1}{2}\Delta x\,. \tag{7.59}$$

Behind the time focus, the difference in the flight time of electrons with $\Delta x \neq 0$ increases linearly. The diagram in Fig. 7.17 confirms the location of the time focus at $s_{\mathrm{f}} \approx 2R = 70\,\mathrm{mm}$ and leads to the conclusion that Δx has to be limited to $|\Delta x| \leq 1\,\mathrm{mm}$ by the electrostatic analyzer.

Due to the existence of a focus in time, one could imagine removing the electrostatic analyzer and replacing the resonant deflector near the time focus. Two important reasons are in opposition to such a simplification of the measuring system:

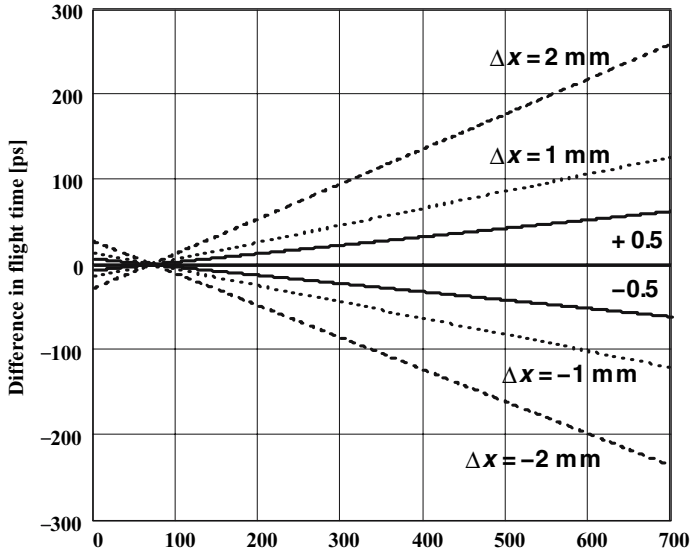

Fig. 7.17. Difference in the time of flight between the reference particle $\Delta x = 0$ and particles starting at $\Delta x \neq 0$. The focus in time occurs approximately at $2R = 70\,\text{mm}$. Remark: According to the definition of the coordinate system, $\Delta x < 0$ corresponds to an electron starting at a potential > than the potential seen by the reference particle. See text for details

- Electrons that pass the time focus nearly at the same time have different energies, which in turn leads to different deflection angles and in consequence to complex profiles on the detector.
- H_2^+ and N_2^+-ions, accelerated to a high voltage plate on the opposite side of the grounded plate, hit the plate and generate secondary electrons, which are accelerated toward the grounded plate, too. Because the heavy ions are much slower than the electrons, these secondary electrons cannot falsify the results, belonging to the bunch from where they are coming. However, comparing the flight times of a H_2^+-ion $t_{H_2} = 58.15\,\text{ns}$ and a N_2^+ ion $t_{N_2} = 217.6\,\text{ns}$ with the rf period of $T = 27.78\,\text{ns}$, it is evident that many secondary electrons may disturb the measurement of the following bunches. This has been confirmed by experiments.

Thus, the analyzing system is an essential part of the measuring system and cannot be omitted.

To figure out the number of electrons remaining in spite of the limitations in Δz and Δx, we define a three-dimensional Gaussian distribution

$$f(x,y,z) = \frac{1}{2\pi\sqrt{2\pi}\sigma_x\sigma_y\,\sigma_z} e^{-\frac{1}{2}\left[\left(\frac{x}{\sigma_x}\right)^2+\left(\frac{y}{\sigma_y}\right)^2+\left(\frac{z}{\sigma_z}\right)^2\right]} \tag{7.60}$$

with $\sigma_x = \sigma_y = R_b / 2.35 = 2.13\,\text{mm}$ and $\sigma_z = 16.5/2.35 = 7.02\,\text{mm}$. The σ_z value results from the bunch length of $\Delta t = 1\text{ns}$ (FWHM) and $\beta c \Delta t = 16.5\,\text{mm}$. Taking $\Delta x = 1\,\text{mm}$, the number of electrons collected from one bunch reduces to

$$NR_b^e = N_b^e \int_{z=-\infty}^{z=\infty} \int_{y=-20}^{y=20} \int_{x=-0.5}^{x=0.5} f(x,y,z)\,dx\,dy\,dz \tag{7.61}$$

$$NR_b^e \approx 889 \tag{7.62}$$

The distribution over the z-coordinate follows from

$$N^e(z) = N_{\text{bunch}}^e \int_{z-0.5}^{z+0.5} \int_{-20}^{20} \int_{-0.5}^{0.5} f(x,y,z)\,dx\,dy\,dz \tag{7.63}$$

and is displayed in Fig. 7.18.

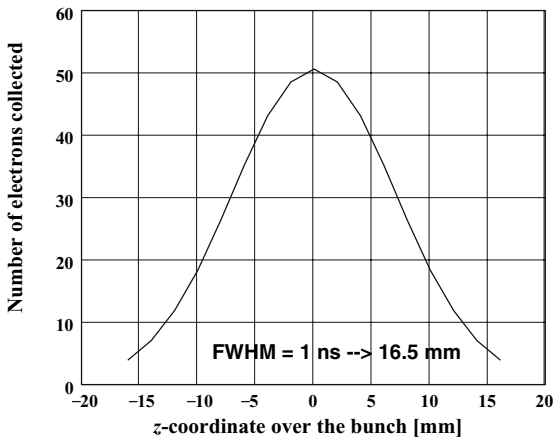

Fig. 7.18. Estimated number of electrons collected from one moving bunch

In practice, measurements are performed over one macropulse and, therefore many more electrons are collected. As a consequence, the measured bunch shapes correspond to an average over one macropulse. The volume from which electrons are collected, can be further reduced by the first aperture, which is a double slit, limiting the extension in the y-direction, too.

Remark. Introducing a second, slow deflection system behind the rf resonator offers the possibility of separating the profiles from different macropulses by an additional deflection perpendicular to the first one [368].

Figure. 7.19 shows part of the monitor looking in the beam direction through the extraction plates. The plate on high voltage is on the bottom, and the grounded plate with a small slit in the y-direction is on top of the rectangular chamber. The resistors on the left and right, connected to rods in

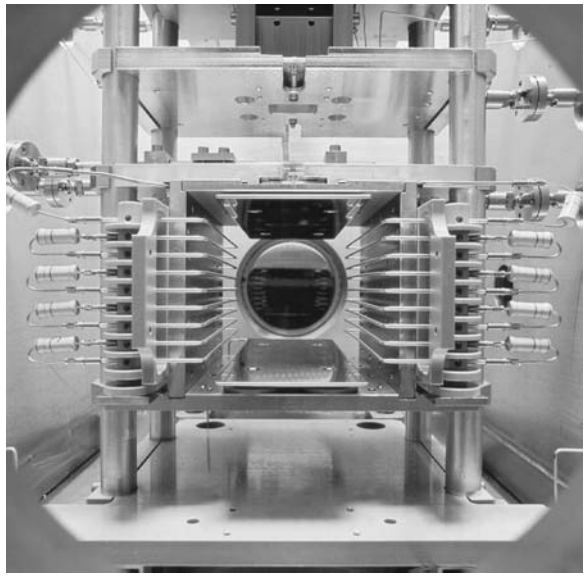

Fig. 7.19. View in beam direction through the extraction plates installed in the rectangular experimental chamber. The extracting E_x field points from bottom to top (charge of the electron assumed to be >0). GSI Foto [373]

parallel with the z-axis, are provided to homogenize the electric field in the x-direction (pointing from bottom to top). Apertures 1 and 2 are adjustable by stepping motors. The corresponding, small feedthroughs are seen on the left and right above the resistors.

Systematic test measurements were performed in the transfer channel from the UNILAC to the SIS. As a consequence, a 5-mm thick steel shielding has been installed behind the energy analyzer to avoid background from X rays, produced from secondary electrons accelerated by the electric field and hitting the housing. As discussed in more detail in Sect. 7.1.2 of this chapter, the longitudinal emittance can be determined by varying the bunch length dependent on the focusing strength of a rebuncher. Figure 7.20 shows the results from a measurement with a 2-mA Ni^{14+}-beam at 11.4 MeV/u [368]. A single gap resonator, acting as a buncher was operated at 108 MHz. Due to the relatively high beam current of 2 mA, the data have been averaged over only four macropulses of 200 µs duration. The solid line in Fig. 7.20 results from a fitting procedure, which is described in more detail in Sect. 7.1.2 of this chapter.

Space Charge Effects

When the number of charges increases within a bunch, electrons are distorted during their accelerated flight by the space charge field of the moving bunch. As shown in Chap. 8, the electric field strength can be up to 100 V/mm, which

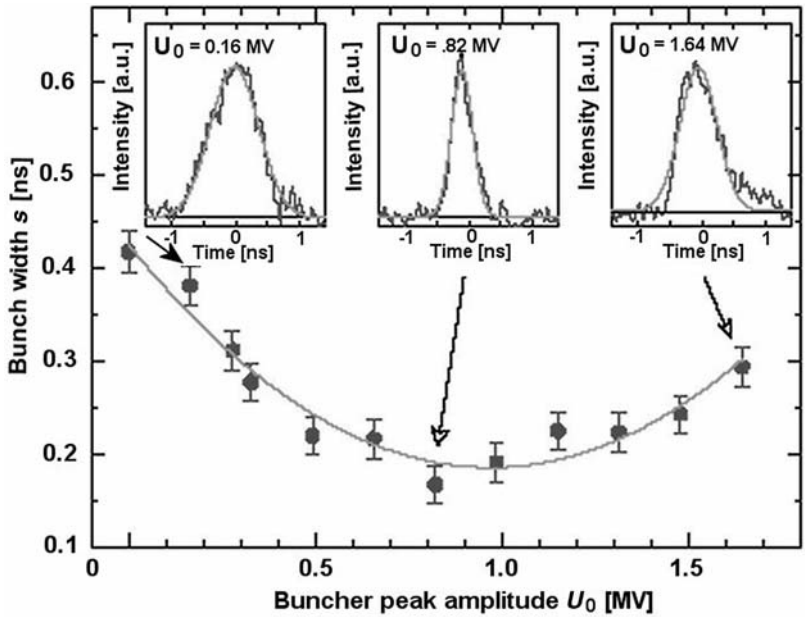

Fig. 7.20. Measurement [368] of the bunch width (one standard deviation) dependent on the buncher gap-voltage located about 31 m upstream from the detector system. The data hold for a 11.4-MeV/u Ni^{14+}-beam with an intensity of about 2 mA

cannot be neglected in comparison to the accelerating E^{ext} field ($\approx 428\,\text{V/mm}$ in the example discussed). An analytical estimation of the effect has to take the following effects into account:

- moving of the bunches along the z-axis with $v = \beta c$;
- accelerated motion of the electrons along the x-axis;
- shape of the bunches; and
- distribution of the charged ions within a bunch, which of course influences only the potential and field strength inside the bunch.

Remark. In the first estimation of the space charge effects, the action of the magnetic field in parallel to the E field (see Fig. 7.15) is not considered.

The first two effects lead to a permanent change in the $\overrightarrow{E}$ vector and, taking into account the external field $E_{\text{x}}^{\text{ext}}$, this results in a permanent change in the components E_{x}, E_{y}, E_{z} acting on the electron. In Chap. 8, the Laplace – and Poisson equations are solved considering four cases of bunch shape and distribution within

- a homogeneously charged sphere,
- a sphere with parabolic charge distribution,

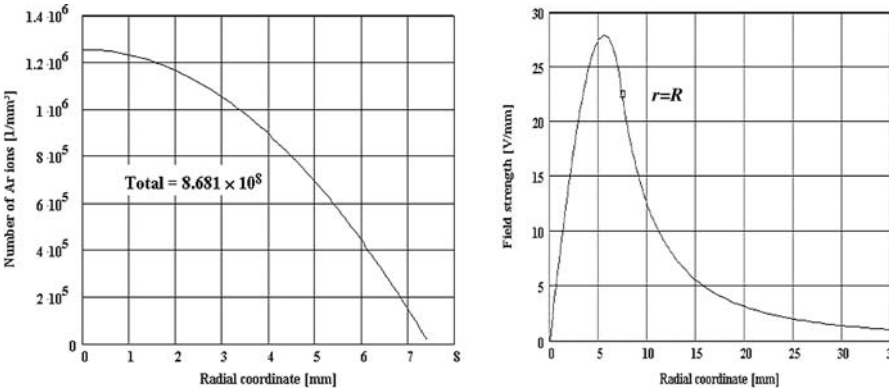

Fig. 7.21. Left: parabolic intensity distribution in a bunch of spherical shape. Right: electrical field strength inside and outside the bunch. See Chap. 8 for details of calculation

- a homogeneously charged ellipsoid, and
- an ellipsoid with parabolic charge distribution.

In the example considered here, the bunch has about the dimensions ($2 \times$ FWHM): $-5\,\mathrm{mm} \leq \Delta x \leq 5\,\mathrm{mm}$, $-5\,\mathrm{mm} \leq \Delta y \leq 5\,\mathrm{mm}$, and $-16.5\,\mathrm{mm} \leq \Delta z \leq 16.5\,\mathrm{mm}$. Therefore, the best approximation would be the rotational symmetrical ellipsoid with a parabolic charge distribution. However, considering the complex formulas (see Chap. 8, App. 8.A), the estimation is based on a sphere with parabolic charge distribution. Due to the moderate ratio between the half-axis Δx, Δy, and Δz, this simplification will not have a large effect on the result. Therefore, we approximate the bunch shape by a sphere with $R_\mathrm{s} = \frac{1}{2}\sqrt[3]{\Delta x\,\Delta y\,\Delta z} = 7.44\,\mathrm{mm}$. Referring to Chap. 8, the electric field strength in a nonrelativistic approximation is given by

$$E_\mathrm{r} = \frac{N_\mathrm{b}^{Ar}\zeta e}{4\pi\varepsilon_0}\frac{r}{2R^3}\left(5 - 3\frac{r^2}{R^2}\right). \tag{7.64}$$

The parabolic charge density distribution and the radial component of the electric field strength according to (7.64) are displayed in Fig. 7.21. The maximum field strength occurs at $r = \sqrt{5}R/3$ (see Chap. 8). Inserting this into (7.64) leads to

$$E_\mathrm{r}^\mathrm{max} = \frac{N_\mathrm{b}^{Ar}\zeta e}{4\pi\varepsilon_0}\frac{1}{R^2}\frac{5\sqrt{5}}{9} = 27.98\,\mathrm{V/mm}. \tag{7.65}$$

Taking the proportionality of $E_\mathrm{r}^\mathrm{max} \sim N_\mathrm{b}\,\zeta/R^2$ into account leads to a practical formula:

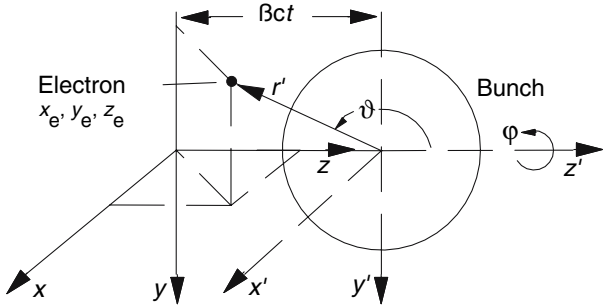

Fig. 7.22. Definition of two Cartesian coordinate systems. The motion of the electron is referenced to the fixed x, y, z-system which has its origin at the center of the extraction system. The origin of the x', y', z'- system is fixed at the center of the bunch and therefore moves with $v = \beta c$ along the z-axis. Note: To make the drawing clearer both systems have been rotated 90° around the z, z'-axes (see Fig. 7.15 for comparison)

$$E_{\mathrm{r}}^{\max}\,[\mathrm{V/mm}] = \frac{1.79 \times 10^{-6} N_{\mathrm{b}}\,\zeta}{R^2},\; R\,[\mathrm{mm}]\;. \tag{7.66}$$

Due to the external extraction field, no space charge compensation can take place within the bunch and therefore one cannot expect any reduction of space charge forces. On the other hand, during the short flight time of the electrons over a distance of about 35 mm down to the grounded plate in roughly 1ns, the bunch moves about 16.5 mm. Because the distance to the next bunch is of the order of 457 mm, only the space charge field of one bunch has to be considered here. This situation changes drastically if N_2^+ and H_2^+ ions are collected, as discussed in Chap. 4, Sect. 4.1.

To calculate the motion of the electron in the combination of the extraction field with the space charge field, we introduce two Cartesian coordinate systems, as illustrated in Fig. 7.22. The origin of the fixed reference system with coordinates x, y, z is exactly at the center of the extraction plates. The movement of the electron is referred to that system. The origin of the second system with coordinates x', y', z' is fixed at the center of the bunch and therefore moves with $v = \beta c$ in the direction of the positive z-axis. Both systems coincide exactly at $t = 0$, the moment when the center of the bunch passes the center of the extraction plates. The magnitude of the E field in the x, y, z-system is given by (7.64) replacing r by r'. Keeping in mind that $x = x', y = y'$, and $z' = z - \beta ct$ $r' = \sqrt{x^2 + y^2 + (z - \beta ct)^2}$, the decomposition of the E vector into its components can by performed by the well-known transformation of spherical coordinates to Cartesian coordinates:

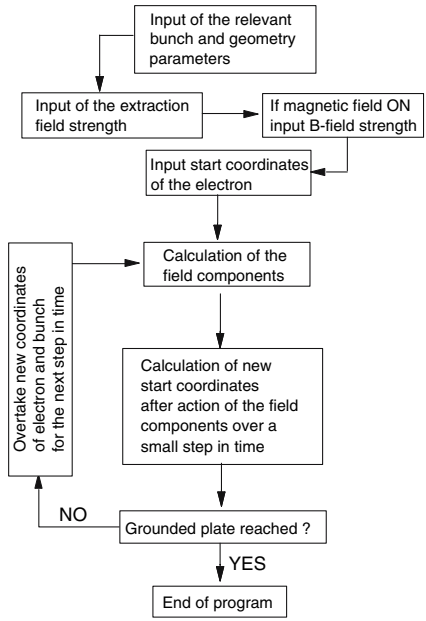

Fig. 7.23. Simplified flow diagram to illustrate the most important steps of a program to evaluate the distortion of the extracted electron by the space charge of a moving bunch

$$E_{\mathrm{x}}(t) = E_{\mathrm{r}}(t)\sin\vartheta(t)\sin\varphi(t) \tag{7.67}$$

$$E_{\mathrm{y}}(t) = E_{\mathrm{r}}(t)\sin\vartheta(t)\cos\varphi(t) \tag{7.68}$$

$$E_{\mathrm{z}}(t) = E_{\mathrm{r}}(t)\cos\vartheta(t) \tag{7.69}$$

$$\cos\vartheta(t) = \frac{z'}{r'} = \frac{z-\beta ct}{\sqrt{x^2+y^2+(z-\beta ct)^2}} \tag{7.70}$$

$$\vartheta(t) = \arccos\frac{z-\beta ct}{\sqrt{x^2+y^2+(z-\beta ct)^2}} \tag{7.71}$$

$$\cos\varphi(t) = \frac{x}{r'\sin\vartheta} \;\rightarrow \varphi(t) = \arccos\frac{x}{r'\sin\vartheta} \tag{7.72}$$

$$\sin\varphi(t) = \frac{y}{r'\sin\vartheta} \;\rightarrow \varphi(t) = \arcsin\frac{y}{r'\sin\vartheta}\,. \tag{7.73}$$

The constant extraction field component $E_{\mathrm{x}}^{\mathrm{ext}}$ has to be added to the x-component. Due to the movement of the bunch, the magnitude of the components change permanently. Therefore, a mathematical algorithm has to be performed in small steps of Δt, according to the scheme shown in Fig. 7.23. The algorithm may be programmed in each modern programming language. From experience with the prototype, the following variables should be included in the program algorithm:

- $\beta = v/c$ of the moving bunch;

- the number of charges within the bunch;
- the shape and size of the bunch;
- the distribution of charges within the bunch;
- the starting coordinates of the electron x_0, y_0, z_0;
- the initial velocity of the created electron $\dot{x}_0, \dot{y}_0, \dot{z}_0$;
- the strength of the electric extraction field;
- the spacing between the plate on high voltage and the grounded one; and
- the magnetic field strength.

Remark. For the shape of the bunch and the distribution of charges within the bunch, analytical solutions for the electric space charge fields can be adapted from the four cases discussed in Chap. 8. Maybe there is also a suitable program for single particle interaction available, allowing ray tracing or Monte Carlo calculations.

Nevertheless, the approximation of the bunch by a sphere with parabolic charge density distribution, resulting in a relatively simple analytical solution of the electric space charge field, gives a good impression of the space charge effects.

The program used to calculate the most important dependencies on the variables, given above, has the following output options:

- coordinate x, y, z and velocity $\dot{x}$, $\dot{y}$, $\dot{z}$ of the electron dependent on flight time,
- magnitude of the electric field components of space charge $E_\mathrm{x}, E_\mathrm{y}, E_\mathrm{z}$ dependent on time.

Some Examples Considering the reference particle, it is of interest to what extent the extraction field will be diminished during the flight time of the electron down to the grounded plate. Figure 7.24 gives the result showing also the z-component of the bunch field. Since the reference particle starts exactly at time $t = 0$ at the center of the bunch, both field components are zero. Due to the relatively fast movement of the bunch, the electron never experiences the maximum magnitude of $E_\mathrm{r}^\mathrm{max} \approx 28\,\mathrm{V/mm}$ (see 7.65). In the program, a step width in time of 0.01 ns has been chosen to recalculate the permanently changing field components. The next four diagrams show the field components E_x and E_z "seen" by electrons, starting near the boundaries of the bunch in the z- and x-directions. Due to symmetry, $E_\mathrm{y}(y_0 = +7\,\mathrm{mm})$ compares with $E_\mathrm{x}(x_0 = +7\,\mathrm{mm})$, and $E_\mathrm{y}(y_0 = -7\,\mathrm{mm})$ compares with $-E_\mathrm{x}(x_0 = +7\,\mathrm{mm})$. From the diagrams, one concludes that the space charge tends to diminish the dimensions of the bunch. This becomes very clear from Fig. 7.26 showing the z-coordinate at $x = 35\,\mathrm{mm}$ with and without space charge forces. The same holds for the transverse coordinate y. Electrons, starting with $y = \pm 7\,\mathrm{mm}$, arrive at $y = \pm 5.95\,\mathrm{mm}$. Due to the high extraction field, the effect does not occur so clearly in the x-direction. From Fig. 7.26, one concludes that the deviations in the z-coordinate at $x = 35\,\mathrm{mm}$ can be more than 1 mm,

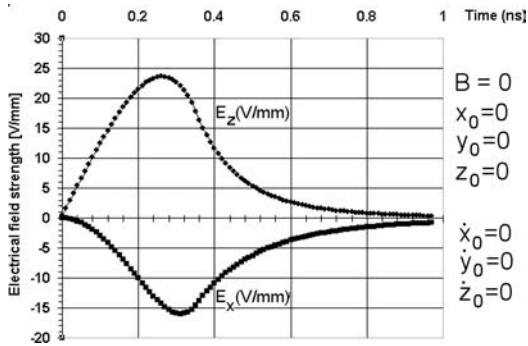

Fig. 7.24. Electrical field components E_x and E_z of the bunch field "seen" by the electron during the flight time of roughly 1 ns down to the grounded plate. Note: For reasons of convenience the charge of the electron has assumed to be $+e$. Therefore, the extraction voltage $E_\mathrm{x}^\mathrm{ext} = +428.56\,\mathrm{V}$

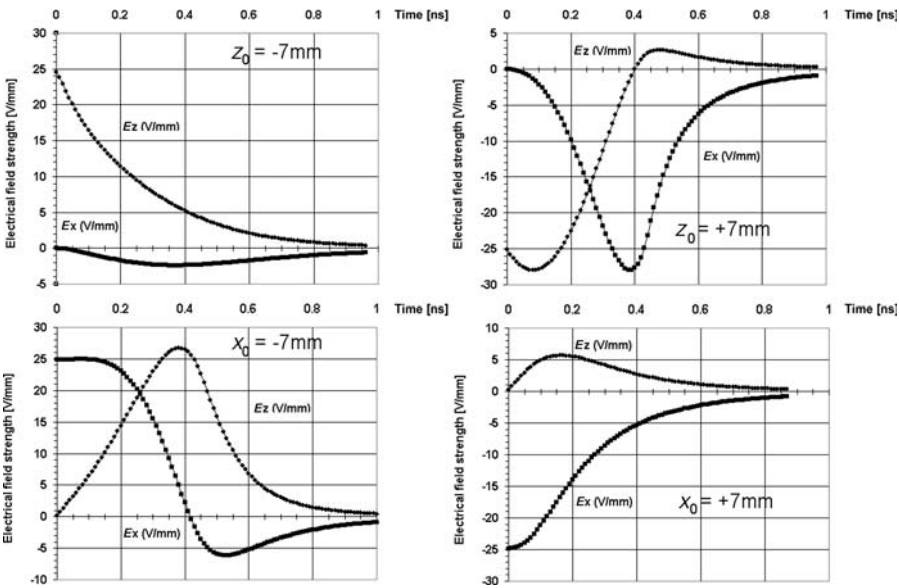

Fig. 7.25. Bunch field components E_x and E_z "seen" by the electron during the flight time down to the grounded plate. Top left: electron starts at $z_0 = -7\,\mathrm{mm}$. Top right: electron starts at $z_0 = +7\,\mathrm{mm}$. Bottom left: electron starts at $x_0 = -7\,\mathrm{mm}$. Bottom right: electron starts at $x_0 = +7\,\mathrm{mm}$. All other remaining initial values are the same as those for the reference particle

which cannot be tolerated based on the resolution required. For this reason, a magnetic field has been introduced in the concept of the monitor, forcing the electrons into a spiral orbit. In the magnetic field, the bending radius ρ_e of the electrons can be derived from the well-known relation,

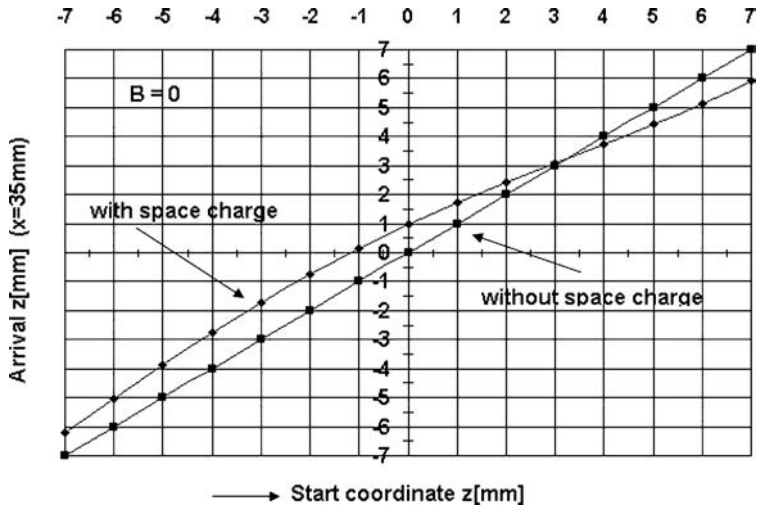

Fig. 7.26. The z-coordinate of the arrival at $x = 35\,\mathrm{mm}$ with and without space charge forces of electrons starting along the z-axis of the bunch. Due to the motion of the bunch in the z-direction, the two straight lines do not conicide at $z = 0$

$$\frac{m_\mathrm{e} v^2}{\rho_\mathrm{e}} = e(\overrightarrow{v}\, x\, \overrightarrow{B})\,, \tag{7.74}$$

which results in

$$\rho_\mathrm{e} = \frac{m_\mathrm{e} v}{eB} \approx 5.68 \frac{v\,[\mathrm{mm/ns}]}{B\,[\mathrm{mT}]}\,[\mathrm{mm}]\ . \tag{7.75}$$

Unfortunately, the relevant components $v_\mathrm{y}, v_\mathrm{z}$ ($B = B_\mathrm{x}$!) change permanently due to the motion of the electron in the external E field and also due to the motion of the bunch. Therefore, (7.75) can be used only to estimates the expected bending radius dependent on v and B. From Fig. 7.26 and the flight time of about 1ns down to the grounded plate, one estimates $v_\mathrm{z}, v_\mathrm{y}$ of the order of 1–1.5 mm/ns. Assuming a reasonable magnetic field strength of 30 mT (= 300 Gauss), the bending radius is well below 1 mm, which should be sufficient to reduce the deviations in the arrival coordinates to the specified tolerances. Taking the magnetic field into account leads to the well-known equation,

$$m_\mathrm{e}\, \overrightarrow{\ddot{r}}\,(x, y, z) = e\left(\overrightarrow{E} + \overrightarrow{v}\, x\, \overrightarrow{B}\right)\ .$$

Supposing again positively charged electrons and a positive B field, the field components given in (7.68) and (7.69) have to be supplemented by

$$E_\mathrm{y} \rightarrow E_\mathrm{y} + v_\mathrm{z} B_\mathrm{x} = E_\mathrm{y}(t) + \dot{z}(t)\, B_\mathrm{x} \tag{7.76}$$

$$E_\mathrm{z} \rightarrow E_\mathrm{z} - v_\mathrm{y} B_\mathrm{x} = E_\mathrm{z}(t) - \dot{y}(t)\, B_\mathrm{x}\,. \tag{7.77}$$

Obviously, the calculation of $\dot{z}(t)$ and $\dot{y}(t)$ can be included very easily in the numerical procedure, according to the simplified flow diagram of Fig. 7.23.

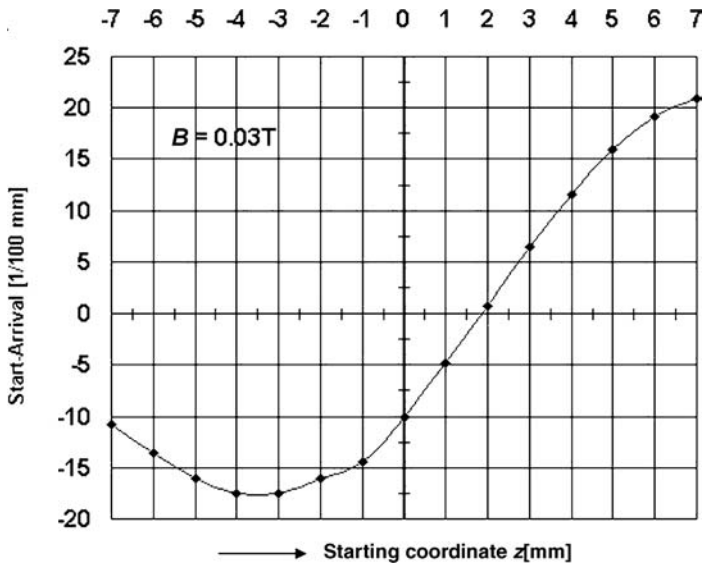

Fig. 7.27. Deviation of the arrival coordinate from the starting coordinate as a function of the starting coordinate. Note that the scale of the ordinate is 1/100 mm

The effect of of the magnetic field is illustrated in Fig. 7.27, which can be compared with Fig. 7.26. The deviations go down to less than about 0.2 mm, which is confirmed by (7.75) inserting $B = 30\,\mathrm{mT}$ and $v = 1$–1.5 mm/ns.

So far, the problem seems to be solved by the introduction of a magnetic field of the order of some 100 gauss. However, beside the realization of a homogeneously magnetic field that confronts the designer with many technical problems, the divergence angles of the electrons arriving at the grounded plate and the apertures behind are changed by the action of the magnetic field. This is demonstrated in Fig. 7.28. The divergence dy/dx ($B = 0$) is $< 10^{-4}$ and thus not shown in the diagram. The effect of an arising divergence dy/dx on the analyzing system has to be studied.

The Analyzing System

The Electrostatic Analyzer The bending radius ρ and the total deflecting angle φ are fixed to $\rho = 30\,\mathrm{mm}$ and $\varphi = 90^\circ = \pi/2$. The required voltages on the bent plates can be derived from the potential of a cylinder capacitor (see Fig. 7.29), resulting from the Laplace equation $\Delta\phi = 0$. In cylindrical coordinates, this simplifies to

$$\left(\frac{1}{r}\frac{\partial}{\partial r} + \frac{\partial^2}{\partial r^2}\right)\phi = 0\,, \tag{7.78}$$

taking into account that $\partial^2/\partial\varphi^2 = \partial^2/\partial z^2 = 0$. In the orbit of the reference electron with radius r_0 ($\equiv \rho$), the potential must vanish. Therefore, an

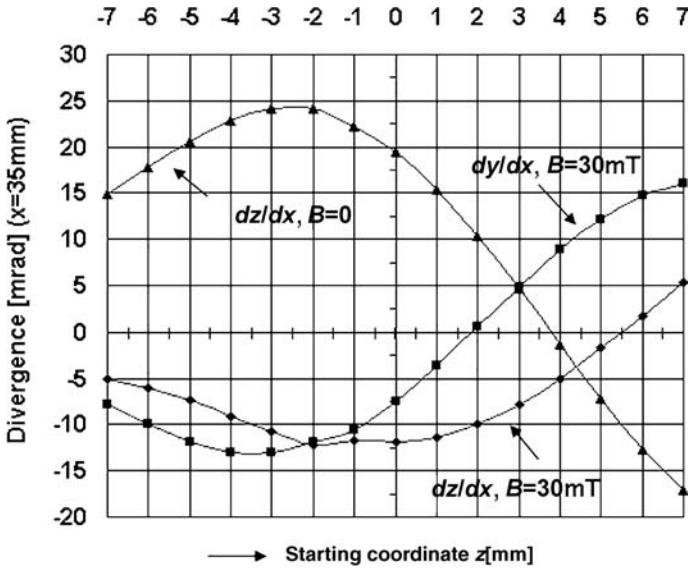

Fig. 7.28. Divergences dz/dx, dy/dx at $x = 35\,\mathrm{mm}$ with and without a magnetic field. Note: dy/dx $(B = 0) < 10^{-4}\,\mathrm{mrad}$

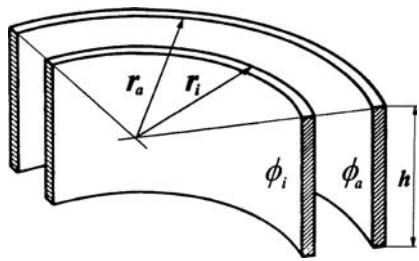

Fig. 7.29. Scheme of a cylinder capacitor ([367]) to derive the required electrical field of the electrostatic analyzer

"Ansatz" $\phi(r) = A \times \ln(r/r_0)$ is reasonable. The constant $A = 2\phi_\mathrm{i}/\ln(r_\mathrm{i}/r_\mathrm{a})$ follows from the conditions $\phi(r_\mathrm{i}) = \phi_\mathrm{i}$ and $\phi(r_\mathrm{a}) = \phi_\mathrm{a} = -\phi_\mathrm{i}$. To guide the reference electron on the radius $r = r_0$, $\phi_\mathrm{i} > 0$. The condition $\phi_\mathrm{a} = -\phi_\mathrm{i}$ also leads to a relation between r_0, r_i, and r_a:

$$2 \ln r_0 = \ln r_\mathrm{a} + \ln r_\mathrm{i} \tag{7.79}$$

$$r_0^2 = r_\mathrm{a} r_\mathrm{i} \tag{7.80}$$

from which r_a and r_i can be determined by specifying an appropriate spacing $r_\mathrm{a} - r_\mathrm{i}$ between the bent plates. In the example, with $r_0 \equiv \rho = 30\,\mathrm{mm}$, $r_\mathrm{i} = 25\,\mathrm{mm}$ and $r_\mathrm{a} = 36\,\mathrm{mm}$ were chosen. The height h (in parallel to the y_s-coordinate) was chosen at $h = 40\,\mathrm{mm}$. The determination of ϕ_i and ϕ_a remains. This can be easily derived from the balance between the force F_E of

the electric field and the centrifugal force F_C:

$$F_E = -\frac{e\Delta\phi/\ln(r_i/r_0)}{r} \quad \text{with} \quad \Delta\phi = \phi_i - \phi_a = 2\phi_i \tag{7.81}$$

$$F_C = \frac{m_e v^2}{r} \tag{7.82}$$

$$F_E = F_C \rightarrow m_e v^2 = -\frac{e\Delta\phi}{\ln(r_i/r_a)} \tag{7.83}$$

$$m_e v^2 = 2eU \rightarrow \Delta\phi = -2\,U \ln(r_i/r_a)\,. \tag{7.84}$$

With $U = 15\,\text{kV}$ holding for the reference electron, $\Delta\phi = 10.940\,\text{kV}$, $\phi_i = \Delta\phi/2 = 5.47\,\text{kV}$, and $\phi_a = -\Delta\phi/2 = -5.47\,\text{kV}$.

The rf Deflector After passing the two electrostatic analyzers, the time information is converted to a spatial profile by the rf deflector. The deflector is a $\lambda/4$ resonator [361, 374] operating at 108 MHz, in the example, the third harmonic of the accelerating frequency. The factor of merit Q is about 100. An input power of 30 W and an impedance of 50 Ω leads to a maximum voltage $U_0 > 5000\,\text{V}$ of the sine wave excitation. To avoid nonlinearities, only about $\pm 30°$ of the sine wave can be used. The resulting maximum deflection angle is then of the order of $\pm 50\,\text{mrad}$. After a drift of about 600 mm, the profile width on the MCP detector is of the order of centimeters. It is evident that a theoretical determination of the conversion factor, time → spatial coordinate, has to be approved and, possibly has to be corrected by experiment. The correct phase setting of the input voltage to the rf resonator can probably be fixed only by experiment.

The Transfer Matrices To transfer an electron through an electrostatic analyzing system, as shown in Fig. 7.15, the well-known matrix formalism can be applied. The coordinates of a specific electron are described by the vector,

$$\overrightarrow{r} = \begin{pmatrix} x_s \\ x'_s \\ y_s \\ y'_s \\ l \\ \Delta \end{pmatrix} . \tag{7.85}$$

To be consistent with the conventions in the literature [326, 330], one has to substitute for the coordinate system x, y, z, defined in Fig. 7.22, for a new one x_s, y_s, s, moving at the velocity of the reference electron v_0 along the trajectory s:

$$-z \rightarrow x_s \tag{7.86}$$

$$y \rightarrow y_s \tag{7.87}$$

$$x \rightarrow s\,. \tag{7.88}$$

Therefore, x_s now defines the "horizontal" plane of the analyzer and is determined by the deviation of the arriving particle in the z-coordinate, and x'_s has to be derived from $-v_\mathrm{z}/v_\mathrm{x} = -\dot{z}/\dot{x} = -dz/dx$. In the "vertical" plane, $y'_\mathrm{s} = v_\mathrm{y}/v_\mathrm{x} = \dot{y}/\dot{x} = dy/dx$. As usual, s is the longitudinal coordinate in the matrix formalism for bending magnets. This coordinate is fixed on the reference electron. Defining l as the local deviation of a specific electron against the reference electron gives $l = -v_0(t - t_0)$. On the other hand, Δ is defined as the relative deviation in the velocity $\Delta = (v_\mathrm{s} - v_0)/v_0$. Taking the small slit in the grounded plate of the extraction system as reference, t_0 and v_0 are given by (7.50) and (7.51), respectively. The coordinate transformation of an electron starting at the grounded plate is determined by the transfer matrices of the following elements:

1. drift $D_1 \rightarrow$ aperture A_1
2. drift $D_2 \rightarrow A_2$
3. drift $D_3 \rightarrow$ left analyzer
4. left analyzer
5. drift $D_4 \rightarrow$ right analyzer
6. drift $D_5 \rightarrow$ aperture A_3
7. drift $D_6 \rightarrow$ rf deflector
8. thin lens (realized by an additional dc-voltage on the deflecting plates).

Behind the deflector is another drift space D_7 up to the stop at the MCP detector. But keeping in mind that the arrival time at the rf deflector determines the spatial profile at the MCP, it is sufficient to transform the electrons up to the thin lens. In the transformation matrices, the apertures as well as the thin lens do not have an extension in the s-direction. In the following, the transfer matrices $A_{11} \ldots A_{66}$ are given for the interested system designer and programmer:

$$\mathrm{Drift}(L) = \begin{pmatrix} 1 & L & 0 & 0 & 0 & 0 \\ 0 & 1 & 0 & 0 & 0 & 0 \\ 0 & 0 & 1 & L & 0 & 0 \\ 0 & 0 & 0 & 1 & 0 & 0 \\ 0 & 0 & 0 & 0 & 1 & L \\ 0 & 0 & 0 & 0 & 0 & 1 \end{pmatrix} . \tag{7.89}$$

Thin lens, focusing in the horizontal plane (x-direction);

$$\mathrm{Lens_x}(f) = \begin{pmatrix} 1 & 0 & 0 & 0 & 0 & 0 \\ -1/f & 1 & 0 & 0 & 0 & 0 \\ 0 & 0 & 1 & 0 & 0 & 0 \\ 0 & 0 & 0 & 1 & 0 & 0 \\ 0 & 0 & 0 & 0 & 1 & 0 \\ 0 & 0 & 0 & 0 & 0 & 1 \end{pmatrix} . \tag{7.90}$$

To get the matrix for a thin lens focusing in the vertical plane (y-direction), one has to replace the elements A_{21} by 0 and A_{43} by $-1/f$.

The matrix for the electrostatic analyzer, deflecting to the left with bending radius ρ and total deflecting angle φ is

$$A_l = \begin{pmatrix} \cos\sqrt{2}\varphi & \frac{\rho}{\sqrt{2}}\sin\sqrt{2}\varphi & 0 & 0 & 0 & -\rho(1-\cos\sqrt{2}\varphi) \\ -\frac{\rho}{\sqrt{2}}\sin\sqrt{2}\varphi & \cos\sqrt{2}\varphi & 0 & 0 & 0 & -\sqrt{2}\sin\sqrt{2}\varphi \\ 0 & 0 & 1 & \rho\varphi & 0 & 0 \\ 0 & 0 & 0 & 1 & 0 & 0 \\ -\sqrt{2}\sin\sqrt{2}\varphi & \rho(1-\cos\sqrt{2}\varphi) & 0 & 0 & 1 & \rho(\varphi-\sqrt{2}\sin\sqrt{2}\varphi) \\ 0 & 0 & 0 & 0 & 0 & 1 \end{pmatrix} . \tag{7.91}$$

To construct the matrix for the analyzer deflecting to the right, one has to replace $A_{16} \rightarrow -A_{16}$, $A_{26} \rightarrow -A_{26}$, $A_{51} \rightarrow -A_{51}$, $A_{52} \rightarrow -A_{52}$, which can also be done by replacing ρ with $-\rho$ and φ with $-\varphi$.

The results from single particle transformations with somewhat typical initial conditions for the starting coordinates of the electron can be summarized as follows:

- Due to the space charge, the resolution of the whole system is diminished.
- The influence of the space charge forces can be reduced by a magnetic field parallel to the electric extraction field as long as the spatial resolution up to the exit of the second analyzer is considered.
- However, the magnetic field has an influence on the resolution of the system for the energy spread of the electrons collected. Considering the vector product

$$W = P\Delta t = (\overrightarrow{v} \cdot \overrightarrow{F})\Delta t = (\overrightarrow{v} \cdot (\overrightarrow{v} x \overrightarrow{B}))\Delta t = 0\,, \tag{7.92}$$

  it follows, that normally a magnetic field $\overrightarrow{B}$ parallel to the vector of the velocity $\overrightarrow{v}$ cannot transfer energy. Of course, the calculated change in energy is caused by the combination of space charge force and the magnetic field. In the calculations, this is confirmed by the transformation of an electron created at the front of the bunch. Such an electron experiences the space charge force for a long time due to the spiraled motion.
- Because the emittance of the electron beam is not changed by the magnetic field, the divergences increase.

Problems in the Technical Design

Beside extensive studies of particle dynamics, space charge forces, and the behavior of a rather complex analyzing and detection system, the design and manufacturing of a similar monitor confronts the engineer with some additional technical problems:

- To avoid distortions from the fringing field of the extraction condenser, homogenization of the edge fields has to be provided. This can be achieved by installing so-called "Herzog apertures" [367, 375] on a well-defined potential in front and behind the condenser.

- Furthermore, the electric field well inside the condenser has to be homogenized. Experiments with ceramic plates on both sides, coated with a thin layer of a resistive material, ended up with high voltage breakdowns. Finally, the problem has been solved by installing rods connected to chains of resistors along both sides of the condenser (see Fig. 7.19).
- The realization of a sufficient homogeneous magnetic field parallel to the electric field, especially near the extraction slit, confronts the designer with some other problems.
- As first experiments have shown, there are many secondary electrons generated somewhere in the system, leading to nearly constant noise in the output of the MCP. This noise has to be reduced by installing additional apertures and baffles.
- Considering beams with relatively low stiffness, the deflection of the primary beam by the electric extraction field may be intolerable and, therefore has to be compensated for by additional steerers in front of and behind the monitor.

Conclusion

A monitor, detecting secondary electrons from a thin wire in the beam or electrons from residual gas ionization, allows a nearly non-destructive measurement of longitudinal intensity distributions. However, both types of monitors are rather complex in technical design as well as in the interpretation of data in the presence of space charge forces. Nevertheless, considering the physical effects that have to be taken into account and the technical problems that have to be solved, design and operation of similar monitors can be an interesting challenge for engineers and physicists.

Determination of Longitudinal Emittances from Bunch Length Measurements

Approximating the particle distribution in the $\Delta W, \Delta\phi$ – plane by ellipses, algorithms analog to the algorithms, discussed in Sect. 6.2.4, can be applied [376]. The simplest method is to measure the bunch length at least at three pickups along a drift space.

Transfer Matrix for Drift Spaces

Taking the deviation in phase $\Delta\phi$ and the energy spread $\Delta W/W$ of a certain particle against the reference particle ($\Delta\phi = 0$, $\Delta W = 0$) as the variables in the longitudinal phase plane, the coordinates after a drift L are determined from the matrix transformation,

$$\begin{pmatrix} \Delta\phi_1 \\ \Delta W_1/W_0 \end{pmatrix} = \begin{pmatrix} 1 & k \\ 0 & 1 \end{pmatrix} \begin{pmatrix} \Delta\phi_0 \\ \Delta W_0/W_0 \end{pmatrix} . \tag{7.93}$$

In a nonrelativistic approximation, the coefficient k is easily derived from

$$\Delta\phi = \omega\Delta t = -\frac{2\pi f\, L}{\Delta v} = -\frac{2\pi f\, L}{\Delta\beta c} \tag{7.94}$$

$$\frac{\Delta\beta}{\beta} = \frac{1}{2}\frac{\Delta W}{W} \rightarrow k\,[\mathrm{rad}] = -\frac{\pi f\, L}{\beta c}\,. \tag{7.95}$$

In practice, the bunch length is measured on the timescale. Measuring the drift space in [meters] and using [nanoseconds] as the unit on the timescale, (7.93) can be converted to

$$\begin{pmatrix} \Delta t_1 \\ \Delta W_1/W_0 \end{pmatrix} = \begin{pmatrix} 1 & k^* \\ 0 & 1 \end{pmatrix} \begin{pmatrix} \Delta t_0 \\ \Delta W_0/W_0 \end{pmatrix} \tag{7.96}$$

$$k^*\,[ns] = -\frac{1000\, L\,[\mathrm{m}]}{2\beta c\,[\mathrm{mm/ns}]}\,. \tag{7.97}$$

Referring to (6.74) (Sect. 6.2.4), the bunch length Δt_1 at position "1" is determined from the length Δt_0 at position "0":

$$\Delta t_1 = \sqrt{\varepsilon\beta_1} = \sqrt{a_{11}^2\,\varepsilon\beta_0 - 2\,a_{11}a_{12}\,\varepsilon\alpha_0 + a_{12}^2\,\varepsilon\gamma_0}\,, \tag{7.98}$$

with $a_{11} = 1$, $a_{12} = k^*$, $a_{21} = 0$, and $a_{22} = 1$. Thus, to determine the Twiss parameters from three or more measured bunch lengths along a drift space, the algorithms discussed in Sect. 6.2.4 can be applied.

Use of a rf Cavity to Vary the Bunch Length

Considering the action of a rf cavity, like a single gap resonator or all kinds of bunchers, on the particles leads to a further analogy to the transverse case. To illustrate this, Fig. 7.30 shows an ellipse in the longitudinal phase plane, representing a bunch in the center of a rf cavity. The particle at the center of the bunch arrives at the center of the cavity at $t = 0$, which is also the reference time of the corresponding sine wave. Particles arriving at $t < 0$ are earlier than the reference particle and, therefore are decelerated by the rf. On the other hand, particles arriving at $t > 0$ are later than the reference particle and are accelerated. From Fig. 7.30, it becomes clear that most of the particles arriving at $t < 0$ have higher energy than the reference particle and most of the particles with $t > 0$ have lower energy than the reference particle. Thus, the action of the cavity results in a reduction of the energy spread. Because the area of the ellipse remains constant, the bunch length will increase. This is a typical application of a debuncher, used mostly behind a linear accelerator as an injector into a circular machine, where a low energy spread is much more important than a short bunch length. Switching the phase of the sine wave $\sin\omega t$ to $\sin(\omega t + \pi)$ changes deceleration to acceleration. A typical example for this phase setting is a rebuncher, used mostly in front of a linear accelerator

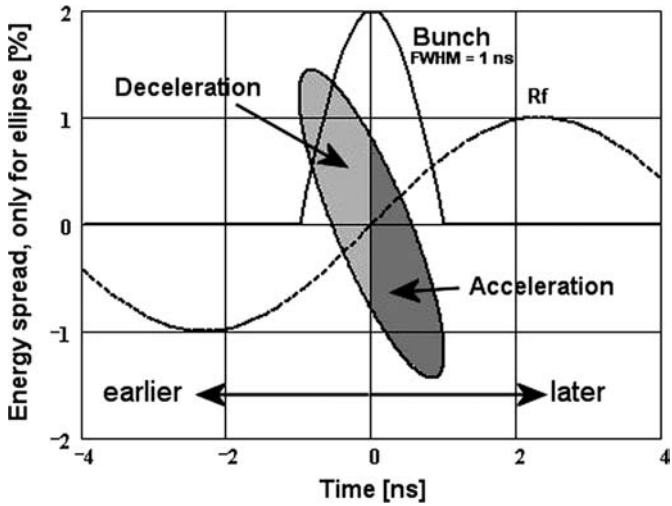

Fig. 7.30. Simplified scheme to explain the determination of longitudinal emittances, changing the bunch length by means of a rf-cavity. Note: The diagram is drawn in the longitudinal phase plane and, therefore the scale of the ordinate holds only for the ellipse with TWISS parameters: $\varepsilon = 0.8\,\%\,\mathrm{ns}$, $\beta = 1.25\,\mathrm{ns}\,/\,\%$, $\gamma = 2.6\,\%/\,\mathrm{ns}$ and $\alpha = 1.5$. The amplitude of the sine-wave as well as the displayed particle density distribution in the bunch are drawn in arbitrarily units

section requiring short bunches. Obviously, the phase setting of the rf cavity can be compared with the action of a focusing and defocusing quadrupole in the transverse phase plane. Figure 7.31 illustrates the change in energy spread dependent on the phase setting of the rf cavity.

Remark. Consider the ellipse, shown in Fig. 7.30. At a certain point without any action of a rf cavity, it becomes clear that the ellipse rotates counterclockwise along a drift. Thus, the particles have their focus in times already passed. The location of the focus in time in front of the observation point can be derived from the condition $\alpha = 0$. For the example of Fig. 7.30 with $\beta = v/c = 0.1$ and $\gamma = 2.6$ [% / ns], this leads to

$$-\alpha + k^* / \gamma = 0 \tag{7.99}$$

$$L = -\frac{\alpha}{\gamma}\frac{2\,\beta c}{1000} \rightarrow -3.46\,\mathrm{m} \tag{7.100}$$

$$\Delta t(\mathrm{FWHM}) \;:\; 1\,\mathrm{ns} \rightarrow 0.555\,\mathrm{ns}\,. \tag{7.101}$$

According to the transfer matrices (7.93) and (7.96), the energy spread does not change during drift.

Transfer Matrix of a rf Cavity

Customarily, in accelerator physics, the reference phase ϕ_s is defined by $\phi_\mathrm{s} = 0$ on top of a sine wave. Therefore, the maximum energy that a particle travers-

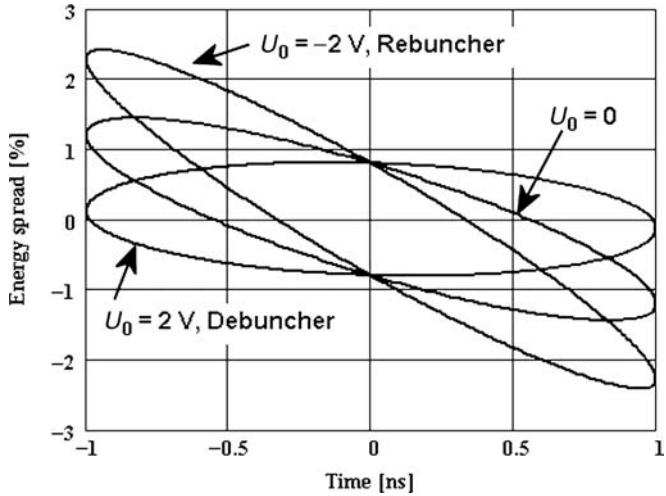

Fig. 7.31. Change of energy spread $\Delta W/W$ due to the action of a rf cavity

ing the cavity can gain is given by

$$\Delta W = \zeta e T_{\text{transit}} U_0 \cos\phi_{\text{s}}. \tag{7.102}$$

The so-called transit time factor T_{transit} takes into account the finite crossing time through the cavity. For a rf cavity with uniform field and a gap length g, $T_{\text{transit}} = \sin(\pi g/\lambda)/(\pi g/\lambda)$ with λ as the wavelength of the accelerating rf. Referring to Fig. 7.30, the rf cavity has to be operated at $\phi_{\text{s}} = \mp\frac{\pi}{2}$ to change the bunch length ($\phi_{\text{s}} = -\pi/2$ corresponds to the example of Fig. 7.30). Thus, particles with small $\Delta\phi$ around the reference particle gain energy:

$$\Delta W = \zeta e T_{\text{transit}} U_0 \sin\Delta\phi \approx \zeta e T_{\text{transit}} U_0 \Delta\phi, \quad -\pi/2 \tag{7.103}$$

$$\Delta W = -\zeta e T_{\text{transit}} U_0 \sin\Delta\phi \approx -\zeta e T_{\text{transit}} U_0 \Delta\phi, \quad \pi/2 \tag{7.104}$$

Equations. (7.103) and (7.104) between the change in energy and phase deviation determine the transfer matrix. Considering especially (7.103), one gets

$$\frac{\Delta W}{W} = \frac{1}{W}\frac{\zeta e}{A} T_{\text{transit}} U_0 \Delta\phi, \tag{7.105}$$

where W and ΔW usually are in units of MeV/u.

In most cases, the transit time factor as well as the exact absolute value of U_0 are not known to the operator. Performing a measurement requires a well-known change in U_0 to vary the bunch length. Usually, this is done by changing a computer-controlled reference voltage (mostly from 0–10 V). To observe the change in bunch length, the corresponding detector (capacitive pickup, or semiconductor) has to be installed at an appropriate distance L behind the cavity. This offers the possibility of determining the unknown

factors in 7.105 by switching the rf phases to values, different from $\phi_s = \pm\pi/2$ (e.g., $\phi_s = \pm 30°, \pm 60°$) and measuring the change in time of flight. Defining $D = \zeta e T_{\text{transit}}/WA$, one obtains an equation to calibrate the product DU_0:

$$\frac{\Delta W}{W} = D\,U_0 \cos\phi_s = DU_0 \sin\phi\,. \tag{7.106}$$

Here, $\phi = \phi_s + \pi/2$ has been introduced, since most phase shifters define $\phi = 0$ at $\phi_s = -\pi/2$. In a nonrelativistic approximation, $\Delta W/W$ can be evaluated from $2\,\Delta t/t_0$ with $t_0 = L\,/\,\beta c$ as the time of flight from the cavity to the detector switching the cavity off ($U_0 = 0$). By measuring Δt for various phase settings, the constant D can be determined with high precision from the slope in a diagram $\Delta W/W = f(\sin\phi)$. Then the transfer matrix is given by

$$\begin{pmatrix} \Delta\phi_1 \\ \Delta W_1/W_0 \end{pmatrix} = \begin{pmatrix} 1 & 0 \\ DU_0 & 1 \end{pmatrix} \begin{pmatrix} \Delta\phi_0 \\ \Delta W_0/W_0 \end{pmatrix}\,. \tag{7.107}$$

By determining $\Delta W/W$ in percent and measuring the reference voltage U_0 in Volts, the constant D comes out in the dimension $[\%\,/\,V\,\text{rad}]$. Conversion to a phase plane with Δt as the variable of the abscissa is straightforward by replacing $\sin\phi$ by $\sin\phi/2\pi f$. A practical dimension of D is $[\%/Vns]$ and the transformation matrix is

$$\begin{pmatrix} \Delta t_1 \\ \Delta W_1/W_0 \end{pmatrix} = \begin{pmatrix} 1 & 0 \\ DU_0 & 1 \end{pmatrix} \begin{pmatrix} \Delta t_0 \\ \Delta W_0/W_0 \end{pmatrix}\,. \tag{7.108}$$

D is determined by the characteristics of the cavity, by the conversion of the reference voltage to the voltage over the gap, and the charge over mass ratio A/ζ. Therefore, D has to be measured only once, introducing a normalized constant of the cavity $D_n = A/\zeta\,D$. Table 7.2 gives the results of a calibration procedure performed on a debuncher cavity with the following relevant parameters:

Beam energy: 11.44 MeV/u *(*$\rightarrow \beta = v/c = 0.155$*)*
Ion: Ne *(*$A = 20$, $\zeta = 10$*)*
rf-frequency: $f = 108.2$ MHz
Drift space from the debuncher to the capacitive pickup: 51.434 m
Reference voltage: $U_0 = 0.54$ V

With the given parameters, $\Delta W/W$ is obtained in a nonrelativistic approximation from

$$\text{TOF}_{U_0=0} = \frac{51.434 \times 10^3\,\text{mm}}{0.155 \cdot 300\,\text{mm/ns}} = 1.11\,\mu\text{s} \tag{7.109}$$

$$\frac{\Delta W}{W}\,[\%] = 200\frac{\Delta t_{\text{TOF}}}{\text{TOF}_{U_0=0}}\,. \tag{7.110}$$

Figure 7.32 illustrates the determination of D from the slope in the diagram $\Delta W/W = f(\sin\phi/2\pi f) = f(\Delta t)$. Figure 7.33 displays the results of a longitudinal emittance measurement, observing the change in bunch length by varying the cavity reference voltage.

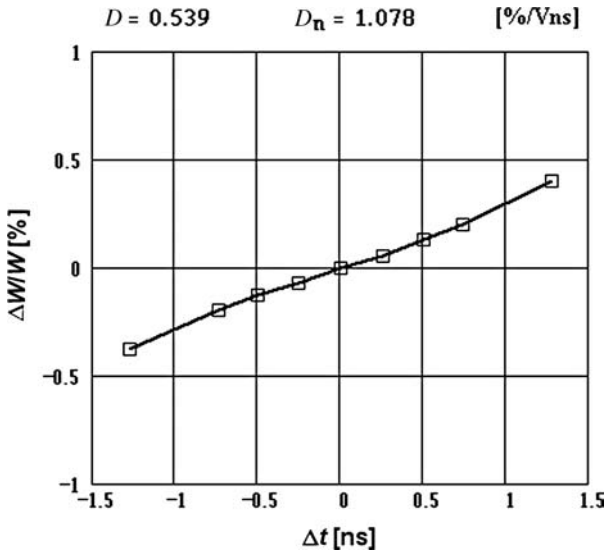

Fig. 7.32. Determination of the characteristic cavity constant D from the slope $\Delta W/W = f(\Delta t)$

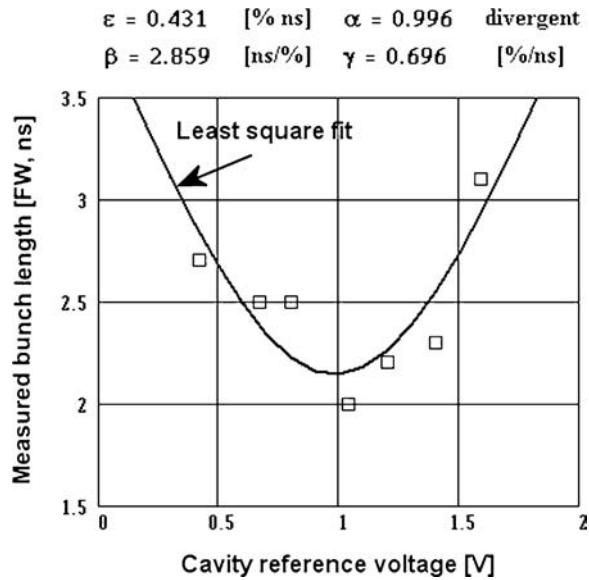

Fig. 7.33. Example of a longitudinal emittance measurement in the transfer channel of the UNILAC to the SIS

Table 7.2. Calibration of a debuncher cavity for longitudinal emittance measurements. The characteristic constant D is determined from the slope $\Delta W/W = f(\sin\phi)/(2\pi f)$, as illustrated in Fig. 7.32

$\phi\,[^0]$	Δt_{TOF}[ns]	$\Delta W/W$ [%]	$\sin\phi/2\pi f$ [ns]
60	2.2	0.398	1.274
30	1.1	0.199	0.735
20	0.7	0.127	0.503
10	0.3	0.054	0.255
0	0	0	0
−10	−0.4	−0.072	−0.255
−20	−0.7	−0.127	−0.503
−30	−1.1	−0.199	−0.735
−60	−2.1	−0.38	−1.274

Combination of Drift Spaces and rf Cavity

Beam transport sections may be equipped with a certain number of capacitive pickups and bunchers or rebunchers in between. With the knowledge of all distances between the relevant elements and the reference voltage settings of the rf cavities, determination of the longitudinal emittance is possible without any change in the reference voltages. An example is taken from the long transfer channel between the end of the UNILAC and the SIS. Figure 7.34 shows the result of such a measurement. Here, the operator has tried to optimize the rf setting of a debuncher to obtain minimum energy spread for injection into the synchrotron. After the longitudinal emittance has been measured, it is very easy to check operator effort by

- transforming the Twiss parameters along the drift space up to the location of the debuncher (= 36.11 m from the first capacitive pickup) and
- determining $\Delta W/W$ dependent on the reference voltage of the debuncher from

$$M(U_0) = \begin{pmatrix} 1 & 0 \\ DU_0 & 1 \end{pmatrix} \begin{pmatrix} \beta & -\alpha \\ -\alpha & \gamma \end{pmatrix}_{\mathrm{Deb}} \begin{pmatrix} 1 & 0 \\ DU_0 & 1 \end{pmatrix}^T , \qquad (7.111)$$

with the result $\Delta W/W(U) = \sqrt{\varepsilon M(U_0)_{22}}$.

Figure 7.35 shows that the setting of the operator could be improved by nearly a factor of 2.

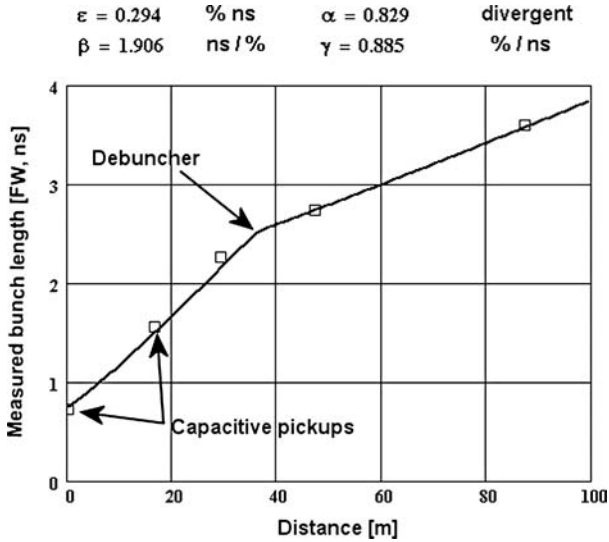

Fig. 7.34. Determination of longitudinal emittance by measuring the bunch length at five capacitive pickups, including the action of a debuncher

7.1.3 Measurements in the Phase Planes of Circular Machines

Basics

In circular machines, particles pass any detector system with the revolution frequency f_0. The corresponding revolution time T_0 depends mainly on the circumference of the machine, on the energy of the particles, and on the kind of ions. Revolution times $100\,\mathrm{ns} < T_0 < 100\,\mu\mathrm{s}$ can be considered typical. Thus, most methods discussed above to determine parameters in phase planes cannot be applied. On the other hand, periodically repeated signals open interesting new possibilities for beam diagnostics. Let us first recall some important formulas of accelerator physics in circular machines:

$$\frac{\Delta L}{L_\mathrm{c}} = \alpha \frac{\Delta p}{p_0} \quad \alpha, \text{ compaction factor} \tag{7.112}$$

$$\gamma_\mathrm{t}^2 = \frac{1}{\alpha} \quad \gamma_\mathrm{t} = \gamma - \text{ transition} \tag{7.113}$$

$$W_\mathrm{t} = \gamma_\mathrm{t} m_0 c^2 \quad \text{energy} \tag{7.114}$$

$$\frac{\Delta f}{f_0} = -\frac{\Delta T}{T_0} = \eta \frac{\Delta p}{p_0} \quad \text{frequency dispersion} \tag{7.115}$$

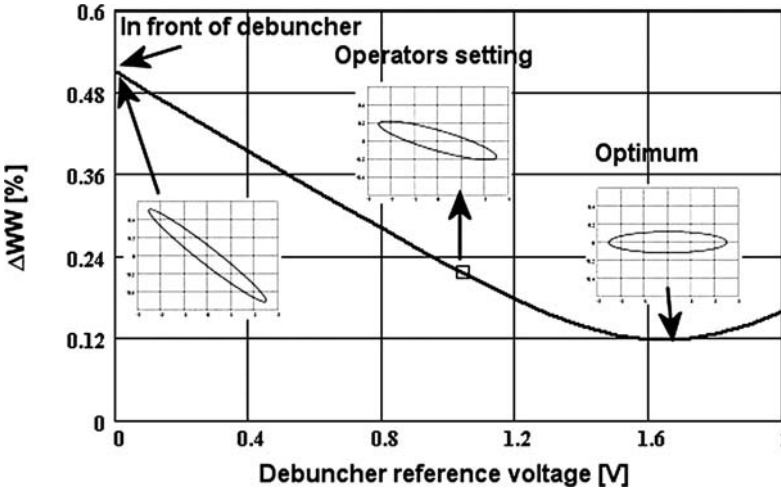

Fig. 7.35. Optimization of a debuncher setting to obtain the mimimum energy spread. The ellipse inserted on the left-hand side with $\Delta W/W_{\max} = 0.51\%$ corresponds to the output of the linac. The ellipse in the middle of the diagram with $\Delta W/W_{\max} = 0.22\%$ shows the change by the debuncher due to the setting of the operator, and the optimum with $\Delta W/W_{\max} = 0.12\%$ corresponds to a higher setting of the debuncher reference voltage as a result from a longitudinal emittance measurement

$$\eta = \frac{1}{\gamma^2} - \frac{1}{\gamma_t^2} = \frac{1}{\gamma^2} - \alpha \tag{7.116}$$

$$\frac{\Delta Q}{Q_0} = \xi \frac{\Delta p}{p_0} \quad \xi, \text{ chromaticity} \tag{7.117}$$

$$f_s = \frac{c}{L_c} \sqrt{\frac{\zeta e}{A} \frac{n\,|\eta|\,U_{rf}}{2\pi\gamma\, m_0 c^2}} \quad \text{synchrotron frequency} \tag{7.118}$$

Where L_0 is the circumference of the machine, p_0 the momentum and Q_0 tune for the reference particle, γ the relativistic factor $1/\sqrt{1-\beta^2}$, c the velocity of light, A the number of particles with charge ζe and rest mass m_0, n the harmonic number, and U_{rf} the amplitude of the accelerating rf. Equation 7.118 holds for small amplitudes of synchrotron oscillations at constant rf.

Various methods of beam diagnostics in the longitudinal phase space of circular machines are discussed in the literature (see, e.g., [1, 6, 28, 285, 329, 377–379].

Measurements, based on evaluating the so-called beam transfer function (BTF) require longitudinal excitation of the beam by a cavity. Because this results in collective modulation of the particles, the signals are relatively high in amplitude and therefore the achievable statistical accuracy can be high.

On the other hand, the observation and analysis of Schottky noise signals is another powerful tool for studying the behavior of a beam in longitudinal and

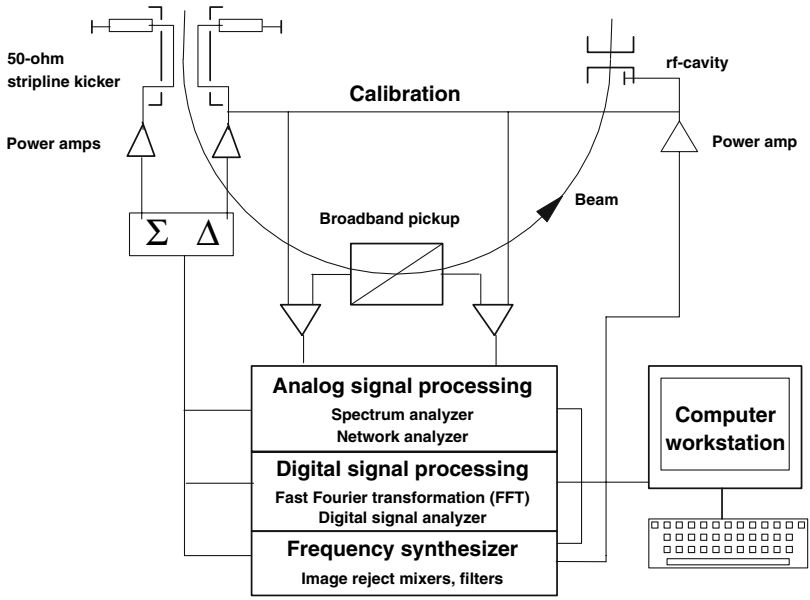

Fig. 7.36. Simplified scheme to illustrate BTF and Schottky signal measurements in circular machines

transversal phase planes. The beam current in a circular machine is generated by a finite number of circulating charged ions, which always are subjected to statistical fluctuations. This leads to noise even from a dc-current. Because the effect was first investigated by Schottky in old-fashioned electron tubes [380], this noise is called Schottky noise, and the term Schottky signals has been introduced in accelerator physics. Because Schottky noise arises from an incoherent intrinsic modulation of the beam, the signals are small in comparison to BTF signals, but do not require any excitation. Figure 7.36 is a simplified scheme to illustrate both methods. In the scheme, longitudinal excitation can be performed by a cavity, as well as by the 50-Ω strip-line kicker. Using the kicker, the power amplifiers have to be in phase (Σ). Excitation in the transverse plane requires a difference of π in phase (Δ). Figure 7.37 shows the main parts of a Schottky pickup, designed to perform Schottky scans in the SIS. To avoid distortions of the signals via the beam pipe, the signal ground is isolated from the grounded beam pipe. Taking advantage of the 50-Ω N-connectors on both ends of the electrodes, the pickup can be operated as an electrostatic monitor (open end) as well as in strip-line mode (50-Ω resistor at the end).

For interpretation and evaluation of BTF and Schottky signals, the beam circulating in a machine has to be classified according to the following characteristics:

- longitudinal
  - unbunched beam (dc, respectively, coasting beam),
  - bunched beam.

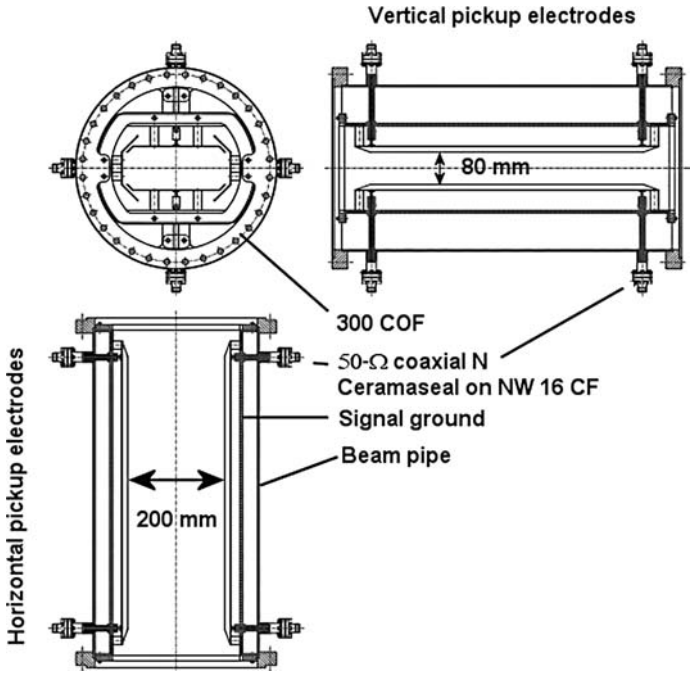

Fig. 7.37. Main parts of a construction drawing of a Schottky pickup. Top left: look into the chamber showing the horizontal and vertical pickup electrodes arranged one system behind the other one. The pickup can be used for longitudinal as well as transverse Schottky scans

- transversal
  - unbunched beam,
  - bunched beam.

Schottky, Longitudinal, Unbunched Beam

Assuming a charge of $1e$, the current in a circular machine is given by $i_{\mathrm{sp}} = e\, f_0$. Now, if there are N charged particles ($j = 1 \ldots N$) with frequencies f_{j} (around f_0), the current of the jth-particle can be written as

$$i_{\mathrm{j}}(t) = e f_{\mathrm{j}} \sum_{m=-\infty}^{+\infty} e^{im\omega_{\mathrm{j}} t} \qquad i \text{ is the imaginary unit}\,. \tag{7.119}$$

Obviously, the term $\sum_{m=-\infty}^{+\infty} e^{im\omega_{\mathrm{j}} t}$ represents the δ function. Assuming positive frequencies ($\omega_{\mathrm{j}} > 0$) because a detector can detect only positive frequencies, (7.119) can be written as

$$i_{\mathrm{j}}(t) = e f_{\mathrm{j}} + 2e f_{\mathrm{j}} \sum_{m=1}^{\infty} \cos m\omega_{\mathrm{j}} t. \tag{7.120}$$

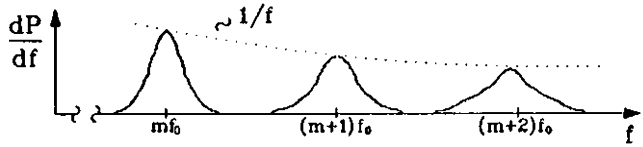

Fig. 7.38. Typical frequency spectrum of longitudinal Schottky noise (from [381])

Averaging over all N particles leads immediately to the dc-current $i_{\mathrm{DC}} = N\,e\,f_0$ ($\langle \cos m\omega_{\mathrm{j}} t\rangle = 0$), where f_0 now is the average of the revolution frequencies. However, looking for the rms current per band, one gets

$$\langle i^2\rangle = [2ef_0]^2\, N\, \langle \cos\Theta_{\mathrm{j}}\rangle^2, \qquad \Theta_{\mathrm{j}} = m\omega_{\mathrm{j}} t \tag{7.121}$$

$$i_{\mathrm{rms}} = 2ef_0\sqrt{\frac{N}{2}} = ef_0\sqrt{2N}. \tag{7.122}$$

Thus, the rms current per band from incoherent statistical fluctuations is independent of m and proportional only to $\sqrt{N}$ and not to N, as holds for coherent modulations. This proportionality to $\sqrt{N}$ confirms the statistical character of Schottky signals. Considering the frequency domain, one finds an infinitely narrow line at frequency mf_{j} for a specific single charged particle. Therefore, many particles having slightly different f_{j} are represented by a band of frequencies (Schottky band), whose width can be derived from (7.115) as

$$\Delta f = m\Delta f_{\mathrm{j}} = mf_0\eta\frac{\Delta p}{p}. \tag{7.123}$$

The spectral power density dP/df is proportional to $\langle i^2\rangle/\Delta f$ and, because the total power in a band is constant, in a diagram of dP/df as a function of frequency f, one expects peaks, centered at frequencies $m\,f_0$, $(m+1)\,f_0$, $(m+2)\,f_0, \ldots$, decreasing in amplitude $\sim 1/f$ and increasing in width $\sim m$ as shown in the example of Fig. 7.38. Longitudinal Schottky signals of a coasting beam lead to relatively simple spectra in the frequency domain. Thus, the momentum spread $\Delta p/p$ can be determined by measuring the width of a peak Δf_{m} at the harmonic m. Equation 7.115 leads immediately to

$$\frac{\Delta p}{p} = \frac{1}{\eta}\frac{\Delta f_{\mathrm{m}}}{mf_0}\,. \tag{7.124}$$

Figure 7.39 shows two Schottky signals measured in the storage ring ESR.

Schottky, Transversal, Unbunched Beam

Due to the betatron oscillations around the beam center, the transverse Schottky signal of a coasting beam becomes more complicated. Because the signals represent the dipole moment and, therefore are gained from the difference of

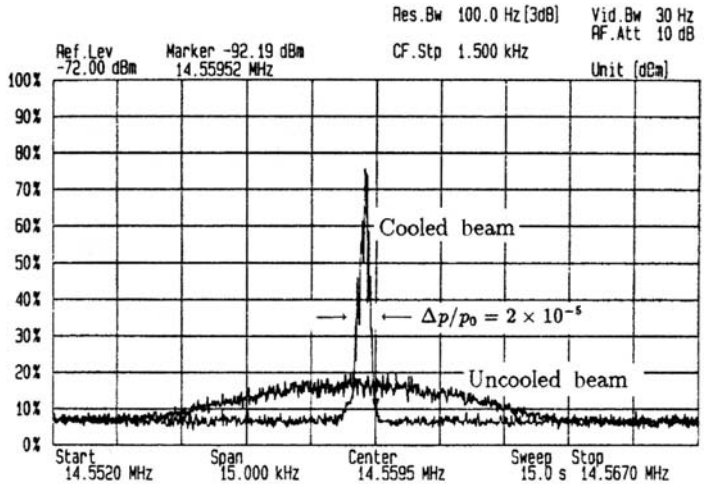

Fig. 7.39. Longitudinal Schottky signals [381], taken at the 10th harmonic from an Ar^{18+}-beam circulating in the ESR. The momentum spread of the uncooled beam is about $\Delta p/p = 1 \times 10^{-3}$. The improvement due to cooling down to $\Delta p/p = 2 \times 10^{-5}$ is illustrated very nicely

a horizontal or vertical pair of electrodes, the signals are smaller (up to two orders of magnitude) than longitudinal sum signals. For the jth particle, the amplitude of sinusoidal oscillation is

$$a_{\mathrm{j}}(t) = a_{\mathrm{j}} \cos(q_{\mathrm{j}} \omega_{\mathrm{j}} t + \varphi_{\mathrm{j}}) \tag{7.125}$$

with q_{j} as the nonintegral part of the betatron tune Q. In the frequency domain representation, the dipole moment of the jth particle follows from $d_{\mathrm{j}}(t) = a_{\mathrm{j}}(t) i_{\mathrm{j}}(\omega)$ [6], [285]:

$$d_{\mathrm{j}}(t) = a_{\mathrm{j}} \cos(q_{\mathrm{j}} \omega_{\mathrm{j}} t + \varphi_{\mathrm{j}}) e f_{\mathrm{j}} \sum_{m=-\infty}^{+\infty} e^{im\omega_{\mathrm{j}} t} \qquad i \text{ is the imaginary unit}. \tag{7.126}$$

Expressing $\cos(q_{\mathrm{j}} \omega_{\mathrm{j}} t + \varphi_{\mathrm{j}})$ by $(e^{i(q_{\mathrm{j}} \omega_{\mathrm{j}} t + \varphi_{\mathrm{j}})} + e^{-i(q_{\mathrm{j}} \omega_{\mathrm{j}} t + \varphi_{\mathrm{j}})})/2$ shows immediately that the spectrum consists of a series of lines, spaced by f_0, but shifted in frequency ($im\omega_{\mathrm{j}} \rightarrow i(m + q_{\mathrm{j}})\omega_{\mathrm{j}}$). This becomes even clearer by evaluation of (7.126) keeping in mind that $\cos x \cos y = \cos(x - y) \cos(x + y)/2$:

$$d_{\mathrm{j}}(t) = e f_{\mathrm{j}} a_{\mathrm{j}} (1 + \sum_{m=1}^{m=\infty} \cos\left[(m - q)\omega_{\mathrm{j}} t + \varphi_{\mathrm{j}}\right] \cos\left[(m + q)\omega_{\mathrm{j}} t + \varphi_{\mathrm{j}}\right] . \tag{7.127}$$

Equation 7.127 describes a frequency modulation, splitting the lines in the longitudinal of a coasting beam at $f_{\mathrm{m}} = m f_0$, into two lines $f_{\mathrm{m}+} = (m + q) f_0$ and $f_{\mathrm{m}+} = (m - q) f_0$. Therefore, measuring the separation of lines

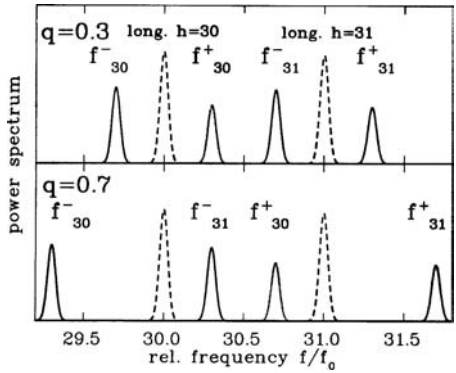

Fig. 7.40. Calculated transverse Schottky spectra ([120]) for $m = 30$ and 31. Top: For a value of $q = 0.3$, the lines are close to the longitudinal peak. Bottom: For a value of $q = 0.7$, the lines are widely separated from the longitudinal peak which in this case leads even to an interchange of the order. Parameters of calculation: $f_0 = 1\,\mathrm{MHz}$, $\Delta p/p = 2 \times 10^{-3}$, $\eta = 1$, $\xi = -1$, and $Q = 4.3$ and 4.7

corresponding to the same harmonic number "little q,"the nonintegral part of the tune, can be determined from

$$q = m\,\frac{f_{\mathrm{m}}^{+} - f_{\mathrm{m}}^{-}}{f_{\mathrm{m}}^{+} + f_{\mathrm{m}}^{-}}. \tag{7.128}$$

Remembering that Schottky signals can be obtained without any excitation of the beam, the q value, derived from (7.128) is the incoherent value of the tune. This value can differ from a BTF measurement, which due to the required beam excitation, delivers the coherent value of the tune. Figure 7.40 shows two calculated transverse Schottky spectra to illustrate the powerful method for determining q. At the same time, it demonstrates that one has to be careful in the interpretation of such spectra. The correct order of lines can be checked by a small variation of the tune and observing the shift of the lines. From the width of the sidebands, it is possible to deduce further information. Differentiation of $f_{\mathrm{m}}^{\pm} = (m \pm q) f_0$, applying the results in

$$\Delta f_{\mathrm{m}}^{\pm} = (m \pm q)\Delta f_0 + \Delta q\, f_0\ , \tag{7.129}$$

and with $\Delta q = Q\,\xi\,\Delta p/p$ from (7.117),

$$\frac{\Delta f_{\mathrm{m}}^{\pm}}{f_0} = \frac{\Delta p}{p}\left[(m \pm q)\,\eta \pm Q\,\xi\right]\ . \tag{7.130}$$

This offers the possibility of determining ξ from a transverse Schottky scan without beam excitation, if the other parameters can be measured independently or are known from the design of the machine.

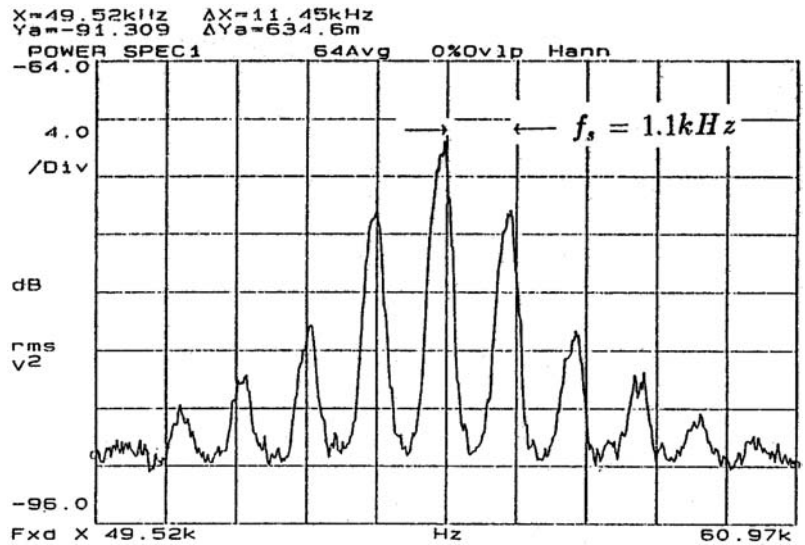

Fig. 7.41. Longitudinal Schottky spectrum [381] of a beam bunched and cooled in the experimental storage ring (ESR) of GSI. Parameters: $W = 164\,\mathrm{MeV}\,/\,\mathrm{u}$, $^{40}\mathrm{Ar}^{18+}$ ions, measured at the 10th harmonic, mixer frequency $f = 14.49\,\mathrm{MHz}$

Schottky, Longitudinal, Bunched Beam

As in linear accelerators, bunches are formed from the action of a rf cavity in a circular machine. If an individual particle does not cross the accelerating gap at a stable angle, defined by $\Delta W = \zeta e \cos\,\phi_\mathrm{s}$, then it will execute synchrotron oscillations around the phase ϕ_s of the synchronous particle, circulating with frequency f_0. This results in a modulation in time for the passage of particles through a pickup. This modulation adds to the Δp effect according to (7.123). In (7.119), t has to be replaced by $t + t_\mathrm{j}(\sin\,\omega_\mathrm{s} t + \varphi_\mathrm{j})$ to derive the equivalent to (7.120). The evaluation of the resulting equation

$$i_\mathrm{j}(t) = e f_\mathrm{j} \sum_{m=-\infty}^{+\infty} e^{im\omega_\mathrm{j}\left[t + t_\mathrm{j}(sin\omega_\mathrm{s} t + \varphi_\mathrm{j}^0)\right]} \tag{7.131}$$

$$\omega_\mathrm{s} = 2\pi f_\mathrm{s} \quad f_\mathrm{s} \rightarrow (7.118) \tag{7.132}$$

is straightforward [6, 285] and leads to a series of Bessel functions J_p. Considering the Schottky signals, each line at frequencies mf_0 in the longitudinal spectrum of a coasting beam splits into an infinite series of lines spaced by f_s. Figure 7.41 shows a spectrum observed at a bunched and cooled Ar-beam in the ESR. Due to the statistic character of the starting phases φ_j^0, the spread $\Delta p/p$ cannot be determined directly from the width of the peak, as of a coasting beam. But, taking advantage of the relation [285, 381]

$$\frac{\Delta p}{p} = \frac{1}{\eta}\frac{\Delta f}{f_0} = \frac{2\pi n}{\eta} f_\mathrm{s}\,\Delta t_\mathrm{b}\ , \tag{7.133}$$

the momentum spread can be determined by performing an additional measurement of the width in time Δt_b.

Schottky, Transversal, Bunched Beam

The transverse Schottky spectra of a bunched beam arise from a combination of betatron oscillations, corresponding to an amplitude modulation and synchrotron oscillations, corresponding to a modulation in time. This leads to quite complex formulas [6, 285]. Each betatron line splits now into an infinite number of synchrotron satellites, and the spectra become rather complex. In consequence, their interpretation and evaluation requires much more effort, as in the three cases discussed. Additionally, the signal-to-noise ratio becomes quite low. Therefore, probably most applications of Schottky scans are based on the measurement of longitudinal spectra. An application of Schottky noise analysis for diagnosis of intense beams in linacs is given in [382].

Remark: No space charge effects have been considered in the discussion of Schottky signals in circular machines. Space charge forces can lead to changes in the relation (7.117) and, therefore, other methods of evaluation are required [383]. Another effect, not considered here, is the deforming and splitting of longitudinal Schottky signals due to plasma waves in highly cooled beams [379].

8

The Electromagnetic Fields of Bunches

8.1 Introduction

For many problems arising in the field of beam diagnostics, it is sufficient to derive influenced or induced signals considering a one-dimensional density distribution of the particles within a bunch or even macropulse. In most cases, the corresponding coordinate is the z-coordinate, respectively, the time t, related to each other by $z = \beta ct$. Typical examples are

- the calculation and interpretation of bunch signals detected with capacitive or inductive pickups, as discussed in Chap. 5;
- the determination of intensity distributions along the time axis from signals measured with coaxial Faraday cups (see Chap. 2); and
- the measurement of the beam intensity with beam current transformers (see Chap. 2).

But, to consider, for example, the effect of space charge on measured signals or a possible space charge compensation within bunches, it becomes essential to take the spatial extensions of bunches into account, as already briefly discussed in Chap. 7.

Although there are computer programs [301–307] for to calculating space charge effects in bunched beams by summing up the interactions of many single particles, analytical solutions have some advantages:

- The dependencies of all parameters become immediately evident.
- The potentials and field strengths generated by a bunch are known at any geometric position within and outside the bunches.
- Once the potentials and electromagnetic fields are known for a single bunch at rest, the evaluation of time-dependent potentials and fields generated by a moving chain of bunches is straightforward.
- The understanding of space charge effects may become clearer by considering a single particle in the potential and electromagnetic fields of a moving bunch.

- The effects of any partial space charge compensation can be easily taken into account mathematically by lowering the number of charges within the bunches.
- There is no need for large computing power to obtain rough estimations of space charge effects.

In the following, relativistic effects and the magnetic fields of bunches will be neglected, which means we consider, first of all, low energy rf accelerators accelerating particles up to β values $\lesssim 0.5$.

If necessary, relativistic effects can be taken into account by applying the well-known transformation laws [39, 245, 351] of the four vectors, respectively, of the second-rank, antisymmetric field strength tensor. A discussion of the relevant transformation laws as well as the relativistic effects arising is postponed to Appendix 8.B at the end of this chapter.

Considering rf accelerators, the geometric dimensions of a bunch are mostly similar in the two transverse directions. Therefore, it is reasonable to assume rotational symmetry of the bunches about the longitudinal axis. Hence, the bunch shape may be approximated by rotational symmetrical ellipsoids [395, 396]. Their shape then depends only on the ratio of the two half-axes a and b. Obviously, the special case $a = b = R$ leads to a spherical bunch resulting in relatively simple expressions for the potential as well as the electrical field strength.

To determine potentials and fields, one has to find analytical solutions of the Poisson equation

$$\Delta\phi = -\frac{\rho(x, y, z)}{\epsilon_0} \tag{8.1}$$

$$\epsilon_0 = 8.85 \times 10^{-12}\,\mathrm{Vs/Am}\,, \tag{8.2}$$

assuming reasonable density distributions $\rho(x, y, z)$ of the particles within bunches. From the mathematical point of view, the simplest case is a homogeneous distribution with $\rho = \rho_0 = \text{const}$, which of course can be only a very rough approximation for $\rho(x, y, z)$. A better approach is achieved with a parabolic density distribution.

8.2 Bunches with a Spherical Shape

8.2.1 Charge Distributions

Homogeneously Charged Sphere

For bunches of spherical shape with radius R and a homogeneous charge density, $\rho(x, y, z)$ is constant and is given by

$$\rho_0 = \frac{3N\zeta e}{4\pi R^3} \tag{8.3}$$

within the limits $0 \leq r \leq R$, where N is the number of particles within the bunch, ζ is their charge, and $e = 1.602 \times 10^{-19}$As. For continuous beams, this corresponds to the well-known distribution function of Kapchinskij-Vladimirskij (KV) [384].

Parabolic Density Distribution

For continuous beams, a parabolic density distribution known as the "waterbag" distribution (WB) [308, 309], is described by

$$\rho^p(r) = \frac{5}{2}\,\rho_0 \left(1 - \frac{r^2}{R^2}\right), \tag{8.4}$$

within the bunch ($0 \leq r \leq R$). Of course, $\rho^p(r) = 0$ for $r \geq R$.

8.2.2 The Potentials

Homogeneously Charged Sphere

The solution of the Poisson equation for a homogeneously charged sphere (8.3) leads to

$$\phi(r)_{r \leq R} = \rho_0 \frac{R^2}{2\epsilon_0}\left(1 - \frac{r^2}{3R^2}\right) \tag{8.5}$$

$$\phi(r)_{r \geq R} = \rho_0 \frac{R^3}{3\,\epsilon_0}\frac{1}{r}\,, \tag{8.6}$$

where (8.5) describes the potential inside the spherical bunch and (8.6) gives the potential outside the bunch ($r > R$). In the solution, the influence of the beam pipe boundary has been neglected.

Sphere with a Parabolic Charge Distribution

For the parabolic distribution according to (8.4), the potential inside the sphere becomes

$$\phi(r)_{r \leq R} = \frac{5}{8}\frac{R^2}{\epsilon_0}\rho_0 \left(1 - \frac{2r^2}{3R^2} + \frac{r^4}{5R^4}\right)\,. \tag{8.7}$$

Of course, there is no difference in the potential outside the sphere from the homogeneous charge distribution, given by (8.6).

As an example, the potentials for the two cases are compared in Fig. 8.1 assuming $N = 1 \times 10^9$, $\zeta = 4$, and $R = 10\,\text{mm}$.

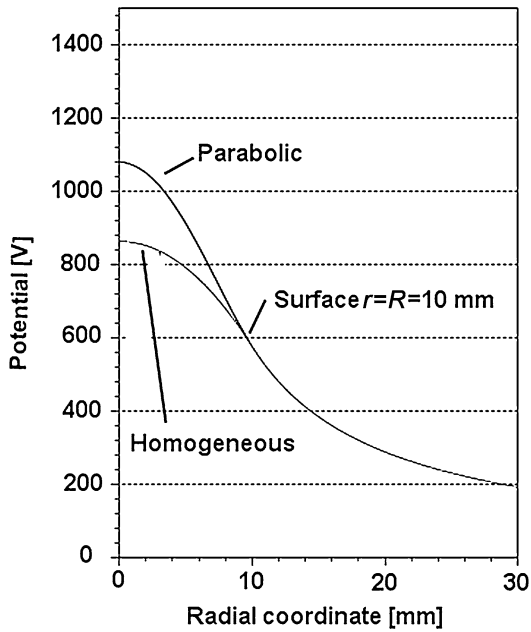

Fig. 8.1. Potential of a homogeneously charged sphere in comparison with a parabolic charge distribution. The data hold for radius $R = 10\,\mathrm{mm}$ and $N = 10^9$ U^{4+}-ions in the sphere

8.2.3 Electric Field Strength

Homogeneously Charged Sphere

There is only a radial component E_r of the electric field, which results from :

$$\overrightarrow{E(r)} = -\overrightarrow{\nabla}\phi(r) = -\frac{d}{dr}\phi(r) \ .$$

Inside the sphere, one obtains from (8.5)

$$E(r)_{\mathrm{r}\,\leq\,R} = \frac{1}{3\,\epsilon_0}\rho_0\, r \ , \tag{8.8}$$

and outside, the field has to be proportional to $1/r^2$, which immediately follows from (8.6):

$$E(r)_{\mathrm{r}\,\geq\,\mathrm{R}} = \frac{R^3}{3\,\epsilon_0}\rho_0\frac{1}{r^2} \ . \tag{8.9}$$

8.2.4 Sphere with a Parabolic Charge Distribution

From (8.7), for the field inside the bunch,

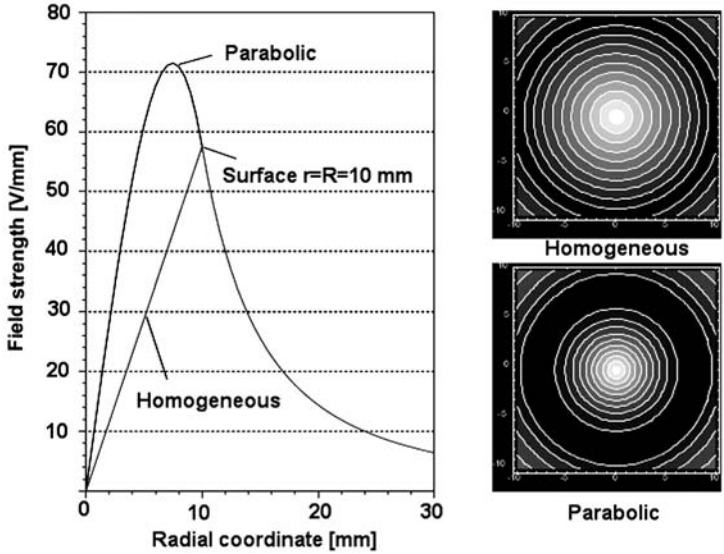

Fig. 8.2. Electrical field strength of a homogeneously charged sphere in comparison with a parabolic charge distribution. The data hold for a radius of $R = 10\,\mathrm{mm}$ and $N = 10^9$ U^{4+}-ions in the sphere

$$E(r)_{r \le R} = \frac{5}{6\,\epsilon_0}\rho_0\, r\, \left(1 - \frac{3}{5}\frac{r^2}{R^2}\right) . \tag{8.10}$$

Of course, the field outside the bunch is the same as given by (8.9). In Fig. 8.2, the two cases are compared. For a homogeneous charge distribution, the maximum field strength occurs at the surface at $r = R$; For the parabolic distribution, the maximum is inside the sphere at $r_\mathrm{m} = \sqrt{5}R/3$, and the corresponding field strength is $E(r_\mathrm{m}) = 5\sqrt{5}\rho_0\, R/(27\varepsilon_0)$. For the example, one obtains $r_\mathrm{m} = 7.454\,\mathrm{mm}$ and $E(r_\mathrm{m}) = 71.46\,\mathrm{V/mm}$.

8.3 Bunches with an Elliptical Shape

8.3.1 Charge Distributions

Here we consider two cases, too:

Homogeneously Charged Ellipsoid

A rotational symmetrical ellipsoid with a homogeneous charge distribution is comparable to the distribution given by (8.3):

$$\rho_0^e = \frac{3N\zeta e}{4\pi ab^2} = \rho_0 \frac{R^3}{ab^2} . \tag{8.11}$$

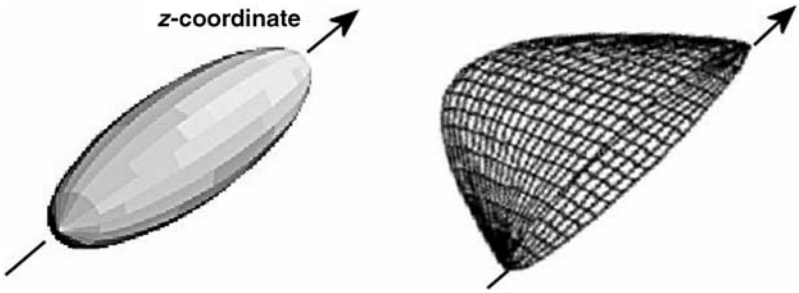

Fig. 8.3. Illustration of a bunch with an elliptical shape (left). In the x, y, z-coordinate system, the r-coordinate is given by $r = \sqrt{x^2 + y^2}$. The figure on the right-hand side illustrates a parabolic density distribution of the charged particles within the ellipsoid

Ellipsoid with a Parabolic Charge Distribution

Figure 8.3 illustrates the shape of a rotational symmetrical ellipsoid (left) with a parabolic distribution in the r- and z-directions, where $r = \sqrt{x^2 + y^2}$. Here we have defined x, y as the transverse coordinates and z as the longitudinal one. The distribution is described by

$$\rho(r, z) = \frac{5}{2}\rho_0^e \left(1 - \frac{r^2}{b^2} - \frac{z^2}{a^2}\right) . \tag{8.12}$$

In (8.12), r and z have to fulfill the relation

$$\frac{r^2}{b^2} + \frac{z^2}{a^2} = 1 \tag{8.13}$$

at the surface of the ellipsoid.

Even in a homogeneous distribution, the boundary conditions at the surface of the ellipsoid lead to very complex expressions in the solution of the Poisson equation. Therefore, it is practical to introduce a system of confocal elliptical coordinates [385, 386], which is more adapted to the problem. But, even in this coordinate system, one arrives at lengthy complex expressions. The solutions are given in Appendix 8.A of this chapter.

8.3.2 Comparison of Potentials

The potential of a homogeneously charged ellipsoid is given by (8.66) and (8.67), and the potential of a parabolically charged ellipsoid is described by (8.83) and (8.82) (see Appendix 8.A).

To compare with the potentials of a sphere, we assume the same number of particles $N = 1 \times 10^9$ with $\zeta = 4$ within an elliptical bunch of the same volume as the sphere with $R = 10\,\text{mm}$. In the example, we assume a relatively long,

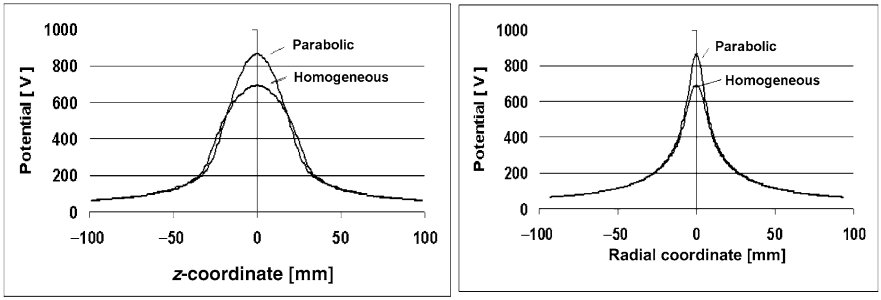

Fig. 8.4. Potentials of an elliptical shaped bunch. Left: Potentials along the z-axis. Right: Potentials along the small axis ($\eta = 0$). In the solution, the influence of the beam pipe boundary has been neglected

slim bunch with $a = 5b$, leading to $b = R/\sqrt[3]{5} = 5.85\,\text{mm}$ and $a = 29.2\,\text{mm}$, which, for example, would correspond to a bunch with $\Delta t \approx 500\,\text{ps}$ at $\beta = 0.2$. Figure 8.4 shows the potentials of homogeneously and the parabolically charged ellipsoids along the z-axis and along the small axis at the center of the ellipsoid ($\eta = 0$).

8.3.3 Comparison of Electric Fields

It is also of interest to compare the components of electric field strength between the homogeneously charged ellipsoid and the parabolically charged one with each other, as well as to compare them with the fields of the charged sphere. Figure 8.5 shows the field components along the z-axis and along the small axis with $\eta = 0$. The calculation of the fields from (8.99)–(8.101) (see Appendix 8.A) has been performed with MATHCAD.

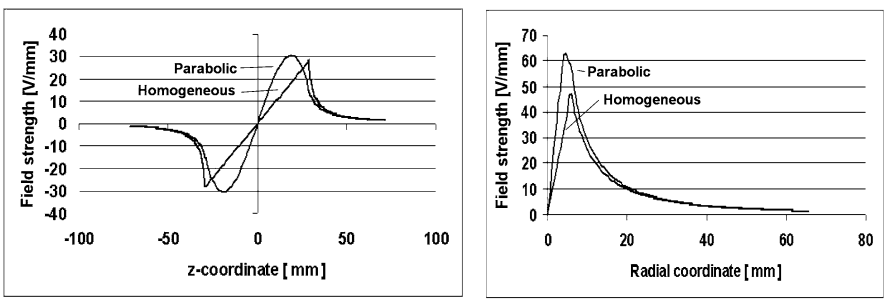

Fig. 8.5. Left: Field components for the elliptical bunches in z-direction. Right: Field components in r-direction

Conclusion

The equations derived for potentials and field strengths are rather complex, especially for the more realistic elliptical bunch shapes. Comparing the potentials and fields inside spherically shaped bunches and elliptically shaped bunches, one finds that the radial components of the field strength do not differ very much, if the number of charges within the bunches as well as their volume are comparable. On the other hand, the axial component of the field strength inside elliptical bunches is reduced, depending on the ratio of the axes. Due to the complexity of the expressions describing potentials and fields within elliptically shaped bunches, analytical estimations of space charge effects are very laborious. But, as experience has shown, in many cases, such estimations can be approximated well using reasonably scaled potentials and fields derived for spherically shaped bunches. In some cases, it is even possible to derive simpler, reasonable approximations of potentials and fields inside of bunches by considering a dc-beam.

8.4 Comparison with a DC-Beam

8.4.1 The Potentials

For a dc-beam with a homogeneous charge distribution along the longitudinal z-coordinate and the transverse r-coordinate, the Poisson equation reduces to

$$\frac{1}{r}\frac{d}{dr}\left[r\frac{d}{dr}V_{\mathrm{ih}}(r)\right] = -\frac{\rho(r)}{\epsilon_0}\ . \tag{8.14}$$

For a homogeneous charge distribution, the well-known relation $i \cdot z = q \cdot v$ leads immediately to

$$\rho(r) = \text{const.} = \rho_0 = \frac{q}{z\,\pi R^2} = \frac{i}{\beta c\,\pi R^2}\ \text{(nonrelativistic)}\ . \tag{8.15}$$

For the potential inside a beam, a solution of the differential equation (8.14) is given by

$$V_{\mathrm{h}}(r)_{r\le R} = -\frac{\rho_0}{4\epsilon_0}r^2\ . \tag{8.16}$$

Outside the beam, we have the well-known potential of a line charge given by

$$V(r)_{r\ge R} = \frac{\rho_0 R^2}{2\epsilon_0}\ \ln\left(\frac{R_{\mathrm{p}}}{r}\right)\ , \tag{8.17}$$

with $V_{\mathrm{h}}(R_{\mathrm{p}}) = 0$ and R_{p} as the pipe radius. The adaptation of the potential given by (8.16) at $r = R$ to the solution given by (8.17) leads to

$$V_{\mathrm{h}}(r)_{r\le R} = \frac{\rho_0\, R^2}{4\epsilon_0}\left[1 + 2\ln\left(\frac{R_{\mathrm{p}}}{R}\right) - \frac{r^2}{R^2}\right]\ . \tag{8.18}$$

For a parabolic density distribution in the transverse coordinate r,

$$\rho_{\mathrm{p}}(r) = 2\,\rho_0 \left(1 - \frac{r^2}{R^2}\right) ,$$

and as a solution for the potential inside a beam,

$$V_{\mathrm{p}}(r)_{r \le R} = \frac{\rho_0}{2\,\epsilon_0} r^2 \left(\frac{r^2}{4R^2} - 1\right) . \tag{8.19}$$

In this case, the adaptation of the potential given by (8.19) at $r = R$ to the solution given by (8.17) leads to

$$V_{\mathrm{p}}(r)_{r \le R} = \frac{\rho_0 R^2}{2\epsilon_0} \left[\frac{3}{4} + \ln\left(\frac{R_{\mathrm{p}}}{R}\right) - \frac{r^2}{R^2} + \frac{r^4}{4R^4}\right] . \tag{8.20}$$

8.4.2 The Radial Fields

Determination of the radial electric field strength is straightforward and leads to

$$E_{\mathrm{h}}(r)_{r \le R} = \frac{\rho_0}{2\epsilon_0} r \tag{8.21}$$

for the homogeneous case inside a beam and to

$$E_{\mathrm{p}}(r)_{r \le R} = \frac{\rho_0}{\epsilon_0} r \left(1 - \frac{r^2}{2R^2}\right) \tag{8.22}$$

for the parabolic distribution inside a beam. Of course, the field outside a beam is the same in both cases:

$$E(r)_{r \ge R} = \frac{\rho_0}{2\epsilon_0} \frac{R^2}{r} . \tag{8.23}$$

Remark. In contrast to the potentials of bunches with spherical and elliptical shapes, the influence of the beam pipe boundary has been considered in (8.18) and (8.19) by setting the potentials at the beam pipe radius R_{p} to zero. But, as follows immediately from (8.21–8.23), this has no influence on the electric field strengths. The radial electric field outside a beam may also be derived from the well-known relation

$$q = \int \rho dV = \varepsilon_0 \int \mathrm{div}\, E\, dV = \varepsilon_0 \oint E_{\mathrm{r}}\, dA \quad \rightarrow \tag{8.24}$$

$$q = 2\,\pi r\, z\, \varepsilon_0 E_{\mathrm{r}} \quad \rightarrow \tag{8.25}$$

$$E(r)_{r \ge R} = \frac{q}{z} \frac{1}{2\pi\varepsilon_0 r} = \frac{\rho_0}{2\varepsilon_0} \frac{R^2}{r} . \tag{8.26}$$

To consider the relativistic effect, (8.15) has to be replaced by $\rho_0 = i/\gamma\beta c\,\pi R^2$.

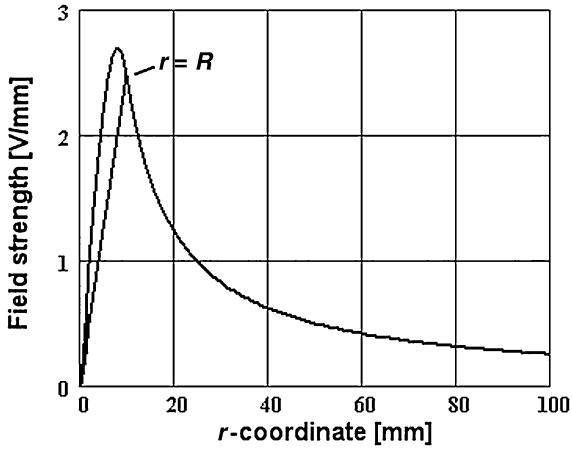

Fig. 8.6. Radial electrical field strength of a dc-beam with homogeneous and parabolic intensity distribution over the radial coordinate. Parameters: $R = 10\,\mathrm{mm}$, $i = 23\,\mathrm{mA}$

8.4.3 Comparison with Bunched Beams

Comparison with a Spherical Bunch

To compare the fields of a dc-beam with those of a bunched beam, one has to specify the electric dc-current i and a ß-value. For a given accelerating frequency f, the dc-beam current is

$$i = N\, f\, \zeta\, e\ .$$

For $N = 10^9$, $\zeta = 4$, and $f = 36\,\mathrm{MHz}$, $i = 23\,\mathrm{mA}$. Concerning the β value, it is reasonable to determine β from the relation $\beta c \Delta t = R$. Figure 8.6 shows the electric field strength for a dc-beam with $R = 10\,\mathrm{mm}$, $\beta = 0.056$ ($W = 1.44\,\mathrm{MeV/u}$), and $\Delta t = 0.6\,\mathrm{ns}$ (FWHM). To compare the field strength of the dc-beam (Fig. 8.6), with the field strength of the spherical bunches (Fig. 8.2), one has to consider the "geometric duty factor" of a bunched beam, which is given by

$$D = \frac{2R}{\beta\lambda} = \frac{2Rf}{\beta c} = 0.043\ . \tag{8.27}$$

Multiplying the values of Fig. 8.6 by $1/D = 23.3$, one finds good agreement between the dc-beam and the spherically shaped bunch.

Comparison with Elliptically Shaped Bunches

Due to the dependency of the r-component on the z-coordinate in an elliptically shaped bunch, a comparison with a dc-beam is more complex. Because

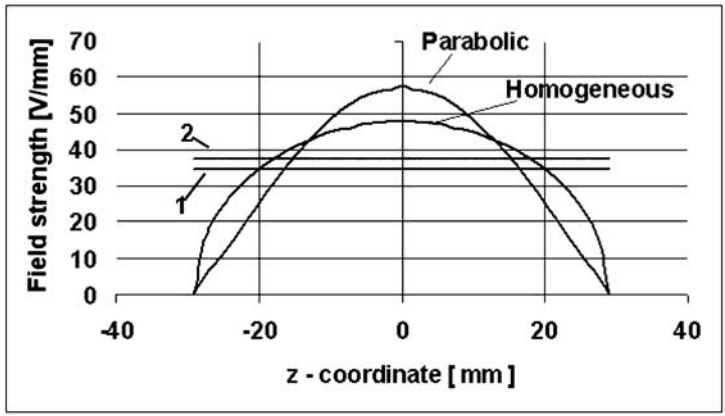

Fig. 8.7. Comparison of the radial components along the surface of elliptically shaped bunches with the maximum field strength of a dc-beam. The line marked 1 corresponds to the maximum field strength of the dc-beam at the surface multiplied by $1/D$, the line marked 2 corresponds to the maximum field strength ($\times 1/D$) for the dc-beam with a parabolic radial intensity distribution. See text for details

the charge density of a dc-beam $\rho(r)$ is proportional to $1/\beta$ (8.15), $\beta = 0.055$. On the other hand, the long axis a of the ellipsoid is determined by $a = \beta\, c\, \Delta t$. In the example, $a = 29.2\,\mathrm{mm}$, which leads to $\Delta t = 1.74\,\mathrm{ns}$. Because the small axis b, is 5.85 mm in the example, for the comparison, the radius of the dc-beam has to be changed to $R = 5.85\,\mathrm{mm}$. Replacing $2R$ by $2a$ in (8.27) results in $D = 0.125$. Figure 8.7 shows the radial field component E_r for elliptical bunches at the surface along the z-axis ($\xi = \xi_0$, $-1 \le \eta \le 1$). For comparison, the line marked 1 gives the radial field strength at the surface of the dc-beam ($R = 5.85\,\mathrm{mm}$) multiplied by $1/D = 8$, the line marked 2 corresponds to the maximum field strength at $r = \sqrt{2/3}R$ for the dc-beam with a parabolic radial density distribution, also multiplied by $1/D$.

Conclusion

Taking the duty factor of bunched beams into account, the mean electric field strength within bunches of spherical and elliptical shape can be roughly estimated from the fields of a dc-beam.

8.5 Estimations of Space Charge Effects

Space charge effects and space charge neutralization are considered in numerous publications. The fundamentals were already discussed in some older basic works, e.g., [387–394], considering theoretical and practical aspects.

8.5.1 Electrons or Ions in the Field of Moving Bunches

With respect to beam diagnostics, the movement of electrons in the field of bunches is of interest for the following reasons:

- To estimate partial neutralization within a bunch by capture of electrons freed by residual gas ionization which, for example, can reduce the signal of capacitive pickups, beam transformers, and Faraday cups or even change the required settings for focusing devices.
- To calculate the distortion of beam profile measurements based on residual gas ionization caused by deflection of the liberated electrons and ions in the electric field of moving bunches (see Chap. 4 for a detailed discussion of this matter).

Capture of Electrons

To discuss the problem and derive the dependencies, the movement of electrons in the potential of a spherical bunch will be considered. Furthermore, the analytical consideration will be restricted to movement of the electrons in the z-direction, which is the direction in which the bunches are moving. Some examples of the three-dimensional case are given from numerical calculations.

The differential equation for the movement of an electron inside a homogeneously charged sphere can be derived directly from (8.8):

$$m_\mathrm{e}\frac{d^2}{dt^2} = m_\mathrm{e}\,\ddot{z} = -E(r \to z)_{z \le R} = \frac{-N\zeta e^2}{4\pi\varepsilon_0 R^3}(z - \beta ct) \tag{8.28}$$

with m_e as the mass of the electron. Introducing $\omega^2 = N\zeta e^2/4\pi\varepsilon_0 m_\mathrm{e} R^3$, (8.28) becomes

$$\ddot{z} = -\omega^2(z - \beta ct), \tag{8.29}$$

which has the solution,

$$z(t) = \frac{v_\mathrm{z}(0) - \beta c}{\omega}\sin(\omega t) + z(0)\cos(\omega t) + \beta ct \tag{8.30}$$

and

$$\dot{z}(t) = (v_\mathrm{z}(0) - \beta c)\cos(\omega t) + z(0)\sin(\omega t) + \beta c\,. \tag{8.31}$$

As an example, we take parameters already used: $N = 1 \times 10^9$, $\zeta = 4$, $R = 10\,\mathrm{mm}$, and $\beta = 0.055$. Figure 8.8 shows the movement of an electron created at the center of the bunch ($z(0) = 0$) with $v_\mathrm{z}(0) = \dot{z}(0) = 0$.

From the oscillating motion with a maximum amplitude of about 15 mm (see Fig. 8.8), it seems that the electron would be captured and moving with the bunch. But the decreasing electric field strength for $z > R$ (see Fig. 8.2) is not considered in (8.29). Therefore, the electron is lost because the space charge force is too weak to catch the electron within the bunch.

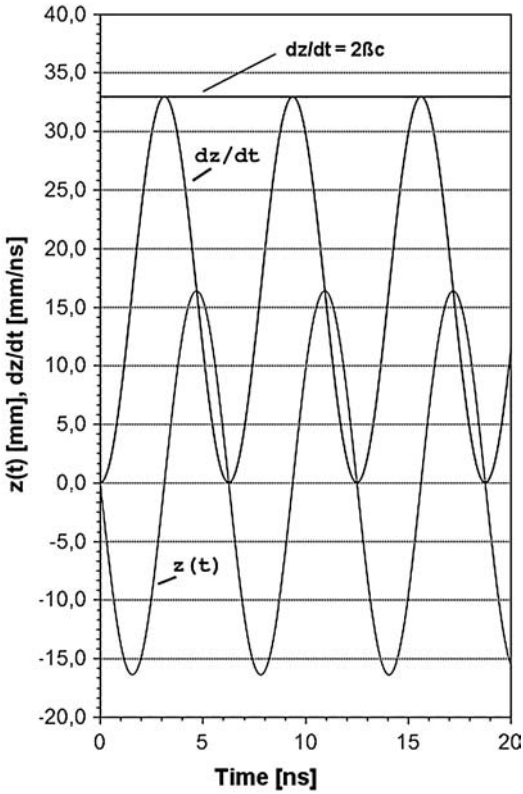

Fig. 8.8. Calculated z-coordinate and velocity dz/dt from the solution of the differential equation (8.29). The electron starts at the coordinate $z(0) = 0$ and velocity $\dot{z}(0) = 0$ at the center of the bunch

To derive a condition for the capture of the electron within the bunch ($z_{\max} = R$), we consider (8.29) for $\beta = 0$ in the phase plane z, $\dot{z}$:

$$\begin{aligned}
\ddot{z} &= -\omega^2 z \\
\dot{z} &= y \\
\dot{y} &= -\omega^2 z \\
\frac{\dot{y}}{\dot{z}} &= \frac{dy}{dz} = -\omega^2 \frac{z}{y} \\
ydy &= -\omega^2 z dz \\
y^2 &= -\omega^2 z^2 + C_1 \\
y = \dot{z} &= \pm\sqrt{C_1 - \omega^2 z^2}\,. \qquad (8.32)
\end{aligned}$$

The dependency $\dot{z} = y = f(z)$ (8.32) describes oscillation in the phase plane. Figure 8.9 shows the corresponding phase plane plot with $C1$ as a

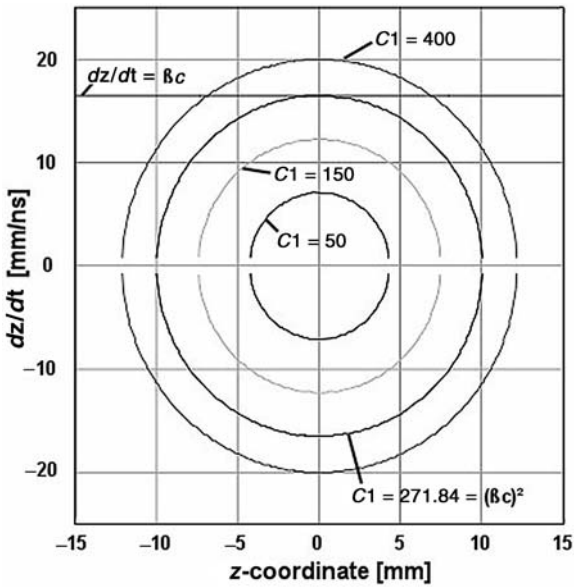

Fig. 8.9. Phase plane plot according to (8.32)

parameter. Obviously, the electron remains inside the bunch if $z_{\max} \leq R = 10\,\mathrm{mm}$ and $\dot{z}_{\max} \leq \beta c = 16.5\,\mathrm{mm/ns}$, which leads immediately to $C1 \leq (\beta c)^2$. Therefore, the condition for stable oscillation within the bunch can be derived from the relation:

$$(\beta c)^2 = \omega^2 R^2, \tag{8.33}$$

which leads immediately to the required number of charges:

$$N^h_{\min} = \frac{4\pi\varepsilon_0\, R\,(\beta c)^2\, m_\mathrm{e}}{\zeta e}\ . \tag{8.34}$$

This estimation is confirmed by the solution of (8.29). Figure 8.10 shows the result of increasing the number of particles in the bunch from $N = 10^9$ (see Fig. 8.8) to $N^h_{\min} = 2.7 \times 10^9$.

It is of interest to see the effect of a parabolic density distribution inside the spherical bunch on the required number of charges. For the sphere with a parabolic density distribution according to (8.10), (8.29) changes to

$$\ddot{z} = -\omega^2 \left(\frac{5}{2} z - \frac{3}{2} \frac{z^3}{R^2} \right) \tag{8.35}$$

which is known as the nonlinear differential equation for an oscillator or pendulum.

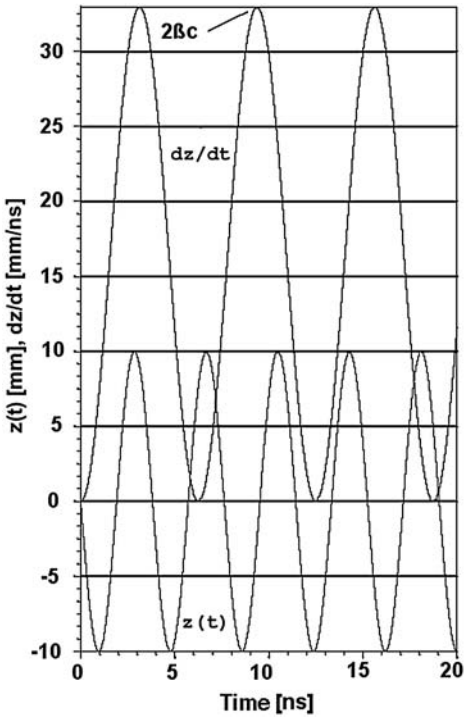

Fig. 8.10. Same as Fig. 8.8, but increasing the number of charges within the bunch; see text

Analogously to (8.32), for the movement in the phase plane,

$$y = \dot{z} = \pm\sqrt{C_2 - \omega_0^2\left(z^2 - b\frac{z^4}{2}\right)}, \tag{8.36}$$

with $\omega_0 = \sqrt{5/2}\omega$ and $b = 3\,/\,5R^2$. Figure 8.11 shows the corresponding phase plot reducing the number of particles in a first guess to $N = 0.6\,N^h_{\min} \simeq 1.6 \times 10^9$.

Obviously, to estimate $N^p_{\min}$ for the parabolically charged sphere, one has to replace (8.33) by

$$(\beta c)^2 = \omega_0^2\left(z^2_{\max} - b\frac{z^4_{\max}}{2}\right). \tag{8.37}$$

There are two changes in comparison to (8.33):

- The oscillation frequency becomes higher because $\omega \to \omega_0 = \sqrt{5/2}\omega$.
- $R \to z_{\max} < R$.

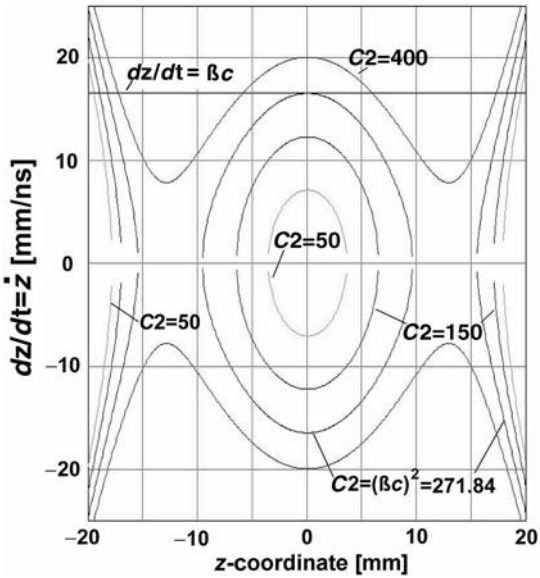

Fig. 8.11. Phase plane plot according to (8.36), see text for details

Comparing the electric field strengths in Fig. 8.2, which represent the attractive forces, it seems reasonable to assume a value between R and $\sqrt{5}R/3$ for $z_{\max}$, where the maximum of the field strengths occurs. Quadratic averaging according to

$$z_{\max}^2 = \frac{\int_{\sqrt{5}R/3}^{R} z^2 (z^2 - b\frac{z^4}{2})}{\int_{\sqrt{5}R/3}^{R} (z^2 - b\frac{z^4}{2})} \tag{8.38}$$

leads to $z_{\max} = \sqrt{41/54}R$, in good agreement with $z_{\max} \sim \sqrt{4/5}R$ from a numerical solution of (8.35). Inserting $b = 3/5\,R^2$, $\omega_0 = \sqrt{5/2}\omega$, and $z_{\max} \simeq \sqrt{4/5}R$ into (8.36),

$$N_{\min}^{p} \sim 0.68\, N_{\min}^{h}\ . \tag{8.39}$$

Of course, there is also a solution of (8.35) in the z-t- plane. Usually this kind of nonlinear differential equation is solved by successive approximation with a Fourier series. Figure 8.12 shows the time dependence of $z(t)$ and $\dot{z}(t)$ from an approximation up to the third harmonic, taking $N = 1.84 \times 10^9 = 0.68\, N_{\min}^{h}$. The result confirms the estimation given in (8.39).

Up to now, the simplest case possible has been considered by assuming

- movement of the electron in only one dimension;
- initial coordinates of the electron $z(0) = 0$, respectively, $z(0) = R$, $\dot{z}(0) = 0$;
- no attracting field outside of the bunch ($|z| > R$); and
- no effect of other bunches within a chain of moving bunches.

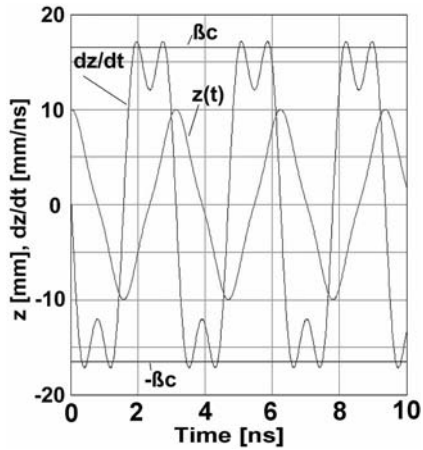

Fig. 8.12. Approximate solution of the differential equation (8.35) up to the third order of a Fourier series. The solution holds for $z(0) = R = 10\,\text{mm}$, $\dot{z}(0) = 0$, and $N = 1.8 \times 10^9$

Because the field outside the bunch always results in an attractive force, electrons can move in closed orbits outside the bunch in the phase plane. This can be shown by taking into account the external field according to (8.9), which leads to

$$\ddot{z} = -\frac{R^3\omega^2}{z^2}\,. \tag{8.40}$$

$$\dot{z} = y \tag{8.41}$$

$$\frac{\dot{y}}{\dot{z}} = \frac{dy}{dz} = -\frac{R^3\omega^2}{z^2 y} \tag{8.42}$$

$$y\,dy = -R^3\omega^2\frac{dz}{z^2} \tag{8.43}$$

$$\frac{1}{2}y^2 = R^3\omega^2\frac{1}{z} + \frac{1}{2}C3 \tag{8.44}$$

$$y = \pm\sqrt{\frac{2R^3\omega^2}{z} + C3}\,. \tag{8.45}$$

The solution for $y = \dot{z}$ holds outside the bunch and has to be matched at $z = R$ to solutions of (8.32) for a homogeneously charged spherical bunch and to (8.36) for a parabolically charged one. The solutions are straightforward in both cases and the results are shown in Fig. 8.13.

In both diagrams of Fig. 8.13, the inner curves correspond to the movement within the bunch, the outer ones correspond to electrons moving also in the external field. Because these electrons move at high speed through the bunch, they will not contribute to neutralization.

Numerous numerical calculations [395,396] have been performed to study the conditions that hold electrons with various starting coordinates inside a

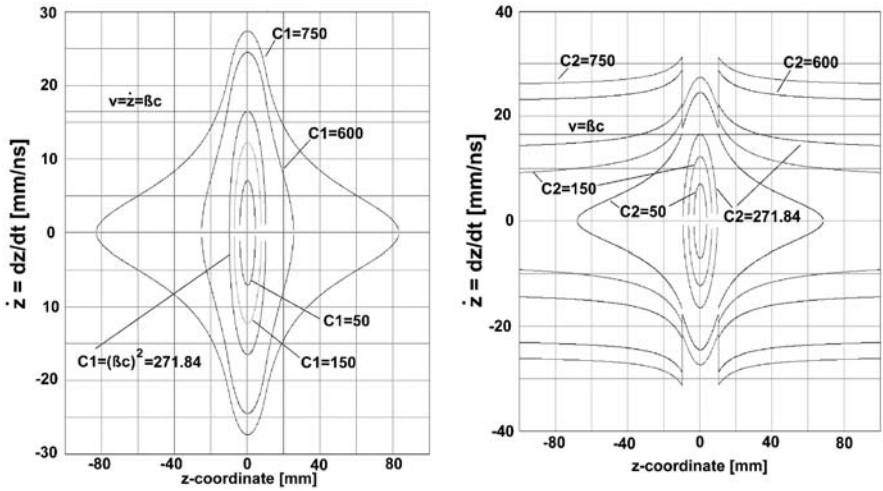

Fig. 8.13. Movement of an electron in the phase plane, considering also the external field. Left: homogeneously charged spherical bunch with 2.7×10^9 U^{4+}-ions. Right: spherical bunch with a parabolic charge density distribution and 1.8×10^9 U^{4+} ions. See text for details

bunch. Special attention was given to the initial velocity of electrons. Electrons are freed from the residual gas by interaction with ions in bunches. Due to the kinematics, the distribution of the velocity is peaked forward and the maximum velocity in the z-direction is just two times the velocity of the bunch. Referring to measured data [397] and calculations for the design of a bunch shape monitor based on detection of electrons freed by residual gas ionization (see Chap. 7), the calculated distribution of the velocities for the z-direction is shown in Fig. 8.14. The maximum is located at about 3% of βc which in the example corresponds to about 0.5 mm/ns.

Figure 8.15 is a phase plane plot obtained from the numerical integration of (8.29) for $|z| < R$ and (8.40) for $|z| > R$ assuming starting parameters $z(0) = 0$, $v_z(0) = +5\,\mathrm{mm/ns}$, $v_z(0) = 2\,\beta c$ (33 mm/ns), and $v_z(0) = -5\,\mathrm{mm/ns}$. Consistent with analytical considerations, the electron with $v_z(0) = 2\,\beta c$ just oscillates inside the bunch and of course an electron starting at $v_z(0) = \beta c$ gives just one point at $z = 0$, $\dot{z} = 0$ in the phase plane. Therefore, with the parameters of the example, all electrons with $0 < v_z(0) < 2\beta c$ remain in the bunch, whereas electrons with $v_z(0) < 0$ are lost.

The calculations have shown that the estimations by (8.34), (8.37), and (8.39) give the right order of magnitude to determine the number N of charges in a bunch of spherical shape, where neutralization by capture of electrons in the space charge field just starts. For a bunch with the parameters of the example, this leads to 10^9 up to about 10^{10} U^{4+}-ions. The differences between the homogeneous density distribution and the parabolic one are marginal and may be neglected in rough estimations. Estimating N for elliptically shaped

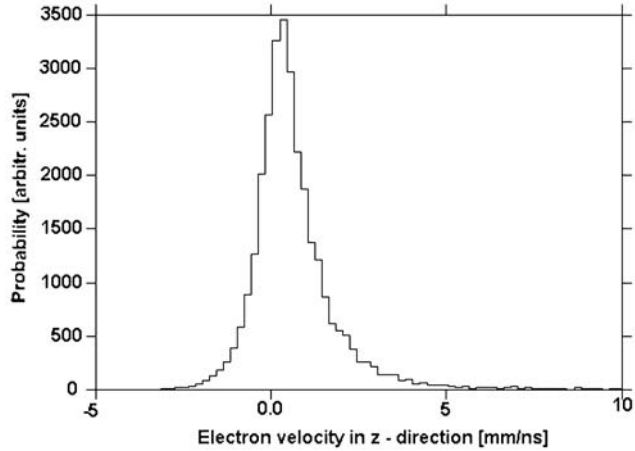

Fig. 8.14. Calculated velocity distribution of electrons freed by residual gas ionization. The data hold for U^{4+}-ions with $\beta = 0.055$ onto N_2 molecules

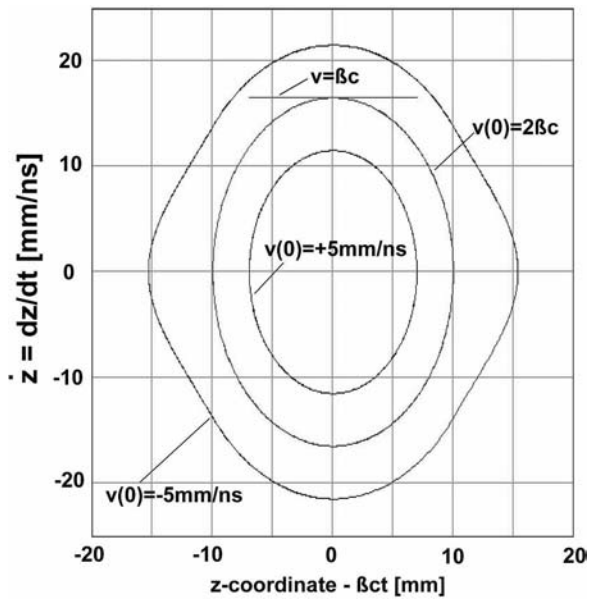

Fig. 8.15. Phase plane plot from the numerical solution of (8.29) and (8.40) with $N = 2.7 \times 10^9$ U^{4+}-ions in the bunch. Inner curve: $v_z(0) = 5\,\mathrm{mm/ns}$; middle: $v_z(0) = 2\beta c$; outer curve: $v_z(0) = -5\,\mathrm{mm/ns}$

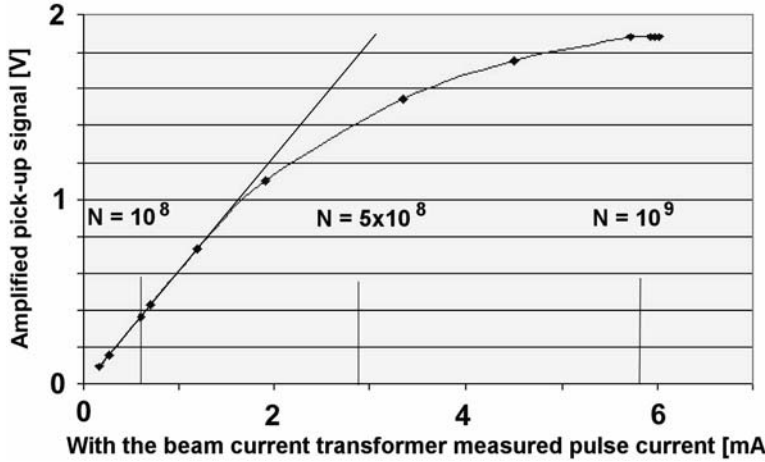

Fig. 8.16. Effect of bunch neutralization observed with a capacitive pickup. See text for details

bunches is more complicated. Reasonable values for N should be estimated very roughly by calculation of N for a spherical bunch and scaling with the ratio of the bunch volume.

Example of a Measurement

A capacitive pickup is installed directly behind the gas stripper at the UNILAC. In an accelerator experiment, an Ar^{1+}-beam with a maximum intensity of about 6 mA (macropulse current) was delivered to the stripper. The stripper works at nearly atmospheric pressure and therefore there should be enough electrons, which can be captured by the bunches crossing the stripper. Because the charge of the Ar-ions goes up from 1^+ to a spectrum with a maximum of intensity at 10^+ by passing the stripper and charge separation has not yet taken place at the position of the capacitive pickup, the effect of neutralization on the signal amplitude of the capacitive pickup should be observable. Figure 8.16 shows the pickup signal dependent on beam intensity, measured with a beam transformer in front of the stripper. Because charge state separation has not yet taken place, the number of particles within the bunch can be calculated from the current measured by the beam current transformer in front of the stripper. Taking the rf period of $T = 27.7\,\mathrm{ns}$ and $\zeta = 1$, the number of Ar-particles in one bunch in front of the stripper can be calculated from

$$N_{\mathrm{Ar}} = \frac{i_{\mathrm{macro}}\, T}{\zeta\, e}\ ,$$

which leads to 1.73×10^8 U^{1+}-ions per mA of macropulse current. On the other hand, from the shape of the stripper spectrum, it is reasonable to assume

$\zeta = 10$ as the mean charge state behind the stripper. With $R = 10\,\mathrm{mm}$ for a spherically shaped bunch, which seems to be very reasonable at the stripper position, (8.34) with $\beta = 0.055$ leads to $N^h_{\mathrm{min}} = 1.08 \times 10^9$ for the homogeneously charged bunch and $N^p_{\mathrm{min}} = 6.45 \times 10^8$ for the parabolic charge density distribution. Considering the complexity of the process, the relations derived for the determination of N^h_{min} (8.34) and N^p_{min} (8.39) seem to be usable for rough estimations.

The Ions in Their Field

It is also of interest to estimate the effect of the space charge on ions in the bunch itself. Of course, exact calculations can be done by considering the action of all particles on each other, as performed in the well-known numerical codes of particle dynamics. Using analytical solutions, the momentum spread of particles due to the action of the space charge force as well as the arising transverse divergence can be estimated.

Momentum Spread

The change of momentum $\Delta p/p$ by the space charge force is given (non-relativistic) by

$$\frac{\Delta p}{p} = \frac{\zeta e \int_0^t \overrightarrow{E}(\overrightarrow{r}, t)\, dt}{A\, m_{\mathrm{u}}\, \beta c} \,. \tag{8.46}$$

For the estimation, ions on the beam axis ($x = 0$, $y = 0$, $z \neq 0$) moving at the same speed βc as the bunch at $t = 0$ are considered. Of course, the estimation using the analytical formulas for the description of the space charge effects holds only as long as the change of position with respect to the start position is small compared to the size of the bunch. This means that there will be no remarkable change in the non-self-consistent charge density distribution [398] within the bunch. Figure 8.17 shows the results for ß-values of 1.6% and 5.5%. In both cases, a parabolic charge density distribution in spherically shaped bunches was assumed. Of course, the calculations hold only if no other forces act on the bunches. The diagrams at the bottom of Fig. 8.17, which correspond to $z(t) = \beta ct$, give an estimate of the drift space that may be tolerated with respect to the increase of the spread by the space charge. The diagrams at the center of Fig. 8.17 show the displacement Δz of particles due to space charge forces. This becomes clear keeping in mind that (non-relativistic) $\Delta v = v\, \Delta p/p$ and $\Delta z = \Delta v\, t$.

Divergence

Considering bunches of spherical shape, estimation of the arising divergence by the space charge can be taken over from the estimation of $\Delta p/p$ in (8.46). In the nonrelativistic case,

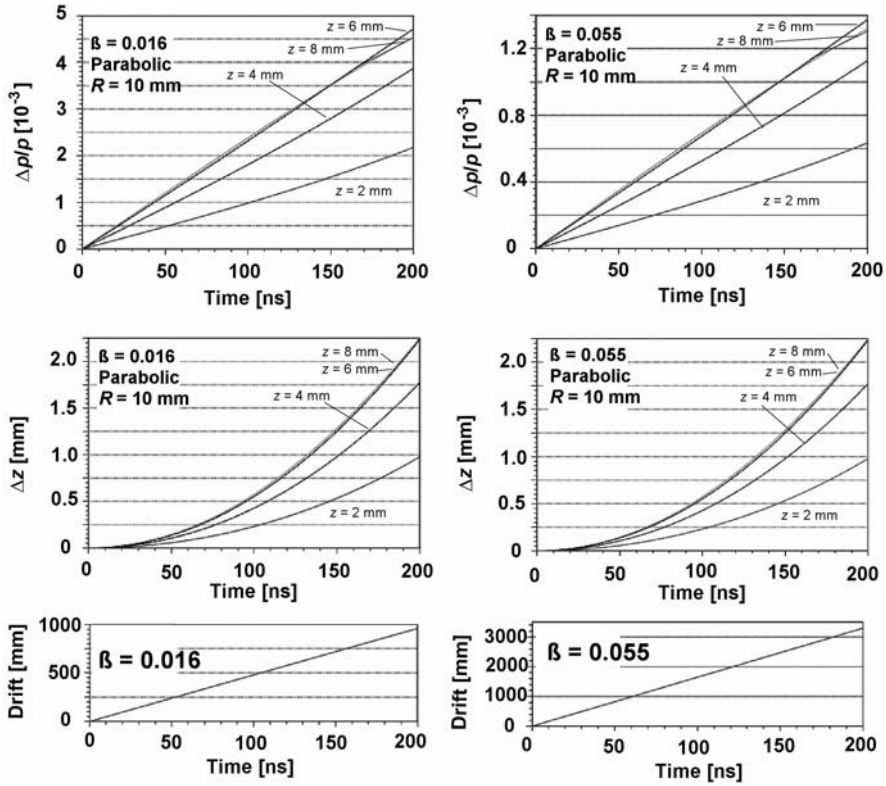

Fig. 8.17. Top: calculated momentum spread $\Delta p/p$ due to the space charge forces within a sperically shaped bunch with a parabolic density distribution. Center: calculated displacement of the particle due to the change of momentum. Bottom: Drift of the bunch dependent on time. For all diagrams, left: $\beta = 1.6\%$ right: $\beta = 5.5\%$

$$\frac{\Delta p_\perp}{p} = \frac{\Delta \beta_\perp}{\beta} = \frac{\dot{x}}{\dot{z}} = \frac{dx/dt}{dz/dt} = x', \text{ resp, } (y') \,, \tag{8.47}$$

where $\perp$ holds for the transverse directions x, y. Therefore, the diagrams of Fig. 8.17 hold also for the estimation of the arising divergence replacing $[10^{-3}]$ by [mrad]. Similar estimations can be performed for bunches of elliptical shape. Obviously, in this case, the Δp values in the longitudinal direction will differ from the values in the transverse directions, depending on the shape of the ellipsoid. For an ellipsoid with $a > b$, we will find $\Delta p_\perp > \Delta p_z$, whereas $\Delta p_z > \Delta p_\perp$ holds for an ellipsoid with $b > a$.

8.6 Special Effects of Moving Charged Particles

A charged particle performing a rectilinear motion at constant velocity does not emit electromagnetic radiation. But this changes if the particle is acceler-

ated or moves through a medium with changing electromagnetic properties. Electromagnetic radiation is emitted because the adaptation of the Coulomb field, moving together with the charge, to the changing boundary conditions is only possible in this way.

8.6.1 Synchrotron Radiation

In the emission of radiation by acceleration of charged particles, there is a big difference between linear accelerators and circular machines. For a one-dimensional accelerated linear motion of an electron, the radiated power is given by [39]

$$P_{\mathrm{s}} = \frac{e^2 c}{6\pi\varepsilon_0 (m_0 c^2)^2} \left(\frac{dp}{dt}\right)^2 . \tag{8.48}$$

Taking into account $\mathrm{d}W = v\,dp$ [358] and $\mathrm{d}W/dx = v dp/dx = dp/dt$, one obtains

$$P_{\mathrm{s}} = \frac{e^2 c}{6\pi\varepsilon_0 (m_0 c^2)^2} \left(\frac{\mathrm{d}W}{dx}\right)^2 . \tag{8.49}$$

For typical values of $\mathrm{d}W/dx$ of 15 MeV/m, one finds that radiated power is negligible. This becomes completely different for circular machines. Remembering that $dp/dt = p\,\omega = p\,v/R$, the equivalent to (8.49) is

$$P_{\mathrm{s}} = \frac{e^2 c}{6\pi\varepsilon_0 (m_0 c^2)^4} \frac{W^4}{R^2} . \tag{8.50}$$

Comparing electrons with protons leads to

$$\frac{P_{\mathrm{s}}^e}{P_{\mathrm{s}}^p} = \left[\frac{931\,\mathrm{MeV}}{511\,\mathrm{keV}}\right]^4 \approx 1.1 \times 10^{13} . \tag{8.51}$$

For applications in beam diagnostics, the angular distribution is important:

- For nonrelativistic particles, the radiation is $\perp$ to dp/dt.
- For relativistic particles, the radiation becomes forward peaked.

Measuring the angular distribution, intensity, and time structure of the emitted synchrotron radiation allows the determination of many parameters in beam diagnostics. A drawback is that the application – with the exception of some very special cases – is limited to circular electron machines.

Example of an Application in Beam Diagnostics

A very sophisticated setup to monitor the particle density distribution in three dimensions in space has been developed for the large electron-positron storage ring (LEP) [399].

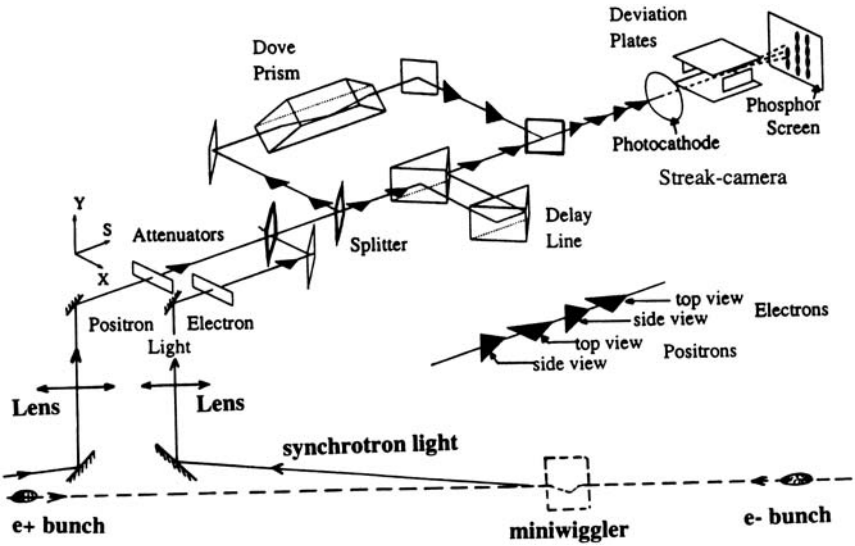

Fig. 8.18. Optical setup of a synchrotron light monitoring system. See Figure 8.19 for details of the streak camera. (From Rossa, E., *AIP* Conference Proceedings 333 (1995), p. 148. With Permission)

Synchrotron radiation is produced by small dipole magnets in the LEP, so-called miniwiggler. The light generated by the electrons and positrons is collected by two beryllium mirrors inside the beam pipe and guided to a system of optical components consisting of lenses, attenuators, a splitter, and a delay line. A Dove prism decomposes the light into two polarization planes to allow top and side views of the synchrotron light bunches. Figure 8.18 illustrates the synoptic of the setup. A special double sweep streak camera [399] is used as a detector, allowing sweep in the horizontal and vertical directions. Figure 8.19 illustrates the operating principle of this device. The measuring system has been used in many accelerator experiments to improve the performance of the machine. Figure 8.20 demonstrates the capability of the system showing longitudinal oscillations of the bunches in the LEP. Because the measuring system is a non-intercepting device, it is also very suitable for routine operation of a circular machine. Synchrotron light interferometry is used at the Jefferson Lab to measure and continuously monitor the energy spread with high resolution [400].

8.6.2 Cherenkov Radiation

A charged relativistic particle moving at constant velocity βc through a medium with a refractive index, where the velocity of light with c/n is smaller than the velocity of the particle, emits Cherenkov radiation (see, e.g., [39]). For the number N of quanta radiated per unit length with frequencies between

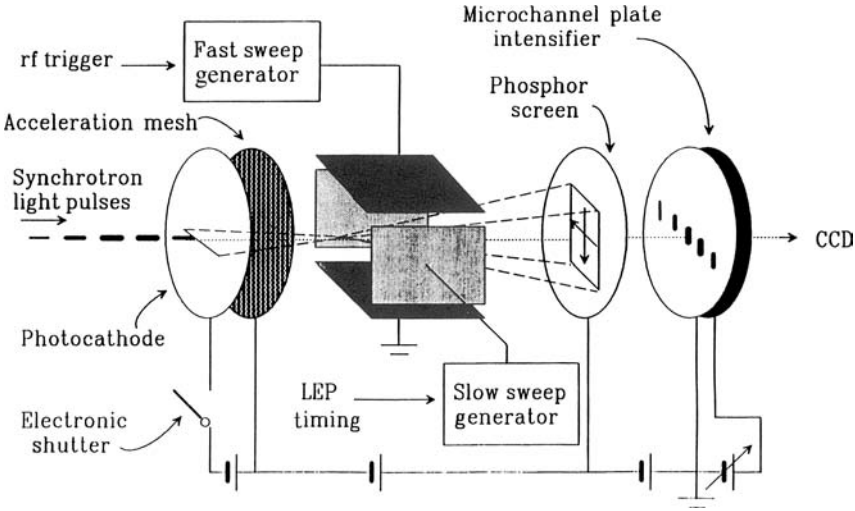

Fig. 8.19. Working principle of the double sweep streak camera. (From Rossa, E., *AIP* Conference Proceedings 333 (1995), p. 148. With Permission)

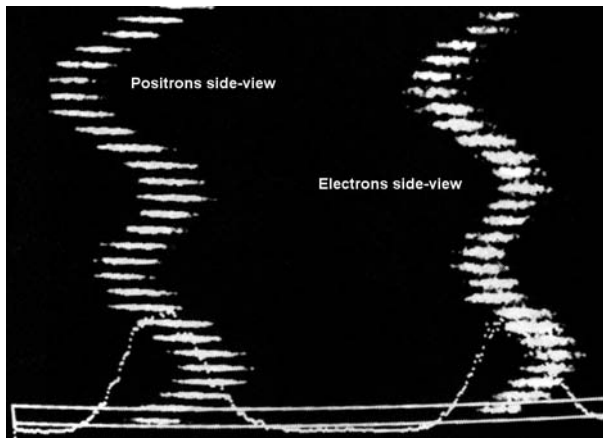

Fig. 8.20. Longitudinal oscillations of the electron and positron bunches when the longitudinal feedback is switched off. (From Rossa, E., *AIP* Conference Proceedings 333 (1995), p. 148. With Permission)

f and $f + df$ [39, 45],

$$dN = \frac{\pi\zeta^2 e^2}{\varepsilon_0 hc}\left(1 - \frac{1}{n^2\beta^2}\right)\frac{df}{c} \; . \tag{8.52}$$

Because the relation $\cos\theta = 1/n\beta$ holds between the angle θ of the light rays and $n\beta$ and $1 - \cos^2\theta = \sin^2\theta$, (8.52) can be rewritten as

$$dN = \frac{\pi\zeta^2 e^2}{\varepsilon_0 hc} \sin^2\theta \frac{df}{c} \ . \tag{8.53}$$

The measure of the angle θ of emitted Cherenkov light can be used to determine the ß-value of the particles and their energy. The combination of a transparent Cherenkov radiator coupled via a light guide to a photo-cathode and a multiplier, known as a Cherenkov counter [360, 401], is often used for monitoring beam intensities.

8.6.3 Wake Fields

The transport of charged particle bunches through a vacuum system with changing aperture, respectively, geometry leads to the generation of wake fields, which is a consequence of the changing impedance. The effect is used in advanced accelerator technique to accelerate particles [402].

8.6.4 Optical Transition Radiation

Charged particles emit optical transmission radiation (OTR) while traveling from a medium with dielectric constant ε_1 into a medium with dielectric constant ε_2 [403]. The phenomenon is well established within electromagnetic theory and its application to beam diagnostics was first demonstrated in 1975 [404].

The general expression for the twofold energy distribution of the radiated energy $d^2W/\, d\omega\, d\Omega$ is rather complex (see, e.g., [405–407, 409], but simplifies when a particle moving in vacuum with $\varepsilon_1 = 1$ hits a target, respectively, this particle leaves from the target into the vacuum. Hence, crossing such a single boundary, the charged particle emits radiation into the backward and forward hemisphere of the target. For a target of metal with $\varepsilon_2 \to \infty$ [407],

$$\frac{d^2W}{d\omega\, d\Omega} = \frac{1}{4\pi\varepsilon_0} \frac{\zeta^2 e^2}{\pi^2 c} \frac{\beta^2 \sin^2\theta}{\left(\gamma^{-2} - \beta^2 \sin^2\theta\right)} = \frac{1}{4\pi\varepsilon_0} \frac{\zeta^2 e^2}{\pi^2 c} f(\theta)\,, \tag{8.54}$$

which holds at a sufficiently large distance between the observation point and the source of radiation. The angle θ is defined in the forward and backward hemisphere according to the scheme of Fig. 8.21. The maximum occurs at $\theta \simeq 1/\gamma$ and, therefore, the separation of the two lobes in each hemisphere is $\theta \simeq 2/\gamma$. The radiation is strictly proportional to the beam intensity and contains information about energy and divergence ($\to$ emittance). Because the radiation is generated at the boundary between two different media, the intensity of the emitted radiation is largely independent of the thickness and material of the foil.

Transition radiation opens a large field of applications, especially,

- Determination of transverse emittances by applying the gradient varying method (see Chap. 6) for beams with very small radial dimensions typical of high energy electron machines [408].

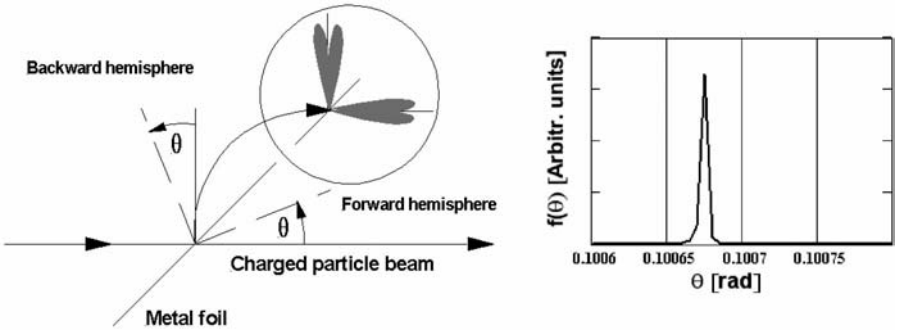

Fig. 8.21. Scheme to illustrate the emission of optical radiation transition with respect to the angle θ, according to (8.54). The diagram on the right-hand side shows the dependency $f(\theta)$ according to (8.54) for $\gamma = 10$ ($\rightarrow \beta = 0.995 \rightarrow 8.4\,\mathrm{GeV/u}$)

- Determination of the energy spread by measuring the size of bunches in a dispersive section of a beam line [408].
- Bunch length measurements in the picosecond-range. In this application, one takes advantage of the coherence of OTR in a region where the wavelength is comparable to the bunch length and applies an auto-correlation technique [407, 408].
- Measurement of bunch shapes and density distributions in the longitudinal phase space by interferometric spectroscopy (see, e.g., [407] and further references given there).

8.6.5 Diffraction Radiation

The radiation produced when a particle goes through a limiting aperture, such as a slit or hole, or passes near the border of a device, such as a screen or scraper, is known as diffraction radiation [405]. Optical diffraction radiation is a special case of transition radiation and wake field generation. The relationship to OTR becomes evident if one considers the twofold energy distribution of the radiated energy $d^2W/\,d\omega\,d\Omega$ for a charged particle passing through a hole with radius r_h [409]:

$$\frac{d^2W}{d\omega\,d\Omega} = \frac{1}{4\pi\varepsilon_0}\frac{\zeta^2 e^2}{\pi^2 c}\frac{\beta^2\sin^2\theta}{\left(\gamma^{-2}-\beta^2\sin^2\theta\right)}\left[1-J_0(k\,r_\mathrm{h})\sin\theta\right]^2 \tag{8.55}$$

$$= \left[\frac{d^2W}{d\omega\,d\Omega}\right]_\mathrm{OTR} \times \left[1-J_0(kr_\mathrm{h})\sin\theta\right]^2 . \tag{8.56}$$

Here k is the wave vector and J_0 is the Bessel function. Optical diffraction radiation may be used for beam diagnostic purposes [410,411] instead of OTR, if the energy loss in thin foils cannot be tolerated due to thermal heating.

8.A Solution of the Poisson Equation in the Elliptical Coordinate System

8.A.1 The Elliptical Coordinate System

The elliptical coordinate system uses two variables ξ, η, defined by

$$z(\xi,\eta) = c\,\xi\,\eta \tag{8.57}$$

$$\rho(\xi,\eta) = c\sqrt{(\xi^2-1)(1-\eta^2)}\,. \tag{8.58}$$

Here c is defined by the two focal points and is related to the two half-axes of the ellipsoid by

$$c = \sqrt{a^2-b^2}\,. \tag{8.59}$$

The elliptical coordinates are limited to $1 \le \xi \le \infty$ and $-1 \le \eta \le 1$. The surface of the ellipsoid is defined by $\xi = \xi_0 = a/c$ with the x, y, z-coordinates

$$\begin{aligned} x &= c\sqrt{(1-\eta^2)\,(\xi_0^2-1)}\sin t, \quad -\pi \le t \le \pi\,, \\ y &= c\sqrt{(1-\eta^2)\,(\xi_0^2-1)}\ \cos t\,, \\ z &= c\,\eta\,\xi_0\,. \end{aligned}$$

Figure 8.22 illustrates the dependencies on the parameters ξ and η of an ellipsoid with $b = 5\,\text{mm}$ and $a = 2b = 10\,\text{mm}$.

In the newly defined coordinate system, the Laplace-operator is transformed to [385, 386]:

$$\Delta\phi(\xi,\eta) = \frac{1}{c^2(\xi^2-\eta^2)}\left[\frac{\partial}{\partial\xi}(\xi^2-1)\frac{\partial\phi(\xi,\eta)}{\partial\xi} + \frac{\partial}{\partial\eta}(1-\eta^2)\frac{\partial\phi(\xi,\eta)}{\partial\eta}\right]. \tag{8.60}$$

Due to the rotational symmetry, there is no dependence of ϕ in (8.60). Equation (8.12) transforms to

$$\rho(\xi,\eta) = \frac{5}{2}\frac{a^2}{b^2}\rho_o^e\left(1-\frac{\xi^2}{\xi_0^2}\right)\left(1-\frac{\eta^2}{\xi_0^2}\right). \tag{8.61}$$

Introducing the definitions,

$$s_1 = \frac{5}{2}\,\rho_0^e\,\frac{a^2}{b^2} \tag{8.62}$$

$$s_2 = -\frac{5}{2}\,\rho_0^e\,\frac{c^2}{b^2} \tag{8.63}$$

$$s_3 = \frac{5}{2}\,\rho_0^e\,\frac{c^4}{a^2\,b^2}\,, \tag{8.64}$$

and rearranging (8.61) in terms of ξ and η results in

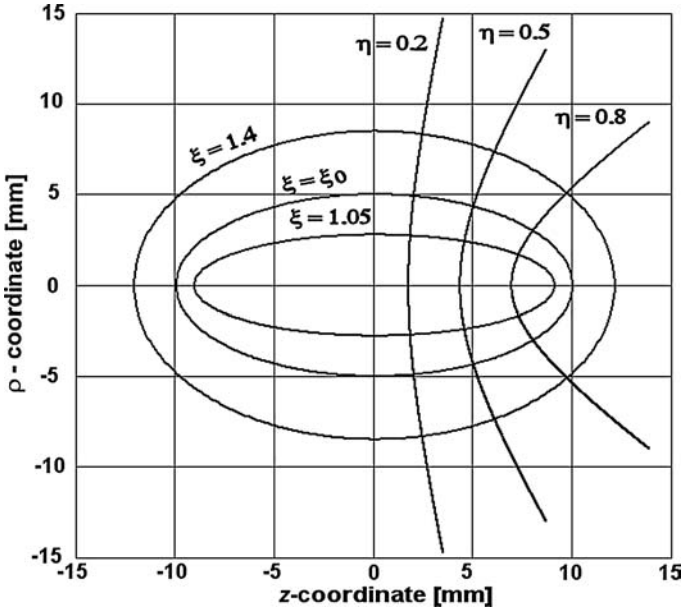

Fig. 8.22. Example to illustrate the dependencies on the elliptical parameters ξ and η. In case ξ =const, η varies from $-1 \cdots +1$, while ξ varies from $1 \ldots 2$ for the lines with $\eta =$ const

$$\rho(\xi, \eta) = s_1 + s_2\,(\xi^2 + \eta^2) + s_3\,\xi^2\,\eta^2\ . \tag{8.65}$$

Remark: In an attempt to generalize the charge distribution inside an elliptical bunch of the type of $\rho(\xi, \eta) = f\ [(1 - \frac{\xi^2}{\xi_0^2})(1 - \frac{\eta^2}{\xi_0^2})]$, with an arbitrary function f, it has been found that there are only two separable cases: homogeneous and parabolic spatial distributions. In all other cases an "Ansatz" in elliptical coordinates will fail [412].

8.A.2 The Potentials

The Homogeneously Charged Ellipsoid

The solution of the Poisson equation can be adapted from [385]. The potentials inside and outside the ellipsoid are expressed by a series of polynomials, functions, and their derivatives:

$$\phi(\xi, \eta)_{\xi \le \xi_0} = c_0 + c_2 P_2(\xi) P_2(\eta) - \frac{3}{2}\sigma(\xi^2 + \eta^2) \tag{8.66}$$

$$\phi(\xi, \eta)_{\xi \ge \xi_0} = a_0 Q_0(\xi) + a_2 Q_2(\xi) P_2(\eta)\ . \tag{8.67}$$

Equation (8.66) holds for the potential inside the ellipsoid where ξ can vary from 1 to ξ_0; the potential outside the ellipsoid is described by (8.67) with

$\xi \geq \xi_0$. The $P_{\rm n}(x)$ are the well-known Legendre polynomials with $Q_{\rm n}(x)$ derived from the recursion formula [386]

$$Q_{n+1}(x) = \left[\frac{(2n+1)\,x\,Q_{\rm n}(x) - n\,Q_{n-1}}{n+1}\right] \tag{8.68}$$

$$Q_0(x) = \frac{1}{2}\ln\left(\frac{x+1}{x-1}\right) \tag{8.69}$$

$$Q_1(x) = \frac{x}{2}\ln\left(\frac{x+1}{x-1}\right) - 1\,. \tag{8.70}$$

From the boundary condition for the potential and its derivative at $\xi = \xi_0$, the coefficients are determined [385]:

$$\sigma = \rho_{eh}\frac{c^2}{9\epsilon_0} \tag{8.71}$$

$$a_0 = -\sigma\frac{P_2'(\xi_0)}{Q_0'(\xi_0)} \tag{8.72}$$

$$a_2 = \sigma\frac{P_2'(\xi_0)}{Q_2'(\xi_0)\,P_2(\xi_0) - Q_2(\xi_0)\,P_2'(\xi_0)} \tag{8.73}$$

$$c_0 = \sigma\left[\frac{P_2(\xi_0)\,Q_0'(\xi_0) - P_2'(\xi_0)\,Q_0(\xi_0)}{Q_0'(\xi_0)} + 1\right] \tag{8.74}$$

$$c_2 = \sigma\left[\frac{Q_2'(\xi_0)}{Q_2'(\xi_0)\,P_2(\xi_0) - Q_2(\xi_0)\,P_2'(\xi_0)}\right]\,. \tag{8.75}$$

$P_{\rm n}'(\xi)$ and $Q_{\rm n}'(\xi)$ are the derivatives $(d/d\xi)$ of $P_{\rm n}(\xi)$ and $Q_{\rm n}(\xi)$.

The Ellipsoid with a Parabolic Charge Distribution

Referring to the definitions in (8.62), a solution of the Poisson equation (8.1) has been found for an "Ansatz" of the type of

$$\phi(\xi,\eta) = A\,(\xi^2+\eta^2) + B\,(\xi^4+\eta^4) + C\,\xi^4\,\eta^4 \tag{8.76}$$

with

$$A = -\frac{c^2}{2\epsilon_0}\left(\frac{s_1}{3} + \frac{s_2}{5}\right) \tag{8.77}$$

$$B = -\frac{s_2\,c^2}{20\,\epsilon_0} \tag{8.78}$$

$$C = -\frac{s_3\,c^2}{12\,\epsilon_0} \tag{8.79}$$

where s_1, s_2, s_3 are defined by (8.62–8.64). In the coordinate system used, the boundary conditions at $\xi = \xi_0$ are

$$\phi(\xi,\eta)_{\xi\le\xi_0} = \phi(\xi,\eta)_{\xi\ge\xi_0} \tag{8.80}$$

and

$$\left[\frac{\partial\phi(\xi,\eta)_{\xi\le\xi_0}}{\partial\xi}\right] = \left[\frac{\partial\phi(\xi,\eta)_{\xi\ge\xi_0}}{\partial\xi}\right] \tag{8.81}$$

which have to be fulfilled for all η.

The solution outside the parabolic ellipsoid compares to the solution (8.67) of the homogeneous ellipsoid adding a term proportional to $Q_4\,P_4$ to fulfill the boundary conditions at $\xi=\xi_0$. This leads to

$$\phi_{\xi\ge\xi_0}(\xi,\eta) = A_0\,Q_0(\xi) + A_2\,Q_2(\xi)\,P_2(\eta) + A_4\,Q_4(\xi)\,P_4(\eta)\,. \tag{8.82}$$

To determine the unknown coefficients A_0, A_2, and A_4, one can add to the "Ansatz" for $\phi(\xi,\eta)$ of (8.76) any solution of the homogeneous differential equation, which is regular inside the ellipsoid and, therefore, given by polynomials $P_{\rm n}(\xi)$ and $P_{\rm n}(\eta)$. This leads to

$$\phi_{\xi\le\xi_0}(\xi,\eta) = \phi(\xi,\eta)_{\xi\ge\xi_0} + C_0 + C_2\,P_2(\xi)\,P_2(\eta) + C_4\,P_4(\xi)\,P_4(\eta)\,. \tag{8.83}$$

Now the coefficients C_0, C_2, C_4 can be determined together with A_0, A_2, A_4 from the boundary conditions by comparing the coefficients of equal power in η. The evaluation of the resulting equations is rather laborious but straightforward. Beginning with the A_4, C_4 coefficients, one gets

$$A_4 = \frac{8}{35\,PQ_4}\,\left[P_4'(\xi_0)\,(B + C\;\xi_0^4) - 4\,C\,\xi_0^3\,P_4(\xi_0)\right] \tag{8.84}$$

$$C_4 = \frac{1}{P_4'(\xi_0)}\,\left[A_4\,Q_4'(\xi_0) - \frac{32}{35}\,C\,\xi_0^3\right] \tag{8.85}$$

with

$$PQ_4 = Q_4(\xi_0)P_4'(\xi_0) - Q_4'(\xi_0)\,P_4(\xi_0)\,. \tag{8.86}$$

Next A_2 and C_2 are determined as

$$A_2 = \frac{2}{3\,PQ_2}\,\left[P_2'(\xi_0)\,\left(A + \frac{15}{4}\,A_{C4}\right) - P2(\xi_0)\,\frac{15}{4}\,A_{C4S}\right] \tag{8.87}$$

$$C_2 = \frac{1}{P_2'(\xi_0)}\,\left[A_2\,Q_2'(\xi_0) - \frac{5}{2}\,A_{C4S}\right] \tag{8.88}$$

with

$$PQ_2 = Q_2(\xi_0)\,P_2'(\xi_0) - Q_2'(\xi_0)\,P_2(\xi_0) \tag{8.89}$$

$$A_{C4} = A_4\,Q_4(\xi_0) - C_2\,P_2(\xi_0) \tag{8.90}$$

$$A_{C4S} = A_4\,Q_4'(\xi_0) - C_4\,P_4'(\xi_0)\,. \tag{8.91}$$

Finally A_0, C_0 are obtained:

$$A_0 = \frac{1}{Q_0'(\xi_0)} \left(2A\,\xi_0 + 4B\,\xi_0^3 + \frac{1}{2}\,A_{C2S} - \frac{3}{8}\,A_{C4S} \right) \tag{8.92}$$

$$C_0 = A_0\,Q_0(\xi_0) - A\,\xi_0^2 - B\,\xi_0^4 - \frac{1}{2}\,A_{C2} + \frac{3}{8}\,A_{C4} \tag{8.93}$$

with

$$A_{C2} = A_2\,Q_2(\xi_0) - C_2\,P_2(\xi_0) \tag{8.94}$$

$$A_{C2S} = A_2\,Q_2'(\xi_0) - C_2\,P_2'(\xi_0)\,. \tag{8.95}$$

The coefficients A, B, and C were already defined in (8.77–8.79). Of course, the dimension of all coefficients is [V].

8.A.3 The Electric Fields

In the system of elliptical coordinates (ξ, η), the absolute values of the electric fields can be determined from [386]

$$\left| \vec{\nabla}\phi(\xi,\eta) \right| = \frac{1}{c \cdot \sqrt{\xi^2 - \eta^2}} \sqrt{(\xi^2-1)\left[\frac{\partial\phi(\xi,\eta)}{\partial\xi}\right]^2 + (1-\eta^2)\left[\frac{\partial\phi(\xi,\eta)}{\partial\eta}\right]^2}\,. \tag{8.96}$$

Evaluation is straightforward but laborious. In most cases, the accelerator physicist is much more interested in the components in the transverse and longitudinal directions to estimate momentum spread, arising divergence, emittance growth, and other effects due to space charge. To determine these field components, one defines an orthonormal basis $\vec{e_\xi}$ and $\vec{e_\eta}$, taken from the vector equation,

$$\vec{s} = z\,\vec{e_z} + r\,\vec{e_r}\,,$$

where $\vec{s}$ is the vector from the origin of the cylindrical coordinates (which is the center of the ellipsoid) to the point under consideration. With the unit vectors in the z-and r-directions $\vec{e_z}$ and $\vec{e_r}$, $\vec{s}$ has the components z and r. The unit vectors $\vec{e_\xi}$ and $\vec{e_\eta}$ can be determined from

$$\vec{e_\xi} = \frac{\frac{\partial\vec{s}}{\partial\xi}}{\left|\frac{\partial\vec{s}}{\partial\xi}\right|} = \frac{\frac{\partial z}{\partial\xi}\vec{e_z} + \frac{\partial r}{\partial\xi}\vec{e_r}}{\sqrt{z_\xi^2 + r_\xi^2}} \tag{8.97}$$

$$\vec{e_\eta} = \frac{\frac{\partial\vec{s}}{\partial\eta}}{\left|\frac{\partial\vec{s}}{\partial\eta}\right|} = \frac{\frac{\partial z}{\partial\eta}\vec{e_z} + \frac{\partial r}{\partial\eta}\vec{e_r}}{\sqrt{z_\eta^2 + r_\eta^2}}\,, \tag{8.98}$$

with $z_\xi = \partial z/\partial\xi$, $r_\xi = \partial r/\partial\xi$. Taking into account the relations (8.57) and (8.58), one obtains

$$\vec{e_\xi} = \frac{\eta\sqrt{\xi^2-1}}{\sqrt{\xi^2-\eta^2}}\vec{e_z} + \frac{\xi\sqrt{1-\eta^2}}{\sqrt{\xi^2-\eta^2}}\vec{e_r} \tag{8.99}$$

$$\overrightarrow{e_\eta} = \frac{\xi\sqrt{1-\eta^2}}{\sqrt{\xi^2-\eta^2}}\overrightarrow{e_\mathrm{z}} + \frac{\eta\sqrt{\xi^2-1}}{\sqrt{\xi^2-\eta^2}}\overrightarrow{e_\mathrm{r}} \tag{8.100}$$

with the well-known relations of orthogonal unit vectors

$$\overrightarrow{e_\xi}\,\overrightarrow{e_\eta} = 0$$

and

$$|\overrightarrow{e_\xi}| = |\overrightarrow{e_\eta}| = 1\,.$$

For the gradient of the potentials in the system of confocal elliptical coordinates, one obtains the vector equation

$$\overrightarrow{\nabla}\phi(\xi,\eta) = \frac{1}{\sqrt{z_\xi^2 + r_\xi^2}}\frac{\partial\phi(\xi,\eta)}{\partial\xi}\overrightarrow{e_\xi} + \frac{1}{\sqrt{z_\eta^2 + r_\eta^2}}\frac{\partial\phi(\xi,\eta)}{\partial\eta}\overrightarrow{e_\eta}\,. \tag{8.101}$$

Taking (8.99) and (8.100) into account, the field components in the z- and r-directions can be derived from the potentials given in (8.66), (8.67) (homogeneously charged ellipsoid) and 8.83, 8.82 (parabolically charged ellipsoid). The resulting analytical expressions become very complex and therefore are not given here. To calculate the electric fields dependent on the parameters, the use of programs [84–86] which allow fast numerical differentiation, is recommended.

8.B Relativistic Effects

As mentioned in the introduction of this chapter, the transformation of electrodynamic quantities between moving coordinate systems and coordinate systems at rest can be performed by use of four vectors to describe the quantities. Using a notation which takes advantage of complex variables [351], the relevant four vectors are defined as

$$\overrightarrow{X_4} = [x_1, x_2, x_3, x_4] = [x, y, z, ict] = [\overrightarrow{x}, ict] \tag{8.102}$$

$$\overrightarrow{J_4} = \left[\overrightarrow{j}(\overrightarrow{x}, t), ic\rho(\overrightarrow{x}, t)\right] \tag{8.103}$$

$$\overrightarrow{A_4} = \left[\overrightarrow{A}(\overrightarrow{x}, t), \frac{i}{c}\varphi(\overrightarrow{x}, t)\right], \tag{8.104}$$

with i as the imaginary unit, $\overrightarrow{j}$ as the current density, $\overrightarrow{A}$ as the vector potential, and the scalar potential φ. The interesting tensor of the field strengths is defined as

$$F = \begin{bmatrix} 0 & B_\mathrm{z} & -B_\mathrm{y} & -\frac{i}{c}E_\mathrm{x} \\ -B_\mathrm{z} & 0 & B_\mathrm{x} & -\frac{i}{c}E_\mathrm{y} \\ B_\mathrm{y} & -B_\mathrm{x} & 0 & -\frac{i}{c}E_\mathrm{z} \\ \frac{i}{c}E_\mathrm{x} & \frac{i}{c}E_\mathrm{y} & \frac{i}{c}E_\mathrm{y} & 0 \end{bmatrix}. \tag{8.105}$$

In the context of this treatise, the following transformations are important:

$$x' = \frac{x - v_\mathrm{x} t}{\sqrt{1 - (\frac{v}{c})^2}} = \frac{x - v_\mathrm{x} t}{\sqrt{1 - \beta^2}} \tag{8.106}$$

$$\rho' = \frac{\rho - v_\mathrm{x}\, j_\mathrm{x}/c^2}{\sqrt{1 - \beta^2}} \tag{8.107}$$

$$j'_\mathrm{x} = \frac{j_\mathrm{x} - v_\mathrm{x}\rho}{\sqrt{1 - \beta^2}} \tag{8.108}$$

$$t' = \frac{t - x v_\mathrm{x}/c^2}{\sqrt{1 - \beta^2}} \tag{8.109}$$

$$\varphi' = \gamma\varphi\left[x \to \gamma(x - v_\mathrm{x} t)\right], \quad \gamma = 1/\sqrt{1 - \beta^2} \tag{8.110}$$

$$A'_\mathrm{x} = \gamma A\left[x \to \gamma(x - v_\mathrm{x} t)\right] \tag{8.111}$$

$$y = y',\ y = y',\ j'_\mathrm{y} = j_\mathrm{y},\ j'_\mathrm{z} = j_\mathrm{z} \tag{8.112}$$

To be consistent with the notation used mostly in the literature, movement in the z-direction is supposed, giving the transformations of the four vectors from the moving coordinate system $\overrightarrow{X_4}$, where $\overrightarrow{J_4}$ and $\overrightarrow{A_4}$ are defined in the fixed coordinate system of the observer, respectively, detector. Assuming $\overrightarrow{A_4} = [0, 0, 0, ic\rho(\overrightarrow{x}, t)]$ in the rest frame of the charges, the fields transform as follows [351]:

$$E'_\mathrm{x} = E_\mathrm{x}, \quad B'_\mathrm{x} = B_\mathrm{x} \tag{8.113}$$

$$E'_\mathrm{y} = \gamma(E_\mathrm{y} - v_\mathrm{x} B_\mathrm{z}), \quad B'_\mathrm{y} = \gamma\left(B_\mathrm{y} + \frac{v_\mathrm{x}}{c^2} E_\mathrm{z}\right) \tag{8.114}$$

$$E'_\mathrm{z} = \gamma(E_\mathrm{z} + v_\mathrm{x} B_\mathrm{y}), \quad B'_\mathrm{z} = \gamma\left(B_\mathrm{z} - \frac{v_\mathrm{x}}{c^2} E_\mathrm{y}\right), \tag{8.115}$$

which simplifies for a moving point charge due to $B_\mathrm{x} = B_\mathrm{y} = B_\mathrm{z} = 0$. Obviously, the most important consequences taking relativistic effect into account are

- In comparison to the rest system of the charge, the electric field strength becomes smaller proportional to $1/\gamma^2$ in the direction of the movement, which means that the field lines are compressed due to the movement.
- On the other hand, the electric field strength will be enhanced $\sim \gamma$ perpendicularly to the direction of movement.
- Even for the moving point charge with $B_\mathrm{x} = B_\mathrm{y} = B_\mathrm{z} = 0$, components of the magnetic field strength arise as a necessary condition from the transformations. As a consequence, the repulsive forces between two electrons flying in parallel at the velocity of light c are canceled by the action of the highly relativistic electromagnetic fields.

- The same arguments hold when $\overrightarrow{A_4} = [0, 0, 0, ic\rho(\overrightarrow{x}, t)]$ which means there are no moving charges in the rest system. It follows from (8.108) that a component arises in the system moving against the rest system of the charges.

9

Beam Loss Monitoring

Beam loss monitoring becomes essential if lost particles cause non-tolerable activation of accelerator components by nuclear reactions. Moreover, components can be destroyed by the radiation or due to thermal heating by lost energetic particles. Sensitive beam loss monitoring can help the operator to achieve high transmission through a machine up to the target, including the optimization of complex beam transport systems. Beam loss monitors should localize a particle loss and additionally give information about the time and intensity of the loss. Beam loss monitoring can be based on

- direct detection of lost particles,
- detection of particles or radiation from nuclear reactions of lost particles with the surrounding material (wall of beam pipe, slits, scrapers,...). The most important processes are [413, 414, 416]:
  1. *Bremsstrahlung:* Because the creation of Bremsstrahlung is based on the deceleration of moving charged particles in material, the process can be compared with the generation of synchrotron radiation. Hence, referring to (8.48) (Chap. 8, Sect. 8.6), the creation of Bremsstrahlung will be significant only for electrons and dominates energy loss from collisions above ∼100 MeV. The high energy γ rays created can produce particles by pair production. Depending on the ratio of the energy between the high energy photons and the rest energy, particle pairs, such as $e^{\pm}$, $\mu^{\pm}$, $\pi^{\pm}$, can be created. Furthermore, as a consequence of the interaction of the high energy photons with the nuclei of the stopping material, processes such as (γ, n), (γ, p), (γ, np) give rise to further particles.
  2. *Direct nuclear interactions:* If a lost high energy particle hits a target with a thickness comparable to the range determined by electronic stopping, nuclear processes become probable. For protons above 1 GeV, the probability is nearly 100%. As a consequence, many channels of particle production are open. Most of the open channels include fast neutron emission.

3. *Fragmentation and Fission:* For heavy ions, the high energy projectiles can be fragmented or fission can be induced. As a consequence, radioactive nuclei are produced together with emission of fast protons and neutrons.

Due to the kinematics of the primary interaction, all secondary particles are emitted more or less in the forward direction. Emitted charged particles can be stopped relatively quickly by the surrounding material. This does not hold for fast neutrons, which can travel large distances through materials. Overviews of the different types of monitors are given in [415–417]. The reliability of beam loss monitors for the LHC has been studied in [418] (see also [419]).

9.1 Principles and Types of Beam Loss Monitors

9.1.1 Ionization Chamber (IC)

The output signal is proportional to the energy loss of ionizing particles. The principle has been already discussed in Chap. 2, Sect. 2.6. An example of a very short ionization chamber is shown in Fig. 2.45 (Chap. 2, Sect. 2.6). Although ionization chambers of this type are more suitable for beam intensity measurements, they can be used for beam loss detection, too. The IC is not sensitive to neutrons and has a rather low efficiency for γ rays; efficiency for charged particles is high. Concerning response time, one has to keep in mind that the ions, created in the gas by the incident ionizing particles, need some time to reach the electrode. The response time can be estimated from the μ of positive and negative ions in gases. The mobility of the mostly used gases Ar and CO_2, at normal pressure and a temperature of 15°C is from 0.8–1.7 (cm/s)/V/cm) [45]. A big advantage of the IC is its very high radiation hardness.

A well-known example is Panowski's long ionization chamber (PLIC, [420]) installed at the Stanford Linear Accelerator Center (SLAC). It consists of a 3.5-km hollow coaxial cable, filled with Ar (95%) and CO_2 (5%). The loss is localized by measuring the time delay between direct and reflected signals.

9.1.2 Plastic Scintillators, Diamond Detectors

All devices, suitable for counting ionizing particles, as described in Chap. 2, Sect. 2.7, can be used to detect lost particles. Due to the better radiation hardness of diamond in comparison to plastic scintillators, this type of detector should be preferred. A very rough number of the destruction threshold for plastic materials is $1\,\mathrm{Mrad} = 10^4\,\mathrm{Gy}$ [120]. At this limit, light transmission is reduced by a factor of $1/e = 0.37$. The radiation hardness of diamond is better by some orders of magnitude.

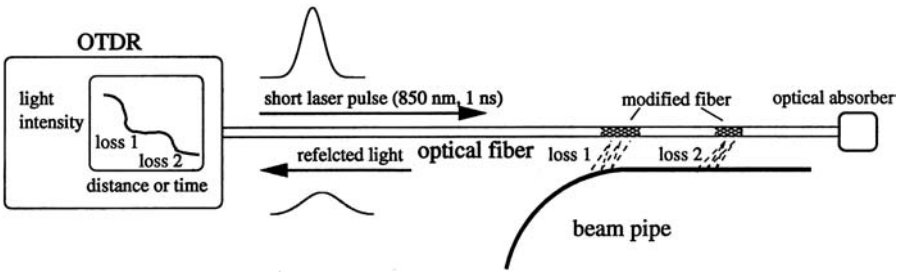

Fig. 9.1. Scheme to illustrate beam loss monitoring with fiber optics [120, 421]

9.1.3 Fiber Optic Radiation Sensing

A newly developed on-line monitor system for long and complex accelerators is based on optical fibers, combined with an optical time domain reflectometer (OTDR) [120, 421]. The principle is illustrated in Fig. 9.1. An optical fiber is installed close to the beam pipe. Because the material is used manifold in telecommunication, it can be fabricated in nearly arbitrary lengths at a low price. Due to radiation destruction, optical fibers change light transmission and reflection coefficients. As a standard technique in telecommunication, the quality is tested with a optical time domain reflectometer using a nanoseconds-laser pulse. A change in the optical properties of the fiber leads to a reflection. Measuring the arrival time with respect to the start of the input pulse gives the localization of the distortion, taking the well-known velocity of light in the fiber into account. Because signal evaluation is performed by OTDR, the system is not suitable for on-line monitoring, but can be very helpful during the commissioning phase of a new large machine, such as the TESLA [421]. The detector can be partly repaired by heating the fiber up to about 150°C.

9.1.4 Scintillation Liquids

A detector of this type consists of a tube, filled with a scintillation liquid, coupled to a photomultiplier. Like plastic scintillators, the device is sensitive to charged particles, γ rays, and neutrons. Applying modern techniques of pulse shape discrimination [126] allows discrimination between different kinds of particles. Due to the special chemical composition of the solvent, the radiation hardness is about a factor of 10 better than that of plastic scintillators.

9.1.5 Cherenkov Counter

Taking advantage of the Cherenkov effect, discussed in Chap. 8, Sect. 8.6, the loss of charged relativistic particles can be detected by a counter, designed similarly to the liquid scintillator. Water can be used as a source of Cherenkov radiation, but in most cases a special mixture is used. Depending on the mixture, the radiation hardness can be very high.

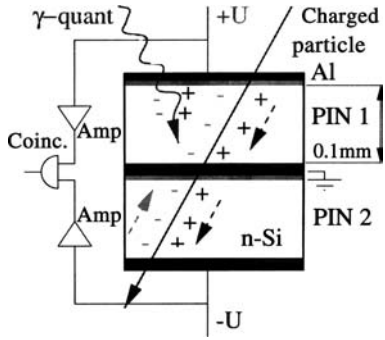

Fig. 9.2. PIN diode operated in coincidence for beam loss monitoring [120]

9.1.6 PIN Diode

Ionizing particles that cross the gap of a semiconductor create electron–hole pairs, which can be separated by an applied voltage over the gap. The signal is amplified by a charge sensitive amplifier and further analyzed. Studying the pulse height distribution leads to coarse information about the energy of the particles. In the application to beam loss monitoring, the corresponding pulses are mostly counted. A beam loss monitor developed at DESY [415] uses PIN diodes as the detector. A device consisting of two face-to-face mounted PIN diodes including amplifier and counter is commercially available [95]. The two PIN diodes are used in coincidence to suppress the signal created by low energy photons emitted by synchrotron radiation. The principle is illustrated in Fig. 9.2. Due to the low penetration depth, the photons are stopped at the first diode and do not reach the other one. A drawback of this detector system is the small size of PIN diodes, typically 1 cm^2, which results in rather low detection efficiency. This holds especially for application to heavy ion machines because the solid angle of lost particles or secondary products is very small for kinematic reasons.

9.1.7 BF_3 Counter

Neutrons can be detected by the well known BF_3 counter [126, 422]. The detector is based on the reaction $^{10}\mathrm{B} + n \rightarrow {}^{7}\mathrm{Li} + \alpha$. For thermal neutrons, the process has a cross section of the order of 1 kBarn (1 Barn $= 10^{-24}$ cm^2). Figure 9.3 illustrates the principle. A glass tube is filled with BF_3 gas and surrounded by paraffin or concentric layers of polyethylene to moderate the incident neutrons to thermal energies. A high electric field between a thin wire in the center of the glass tube and the metallized surface of the tube ionizes the particles. The fast signal is coupled via a capacitor, amplified and fed to a counter. To increase the sensitivity with respect to the angle of incidence, the paraffin or polyethylene moderator can be surrounded by two

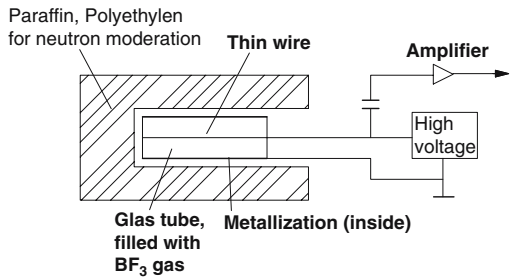

Fig. 9.3. Scheme of a BF_3 counter for neutron detection

additional layers consisting of polyethylene doped with boron or B_2O_3 and another paraffin/polyethylene layer [45, 422]. The counting rate is limited by the time needed to recharge the wire inside the tube.

9.1.8 Example from Measurements at a Test Setup

Due to the great variety of accelerated ion species in the SIS, the setting of the extraction system requires beam loss monitoring to optimize parameters for beam losses. A setup of four suitable beam loss monitors, an IC, a liquid scintillator, a plastic scintillator, and a BF_3 counter has been installed around the extraction system of the SIS and tested in accelerator experiments [424]. Figure 9.4 shows the results [423], comparing the counts from the different types of beam loss monitors with the signal from a beam transformer and data measured in the experiment.

9.1.9 Other Applications of Beam Loss Monitoring

Beam loss monitors are relatively cheap and do not require a complex signal processing system. They can be installed outside the vacuum system, fixed at critical locations along an accelerator and beam transport system, or even moved on demand to positions that require surveillance of beam losses. Relating typical count rates to the primary particle flux, the sensitivity is very high and in general cannot be achieved with other non-destructive beam diagnostic devices. Referring to Fig. 9.4, a counting rate of some thousand counts per spill allows optimization of the intensity in an experiment with 10^9–10^{10} particles per spill. Thus, beam loss monitoring can be a useful tool for operators and accelerator physicists in applications such as:

- optimization of complex machine settings during the commissioning phase of a new accelerator facility;
- quench protecting of superconducting parts, such as magnets, quadrupoles, and cavities;
- optimization of extraction systems, septa parameters, and scraper positioning during routine machine operation;

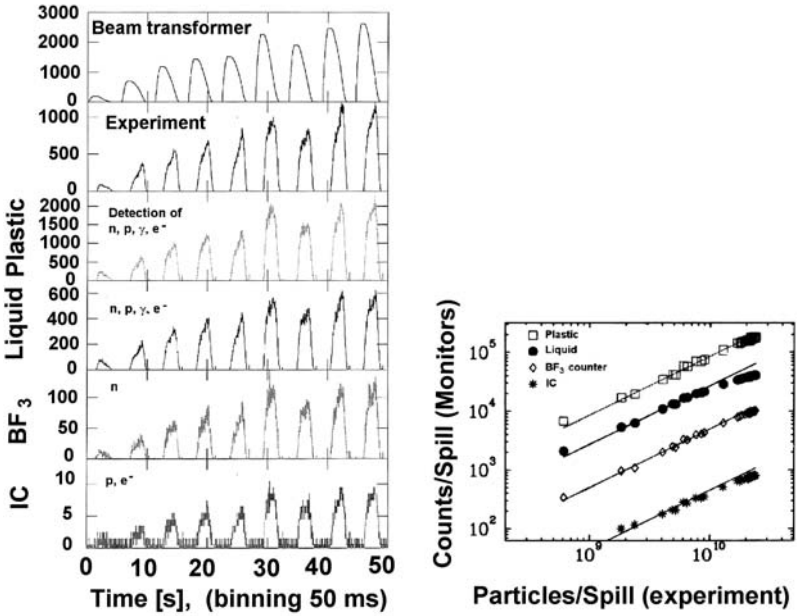

Fig. 9.4. Left: Counting rates/spill from different types of beam loss monitors for an O^{18+}-beam accelerated from about 11 to 800 MeV/u with up to 4×10^4 particles/spill. Right: output of the counters as a function of the intensity. The lines are fits of straight lines to illustrate the linearity [424]

- fast failure detection of important beam transport systems, such as bending magnets and focusing elements; and
- recording beam loss at critical locations during a long period of machine operation may be used as a criterion in kind of a high score, for parameter optimization and machine operation.

10

Some Interesting Specialized Aspects of Beam Diagnostics

One may compare the fitting out of accelerator facilities with more and more sophisticated diagnostic tools to the development in the car industry, where ingenious computer-controlled electronic circuits are increasing in support of the car driver. In both cases, this trend will continue and there will be no limits for the engineers and physicists in the implementing new ideas. It is beyond the scope of this book to cover all new developments and specialized aspects of beam diagnostics. Nevertheless, some modern, specialized beam diagnostic tools are discussed briefly in the following.

10.1 The Laserwire

For the newest developments in linear collider design, the expected beam sizes in electron or positron machines are of the order of some micrometers or even less. The performance of those machines depends very much on the determination and control of the transverse beam size and emittance. An idea for non-destructive measurement is based on Compton scattering between the electrons (positrons) in a bunch and the photons of a laser beam. The theory is based on the classical Thomson formula for scattering of radiation by a free charge [425]. In this formula, the momentum of the incident photon has been neglected. Applying two-body relativistic kinematics to the process leads to the Compton formula [39, 426, 427],

$$\lambda_{\mathrm{f}} - \lambda_{\mathrm{i}} = \frac{h}{m_0 c}\,(1 - \cos\theta). \tag{10.1}$$

Here θ is the scattering angle in the laboratory system, which is the rest frame of the electron or positron, and $\lambda_{\mathrm{i}}, \lambda_{\mathrm{f}}$ are the wavelengths of the photon before and after scattering. The quantity $h/m_0 c = 2.426 \times 10^{-12}$ m is the Compton wavelength. The interaction between a laser beam and an electron beam has been studied more in general in [430].

In practical application of a laserwire, a highly intense thin laser beam is scanned horizontally and vertically across the electron beam. The Compton scattered photons are detected downstream behind a deflecting magnet with a photon detector system, e.g., a CsI scintillator. Obviously, the thin laser beam takes over the role of a scanning wire in a conventional system. Applying the method, an ultralow vertical emittance of $\epsilon = 1.18 \times 10^{-11}$ mrad has been determined at the accelerator test facility (KEK) (ATF) [431]. Recent measurements with micron and submicron resolution using the laserwire are reported in [432].

An international collaboration "Laser Beam Based Diagnostics" (LBBD) has been established to study the feasibility of laser based diagnostic tools. The principle of the laserwire, which is one possible application of lasers in beam diagnostics (see, e.g., [433–435]), is shown schematically on the homepage of LBBD [436]. Publications about the laserwire as a powerful diagnostic tool are summarized in the "Laserwire Bibliography" [428].

10.2 The Fresnel Zone Plate Beam Profile Monitor

A newly developed real-time high-resolution monitor for the accelerator test facility (KEK) (ATF) [437] is based on detecting synchrotron radiation, using two Fresnel zone plates (FZP) to magnify monochromatized synchrotron light. An X-ray CCD camera is used to detect synchrotron radiation (see also [438]). The monitor takes real-time images of the electron beam with a resolution of 1 μm.

10.3 Beam Profile Monitor Based on a GEM Detector

A new type of beam profile monitor based on a gas electron multiplier (GEM) is under development at CERN for the antiproton decelerator [439]. The principle is similar to the multiwire proportional chambers (MWPC) but is more suitable at low energies. Because at low energies (5.3-MeV antiprotons in the case under discussion), MWPC's are destructive to the beam and antiprotons can be annihilated, the new monitors are considered as a possible replacement of the MWPCs.

10.4 High-Resolution Bunch Shape and Length Measurements

To measure the shape and length of electron bunches in the picosecond region, a new technique combines the electro-optical detection of the Coulomb field of an electron bunch and the single-shot cross-correlation of optical pulses [440].

The measuring system works in real time and non-destructive. Single bunches of 50-MeV electrons with a length of around 650 fs (FWHM) could be analyzed by this method. The method takes advantage of the fact that the electric field lines of a highly relativistic bunch is concentrated perpendicularly to the direction of movement.

10.5 Electron Beam Scanner

A very thin scanning electron beam is proposed for beam profile determination [441]. The electrons crossing the beam are scattered by Rutherford scattering, detected, and analyzed based on the Rutherford scattering formula. The method has some advantages in comparison with residual gas ionization monitors and can be applied in very high vacuum systems. High velocity and low energy spread of the scattered electrons allow fast longitudinal bunch shape measurements, too.

10.6 AC Modulation of System Parameters

Taking advantage of lock-in averaging techniques in signal analysis, the precision of measurements can be enhanced considerably. One application is k-modulation, as described in Chap. 5, Sect. 5.4.6. The technique can be extended to measure other beam parameters by slow modulation of the relevant accelerator components. An overview of very precise determination of various beam parameters by ac-modulation is given in [442].

References

1. Borer, J., Jung, R., Diagnostics, CAS-CERN, Accelerator School, Aarhus (Denmark), (October 1983), CERN 84-15, (1984), p. 385
2. Beam Diagnostics, CERN/PS 88-09(AR)
3. Koziol, H., Beam Diagnostics for Accelerators, CAS-CERN Accelerator School, Jyväskylä, Finland, (September 1992), CERN 94-01 (1994)
4. Strehl, P., Rev. Sci. Instrum. **63** (4), 26–52 (1992)
5. Hofmann, A., Accelerator Needs for Diagnostics, p.1 in [20]
6. Bosser, J., Beam Instrumentation, CERN-PE-ED, 001–92, (Nov. 1994)
7. Koziol, H., Some Physics Aspects in Beam Diagnostics, p. 87 in [6]
8. Hofmann, A., Beam Diagnostic and Applications, p. 3 in [16]
9. Strehl, P., Diagnostics in Heavy Ion Machines, p. 27 in [23]
10. Hinterberger, F., Physik der Teilchenbeschleuniger und Ionenoptik (Springer Verlag, Berlin Heidelberg New York, 1997)
11. Handbook of Accelerator Physics and Engineering, Editors: Chao, A. W., Tigner, M., (World Scientific, Singapore, 1999, reprinted 2002)
12. Wille, K., Physik der Teilchenbeschleuniger und Synchrotronstrahlungsquellen (B. G. Teubner, Stuttgart 1992)
13. *AIP* Conference Proceedings 319, Beam Instrumentation Workshop 1993, Santa Fe, NM, October 1993
14. *AIP* Conference Proceedings 333, Beam Instrumentation Workshop 1994, Vancouver, B.C., Canada, October 1994
15. *AIP* Conference Proceedings 390, Beam Instrumentation Workshop 1996, Argonne, Illinois, 1996
16. *AIP* Conference Proceedings 451, Beam Instrumentation Workshop 1998, Stanford, CA, May 1998
17. *AIP* Conference Proceedings 546, Beam Instrumentation Workshop 2000, Cambridge, MA, May 2000
18. *AIP* Conference Proceedings 648, Beam Instrumentation Workshop 2002, Upton, New York, May 6–9, 2002
19. *AIP* Conference Proceedings 732, Beam Instrumentation Workshop 2004, Knoxville, TN, May 3–6, 2004
20. Proceedings of the First European Workshop on Beam Diagnostics and Instrumentation for Particle Accelerators (DIPAC 1993), Montreux, Switzerland, May 3–5, 1993, CERN PS/93–35 (BD), CERN SL/93–35 (BI)

21. Proceedings of the Second European Workshop on Beam Diagnostics and Instrumentation for Particle Accelerators (DIPAC 1995), Travemünde, Germany, May 28–31, 1995
22. Proceedings of the Third European Workshop on Beam Diagnostics and Instrumentation for Particle Accelerators (DIPAC 1997), Laboratory Nazionali di Frascati, LNF-INFN, Frascati (Rome), Italy, October 12–14, 1997
23. Proceedings of the Fourth European Workshop on Beam Diagnostics and Instrumentation for Particle Accelerators (DIPAC 1999), Daresbury, Warrington, UK, May 16–18, 1999
24. Proceedings of the Fifth European Workshop on Beam Diagnostics and Instrumentation for Particle Accelerators (DIPAC 2001), ESRF, Grenoble, France, May 13–15, 2001, http://www.esrf.fr/conferences/DIPAC/DIPAC2001Proceedings.html
25. Proceedings of the Sixth European Workshop on Beam Diagnostics and Instrumentation for Particle Accelerators (DIPAC 2003), Mainz, Germany, May 5–7, 2003, www.jacow.org
26. Contributions to Conferences via Internet: PAC65,..., EPAC96,..., LINAC96,..., APAC01,..., DIPAC01,..., ICALEPCS01,..., www.jacow.org (CERN server)
27. Karlsruher Virueller Katalog (KVK): www.ubka.uni-karlsruhe.de/kvk.html
28. Minty, M. G., Zimmermann, F., Measurement and Control of Charged Particle Beams (Springer-Verlag, Berlin Heidelberg New York, 2003)
29. Barth, W., Klabunde, J., GSI-Darmstadt, private communication
30. Webber, R. C., Tutorial on Beam Current Monitoring, *AIP* Conference Proceedings 546, 2000, p. 83
31. Peters, A., Vodel, W., Dürr, V., Koch, H., Reeg, H., Schroeder, C. H., A Cryogenic Current Comparator for Low Intensity Ion Beams, p. 100 in [20]
32. Peters, A., Vodel, W., Koch, H., Neubert, R., Reeg, H., Schroeder, C. H., A Cryogenic Current Comparator for the Absolute Measurement of nA Beams, p. 163 in [16]
33. PET, Physik Elektronik Technik, Engineering Office, Strehl, P., Kraus, H., Smetanaweg 6, D-64291 Darmstadt, Germany, e-mail: petdarmstadt@aol.com
34. Carter, G., Colligon, J., Ion Bombardment of Solids (Heinemann, London, 1969)
35. Goodfellow GmbH, Bad Nauheim, Germany. Goodfellow Cambridge Limited, Huntington, England
36. Meinke, H., Gundlach, F. W., Taschenbuch der Hochfrequenztechnik (Springer-Verlag, Berlin Heidelberg New York Tokyo, 1986)
37. MECL System Design Handbook, Motorola Semiconductor Inc., (1971)
38. Nührmann, D., Das große Werkbuch Elektronik (Franzis' Verlag GmbH, Poing, 1998)
39. Jackson, J. D., Classical Electrodynamics (John Wiley & Sons, New York, 1975) third edition: 1999, ISBN 0-471-30932-X
40. Kaufmann, W., GSI-Darmstadt, Germany, private communication
41. Bethe, H. A., Z. f. Physik **76**, 293 (1932)
42. Bethe, H. A., Heitler, W., Proc. R. Soc., A **146,** 83 (1934)
43. Bloch, F., Z. f. Physik **81**, 363 (1933)
44. Bethe, H. A., Askin, J., Passage of Radiations Through Matter, in: Ségre, E., Experimental Nuclear Physics (Wiley, New York, 1953–1959)

45. Segré, E., Nuclei and Particles (W. A. Benjamin, New York Amsterdam, 1964)
46. Rutherford, E., Philas. Mag. **21**, 672 (1911)
47. Sternheimer, R. M., Phys. Rev. **115** (1), 137 (1959)
48. Heitler, W., The Quantum Theory of Radiation, 3rd ed. (Oxford University Press, New York, 1954)
49. Kantz, A. D., Hofstadter, R., Phys. Rev. **89** (3), (1952)
50. Hofstadter, R., Kantz, A. D., Nucleonics **12** (3), 36 (1954)
51. Brown, K. L., Tautfest, G. W., Rev. Sci. Instrum. **27** (9), 696 (1956)
52. Nelms, Energy Loss and Range of Electrons and Positrons, National Bureau of Standards, NBS Circular 577 (1956), supplemented 1958. Katz and Penfold, RMP (1952), 24, p. 28
53. Yung-Su Tsai, Rev. Mod. Phys. **46** (4), 828 (1974)
54. Sanders, J. H., J. Sci. Instrum. **26**, 36 (1949)
55. Harrison, E. R. J. Sci. Instrum. **34**, 242 (1957)
56. Gunn, S. R., Nucl. Instrum. Methods **29**, 1 (1964)
57. Andersen, H. H., Radiat. Effects **3**, 51 (1970)
58. Van de Runstraat, C. A., Wijnaendts van Resandt, R., Los, J., J. Phys. E **3**, 575 (1970)
59. Christodoulides, C. E., Freeman, J. H., Nucl. Instrum. Methods **135**, 13 (1976)
60. Yamada, R., Jp. J. Appl. Phys. **1** (2), 92 (1962)
61. Internal Cern-Report, The Inductionn Type Beam Monitor for the PS, ("Hereward Transformer"), MPS/Int. CO 62–15, (1962)
62. Unser, K. B., IEEE Trans. Nucl. Sci. NS-**16**, 934 (1969)
63. Gardiner, S. N., Matthews, J. L., Owens, R. O., Nucl. Instrum. Methods **87**, 285 (1970)
64. Steiner, R., Merle, K., Andresen, H. G., Nucl. Instrum Methods **127**, 11 (1975)
65. Dunn, P. C., Nucl. Instrum. Methods **165**, 163 (1979)
66. Tokuda, N., Watanabe, S., Electrostatic and Ferrite-core Monitors, INS, University of Tokyo, report, INS-NUMA-21
67. Loyer, F., Andre, T., Ducoudret, B., Rataud, J. P., IEEE Trans. Nucl. Sci., NS-**32** (5), 1938 (1985)
68. Sato, Y., Yamada, T., Ogawa, H., Fujii, R., Nucl. Instrum. Methods **228**, 576 (1985)
69. Reeg, H.-J., Dimensionierung, Konstruktion, Bau und Erprobung eines elektromagentisch abgeschirmten Strahltransformators mit einer Zeitkonstanten von etwa $0,5\,\mu s$, Diplomarbeit, FH-Wiesbaden, GSI-Darmstadt, Germany, (1986)
70. Degueurce, L. Nucl. Instrum. Methods A **260**, 538 (1987)
71. Unser, K. B., Design and Preliminary Tests of a Beam Intensity Monitor for LEP, Proc. IEEE Particle Accelerator Conference, 1989, Chicago, Vol. 1, p. 71
72. Unser, K. B., Measuring Bunch Intensity, Beam Loss and Bunch Lifetime in LEP, Proc. of the Second European Particle Accelerator Conference, Nice, June 12–16, 1990, Vol. 1, p. 786
73. Burtin, G., Colchester, R., Fischer, C., Hemery, J. Y., Jung, R., Vanden Eynden, M., Vouillot, J. M., Mechanical Design, Signal Processing and Operator Interface of the LEP Beam Current Transformers, Proc. of the Second European Particle Accelerator Conference, Nice, June 12–16, 1990, Vol. 1, p. 794
74. Schneider, N., Walter, H., Beam Current Measurements, GSI Scientific Report (1990), GSI 91–1, March 1991, p. 386

75. Unser, K. B., The Parametric Current Transformer, Particles and Fields, Series 46, Conference Proceedings No. 252 of the Third Annual Workshop on Accelerator Instrumentation, CEBAF, Newport News, 1991, p. 266
76. Unser, K. B., Recent Advances in Beam Current Transformer Technology and Avenues for Further Developments, p. 105 in [20]
77. Schneider, N., Beam Current Monitors at the Unilac, p. 502 in [16]
78. Reeg, H., Schneider, N., Current Transformers for GSI's keV/u to GeV/u Ion Beams, an Overview, p. 120 in [24]
79. Reeg, H.-J., GSI-Darmstadt, Germany, private communication
80. Schlegel, H., Nowak, A., Impulstechnik (C. F. Winter'sche Verlagsbuchhandlung, Prien, 1961)
81. Stegmeier, H., Der Entwurf von Impulstransformatoren im ns-Bereich, Archiv Elektrische Übertragung 19/1965
82. Boll, R., Weichmagnetische Werkstoffe (Vacuumschmelze GMBH, Verlag: Siemens AG, Berlin und München, 1965)
83. FS-M 7, Weichmagnetische Werkstoffe (Firmenschrift, Vacuumschmelze Hanau GmbH, Germany, 1983)
84. Mathsoft Engineering & Education, Inc., Cambridge, MA, (1986–2004)
85. Wolfram Research, Inc., Champaign, IL
86. The Math Works, Inc., Natick, MA
87. Ott, H., Noise Reduction Techniques in Electronic Systems (John Wiley & Sons, New York, 1976)
88. Miteq, Inc., Hauppauge, NY
89. Fa. Dr. Friedrich Foerster, Reutlingen, Germany.
90. Lemme, H., Sensoren in der Praxis (Franzis Verlag München, 1990)
91. DRP-Anmeldung, H 138715, (1937)
92. Colchester, R., Turner, S., Unser, K. Beam Current Transformers for the ISR and West Hall Beam Transfer System, CERN-ISR-OP/72–2, (1972)
93. Unser, K., IEEE Trans. Nucl. Sci. NS-**28** (3), 2344 (1981)
94. Unser, K. B., Atomenergie-Kerntechnik **47** (1), 48 (1985)
95. Bergoz, J., BERGOZ Comp., 01170 Crozet, France
96. Schamass, A., Schneider, N., Steiner, R., A Beam Intensity Monitor for Synchrotron Beams with Fast Beam Extraction Mode, Internal Technical Report GSI (1996)
97. Steiner, R., Diploma Thesis, Institut für Kernphysik, Universität Mainz, Germany, (1973)
98. Harvey, I. K., A precise low temperature dc ratio transformer, Rev. Sci. Instrum. **43**, 1626 (1972)
99. Grohmann, K., Hahlbohm, H.-D., Lübbig, H., Ramin, H., *PTB* Jahresbericht p. 204 (1972)
100. Grohmann, K., Hechtfischer, D., Jakschik, J., Lübbig, H., A Cryodevice for Induction Monitoring of DC Electron or Ion Beams with Nano-ampere Resolution, in: Superconducting Quantum Interference Devices and their Applications, Walter de Gruyter & Co., (1977), p. 311
101. Grohmann, K., Hahlbohm, H.-D., Hechtfischer, D., IEEE Trans. Instrume. Meas. IM-**28** (3), 206 (1979)
102. Peters, A., GSI-Darmstadt, Germany, private communication
103. Vodel, W., Nietzsche, S., Neubert, R., Peters, A., Knaack, K., Wendt, M., Wittenburg, K., Low-Tc-SQUID based CCC for Applications in High Energy Physics, EUCAS 2003 Proc., Inst. of Physics Conference, Series 181 Nov. 2004

104. Hatton, V. W., Lowndes, S. A., Proceedings, DNPL/R1, Symposium on Beam Intensity Measurement, April 22–26, Daresbury, 1968
105. Forck, P., Heeg, P., Peters, A., Intensity Measurement of High-Energy Heavy Ions at the GSI Facility, p. 422 in [15]
106. Ferioli, G., Jung, R., Evolution of the Secondary Emission Efficiencies of Various Materials Measured in the CERN SPS Secondary Beam Lines, p. 168 in [22]
107. Chu, W. T., Instrumentation for Medical Beams, p. 160 in [14]
108. Kraft, G., et al., The Darmstadt Program HITAG: Heavy Ion Therapy at GSI (Elsevier Science B. V. 1994) Hadrontherapy in Oncology editors: Amaldi, U., Larsson, B
109. Forck, P., Heeg, P., Peters, A., Strehl, P., A Scintillator based Halo-Detector for Beam Position Monitoring, Proc. 5th European Part. Acc. Conference, Sitges (Barcelona), EPAC 96, IoP (1996) p. 2644
110. Schardt, D., Beam Delivery Systems and Dose Verification Techniques at Heavy-Ion Therapy Facilities, p. 6 in [22]
111. Dölling, R., Profile, Current, and Halo Monitors of the PROSCAN Beam Lines, p. 244 in [19]
112. Mitsuhashi, T., Design and Construction of Coronagraph for Observation of Beam Halo, Proceedings of the EPAC 2004, Lucerne, Switzerland (Web Version), p. 2655
113. Haberer, Th., Becher, W., Schardt, D., Kraft, G., Magnetic Scanning System for Heavy Ion Therapy, GSI-93–15, (März 1993) and Nucl. Instrum. Methods A **330**, 296 (1993)
114. Kraft, G., Medical Application of Accelerators in Tumor Therapy, *CAS,* Rhodes, Greece, CERN 95–06, 1995, p. 1083
115. Eickhoff, H., Haberer, Th., Kraft, G., Krause, U., Poppensieker, K., Richter, M., Steiner, R., The GSI Cancer Therapy Project, Proc. Part. Acc. Conf., PAC 97, Vancouver, B.C., Canada, 1997, p. 3801
116. Proposal for a Dedicated Ion Beam Facility for Cancer Therapy, submitted in September 1998, Radiologische Universitaetsklinik Heidelberg, DKFZ-Heidelberg, GSI-Darmstadt, FZR-Rossendorf
117. Amaldi, U., Z. Med. Phys. **14**, 7 (2004)
118. Heeg, P., GSI-Darmstadt, Germany, private communication
119. Strehl, P., Beam Instrumentation and Diagnostics, Joint Universities Accelerator School 2001, Archamps, January–March 2001
120. Forck, P. Lecture Notes on Beam Instrumentation and Diagnostics, Joint Universities Accelerator School 2003, Archamps, January–March 2003
121. Northcliffe and Schilling, Nuclear Data Tables, Vol. 7, No. 3–4, (Jan 1970), p. 233
122. Ziegler, F. J., Handbook of Stopping Cross Sections for Energetic Ions in all Elements, Vol. 5, The Stopping Power and Ranges of Ions in Matter (Pergamon Press, New York, 1984, 1985)
123. Hubert, F., Fleury, A., Bimbot, R., Gardes, D., Annales de Physique **5** (Suppl.), 1–214 (1980)
124. Hubert, F., Bimbot, R., Gauvin, H., Atomic Data and Nuclear Data, **46**, (1), (Sept. 1990)
125. Sauli, F., Principles of Operation of Mulitwire Proportional and Drift Chambers, CERN 77–09, (May 1977)

126. Knoll, G. F., Radiation Detection and Measurement, 2nd ed., (John Wiley & Sons, New York, 3rd ed. 2000)
127. Leo, W.R., Techniques for Nuclear and Particle Physics Experiments (Springer-Verlag, Berlin, 1994)
128. Keller, O., Untersuchungen zum Betrieb eines Szintillationsdetektors im Strom-Mode, Diplomarbeit, FH-Darmstadt, Germany, (1994)
129. Heeg, P., Intensity Measurements of Energetic Heavy Ion Beams between 10^5 and 10^9 pps, p. 96 in [20]
130. Heeg, P., Keller, O., A Scintillator - Photodiode - Beam Intensity Monitor, Proc. of the Fourth European Particle Accelerator Conference, EPAC, London, GB, June 27–July 1, 1994, p. 1725
131. Heeg, P., Peters, A. Strehl, P.: Intensity Measurements of Slowly Extracted Heavy Ion Beams from the SIS, p. 287 in [14]
132. Rossa, E., Schmickler, H., Brambilla, A., Verger, L., Mongellaz, F., New Development of Radiation-Hard Polycrystalline CdTe Detector for LHC Luminosity Monitoring, p. 94 in [24]
133. Tapper, R. J., Rep. Prog. Phys. **63**, 1273 (2000)
134. Berdermann, E., Blasche, K., Daues, H. W., Moritz, P., Stelzer, H., Voss, B., The Diamond Project at GSI - Perspectives, Proc. 7th Int. Conf. Advanced Tech. & Part. Physics, (ICATPP-7), ed. Barone, M. et al., p. 246
135. Berdermann, E., Moritz, P., Stelzer, H., Zeytoni, F., Diamond Detectors for Heavy Ion Measurements, 36th Int. Winter Meeting on Nuclear Physics, Bormio, Italy, Jan. 1998
136. Berdermann, E., Blasche, K., Moritz, P., Stelzer, Voss, B., H., Zeytoni, F., First Applications of CVD Diamond Detectors in Heavy Ion Experiments, Nucl. Phys. B (Proc. Suppl.) **78**, (1999)
137. The RD42 Collaboration (CERN), A CVD Diamond Telescope for Charged Particle Tracking, Proc. of the IEEE, San Diego, 2001
138. Moritz, P., Berdermann, E., Blasche, K., Stelzer, H., Zeytoni, F., Diamond Detectors for Beam Diagnostics in Heavy Ion Accelerators, p. 153 in [22]
139. Moritz, P., Berdermann, E., Blasche, K., Roedl, H., Stelzer, H., Zeytouni, F., Diamond Detectors with Subnanosecond Time Resolution for Heavy Ion Spill Diagnostics, p. 514 in [16]
140. Moritz, P., Berdermann, E., Blasche, K., Stelzer, Voss, B., Broadband Electronics for CVD-Diamond Detectors, Proc. of the 7th International Conference on New Diamond Science & Technology, ICNDST-7, July 24–28, 2000, University of Hong Kong
141. Meier, D., for the RD42 Collaboration (CERN), 5. Symposium on Diamond Materials, Electrochemical Society, Paris, 1997
142. Moritz, P., GSI-Darmstadt, Germany, private communication
143. Moritz, P., Broadband Preamplifiers for Fast Particle Detectors, GSI-Darmstadt, Germany, Internal Report
144. Walter, H., Ingenieurbüro Horst Walter, Kleine Ostergasse 6, D-55291 Saulheim, Germany, e-mail: horst.walter@ing.twinwave.net
145. Gröber, E. H., Erk, S., Grigull, U., Grundgesetze der Wärmeübertragung (Springer-Verlag, Berlin Heidelberg New York, 1981)
146. Hell, F., Grundlagen der Wärmeübertragung (VDI-Verlag GmbH, Düsseldorf, 1982)
147. Cerbe, G., Hoffmann, H.-J., Einführung in die Wärmelehre (Carl Hanser Verlag, München Wien, 1980)

148. Wagner, W., Wärmeübertragung (Vogel Verlag, Würzburg, 1981)
149. Schlünder, E.-U., Einführung in die Wärmeübertragung (Friedr. Vieweg & Sohn Verlagsgesellschafta GmbH Braunschweig, 1981)
150. Strehl, P., Thermische Berechnungen zum Hochstrombetrieb, GSI-Report 94–03, (1994)
151. Strehl, P., Thermal Aspects of Beam Intercepting Diagnostic Devices, Proc. 5th European Part. Acc. Conference, EPAC96, Sitges, Spain, 1996, p. 1603
152. Zienkiewicz, O. C., Cheung, Y. K., The Engineer, September 24, (1964)
153. Wilson, E. L., Nickell, R. E., Nucl. Eng. Design (Holland) **4**, 276 (1966)
154. Zienkiewicz, O. C., The Finite Element Method in Engineering Science, 2nd ed. (McGraw-Hill, New York, 1971)
155. Strang, G., Fix, G. J., An Analysis of the Finite Element Method (Prentice Hall, Englewood Cliffs, NJ, 1973)
156. Polivka, R. M., Wilson, E. L., Finite Element Analysis of Nonlinear Heat Transfer Problems, Structural Engineering and Structural Mechanics Department of Civil Engineering, University of California, Berkeley
157. Hinton, E., Owen, D. R. J., Finite Element Programming Academic Press London, 1977)
158. Link, M., Finite Elemente in der Statik und Dynamik, (B.G. Teubner Stuttgart, 1984)
159. Jordan-Engeln, G., Reutter, F., Numerische Mathematik für Ingenieure (Bibliographisches Institut (BI), Mannheim Wien Zuerich, 1982)
160. Großmann, Ch., Roos, H.-G., Numerik partieller Differentialgleichungen (B. G. Teubner, Stuttgart, 1992)
161. Marsal, D., Die numerische Lösung partieller Differentialgleichungen in Wissenschaft und Technik (Bibliographisches Institut (BI), Mannheim Wien Zuerich, 1976)
162. Rossi, B., High Energy Particles (Prentice Hall Physics Series, 1952)
163. Handbook of Chemistry and Physics, 56th ed. (CRC Press, Cleveland, OH 1975–1976)
164. Müller, R. W., Strehl, P., Protection of Storage Rings and Ion-Beam Devices from Melting, Proc. of the 12th Int. Symposium on Heavy Ion Inertial Fusion, Heidelberg, Germany, Sept. 1997, Nucl. Instrum. Methods Phys. Res. A **415**, 305 (1998)
165. Smirnow, W. I., Lehrgang der höheren Mathematik, Teil II (VEB Deutscher Verlag der Wissenschaften, Berlin, 1960)
166. Riedel, C., GSI-Darmstadt, Germany, private communication
167. Bock, R., Hofmann, I., Meyer-Ter-Vehn, Proc. Int. Symp. Heavy Ion Inertial Fusion (North-Holland, Amsterdam, 1989), reprinted from Nucl. Instrum. Methods Phys. Res. A **278** (1)
168. High Energy Density in Matter Produced by Heavy Ion Beams, GSI-Report, GSI-96–02
169. Nickel, F., Festkörpertargets bei hoher Strahlbelastung, Inaugural-Dissertation, Universität Giessen, (1976)
170. Nickel, F., Marx, D., Ewald, H., Nucl. Instrum. Methods **134**, 11 (1976)
171. Umstätter, H. H., Energy Absorption, Temperature Rise and Heat Diffusion in SEM-grid Strips for 10 MeV Protons, CERN, PS/HI/Note 96–07, (April 1996)
172. Gilpatrick, J. D., Techniques for Intense-Proton-Beam Profile Measurements, p. 110 in [16]

173. IBT Elektronik GmbH, Mühltal, Germany
174. Grimm, H., Graf, H., GSI-Darmstadt, Germany, private communication
175. Gilbert, P., J. Theor. Biol. **36**, 105 (1972a)
176. Herman, G. T., Lent, A., Rowland, S. W., J. Theor. Biol. **42**, 1 (1973)
177. Gordon, R., Herman, G. T., Int. Rev. Cytol. **38**, 111, (1974)
178. Oppenheim, B. E., IEEE Trans. Nucl. Sci. NS-**21**, 72 (June 1974)
179. Colsher, J. G., Comput. Graph. Image Proc. **6**, 513 (1976)
180. Fraser, J. S., Beam Tomography or ART in Accelerator Physics, Los Alamos Scientific Laboratory Report, LA-7498-MS, (Nov. 1978)
181. Minerbo, G. N., Sanderson, J. G., Reconstruction of a Source from a few (2 or 3) Projections, Los Alamos Scientific Report, (July 1978)
182. Minerbo, G., Comput. Graph. Image Proc. **10**, 48 (1979)
183. Chamberlin, D. D., Jameson, R. A., Minerbo, G. N., Sander, O. R., Beam Tomography in Two and Four Dimensions, Proc. of the 1979 Linac Accelerator Conference, Los Alamos, (1979), p. 314
184. Connolly, R., Michnoff, R., Moore, T., Shea, T., Tepikian, S., Nucl. Instrum. Methods Phys. Res. A **443**, 215 (2000)
185. Eckert, G., Winter, J., Strahlrekonstruktion aus Profilmessungen, Diplomarbeit, Fachhochschule Darmstadt, Fachbereich Informatik, durchgeführt bei GSI-Darmstadt, Germany, (1986)
186. Breskin, A., Charpak, G., Majewski, S., Melchart, G., Petersen, G., Sauli, F., Nucl. Instrum. Methods **161**, 19 (1979)
187. Physikalische Nachweisgeräte, Herbert Stelzer, Messel, Germany
188. Stelzer, H., Physikalische Nachweisgeräte, Herbert Stelzer, Messel, Germany, private communication
189. Stelzer, H., Nucl. Instrum. Methods Phys. Res. A **310**, 103 (1991)
190. Hortig, G., Nucl. Instrum. Methods **30**, 355 (1964)
191. Danfysik A/S, DK-4040 Jyllinge, Danmark, Beam Profile Monitoring Systems
192. Colchester, R. J., Jung, R., Proc. Part. Acc. Conf. (PAC97), Vancouver, IEEE Trans. Nucl. Sci. NS-**32**, 1917 (1985)
193. Steinbach, Ch., van Rooij, M., A Scanning Wire Beam Profile Monitor, IEEE Trans. Nucl. Sci. NS-**32** (5), 1920 (1985)
194. Fischer, C., et al., Proc. Euro. Part. Acc. Conf. (EPAC88), Rome, 1988, p. 1081
195. Soukup, J., et al., Rotating Scanning Polarization Profile Monitor, p. 492 in [14]
196. Fischer, C., Jung, R., Koopmann, J., Quartz Wires versus Carbon Fibres for Improved beam Handling Capacity of the LEP Wire Scanners, p. 290 in [15]
197. Field, C., McCormick, D., Raimond, P., Ross, M., Wire Breakage in SLC Wire Profile Monitor, p. 440 in [16]
198. O'Hara, J. F., Gilpatrick, J. D., Day, L. A., Kamperschroer, J. H., Madsen, D. W., Slow Wire Scanner Beam Profile Measurements for LEDA, p. 510 in [17]
199. Burger, S., Carli, C., Ludwig, M., Priestnall, K., Raich, U., The PS Booster Fast Wire Scanner, p. 122 in [25]
200. El-Sisi, A. B., Wire Scanner Beam Profile Measurement for ESRF, p. 131 in [25]
201. Jung, R., Image Acquisition and Processing for Beam Observation, p. 54 in [20]
202. Morgan Matroc, Ltd., Siegburg, Germany
203. Jung, R., Beam Intercepting Monitors, Joint US-CERN School on Particle Accelerators; Frontiers of Particle Beams, Lecture Note in Physics, No. 343, Anacapri, Italy, (October 1988), p. 403

204. Jung, R., CERN, Geneve, Switzerland, private communication
205. Budker, G. I., Dimov, G. I., Dudnikov, V. G., Sov. At. Energy **22** (5), 441 (May 1967)
206. Hornstra, F., Deluca, W. H., Nondestructive Beam Profile System for the Zero Gradient Synchrotron, Proc. Sixth International Conference on High Energy Acclerators, M. I. I., Cambridge, MA 1967, p. 374
207. De Luca, W., H., IEEE Nucl. Sci., NS-**16**, 813 (1969)
208. Hornstra Jr. F., Simanton, J. R., Nucl. Instrum. Methods **68**, 138 (1969)
209. Dimov, G. I., Dudnikov, V. G., Instrum. Exp. Tech. **3**, 553 (1969)
210. Johnson, C.D., Thorndahl, L., IEEE Nucl. Sci. NS-**16** (3), 227 (1969)
211. Weisberg, H., Gill, E., Ingrassia, P., Rodger, E., IEEE Trans. Nucl. Sci., NS-**30** (4), 2179 (1983)
212. Krider, J., Nucl. Instrum. Methods A **278**, 660 (1989)
213. Samulat, G., Strahlprofilmessungen in den HERA-Protonen-Beschleunigern unter Ausnutzung der Restgasionisation, Diplomarbeit, Universität Hamburg, (September 1989)
214. Berg, H., Schmidt-Böcking, H., Residual Gas Beam Profile Monitor for SIS beams, GSI-Scientific Report 1989, GSI 90–1, (March 1990), p. 280
215. Hochadel, B., Ein Strahlprofilmonitor nach der Methode der Restgasionisation für den Heidelberger Testspeicherring TSR, Report MPI Heidelberg, MPI H-1990-V-19, (1990)
216. Gabel, A., Entwicklung eines Restgas-Monitors für Strahlprofilmessungen im Bereich höherer Teilchenströme, Durchführung von Messungen, Diplomarbeit im Fachbereich Physikalische Technik der Fachhochschule Wiesbaden, durchgeführt bei der GSI-Darmstadt, (1990)
217. Schippers, J. M., Kiewiet, H. H., Zijlstra, J., Nucl. Instrum. Methods A **310**, 540 (1991)
218. Wittenburg, K., Experience with the Residual Gas Ionisation Beam Profile Monitors at the DESY Proton Accelerators, Proc. of the Third European Particle Accelerator Conference (EPAC92), Berlin, March 1992, p. 1133
219. Vignet, J.-L., P., Anne, R. M., Georget, Y. R., Hue, R. E., Tribouillard, C. H., Beam Monitors Based on Residual Gas Ionization, p. 223 in [15]
220. Connolly, R., Michnoff, R., Moore, T., Tepikian, S., Beam Profile Measurement on RHIC, p. 330 in [17]
221. Fischer, C., Koopmann, J., Measurements made in the SPS with a Rest Gas Profile Monitor by Collecting Electrons, p. 191 in [17]
222. Kamerdzhiev, V., Dietrich, J., Ionization Beam Profile Monitor at the Cooler Synchrotron COSY-Jülich, p. 140 in [25]
223. Venica, E., Utilisation d'un detecteur base sur le principe de l'ionisation d'un gaz pour la mesure du profil d'un faisceau d'ions dans la domaine des hautes energies, GSI-Darmstadt, Germany, Report (June 1993)
224. Schotmann, Th., Das Auflösungsvermögen der Restgas Ionisations Strahlprofil Monitore für Protonen in PETRA und HERA, Diplomarbeit, DESY-Hamburg, Germany, DESY HERA 93–09, (1993)
225. Lindhard, J., Scharff, M., Phys. Rev. **124**, 128 (1961)
226. Sandoval, D. P., et al., Fluorescence-Based Video Profile Beam Diagnostics, p. 273 in [13]
227. Burtin, G., et al., Proc. 6th Euro. Part. Acc. Conf. (EPAC), Vienna, 2000, p. 256

228. Bank, A., Forck, P., Residual Gas Fluorescence for Profile Measurements at the GSI UNILAC, p. 137 in [25]
229. Smith, K., Exp. Methods Phys. Sci. A **29**, 253 (1995)
230. Hamamatsu Photonic System Corporation, Bridgewater, NJ, Technical Infromation 1994, MCP Assembly
231. Ferioli, G., Fischer, C., Koopmann, J., Sillanoli, M., Sensitive Studies with the SPS Rest Gas Profile Monitor, p. 201 in [24]
232. Unverzagt, M., Entwicklung eines Strahlprofilmonitors für den ESR, Diplomarbeit, Institut für Kernphysik der Johann-Wolfgang-Goethe-Universität Frankfurt, (September 1992)
233. Kawabuko, T., et al., Nucl. Instrum. Methods A **302**, 397 (1991)
234. Heeg, P., Restgas – Profilmonitor für das SIS, Projektstudie, (1993), unpublished
235. Forck, P., Giacomini, T., Golubev, A., Liakin, D., Skachkov, V., Vetrov, A., Advanced Residual Gas Profile Monitor for High Current Synchrotrons and Cooler Rings, p. 134 in [25]
236. Giacomini, T., Barabin, S., Forck, P., Liakin, D., Skachkov, V., Development of Residual Gas Profile Monitors at GSI, p. 286 in [19]
237. Skachkov, V. S., et al. Drift Tubes for a Focusing Channel of Ion Linear Accelerator, Proc. PAC-89, IEEE **2**, (1989), p. 1073
238. Taken from "Operators Protocol Book," GSI-Darmstadt, Germany
239. Strehl, P., Composition - Ions Beams, p. 551 in [11]
240. Scheeler, U., GSI-Darmstadt, Germany, private communication
241. Glatz, J., Langenbeck, B., A High Duty Foil Stripper System in the Injection Line to the Heavy Ion Synchrotron SIS at GSI, Proc. 5th European Part. Acc. Conference, Sitges (Barcelona), EPAC 96, IoP 1996, p. 2406
242. Strehl, P., Charge State - Ion Beams, p. 555 in [11]
243. Dahl, L., Computer-Aided Tuning Procedures at the Unilac, 9th International Conf. Cyclotrons Their Appl., Caen University, France, 1981, p. 575
244. Recknagel, A., PHYSIK, Elektrizität und Magnetismus (VEB Verlag Technik Berlin, 1980)
245. Feynman, P., R., Leighton, R. B., Sabds, M., Feynmann Vorlesungen über Physik, Band II R. Oldenburg Verlag GmbH, München, 1991
246. Linnecar, T., P. R., IEEE Trans. Nucl. Sci. NS-**26** (3), 3409 (1979)
247. Fellenz, B., Crisp, J., An Improved Resistive Wall Monitor, p. 446 in [16]
248. Odier, P., A New Wide Band Wall Current Monitor, p. 216 in [25]
249. Strehl, P., Klabunde, J., Schaa, V., Vilhjalmsson, H., Wilms, D., Das Phasensondensystem am Unilac : Sondendimensionierung und Signalauswertung, GSI-Report 79–13, (1979), translated for the Los Alamos Scientific Laboratory by : Leo Kanner Associates, Redwood City, (1980), LA-TR-80–43
250. Durcansky, G., EMV-gerechtes Gerätedesign (Franzis Verlag, München, 1995)
251. Tinschert, K., Bossler, J., Schennach, S., Schulte, H., Status Report on ECR Ion Source Operation at the GSI Accelerator Facilities, Proc. 7th Int. Conf. on Ion Sources, Taormina, Italy, Sept 7–13 1997, ed. by Ciavola, G., Gammino, S., RSI **69** (2), Part II, (1998), p. 709
252. Schneider, S., Franklin, E., Derivation of an Expression for the Beam Pulse Signal from a Parallel-Plate Capacitive Phase Probe, National Acclerator Center, South Africa, NAC BD 83–01, (1983)
253. Stöcker, H., Taschenbuch mathematischer Formeln und moderner Verfahren (Verlag Harri Deutsch, Frankfurt/Main, 1993)

254. Spiegel, R. M., Complex Variables in: Schaums Outline Series (Schaum, New York, 1964)
255. Neue Technologien Gesellschaft mbH & Co KG, Gelnhausen, Germany
256. Gröhn, K., Raulien, W., Reinhard, A., Timm, J., Die gesetzlichen Einheiten in Technik und fachbezogener Naturwissenschaft (Verlag Handwerk und Technik GmbH Hamburg, 1975)
257. Feinberg, B., Meaney, D., Thatcher, R., Timossi, C., Nucl. Instrum. Methods Phys. Res. A **270**, 1 (1988)
258. Beam Intensity Upgrade of the GSI Accelerator Facility, GSI Report, GSI-95–05
259. Forck, P., Strehl, P., Measurements with a Versatile Test Bench for the Commissioning of the New GSI High Current Linac, Proc. p. 42 in [23]
260. Geissel, H., Laichter, Y., Albrecht, R., Kitahara, T., Klabunde, J., Strehl, P., Nucl. Instrum. Methods **206**, 609 (1983)
261. Boccard, C., Bogey, T., Papis, J.-P., Vos, L., Intensity and Bunch Length Measurement for Lepton Beams in the Injection Lines of the SPS and LEP, p. 42 in [21]
262. Bellato, M., Dainelli, A., Poggi, M., Bunch Length Measurements in the ALPI Linac at LNL, p. 145 in [21]
263. Ferianis, M., Pros, M., Carniel, A., De Monte, R., Bunch Length Measurements at ELLETRA, p. 201 in [22]
264. Hanke, K., Electron Bunch Length Monitors for the TESLA Test Facility Linac, p. 224 in [22]
265. Geitz, M., Bunch Length Measurements, p. 18 in [23]
266. Burns, A. J., Schmickler, H., Bunch Length Measurements in LEP, p. 56 in [23]
267. Forck, P., Heymach, F., Meyer, U., Moritz, P., Strehl, P., Aspects of Bunch Shape Measurements for Slow, Intense Ion Beams, p. 176 in [23]
268. Rawnsley, W. R., Laxdal, R. E., Root, L., Mackenzie, G. H., Bunch Shape Measurements Using Fast Faraday Cups and an Oscilloscope by LabVIEW Over Ethernet, p. 547 in [17]
269. Proc. Part. Acc. Conf., PAC 95, Dallas, 1995, p. 2512
270. Smith, S. R., Beam Position Monitor Engineering, p. 50 in [15]
271. Schneider, G., Messwerterfassung und -Übertragung zur Strahllagebestimmung beim 28-GeV-Protonen-Synchrotron, Dissertation, CERN, 1971
272. Kaufmann, W., Kraus, H., Strehl, P., Viljalmsson, H., Calibration of Capacitive Beam Position Monitors for SIS18 and ESR, GSI Report 88–1, (1988), p. 373
273. Vismara, G., The Comparison of Signal Processing Systems for Beam Position Monitors, p. 11 in [23] and Vismara, G., Signal Processing for Beam Position Monitors, p. 36 in [17]
274. Strehl, P., Vilhjalmsson, H., The SIS Beam Diagnostic System, Euro. Part. Acc. Conf. EPAC88, Rome, 1988, p. 1413
275. Moritz, P., Beckert, K., Synchronous Swept Narrowband Measurement of Beam Position, Tune, and Chromaticity of Heavy Ion Beam Accelerators, p. 131 in [20]
276. Teytelman, D., Claus, R., Fox, J., Hindi, H., Linscott, I., Prabhakar, S., Drago, A., Stover, G., Feedback Control and Beam Diagnostic Algorithms for a Multiprocessor DSP System, p. 390 in [15]
277. Fox, J. D., Kikuzani, E., Bunch Feedback System and Signal Processing, Proc. School Beam Measure. Montreux, World Scientific Singapore, 1999, p. 579

278. Fox, J., et al., Programmable DSP-Based Multi-Bunch Feedback - Operational Experience from Six Installations, p. 226 in [17]
279. Kamerdzhiev, V., Dietrich, J., Transverse Feedback System for the Cooler Synchrotron COSY-Jülich – First Results, p. 214 in [25]
280. Moritz, P., Peters, A., Beam Position Measurements at the SIS, GSI Report 91–1, (March 1991), p. 391
281. Mohos, I., Dietrich, J., 500 MHz Narrowband Beam Position Electronics for Electron Synchrotrons, p. 299 in [16]
282. Fröhlich, G., Software zur Berechnung des Q-Faktors im SIS, Internal Notiz, (1983), GSI-Darmstadt, Germany
283. Hereward, H. G., Landau Damping, in: *CAS* Oxford 1985, CERN87–03, (April 87), p. 255
284. A. W. Chao, Zotter, B., Landau Damping, p. 124, in [11]
285. Boussard, D., Schottky Noise and Beam Transfer Function Diagnostics, p. 749 in *CAS* Proceedings, CERN 95–06
286. Moritz, P., Improved Narrowband Signal Conditioner for SIS and ESR, GSI Report 94–1, (March 1995), p. 237
287. Rice, D., IEEE Trans. Nucl. Sci., Vol. NS-**20** (4), (Aug. 1983)
288. Berrig, O., Fischer, C., Schmickler, H., Measuring Beta-Functions with K-Modulation, p. 85 in [24]
289. Bell, J. S., Hamiltonian Mechanics (*CAS* Oxford, England, CERN 87–03, 5 (1987))
290. Van Steenbergen, A., IEEE Trans. Nucl. Sci. NS-**14**, 746 (1965)
291. Van Steenbergen, A., Nucl. Instrum. Methods **51**, 245 (1967)
292. Lejeune, C., Aubert, J., Adv. Electron. Electron Phys. Supplement **13A**, 159 (1980)
293. Tolman, R. C., The Principles of Statistical Mechanics University Press, Oxford, Great Britain, 1938), Chap. II, III
294. Wilson, E., Transverse Beam Dynamics, CAS-CERN Accelerator School, Gif-sur-Yvette, Paris, France, (1984), CERN 85–19, (1985), p. 64
295. Bovet, C., Fischer, C., Jung, R., Comparison of Different Methods for Transverse Emittance Measurements and Recent Results from LEP, p. 36 in [22]
296. Joho, W., Representation of Beam Ellipses for Transport Calculations, SIN-report, TM-11–14, (1980), p. 1
297. Courant, E.D., Snyder, H. S., Ann. Phys., **3**, 1 (1958)
298. Brown, K. L., Carey, D. C., Iselin, Ch., Rothacker, F., TRANSPORT A Computer Program for Designing Charged Particle Beam Transport Systems, CERN 80–04, (March 1980)
299. PET, Physik Elektronik Technik, Engineering Office, Strehl, P., Kraus, H., Smetanaweg 6, D-64291 Darmstadt, Germany, Emittanz-Messsystem für die Universität Frankfurt, Inst. Angewandte Physik, Germany, interne Spezifikation
300. Strehl, D., Ing. Büro für Softwareentwicklung, D-64331 Weiterstadt, e-mail: dirk@team-strehl.de, Software für ein Emittanz-Messsystem der Universität Frankfurt, Inst. Angewandte Physik, Germany, interne Spezifikation
301. Garnett, R. W., Status of the Los Alamos Accelerator Code Group (LAACG), Los Alamos National Laboratory, NM 87545, http://laacgl.lanl.gov/laacg/componl.html
302. Stovall, J. et al., Beam Simulation Codes Comparisons, ASAC Review, Los Alamos, SNS-104050000-PS006-R00

303. Willeke, F., Modern Tools for Particle Tracking, in: *CAS* CERN 95–06, (1995), p. 213
304. Holzschuh, G., Klabunde, J., Struckmeier, J., Trautmann, H., Parmila - GSI - A Computer Program for Beam Dynamics in Acclerators with Space Charge, GSI-Scientific Report, (1980), p. 267
305. Struckmeier, J., Charge Calculations in Monte Carlo Computer Codes, GSI-Scientific Report, (1981), p. 310
306. Struckmeier, J., GSI-Darmstadt,Germany, private communication, (2004)
307. Sacherer, F. J., Sherwood, T. R., The Effects of Space Charge in Beam Transport Lines, CERN/MSP-SI/Int. LIN/71–2
308. Sacherer, F. J., Some Useful Formulae Concerning rms Values of Various Density Distributions, CERN/MPS/LIN/74–1, Appendix I
309. Struckmeier, J., Klabunde, J., Reiser, M., Particle Accelerators **15**, 47 (1984)
310. Strehl, P., Beam Diagnostic Devices for a Wide Range of Currents, 9th International Conference on Cyclotrons and Their Applications, Caen University, France, (1981), p. 575
311. Strehl, P., Englert, G., Hartung, M., Horneff, H., A New Emittance Measuring Device of the UNILAC, IEEE Proc. PAC-81, NS-**28**, 10
312. Wenzler, F., Konstruktion und Aufbau eines Strahldiagnosesystems zur gleichzeitigen Messung der horizontalen und vertikalen Emittanz, Diplomarbeit, FH-Wiesbaden, GSI-Darmstadt, Germany, (1988)
313. Domke, M., Dorn, Chr., Forck, P., Kraus, H., Peters, A., Strehl, P., A Single Shot Emittance Measuring System for Intense Heavy Ion Beams, p. 141 in [22]
314. PCO AG, Kelheim, Germany, e-mail: info@pco.de
315. Dolinska, M., Domke, M., Forck, P., Hoffmann, T., Liakin, D., Peters, A., Strehl, P., Emittance Measurements at the New UNILAC Pre-Stripper Using a Pepper-Pot with a PC-Controlled CCD-Camera, p. 161 in [23]
316. Hoffmann, T., Barth, W., Forck, P., Peters, A., Strehl, P., Emittance Measurements of High Current Heavy Ion Beams Using a Single Shot Pepperpot System, p. 432 in [17]
317. Hutter, R., Beams with Space-charge, in : Focusing of Charged Particles, ed. by A. Septier (Academic Press, New York, 1967) Vol. II, p. 3
318. Larson, J. D., Nucl. Instrum. Methods **189**, 71 (1981)
319. Barth, W., GSI-Darmstadt,Germany, private communication
320. Hoffmann, T., Liakin, D. A., Control and Data Analysis for Emittance Measuring Devices, p. 126 in [24]
321. Crescenti, M., Raich, U., A Single Pulse Beam Emittance Measurement for the CERN Heavy Ion Linac, p. 66 in [21]
322. Cianchi, A., et al., Design Study of a Movable Emittance Meter Device for the SPARC Photoinjector, Proceedings of the EPAC 2004, Lucerne, Switzerland, (Web Version) (CD-ROM), p. 2622
323. Riehl, G., Untersuchung der mehrdimensionalen transversalen Phasenraumverteilungen von intensiven Ionenstrahlen, Dissertation, Institut für Angewandte Physik, J. W. Goethe Universität Frankfurt (1992)
324. Mukoyama, T., Nucl. Instrum. Methods **125**, 289 (1975)
325. Schönauer, H., IEEE Trans. Nucl. Sci., Vol. NS-2**6**, p. 3294 (1979), and Proc. Work. Adv. Beam Instrum., Tsukuba, April 22–24, 1991, Vol. 2, p. 453
326. Steffen, K. G., High Energy Beam Optics (Interscience, John Wiley & Sons New York London Sydney, 1965)

327. Banford, A. P., Transport of Charged Particles (Spon London, 1966)
328. Septier, A., Focusing of Charged Particles, (Academic Press, New York, 1967) Vol. II
329. Hinterberger, F., Physik der Teilchenbeschleuniger und Ionenoptik (Springer Verlag, Berlin Heidelberg New York, 1997)
330. Enge, H. A., Deflecting Magnets, in: Focusing of Charged Particles, ed. by A. Septier (Academic Press, New York, 1967) Vol. II, p. 203
331. Sheppard, J. G., Clendenin, J. E., Helm, R. H., Lee, M. J., Miller, R. H., Blocker, C. A., IEEE Trans. Nucl. Sci., NS-**30**, 2161 (1981)
332. Ploss, H., Blumberg, L. N., Methods of Emittance Measurement in External Beam Lines Using Ellipse Approximations, BNL Acc. Dept. Int. Report AGS DIV 68–4, (1968)
333. Bovet, C., Guignard, C., Mesure de l'emittance d'un faisceau primaire, CERN SI/Note DL/68–7, (1968)
334. Metzger, C., Mesures des emittances et du centrage des faisceau dans la ligne de mesure "800 MeV" du PSB, CERN/SI/Int. DL69–10
335. Witkover, R. L., Automatic Electronic Emittance Device for the BNL 200 MeV Linac, Proc. of the 1970 Proton Linear Acclerator Conference, Batavia, IL 1970 Vol. 1, p. 125
336. Goodwin, R. W., Gray, E. R., Lee, G. M., Shea, M. F., Beam Diagnostics for the NAL 200-MeV Line, Proc. of the 1970 Proton Linear Accelerator Conference, 1970, p. 107
337. Koziol, H., Reich, K. H., IEEE Trans. Nucl. Sci. NS-**18**, 347 (1971)
338. Fewell, N., Witkover, R. L., Beam Diagnostic at the BNL 200-MeV Linac, Proc. Proton Lin. Acc. Conf., 1972, p. 54
339. Baribaud, G., Metzger, C., IEEE Trans. Nucl. Sci. NS-**20** (3), 659 (June 1973)
340. Franczak, B., Emittanzmessung mit Quadrupolen - Auswertung, Internal Note, GSI-Darmstadt, AN-F-060673-3, (1973)
341. Schaa, V., Emittance Measurements with Profile Grids, Dissertation, TH-Darmstadt, GSI-Darmstadt (1978)
342. Ebihara, K., et al. Nucl. Instrum. Methods **202**, 403 (1982)
343. Qian, Y. L., Riedel, C., Schaa, V., Strehl, P., Determination of Beam Emittance by Profile Measurements, Internal report, GSI-Darmstadt, (1990) and GSI-Report 89–1, (March 1989), p. 391
344. Franczak, B., Einstellung von Steerern, Internal Note, GSI-Darmstadt, AN-229776, (1976)
345. Franczak, B. J., Mirco Expert, Mirkodok.ps and MExDok0904 (HTML-Version), available on the server of GSI-Darmstadt, Germany
346. Dahl, L., et al., Longitudinal and Transverse Beam Optimization at the Unilac, Proc. Lin. Acc. Conf., Montauk, N. Y., BNL 51134, (1979), p. 291
347. Kneis, W., Rechnergesteuerte Strahldiagnostik und Strahloptimierung am Karlsruher Isochronzyklotron (Kernforschungszentrum Karlsruhe, KFK, 1979) 2835
348. Bock, F., Strehl, P., Process Control of the Heavy Ion Accelerator Unilac by T85 Computers, Teleflyer, Vol. 9, (August 86), Special Issue from Telefile, Computer Products, Inc., Irvine, CA
349. See Contributions: Proc. Int. Conf. Acc. Large Exp. Phys. Contr. Systems, ICALEPS, via [26]
350. Macke, W., Mechanik der Teilchen und Continua (Akademische Verlagsgesellschaft Geest & Portig K.-G., Leipzig, 1962)

351. Joos, G., (bearbeitet von Fricke, B., Schäfer, K.), Lehrbuch der Theoretischen Physik (AULA-Verlag GmbH Wiesbaden, 1989)
352. Reiser, M., Theory and Design of Charged Particle Beams (John Wiley & Sons New York, 1994)
353. Cottingame, W. B., Cortez, J. H., Higgins, W. W., Sander, O. R., Sandoval, D. P., Longitudinal Emittance Measurements on the ATS, Proc. 1986 Linear Acc. Conf., Stanford Linear Accelerator Center
354. Finocchiaro, P., Amato, A., Ciavola, G., Gu, M., Raia, G., Rovelli, A., Low Intensity Ion Beam Diagnostic with Particle Detectors, Proc. Diag. Instrum. Part. Acc., DIPAC 1997, p. 53
355. Ratzinger, U., Proc. XVIII Int. Lin. Acc. Conf., Geneva, Switzerland, (1996), p. 288 and W. Barth et al., Proc. XIX Int. Lin. Acc. Conf., Geneva, Switzerland, 1998
356. Forck, P., Heymach, F., Hoffmann, T., Peters, A. Strehl, P., Proc. XX Int. Linac Conf., Aug. 21–25, 2000, Monterey, CA, p. 166
357. Barth, W., Forck, P., The New Gas Stripper and Charge State Separator of the GSI high Current Injector, Proc. XX Int. Linac Conf., Monterey, CA, Aug. 21–25, 2000
358. Evans, R. D., The Atomic Nucleus (McGraw-Hill, New York, 1955)
359. Ziegler, J. F., Biersack, J. P., SRIM-2003.20 – The Stopping and the Range of Ions in Matter, (1998), 1999 by IB77M Co.
360. Ahlen, S. P., Rev. Mod. Phys. **52**, 121 (1980)
361. Bylinsky, V., Feschenko, A. V., Ostroumov, P. N., IEEE Proc. Part. Acc. Conf., San Franzisko, (1991), p. 3062 and Proc. 4th European Part. Acc. Conf. (EPAC94), London, 1994, p. 1702
362. Feschenko, A. V., Proc. Part. Acc. Conf., PAC2001, Chicago, p. 517
363. Esin, S. K., et al., Proc. XVIII Int. Linear Acc. Conf., Geneva, Switzerland, 1996, p. 193
364. Ostroumov, P. N., et al., Proc. XIX Int. Lin. Acc. Conf., Geneva, Switzerland, 1998, p. 905
365. Fachlexikon ABC Physik (Verlag Harri Deutsch, Zürich, 1974) p. 1314
366. Feschenko, A. V., Space Charge Effects in Bunch Shape Monitors, Proc. XX Int. Lin. Acc. Conf., Monterey, CA, 2000, p. 178
367. Mehler, S., Auslegung eines Systems zur Messung der zeitlichen Struktur eines gepulsten Schwerionenstrahls, Diplomarbeit, FH Wiesbaden, GSI-Darmstadt, Germany, 1998
368. Forck, P., Dorn, Ch., Herty, M., Strehl, P., Peplov, V., Sharamentov, S., A Novel Device for Non-Intersepting Bunch Shape Measurements at the High Current GSI-LINAC, Proceedings of the EPAC 2004, Lucerne, Switzerland (Web Version) (CD-ROM), p. 2541
369. Zieher, K. W., Inst. Exp. Kernphysik, Interne Notiz Nr. 132, (1971)
370. Stolterfoht, N., Phys. Rev. Lett. **33** (2), 59 (1974)
371. Bechthold, U., Phys. Rev. Lett. **79** (2), 2034 (1997)
372. Ramm, U., Systematische Untersuchung der $\delta-$ Elektronenemission in Stößen schneller, schwerer Ionen mit Atomen und einfachen Molekülen: Eine Grundlage zur Dosisberechnung von Schwerionenspuren in Materie, Dissertation, Johann Wolfgang Goethe - Universiät Frankfurt/Main, 1994
373. Dorn, Ch., GSI-Darmstadt, Germany, private communication
374. Vinogradov, N. Y., et al., Proc. XXI Linear Acc. Conf., Gyeongju, 2002, p. 61

375. Herzog, R., Archiv für Elektrotechnik **29**, 790 (1935)
376. Strehl, P., A New Method for Longitudinal Emittance Measurement, Proc. of the 1983 Particle Accelerator Conference, IEEE Trans. Nucl. Sci., NS-**30**, 2198 (August 1983)
377. Borer, J., Bramham, P., Hereward, H. G., Hübner, K., Schnell, W., Thorndahl, L., Non-Destructive Diagnostics of Coasting Beams with Schottky Noise, Proc. IX. Int. Conf. on High Energy Accelerators, Stanford, 1974
378. Borer, J., et al., IEEE Trans. Nucl. Sci. NS-**26**, 3405 (1979)
379. Nolden, F., Instrumentation and Diagnostics Using Schottky Signals, Proc. Diag. Instrum. Part. Acc., DIPAC 2001, p. 6
380. Schottky, W., Annalen der Physik **57**, (1918)
381. Schaaf, U., Schottky-Diagnose und BTF-Messungen an gekühlten Strahlen im Schwerionenspeicherring ESR, GSI-91–22 Report, Juli 1991
382. Oguri, Y., Müller, R. W., Schottky Noise Analysis in Linear Accelerators, GSI-Report, GSI-88–07 (März 1988)
383. Van der Meer, S., Diagnostics with Schottky Noise, presented at the US-CERN School on Beam Observation, Capri, Italy, 1988 (CERN-PS-88-60-AR, Geneva, CERN, Oct. 1988)
384. Kapchinskij, I.M. and Vladimirskij, V.V., Proc. Conf. High Energy Acc., CERN, Geneva, 1959, p. 274
385. Flügge, S., Zeitschrift für Physik, **130**, 159 (1951)
386. Wendt, G., Statische Felder und stationäre Ströme, Handbuch der Physik, Bd. XVI, p. 1
387. Nezlin, M. V., Plasma Phys. **10**, 337 (1968)
388. Evans, L. R., Warner, D. J., Space-charge Neutralisation of Intense Charged Particle Beams: Some Theoretical Considerations, CERN/MPS/DIN. 71–2, (August 1971)
389. Holmes, A. J. T., Phys. Rev. A **19** (1), 389 (1979)
390. Hofmann, I., Nucl. Instrum. Methods **187**, 281 (1981)
391. Ramirez, J. J., Nucl. Instrum. Methods **187**, 289 (1981)
392. Holmes, A. J. T., Neutralization of ion beams, *CAS*-CERN accelerator school, Aarhus, Denmark, (Sept. 1986), CERN 87-10, 1987, p. 79
393. Schönlein, A., Emittanzwachstum und Raumladungskompensation beim Transport intensiver Ionenstrahlen, GSI-Report, GSI-87–4, (Januar 1987)
394. Dölling, R., Raumladungskompensation driftender intensiver Strahlen niederenergetischer Ionen und Techniken zu ihrer Vermessung, Dissertation, Johann Wolfgang Goethe-Universität Frankfurt/Main, (1994), DF1
395. Strehl, P., Dolinska, M., The electrical fields of Bunches, GSI-Internal Report
396. Dolinska, M., Modeling of Inner Beam Processes and Their Account at Carrying out of Beam Diagnsotics on Acclerators of the Charged Particles, Dissertation, Institut for Nuclear Research, 252028 Kiev, Ukraine, 2003
397. M. Krämer, G. Kraft, Radiat. Environ. Biophys. **33**, 91 (1994)
398. Selbstkonsistente und nicht-selbstkonsistente Phasenraumverteilungen intensiver Ionenstrahlen, GSI-Report, GSI-85–14, (Mai 1985)
399. Rossa, E., Real Time Single Shot Three-dimensional Measurement of Picosecond Photon Bunches, *AIP* Conf. Proc. **333**, 1995, p. 148
400. Chevtsov, P., Day, A., Freyberger, A. P., Hicks, R., Denard, J-C., Proceedings of the EPAC 2004, Lucerne, Switzerland, 231–2 (Web Version), (CD-ROM), p. 2846

401. Kantz, A., Hofstadter, R., Nucleonics **12** (3), 36 (1954)
402. Simpson, J., Wakefield Accelerators, p. 49, in [11]
403. Ginzburg, V. L., Frank, I. M., JETP **16**, 15 (1946)
404. Wartski, L., Roland, S., Lasalle, J., Bolore, M., Fillipi, G., J. Appl. Phys. **46**, 3644 (1975)
405. Ter-Mikaelian, M. L., High Energy Electromagnetic Processes in Condensed Media (Wiley-Interscience New York, 1972)
406. Ginzburg, V. L., Phys. Rep. **49**, 1 (1979)
407. Loos, H., Bestimmung der longitudinalen Struktur der Elektronenbunche im Strahl von supraleitenden Beschleunigern, Dissertation D17, TU-Darmstadt, Germany, (2001)
408. Döbert, S., et al., Transverse and Longitudinal Beam Diagnostics Using Transition Radiation, in: V. Palmieri, A. Lombardi, Proc. 8th RF Superconducting Workshop, Abano Terme, Italy, 1997 (1998), p. 184
409. Carr, R., Wiedemann, H., Other Radiation Sources, p. 192, in [11]
410. Muto, T., et al., Development of the Non-invasive Beam Size Monitor Using ODR, Proceedings of the EPAC 2004, Lucerne, Switzerland (Web Version), (CD-ROM), p. 256
411. Karataev, p., et al., Development of Optical Diffraction Radiation Beam Size Diagnostics at KEK Accelerator Test Facility, Proceedings of the EPAC 2004, Lucerne, Switzerland (Web Version), (CD-ROM), p. 2646
412. Müller, R. W., GSI-Darmstadt, Germany, private communication
413. Sullivan, A. H., A Guide to Radiation and Radioactivity Level near High Energy Particle Accelerators (Nuclear Technology, Ashford, 1992)
414. Thomas, R. H., Radiation Effects and Protection, p. 599 in [11]
415. Wittenburg, K., Beam Loss Detection, p. 11 in [20]
416. Shafer, R. E., A Tutorial in Beam Loss Monitoring, p. 44 in [18]
417. Hoffmann, T., Liakin, D. A., Forck, P., Moritz, P., Experiences on Counter Applications and Beam Loss Measurements at the GSI Synchrotron, p. 294 in [19]
418. Guaglio, G., Dehning, B., Santoni, C., Reliability of Beam Loss Monitors System for the Large Hadron Collider, p. 141 in [19]
419. Holzer, E. B., et al., Design of the Beam Loss Monitoring System for the LHC Ring, Proc. EPAC 2004, Lucerne, Switzerland (Web Version), (CD-ROM), p. 2487
420. Panofski, W. K. H., SLAC Internal Report TN-63–57, (1963)
421. Henschel, H., Körfer, M., Wulf, F., Fibre Optical Sensing System for TESLA, p. 73 in [24]
422. Stoll, P., Experimentelle Methoden der Kernphysik (Springer Verlag, Berlin Heidelberg, 1966)
423. Forck, P., Hoffmann, T., Test of Different Beam Loss Detectors at the GSI Heavy Ion Synchrotron, p. 129 in [24]
424. Forck, P., GSI-Darmstadt, Germany, private communication
425. Thomson, J.J., Recent Researches in Electricity and Magnetism (Clarendon Press, Oxford, 1893)
426. Compton, A.H., Phys. Rev. **21**, 483 (1923a); **22**, 409 (1923b)
427. Hering, E., Martin, R., Stohrer, M., Physik für Ingenieure (VDI-Verlag GmbH, Düsseldorf, 1989).
428. Laserwire Bibliography, www.pnp.physics.ox.ac.uk/˜delerue/laserwire/bibliography.php

429. Phys. Rev. Spec. Topics - Accelerators and Beams, Vol. 5, (2002)
430. Salamin, Y. I., Mocken, G. R., Keitel, Ch. H., Electron Scattering and Acceleration by a Tightly Focused Laser Beam, p. 101303 in [429]
431. Sakai, H., et al., Measurement of a Small Vertical Emittance with a Laser Wire Beam Profile Monitor, p. 122801 in [429]
432. Balewski, K. et al., Beam Profile Measurements at PETRA with the Laserwire Compton Scattering Monitor, Proceedings of the EPAC 2004, Lucerne, Switzerland (Web Version), (CD-ROM), p. 2529
433. Beche, J.-F., Byrd, J., De Santis, F., Denes, P., Placidi, M., Turner, W., Zolotorev, M., Measurement of the Beam Longitudinal Profile in a Storage Ring by Non-linear Laser Mixing, p. 112 in [19]
434. Beche, J.-F., Byrd, J., Datte, P., De Santis, F., Placidi, Riot, V., Schoenlein, R., M., Turner, W., Zolotorev, M., A Laser Based Longitudinal Density Monitor for the Large Hadron Collider, Proceedings of the EPAC 2004, Lucerne, Switzerland (Web Version), (CD-ROM), p. 2789
435. Blokland, W., et al., SNS Laser Profile Monitor Progress, Proceedings of the EPAC 2004, Lucerne, Switzerland (Web Version), (CD-ROM), p. 2852
436. LBBD Laserwire, www.hep.ph.rhul.ac.uk./˜kamps/lbbd/
437. Nakamura, N. Developments of the FZP Beam Profile Monitor, Proceedings of the EPAC 2004, Lucerne, Switzerland (Web Version), (CD-ROM), p. 2353
438. Fisher, A. S., et al., Design of an X-Ray Imaging System for The Low-Energy Ring of PEP-II, Proc. EPAC 2004, Lucerne, Switzerland (Web Version), (CD-ROM), p. 2819
439. Bosser, J., Gnanvo, K., Spanggaard, J., Tranquille, G., New Beam Profile Monitor Based on GEM Detector for the AD Transfer and Experimental Lines, Proc. EPAC 2004, Lucerne, Switzerland (Web Version), (CD-ROM), p. 2472
440. Berden, B., Redlich, G., van der Meer, A. F. G., Jamison, S. P., MacLeod, A. M., Gillespie, W. A., High Temporal Resolution, Single-Shot Electron Bunch-Length Measurements, Proceedings of the EPAC 2004, Lucerne, Switzerland (Web Version), (CD-ROM), p. 2700
441. Liakin, D., Analysis of the Electron Beam Scanning Method for Beam Profile Monitoring, Proceedings of the EPAC 2004, Lucerne, Switzerland (Web Version), (CD-ROM), p. 2721
442. Tiefenback, M., Beam Diagnostics Based on AC Modulation of System Parameters, p. 88 in [19]

Index